CRITICAL HEIGHT AND SURFACE DEFORMATION OF COLUMN-SUPPORTED EMBANKMENTS

Michael P. McGuire

Dissertation submitted to the faculty of the Virginia Polytechnic Institute and State University in partial fulfillment of the requirements for the degree of

Doctor of Philosophy
In
Civil Engineering

George M Filz (Chair)
Thomas L. Brandon
Russell A. Green
James R. Martin
Raymond H. Plaut

November 1, 2011
Blacksburg, VA

Keywords:
Critical height
Column-supported embankment
Geosynthetic reinforcement
Settlement

CRITICAL HEIGHT AND SURFACE DEFORMATION OF COLUMN-SUPPORTED EMBANKMENTS

Michael P. McGuire

ABSTRACT

Column-supported embankments with or without basal geosynthetic reinforcement can be used in soft ground conditions to reduce settlement by transferring the embankment load to the columns through stress redistribution above and below the foundation subgrade level. Column-supported embankments are typically used to accelerate construction and/or protect adjacent facilities from additional settlement. The column elements consist of driven piles or formed-in-place columns that are installed in an array to support a bridging layer or load transfer platform. The bridging layer is constructed to enhance load transfer using several feet of compacted sand or sand and gravel that may include one or more layers of high-strength geotextile or geogrid reinforcement.

Mobilization of the mechanisms of load transfer in a column-supported embankment requires some amount of differential settlement between the columns and the embankment as well as between the columns and the foundation soil. When the embankment height is low relative to the clear spacing between columns, there is the risk of poor ride quality due to the reflection of the differential foundation settlement at the surface of the embankment. The minimum embankment height where differential surface settlement does not occur for a particular width and spacing of column is the critical height. The conventional approach is to express critical height as a fixed ratio of the clear span between adjacent columns; however, there is no consensus on what ratio to use and whether a single ratio is applicable to all realistic column arrangements.

The primary objective of this research is to improve the understanding of how column-supported embankments deform in response to differential foundation settlement. A bench-scale experimental apparatus was constructed and the equipment, materials, instrumentation, and test procedures are described. The apparatus was able to precisely measure the deformation occurring at the sample surface in response to differential settlement at the base of the sample. Critical heights were determined for five combinations of column diameter and spacing representing a wide range of possible column arrangements. In addition, tests were performed using four different column diameters in a single column configuration with ability to measure the load

acting on the column and apply a surcharge pressure to the sample. In total, 183 bench-scale tests were performed over a range of sample heights, sample densities, and reinforcement stiffnesses. Three-dimensional numerical analyses were conducted to model the experiments. The critical heights calculated using the numerical model agreed with the experimental results.

The results of the laboratory tests and numerical analyses indicate that critical height depends on the width and spacing of the columns and is not significantly influenced by the density of the embankment fill or the presence of reinforcement. A new method to estimate critical height was developed and validated against extensive case histories as well as experimental studies and numerical analyses performed by others.

ACKNOWLEDGEMENTS

I would like to thank my advisor Dr. George Filz for being a role model in my life over the past seven years. He has been a caring mentor in my endeavors as a researcher, teacher, and engineer.

I would also like to thank the other members of my committee, Dr. Thomas Brandon, Dr. Russell Green, Dr. James Martin, and Dr. Raymond Plaut for their guidance during this research.

I am thankful for the help and support provided by Brett Farmer, Dennis Huffman, Clark Brown, and Bonnie Franklin during the laboratory work. Every component of the lab apparatus had to pieced together from an assortment suppliers or fabricated from scratch. While I am far from being a machinist, carpenter, or electronics specialist, I have learned a great deal from these talented people.

I would like to thank Alfredo Arenas for sharing his expertise in numerical modeling. The learning curve with FLAC can be very steep and Alfredo helped to flatten the grade.

I am also thankful for my experience at the Sligo Institute of Technology in Ireland. I appreciate Dr. Patrick Naughton's willingness to host me and expose me to research in the Emerald Isle.

This research would not be possible without the financial support of the National Science Foundation. My doctoral studies would not be possible without the Charles E. Via Fellowship, the GAANN Fellowship, and the Geosynthetics Institute Fellowship.

I am grateful for the value my parents placed on my education. I am also deeply grateful to have my wife, Tish, in my life. This experience has truly been a team effort.

TABLE OF CONTENTS

LIST OF FIGURES

Appendix A

Appendix B

Appendix C

Appendix D

Appendix E

Appendix G

Appendix H

Appendix I

Appendix K

Appendix L

LIST OF TABLES

Appendix F

Appendix G

Appendix H

Appendix I

LIST OF SYMBOLS

a	Square column or pile cap width (L)
A_s	Area replacement ratio (unitless)
c_c	Coefficient of curvature (unitless)
C	Clay compressibility (unitless)
C_{col}	Vertical elastic compression of the column (L)
COV	Coefficient of variation (unitless)
CSR	Column stress ratio (unitless)
c_u	Coefficient of uniformity (unitless)
d_{10}	10^{th} percentile grain size (L)
d_{30}	30^{th} percentile grain size (L)
d_{50}	50^{th} percentile grain size (L)
d_{60}	60^{th} percentile grain size (L)
d	Round column or pile cap diameter (L)
d’	Influence diameter (L)
D_o	Position of vertical slide of profiler when sample tank is empty (L)
D	Position of vertical slide of profiler when sample tank is not empty (L)
D_r	Relative density (unitless)
DSBR	Generic form of the ratio of differential surface settlement to base settlement (unitless)
$DSBR_d$	Ratio of differential surface settlement between the column, S_c, and S_d, a distance s’ away from any pile cap, to base settlement (unitless)
$DSBR_i$	Ratio of differential surface settlement between column, S_c, and S_i, mid-span along column line, to base settlement (unitless)
E	Young’s Modulus (F/L^2)
e_{max}	Maximum void ratio (unitless)
e_{min}	Minimum void ratio (unitless)
F	Vertical distance between hopper and upper diffuser screen in pluviator (L)
F_y	Rowe and Davis (1982) baseline breakout factor for plane strain conditions (unitless)
G_s	Specific gravity (unitless)
H	Height of embankment or sample (L) or vertical distance between lower diffuser screen and sample surface in pluviator (L)
H^*	Critical anchor embedment depth (L)
H_i	Interaction height of embankment (L)
H_{crit}	Critical height of embankment (minimum height with zero differential surface settlement) (L)
$H_{crit,traffic}$	Critical height of embankment subjected to traffic loading (L)
H_{min}	Minimum recommended embankment height (L)
H(x)	Sample height at profile position x (L)
$H(x)_n$	Sample height at profile position x at the n^{th} increment of base settlement (L)
J	Stiffness of geosynthetic reinforcement (F/L)
k	Fitting parameter used by Bolton (1986) correlation (unitless), also the ratio of the vertical embankment stress to the average initial vertical stress in the compressible clay foundation (unitless)

K_p	Rankine passive earth pressure coefficient (unitless)
$L(x)_o$	Distance between profiling laser and base of sample tank at profiling position x (L)
$L(x)$	Distance between profiling laser and sample surface at profiling position x (L)
N^*	Parameter for estimating peak vertical stress on the column or anchor (unitless)
P	Net vertical stress acting on reinforcement (F/L^2)
Q	Fitting parameter used by Bolton (1986) correlation (unitless)
q	Embankment surcharge pressure (F/L^2)
R	Fitting parameter used by Bolton (1986) correlation (unitless)
R_ψ,	Rowe and Davis (1982) correction factor for dilatency
R_R	Rowe and Davis (1982) correction factor for anchor roughness
R_K	Rowe and Davis (1982) correction factor for initial stress state
s	Column center-to-center spacing (L)
s_1,s_2	Column center-to-center spacing along lines of columns with different in-line center-to-center spacings (L)
s’	The maximum distance a location within the unit cell can be from the edge of any round column
s^*	Shape factor in Meyerhof and Adams (1968) correlation (unitless)
S	Vertical distance between upper and lower diffuser screens in pluviator (L)
S_b	Uniform differential settlement between columns and base of sample tank (L)
$S_{b,avg}$	Average base settlement (L)
$S_{b,i}$	Base settlement mid-span along a line of columns (L)
$S_{b,d}$	Maximum base settlement, which occurs a distance s’ from any round pile cap (L)
$S_{b,max}$	Base settlement corresponding to maximum column stress (L)
$S_{b,res}$	Base settlement corresponding to residual column stress (L)
S_c	Surface settlement over the center of the column(s) (L)
S_i	Surface settlement mid-span along a line of columns (L)
S_{i1}, S_{i2}	Surface settlement mid-span along lines of columns with different in-line center-to-center spacings (L)
S_d	Surface settlement a projected distance s’ from any pile cap (L)
$S_{tot,post}$	Post-construction uniform surface settlement (L)
$S_{b,avg,post}$	Post-construction average base settlement (L)
$S(x)_n$	Settlement of sample surface at profile position x at the n^{th} increment of base settlement (L)
SBR	Generic form of the ratio of surface settlement to base settlement (unitless)
SBR_c	Ratio of surface settlement above column to base settlement (unitless)
SBR_d	Ratio of surface settlement a distance s’ from any pile cap to base settlement (unitless)
SBR_i	Ratio of surface settlement at mid-span along column line to base settlement (unitless)
SBR_{tot}	Ratio of total surface settlement to maximum base settlement above the critical height (unitless)
SRF	Generic form of the ratio of settlement for an embankment supported on columns to settlement without columns (unitless)
SRF_{base}	The ratio of the settlement of the base of an embankment supported on columns to the settlement without columns (unitless)

SRF_{surf}	The ratio of the settlement of the surface of an embankment supported on columns to the settlement without columns (unitless)
SRR	Stress reduction ratio (unitless)
SRR_{emb}	Stress reduction ratio above reinforcement (unitless)
SRR_{fndn}	Stress reduction ratio below reinforcement (unitless)
SRR_{net}	Increment of stress reduction ratio due to reinforcement (unitless)
t	Thickness of stiff near-surface soils (L)
V_f	Volume of soil influenced by the column (L^3)
$V_{rectangle}$	Rectangular volume used to calculate volume of unit cell (L^3)
V_{sample}	Volume of sand in sample tank (L^3)
$V_{soil\ ring}$	Annular volume used to calculate volume of sand in sample tank (L^3)
V_u	Volume of unit cell (L^3)
$\Delta V_{u,20}$	Volume change in unit cell at S_b/d equal to 0.2 (L^3)
x	Quantized location along a scanning profile (L)
x_{center}	Location along scanning profile corresponding to the center of the sample tank (L)
x'	Quantized location along 45 degree profile corresponding to location x along 0 degree profile (L)
x_{center}	Quantized profile position at center of tank (L)
α	Orientation of linear shear surface from vertical (deg)
β	Angle defining the trend between DSBR and H/d below H_{crit} (deg)
δ_{max}	Displacement at peak anchor capacity (L)
ε	Average strain in reinforcement between columns (unitless)
ϕ_{crit}	Friction angle at critical state (deg)
ϕ_{peak}	Peak friction angle (deg)
ϕ_{trial}	Trial friction angle used in adapted version of Bolton (1986) correlation (deg)
γ	Unit weight (F/L^3)
κ	Coefficient to account for the influence of traffic loading on critical height (unitless)
ψ_{peak}	Peak dilation angle (deg)
σ'_3	Confining stress (F/L^2)
$\sigma_{col,max}$	Peak vertical stress acting on column top (F/L^2)
$\sigma_{col,res}$	Residual, or approximately stable post-peak, column stress (F/L^2)
$\sigma_{col,geobot}$	Average stress acting over column below reinforcement (F/L^2)
$\sigma_{col,geotop}$	Average stress acting over column above reinforcement (F/L^2)
$\sigma_{soil,geobot}$	Average stress acting over soil below reinforcement (F/L^2)
$\sigma_{soil,geotop}$	Average stress acting over soil above reinforcement (F/L^2)
σ_o	Initial vertical overburden stress (F/L^2)

Fundamental Units

F Force

L Length

1 Introduction

1.1 Background and Motivation

Geosynthetic-Reinforced, Column-Supported Embankments (GRCSEs) can be used in soft ground conditions to reduce settlement that would otherwise be induced by the new embankment load. The columns in column-supported embankments can be driven piles or various types of formed-in-place columns. If driven piles are used, they are often fitted with pile caps to help transfer the embankment load to the piles. A bridging layer consisting of several feet of sand or sand and gravel is often used to help transfer the embankment load to the columns.

GRCSEs concentrate the embankment stress and live loads to the stiff columns through stress redistribution both above and below the foundation subgrade level. Mechanisms of load transfer present above the subgrade level consist of (1) arching within the embankment fill and (2) the vertical component of tension developed in the geosynthetic reinforcement. Below the foundation subgrade level, load transfer occurs via negative skin friction acting down on the column. Mobilization of these load transfer mechanisms requires differential settlement between the column and the soft foundation soil. While differential settlement is necessary for initiating load transfer, important design considerations include limiting the tension in the reinforcement and preventing expression of the differential foundation settlement at the embankment surface.

Increasingly, column-supported embankment technology is being applied to low height embankments. Referencing the British Standard Code of Practice BS8006, Gwede and Horgan (2008) define low-height GRCSEs as those with heights above the pile caps less than 1.4 times the clear spacing between adjacent pile caps.

Examples of low height embankments are provided by Rogbeck et al. (1998), Almeida et al. (2008), Gwede and Horgan (2008), Livesey et al. (2008), and others. More attention is being paid to low height GRCSEs due to their attractiveness as compared with traditional surcharge methods and use of pile-supported structural slabs, but also due to several documented examples of failure. When the clear spacing between adjacent columns is large relative to the embankment height, there is the risk of excessive levels of strain developing within the geosynthetic reinforcement and surface expression of the differential settlement that occurs at the base of the

embankment. This mode of failure is often referred to as 'dimpling'. Examples of this type of failure are reported by Coghlin (2005), Camp and Siegel (2006), and Ting et al. (1994). Currently, consensus has not been established regarding procedures to design embankments to be safe against such surface deformation.

1.2 Objectives and Scope

The primary objective of this research is to improve understanding of GRCSE deformation in response to differential settlement occurring between the relatively stiff column elements and the soft foundation soil. Embankment deformation resulting from lateral spreading or slope instability is outside the scope of this research. The outcome of this research is a set of design recommendations for selecting a unit cell geometry that provides acceptable ride quality and settlement.

The scope of the research includes the following tasks:

- Literature review
- Bench-scale experimental modeling
- Three-dimensional numerical modeling
- Comparison of results to previous studies and published case histories
- Analysis of findings and development of recommendations

A complete summary of activities performed during this research is provided in Section 8.1

1.3 Organization

This dissertation is organized into eight chapters and twelve appendices, which are described below. Readers wanting to navigate directly to the key findings, conclusions, and recommendations can find them in Chapters 7 and 8, which require knowledge of the notation and terminology defined in Section 1.4.

Chapter 2 provides a review of existing guidance for the design of GRCSEs, including estimating the critical height. Chapter 2 also introduces the list of previous experimental and numerical studies, as well as published case histories, reviewed as part of this research. Section

2.5 presents a separate literature review focused on the propagation of fault rupture through a soil profile and load-displacement behavior of embedded anchors during pullout. These areas of research were identified as being analogous to embankment deformation and load transfer to the columns resulting from differential settlement occurring at the foundation level.

Chapter 3 describes the attributes and capabilities of the bench-scale experimental apparatus designed and built for this research. A description of sample preparation, testing procedures, and methods of data reduction is included in the discussion. The selection of material property values of the sand used in the bench-scale experiments is also discussed.

Chapters 4 and 5 present the results, analysis, and discussion of the single and multi-column bench-scale experiments described in Chapter 3. The results highlight the influences of the magnitude of differential base settlement, sample height, initial sample density, column diameter, column spacing, presence and stiffness of reinforcement, and application of surcharge pressure on measured deformation of the sample surface. Chapter 4 also provides a discussion of the results from single column experiments associated with the relationship between base settlement and the vertical stress acting on the column.

Chapter 6 presents the development, analyses, and results from the numerical model developed using FLAC3D.

The conclusions from Chapters 4 through 6 are evaluated and expanded in Chapter 7 using the findings from previous investigations and case histories. Chapter 8 provides a summary of the work accomplished as part of this research, the primary conclusions, and practice-oriented recommendations.

In addition, this dissertation includes the following appendices:

Appendix A: McGuire, M. P., and Filz, G. M. (2008). "Quantitative comparison of theories for geosynthetic reinforcement of column-supported embankments."
Appendix B: McGuire, M. P., Filz, G. M., and Almeida, M. S. S. (2009). "Load-displacement compatibility analysis of a low-height column-supported embankment."
Appendix C: McGuire, M. P., and Filz, G. M. (2010). "Incorporation of slack and creep in the British Standard code of practice for calculating tension and deflection of geosynthetic reinforcement used in column-supported embankments."
Appendix D: Summary and interpretation of experimental study conducted by Chen et. al (2008)

Appendix E: Summary and interpretation of experimental and numerical studies conducted by Demerdash (1996)
Appendix F: Summary and interpretation of experimental study conducted by Ellis and Aslam (2009a,b)
Appendix G: Summary and interpretation of numerical study conducted by Han and Gabr (2002)
Appendix H: Summary and interpretation of experimental and numerical studies by Jenck et al. (2007)
Appendix I: Summary and interpretation of Penang Bridge Approach case history described by Ting et al. (1994)
Appendix J: List of test parameters
Appendix K: Instrumentation calibration
Appendix L: Vacuum triaxial test results

1.4 Notation, Terminology, and Geometric Relationships

This section provides the most important background notation, terminology, and geometric relationships defined and used in this study. Some additional notation that builds on the concepts presented in the dissertation is not presented in this section. In such cases, the notation is clearly defined in the section it is introduced. A complete list of symbols is provided on Pages xxiii through xxv of the front material.

Most of the notation and terminology used in this study can be lumped into three broad headings. The first category deals with the geometry of column supported embankments (Section 1.4.1), the second category involves deformations (Section 1.4.2), and the third category describes stresses (Section 1.4.3).

Column-supported embankments may incorporate one or more layers of geosynthetic reinforcement positioned low in the embankment near the elevation of the pile caps. In some situations, no pile caps are used over the tops of the columns. To improve readability, the term 'column' is used to refer to the pile cap or to the top of the column if pile caps are not used. A distinction between the top of the column and the top of the pile cap is not necessary within the scope of this research, which focuses on embankment response. Another simplification involves the use of the acronym GRCSE, which stands for Geosynthetic-Reinforced Column-Supported Embankment, to refer to column-supported embankment systems with and without geosynthetic reinforcement. Conceptually, a GRCSE without reinforcement is equivalent to an embankment with reinforcement that has zero tensile and flexural stiffness.

Figure 1.1 shows an exploded sketch of the major components and geometric parameters of a typical GRCSE.

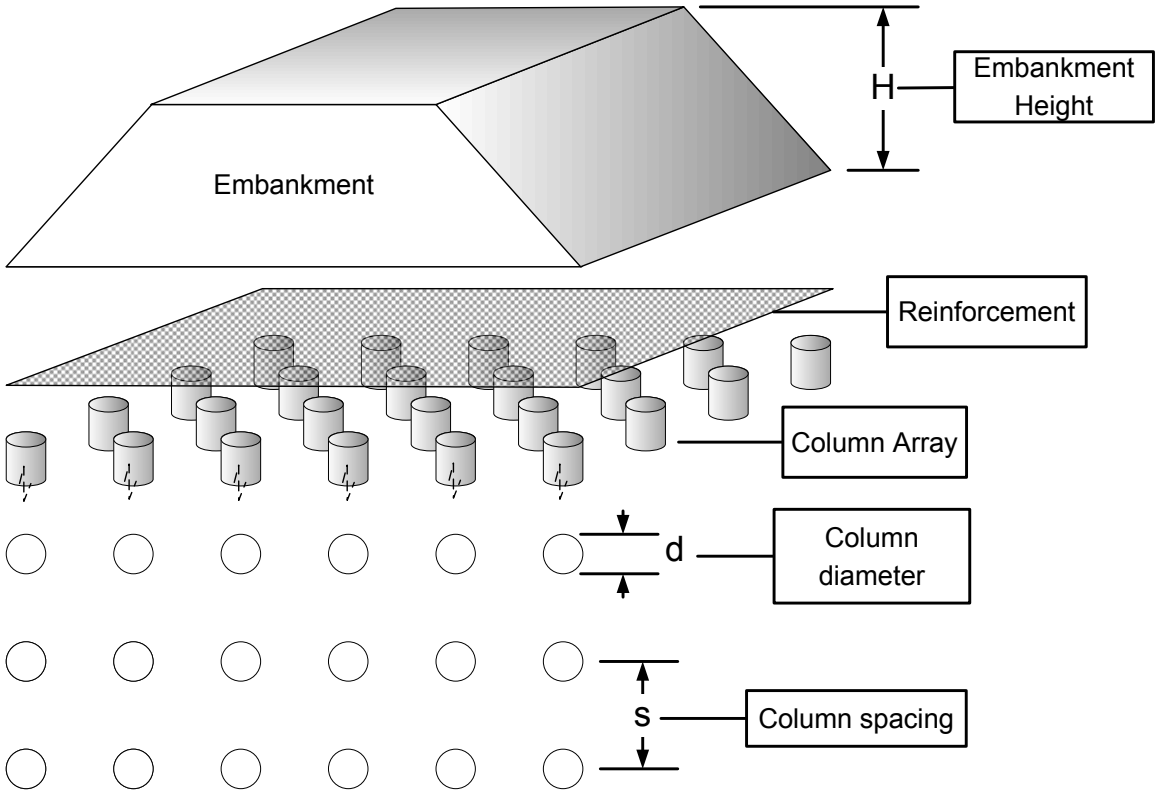

Figure 1.1 Definition sketch of major components and geometric parameters of a GRCSE

1.4.1 Geometry terms and relationships

It is convenient to study the loads and deformations in a GRCSE from sources other than lateral spreading and slope stability by defining a unit cell. Unit cells can be equivalently defined either around the center of a column or around the center of soil between columns. For practical purposes, four types of three-dimensional column arrays can be defined: square, rectangular, equilateral triangular, isosceles triangular. Additionally, unit cells can be defined for plane strain and axisymmetric conditions. The unit cells for these geometries are defined in Figure 1.2 through Figure 1.8. In addition to representing column diameter, d also represents the width of the plane strain representation of the column or cap beam.

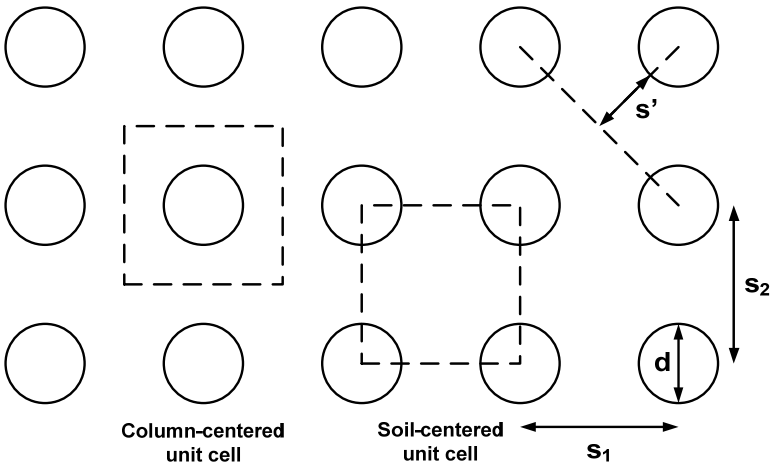

Figure 1.2: Definition of unit cell for square ($s_1=s_2$) and rectangular ($s_1 \neq s_2$) arrays

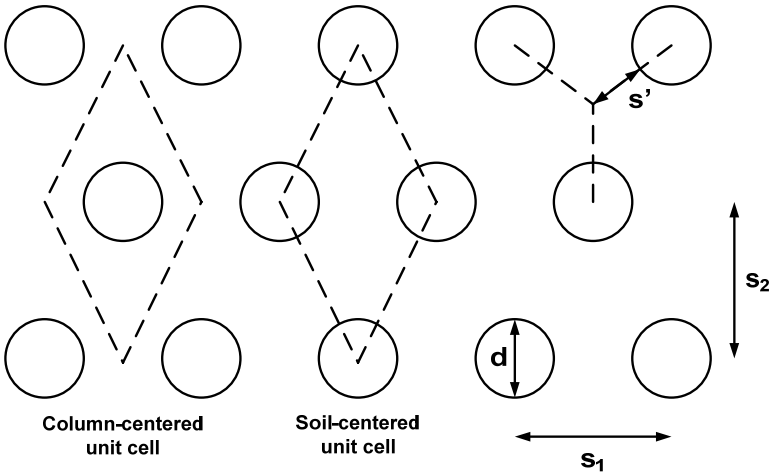

Figure 1.3: Definition of unit cell for isosceles triangular array

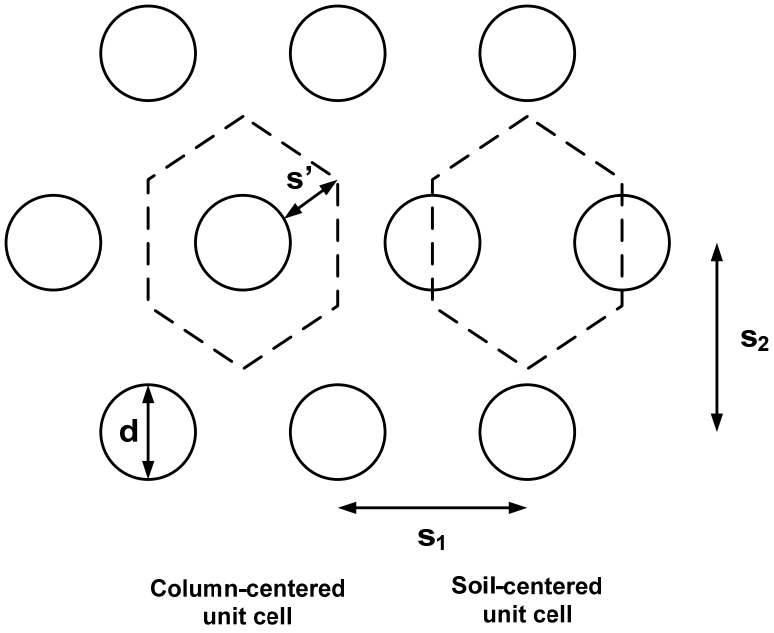

Figure 1.4: Alternate definition of unit cell for isosceles triangular array

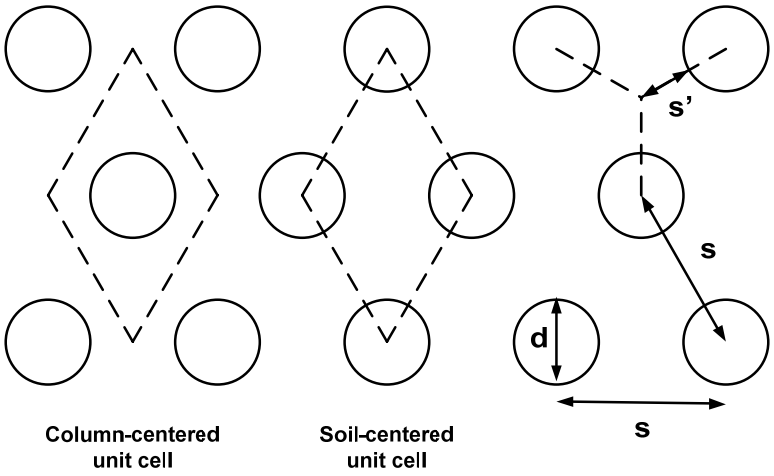

Figure 1.5: Definition of unit cell for equilateral triangular array

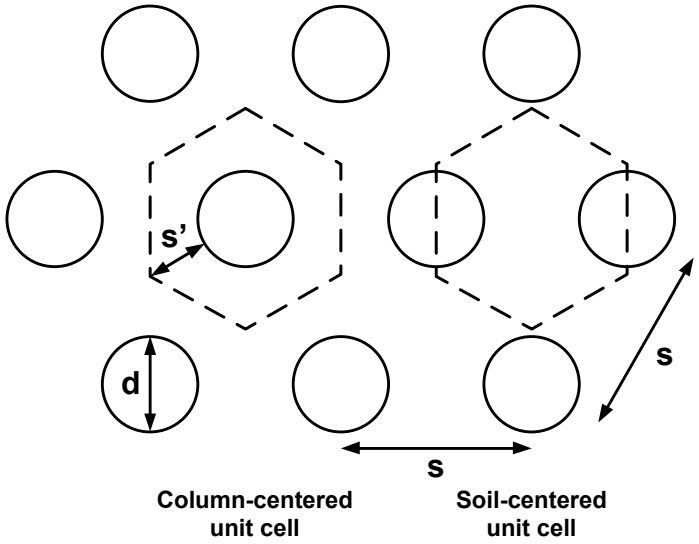

Figure 1.6: Alternate definition of unit cell for equilateral triangular array

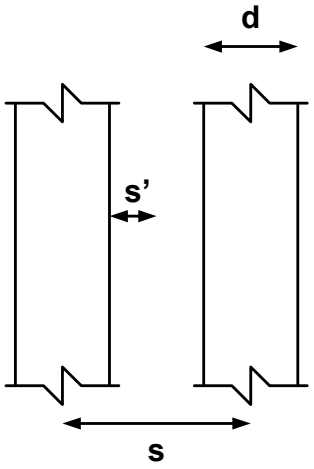

Figure 1.7 Definition of plane strain unit cell

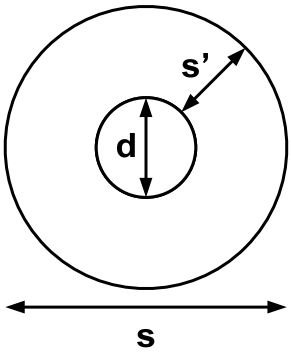

Figure 1.8 Definition of axisymmetric unit cell

The dimension s', which is referred to here as the centroid distance, is the location that is equidistant from the nearest four columns for a square or rectangular array and from the nearest three columns for a triangular array. The centroid distance is the maximum horizontal distance any location within the unit cell can be from the projected edge of a round column. Table 1.1 provides the geometric relationships between the centroid distance and column spacing and cap diameter. A square array is a special case of an isosceles triangular array rotated 45 degrees where $s_1=2s_2$.

Table 1.1 Geometric properties of unit cells

Array Type	s'	Spanning ratio
Square ($s_1 = s_2$)	$\frac{\sqrt{2}s - d}{2}$	$\frac{s}{\sqrt{2}d} - \frac{1}{2}$
Rectangular ($s_1 \neq s_2$)	$\frac{\sqrt{s_1^2 + s_2^2} - d}{2}$	$\frac{\sqrt{s_1^2 + s_2^2}}{2d} - \frac{1}{2}$
Isosceles Triangular ($s_1 = s_2$)	$0.625s - \frac{d}{2}$	$0.625\frac{s}{d} - \frac{1}{2}$
Isosceles Triangular ($s_1 \neq s_2$)	$\frac{4s_2^2 s_1 + s_1^3}{8s_1 s_2} - \frac{d}{2}$	$\frac{4s_2^2 s_1 + s_1^3}{8s_1 s_2 d} - \frac{1}{2}$
Equilateral Triangular	$\frac{s}{\sqrt{3}} - \frac{d}{2}$	$\frac{s}{\sqrt{3}d} - \frac{1}{2}$
Plane Strain	$\frac{s-d}{2}$	$\frac{s}{2d} - \frac{1}{2}$
Axisymmetric	$\frac{s-d}{2}$	$\frac{s}{2d} - \frac{1}{2}$

The terms 'support' and 'influence' will be used to describe how columns affect surface deformations resulting from differential settlement between the columns and foundation soils. The term 'support' refers to how surface deformations are limited due to the spatial characteristics of the unit cell geometry. The term 'influence' refers to how surface deformations of a particular unit cell are affected by changes in embankment height.

The spanning ratio, s'/d, is a dimensionless quantity that provides an indication of the amount of support provided to the embankment by the column array. As the spanning ratio decreases, the amount of support provided by the columns to the overlying embankment increases. As support provided by the columns increases for a constant embankment height, the

surface deformations resulting from differential settlement at the base of the embankment are reduced to a greater extent.

Another useful geometric parameter that is frequently used in the literature is the area replacement ratio, A_s, which is defined as the area of the column divided by the total area of the unit cell. One reason area replacement ratio is useful is that the material costs for the project are proportional to the area replacement ratio for given unit material cost for the columns, project footprint, and column length. Since the spanning ratio gives an indication of the support provided to the embankment by the columns, it is useful to express the spanning ratio in terms of area replacement ratio because it provides an indication of how much support is provided for a certain investment of materials. When s_1 equals s_2 in a type of column array, there is a unique relationship between A_s and s'/d which is provided in Table 1.2. When s_1 does not equal s_2 in a type of column array, the spanning ratio is higher than when s_1 equals s_2 indicating that less support is provided to the embankment by the column array.

Table 1.2: Relationship between area replacement ratio and spanning ratio

Array Type	Area of Unit Cell	Area replacement ratio, A_s	Spanning ratio, s'/d
Square ($s_1 = s_2$)	s^2	$\frac{\pi}{4}\left(\frac{d}{s}\right)^2$	$\sqrt{\frac{\pi}{8A_s}} - \frac{1}{2}$
Rectangular ($s_1 \neq s_2$)	$s_1 s_2$	$\frac{\pi}{4}\frac{d^2}{s_1 s_2}$	$\geq \sqrt{\frac{\pi}{8A_s}} - \frac{1}{2}$
Isosceles Triangular ($s_1 = s_2$)	s^2	$\frac{\pi}{4}\left(\frac{d}{s}\right)^2$	$0.625\sqrt{\frac{\pi}{4A_s}} - \frac{1}{2}$
Isosceles Triangular ($s_1 \neq s_2$)	$s_1 s_2$	$\frac{\pi}{4}\frac{d^2}{s_1 s_2}$	$\geq 0.625\sqrt{\frac{\pi}{4A_s}} - \frac{1}{2}$
Equilateral Triangular	$\frac{\sqrt{3}s^2}{2}$	$\frac{\pi}{2\sqrt{3}}\left(\frac{d}{s}\right)^2$	$\sqrt{\frac{\pi}{6\sqrt{3}A_s}} - \frac{1}{2}$
Plane Strain (per unit out-of-plane depth)	s	$\frac{d}{s}$	$\frac{1}{2A_s} - \frac{1}{2}$
Axisymmetric (area of revolution about axis)	$\frac{\pi}{4}s^2$	$\left(\frac{d}{s}\right)^2$	$\sqrt{\frac{1}{4A_s}} - \frac{1}{2}$

The volume of the unit cell, V_u is equal to the area of the unit cell multiplied by the embankment height, H.

In this study, the analyses and conclusions are based on circular columns. The two primary reasons for this approach are that the bench scale experiments performed in this study and the companion field study performed by Sloan (2011) used round columns and the findings by Filz and Plaut (2009) and Almeida et al. (2008) suggest that circular columns are less prone to damaging the reinforcement than columns with corners. In the cases where square columns are used, the approach used by Smith (2005) recommends converting the square column to a circular column with the same area. If the square column is not converted based on equal area, there are basically two options for determining spanning ratio. The first option is to use the diagonal dimension √2a, where *a* is the width of the column. This approach is equivalent to treating the square column as a circular column with a diameter equal to √2a. The spanning ratio in this case would be lower than the equal area approach which suggests more support is provided by the column. The other option is to base the spanning ratio on the width dimension of the square column cap. This is equivalent to treating the square column as a circular column with a diameter equal to the width of the square column. In this case, the spanning ratio would be greater than the equal area approach, suggesting less support is provided. The three options for determining spanning ratio for square columns are shown in Table 1.3. Since the equal area approach makes intuitive sense and the spanning ratio falls between the other two approaches, it is used in this research when analyzing the results from other experimental studies and case histories.

Table 1.3: Three alternatives for converting a square column into an equivalent circular column

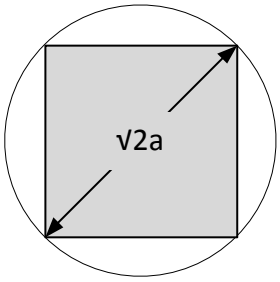	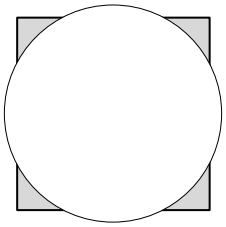 (equal area)	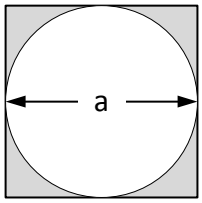
$d = \sqrt{2}a$	$d = \sqrt{\frac{4}{\pi}}a$	$d = a$
For Square Array		
$s' = \frac{s-a}{\sqrt{2}}$	$s' = \frac{2}{\sqrt{2}} - \frac{a}{\pi}$	$s' = \frac{\sqrt{2}s-a}{2}$
$\frac{s'}{d} = \left(\frac{1}{2}\right)\frac{s}{a} - \frac{1}{2}$	$\frac{s'}{d} = \left(\sqrt{\frac{\pi}{8}}\right)\frac{s}{a} - \frac{1}{2}$	$\frac{s'}{d} = \left(\frac{1}{\sqrt{2}}\right)\frac{s}{a} - \frac{1}{2}$
Spanning Ratio for Square Array when s = a (for comparison)		
$\frac{s'}{d} = 0$	$\frac{s'}{d} = 0.127$	$\frac{s'}{d} = 0.207$

1.4.2 Deformation terms

In this study, settlement is measured relative to the top of the columns, which is taken as a reference point. Settlement of the embankment surface can be described by the minimum settlement that occurs directly over the axis of the columns, S_c, the maximum settlement which occurs at locations in the unit cell a distance s' from any column, S_d, and the settlement which occurs mid-span between lines of columns, S_i. For arrays where s_1 does not equal s_2, S_{i1} and S_{i2} are the settlements at midspan along column lines of different spacing. Table 1.4 summarizes the locations of the surface settlements and defined symmetrical sub-unit cells for three dimensional column arrays.

Table 1.4: Definition of sub-unit cell and surface settlement locations for different types of column arrays

Array Type	Shaded fraction of unit cell area	Shaded sub-unit cell and location of surface settlements
Square Array	1/8	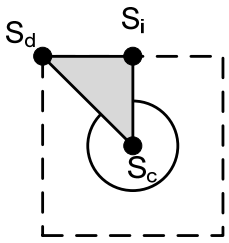
Rectangular Array	1/4	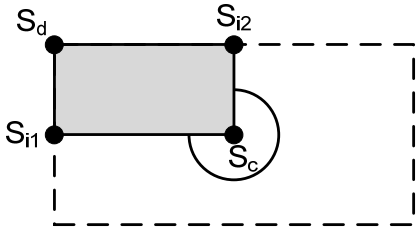
Isosceles Triangular Array	1/4	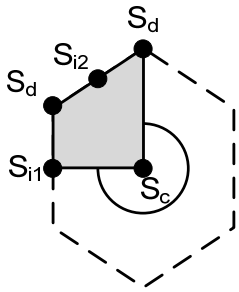
Equilateral Triangular Array	1/12	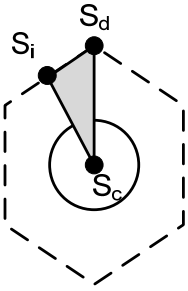

Settlements can also be defined at the base of the embankment, which is assumed to initially be at the same elevation as the column tops. The notation to describe base settlement is consistent with the notation to describe surface settlement, except with the addition of a subscript 'b' to indicate 'base'. For example the base settlement $S_{b,d}$ occurs at the same location(s) in the unit cell where the surface settlement S_d occurs. Because the centroid locations are farthest from the columns, S_d and $S_{b,d}$ respectively represent the maximum settlements at the surface and base of the embankment. As described in Chapter 3, the base settlements are uniform for the bench-

scale experiments performed as part of this study. The simplified notation, S_b, is used herein to describe the magnitude of uniform base settlement. When base settlement is non-uniform, as is typical in the field, $S_{b,avg}$ is used to represent the average base settlement. Uniform and average base settlements are distinguished because surface settlements are influenced by both the magnitude and distribution of base settlements.

It is useful to express surface settlements as a ratio with the maximum base settlement, as defined in Table 1.5. This approach is consistent with the ratio of surface to base settlement defined by Russell et al. (2003). When base settlement is uniform, the maximum base settlement is equal to the uniform settlement, S_b. The acronym SBR is an abbreviation for '**S**urface to **B**ase settlement **R**atio' while DSBR is short for '**D**ifferential **S**urface to **B**ase settlement **R**atio'

Table 1.5: Surface settlement definitions and ratios

Settlement Ratio	Definition
SBR_c	$S_c / S_{b,d}$
SBR_d	$S_d / S_{b,d}$
SBR_i	$S_i / S_{b,d}$
$DSBR_d$	$(S_d - S_c) / S_{b,d}$
$DSBR_i$	$(S_i - S_c) / S_{b,d}$

Note: $S_{b,d} = S_b$ when base settlement is uniform

When embankment or sample height is very low, the columns act individually to support the embankment, rather than collectively as an array, and portions of the surface of the unit cell are not influenced by the columns. As described above, 'influence' means that the columns reduce surface settlement to some value below the magnitude of the differential base settlement. As the embankment or sample becomes taller, more of the unit cell is influenced by the columns. Locations in the unit cell least influenced by the presence of the columns are located a distance s' from any column. The embankment height at which these locations are influenced (i.e. lowest embankment height for which $S_d < S_{b,d}$) is defined here as the interaction height, H_i, since columns influence surface deformations collectively as an array for embankment heights greater than H_i.

As explained in Chapters 4 and 5, further increase in embankment or sample height beyond the interaction height influences surface deformation by reducing S_d and S_i and increasing S_c, with the net effect of reducing $DSBR_d$ and $DSBR_i$. The term 'critical height', H_{crit},

or the height of the 'plane of equal settlement' is used by Chen et al. (2008), Naughton (2007), and Demerdash (1996) to refer to the embankment height above which there is no longer surface expression of the differential foundation settlement (i.e. $DSBR_d = DSBR_i = 0$). Since the location(s) in the unit cell a distance s' from any column receive the least support from the columns, the critical height is determined when $DSBR_d$ reaches zero.

For embankments taller than the critical height, the surface of the unit cell settles uniformly in response to differential settlement occurring at the foundation level. The ratio of the total surface settlement to the base settlement, $S_{tot}/S_{b,d}$, is given by SBR_{tot}. Since surface settlements are uniform, $S_{tot} = S_c = S_d = S_i$ and $SBR_{tot} = SBR_c = SBR_d = SBR_i$.

1.4.3 Stress terms

Filz and Smith (2006) present terminology to describe load transfer to the columns by soil arching within the embankment and tension developed in the reinforcement. A summary of the terms is provided here. It is important to note that without differential movement between the columns and the foundation soil, the stress acting on the columns and soil would be the same and equal to $\sigma_o + q$, where σ_o is the initial vertical overburden pressure from the embankment equal to γ, the unit weight of the embankment material, multiplied by the embankment height, H, and q is the pressure due to a surcharge. With the onset of differential settlement between the column elements and the foundation soils, the stresses acting on the column become greater and the stresses acting on the foundation soil decrease. The average stresses acting above the reinforcement are expressed as $\sigma_{col,geotop}$ for the stress over the column and $\sigma_{soil,geotop}$ for the average stress over the soil. The difference between $\sigma_{col,geotop}$ and $\sigma_{soil,geotop}$ is due to arching within the embankment. Additional load transfer to the columns occurs when the reinforcement deforms and develops tension in response to the out-of-plane application of $\sigma_{soil,geotop}$. The average stresses below the reinforcement are $\sigma_{col,geobot}$ and $\sigma_{soil,geobot}$ for column and soil stresses, respectively. The difference between $\sigma_{soil,geotop}$ and $\sigma_{soil,geobot}$ is that the average stress acting on the soil below the reinforcement has been reduced by load transfer to the column through the reinforcement.

To describe load transfer within a unit cell, it is convenient to normalize the average stresses acting over the column and soil by the overburden pressure acting uniformly within the unit cell prior to differential settlement, $\sigma_o + q$. These ratios are referred to as the Column Stress

Ratio (CSR) and Stress Reduction Ratio (SRR), respectively. The relationship between CSR and SRR is provided in Equation 1.1.

$$1 = \mathrm{CSR}\left(\mathrm{A_s}\right) + \mathrm{SRR}\left(1 - \mathrm{A_s}\right) \tag{1.1}$$

Values of SRR and CSR can be determined for load transfer in the embankment, $\mathrm{SRR_{emb}}$ and $\mathrm{CSR_{emb}}$, load transfer in the reinforcement, $\mathrm{SRR_{net}}$ and $\mathrm{CSR_{net}}$, and the combined effects of load transfer at the foundation level, $\mathrm{SRR_{fndn}}$ and $\mathrm{CSR_{fndn}}$. Equations 1.2 through 1.4 show how $\mathrm{SRR_{emb}}$, $\mathrm{SRR_{net}}$, and $\mathrm{SRR_{fndn}}$ are determined from $\sigma_{\mathrm{soil,geotop}}$, $\sigma_{\mathrm{soil,geobot}}$ and σ_o+q. Values of CSR for a known area replacement ratio can be determined by applying Equation 1.1. Figure 1.9 is reproduced from Filz and Smith (2006) and illustrates load transfer occurring above the foundation level.

$$\mathrm{SRR_{emb}} = \frac{\sigma_{\mathrm{soil,geotop}}}{\gamma \mathrm{H} + \mathrm{q}} \tag{1.2}$$

$$\mathrm{SRR_{net}} = \frac{\sigma_{\mathrm{soil,geotop}} - \sigma_{\mathrm{soil,geobot}}}{\gamma \mathrm{H} + \mathrm{q}} \tag{1.3}$$

$$\mathrm{SRR_{fndn}} = \frac{\sigma_{\mathrm{soil,geobot}}}{\gamma \mathrm{H} + \mathrm{q}} \tag{1.4}$$

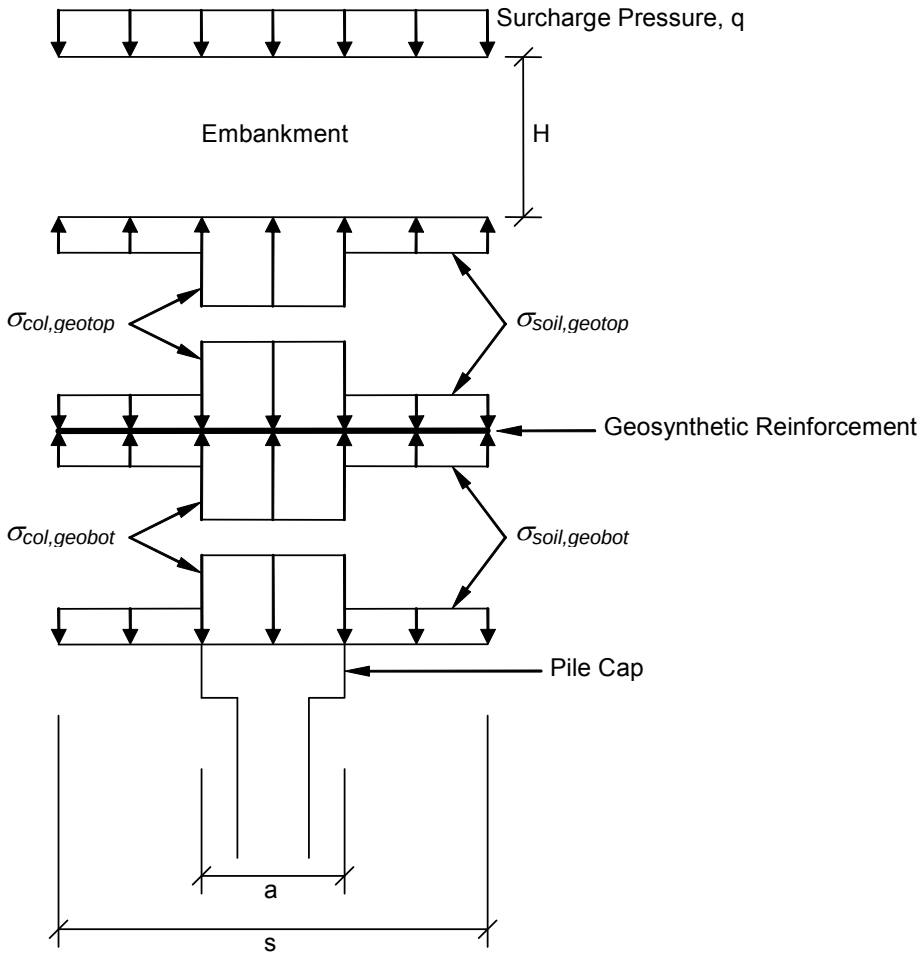

Figure 1.9: Stresses within the unit cell with onset of load transfer (Filz and Smith 2006, with permission from VDOT)

For an isolated column not part of any array, there is no arching between adjacent columns and no defined unit cell. In Chapters 2 and 4, load transfer occurring for a single column or embedded plate anchor is discussed. The column stress-displacement relationship observed during the bench-scale tests and reported by others (Dickin and Laman 2006, Fadl 1981, and Ilamparuthi and Muthukrishnaiah 1999) for embedded plate anchors can be characterized by a sharp increase in stress to a peak value followed by a decline to a residual value that is approximately constant, or decreases gradually, with continued differential movement. In this research, $S_{b,max}$ refers to the maximum base settlement at maximum column stress, $\sigma_{col,max}$ and $S_{b,res}$ refers to the maximum base settlement at residual column stress, $\sigma_{col,res}$. These terms are summarized in Table 1.6. To avoid confusion with the column stress ratio, which includes load transfer by arching, the ratio of the vertical stress acting on the column to the initial vertical stress is defined as the column stress factor. As described in Chapter 3, the

single column tests measured the load acting on the column; however, for tests that included reinforcement, it was not feasible in the bench-scale tests to separately measure the load transfer due to arching and from tension in the reinforcement.

Table 1.6 Key descriptors to define relationship between column stress and base settlement

Base Settlement	Column Stress	Description
$S_b = 0$	σ_o+q	The column stress before any base settlement
$S_{b,max}$	$\sigma_{col,max}$	The base settlement corresponding to the maximum measured column stress
$S_{b,res}$	$\sigma_{col,res}$	The base settlement at the onset of an approximately stable post-peak column stress

In Chapter 4, the measured column stress for tests that include reinforcement is equivalent to $\sigma_{col,geobot}$. In other studies described in Chapters 2 and 7, it is clarified whether the column stress is measured above and/or below the reinforcement.

2 Literature Review

This section covers the literature review associated with the current research project. The general approach taken is to provide key information in a concise format and direct the reader to appendices for supplemental information. The material presented in Chapter 2 is used in Chapter 6 to compare to the current experimental tests.

Chapter 2 is organized into the following sections:

Section 2.1: Current methods for calculating load transfer to columns and tension in reinforcement
Section 2.2: Current recommendations for minimum embankment height
Section 2.3: Previous experimental and numerical studies
Section 2.4: Selected case histories
Section 2.5: Examination of analogous systems

In addition to the content provided in the body of the dissertation, the appendices listed below are provided to give supplemental information and describe the processes used to interpret the findings of others. Relevant appendices are re-introduced in each section.

Appendix A: McGuire, M. P., and Filz, G. M. (2008). "Quantitative comparison of theories for geosynthetic reinforcement of column-supported embankments."
Appendix B: McGuire, M. P., Filz, G. M., and Almeida, M. S. S. (2009). "Load-displacement compatibility analysis of a low-height column-supported embankment."
Appendix C: McGuire, M. P., and Filz, G. M. (2010). "Incorporation of slack and creep in the British Standard code of practice for calculating tension and deflection of geosynthetic reinforcement used in column-supported embankments."
Appendix D: Summary and interpretation of experimental study conducted by Chen et. al (2008)
Appendix E: Summary and interpretation of experimental and numerical studies conducted by Demerdash (1996)
Appendix F: Summary and interpretation of experimental study conducted by Ellis and Aslam (2009a,b)
Appendix G: Summary and interpretation of numerical study conducted by Han and Gabr (2002)

Appendix H: Summary and interpretation of experimental and numerical studies by Jenck et al. (2007)
Appendix I: Summary and interpretation of Penang Bridge Approach case history described by Ting et al. (1994)

The recent dissertation by Sloan (2011) provides a comprehensive background on GRCSE technology and review of current design methods. An electronic version of Sloan (2011) is available on Virginia Tech Library's electronic thesis and dissertation website at http://www.lib.vt.edu/find/byformat/etds.html.

2.1 Current Methods for Calculating Column Load and Reinforcement Tension

A significant body of published work is available that provides guidance on calculating the distribution of loads between the foundation soils and the columns and determining the tension developed in the reinforcement based on the column spacing, pile cap size, embankment height, properties of the embankment material, and reinforcement condition. With few notable exceptions (Filz and Smith, 2006, Kempfert et al. 2004), the literature largely ignores the influence of support provided by the subgrade on the load transfer mechanisms above the foundation level. A study by McGuire and Filz (2008) compared the existing design methods using parametric analysis. Table 2.1 and Table 2.2 provide a list of the methods evaluated in the study.

Table 2.1 Existing methods for calculating loads carried by the columns and foundation soil evaluated in McGuire and Filz (2008)

Method	Reference
The British Standard BS8006	Jones et al. (1990)
Adapted Terzaghi Method 1	Russell and Pierpoint (1997)
Adapted Terzaghi Method 2	Russell et al. (2003)
Hewlett and Randolph Method	Hewlett and Randolph (1988)
EBGEO / German Method	Kempfert et al. (2004)
Adapted Guido Method	Russell and Pierpoint (1997)
NGG / Swedish Method	Carlsson (1987)
Naughton Method	Naughton (2007)
Collin Method	Collin (2004, 2007)
Load-Displacement Compatibility Method	Filz and Smith (2006, 2007)

Table 2.2: Existing methods for estimating tension developed in reinforcement evaluated by McGuire and Filz (2008)

Method	Reference
Parabolic Method	Jones et al. (1990)
Tensioned Membrane	Collin (2004, 2007)
EBGEO / German Method	Kempfert et al. (2004)

The study by McGuire and Filz (2008), as well as studies by Habib et al. (2002), Horgan and Sarsby (2002), and Naughton and Kempton (2005), demonstrated inconsistencies among existing methods for determining the vertical stress on the reinforcement and the tension developed in the reinforcement.

Several studies, including Demerdash (1996), Van Eekelen et al. (2008), McGuire and Filz (2009), have evaluated existing methods to assess the suitability of different approaches for estimating magnitudes of column stress and reinforcement tension. Sloan (2011) assessed twelve existing methods using a variety of performance criteria/indicators. Based on his review, comparison to measurements from a series of field-scale experiments, and consultation with practitioners, Sloan (2011) recommends the Load-Displacement Compatibility Method (LDC), which is also known as the Filz and Smith Method, for estimating load transfer and reinforcement tension.

The LDC approach to GRCSE design is described in detail in Filz and Smith (2006, 2007) and is based on load and displacement compatibility among the embankment, columns, geosynthetic reinforcement, and foundation soil. Figure 2.1 shows the load-displacement relationships currently incorporated in the LDC approach. Differential settlement between the columns and the foundation soil is determined as the difference between the vertical elastic deformation of the column, C_{col}, and the settlement of the foundation soil, S_b, which includes linear compression of existing granular soil, if present, and nonlinear compression of clay. Shear stress between the settling foundation soils and the columns, τ, is accounted for by considering the interface friction angle and the effective lateral stress, σ_h, produced by column installation as well as Poisson effects from the embankment load determined according to a concentric cylinder model (Poulos and Davis 1974).

The load-deflection response of geosynthetic reinforcement is obtained from axisymmetric numerical analyses of an annular membrane described in Smith (2005). The load-deflection relationship for the column or pile cap penetrating up, relatively, into the embankment is assumed to be linear up to a maximum load condition. The linear part is approximated using the linear solution for displacement of a rigid circular loaded area on a semi-infinite mass (Poulos and Davis 1974). The maximum load condition on the column area above the reinforcement level is established by setting a lower limit on the value of total vertical pressure acting down on the reinforcement using the Adapted Terzaghi Method with an earth pressure coefficient, K, equal to 0.75, which falls between the values of 1.0 used by Russell and Pierpoint (1997) and 0.5 used by Russell et al. (2003).

The simultaneous solution among the load-displacement compatibility relations for the embankment fill, geosynthetic reinforcement, columns, and foundation soils is performed using an iterative technique implemented in a Microsoft Excel® spreadsheet entitled GeogridBridge 1.1, which is available by searching "GeogridBridge" at http://vtrc.virginiadot.org/PUBS.aspx. Additional details regarding GeogridBridge 1.1 and the LDC approach are provided by Sloan (2011) and Filz and Smith (2006, 2007).

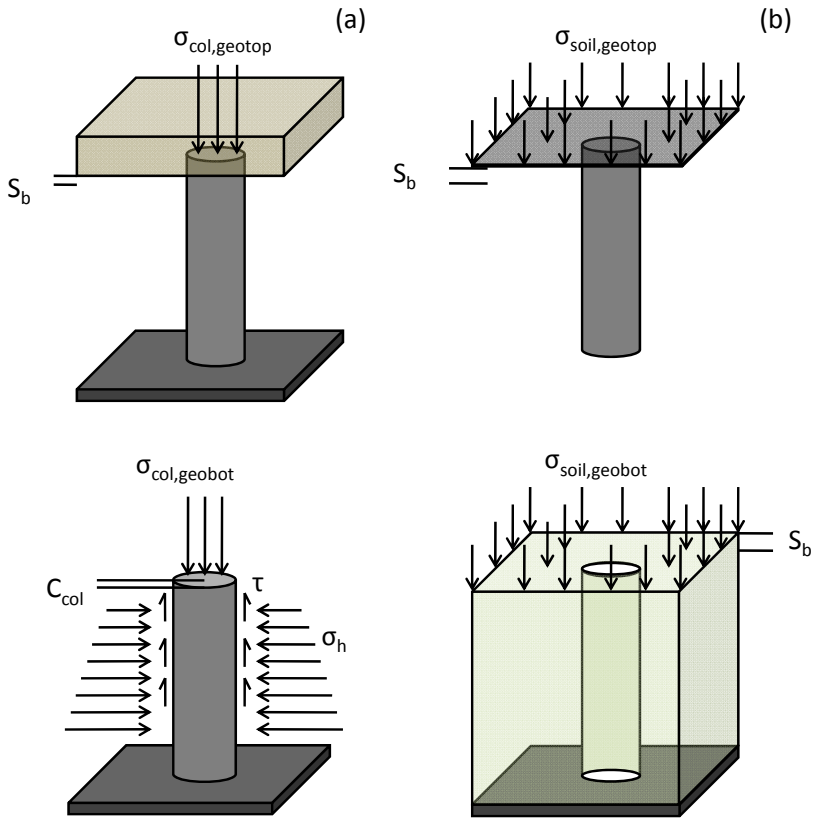

Figure 2.1 Load-Displacement compatibility relations: (a) settlement and arching within the embankment, (b) vertical deflection and development of tension in the reinforcement, (c) compression of the column due to applied load on pile cap and downdrag, and (d) settlement of soft foundation soils

2.2 Current Recommendations for Minimum Embankment Height

Table 2.3 lists recommendations for minimum embankment heights based on load transfer and surface deformation performance criteria as well as assumptions regarding the shape of the soil 'arches' believed to form between adjacent columns. The current convention is to express the minimum recommended height as a ratio of the clear spacing between adjacent columns (i.e. $H_{min}/(s-d)$) or the column spacing, s.

Authors have assumed the shape of the soil arches or differentially yielding soil masses above the columns to be wedges in plane strain (Carlsson, 1987), pyramids (Svanø et al. 2000, Collin 2007, and Russell and Pierpoint 1997), hemispherical domes (Hewlett and Randolph 1988, Kempfert et al. 2004, Jones et al. 1990), and a cruciform (Russell et al. 2003, Russell and Pierpoint 1997).

Table 2.3 Existing recommendations for minimum embankment height

Source	Recommended relationship between column size, spacing, and minimum embankment height	Remarks
Bell et al. (1994), Maddison et al. (1996)	No recommendations given.	GRCSE for Second Severn Crossing was designed by adapted work by Guido et al (1987). Russell and Pierpoint (1997) describe that load transfer using this method assumes a pyramid of unsupported soil between pile caps with ridge lines inclined at 45 degrees. Therefore the height of arching is equal to (s-a)/√2
BS8006 (1995)	Full arching is developed when embankment height is at least 1.4(s-a). BS8006 (1995) states that H>0.7(s-a) to ensure localized differential deformations cannot occur at the surface of embankments	According to Horgan and Sarsby (2002), BS8006 defines critical height as the fill thickness whereby full arching is developed and any additional fill or surcharge is distributed completely to the pile caps.
Carlsson (1987) as reported in Rogbeck (1998)	To limit surface displacements, the height of embankment should be at least equal to the greater of 1 meter and the distance between pile caps. The area replacement ratio should be at least 10 percent.	The height of the soil arches considered in Carlsson's approach are equal to 1.87(s-a)
Chen et al. (2008)	To ensure that no differential settlement occurs at the embankment surface, a minimum embankment height equal to 1.6(s-a) is necessary	Plane strain experimental testing indicated that the plane of equal settlement occurs at height above the pile caps equal to 1.4 to 1.6 times the clear spacing, (s-a). Chen et al. use the term 'plane of equal settlement' to indicate the embankment height above which no differential settlement occurs and the term 'critical height' to define the height above which all embankment weight and surcharge is carried by the pile caps.

Source	Recommended relationship between column size, spacing, and minimum embankment height	Remarks
Collin (2007)	The thickness of the load transfer platform reinforced with at least four layers of reinforcement must be equal to or greater than 0.5(s-d)	Soil unsupported by arching forms a pyramid with sides inclined at 45 degrees.
Combarieu (1989)	A design curve can be found in the original source.	Modified version of the design curve developed by the Swedish Road Board (1974).
Demerdash (1996)	To prevent differential surface settlement, H>1.7(s-a)	Demerdash reports the "Plane of equal settlement", which is the elevation within the embankment where settlement becomes uniform, was experimentally found to equal 1.7 to 2.0 times (s-a)
Ellis and Aslam (2009a,b)	No recommendations given.	Based on the results from centrifuge modeling, Ellis and Aslam report that little to no differential surface settlement occurs for unreinforced embankments when the height is equal to or greater than twice the clear span between pile caps, (s-a).
Hewlett and Randolph (1988)	For square grid of square pile caps, the minimum height of high-grade (K_p>3) fill should not be less than the pile spacing and the total embankment height should not be less than twice the pile spacing. The pile cap width should be selected such that a/s≥1/3.	Soil arching forms hemispherical domes between adjacent pile caps with a height equal to s/√2. Failure of the arches can occur either at the base or crown of the arch. The recommendations select geometries where the limiting condition for the arch is at the base where bearing capacity can be improved by use of high quality fill and geosynthetics.
Horgan and Sarsby (2002)	No recommendations given.	Based on the results of model tests, Horgan and Sarsby report a significant increase in load transfer by arching when embankment height increases from 1.545 to 1.92 times the clear spacing, (s-a).

Source	Recommended relationship between column size, spacing, and minimum embankment height	Remarks
Huat et al. (1994)	The thickness of high quality fill need not extend higher than the pile spacing. Higher area replacement ratio increases efficacy.	Huat et al. report no significant increase in load transfer to the columns for fill thicknesses greater than 1 to 2 times the pile spacing, depending on area replacement ratio.
Kempfert et al. (2004)	Kempfert defines s as the greatest column spacing. For a square array, s equals √2 times the center-to-center spacing. The clear spacing, (s-d), should be less than or equal to 3.0 m for static loads, 2.5 m for heavy live loads. The clear spacing should also be less than or equal to 1.4 times the embankment height above the reinforcement. The ratio of cap diameter to column spacing, d/s, should be equal to or greater than 0.15.	Using Kempfert's definition for s, the height of the soil arches is considered to equal s/2. When the embankment height is less than s/2, the height of the arches is considered to equal the embankment height.
Naughton (2007)	Assuming the shear planes follow a log spiral path, the critical height is equal to C(s-a), where $C = 0.5 * e^{0.5*\pi*\tan\phi}$, typically C = 1.24 - 2.40	The term 'critical height' is defined as the distance from the top of the pile caps to the height of the plane of equal settlement in the embankment.
Nordic Handbook (2002)	To limit surface deformation, the embankment height should at least be as large as 1.2 times the distance between pile caps. The area replacement ratio should be at least 10 percent. Lower embankment heights are permitted if the design includes finite element calculations	

Source	Recommended relationship between column size, spacing, and minimum embankment height	Remarks
Rathmayer (1975)	Table relating embankment height to minimum recommended area replacement ratio is provided in original source.	The recommendations are based on review of 46 column-support embankments designed according to the code of the Finnish Board of Public Roads and Waterways, which at the time required a minimum area replacement ratio of 30 percent. The study found that, in general, embankment at least 2.5 m high did not experience differential surface settlement.
Svanø et al. (2000)	No recommendations provided	Pile caps are assumed to carry a 3D wedge of the embankment with slope β:1, where β varies from 2.5 to 3.5
Swedish Road Board (1974), Broms (1979)	A design curve can be found in the original source. The early Scandinavian methods relied on closely-spaced pile caps to support the embankment	Design curve relating column size, spacing, and embankment height was developed using scale model tests.
Terzaghi (1943)	Does not directly address column-supported embankments, however for plane strain conditions, it is recommended that the zone of arching be considered to extend 2 to 3 times the separation distance between fixed supports.	Zone of arching was determined based on experimental and analytical findings, the vertical pressure acting on a yielding strip is practically independent of the state of stress that exists beyond a distance above the strip equal to 2 to 3 times the width of the strip.

2.3 Previous Experimental and Numerical Studies

Table 2.5 and Table 2.6 list relevant experimental and numerical studies performed by others identified during the literature review. A key to interpreting both tables is provided at the top of Table 2.5. For the description of experimental scale given in Table 2.4, 'bench-scale' refers to a model that is roughly table-top sized, while 'laboratory-scale' refers to a model housed in a lab that is larger than bench-scale, but smaller than field-scale. In total, 24 experimental studies and 29 numerical studies performed by others were identified and are

summarized in Table 2.5 and Table 2.6. Table 2.7 provides a breakdown of the experimental and numerical studies by model type, array type, and whether the influence of reinforcement was included in the study.

Table 2.4 Key to Table 2.5 and Table 2.6

Focus of Study		**Experimental Scale**	
embankment deformation	D	benchtop scale	B
load transfer	L	centrifuge modeling	C
performance of reinforcement	R	laboratory scale	L
foundation settlement	S	field scale	F
other	O		

Displacement/Load Control		**Array Type**	
moveable base or columns	M	square	S
air bladders	A	equilateral triangular	ET
water bladders	W	isoceles triangular	IT
compressible foam/rubber	R	rectangular	R
soil	E	plane strain	P
		axisymmetric	A

Table 2.5 Previous experimental studies by others

Experimental Study	Focus of Study	Scale	Load-controlled with subgrade support	Load-controlled without subgrade support	Displacement-controlled	Number of column spacings tested	Number of pile caps sizes tested	Number of embankment materials tested	Considered influence of sample density	Geosynthetic reinforcement used in embankment	No geosynthetic incorporated in embankment	Considered influence of reinforcement stiffness	Considered influence of multiple reinforcement layers	Critical height(s) reported
						Array type								
Current Study	D,L	B			M	S	2	3	1	•	•	•	•	•	•
Abdullah and Edil (2007a)	D,L,R,S	F	E			S	2	1	1		•		•	•	
Almeida et al. (2008, 2007)	S,R	F	E	•		S,P	2	2	1		•				
Chen et al. (2008)*	D,L	L			W	P	1	3	1		•	•	•		
Chew et al. (2004)	D,L,R	F	E	•		R	1	1	1		•			•	
Demerdash (1996)*	D,L,R	L		•	M	S	1	3			•		•		•
Ellis and Aslam (2009a,b)*	D,L	C	R			S	2	1	2			•			•
Fluet et al. (1986)	D,R	L	A	•		P	1	0	1		•				
Hewlett and Randolph (1988)	D,L	B	R			S,P	2	2	1			•			
Horgan and Sarsby (2002)	D,L,R	L			M	P	1	1	2		•				
Hossain and Rao (2006)	D,S	F	E			S	1	1	1						
Huat et al. (1994)	D,L	C	E			S	1	1	1			•			
Huat et al. (1994)	D,L	L			M	S	1	1	1			•			

Table 2.5 Previous experimental studies by others (continued)

Experimental Study	Focus of Study	Scale	Load-controlled with subgrade support	Load-controlled without subgrade support	Displacement-controlled	Number of column spacings tested	Number of pile caps sizes tested	Array type	Number of embankment materials tested	Considered influence of sample density	Geosynthetic reinforcement used in embankment	No geosynthetic incorporated in embankment	Considered influence of reinforcement stiffness	Considered influence of multiple reinforcement layers	Critical height(s) reported
Current Study	D,L	B				M	S	2	3	1	•	•	•	•	•	•
Jenck et al. (2007)*	D,L	B	R				P	3	1	1						
Kempfert et al. (2004)	L,R	L	E				S	1	1	1		•				
Low Tang and Choa (1994)	L,R	B	R				P	4	1	1		•	•			
Miki (1997)	L,D	F				M	S	3	1	1			•			
Oh and Shin (2007)	L,R,S	F	E				S	3	1	1		•	•			
Quigley et al. (2003)	D,L,R	F	E				ET	1	1	1		•			•	
Rogbeck et al. (1998)	R	F	R,E				S	1	1	1		•				
Sloan (2011)	D,L,R	F	R	•			S	2	1	2		•			•	•
Van Eekelen et al (2003)	D,L	L	W,R				P	1	1	1						
Van Eekelen et al (2008)	L,R	F	E				S	1	1	1		•				
Villard et al. (2004)	D,L,R	F	E	•			T	1	1	1		•		•		
Xu et al. (2007)	L	F	E				T	1	1	1		•				

Table 2.6 Summary of numerical modeling studies by others

Numerical Modeling Study	Focus of Study	Model Type	Array type	Number of column spacings tested	Number of pile caps sizes tested	Embankment material properties varied in analysis	Geosynthetic reinforcement used in analysis	Reinforcement properties varied in analysis	Critical height(s) reported
Current Study	D,L	3D	S	2	3	1			•
Abdullah and Edil (2007b)	L,R,S	2D	P	2	1		•	•	
Berilgen et al. (2008)	O	2D,3D	P,S	1	1		•		
Chen et al. (2006)	L,S	2D	A	1	1				
Collin et al. (2006), Huang et al. (2005)	D,L,R,S	3D	S	4	2	•	•	•	
Demerdash (1996)*	D,L,R	2D	P	6	4	•	•	•	•
Habib et al. (2002)	L	2D	A,P	1	1		•		
Halvordson et al. (2010)	R	3D	S	1	1		•	•	
Han and Akins (2002)	D	2D	P	2	1		•		
Han and Gabr (2002)*	D, L, R,S	2D	A	1	1		•	•	•
Han et al. (2005), Han and Huang (2007), Han et al. (2007), Huang et al. (2008), Huang et al. (2009)	R,O	2D	P	3	1		•	•	
Han and Huang (2007)	R,O	3D	S	1	1		•		
Huang and Han (2006a, 2006c)	L,S	2D,3D	P,S	3	3		•		
Huang and Han (2006b)	R	3D	ET	1	1		•		
Huang and Han (2008)	S	2D	P	5	3				

Table 2.6 Summary of numerical modeling studies by others (continued)

Numerical Modeling Study	Focus of Study	Model Type	Array type	Number of column spacings tested	Number of pile caps sizes tested	Embankment material properties varied in analysis	Geosynthetic reinforcement used in analysis	Reinforcement properties varied in analysis	Critical height(s) reported
Current Study	D,L	3D	S	2	3	1			•
Hossain and Rao (2006)	D,S	2D	P	1	1				
Jenck et al. (2007)*	D,L	2D	P	3	1	•			
Jones et al. (2010)	R	3D	S	1	3		•		
Jones et al. (1990)	L,R,S	2D	P	4	4	•	•		
Kempton and Naughton (2002),	L,R	3D	S	1	2	•	•	•	
Kempfert et al. (2004), Zaeske (2001)	L,R	2D	A	1	1		•		
Kempton et al. (1998)	L,R	2D,3D	P,S	1	8		•		
Liu et al. (2007)	L,D,R,S	3D	S	1	1		•		
Miki and Nozu (2004)	D,L,S	2D	P	1	1				
Oh and Shin (2007)	L,R,S	2D	P	3	1		•		
Pearlman and Porbaha (2006)	R,S	2D	A	2	2		•		
Rogbeck et al. (1998)	R	2D	P	1	1		•		
Plaut and Filz (2010)	R	2D	A	1	1		•	•	
Russell and Pierpoint (1997)	L,R,S	3D	S	1	2	•	•	•	
Smith (2005), Smith and Filz (2007), Filz and Smith (2006), Stewart and Filz (2005a), Stewart and Filz (2005b), Stewart et al. (2004)	L,R,S	2D,3D	S,ET,A	3	3	•	•	•	
Smith (2005)	L	2D	A	12	3	•			
Smith (2005)	L	2D	A	13	3	•	•	•	
Yan et al. (2006)	D,R	2D	P	1	1		•	•	

Table 2.7 Summary of the key aspects of the experimental and numerical studies summarized in Table 2.5 and Table 2.6

	Study type	
	Experimental	Numerical
Experimental scale		
benchtop scale	4	
centrifuge modeling	2	
laboratory scale	7	
field scale	12	
Dimensionality of numerical model		
2D		24
3D		13
Column array type		
square	15	12
equilateral triangular	1	2
isoceles triangular	0	0
rectangular	1	0
plane strain	8	16
axisymmetric	0	9
Includes reinforcement		
	17	26

Studies listed in Table 2.5 and Table 2.6 that are marked with an asterisk are summarized and interpreted in the appendices listed below:

Appendix D: Summary and interpretation of experimental study conducted by Chen et. al (2008)
Appendix E: Summary and interpretation of experimental and numerical studies conducted by Demerdash (1996)
Appendix F: Summary and interpretation of experimental study conducted by Ellis and Aslam (2009a,b)
Appendix G: Summary and interpretation of numerical study conducted by Han and Gabr (2002)
Appendix H: Summary and interpretation of experimental and numerical studies by Jenck et al. (2007)

Interpretation of the studies involved using reported measurements of surface deformation to determine critical heights and/or using load-displacement measurements to determine the magnitude of differential base settlement corresponding to peak load transfer to

the column. From the experimental studies, including the current study, critical heights for 10 unique 3D unit cell geometries were determined. For 2D plane strain conditions, 8 unique critical heights were determined from the numerical analyses and experiments. A summary of the critical heights determined using the experimental and numerical studies, excluding the current study, is provided in Table 2.8. Details and comparison to the results from the current experimental study are presented in Chapter 6 and in the appendices listed above.

Table 2.8 Summary of critical heights interpreted from experimental and numerical studies by others

Reference	(E)Xperimental study, (N)umerical study	Reinforcement Array Type	Column spacing,s (in.)	Column diameter, d [1] (in.)	Spanning ratio, s'/d	Critical height, H_{crit} [2] (in.)	H_{crit}/d
Chen et al. (2008)	E	P		29.5	5.9	2.00	33.1 to 37.8	5.60 to 6.41
Demerdash (1996)	E	S	•[3]	23.6	8.9	1.38	27.5 to 31.5	3.10 to 3.55
Demerdash (1996)	E	S	•[4]	23.6	8.9	1.38	25.3 to 31.5	2.85 to 3.55
Demerdash (1996)	E	S	•[5]	23.6	8.9	1.38	27.1 to 31.5	3.05 to 3.55
Demerdash (1996)	E	S	•[3]	23.6	11.1	1.00	28.9 to 31.6	2.60 to 2.84
Demerdash (1996)	E	S	•[3]	23.6	13.3	0.75	20.0 to 23.6	1.50 to 1.77
Demerdash (1996)	N	P	•	78.7	39.4	0.91	118.0	3.00
Demerdash (1996)	N	P	•	118.1	39.4	1.62	157.0	4.00
Demerdash (1996)	N	P	•	157.5	39.4	2.33	236.0	6.00
Ellis and Aslam (2009a,b)	E	S		118.1	40.0	1.59	130.6	3.27
Han and Gabr (2002)	N	A	•	118.1	27.6	1.64	118.1	4.29
Jenck et al. (2007)	E,N	P		12.6	3.9	1.10	10.2 to 13.4	2.60 to 3.40
Jenck et al. (2007)	E,N	P		17.7	3.9	1.75	15.8 to 19.7	4.00 to 5.00
Jenck et al. (2007)	E,N	P		25.6	3.9	2.75	15.8 to 23.6	4.00 to 6.00
Sloan (2011)	E	S	•	72.0	24.0	1.62	78.0	3.25

Notes:

1. Square pile caps are expressed as circular caps of equal area
2. Range of heights reflect max. and min. interpretation of data. See corresponding appendices for details.
3. Default reinforcement stiffness. See Appendix E for details.
4. 1/3 of default reinforcement stiffness. See Appendix E for details.
5. 4/7 of default reinforcement stiffness. See Appendix E for details.

2.4 Selected Case Histories

Table 2.9 provides essential details on unit cell geometry and embankment height for 24 case histories identified during the literature review. The key provided at the beginning of Table 2.4 is also applicable to Table 2.9. English units are used in the table to be consistent with the presentation of the current experiments in other chapters. The table also indicates whether reinforcement was used and whether differential surface settlement was observed. In some cases, the embankment surface was described as having 'insignificant' differential settlement or the embankment was reported to be in service without any problems. These instances were interpreted as not having differential surface settlement.

To supplement the case history data, the unit cell geometries and embankment heights from 16 experimental studies are provided in Table 2.10. It was not possible, with the information available, to determine critical heights for the cases listed in Table 2.10. The studies listed in Table 2.5 that are not included in Table 2.10 had ambiguous descriptions of either unit cell geometry, sample height, or whether the surface was observed for evidence of differential settlement. In Table 2.9 and Table 2.10, square pile caps are dimensioned as circular pile caps of equal area. Appendix I describes the process used to interpret the case history presented by Ting et al. (1994) to determine a value of critical height for the unit cell geometry. The information presented in Table 2.9 and Table 2.10 and in Appendix I is used in Chapter 7, along with the critical heights determined from previous experimental an numerical studies, to validate the findings from the experimental tests described in Chapters 3, 4, and 5.

Table 2.9 Embankment heights and unit cell geometries reported for case histories identified during the literature review

Case History	Array type	Column spacing (ft)	Cap diameter or equivalent diameter (ft)	Embankment height (ft)	Spanning Ratio	Reinforcement used in embankment	Differential surface settlement reported
Alexiew (2000, 1996)	S	6.23	1.13	6.56	3.40	•	
Alexiew (2000)	ET	5.24	1.96	7.54	1.04	•	
Camp and Siegel (2006) and S&ME (2004)	ET	8.20	3.00	2.16 to 3.6	1.07	•	•
Chen et al. (2010)	S	6.56 to 9.84	3.70 to 5.92	19.68	0.68 to 0.75		
Chen et al. (2010)	S	6.56 to 8.20	3.33 to 3.70	13.12	0.89 to 1.07	•	
Chen et al. (2010)	T	7.21 to 8.86	4.59	16.40	0.61 to 0.86	•	
Chin (1985)	ST	10.49 to 12.47	6.66	10.95 to 18.96	0.48 to 0.67		
Coghlin (2005)	ET	?	?	?		•	•
Collin et al. (2005b)	ET	8.00 to 8.86	2.00	11.48	1.80 to 2.06	•	
Gwede and Horgan (2008)	S	8.20	3.33	6.56	1.24	•	
Han and Akins (2002)	?	8.53 to 9.84	2.25	12.14	?	•	
Habib et al. (2002)	ET	8.20	2.59	5.08	1.33	•	
Hoppe and Hite (2006)	S	7.00	3.38	4.3 to 6.3	0.96	•	
Liu et al. (2007)	S	9.84	3.28	18.37	1.62	•	
Livesey et al. (2008)	R	9.51 x 8.20	2.95	<16.4	1.62	•	
Maddison et al. (1996)	ET	7.21 to 8.86	1.80	7.21 to 18.7	1.81 to 2.34	•	•
Pearlman and Porbaha (2006)	S	3.28	1.38	9.84 to 24.61	1.68	•	
Russell and Pierpoint (1997)	S	8.20	3.70	19.02	1.07		
Ryan et al. (2004)	R	6.89 x 3.28	0.49 to 0.66	3.94	5.28 to 7.29	•	•
Ryan et al. (2004)	R	6.89 x 6.56	0.98	3.94	4.35	•	•
de Mello et al. (2008)	ET	5.90 to 7.22	2.30	16.4 to 27.9	0.98 to 1.31		
Smith (2005), Stewart et al. (2004)	T	6.00 to 10.00	2.66	21	0.8 to 1.67		
Ting et. al (1994)	ST	11.15 to 13.78	6.66	10.83 to 19.03	0.55 to 0.79		•
Wood et al. (2004)	S	8.86 to 10.50	2.95	13.12 to 31.17	1.62 to 2.02	•	

Table 2.10 Embankment heights and unit cell geometries reported for experimental studies

Experimental studies	Array type	Column spacing (ft)	Cap diameter or equivalent diameter (ft)	Embankment height (ft)	Spanning Ratio	Reinforcement used in embankment	Differential surface settlement reported
Abdullah and Edil (2007a)	S	8.20 to 10.66	2.46	11.48	1.86 to 2.56	•	
Almeida et al. (2008, 2007)	S	8.2	2.96	3.94	1.46	•	•
Almeida et al. (2008)	S	9.20	3.70	4.59	1.26	•	•
Chew et al. (2004)	R	6.82 x 3.94	0.69	1.64 to 3.28	5.20	•	•
Fluet et al. (1986)	P	15.42	8.20	4.92	0.44	•	•
Hossain and Rao (2006)	S	3.94	1.31	6.56	1.63		
Miki (1997)	P	4.26 to 7.54	3.28	6.56	0.15 to 0.65		
Oh and Shin (2007)	S	1.97	0.56	8.86	1.99		
Oh and Shin (2007)	S	1.97 to 3.11	0.56	8.86	1.99 to 3.43	•	
Quigley et al. (2003)	ET	9.02	2.95	6.07	1.26	•	
Rogbeck et al. (1998)	S	7.87	4.44	5.58	0.75		
Sloan (2011)	S	10.00	2.00	4.10	3.04	•	•
Van Eekelen et al (2008)	S	4.17	0.98	3.77	2.51		
Van Eekelen et al (2003)	P	3.77	0.49	2.30	3.33		•
Villard et al. (2004)	ET	3.94	0.67	1.64 to 3.28	2.90	•	•
Xu et al. (2007)	ET	6.56	1.31	20.64	2.39	•	

2.5 Examination of Analogous Systems

Two systems, the pullout of embedded anchors and propagation of fault rupture, were identified as sharing characteristics similar to the single column tests described in Chapter 3 and reported in Chapter 4. These systems are shown in Figure 2.2 and Figure 2.3 with the current

notation presented alongside the notation typically used in the literature for the similar systems. The current notation is used in the review presented herein.

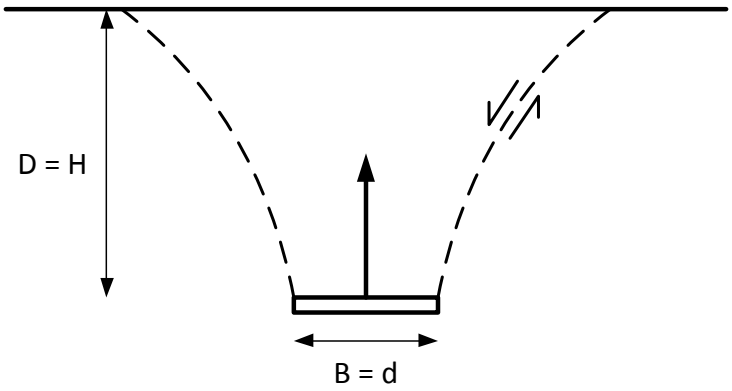

Figure 2.2 Pullout of an embedded anchor with a vertical axis. The embedded depth of the anchor, D, is analogous to the embankment height, H, and the anchor dimension, B, is analogous to the pile cap diameter, d

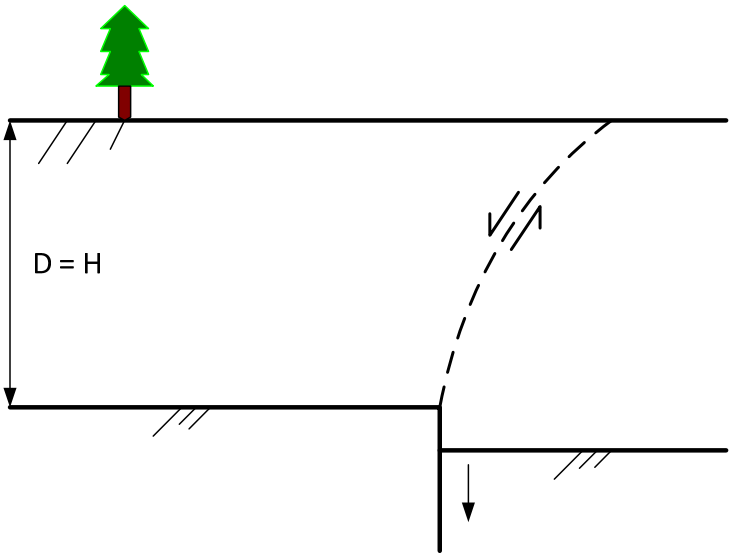

Figure 2.3 Propagation of vertical faulting through a soil profile. The thickness of the soil profile, D, is analogous to the embankment height, H

Considerable research has been done to investigate how shearing propagates through soil overlying an embedded anchor during pullout or over a fault during rupture. Much research has also been done to evaluate the load-displacement behavior of anchors. A limited amount of research identified during this study investigates the behavior of a group of anchors. Bray et al. (1994a) underscored the utility of studying analogous problems, such as the behavior of embedded anchors during pullout, to gain insights on the propagation of fault rupture. The purpose of this review is to leverage the findings from these studies to better understand the

interaction between a single column and an embankment when the embankment foundation settles around the column.

The review of anchor pullout and fault rupture propagation research is organized into four sections. Section 2.5.1 introduces the literature that was reviewed, Section 2.5.2 summarizes the findings related to propagation of shearing through a sand profile, Section 2.5.3 discusses the load-displacement behavior of anchors and evaluates different methods to estimate the ultimate pullout load on the anchor, and Section 2.5.4 presents some findings related to surface deformation over an anchor during pullout.

2.5.1 Review of published material

Table 2.12 summarizes the literature that was reviewed and found to be relevant to the current study. The table indicates the focus area of the study, what methods were used, and the relevancy of the findings to the current research. The table also indicates whether the reference introduces a method to estimate the pullout capacity of an anchor and whether the method can be readily adapted to estimate the stress acting on a column due to settlement of an embankment around a column. A key for interpreting Table 2.12 is provided in Table 2.11.

Table 2.11 Key for Table 2.12

Focus of Study		Anchor Shapes	
Fault rupture progagation	F	Circular / axisymmetric	C
Anchor pullout	A	Square	S
		Rectangular / strip	R

Relevancy Rating

No relevant content *(blank)*

1 - Topic is mentioned but no significant insights are presented

2 - Topic is discussed and some insights are presented

3 - Topic is extensively discussed and significant insights are presented

Table 2.12 Summary of analogous research reviewed

Publication	Focus of study	Experimental study	Theoretical study	Numerical modeling study	Integrated investigation using previous studies	Presents method for estimating pullout resistance?	Anchor shapes considered	Method readily adaptable to current study?	Multiple anchor pullout methods evaluated?	Relevant insights on load-displacement relationship?	Relevant insights on shearing through soil profile?
Anastasopoulos et al. (2007)	F	•		•							1
Bray et al. (1994a)	F				•						1
Cole and Lade (1984)	F	•	•								3
Das and Seely (1975)	A	•					S,R				
Dickin and Laman (2006)	A	•		•			S,R			2	
Fadl (1981)	A	•	•	•	•	•	C	Y	•	3	3
Ilamparuthi and Muthukrishnaiah (1999)	A	•					C			3	3
Kumar and Kouzer (2008a)	A			•			R		•		1
Kumar and Kouzer (2008b)	A		•								3
Koutsabeloulis and Griffiths (1989)	A			•		•	C,R	Y	•	2	1
Matsuo (1968)	A	•	•			•	C	N		1	1
Matsuo (1967)	A	•	•			•	C,S,R	N		1	1
Merifield and Sloan (2006)	A			•			R		•		
Meyerhof and Adams (1968)	A	•	•			•	C,S,R	Y			
Murray and Geddes (1989)	A	•				•	C,S,R	Y		2	1
Rowe and Davis (1982)	A	•		•		•	S,R	Y	•	3	
Sutherland (1965)	A	•					C		•		
Sutherland (1988)	A				•				•		
Tanaka and Sakai(1993)	A	•		•			R			2	2
Vardoulakis et al. (1981)	A	•	•			•	R	N			2
Vermeer and Sutjiadi (1985)	A		•	•			S,R	Y	•	1	1
Vesic (1971)	A		•			•	C,S,R	Y	•		2

2.5.2 Propagation of shearing through a sand profile

This section discusses some key findings and discussion related to how shearing propagates from the boundary of a fault or anchor through a sand profile. There are studies, such as by Vesic (1971) and Bray et al. (1994b), which investigate shearing through a clay profile; however, the current focus is on cohesionless materials, which are often used in engineered embankments. Depending on the profile thickness, magnitude of base displacement, and material density, shearing can either reach the ground surface or be contained within the soil profile. Using experimental model tests, Bray et al. (1994a) found that a vertical base displacement with a magnitude of about 4 percent of the profile thickness is needed to fully develop the shearing surface. Bray et al. (1994a) indicate that loose profiles are more compressible and require larger base displacements. In the context of embedded anchors, anchor failures are typically described as being either 'shallow' or 'deep' (Meyerhof and Adams, 1968, Fadl 1981, Das and Seely, 1975, Ilamparuthi and Muthukrishnaiah, 1999, and others). Shallow anchor failures are characterized by shearing that reaches the ground surface, whereas deep failures are contained in a bulb of soil, with no differential deformation of the ground surface. Several authors have investigated the transition height between shallow and deep failure modes, which is often normalized by the anchor width and referred to as the critical embedment ratio. Meyerhof and Adams (1968), Ilamparuthi and Muthukrishnaiah (1999), and Fadl (1981) show that the critical embedment ratio increases with increasing friction angle of the sand. Since the single column tests described in Chapter 3 and discussed in Chapter 4 all exhibited differential surface deformation, the focus herein will be primarily on the shallow mode of failure; however, it is interesting to consider the parallels between the critical embedment depth for anchors and the critical height for GRCSEs.

Different shapes have been used to describe the failure surface produced by the shallow mode of anchor failure. The most common shapes are a vertical cylinder, cone, trumpet, circular arc, and log spiral. Approximate sketches of these shapes are provided in Figure 2.4. The failure surfaces are the result of the formation of shear bands, which are localized zones of shearing. Vardoulakis et al. (1981), Cole and Lade (1984), and others indicate that the tendency to form shear bands and their path of propagation is highly tied to the dilation angle of the sand. This is primarily due to the tendency for dilative soils to weaken at the location of shearing which further concentrates shear deformations in the weakened zones. This behavior is frequently seen

during triaxial testing of sands which dilate during shear resulting in a localized failure surface as opposed to a diffused 'barrel' failure for contractive materials.

Figure 2.4 Idealized shapes of failure surface for shallow mode of failure. Left to right: cylinder, cone, trumpet, circular arc, log spiral

Many authors agree that curved failure surfaces can be approximated by a linear failure surface as shown in Figure 2.5 defined by a line between the origination point of shearing and the location where the shearing intersects the ground surface. Table 2.13 provides various authors' recommendations for estimating the angle of a linear failure surface with respect to vertical, α. Most of the recommendations express α as a fraction of the peak friction angle of the sand, however Vermeer and Sutjiadi (1985) suggest the orientation is equal to the peak dilation angle, ψ.

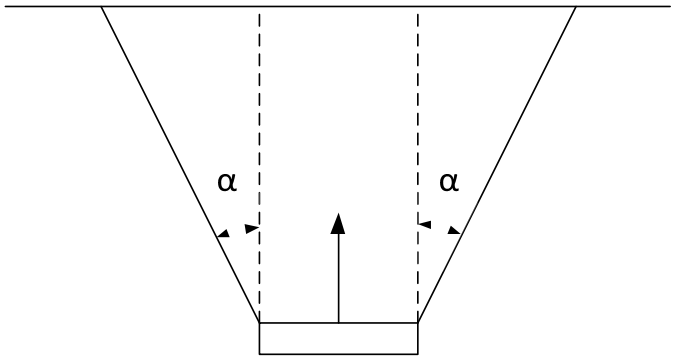

Figure 2.5 Orientation of linear failure surface from vertical

Table 2.13 Recommendations for estimating orientation of linear failure surface

Publication	**Angle of linear failure surface from vertical, α**
Fadl (1981)	$\frac{\phi}{4}\left[D_r\left(\frac{1+\cos^2\phi}{2}\right)+\left(\frac{1+\sin^2\phi}{2}\right)\right]$
Meyerhof and Adams (1968)	$\phi/3$
Ilamparuthi and Muthukrishnaiah (1999)	$\phi/2 \pm 2^o$
Kumar and Kouzer (2008a)	ϕ
Murray and Geddes (1989)	$\phi/2$
Vardoulakis et al. (1981)	18^o – For dense sands, 0^o- At critical state
Vermeer and Sutjiadi (1985)	ψ

Cole and Lade (1984) developed a theoretical model for estimating the orientation of a failure surface approximated as linear using the assumption that the actual failure surface follows a log spiral. They validated their theoretical model against laboratory model testing and achieved good agreement between their predicted and measured results. Figure 2.6 was developed using their model for the case where the fault orientation is vertical, which is similar to the boundary between a pile cap and the settling foundation soil.

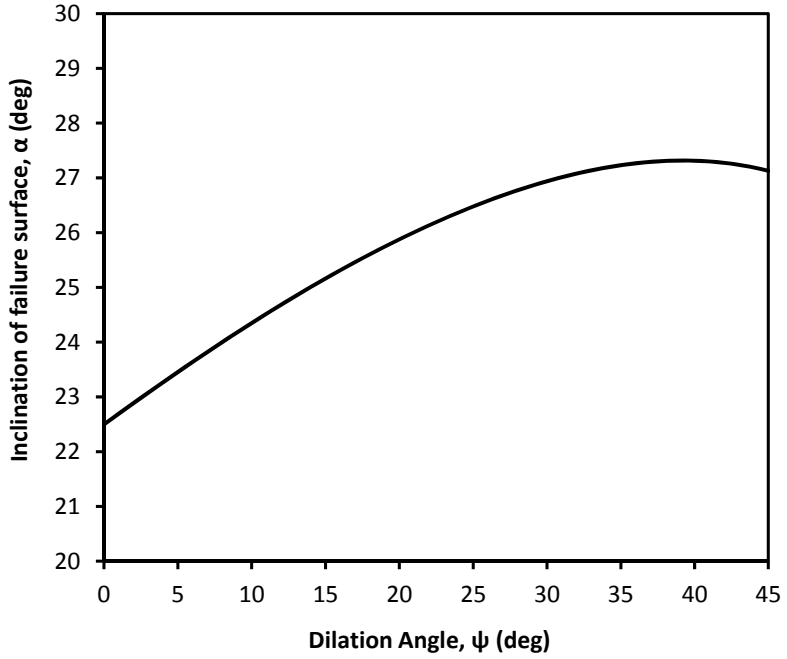

Figure 2.6 Orientation of linear failure surface versus dilation angle using model by Cole and Lade (1984)

As discussed in Chapter 4, the failure surface through the sample was delineated using measurements of surface deformation. Based on all the tests using the single column configuration, the inclination of a line from the column edge to the outermost limit of surface deformation, α, was oriented approximately at an angle equal to the estimated peak dilation angle or 0.55 times the peak friction angle. These ratios are similar to the recommendations by Ilamparuthi and Muthukrishnaiah (1999), Murray and Geddes (1989), and Vermeer and Sutjiadi (1985).

2.5.4 Load-displacement relationships

As discussed in Dickin and Laman (2006), Fadl (1981), and Ilamparuthi and Muthukrishnaiah (1999), the load displacement behavior of shallow embedded anchors is characterized by three primary phases: 1) rapid rise in load to peak value with onset of displacement, 2) rapid decrease in load following peak, 3) leveling-off of load even at large displacements. This pattern of load displacement behavior is illustrated in Figure 2.7 and agrees with the findings from the single column test results reported in Chapter 4. At greater embedment ratios, H/d, the displacement at peak load increases and the drop in load following peak becomes less pronounced.

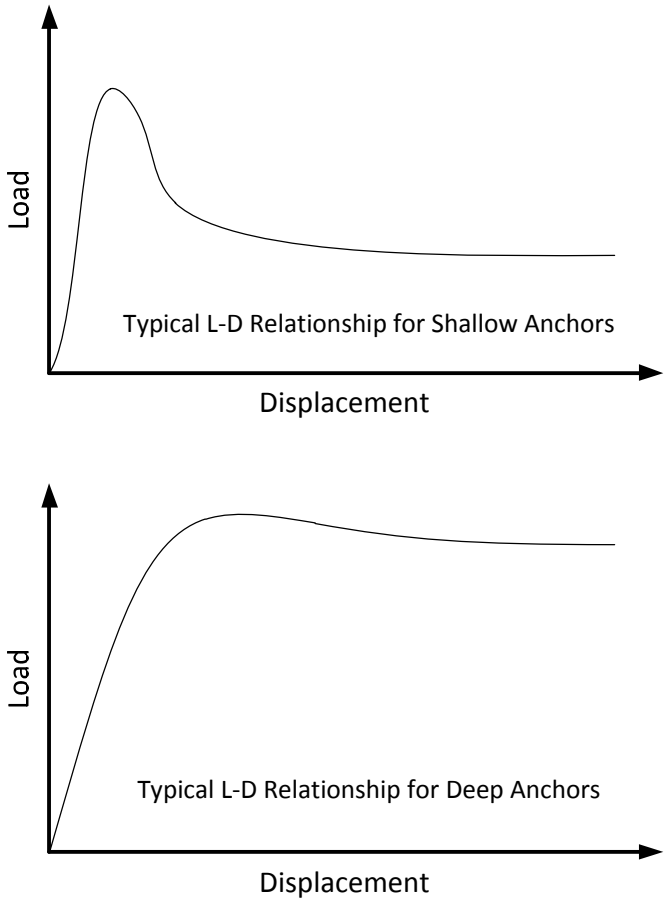

Figure 2.7 Typical load displacement relationships for shallow and deep anchors

Several authors have investigated the displacement required to reach the peak anchor capacity. Table 2.14 through Table 2.16 summarize the findings from experimental studies by others for anchors embedded in sand. The displacement at peak anchor capacity, δ_{max}, can be made dimensionless by normalizing by the anchor dimension, d. The results show that δ_{max}/d increases with increasing embedment ratio and decreasing relative density. Due to equivalence

discussed in Section 3.7.1 between fixing the column and lowering the base and holding the base fixed and raising the column, the anchor displacement δ is analogous to base settlement, S_b.

Table 2.14 δ_{max}/d determined by Dickin and Laman (2006) for strip anchors

	H/d=3	H/d=7
Dense sand	0.062	0.264
Loose sand	0.170	-

Table 2.15 δ_{max}/d determined by Murray and Geddes (1989) for circular anchors

	H/d=6
Dense sand	0.022
Medium Dense sand	0.105

Table 2.16 δ_{max}/d determined by Rowe and Davis (1982) for strip anchors

	H/d=3	H/d=5	H/d=8
Loose sand	0.045	0.149	0.184

Fadl (1981) and Ilamparuthi and Muthukrishnaiah (1999) provide tables of testing results, which were used to develop Figure 2.8 and Figure 2.9. The data suggest that δ_{max}/d increases with embedment ratio, but it is difficult to argue that the range of densities considered have a significant impact.

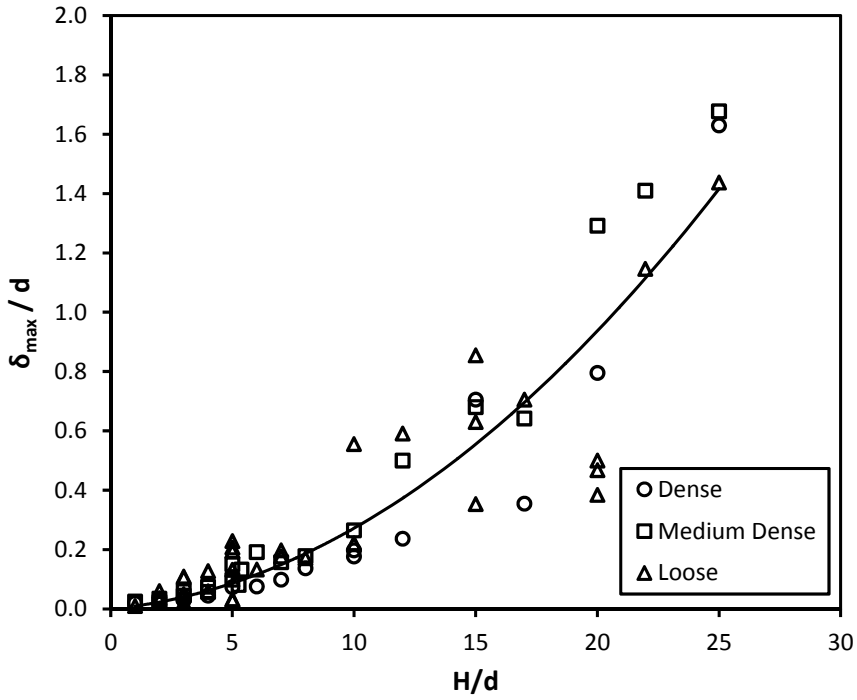

Figure 2.8 Normalized anchor displacement at peak capacity versus embedment ratio for circular anchors using data by Fadl (1981)

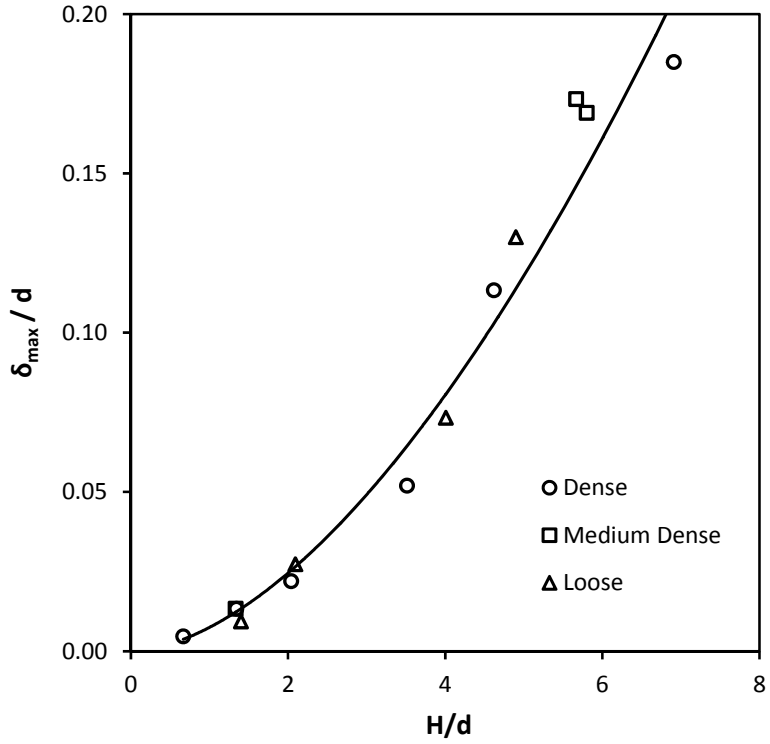

Figure 2.9 Normalized anchor displacement at peak capacity versus embedment ratio for circular anchors using data by Ilamparuthi and Muthukrishnaiah (1999)

As shown in Table 2.12, many authors provide methods to estimate the soil stress acting on the anchor at peak capacity. Eight of the methods listed in Table 2.12 can be readily adapted to estimate the ratio of peak stress acting on the column to the initial overburden stress, $\sigma_{col,max}/\sigma_o$. For embedded anchors, the ratio of peak anchor stress to initial vertical stress is often referred to in the literature as the 'breakout factor'. Since the breakout factor is analogous to the ratio $\sigma_{col,max}/\sigma_{o,}$ it is used in this section. In Chapter 4, the ratio $\sigma_{col,max}/\sigma_o+q$ is defined as the peak column stress factor. Most of the published methods do not consider the influence of an applied surcharge on anchor capacity, since surcharges are often considered to be nonpermanent. Each method is introduced below in outline format and presented in an adapted form. Some of the methods require considerable algebraic manipulation and digitization of chart solutions to obtain the forms presented herein. The current set of notation is used in all equations, and no intermediate steps in the adaptations are provided. Any unique notation is defined using the notation found in the published source. It is noted where the original notation conflicts with the current set of notation.

1. Fadl (1981): In his dissertation, Fadl presents what he calls 'the approximate method' for estimating the pullout capacity of circular anchors at shallow and deep embedment ratios.

He developed his theory using the theory by Matsuo (1968) as a starting point. Matsuo's theory assumes a log spiral failure surface and is too complex to be readily adapted to the current problem. Fadl validated his method against extensive experimental tests, a numerical model, and comparison to testing and theories developed by others. Fadl's methods for shallow and deep failure modes are both presented here. The method for the deep failure mode is included because it gives an example of how the shallow pullout capacity compares to capacity for anchors deeper than the critical embedment ratio. Equation 2.1 provides Fadl's expression for estimating the breakout factor, $\sigma_{col,max}/\sigma_o$, for shallow anchors. After some manipulation, the expression reduces to the form given in Equation 2.2. Recall that α is the straight line approximation of the angle between the failure surface and a vertical projection of the anchor boundary. The equivalent expression for the deep failure mode is given by Equation 2.3. Again, after some manipulation, the expression reduces to the form given by Equation 2.4. The height of the critical embedment depth above the anchor is given by H^* and the shearing resistance along the failure surface above the critical embedment depth to the ground surface ($H-H^*$) is given by T^*. When the embedment depth, H, equals the critical embedment depth, Equation 2.4 reduces to Equation 2.2

$$\frac{\sigma_{col,max}}{\sigma_0} = \frac{1}{3d^2}\left[\left(4H^2\tan^2\alpha + 6Hd\tan\alpha + 3d^2\right) + 2H\tan\alpha\left(3d + 2H\tan\alpha\right)\right] \quad (2.1)$$

$$\frac{\sigma_{col,max}}{\sigma_0} = \frac{8}{3}\left[\tan\alpha\left(\frac{H}{d}\right)\right]^2 + 4\left[\tan\alpha\left(\frac{H}{d}\right)\right] + 1 \quad (2.2)$$

$$\frac{\sigma_{col,max}}{\sigma_0} = \frac{1}{3d^2H}\left[\begin{array}{l} 4H^{*3}\tan^2\alpha + 6H^{*2}d\tan\alpha + 3d^2H + 12H^*\tan\alpha\left(H - H^*\right) \\ \left(d + H\tan\alpha\right) + 2\tan\alpha\left(3d\left(2H - H^*\right) + 2H^*\left(3H - 2H^*\right)\tan\alpha\right) \end{array}\right] + T^* \quad (2.3)$$

$$\frac{\sigma_{col,max}}{\sigma_0} = \frac{8}{3}\left[\tan\alpha\left(\frac{H}{d}\right)\right]^2\left(3 - \frac{2H^*}{H}\right) + 4\left[\tan\alpha\left(\frac{H}{d}\right)\right]\left(2 - \frac{H^*}{H}\right) + T^* + 1 \quad (2.4)$$

2. Koutsabeloulis and Griffths (1989): This method was developed to fit the results of numerical analysis and the results obtained by Rowe and Davis (1982). Equation 2.5 presents the original version of the method. The factors R_ϕ and $R_{\phi\theta}$ adapt the plane strain solution to axisymmetric conditions. These factors are determined from a chart as a function of friction angle. For this study, the chart was digitized and best fit lines were developed which had R^2 values of 0.99 and 0.93 for R_ϕ and $R_{\phi\theta}$, respectively. Beyond a friction angle of 35°, the correction for axisymmetric conditions becomes insensitive to ϕ and can be expressed by $e^{0.318H/d}$.

$$\frac{\sigma_{col,max}}{\sigma_o} = \left[\frac{H}{d}\sin\left(\phi+\psi\right)+1\right]\left(R_\phi^{-R_{\phi\theta}H/d}\right)$$

where

$$\text{for } 0 \le \phi \le 35^o,\ \begin{cases} R_\phi \approx 0.0002\phi^3 - 0.0189\phi^3 + 0.7254\phi \\ R_{\phi\theta} \approx 0.001\phi^3 - 0.0167\phi^2 + 0.8316\phi \end{cases} \tag{2.5}$$

$$\text{for } \phi > 35^o,\ \left(R_\phi^{-R_{\phi\theta}H/d}\right) \approx e^{0.318H/d}$$

3. Merifield and Sloan (2006): The author presents chart solutions for $\sigma_{col,max}/\sigma_o$ as a function of friction angle and embedment ratio for plane strain conditions. For embedment ratios up to 5, the chart solutions can be represented by Equation 2.6 with R^2 value of 1.00.

$$\frac{\sigma_{col,max}}{\sigma_o} = \tan\phi\left(\frac{H}{d}\right)+1 \tag{2.6}$$

4. Meyerhof and Adams (1968): The authors developed theoretical methods for shallow and deep failure modes for plane strain conditions. Their methods were validated using laboratory tests. Meyerhof and Adams adapt their plane strain solutions to circular and rectangular areas by defining a shape factor, s. Equation 2.7 provides their method for estimating $\sigma_{col,max}/\sigma_o$ for shallow embedment in a cohesionless soil profile. The original version of the expression includes an uplift earth pressure coefficient; however, it is stated that the coefficient can be taken to have a value of 0.95 for a wide range of conditions. The shape factor, s, is expressed as s^* in Equation 2.7 to avoid confusion with the notation used elsewhere for column spacing. The shape factor is given in table form as a function of friction angle and embedment ratio. The expressions for s^* given in Equation 2.7 were developed using best fit lines having $R^2 = 1.00$

$$\frac{\sigma_{col,max}}{\sigma_o} = 1.9s^*\left[\tan\phi\left(\frac{H}{d}\right)\right]+1$$

where (2.7)

$$s^* = \min\begin{cases} 1+\left(1.1\cdot10^{-5}\right)\phi^{2.815}\left(\dfrac{H}{d}\right) \\ 1+\left(1.1\cdot10^{-5}\right)\phi^{2.815}\left(0.809e^{0.536\phi}\right) \end{cases}$$

5. Murray and Geddes (1989): The authors used theory and empirical observations from their laboratory testing program to develop a method to estimate the breakout factor for circular anchors. Their expression is given by Equation 2.8.

$$\frac{\sigma_{col,max}}{\sigma_o} = \frac{2H}{d}\left(\sin\phi + \sin\frac{\phi}{2}\right)\left(\frac{2H}{3d}\tan\left(\frac{\phi}{2}\right)\left(2-\sin\phi\right)+1\right)+1 \tag{2.8}$$

6. Rowe and Davis (1982): This method was developed from the results of a numerical parametric study for plane strain conditions. The approach was validated using 47 model tests, only 2 of which used anchors with a length-to-width aspect ratio of 1:1. Rowe and Davis state that the unit area anchor capacity for the 1:1 anchors is 220% of the unit capacity for strip anchors. Sutherland (1988) used Rowe and Davis' plane strain approach for estimating the capacity of circular anchors by multiplying the plane strain result by 2.2. This approach is adopted herein and is given by Equation 2.9. The factor F_y is the baseline breakout factor for plane strain conditions and is a function of embedment and friction angle. The factors R_ψ, R_R, and R_K are correction factors for the effects of soil dilatency, anchor roughness, and initial stress state, respectively. Based on their findings, Rowe and Davis concluded that the effects of anchor roughness and initial stress state are small, and therefore R_R and R_K can be assumed to be equal to unity. The factors F_y and R_ψ are determined using chart solutions. The chart solutions were digitized, and best fit lines were applied with R^2 values equal to 1.00. The best fit expressions for F_y and R_ψ are given by Equations 2.10 and 2.11, respectively.

$$\frac{\sigma_{col,max}}{\sigma_o} = 2.2F_yR_\psi R_R R_K \tag{2.9}$$

$$F_y \approx 2.317F_y^* - 1.1308$$

where (2.10)

$$F_y^* = \tan\left(\frac{\phi}{3}\right)\left(\frac{H}{d}\right)^{1.1} + 1$$

$$R_\psi = 0.14R_\psi^{*2} - 0.018R_\psi^* + 1$$

where (2.11)

$$R_\psi^* = \tan\left(\phi\right)\left(\frac{H}{d}\right)^{0.5}$$

7. Vermeer and Sutjiadi (1985): Vermeer and Sutjiadi developed a simple theoretical method for estimating the pullout capacity of rectangular anchors. Equation 2.12 represents their method for anchors with a 1:1 aspect ratio, where ϕ_{crit} represents the critical state friction angle. They validated their model by comparing their predicted pullout capacities to those calculated from a numerical model and the model tests conducted by Rowe and Davis (1982).

$$\frac{\sigma_{col,max}}{\sigma_o} = 2\cos\phi_{crit}\tan\phi\left(\frac{H}{d}\right)+1 \tag{2.12}$$

8. Vesic (1971): Vesic developed a method for estimating the pullout capacity of shallow anchors by developing a theoretical solution for the expansion of a spherical cavity in a semi-infinite rigid-plastic solid. The solution is presented in table format, which was digitized as part of this study. Equation 2.13 fits Vesic's table solution with an R^2 value equal to 1.00. Vesic validate his solution against several model and field tests performed by others.

$$\frac{\sigma_{col,max}}{\sigma_0} = 1.178K^* - 0.0189K^{*2}$$

where (2.13)

$$K^* = \tan(\phi)\left(\frac{H}{d}\right)^{1.7} + 1$$

There is considerable commonality among the methods described above in terms of how the friction angle and embedment ratio influence the breakout factor. This likeness allows the methods to be expressed in a consistent format and compared. The consistent format is based on the derivation of a simple method for estimating the breakout factor based on Figure 2.10 for plane strain conditions.

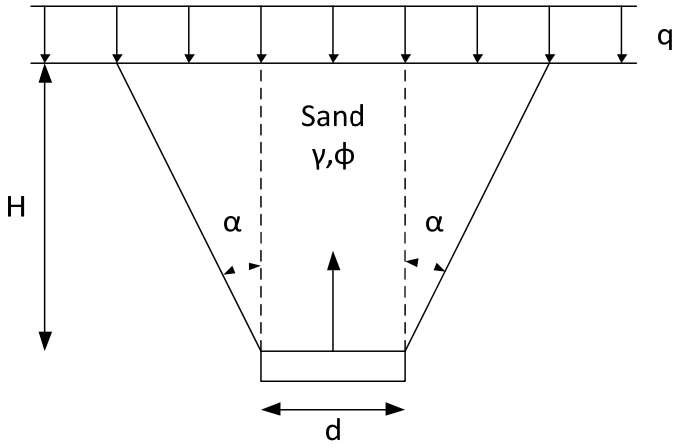

Figure 2.10 Basis for derivation of simplified method for estimating breakout factor

$$\sigma_{col,max} d = \left(d + 2H\tan(\alpha)\right)q + \tan\alpha\left(Hd + H^2\tan(\alpha)\right)\gamma \quad (2.14)$$

$$\frac{\sigma_{col,max}}{\sigma_o + q} = \tan\alpha\left(\frac{H}{d}\right)\left(\frac{2q + \sigma_o}{q + \sigma_o}\right) + 1 \quad (2.15)$$

where $\sigma_o = \gamma H$

$$\frac{\sigma_{col,max}}{\sigma_o + q} = A\left(N^*\right)^2 + B\left(N^*\right) + 1$$

where (2.16)

$$N^* = \tan\phi\left(\frac{H}{d}\right)\left(\frac{2q + \sigma_o}{q + \sigma_o}\right)$$

$$N^* = \tan\phi\left(\frac{H}{d}\right) \text{ when } q = 0 \quad (2.17)$$

The load acting on the column due to the weight of the sand and surcharge pressure within the failure surface can be determined according to Equation 2.14. Equation 2.15 is obtained by dividing Equation 2.14 by (γH+q)d, which is the load on the two-dimensional column due to the overburden from the soil and surcharge directly overlying the column. To account for 3D effects of a circular anchor, the difference between α and ϕ, and the contribution of shearing resistance along the failure surface, Equation 2.16 introduces an additional term and fitting parameters A and B. When there is no applied surcharge pressure, the dimensionless parameter N^* defined in Equation 2.16 reduces to the form given in Equation 2.17. For each method, Table 2.17 provides the best-fit values of the fitting parameters A and B determined by comparing the breakout factor calculated using Equations 2.1 through 2.13 for values of (tan ϕ)(H/d) ranging from approximately 0.7 to 7. Any assumptions made when converting the methods from the versions given in Equations 2.1 through 2.13 to the format given in 2.17 is provided in Table 2.17. The quality of the best fit values of coefficients A and B as determined by R^2 is also expressed in Table 2.17. As indicated by the values of R^2, all of the methods except for the method by Koutsabeloulis and Griffiths (1989) can be adapted to the form given by Equation 2.17 without significant change to the calculated value of breakout factor. Also included in Table 2.17 are the values of A and B which provided a reasonable fit to the results from the single column tests described in Chapters 3 and 4.

Table 2.17 Adaptation of methods for estimating ultimate pullout resistance to form given by Equation 2.17

Method	A	B	R^2	Assumptions
Fadl (1981)	0.101	1.485	0.98	$D_r = 0.866$ (Density 2 in Chap. 3)
Koutsabeloulis and Griffiths (1989)	0.164	3.153	0.65	
Meyerhof and Adams (1968)	1.310	0.640	0.99	
Merifield and Sloan (2006)	0.000	1.000	1.00	
Murray and Geddes (1989)	0.253	3.940	0.93	
Rowe and Davis (1982)	1.513	2.560	1.00	
Vermeer and Sutjiadi (1985)	0.000	1.700	0.98	$\phi_c = 32^o$
Vesic (1971)	0.263	1.877	0.96	
Current single column tests	0.298	1.409	0.92*	

*Based on unreinforced tests with applied surcharge pressure

The range of values for coefficients A and B in Table 2.17 suggests that there are significant differences among the methods. Figure 2.11 shows the values of breakout factor calculated using the methods listed in Table 2.17, except for the method by Koutsabeloulis and Griffiths (1989) which did not adapt well to the expression given by Equation 2.17. It is interesting that the relationship developed using the current single column tests predicts breakout factors essentially in the middle of the group.

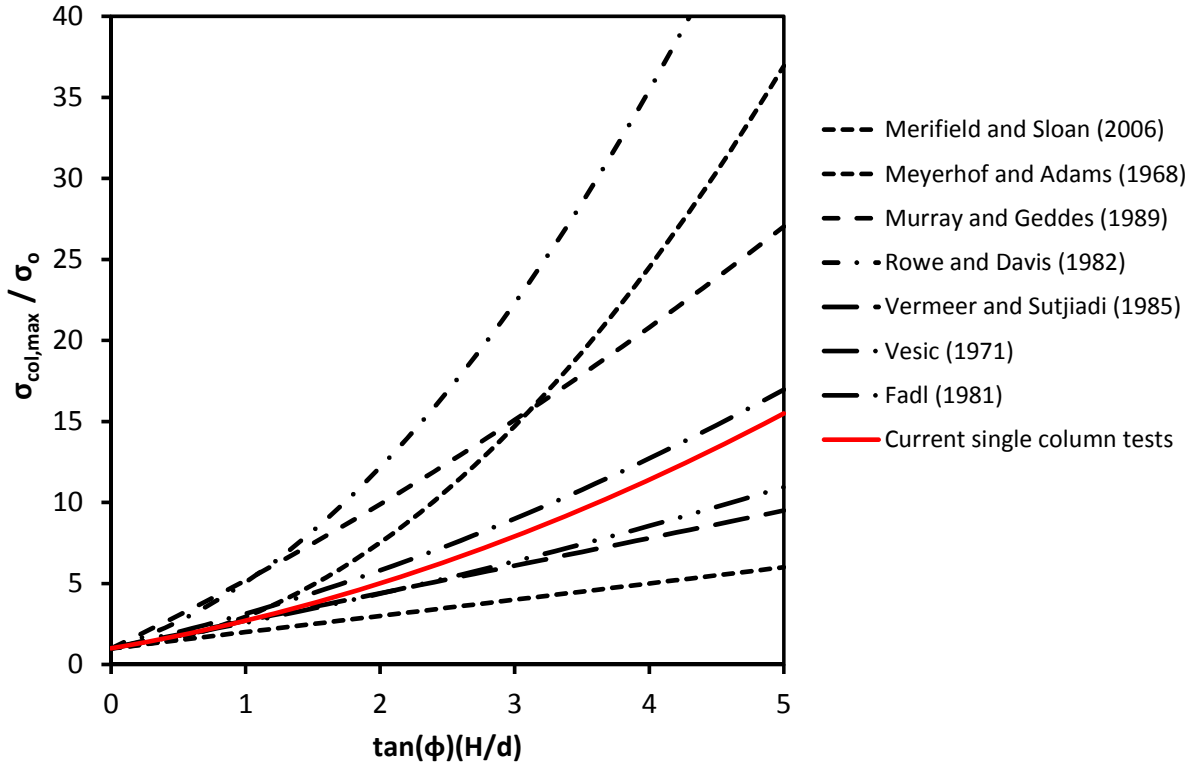

Figure 2.11 Graphical comparison of various methods for estimating breakout factor

The capacity of a group of embedded anchors was discussed by Kumar and Kouzer (2008b). They proposed a simple approach based on whether the failure surfaces from individual anchors interfered with the failure surfaces from adjacent columns. The variables determining whether such interference occurs are the embedment depth, the anchor spacing, and the inclination of the linear failure surface from vertical. This concept is illustrated in Figure 2.12. This approach is relevant to the current research since it proposes a way that the behavior of single columns can be used to understand the behavior of column arrays found in GRCEs.

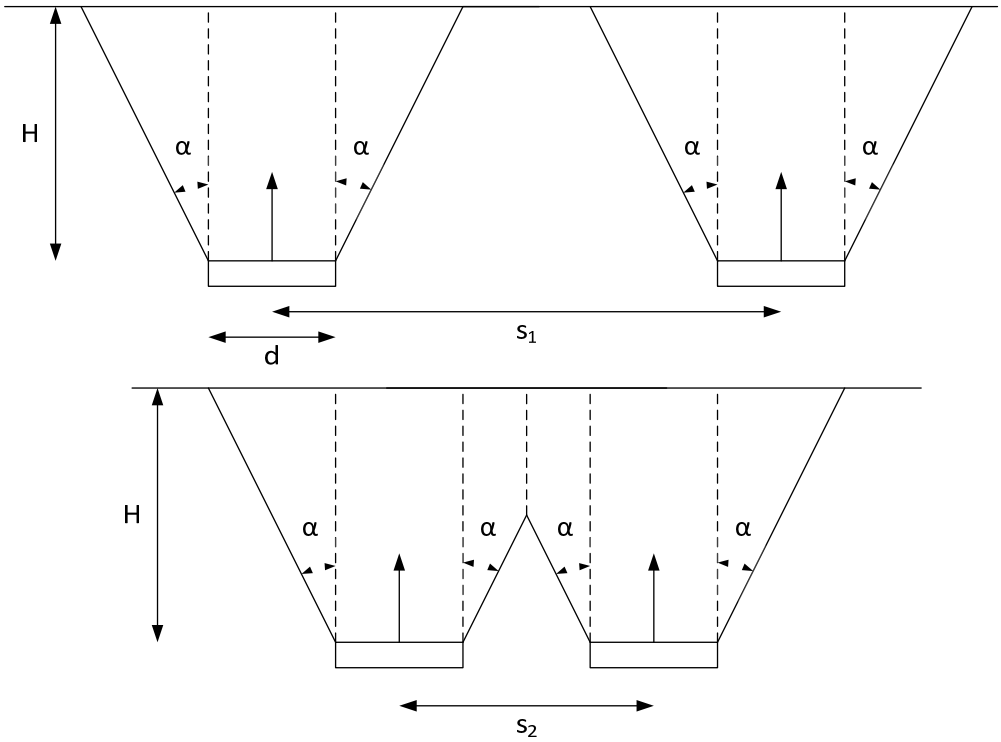

Figure 2.12 Concept proposed by Kumar and Kouzer (2008) for estimating the capacity of a group of embedded anchors. Top figure: Two isolated anchors ($s_1 > 2Htan\alpha+d$). Bottom figure: Two interacting anchors ($s2 < 2Htan\alpha+d$)

2.5.5 Surface deformation

There is not much in the literature about surface deformation resulting from shallow anchor failure. Fadl (1981) took surface measurements during his tests directly over the axis of the anchor and reported the ratio of magnitude of surface displacement to anchor displacement. Fadl tested sample heights ranging from 3 to 25 inches using circular anchors with diameters of 1, 1.5, 2, 2.5, and 3 inches. This means that Fadl's tests cover a wider range of sample heights than the current single column tests, but covers about the same range of diameters. All of his tests were performed using Leighton Buzzard Sand prepared at one of three densities described as dense, medium, and loose. Fadl reports friction angles of 41.0, 36.5, and 33.6 degrees respectively for the dense, medium, and loose samples. In Section 3.3.1, the peak friction angles

for Light Castle sand prepared at the three densities used in current testing are 56, 52, and 48 degrees listed in order of decreasing sample density. Figure 2.13 shows the relationship between surface deformation over the column normalized by anchor displacement versus the embedment ratio, H/d. The figure has been modified to reflect the notation used in this study. The change in sample height over the axis of the anchor is analogous to the change in sample height directly over the center of a single column, ΔH_c, and the anchor displacement is analogous to the magnitude of base settlement, S_b.

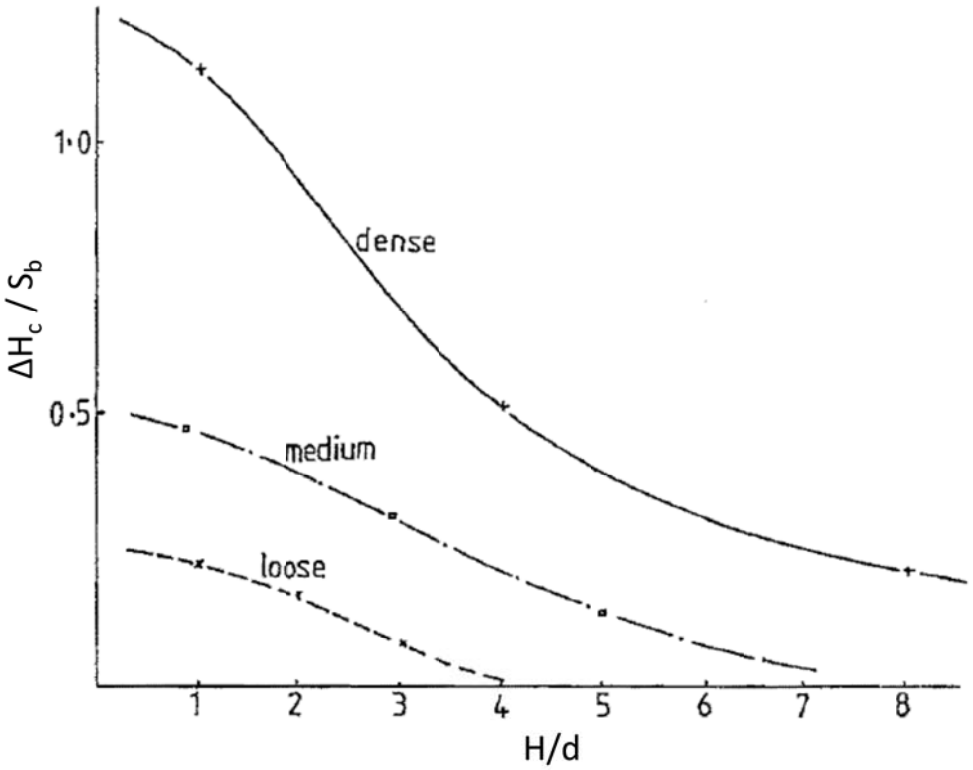

Figure 2.13 Relationship between normalized displacement over the axis of the anchor at maximum anchor capacity versus embedment ratio (adapted from Fadl, 1981, fair use)

As described in Section 3.7.1 there is equivalence between displacing the column, or anchor in this case, and holding the sample tank fixed and keeping the column fixed and lowering the sample tank. This means that there is equivalence between the displacement of the anchor and settlement of the base, S_b. Therefore, Fadl's results in Figure 2.13 can be converted to express the ratio of surface settlement over the anchor versus base settlement using Equation 3.8, which is repeated below as Equation 2.18. Since we are focusing on the location directly over the anchor, the term $(H(x)_n\text{-}H(x)_1)$ can be replaced with ΔH_c and the left side of the equation, $S(x)_n$, can be replaced with S_c, which is the settlement over the column. Dividing both sides of

Equation 2.18 by the base settlement to produce Equation 2.19 yields the settlement ratio over the column, SBR_c.

$$S(x)_n = S_b - \left(H(x)_n - H(x)_1\right) \tag{2.18}$$

$$SBR_c = \frac{S_c}{S_b} = 1 - \frac{\Delta H_c}{S_b} \tag{2.19}$$

After digitizing Fadl's results shown in Figure 2.13, Equation 2.19 was applied to convert the ratio of surface displacement to anchor displacement to the settlement ratio over the column, SBR_c. Figure 2.14 shows the result of this conversion, along with the settlement ratios calculated from the single column tests described in Chapter 3 and reported in Chapter 4. The current test results are not distinguished by sample density since most of the samples would be considered dense.

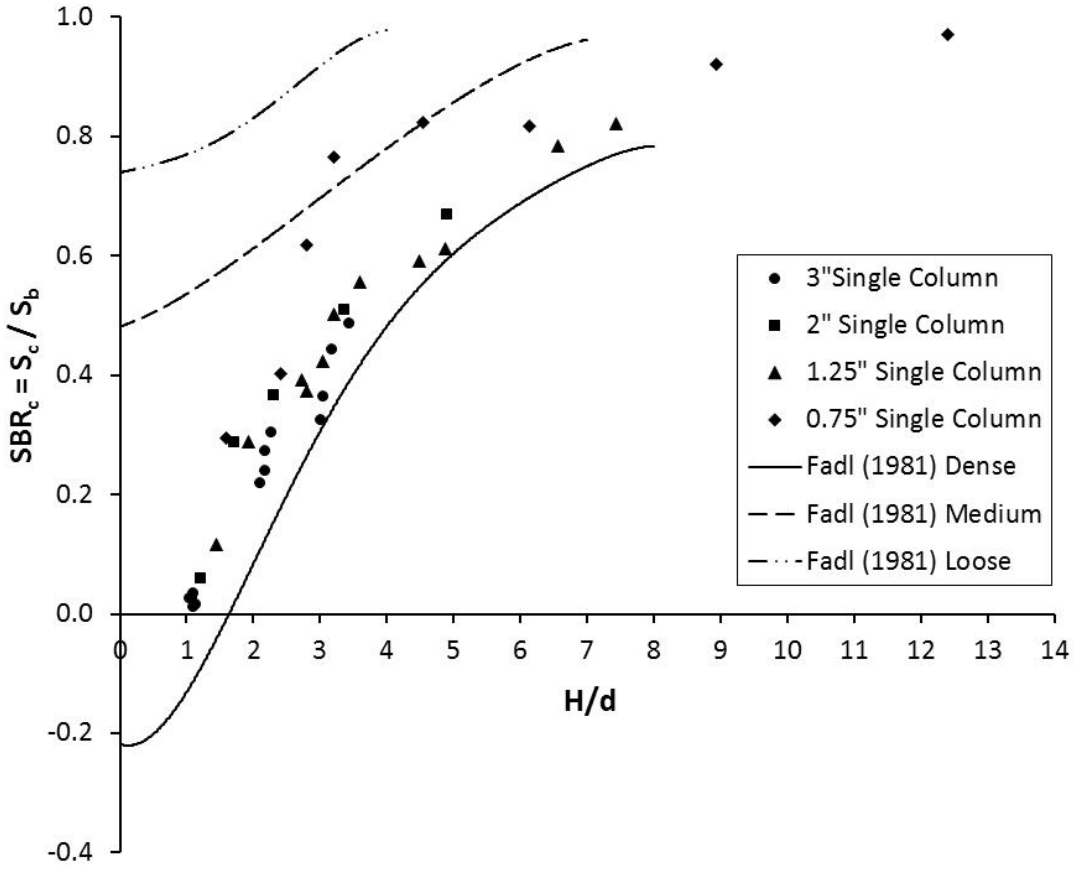

Figure 2.14 Settlement ratio, SBR_c determined using results by Fadl (1981) with results from single column tests described in Chapters 3 and 4.

Almost all of the results from the single column tests fall between Fadl's relationships for medium and dense samples, with better agreement with the relationship for dense samples. The agreement between the two sets of laboratory data represents a significant outcome since, as discussed in Chapter 5, the surface-to-base deformation relationship over the column obtained from single column testing is applicable to column arrays below the critical height. Another interesting observation is that, below an embedment ratio of about 1.7, Fadl's results for dense samples suggests that the ground surface over the column rises above its initial elevation in response to base settlement. This behavior was also observed by Ilampurathi and Muthukrishnaiah (1999) during their laboratory testing. They attributed the behavior to high levels of dilation occurring in the sand overlying the anchor during anchor displacement.

Meyerhof and Adams (1968) provide a relationship between friction angle and the critical embedment depth, H^*/d, which is shown in Figure 2.15. Since the critical embedment depth is defined by the anchor embedment where the failure surface is contained below the ground surface, it is analogous to the sample height at which a single column no longer influences ground settlement. From Figure 2.14, the current test results suggest that the ground settlement over the column equals the base settlement, corresponding to a SBR_c equal to unity, at an embedment ratio equal to about 13.5. Figure 2.15 shows that the embedment depth where SBR_c is projected to reach unity falls on the trend line defined by the relationship proposed by Meyerhof and Adams (1968).

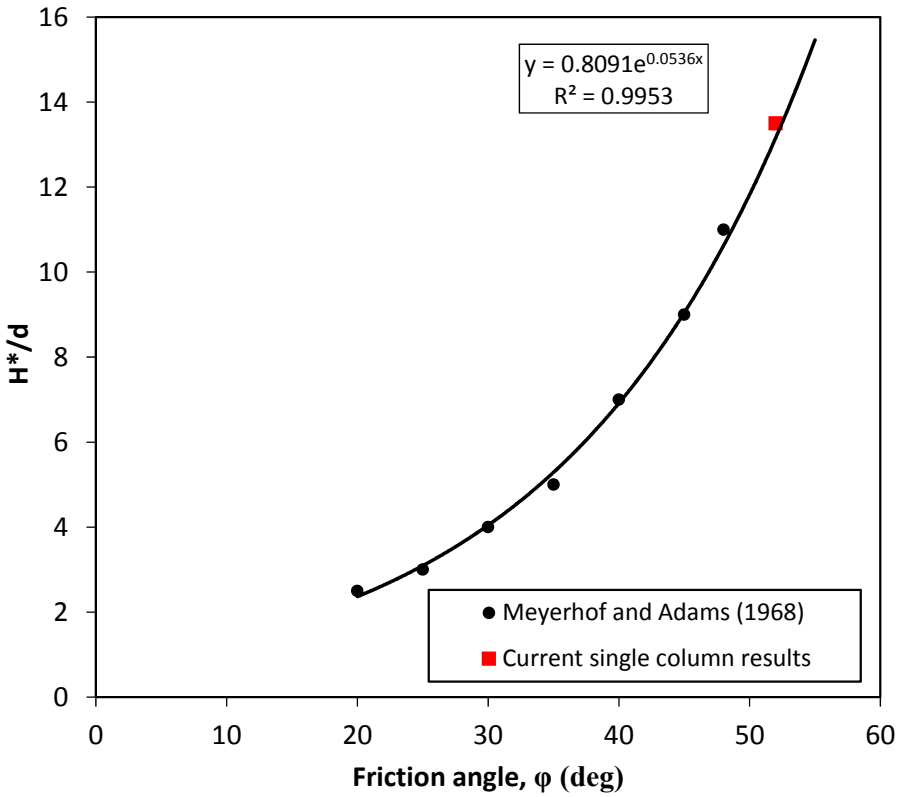

Figure 2.15 Plot showing Meyerhof and Adam's (1968) relationship between critical embedment ratio, H^*/d, and friction angle. Extrapolation of current results shown in red ($\phi = 52^o$ at Density 2, Section 3.3.1)

3 Laboratory Testing Equipment and Procedures

3.1 Objectives, Capabilities, and Overview of Testing Equipment

The primary objective of the experimental study is to investigate the influence of the parameters shown in Table 3.1 on surface deformation and critical height of samples of prepared sand. A second objective is to study the relationship between the vertical load acting on a single column and the relative displacement of the column into the base of the sample.

Table 3.1 Parameters investigated and associated capabilities of the bench scale apparatus

Parameter	Capability of equipment to evaluate parameter
Column Diameter	The apparatus can be configured to evaluate 5 different unit cell geometries with area replacement ratios ranging from 1 to 26 percent.
Column Spacing	
Sample Height	Sample heights up to about 10 inches can be tested. This height was sufficient to evaluate the critical height of the 5 unit cell geometries.
Presence and stiffness of reinforcement	Samples can be prepared with one or more layers of model reinforcement comprised of polypropylene netting with one of three tensile stiffnesses.
Surcharge pressure	Testing with a single column can be performed under subatmospheric conditions to produce an equivalent surcharge pressure up to 425 psf.
Base Settlement	The apparatus can continuously increase differential movement between the base of the sample and the column(s)

The current body of experimental work evaluating the internal and surface deformation of GRCSEs lacks a study that evaluates a wide range of area replacement ratios using a large number of tests performed with precise displacement measurements. Furthermore, a literature search could not identify a study that utilized a single apparatus to evaluate the influence of sample density and the presence, stiffness, and number of reinforcement layers on critical height.

The capabilities unique to this apparatus include the ability to configure columns in a 5x5 array with 3.5 inch c-c spacing, a 2x2 array with a 7.0 inch spacing, or a single column arrangement. When configured for testing columns arrays, the apparatus can evaluate 5 different unit cell geometries with area replacement ratios ranging from 1 to 26%, thus spanning the range of realistic values of replacement ratio. In a single column arrangement, the apparatus can evaluate four different column diameters.

Samples are prepared dry at one of three relative densities using the process of air pluviation. Samples can also be prepared with one or more layers of reinforcement modeled using polypropylene netting. Three different stiffnesses of netting can be used as reinforcement.

Differential movement between the columns and the base of the sample is displacement controlled using a motorized jack. To simplify the equipment, the base and lateral boundaries of the sample are held fixed and the columns are displaced upwards into the sample. This differential movement is exactly equivalent to fixing the columns and having the base and lateral boundaries of the sample settle uniformly. Surface deformations resulting from the differential movement at the base are measured using a non-contact laser distance transducer mounted to a linear motion carriage outfitted with a draw wire sensor. This arrangement provides the ability to obtain a profile of surface deformation without disturbing the sample surface.

Another unique feature of the testing equipment is the ability to apply a surcharge pressure to the sample by testing under subatmospheric conditions.

Influences of the lateral model boundary are mitigated by keeping the area of interest (unit cell or single column) away from the walls of the sample tank and, when possible, including extra rows of columns around the unit cell.

Performing the tests at the bench scale affords the ability to conduct a large number of tests and evaluate a wide range of parameter values. Bench scale testing also has the luxury of a controlled laboratory setting, which reduces the severity of environmental factors such as temperature and moisture. It also could be argued that obtaining reliable measurements is easier at the bench scale than at field scale.

The primary limitation to working at the bench scale is that scaling may influence how closely the model represents the full-scale system. The current apparatus represents a 1:10 to 1:20 scale model of field conditions by approximate application of scaling laws. One significant different between the bench scale testing conditions and field conditions are the low confining pressures present in the sample when testing under atmospheric conditions. The influence of confining pressure was found to have a minimal impact on surface deformation relative to base deformation by comparing the results from tests performed with and without applied surcharge pressures.

Another limitation of the testing equipment involves the relative movement between the base of the sample and the column. Since the base of the tank containing the sample is essentially rigid, the magnitude of differential settlement between the columns and the base of the sample is uniform. In field conditions, compression of the soils beneath the embankment is stress

controlled. Transfer of embankment and surcharge loads to the columns by arching within the embankment, tension developed in the reinforcement, and skin friction between the columns and the foundation soil, cause changes in stress in the compressible soils, and resulting settlement of the base of the embankment, to be non-uniform. As discussed in Section 7.2.2, the inclusion of reinforcement in the sample was found to introduce nonuniformity in the displacement of the base of the sample relative to the columns.

A final consideration is that, since the tests are displacement controlled, there is not a straightforward way to study the ability of the geosynthetic reinforcement to limit surface deformation by transferring load to the columns, thus reducing compression of the foundation soils. In a displacement controlled setup, the inclusion of reinforcement has two influences on the deformation behavior of the sample: 1) the reinforcement provides some vertical support to the overlying sand which has the effect of making the vertical displacement of the sample near the base non uniform and 2) the reinforcement provides some resistance to lateral movement of the sand due to interface friction and interlock of material in the reinforcement apertures. The vertical support provided is limited not only by the tensile stiffness of the reinforcement but also the ability of the sand to arch over the apertures and not pass through the reinforcement.

The testing program included performing 63 single column tests and 120 tests using column arrays. A summary of the parameter variation is provided in Section 3.6 and the details of parameter values for each test are provided in Appendix J.

Chapter 3 includes descriptions of the major components of the apparatus, a description of the data acquisition system, discussion of the material properties of the sand and reinforcement, details on sample preparation, an outline of test procedures, a summary of testing parameters, and a description of how data is reduced for analysis.

3.2 Description of the Apparatus

A bench-scale test apparatus was developed to investigate the relationship between embankment surface deformations and differential settlement of the foundation. The apparatus consists of a circular open PVC tank with an inside diameter of 22.83-inches that can be configured to study the column arrangements depicted in Table 3.2. For the 5x5 square array of columns, a column-centered unit cell can be defined according to Figure 1.2 around the central column. This unit cell definition requires a minimum of a 3x3 array, so the additional rows of

columns were considered sufficient to mitigate boundary effects. A soil-centered unit cell defined according to Figure 1.2 was used for the 2x2 array. While arguably not as insulated from boundary effects as the 5x5 array unit cell, a minimum distance of just under 6.5 inches is provided between the tank wall and the unit cell boundary. A schematic and a photo of the apparatus in elevation view are provided in Figure 3.1 and Figure 3.2.

Table 3.2 Unit cell geometry and column configurations evaluated in this study

	Single Column	2x2 Array	5x5 Array
Apparatus Configuration	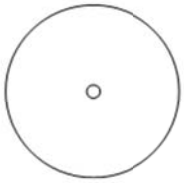	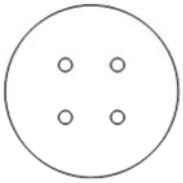	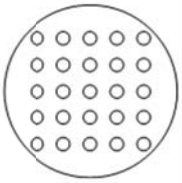
Column Spacing (s), inches	Not applicable	7.00	3.50
Column Diameter (d), inches	0.75 1.25 2.00 3.00	0.75 - 2.00 -	0.75 1.25 2.00 -
Area Replacement Ratio (a_s), %	Not applicable	1 - 6 -	4 10 26 -

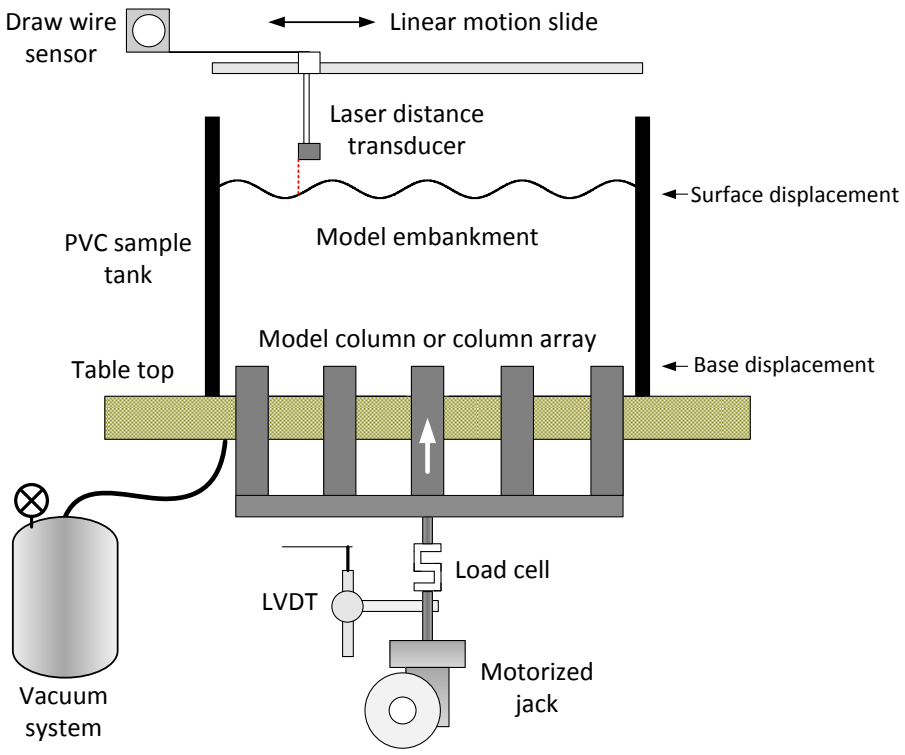

Figure 3.1 Elevation view schematic of the apparatus

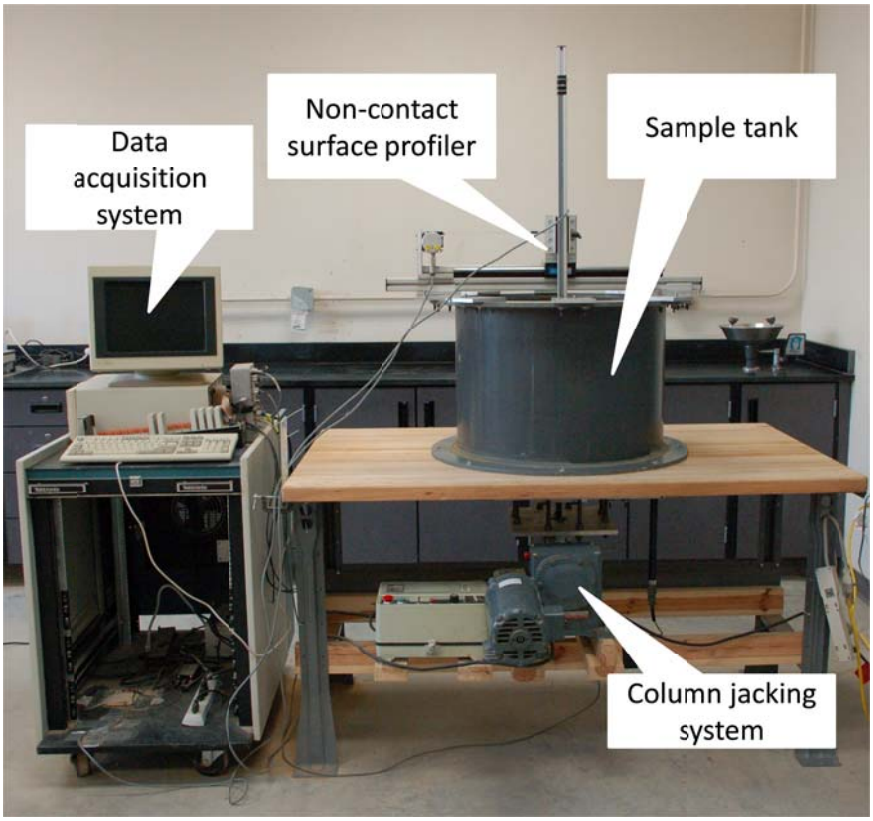

Figure 3.2: The apparatus configured with 5x5 array of columns

Each component of the apparatus is described in the following subsections. Section 3.2.1 describes the sample tank, model columns, and jacking system. Section 3.2.2 describes the laser profiling system. The vacuum system used during testing with a single 3-inch diameter column is described in Section 3.2.3, and the data acquisition system is described in Section 3.2.4. Appendix K presents the calibration results of the instruments at the time the apparatus was constructed.

3.2.1 Description of tank, model columns, and jacking system

Two butcher-block work benches with heavy duty steel frames were selected as platforms for the apparatus because the table tops could be easily modified to accommodate the model columns and the underlying steel frame provided sufficient stiffness to prevent significant deflections of the table when the tank was fully loaded with sand. One of the tables was adapted for testing with a single 3-inch diameter column and the other table was used for testing with column arrays. In both cases, the wooden tops were cut to allow passage of the columns and

associated mounting hardware. The table top using for single column testing also included ports for the vacuum system described in Section 3.2.3. From the vantage point of looking down into the empty tank, Figure 3.3 shows the column array and mounting plate positioned in the table top. In the figure, the columns are partially displaced for illustration and the laser profiler described in Section 3.2.2 is visible.

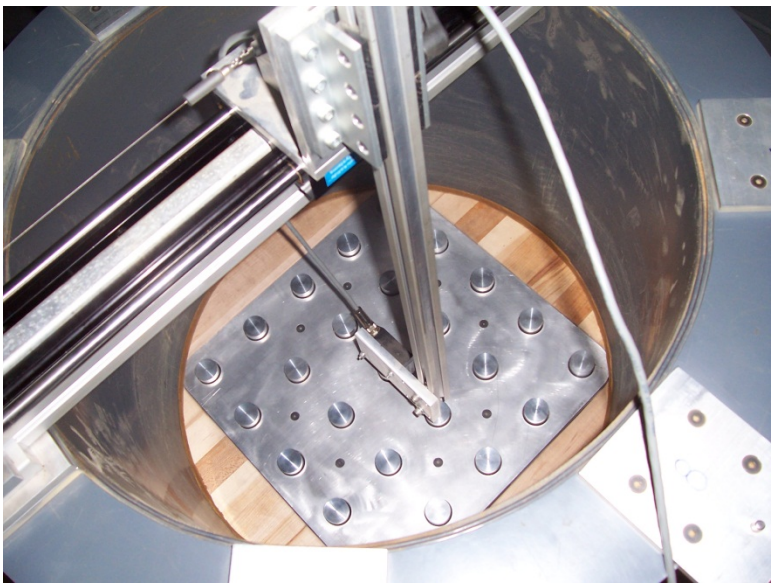

Figure 3.3 Table top, column array, mounting plate, and laser profiler

An 18-inch section of 24-inch diameter PVC pipe was used for the sides of the tank. Plastinetics of Towaco, New Jersey, welded PVC flanges to the top and bottom of the pipe section to allow the tank to be bolted to the table top and to attach aluminum mounting plates for the laser profiler.

The model columns were machined from aluminum rod in the following diameters: 0.75, 1.25, 2.00, and 3.00 inches. The 3-inch column was only used for single column testing and had a threaded base to attach the S-beam load cell. The other column sizes had a 0.5 inch diameter post extending from the base to attach them to the jacking system described later in this section. The alignment of the columns was maintained using aluminum mounting plates with rubber gaskets to provide a close, low-friction fit for the columns to pass through the plane of the table top.

The column(s) displace upwards, above the plane of the table top, using a motorized 2-ton acme screw jack. Displacing the columns up into the base of the sample tank, while holding the tank fixed, is equivalent to holding the columns fixed and lowering the base of the sample

tank. This arrangement (raising the columns instead of lowering the tank) made the equipment easier to fabricate, and it still allows for describing deformation of the sample in terms of settlements. The motor and gear box were manufactured by Boston Gear and feature a voltage-feedback motor speed controller with dynamic braking to ensure a consistent rate of motion regardless of load. During operation, the columns were displaced slowly at a rate of 1 inch in 20 minutes. Figure 3.4 shows the basic components of the jacking system when the apparatus is configured for testing using a single 3-inch column. The jacking system for the other configurations is shown in Figure 3.5. The systems are similar, except that an S-beam load cell was installed between the jack and the column for the 3-inch single column configuration to capture the load-displacement relationship for the load acting on the column. For testing at low sample heights under atmospheric conditions, a 250-lb load cell manufactured by Omegadyne (Model LC 101-250) was used, while a 500-lb load cell manufactured by Interface (Model SSM500) was used for testing at higher sample heights and under sub-atmospheric conditions. In all configurations of the apparatus, a gaging LDVT manufactured by Trans-Tek (Model 354) with a 2-inch measuring range was used to measure the displacement of the columns. Calibrations for the load cells and LVDT were performed and periodically checked. Calibration data is available in Appendix K. The load cells were calibrated using weights and the load acting on the column was determined by subtracting the load due to friction between and column and the rubber gasket from the total measured load. The friction load was accounted for by measuring the registered load as the column was displaced into the tank (at a rate of 1 inch in 20 minutes) when empty and subtracting this value from the load readings taking during experiments.

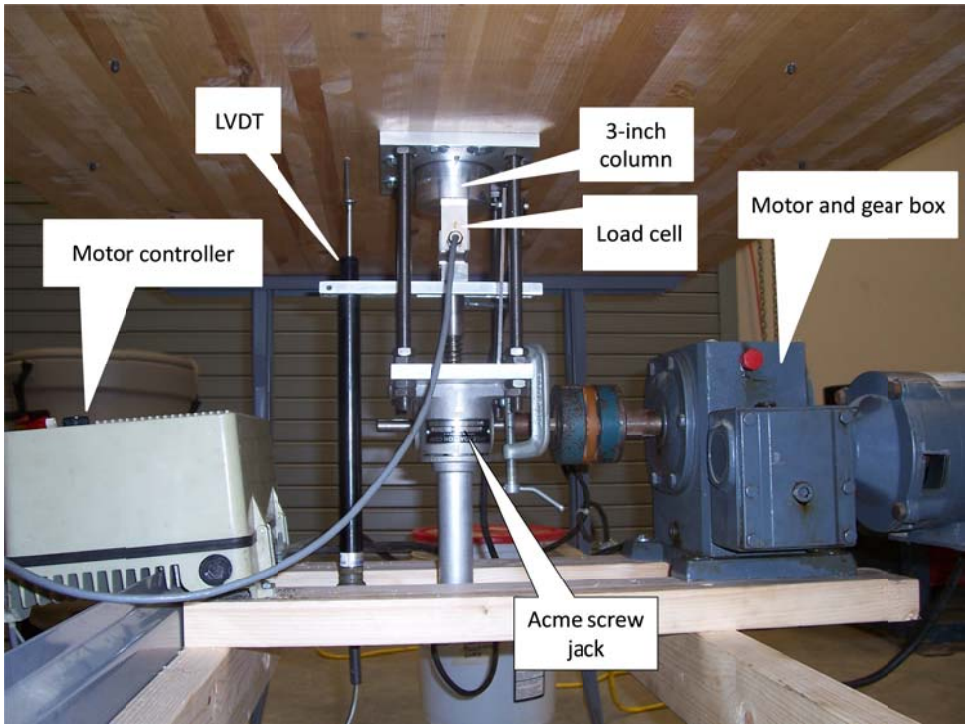

Figure 3.4: Jacking system for 3-inch single column testing configuration

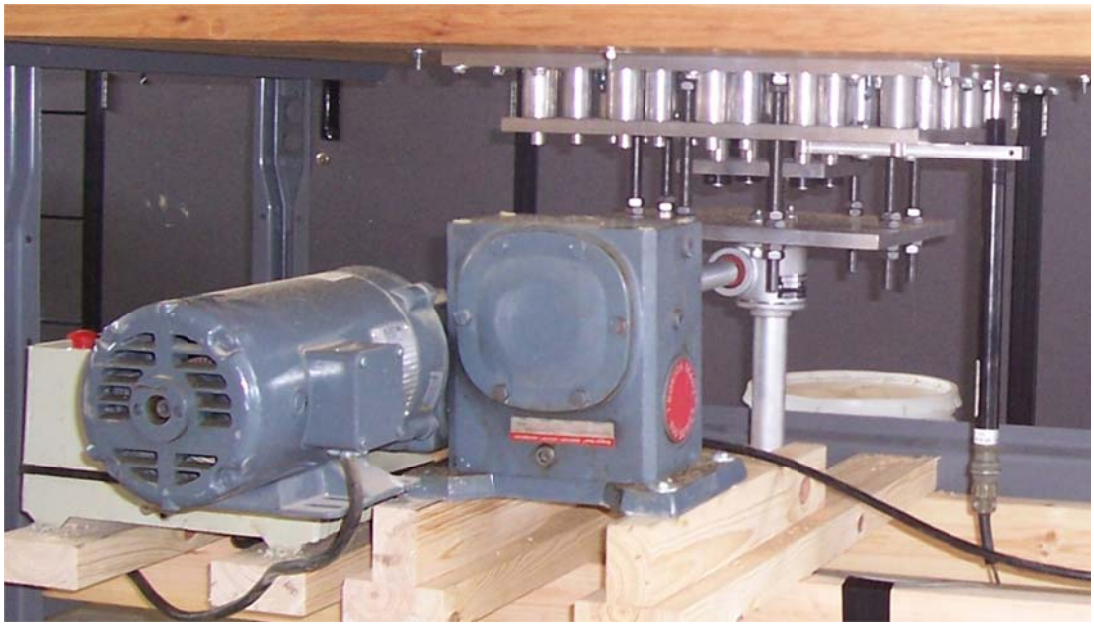

Figure 3.5: Jacking system for other testing configurations (5x5 array of 1.25-inch diameter columns shown)

3.2.2 Description of non-contact surface profiler

At various increments of column displacement, the column motion was stopped and the surface of the sample was scanned using a two-dimensional laser profiling device. The basic components of the profiler consisted of a non-contact laser distance transducer and a draw-wire sensor. The laser device measured the distance from the instrument to the sample surface and the draw-wire measured the horizontal position of the laser. As shown in Figure 3.6 and Figure 3.7, the laser distance transducer was mounted on an adjustable slide that allowed it to be positioned within its measuring range of the sample surface. The measuring range of the laser was sufficient so that the laser height did not need to be changed during a test. The laser and vertical slide were mounted on a freely traveling linear motion carriage. The draw-wire sensor was connected to the carriage to record the horizontal location of the laser. To obtain a profile of the sample surface, the carriage was moved slowly by hand from one edge of the tank to the other at a rate of approximately 1 inch every 5 seconds. The profiling system was capable of capturing the shape of the sample surface with a high degree of accuracy and resolution at the orientations around the circular sample tank shown in Figure 3.8. As discussed in Section 3.2.4, profiler readings were taken at a rate of 5Hz, so approximately 25 measurements are taken per inch of the sample surface. While the columns were displaced using the jack, the laser profiler remained positioned directly over the center of the unit cell to record surface displacement.

The non-contact laser distance transducer used for the profiling system was manufactured by Micro-Epsilon (model number ILD1300-50). This type of optoelectronic displacement measuring device uses a CMOS sensor similar to those found in digital cameras, a laser source which projects a beam to the target object, and basic triangulation of the reflected light path to determine distance. The transducer has a measuring range of approximately 2 inches and has a specified accuracy of about ±0.004 inches. Robust on-board digital signal processing allowed the instrument to provide reliable measurements even though the surface of the sand was highly irregular and faceted at the scale of the laser beam which has a spot diameter of about 0.004 inches. The ability of the instrument to accurately measure sand-covered surfaces was validated by performing a series of exercises whereby the surface of objects with known geometries were covered in sand paper and scanned using the profiling device. Final calibration was performed using a target comprised of Light Castle sand. Calibration data is contained in Appendix K.

The draw-wire sensor used in the profiling system was also manufactured by Micro-Epsilon (model number WDS 750-P60-SR-U). The sensor has a measuring range of about 29.5

inches and a measuring accuracy of about ±0.03 inches. Information regarding calibration of the draw wire sensor is contained in Appendix K.

The linear motion device used to mount the vertical slide and laser was manufactured by Danaher Motion (Model 2DA-08-00A). The slide consists of dual shaft rails and an integrated carriage.

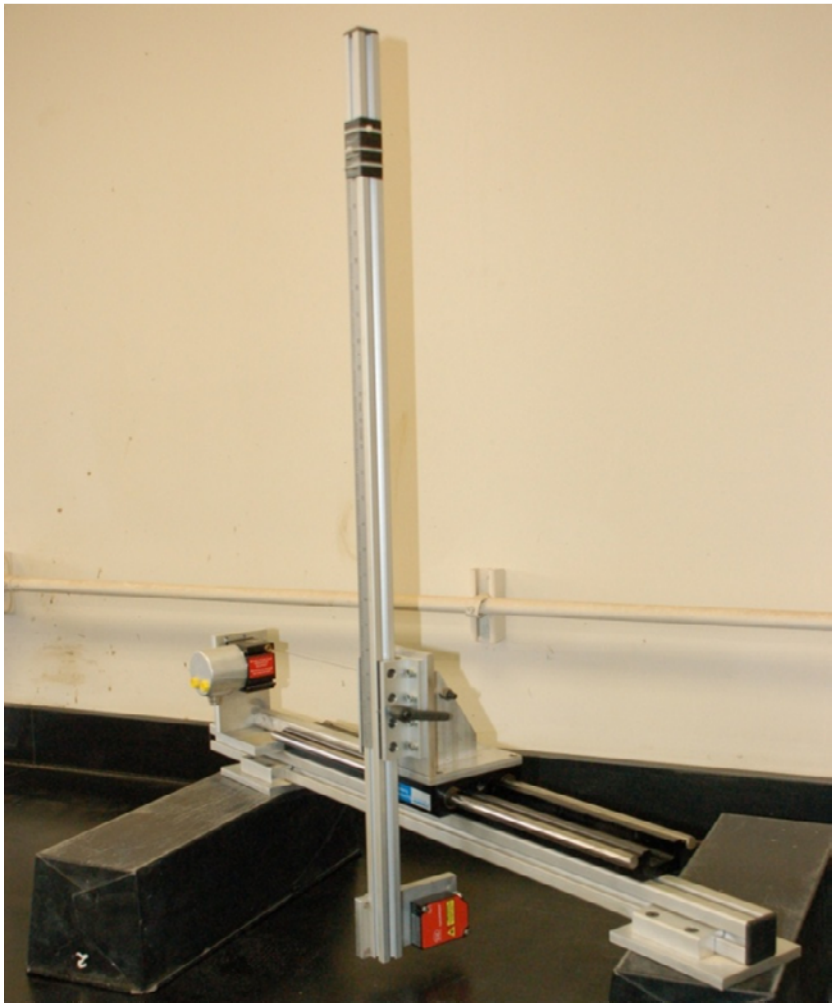

Figure 3.6: Non-contact profiling system

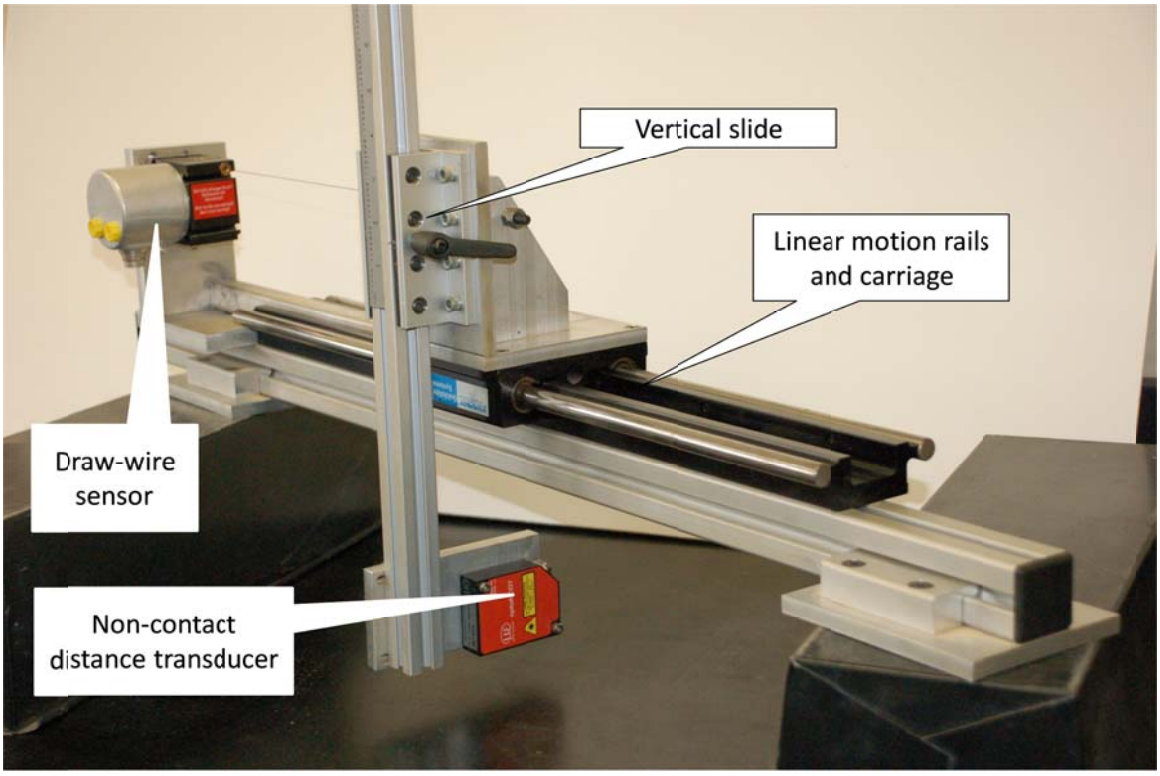

Figure 3.7: Detail of non-contact profiling system

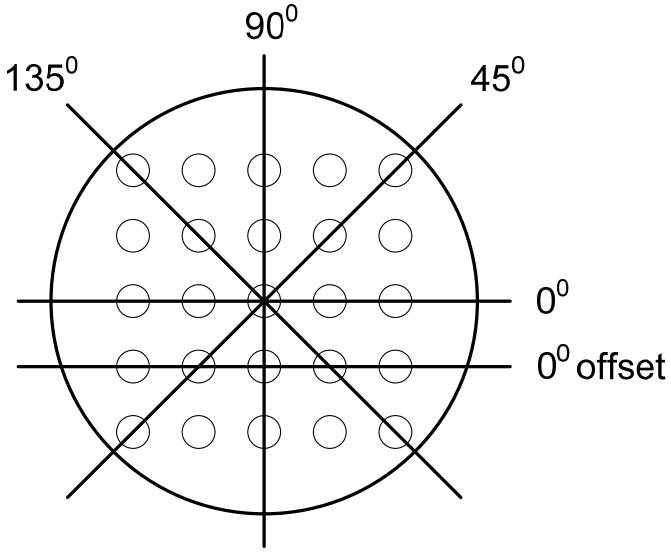

Figure 3.8: Plan view of available profiling orientations

3.2.3 Description of vacuum system

A vacuum system was incorporated into the testing equipment for the 3-inch single column configuration in order to investigate the influences of effective stress on the measured surface deformation. The tank and sample needed to be airtight for a vacuum system to work properly. The interface of the PVC tank to the benchtop and the column mounting hardware were sealed with silicone caulk. The fit between the column and rubber gasket was made airtight by covering the column and gasket with a thin latex sheet which was secured to the benchtop using tape. A novel solution using a thin latex sheet and a bicycle wheel was used to seal the top of the sample without causing significant effects on the surface deformation. A bicycle rim without spokes and a tire with minimal tread were selected to provide a close fit to the inside diameter of the PVC tank when the tire was deflated. After forming the sample of sand, the seal was prepared by securing the latex sheet between the PVC tank walls and the bicycle tire and then inflating the tire to create the seal. The latex sheet/bicycle wheel seal is shown in Figure 3.9.

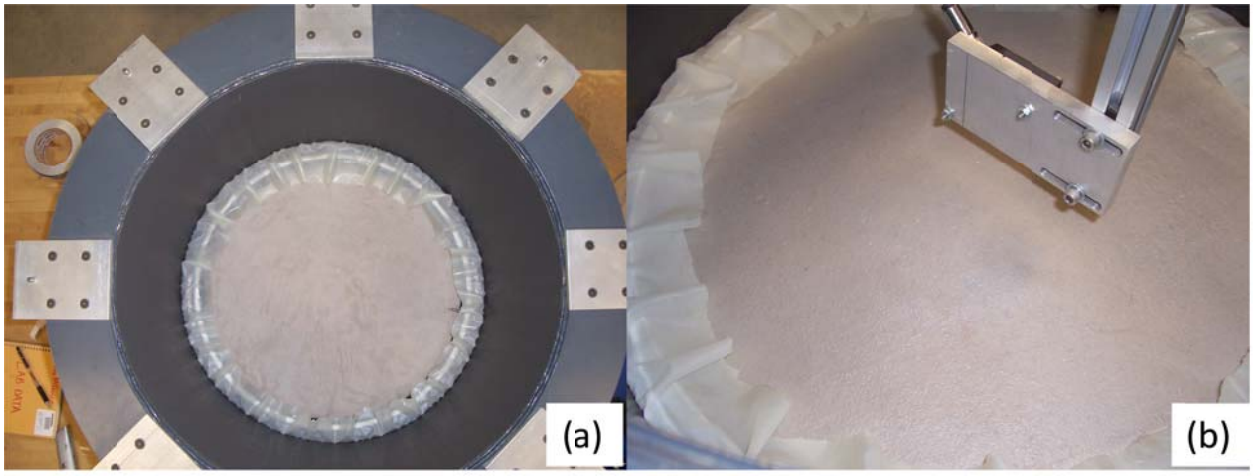

Figure 3.9: Latex sheet and bicycle wheel clamp used for sealing the top of the sample, (a) Looking down into sample tank, (b) Sealed sample being scanned using laser profiler.

The laboratory vacuum pump was used in conjunction with a vacuum regulator to draw the interior pressure of the tank down to the desired level. Four ports were installed in the bottom of the tank to draw and monitor vacuum pressure. Vacuum pressures up to 6 inHg (~3psi) were possible using this system.

3.2.4 Data acquisition

Data acquisition was performed using a rack-mounted Keithley Metrabyte backplane with MB Series signal conditioning modules. Analog signals were converted to digital using a Keithley Metrabyte DAS 1600/1400 Series board installed in an IBM 486 PC. Digital signals were processed in LabTech Notebook Pro v8 (1994). A sampling rate of 50 Hz was used and moving average values were recorded to disk at 5Hz.

3.3 Material Properties and Sample Preparation

This section describes the material properties of Light Castle sand and the method used to prepare samples for testing in the equipment described in Section 3.2. All experimental tests were performed using Light Castle sand prepared dry using the technique of air pluviation.

3.3.1 Properties of Light Castle sand used during experimental testing

Light Castle sand is a poorly-graded manufactured sand classifying as SP according to ASTM D-2487 with sub-angular quartz grains that has been used for a variety of laboratory investigations and physical modeling programs at Virginia Tech. Studies by Gomez (2000), Bonita (2000), Porter (1998), Duncan and Filz (1995), and Filz (1992) include information about the material properties of Light Castle sand. Table 3.3 summarizes the index property values reported by these studies. In some cases, the reported values in one study were also reported in a subsequent study.

Table 3.3 Some reported index properties for Light Castle Sand

Index property	Current Study	Gomez (2000)	Bonita (2000)	Porter (1998)	Duncan and Filz (1995)	Filz (1992)
G_s		2.66	2.65	2.65	2.66	2.65
e_{max}	0.789	0.903	0.868	0.809	0.876	0.868
e_{min}	0.545	0.561	0.560	0.528	0.566	0.560
d_{60} (mm)		0.45	0.45	0.382		0.382
d_{50} (mm)			0.41	0.351		0.351
d_{30} (mm)		0.32	0.33	0.287		0.287
d_{10} (mm)		0.25	0.25	0.192		0.220
c_u		1.8	1.8	1.99	1.8	
c_c		0.9	0.97	1.12	0.9	

The studies listed above also report results from shear strength testing on Light Castle sand using direct shear testing, vacuum triaxial testing, consolidated-drained triaxial testing (CD), and isotropic consolidated-undrained (ICU) triaxial testing. The variation in reported values among the studies listed in Table 3.3 could be attributed to variation in the source quarry for Light Castle sand and/or testing variation. To establish representative shear strength parameters for Light Castle sand under the conditions present during the bench scale testing, the influences of relative density and confining pressure were considered. Using values of e_{max} and e_{min} determined during the current study, the samples used for the bench scale testing were prepared at three relative densities described in Section 3.3.2 ranging from 73 to 105 percent and ranging in height from about 1 to 10 inches. Using approximate values of 100 pcf for unit weight and 0.5 for the lateral earth pressure coefficient, the confining pressure at mid-height of the sample over the range of sample heights varies from about 0.014 to 0.145 psi for tests without an applied surcharge. At maximum applied surcharge pressure equal to 3 psi, the confining pressure at mid-height is approximately 1.59 psi. The combination of high relative density and very low confining pressure means that the friction angle of Light Castle sand under the testing conditions is likely quite high. Obtaining reliable measurement of shear strength at very low confining pressure is difficult (Fukushima and Tatsuoka 1984) because measuring appropriate stresses in the sample requires special consideration of the weight of the sample and components used to load the specimen, the instruments used to measure loads and pore pressures, and the stiffness of the membrane used in triaxial testing. Vacuum triaxial testing provides a straightforward way to obtain reasonable estimates of the friction angle of dry sands at fairly low confining pressures; however, it is difficult to accurately determine the volume change of the specimen during shear. This limitation means that the angle of dilation needs to be estimated using correlations with other material properties.

In his dissertation, Filz (1992) describes the results of two ICU tests performed using samples prepared at a relative density of 74 percent and confining pressures of 5 and 10 psi. A friction angle of 38.1 degrees was reported as being representative of both tests. Using the stress path plots provided by Filz (1992), it was not possible to interpret separate friction angles for each test. Filz also performed direct shear tests on samples at 74 percent relative density using applied normal stresses of approximately 15.3, 27.8, and 55.6 psi. Filz (1992) reports a representative friction angle of 38.6 degrees for all three tests; however, interpreting the results of each test separately yields friction angles of 40.9, 38.6, and 37.9 degrees for the three respective normal stresses. Filz (1992) determined the angle of repose to be 33.6 degrees.

Cornforth (1973) suggests that the angle of repose provides an estimate of critical state friction angle with an accuracy of about 1 degree.

In the study by Duncan and Filz (1995), five vacuum triaxial tests were performed at relative densities of 71 to 77 percent and confining pressures ranging from 2.5 to 10 psi. The resulting friction angles varied from 46.5 to 41.8 over the range of confining pressures evaluated.

Porter (1998) reports the results of nine CU tests performed using conventional end platens over a range of confining pressures from 29 to 47 psi. The samples were prepared at an average relative density of 22 percent. Porter (1998) also performed CU tests using lubricated end platens; however, the results from those tests will not be considered here to maintain consistency with the other tests used in the current analysis. Porter does not report values for shear strength parameters from individual tests; however, he does determine a steady state friction angle between 29 and 30 degrees. The axial strain to reach steady state was approximately 15 percent. Poulos (1981) defines steady state deformation as continuous deformation under constant volume, constant normal effective stress, constant shear stress, and constant velocity. Critical state is defined by Casagrande (1936) as the void ratio at which a cohesionless soil can undergo any amount of deformation without volume change. Steady state is applicable to drained and undrained conditions, while critical state is limited to drained conditions. Steady state also has the additional requirements that the initial soil fabric is completely destroyed and that deformation is actively occurring. For continuous deformation, at large strains, under drained conditions the steady state friction angle is equal to the critical state friction angle. It should be noted that Tatsuoka et al. (1986) found that at very low confining stress, the axial strain required to reach critical state is higher than at greater confining stress. If the results of the individual tests are interpreted from the stress paths and the peak principal stress ratios, values of internal friction are equal to about 33.5±1 degrees at the lower range of confining pressures and 31.5 degrees at the upper range of confining pressure. Using the results from three of Porter's CU tests performed at confining pressures of 29, 40, and 47 psi, Bonita (1999) reports a peak friction angle of 30.8 for Light Castle Sand.

Bonita (2000) performed three ICU tests at a relative density of 55 percent using confining pressures of approximately 7.25, 16, and 40 psi. Bonita (2000) reports a friction angle of 40.5 to be representative of the test results; however, interpreting the tests individually yields friction angles of 43.0, 42.1, and 40.5 degrees for the confining pressures used during testing.

Gomez (2000) performed two series of CD triaxial tests on samples of Light Castle sand. Each series consisted of three tests performed at confining pressures of approximately 6.5, 14.9, and 40.6 psi, with the first using samples prepared at a relative density of 50 percent and the second using samples prepared at 80 percent. The measured friction angles for the medium dense samples were 37.4, 37.8, and 36.4 degrees corresponding to low, medium, and high confining pressures. The friction angles measured for the dense samples were 45.0, 41.5, and 40.1 degrees for the tests at low, medium, and high confining pressures. Gomez (2000) reports constant volume friction angles measured at 15 percent axial strain of 33.2 degrees for samples at 50 percent relative density and 36.5 degrees for samples at 80 percent relative density.

To supplement the existing shear strength testing of Light Castle sand, six vacuum triaxial tests were performed at confining pressures ranging from about 0.5 to 11 psi on samples prepared at the relative densities shown in Table 3.4. The samples had an initial height of about 6.9 inches and an initial diameter of about 2.8 inches. The strain rate used during shearing was 0.5 percent per minute. The test results were area corrected using the parabolic area correction. Porter (1998) found that typically the parabolic area correction uses the sample area at mid-height for determining the axial stress. Since volume change occurs during shearing which is difficult to measure during vacuum triaxial testing, Pi tape was used to directly measure the sample diameter at mid-height. The data was corrected for membrane effects using the guidance provided in ASTM D4767 for CU testing of cohesive soils. The results of the testing are summarized in Table 3.4. Detailed results are provided in Appendix K.

Table 3.4: Results from vacuum triaxial testing

Confining Pressure (psi)	Relative Density (%)[1]	Peak friction angle (deg)
0.49	62	59.0
0.74	72	55.1
0.98	53	52.8
2.45	58	45.2
5.40	55	42.8
10.81	52	39.6

1. Calculated using e_{min} and e_{max} determined during the current study

To evaluate the relationship between confining pressure and friction angle using the results from the vacuum triaxial tests performed as part of this study as well as the results from testing performed by others, the values of friction angle were plotted against the confining pressure normalized by atmospheric pressure (14.7 psi). For the direct shear test results performed by Filz (1992), Duncan and Filz (1995) used the values of σ'_3 determined at failure as the values of confining pressure, and that approach is retained here. The results of this comparison are

provided in Figure 3.10. Also shown in Figure 3.10 are the values of ϕ_o and $\Delta\phi$ estimated using the current vacuum triaxial test results and the values estimated by Duncan and Filz (1995) using their vacuum triaxial test results and the direct shear test results by Filz (1992). Gomez (2000) determined values of ϕ_o and $\Delta\phi$ for Light Castle sand at relative densities of 50 and 80 percent based on the results of three CD tests performed on samples at each density. The values of ϕ_o and $\Delta\phi$ obtained for the samples at Dr=80% were very close to the values obtained by Duncan and Filz (1995) for samples at Dr=74%. Since the values of ϕ_o and $\Delta\phi$ determined by Duncan and Filz (1995) were based on more extensive testing than the values reported by Gomez (2000), a separate trend line reflecting Gomez's findings is not provided in Figure 3.10.

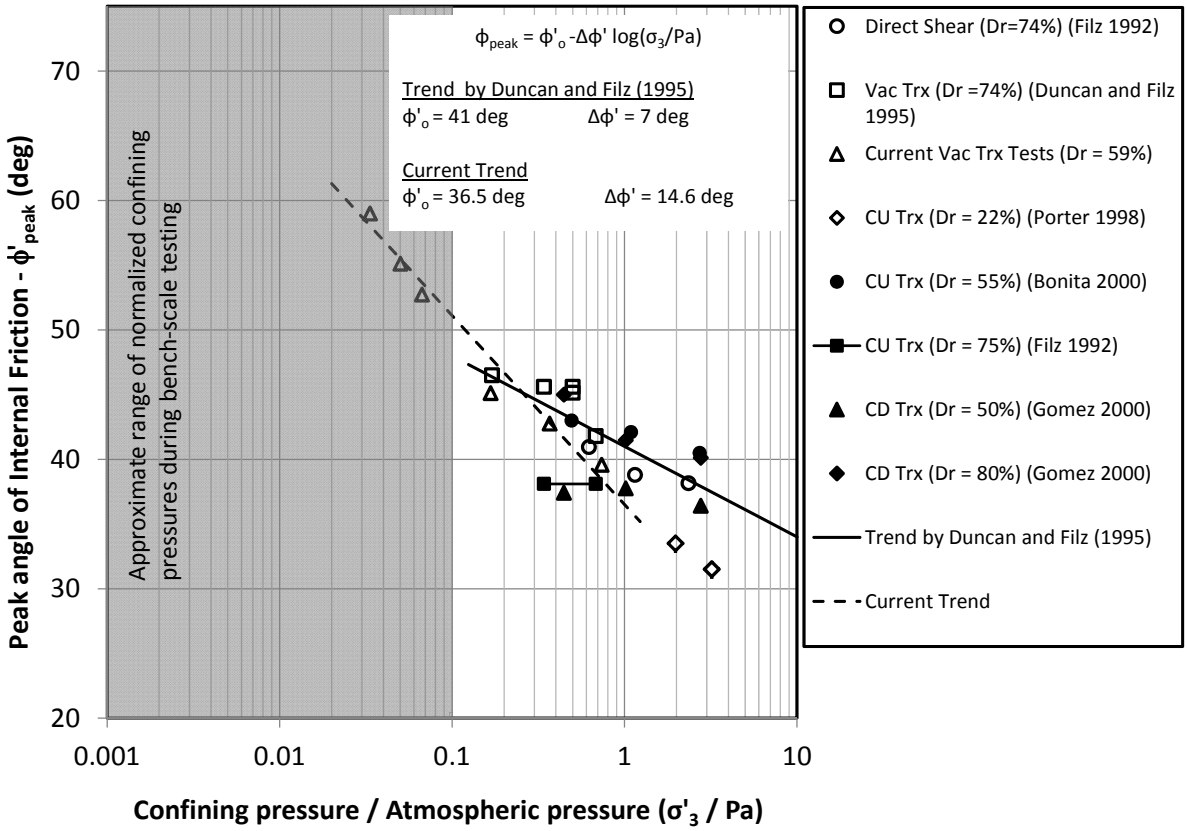

Figure 3.10 Some reported trends for the shear strength of Light Castle sand

The correlation proposed by Bolton (1986) was applied to determine whether the trends developed from the current vacuum triaxial testing and Duncan and Filz (1995) reasonably

estimate the relationship between peak friction angle, ϕ_{peak}, and confining pressure for Light Castle sand. Bolton's correlation is useful for estimating the peak friction angle of sands since it considers the influences of confining pressure, density, minerology, and whether shear is plane strain or triaxial. Inputs to the correlation are the relative density, D_r, critical state friction angle, ϕ_{crit}, and mean effective confining pressure at failure. For shearing under drained conditions, it is possible to estimate the effective mean stress at failure for triaxial conditions as $\sigma'_3(K_p+2)/3$, where σ'_3 is the initial confining stress and $K_p = \tan(45+0.5\phi_{trial})$. Substituting the estimate for effective mean stress at failure into Bolton's correlation is expressed in Equation 3.1, where k is a coefficient equal to 3 for triaxial conditions and 5 for plane strain conditions. The coefficients Q and R are fitting parameters which Bolton found have values of Q=10 and R=1 for clean silica sands. Salgado (2008) provides values of Q and R for sands with small amounts of silt and clay fines. The peak friction angle can be estimated by iteratively solving for $\phi_{peak} = \phi_{trial}$. Bolton suggests limiting the correlation to values of $\phi_{peak} \leq \phi_{crit}+12$ for triaxial conditions and $\phi_{peak} \leq \phi_{crit}+20$ for plane strain conditions. He indicates that the suggested limitation is not due to a breakdown of the correlation itself, but rather due to insufficient experimental testing at low confining pressures.

$$\phi_{peak} = \phi_{crit} + kD_r\left[Q - 2.3\log\left(\frac{\tan^2\left(45+\frac{\phi_{trial}}{2}\right)+2}{3}\sigma'_3\right)\right] - kR \qquad (3.1)$$

The critical state friction angle of Light Castle sand was estimated to be 31.8 degrees by averaging the value of steady state friction angle determined by Porter (1998) with the angle of repose determined by Filz (1992). Equation 3.1 was applied to the trend established by Duncan and Filz (1995) by taking Dr =0.74 and k = 4 since both triaxial and plane strain tests were used in the development of the trend. Equation 3.1 was applied to the trend suggested by the current vacuum triaxial tests using Dr = 0.59 and k = 3. The comparison of Bolton's correlation to the trend derived from experimental testing is shown in Figure 3.11.

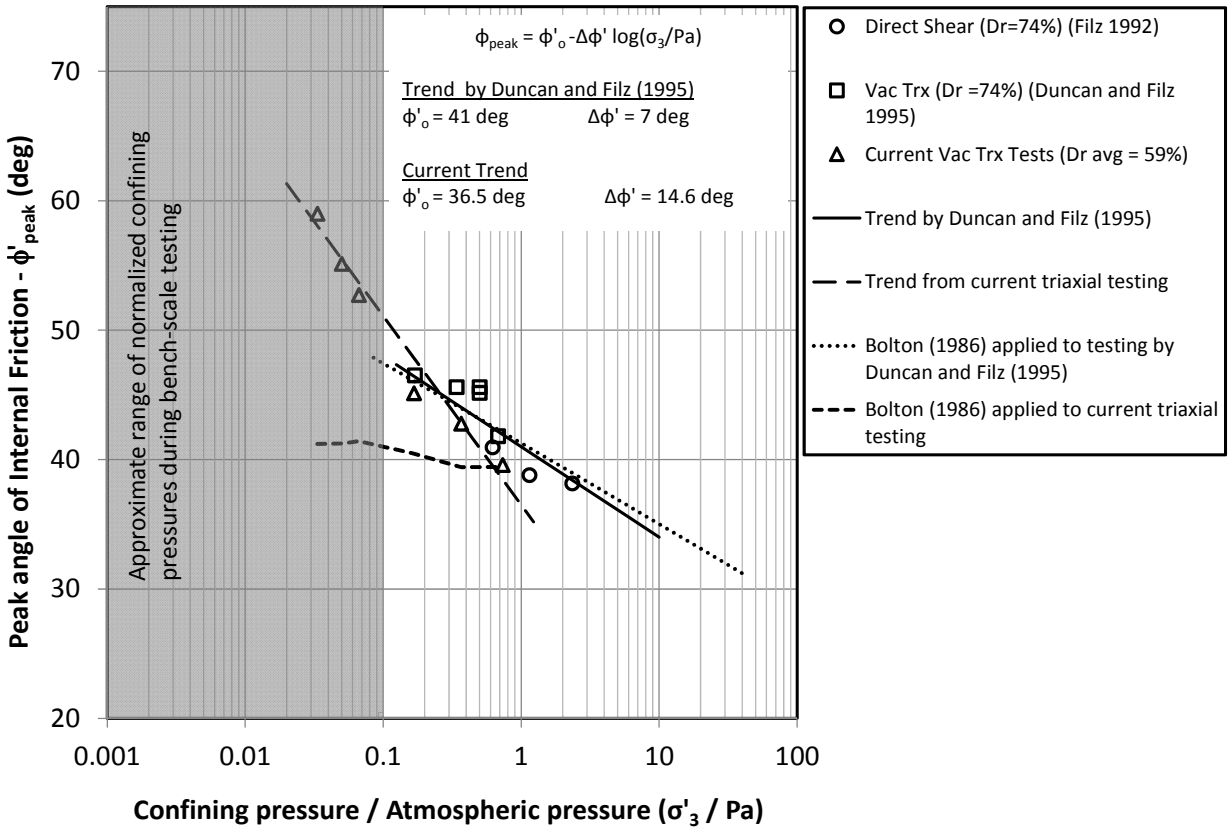

Figure 3.11: Relationships between friction angle and confining pressure derived from testing compared to correlation by Bolton (1986)

Bolton's correlation strongly supports the relationship between friction angle and confining pressure proposed by Duncan and Filz (1995), however the correlation does not support the relationship derived from the current vacuum triaxial testing. A variety of factors could be contributing to the deviation between the measured friction angle and the correlated value including errors in determining membrane effects, area correction, and sample relative density. Since the trend proposed by Duncan and Filz (1995) supports the correlation by Bolton (1986), the correlation rather than the current vacuum triaxial tests was used to estimate the strength parameters of Light Castle sand at low confining pressure. Figure 3.12 shows Bolton's correlation applied to the three relative densities used during experimental testing. In this case, Bolton's correlation is extrapolated back to the confining pressures experienced during testing, acknowledging that the estimated frictions angles exceed Bolton's suggested limits due to an insufficient testing at low confining pressure. Values of ϕ'_o and $\Delta\phi'$ determined from Bolton's correlation are also provided on the plot.

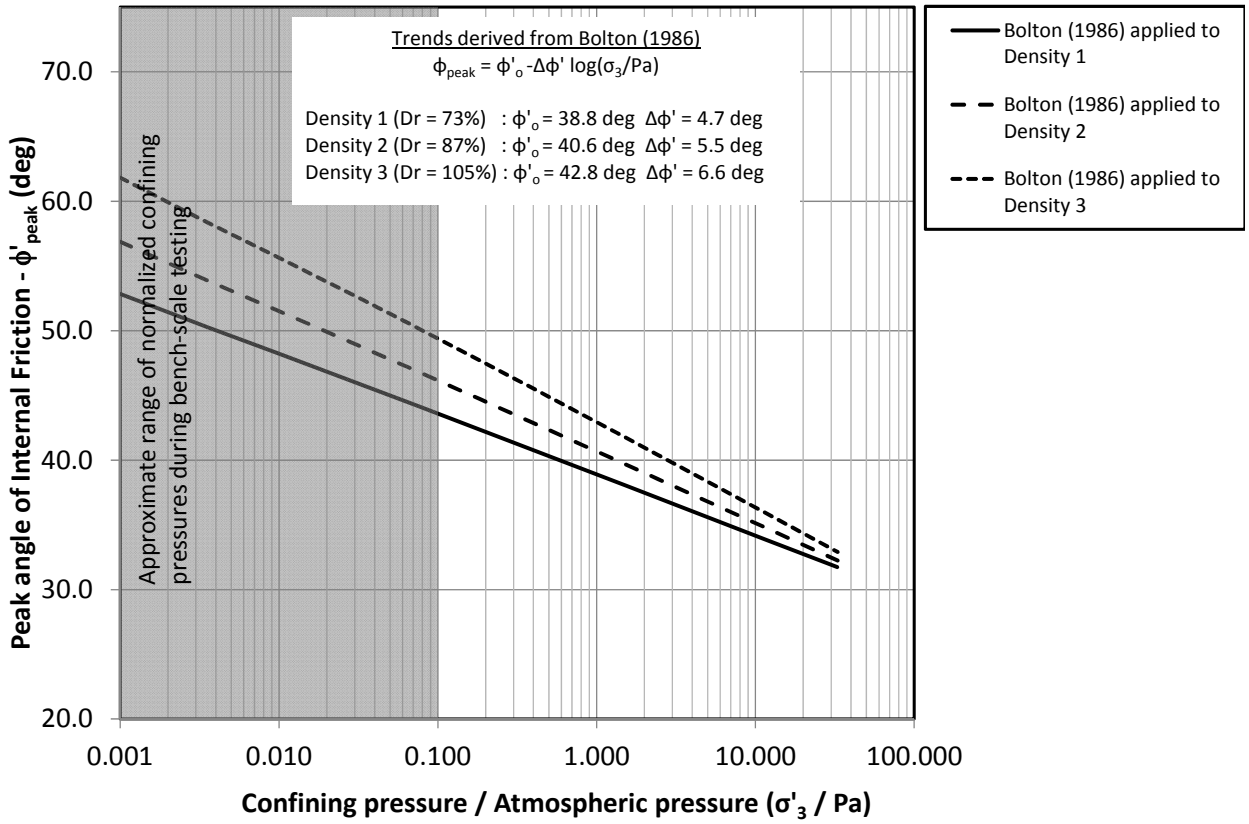

Figure 3.12: Estimated peak friction angle versus confining pressure for three densities as predicted by Bolton (1986) and extrapolated to low confining pressure.

As a check of whether extrapolating Bolton's correlation is reasonable, the correlation proposed by Duncan (2004) for sands with a coefficient of uniformity less than 6 was applied to Densities 1, 2, and 3, defined in Section 3.3.2. In Figure 3.13, the relationship between friction angle and confining pressure predicted by Duncan (2004) is superimposed on the trends predicted by Bolton (1986). The agreement between the correlations is fairly good with Bolton's values generally falling below the friction angles predicted by Duncan. It appears that Bolton's correlation is slightly more sensitive to relative density and confining pressure, since the slope of Bolton's trend lines are steeper and the spacing between lines of constant relative density are farther apart except at higher confining pressures. This observation is supported by comparing values of ϕ'_o and $\Delta\phi'$ predicted using the two correlations. Despite the small differences in

estimated values of friction angle, the correlation by Duncan (2004) supports the extrapolated trends predicted by Bolton (1986).

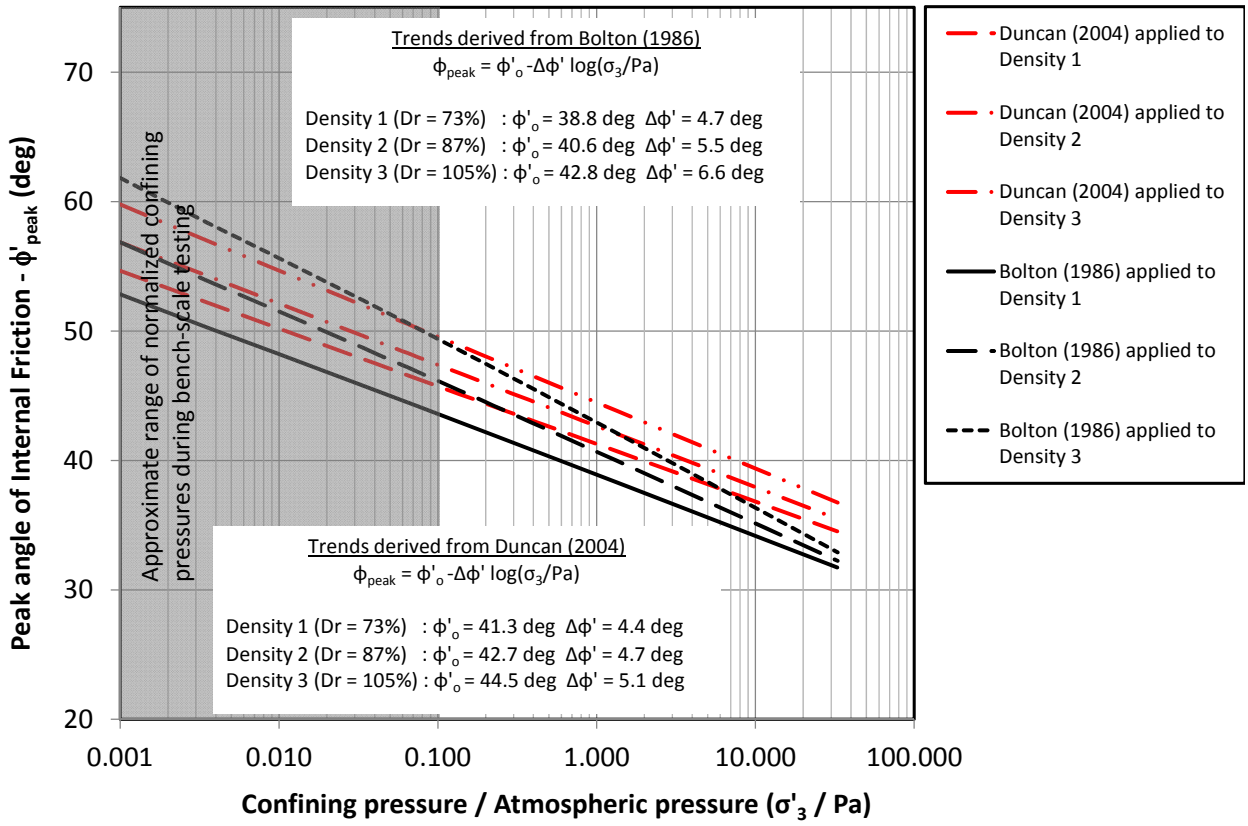

Figure 3.13: Comparison of extrapolated trends using Bolton (1986) to trends predicted by Duncan (2004)

Schwanz and Vermeer (1996) proposed a correlation between a soil state parameter defined by Bolton (1986) and the peak dilation angle. By substituting in the relationship between the soil state parameter and the angles of peak and critical state friction, the correlation can be expressed according to Equation 3.2, where k is a coefficient equal to 3 for triaxial conditions and 5 for plane strain conditions.

$$\psi_{peak} = a\sin\left[\frac{\phi_{peak} - \phi_{crit}}{6.7k + \phi_{peak} - \phi_{crit}}\right] \tag{3.2}$$

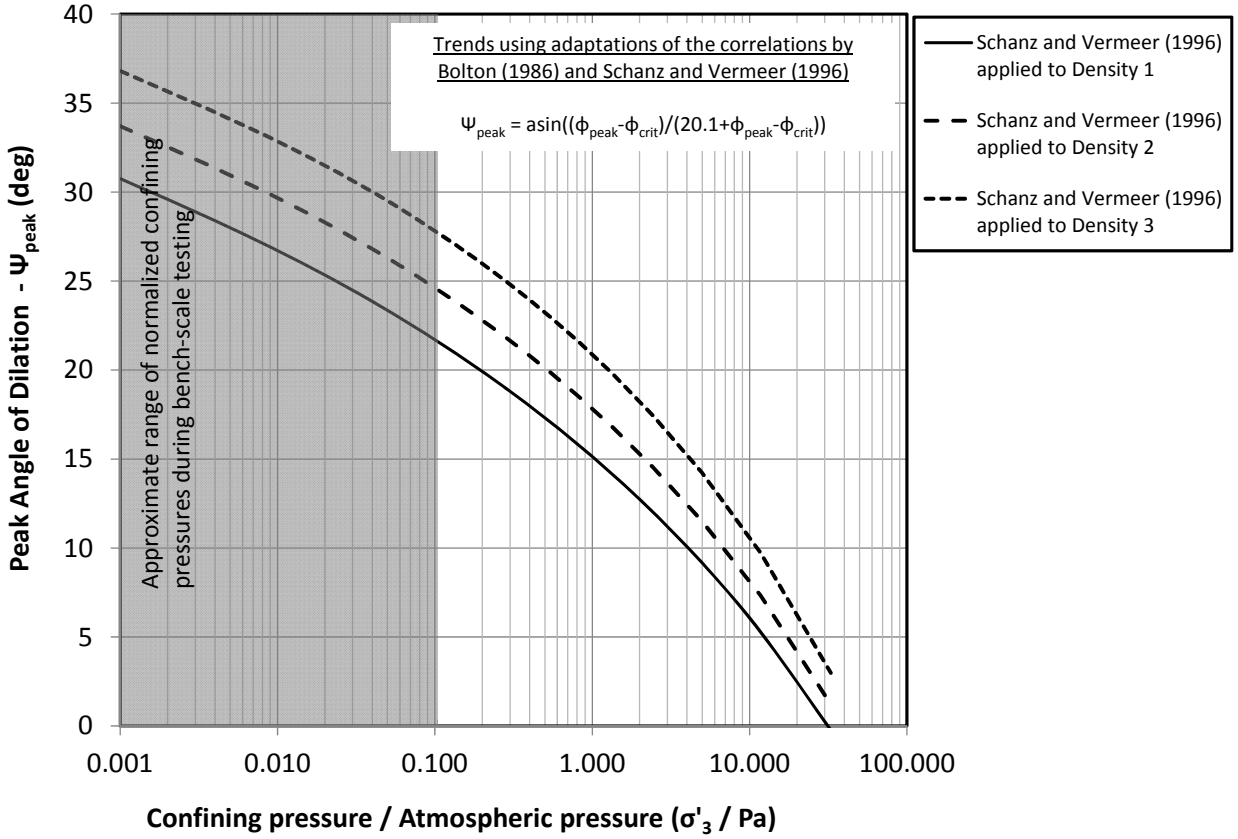

Figure 3.14: Peak dilation angle versus confining pressure predicted at three densities using estimated values of peak friction angle and correlation by Schanz and Vermeer (1996).

Figure 3.14 shows the estimated relationship between confining pressure and peak dilation angle for the three relative densities used during experimental testing. The trends were generated by estimating peak friction angle using Equation 3.1 and then estimating peak dilation angle using Equation 3.2.

Extrapolation of the results shown in Figure 3.12 and Figure 3.14 is necessary to estimate the friction angle of Light Castle sand during testing at the bench-scale. Studies by Sture et al. (1998), Alshibli et al. (2003), Tatsuoka et al. (1986), Fukushima and Tatsuoka (1984), and Ponce and Bell (1971) evaluated the influences of extremely low confining pressure on the shear strength of sands. The studies by Tatsuoka et al. (1986) and Fukushima and Tatsuoka (1984) observed little increase in friction angle below a confining pressure of about 7 psi in triaxial and plane strain testing of samples of angular to subangular uniform Toyoura sand comprised of

primarily quartz grains with a mean grain size of 0.16 mm and uniformity coefficient of 1.46. They attribute the continual increase in friction angle with decreasing confining pressure typically observed to misrepresentation of membrane forces and self-weight of the sample. The studies by Sture et al. (1998) and Alshibli et al. (2003) describe triaxial testing performed on subangular quartz Ottowa F-75 sand (d_{50} = 0.22 mm) under 1-g conditions and under microgravity conditions aboard the Space Shuttle. These testing environments allowed for confining pressures from about 0.00725 psi to 10 psi to be applied. The results of their testing are reproduced below as Figure 3.15 for peak friction angle and Figure 3.16 for peak dilation angle. Shading has been added to these figures to highlight the approximate range of confining pressures experienced during the bench-scale testing.

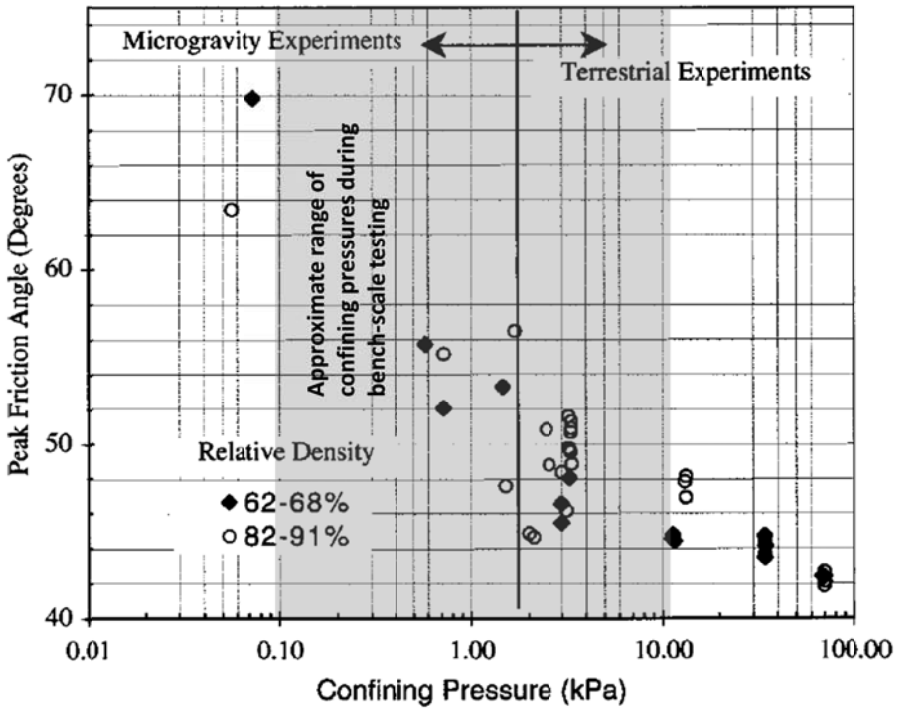

Figure 3.15: Measured peak friction angle of Ottawa F-75 sand, adapted from Alshibli et al. (2003) with permission from ASCE

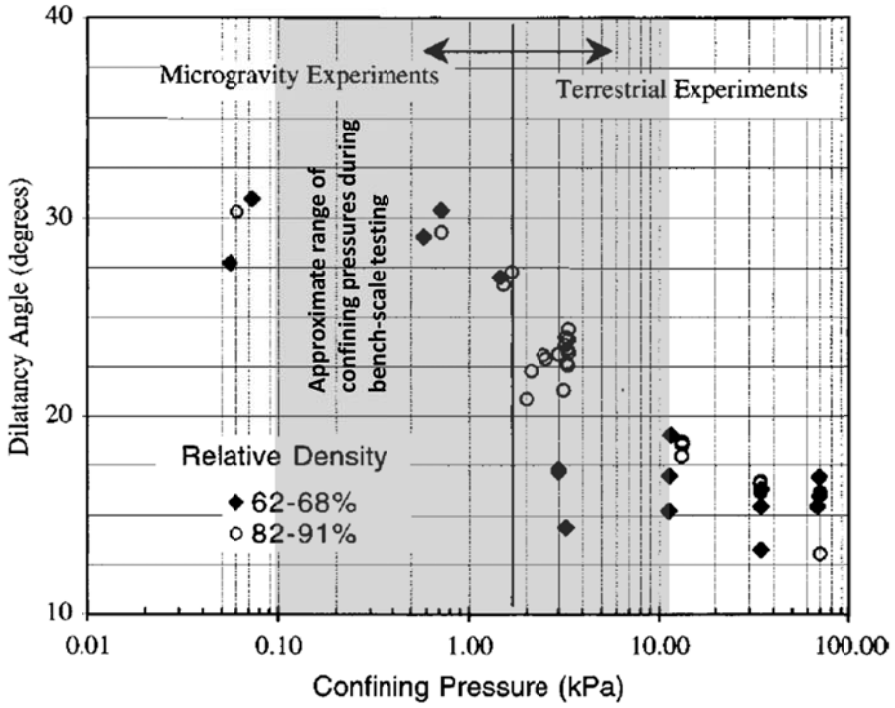

Figure 3.16: Dilation angle of Ottawa F-75 sand, adapted from Alshibli et al. (2003) with permission from ASCE

The somewhat conflicting findings from these studies suggest that certain sands may exhibit continual increases in friction angle with decreasing confining pressure while other sands may exhibit little increase in friction angle below a certain level of confining pressure. Since the experimental results in Figure 3.10 show friction angle of Light Castle sand increasing below 7 psi (normalized confining pressure of about 0.5), it is quite possible that even with more sophisticated testing methods and accurate correction for membrane effects, the peak friction angle could be quite high within the range of confining pressures experienced during bench-scale testing.

Referring to the relationship between dilation angle and confining stress for Ottowa F-75 sand shown in Figure 3.16, there appears to be a limit to the dilation angle reached below a confining pressure of about 1 kPa (0.14 psi), which happens to define the upper end of the range of confining stresses experienced during bench scale testing without applied surcharge pressure. It seems logical for there to be a limit on the dilation angle since the value is directly related to the rate of dilation and it makes sense for there to be a limit to how much volume change can occur due to an increment of shear strain. Bolton (1986) also suggests that there may be an absolute limit to the rate of dilation. Using the estimated values of ψ_o and $\Delta\psi$ for Light Castle

sand and a confining pressure of 0.14 psi to define the point where the limiting rate of dilation is reached, peak values of dilation angle defined in Table 3.5 for the sample three densities can be used over the entire range of confining pressures experienced during bench-scale testing without applied surcharge pressure.

If it is accepted that there is a limit on the rate of dilation, and thus the dilation angle, and Equation 3.2 defines the relationship between dilation angle and friction angle, there should also a limit on the friction angle. Using a cutoff confining pressure of 0.14 psi where the maximum rate of dilation is assumed to occur, the peak friction angles defined in Table 3.5 can be used over the entire range of confining pressures experienced during bench-scale testing without applied surcharge pressure. The values in Table 3.5 consider the testing results discussed herein combined with judgment about extrapolation of strength property values to the range of confining pressures experienced during the bench scale testing program.

Other relevant material property values available for Light Castle sand include interface properties reported by Porter (1998) and parameter values for the Duncan-Chang hyperbolic model reported by Gomez (2000). A discussion of elastic and interface properties for Light Castle Sand is provided in Chapter 6.

Table 3.5: Material properties of Light Castle sand considered in the current study

Parameter	Value		
G_s	2.65		
e_{max}	0.789		
e_{min}	0.545		
d_{60} (mm)	0.382		
d_{50} (mm)	0.351		
d_{30} (mm)	0.287		
d_{10} (mm)	0.220		
c_u	1.8		
c_c	0.9		
	Density 1 (D_r = 73%, γ = 103pcf)	Density 2 (D_r = 87%, γ = 105pcf)	Density 3 (D_r = 105%, γ = 108pcf)
ϕ_{peak} (deg)	$\min\left\{\begin{matrix} 38.8 - 4.7\log\left(\frac{\sigma'_3}{P_a}\right) \\ 48 \end{matrix}\right.$	$\min\left\{\begin{matrix} 40.6 - 5.5\log\left(\frac{\sigma'_3}{P_a}\right) \\ 52 \end{matrix}\right.$	$\min\left\{\begin{matrix} 42.8 - 6.6\log\left(\frac{\sigma'_3}{P_a}\right) \\ 56 \end{matrix}\right.$
ψ_{peak} (deg)	$\min\left\{\begin{matrix} a\sin\left[\frac{\phi_{peak} - 31.8}{20.1 + \phi_{peak} - 31.8}\right] \\ 27 \end{matrix}\right.$	$\min\left\{\begin{matrix} a\sin\left[\frac{\phi_{peak} - 31.8}{20.1 + \phi_{peak} - 31.8}\right] \\ 30 \end{matrix}\right.$	$\min\left\{\begin{matrix} a\sin\left[\frac{\phi_{peak} - 31.8}{20.1 + \phi_{peak} - 31.8}\right] \\ 33 \end{matrix}\right.$
ϕ_{crit} (deg)	32		

3.3.2 Sample preparation

Samples were prepared dry at one of three densities using the technique of air pluviation. This approach is intended to produce a sample of sand that has a known, and reasonably uniform, relative density. Eid (1987) provides a thorough background on air pluviation and the results from parametric studies he performed using two prototype pluviators. Fundamentally, the higher the intensity of deposition, defined as the mass of sand deposited per unit area over a period of time, the lower the relative density of the sample. The explanation for this relationship is that sand grains deposited at lower intensity have more opportunity to find an efficient packing arrangement, thus producing a sample with higher relative density. The velocity of the sand at impact with the sample surface also influences density. Faster moving sand grains carry more kinetic energy to bounce themselves and nearby sand grains into more dense arrangements.

The basic concept for the air pluviator used in the current study, as shown in Figure 3.17, was derived from one of Eid's prototypes. Figure 3.17 also provides a photo of the actual pluviator constructed of 4-inch PVC pipe that was used for sample preparation. The pluviator is shown with the sand hopper removed. In this design, sand is placed in a hopper vessel atop the pluviator column. The base of the hopper has circular openings to allow sand to exit the hopper and free-fall a distance, F, through the upper portion of the pluviator column. After falling through the upper chamber, the sand strikes two diffuser screens separated by a distance, S, which breaks up the sand jets into a uniform 'rain'. The diffused rain of sand then falls a distance, H, before striking the sample surface. The selection of the fall distances F, S, and H are described later in this section. In the current pluviator design, distances F and S are fixed and there is a threaded coupling just below the diffuser screens to allow the distance H to be changed by adding different lengths of pipe as the sample height increases. The pipe sections keep the sand confined over the fall distance H as close as practically possible to the sample surface to maintain depositional intensity. Since the pipe sections reduce H incrementally, there is a small air gap between the bottom of the pluviator and the top of the sample surface. For sample heights 6 inches or less, the maximum air gap between the lower pluviator chamber and the sample surface was 1 inch. For samples taller than 6 inches, the maximum air gap was 2 inches.

Unlike Eid's prototype, the current pluviator is smaller in diameter than the tank opening so it was necessary to be able to move the pluviator to build the sample height in a roughly uniform manner. To add this capability, the PVC support frame shown in Figure 3.17 allowed the pluviator to rest on a wooden frame, which is positioned on the top flange of the tank during sample preparation. The wooden frame provided a level, low friction, surface for the pluviator and support frame to slide around the tank opening.

After pluviating sand to the target sample height, the sample surface was leveled using a screed. The amount of leveling was small such that the leveling process likely did not have a large influence on the relative density of the sample. For samples incorporating geosynthetic reinforcement, a 0.5 inch of sand was deposited and leveled before laying out the first layer of reinforcement. In cases where a second layer of reinforcement was used, a 0.5 inch of sand was deposited and leveled to provide separation from the bottom layer.

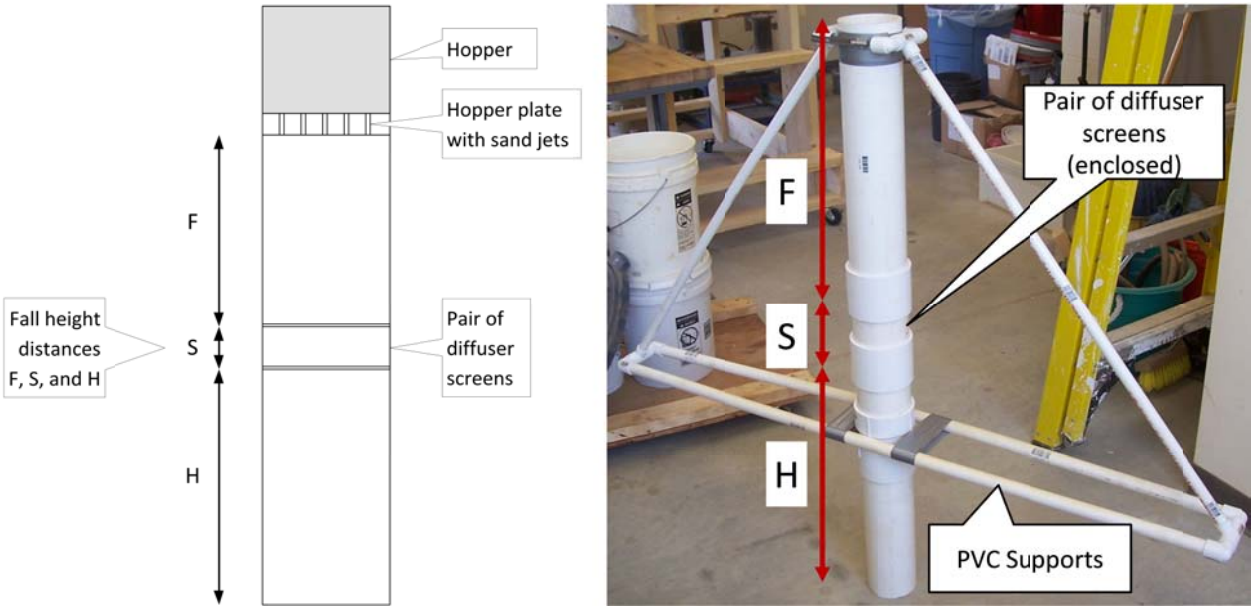

Figure 3.17 Schematic of pluviator concept and photo of actual pluviator used to prepare samples

Eid (1987) explored the impact of the parameters listed in the first column of Table 3.6 on the performance of the pluviator (the density of the deposited sand). Explanations of how each parameter impacts the pluviator performance can be found in Eid's writeup of his parametric study. The primary sand used in the parametric study was Monterey #0/30, which is slightly coarser (D_{50} = 0.45mm) than Light Castle sand (D_{50} = 0.35mm). He also used Monterey #1/20 (D_{50} = 0.75mm) and Monterey #60 (D_{50} = 0.32mm) to test the influence of grain size. The conclusions of his work suggest that, with all other parameters fixed, relative density is inversely proportional to the porosity of the hopper plate. In this case, porosity is defined as the area of openings divided by the total area of the hopper base. Therefore, as more holes are added to the hopper plate, the intensity of sand flow increases, and the relative density of the deposited sand decreases. The level of sand in the hopper tank was found to have no influence on relative density. In the current study, plastic jugs were used as the sand hopper for the pluviator. The jugs could hold about 6.5 lbs of sand when filled and have screw-on caps which were used as the base plate of the hopper. Holes with a diameter of 0.4 inches were drilled in the caps to provide porosity. Hopper plate porosities of 2, 8, and 15% were used to create Density 3, Density 2, and Density 1.

Table 3.6 Parameters studied by Eid (1987) to determine influences on pluviator performance and values used for design of current pluviator.

Parameters controlling pluviator performance	Values for current pluviator
Sand type (grain size)	Light Castle Sand
Level of sand in hopper tank	varies
Porosity of hopper base	2%, 8%, and 15%
Fall distance, F, through upper pluviator chamber	20 inches
Diffuser screen aperture size	0.25 inches
Separation distance, S, between diffuser screens	5.5 inches
Fall distance, H, through lower pluviator chamber	Minimum of 20 inches

The separation distance, *S*, between the diffuser screens was found by Eid (1987) to have no influence on relative density, however when *S* was less than 10 cm (3.9 inches), the sand was not evenly diffused over the area of the pluviator column. In the current pluviator design, a separation distance of 5.5 inches was selected. For the aperture size of the diffuser screens, Eid found that the preferred size is small enough to break up the sand jets completely but large enough to avoid accumulation of sand on the diffuser screens. In his prototypes, Eid used diffuser screens offset by 45 degrees with an aperture size of 0.25 inch. The arrangement yielded satisfactory performance for sands which were finer (Monterey #60) and coarser (Monterey #0/30 and #1/20) than Light Castle Sand, thus the same set up was used in the current pluviator design.

The fall distances H and F both influence the relative density of the sample since they influence the impact velocity of the sand with the sample surface. As H becomes smaller, the impact velocity of the sand decreases and the grains carry less energy to move themselves and neighboring particles into a more dense packing arrangement. The distance F also influences the final impact velocity because the initial velocity of the sand exiting the diffuser screens increases as F is increased. Eid (1987) found that higher relative densities were achieved by increasing F and H until the terminal velocity of the sand was reached. Further increases to F and H had no influence on density. This is a helpful finding since as a sample builds in height, it is satisfactory to keep certain elements of the pluviator fixed and reduce the distances F and/or H without influencing the relative density, as long as the terminal velocity is reached. Eid (1987) found that for Monterey 0/30 sand and an F distance of 45 cm (17.7 in), the relative density of the sample became insensitive to the fall distance H for distances equal to or greater than 50 cm (19.7 in). Eid reports that terminal velocity increases with the mass of the sand particles, thus requiring greater fall height. For the coarser Monterey #1/20 sand and an F distance of 45 cm, H needed to

be 65 cm (25.6 in) before relative density became insensitive to fall height. For finer sands, Rad and Tummay (1986) report that the fall height required to reach terminal velocity for Monterey #0 sand (D_{50} = 0.36mm), which is similar to Light Castle sand, is 25 cm (9.8 inches). In light of this information, for the current pluviator, the main body of the pluviator was designed to be held at a fixed elevation relative to the sample tank and the lower chamber of the pluviator was threaded to allow sections of different lengths to be added as the sample height increased. The distance F was set at 20 inches and H was selected to be 20 inches for the tallest expected sample height of about 10 inches. Therefore at the start of sample preparation, when the tank is empty, the distance H was 30 inches. An F distance of 20 inches and a minimum H distance of 20 inches seem to be conservatively above the height necessary for the Light Castle sand to reach terminal velocity. This means that, when calibrated for Light Castle sand, the only variable that influences relative density is hopper plate porosity.

The relative densities produced by the pluviator using the hopper plates with porosities of 2, 8, and 15% were evaluated two ways. The first approach involved repeatedly preparing samples into a 0.1 ft^3 compaction mold with a 6 inch diameter using the three hopper plates. The results of this exercise are shown in Figure 3.18. Over the range of hopper plate porosities used, the relationship between relative density and porosity is linear. Table 3.7 summarizes the average and standard deviation of relative density produced in the compaction mold using the three different hopper plates.

The second approach for determining the relative density produced by the pluviator was to use the relative density calculated during the experiments using the procedures described in Section 3.7.2. Unreinforced samples higher than 5 inches tested at atmospheric conditions were included in the evaluation of the pluviator performance. Only samples at least 5 inches in height were included because the shape of sample surface beyond the scanning limits of the profiler needs to be assumed as described in Section 3.7.2. The impact of the assumed surface shape on the calculated relative density decreases as sample height increases since the difference between the actual soil volume beyond the scanning limits and the assumed volume becomes a smaller percentage of the total sample volume. Samples incorporating reinforcement were excluded since the samples are leveled during placement of the reinforcement and the leveling process introduces some disturbance in the sample. Samples tested under vacuum were excluded since the bicycle rim and latex used to seal the top of the tank may interfere with surface measurements made near the tank boundary.

The average relative densities measured in the sample tank using the three hopper plates are shown in Figure 3.18 and summarized in Table 3.7. For a fixed hopper plate porosity, the

relative density produced by the pluviator is higher for the sample tank than for the 6 inch diameter compaction mold. The likely reason for this difference is that there is a small air gap between the bottom pluviator chamber and the sample surface. This gap is necessary so the pluviator can be moved around to cover the entire tank interior. Over the distance of the air gap, which is 2 inches or less, there is no lateral confinement provided to the falling sand. As the sand strikes the sample surface, the sand particles can move laterally before coming to rest. The lateral movement effectively lowers the intensity of deposition, which increases density. Since the walls of the 6 inch diameter compaction mold provide more lateral confinement to the falling sand than the sample tank, more depositional intensity is retained, which has the effect of lowering relative density. The difference between the relative densities produced in the compaction mold and the sample tank is greatest when the hopper plate porosity is high, corresponding to high depositional intensity when lateral confinement is maintained.

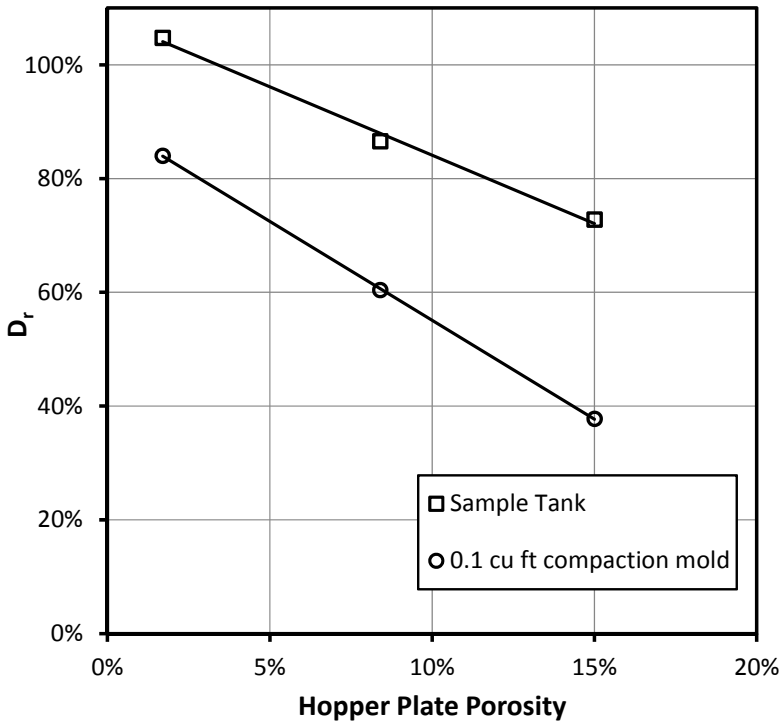

Figure 3.18: Relationship between relative density and hopper plate porosity for pluviator used for sample preparation

Table 3.7: Summary of relative densities produced by pluviator

Vessel	Hopper plate porosity and density designation					
	15% - Density 1		8% - Density 2		2% - Density 3	
	Dr_{avg}	COV	Dr_{avg}	COV	Dr_{avg}	COV
Compaction mold	37.8%	0.048	60.4%	0.055	84.0%	0.015
Sample Tank	72.8%	0.067	86.6%	0.040	104.8%	0.022

3.4 Model Geosynthetic Reinforcement

Three types of biaxial polypropylene netting with different tensile stiffnesses, J (lbs/ft), were selected for use as the geosynthetic reinforcement. The netting was selected based on stiffness determined to be appropriate by approximate application of scaling laws for a 1:10 to 1:20 length scale model.

The relationship among model geometry, gravity forces, and strain in the reinforcement can be assumed to follow the BS8006 (1995) recommendation given below in Equation 3.3, where p is the net vertical stress acting on the reinforcement equal to $SRR(\gamma_{emb}H)$. Eliminating dimensionless terms and expressing embankment height, column spacing, and cap width in fundamental units of length, l, leaves the expression given in Equation 3.4.

$$\varepsilon J = p\frac{\left(s^2 - a^2\right)}{4a}\sqrt{1+\frac{1}{6\varepsilon}} \tag{3.3}$$

$$J = \gamma_{emb}\left(\ell^2\right) \tag{3.4}$$

Using superscripts *model* and *prototype*, the ratio between the stiffness of the model reinforcement to the prototype reinforcement is provided in Equation 3.5.

$$\frac{J^{model}}{J^{prototype}} = \frac{\gamma_{emb}^{model}}{\gamma_{emb}^{prototype}}\left(\frac{\ell^{model}}{\ell^{prototype}}\right)^2 \tag{3.5}$$

Since the unit weight of the model sand is approximately equal to actual embankment material, the model geometry is what governs the scaling of the reinforcement stiffness. If the model is assumed to be a 1:10 to 1:20 length scale model, the ratio of model reinforcement stiffness to the stiffness of the prototype reinforcement should be about 1:100 to 1:400.

In addition to proper scaling, another consideration in selecting model reinforcement was the tendency for very low stiffness netting to be prone to rupture near the column locations. For this reason, the netting selected for use is a bit stiffer when scaled up than many commercially available geogrids, particularly if the model is considered to be a 1:20 length scale model. This limitation is acceptable since the main goal of incorporating reinforcement in the sample is to study the impact of reinforcement on surface deformations rather than the mechanical behavior of the reinforcement itself.

A series of tension tests were performed on each of the reinforcement materials at a 10%/min constant rate of strain in both the machine (MD) and cross-machine directions (XMD). The tests were performed in general accordance with ASTM D 4595, except that the width of the specimens was reduced to 2 inches in order to fit the available clamps. The tests results for each material were averaged and are presented in Figure 3.19. The average of the directional stiffnesses at 5% strain for each of the materials are reported in Table 3.8. The influence of reinforcement stiffness on surface deformation is investigated by changing either the stiffness or number of the reinforcement layers. The bottom layer of reinforcement is placed ½ inch above the base of the bench-scale embankment with ½ inch separating any overlying layers.

Table 3.8 Stiffnesses of reinforcement used in the study

Reinforcement Designation	Average of MD and XMD Secant Stiffness at 5% Strain, J (lbs/ft)
Stiffness 1	294
Stiffness 2	1212
Stiffness 3	1770

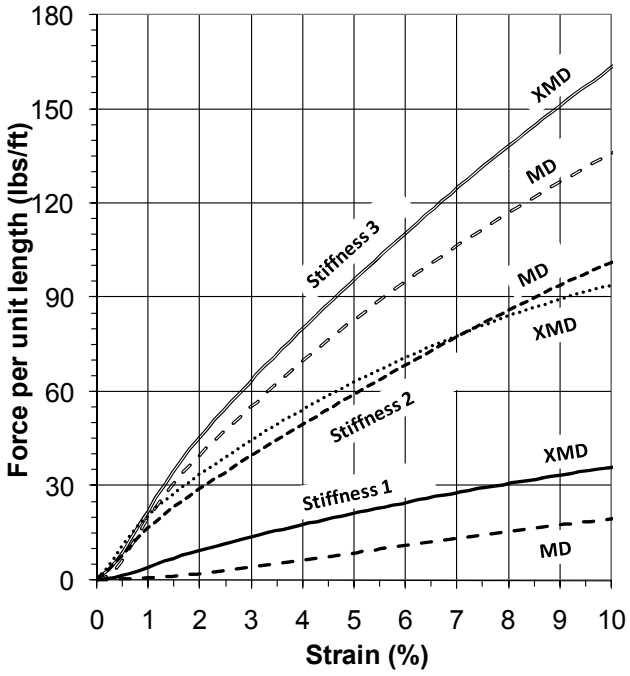

Figure 3.19 Tension test results for reinforcement used in the study

3.5 Test Procedures

This section outlines the procedures followed during experimental testing. It is noted when certain steps are applicable only to a particular set of testing conditions. Reconfiguring the apparatus from one columns arrangement to another is an involved process requiring partial disassembly of the jacking system, and therefore, the steps required to switch from one testing configuration to another are not provided.

Steps 1-21 describe preparation of the sample

1. With an empty tank, the position of the column(s) are checked so that they are level with the table top.
2. A freestanding working platform mounted on rollers is parked next to the bench top apparatus to allow the pluviator to be operated in a comfortable and controlled manner.
3. The wooden frame used to support the pluviator is positioned on the top flange of the sample tank. Periodically, paraffin wax is applied to the wooden frame to provide smooth movement between the frame and the pluviator.
4. The pluviator is assembled with the longest lower attachment that provides a minimal gap between the bottom of the pluviator and the base of the empty sample tank. The pluviator is positioned on top of the wooden frame.

5. The pluviator hopper is filled with Light Castle sand from a stockpile kept in the same laboratory room. The hopper+sand is weighed using an electronic scale and the weight of the sand is obtained by subtracting the weight of the empty hopper.
6. The appropriate hopper disk to achieve the desired sample relative density is screwed onto the top of the hopper bucket.
7. The hopper is quickly inverted over the open top of the pluviator and sand immediately begins to fall through the pluviator column. With a bit of practice, it is easy to perform this operation without losing any significant amount of sand in the process.
8. The pluviator is moved by hand in a spiraling pattern, beginning at the edge of the tank and working towards the center. The movement is intended to build the sample up in a uniform manner over the entire area of the tank opening.

Steps 9-13 are only applicable to tests incorporating layer(s) of the model reinforcement

9. After 0.5 inches of sand has been placed in the tank, the surface is leveled using a screed.
10. On another workbench, the desired model reinforcement is cut into a circle with a diameter equaling the inside diameter of the sample tank using a template and razor blade.
11. The first layer of reinforcement is placed in the tank with the stiffer cross-machine direction oriented parallel to the 0 degree profile orientation shown in Figure 3.20.
12. The pluviation process is continued to provide 0.5 inches of sand separating a second layer of reinforcement, if used.
13. For tests with a second layer of reinforcement, the surface is re-leveled and the reinforcement is placed in the tank with the cross-machine direction oriented parallel to the 90 degree profile orientation.
14. The pluviation process is continued. Each time the hopper is filled, the weight of the sand is obtained. When the sample surface gets close to contacting the bottom of the pluviator chamber, the lower attachment is removed and replaced with the next shorter length section.
15. During pluviation, the height of the sample is tracked using the weight of sand in the tank and the length of the lower attachment on the pluviator. Once the desired sample height is reached, the pluviator and wooden frame are removed from the tank and the sample is leveled using a screed.

Steps 16-21 are only applicable to tests performed under sub-atmospheric conditions.

16. The latex sheeting used to seal the top of the tank is inspected for any defects. If defects are found, a new sheet is cut using a circular template that is a bit larger than the inside diameter of the tank.
17. The latex sheeting is taped to a circular plywood jig that evenly drapes the latex over the bicycle wheel used to clamp the latex to the tank wall.

18. The assembly comprised of the latex, tape, jig, and bicycle wheel are carefully positioned in contact with the sample inside the tank. Once in position, the tape and jig are removed leaving the latex membrane and bicycle wheel.
19. The tire mounted on the bicycle wheel is inflated, which firmly presses the latex against the wall of the tank.
20. The desired vacuum pressure is applied using a regulator connected to the laboratory vacuum pump.
21. The tank is checked for leaks by monitoring the vacuum pressure gauge, which measures pressure inside the tank. If any leaks are detected, the bicycle wheel and latex are removed and Steps 16-20 are repeated. If the sample is disturbed during removal of the latex, the sample is scrapped and a new sample is prepared.

Steps 22-28 describe preparation of the apparatus for testing

22. The data acquisition computer and signal conditioners are powered up.
23. The laser profiler is set in the 45 degree position. A metal prop keeps the linear motion carriage holding the laser directly over the center of the tank.
24. The power supplies to the laser distance transducer, draw wire sensor, LVDT, and load cell (if used) are turned on.
25. The instruments are allowed 15 minutes to warm up. The manufacturer of the laser distance transducer recommends a 15 minute warm-up period to ensure reliable measurements.
26. The vertical slide holding the laser is adjusted to position the laser at its mid-range measuring distance.
27. The jacking system motor controller is powered up. The motor controller is set to the calibrated setting to give a column displacement rate of about 1 inch in 20 minutes. The motor remains stationary until Step 34 when the 'Start' button is pressed.
28. Data acquisition is initiated.

Steps 29-33 describe actions performed during testing to obtain the initial sample height and volume. Figure 3.20 is a reproduction of Figure 3.8 with arrows added to show the direction the profiler is moved across the tank (positive x-direction).

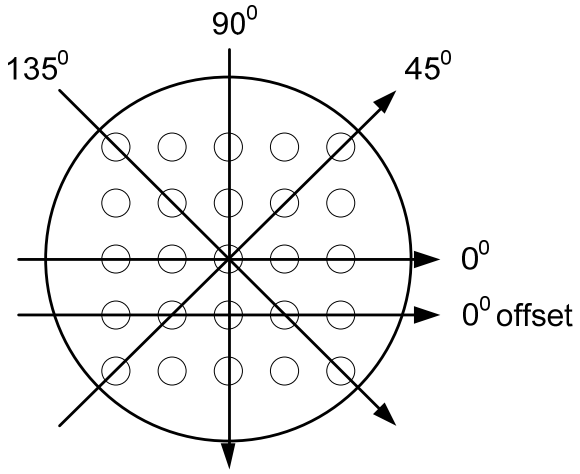

Figure 3.20 Possible profiling orientations showing the direction of profiler sweep

29. The metal prop holding the laser over the tank center is removed and the profiler is moved to the starting position at the tank wall.
30. The scanner is moved slowly by hand in the forward direction along the profile orientation at a rate of about 1 inch in 5 seconds.
31. When the profiler reaches the opposite tank wall, the profiler is returned to the tank center position with the metal prop in place.
32. Steps 29-31 are repeated for the 0, 135, and 90 degree profiling orientations.
33. The profiler is positioned in the 0 degree orientation with the laser held over the center of the tank.

Steps 34-38 describe actions performed during testing to displace the columns and measure the resulting surface deformation.

34. The jacking system motor is started and the columns are advanced an increment of displacement. Increments of displacement are tracked by measuring motor run time using a stop watch. Table 3.9 shows typical displacement intervals tracked during testing using motor run time. Actual column displacements used for analysis of the data are measured with the LVDT mounted to the jacking system.

Table 3.9 Typical intervals of displacement used during testing

Displacement Increment	Interval of motor run time (minutes)	Cumulative motor run time (minutes)	Approximate column displacement (inches)
1	1	1	0.05
2	1	2	0.10
3	1	3	0.15
4	2	5	0.25
5	2	7	0.35
6	4	11	0.55

35. The motor is stopped once a displacement increment is reached.
36. Scans of the sample surface are performed by following Steps 29-31. Typically, scans are performed in the orientations shown in Table 3.10

Table 3.10: Typical orientations of profiles obtained at each increment of column displacement

Test configuration	Profile Orientation				
	0^0	45^0	90^0	135^0	0^0 offset
Single Column	X				
5x5 Column Array	X	X			
2x2 Column Array	X	X			X

37. Steps 34-36 are repeated for each increment of column displacement.
38. Following completion of the test, the tank is emptied and the sand is returned to the stockpile for re-use. The columns are lowered using by reversing the direction of the jacking system motor.

3.6 Test Parameters

The following parameters were varied during testing: column diameter, column spacing, sample height, sample density, presence and stiffness of reinforcement, surcharge pressure, and magnitude of base settlement. In most cases, base settlements ranged from 0 to about 0.6 inches. Table 3.11 summarizes the variations of the other parameters during the testing program. The

table provides the number of tests performed using a particular parameter value. Appendix J provides a complete list of tests and parameter values.

Table 3.11 Summary of parameter variations using during the bench-scale testing program

Parameter		Column Configuration								
		Single Column				5x5 Column Array			2x2 Column Array	
Column diameter (in.)		0.75	1.25	2.00	3.00	0.75	1.25	2.00	0.75	2.00
Column spacing (in.)		-	-	-	-	3.50	3.50	3.50	7.00	7.00
Min. Sample Height (in.)		1.2	1.8	2.4	3.2	1.2	2.2	2.3	4.4	4.6
Max. Sample Height (in.)		9.3	9.3	9.8	10.3	6.7	9.3	9.4	8.7	9.9
Sample Density (# of tests)	Density 1 (D_r = 73%)	-	-	-	5	5	6	5	-	-
	Density 2 (D_r = 87%)	8	11	5	29	23	17	30	9	12
	Density 3 (D_r = 105%)	-	-	-	5	5	5	3	-	-
Model Reinforcement (# of tests)	Unreinforced	8	11	5	24	25	21	21	9	9
	Stiffness 1 294 lbs/ft	-	-	-	6	-	1	5	-	-
	Stiffness 2 1212 lbs/ft	-	-	-	-	-	2	6	-	3
	Stiffness 3 1770 lbs/ft	-	-	-	-	-	1	4	-	-
	2 Layers Stiffness 1	-	-	-	6	-	1	1	-	-
	2 Layers Stiffness 2	-	-	-	2	8	1	1	-	-
	2 Layers Stiffness 3	-	-	-	1	-	1	-	-	-
Equivalent surcharge induced by vacuum (# of tests)	200-300 psf	-	-	-	5	-	-	-	-	-
	300-350 psf	-	-	-	1	-	-	-	-	-
	350-425 psf	-	-	-	9	-	-	-	-	-

Number of tests		8	11	5	39	33	28	38	9	12
		63				120				
		183								

3.7 Data Reduction

The raw data from the experimental testing was reduced using a series of Microsoft Excel spreadsheets and macro code. Reducing data from the load cell and LVDT mounted on the jacking system involved plotting net load (i.e. friction subtracted from measured load) versus column displacement. Since this process was fairly straightforward, further discussion is not necessary. Reducing the data from the laser profiler was considerably more involved. The basic objectives were to use the raw data to determine the sample height and sample volume at various increments of column displacement. Section 3.7.1 describes procedures for obtaining the sample height and Section 3.7.2 describes calculation of the sample volume.

3.7.1 Calculation of sample height and surface settlement

The laser profiler described in Section 3.2.2 was used to determine the height of the sample surface along the profiles transecting the sample tank shown in Figure 3.8 in Section 3.2.2 (Figure 3.20 in Section 3.5) by measuring the distance from the laser transducer to the sample surface, L(x), at a particular position, x, measured by the draw wire sensor. The laser was positioned within its measuring range of the surface using a locking slide with a machinists scale affixed to the side to record the slide position relative to the linear motion rails. As described in Section 3.2.4, measurements from the laser profiler were sampled at a rate of 50 Hz and a moving average was recorded at a rate of 5Hz. Since the profiler was moved by hand across the tank at a rate of about 1 inch in 5 seconds, there were roughly 25 readings per inch of the profile surface. In order to accurately measure increments of surface deformation with base settlement, readings were quantized to a set of positions, *x*, by linearly interpolating from the nearest readings bracketing the location. The increment of distance between quantized positions was 0.05 inches within a 6 inch radius of the tank center and 0.1 inches beyond a 6 inch radius.

In order to accurately measure the height of the sand in the tank, the tank was scanned empty along all the possible profile locations. During the scans, the vertical slide was positioned and locked to hold the laser a distance D_o below the rails of the linear motion slide. The laser readings provide the distance from the transducer to the base of the tank, $L(x)_o$, at each position along the profile. As shown in the left-hand sketch in Figure 3.21, the sum of D_o and $L(x)_o$ gives the baseline distance between the rails of the linear motion slide and the base of the tank. There are minute changes in distance with position since the base of the tank is not perfectly flat and the rails of the linear motion slide are not perfectly co-planar with the workbench top comprising the tank base.

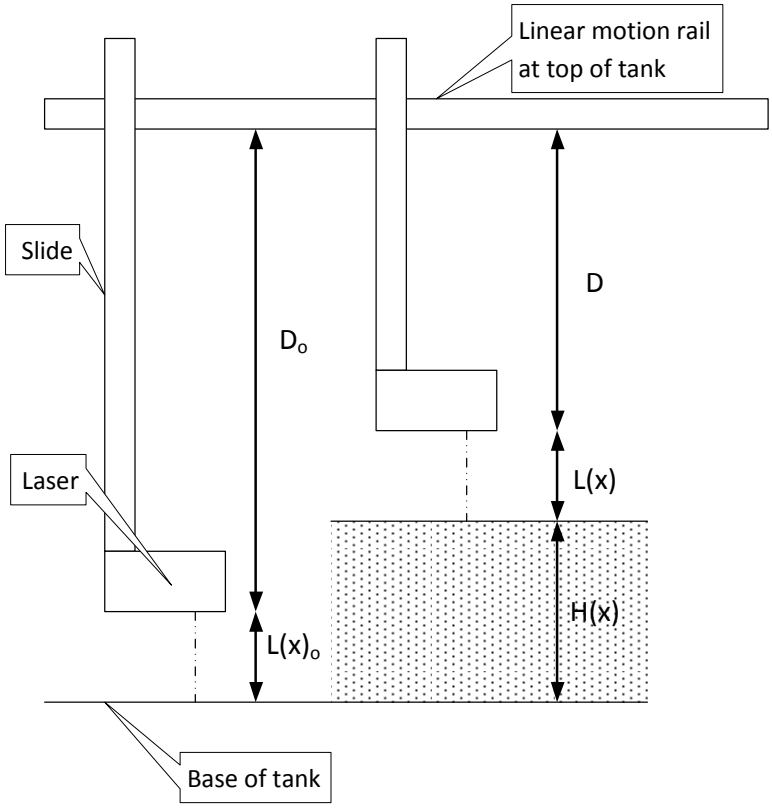

Figure 3.21 Scheme used to measure the height of sand in the tank

Along a given profile, the height of the sand at a particular position, H(x), is given by Equation 3.6 where D is the set position of the vertical slide mounting the laser and L(x) is the measured distance from the laser to the top of the sample at position x. The right-hand sketch in Figure 3.21 illustrates this measurement scheme.

$$H(x) = \left(D_o + L(x)_o\right) - \left(D + L(x)\right) \tag{3.6}$$

During testing, the surface of the sample is scanned at the 0, 45, 90, and 135 degree orientations prior to displacing the column(s) to obtain the initial height of the sample surface. At various magnitudes of column penetration, CP, into the base of the sample, the surface is scanned to measure the resulting surface deformation. If $H(x)_n$ is the height of the sample at a particular location and magnitude of column penetration, beginning with n=1 for the initial scans with no column movement, then the change in sample height $\Delta H(x)_n$ is given by Equation 3.7.

$$\Delta H(x)_n = H(x)_n - H(x)_1 \tag{3.7}$$

If the plane defined by the top of the column(s) is treated as the datum, it is easy to visualize the equivalence between holding the columns fixed and lowering the apparatus and holding the apparatus fixed and raising the columns. Therefore, the magnitude of column penetration, CP, is equal to an equivalent base settlement magnitude, S_b. Using this concept of equivalence, Equation 3.8 shows that the settlement of the sample surface at a certain location and time, $S(x)_n$, is equal to the base settlement magnitude minus the change in sample height.

$$S(x)_n = S_b - \left(H(x)_n - H(x)_1\right) \tag{3.8}$$

3.7.2 Calculation of sample volume

The volume of the sample was determined using the profiler measurements of sample height described in Section 3.7.1. The volume of a ring of soil defined according to Figure 3.22 was calculated at each quantized profiler measuring position. The radius of each ring was determined by taking the absolute value of the difference between the current profile position, x, and the position at the center of the tank, x_{center}. With each complete sweep of the profiler, two sets of soil rings are generated with one set representing the height measurements for $x<x_{center}$ and the second set representing the height measurements for $x>x_{center}$. The volume of soil in the tank is calculated using the complete profile sweep by taking the average of the integrated volumes of the two sets of soil rings. The calculation of the volume of an individual soil ring is given in Equation 3.9 and the calculation of the sample volume based on a single profile sweep is expressed in Equation 3.10. At either limit of each profiler sweep, there is a portion of the sample surface, measuring about an inch, that is beyond the reach of the profiler because the profiler makes contact with wall of the tank. The volume of the ring of soil beyond the reach of the profiler was estimated using the closest measurement of sample height and assuming that the sample slopes down at 1V:6.7H. This slope was estimated from many tests using hand measurements of the slope and extrapolating the slope of the measurements of sand height near the limits of the profiler. To obtain a better measurement of the sample volume, profiles are taken along 0, 45, 90, and 135 degree orientations as defined in Figure 3.8 in Section 3.2.2. The sample volume calculated using individual profiles are averaged to determine sample volume. The sample unit weight was calculated by dividing the weight of sand in the tank by the sample volume determined using the four profile sweeps.

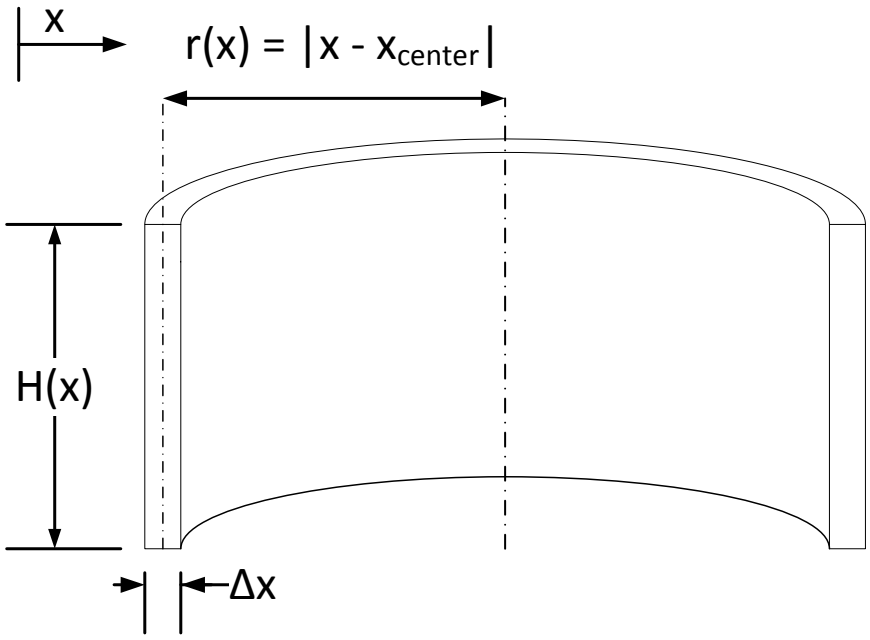

Figure 3.22: Calculation of sample volume using measured sample height at each profiler position

$$V_{soil\ ring} = 2\pi H(x)\left|x - x_{center}\right|\Delta x \tag{3.9}$$

$$V_{sample} = \pi\sum\left[H(x)\left|x - x_{center}\right|\Delta x\right] \tag{3.10}$$

When testing using 5x5 column arrays, the volume within the unit cell defined around the central column was calculated from profiles taken along the 0 and 45 degree orientations. Since the boundaries of the unit cell are square, a different approach than described above was used to obtain volume. Because of the symmetries that exist, surface deformation can be represented by $1/8^{th}$ of the unit cell. The volume within the $1/8^{th}$ slice of the unit cell is divided into rectangular volumes with a width equal to Δx, a length equal to the distance from the current position along the 0^o profile to the center of the tank, l(x), and a height equal to the average of the height measured at the current position along the 0^o profile, H(x) and the height at H(x') along the 45^o profile. Here, x' refers to the x position along the 45 degree profile which corresponds to the x position along the 0 degree profile. This approach to measuring volume is illustrated in Figure 3.23 and expressed mathematically in Equation 3.11. Since profiles along the 0 and 45 degree orientations capture a combined volume equal to $1/4^{th}$ of the unit cell, the integrated volumes of the two $1/8^{th}$ slices were added together and multiplied by 4 as shown in Equation 3.12. To calculate volume change in the soil in response to a magnitude of base settlement, the volume of

the column above the base of the tank is subtracted from the volume calculation, where d is the column diameter and S_b is the displacement of the column relative to the base of the tank.

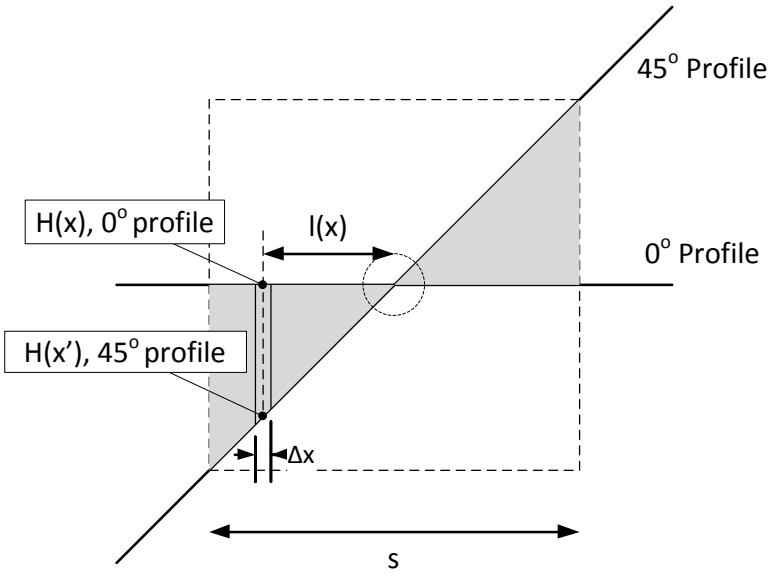

Figure 3.23: Method used to calculate volume within the unit cell

$$V_{rectangle} = \frac{1}{2}\left(H(x)^{0\,deg\,profile} + H(x')^{45\,deg\,profile}\right)\left|x^{0\,deg\,profile} - x_{center}^{0\,deg\,profile}\right|\Delta x$$
$$\text{where } x' = x_{center}^{45\,deg\,profile} + \sqrt{2}\left(x^{0\,deg\,profile} - x_{center}^{0\,deg\,profile}\right) \quad (3.11)$$

$$V_u = 2\sum\left[\left(H(x)^{0\,deg\,profile} + H(x')^{45\,deg\,profile}\right)\left|x^{0\,deg\,profile} - x_{center}^{0\,deg\,profile}\right|\Delta x\right] - \frac{\pi}{4}d^2\left(S_b\right) \quad (3.12)$$

4 Single Column Test Results

This section describes the results from the laboratory testing using a single column configuration. As described in Chapter 3, a total of 63 single column tests were performed using column diameters of 0.75, 1.25, 2.00, and 3.00 inches. For the 3-inch diameter columns tests, the testing equipment allowed for the application of a surcharge pressure using a vacuum system. The 3-inch diameter column tests also included a load cell installed between the column jacking system and the column to measure the load on the column with column displacement. Due to the equivalence described in Section 3.7.1 between raising the column with the sample tank fixed and keeping the column fixed and lowering the sample tank, the results are discussed herein in terms of settlements. The notation used in this section is outlined in Section 1.4 and a list of symbols is provided in the front material. The review of analogous systems provided in Section 2.5 is relevant to the observations made during the single column tests.

Chapter 4 will proceed using an example test in order to detail each component of the analysis. The test parameter values associated with the example are provided below in Table 4.1.

Table 4.1 Test parameter values for test highlighted as example

Test used for example	
Test parameter	Value
Test ID	MD6V2
Column diameter (in.)	3.00
Sample height (in.)	6.5
Sample density	Density 2 (D_r = 87%)
Reinforcement	None
Surcharge induced by vacuum (psi, psf))	2.7, 389

The primary purposes for conducting the single column tests are to 1) delineate the limits of differential surface settlement, 2) observe the relationship between surface settlement directly over the column axis and base settlement, 3) determine the degree of volume change occurring in the sample due to base settlement, and 4) capture the relationship between column stress and displacement. Chapter 4 is organized according to these primary objectives as follows: Section 4.1 describes the settlement profile including delineation of the boundary of differential surface settlement and the relationship between surface settlement over the column and base settlement,

Section 4.2 describes the amount of volume change inferred from surface measurements occurring in the sample due to base settlement, and Section 4.3 describes the column stress-displacement relationships observed during testing with the 3-inch diameter column. A brief chapter summary highlighting key findings is provided in Section 4.4.

4.1 Surface Settlement Profile

This section describes the surface settlement profile, including the radial extent of differential surface settlement resulting from differential settlement of the base around the column and the relationship between surface settlement over the column axis and differential base settlement.

4.1.1 Limits of differential surface settlement

When differential settlement occurs between the column and the base of the sample tank, the sample surface a distance beyond the influence of the column settles the same magnitude as the base. Closer to the projected location of the column, the surface settles some magnitude less than the base settlement due to the support provided by the column. Viewed from above, the limits of the sample surface influenced by the column forms a circle with a diameter equal to d'. The dimension d' will be referred to herein as the *influence diameter*. Using the profiling technique described in Section 3.5, the diameter of the limits of differential surface settlement can be determined for each increment of base settlement, S_b. Figure 4.1 shows the profile of surface settlement measured at each increment of base settlement, $S_{b,n}$, for the example test. The scatter visible beyond a profiling position of 19 inches is due to the presence of the latex sheet and bicycle rim used to seal the top of the tank when testing under sub-atmospheric conditions. A key observation from Figure 4.1, is that the influence diameter, d', does not change significantly with the magnitude of base settlement.

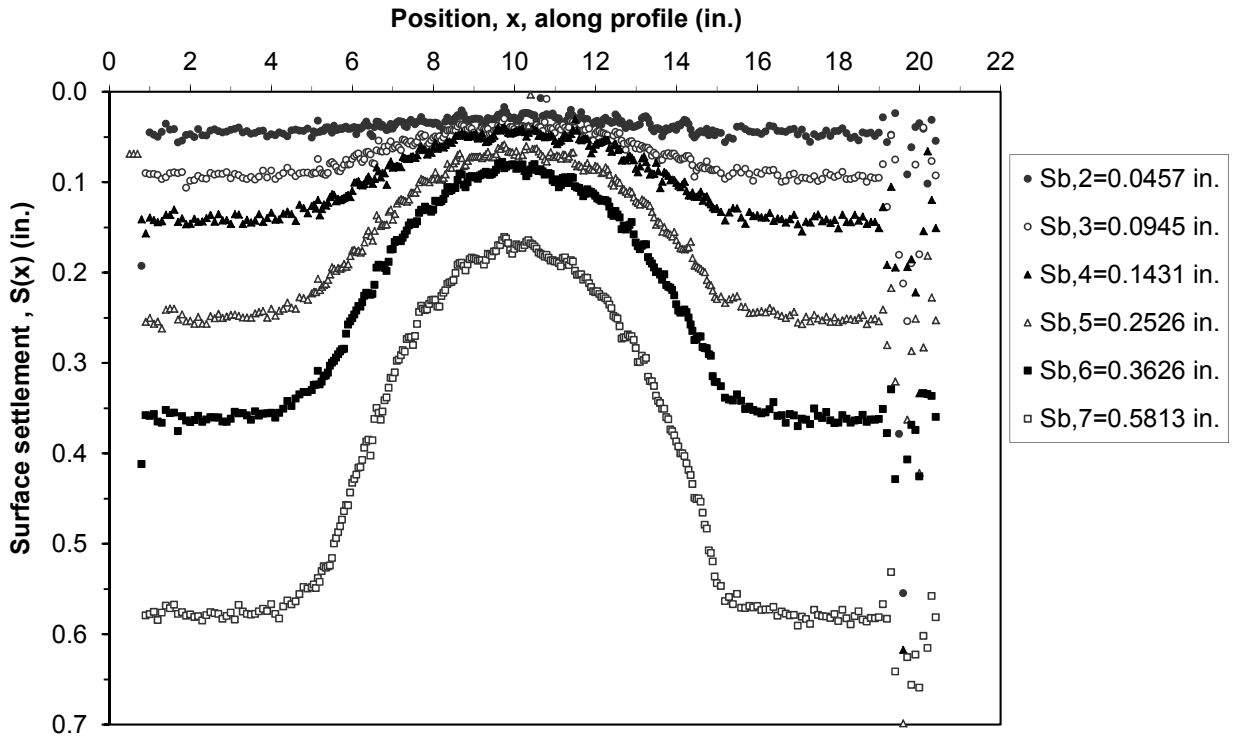

Figure 4.1 Example of settlement profiles at increments of base settlement

From the review of research on embedded anchors provided in Section 2.5, a shearing surface is produced by the differential settlement between the base and the column. The shearing surface initiates at the edge of the column and intersects the sample surface at limits of the column's influence on surface settlement. As illustrated in Figure 4.2, the linear approximation of the failure surface occurs at an angle α with the vertical cylinder above of the column boundary. Using the approach shown in Figure 4.2, the influence diameter can be determined according to Equation 4.1, where d is the column diameter and H is the sample height.

$$d' = d + 2H\tan\alpha \tag{4.1}$$

The angle α can be determined by comparing the values of d' determined for multiple tests performed over a range of sample heights. Figures 4.3 through 4.10 show profiles of the sample surface obtained from different tests provided on plots organized by testing condition. Using the measuring approach described in Section 3.7.1, the height of the sample surface at each profiling position, H(x), rather than settlement, S(x), is plotted so that the surface profiles align vertically beyond the influence diameter. Plotting surface deformation this way makes it easier to see how sensitive the influence diameter is to the magnitude of base settlement. To

make the surface profiles reflect consistent magnitudes of base settlement, the profiles from each test were interpolated to represent the surface deformation occurring from 0.25 and 0.5 inches of base settlement. Therefore, for the settlement profiles shown in Figure 4.1, the surface deformation resulting from 0.25 inches of base settlement is obtained by interpolating the results from $S_{b,4}$ = 0.1431 inches and $S_{b,5}$ = 0.2526 inches. In Figures 4.3 through 4.10, the surface deformation resulting from 0.25 inches of base settlement is shown in red, while the deformation resulting from 0.5 inches of base settlement is shown in blue.

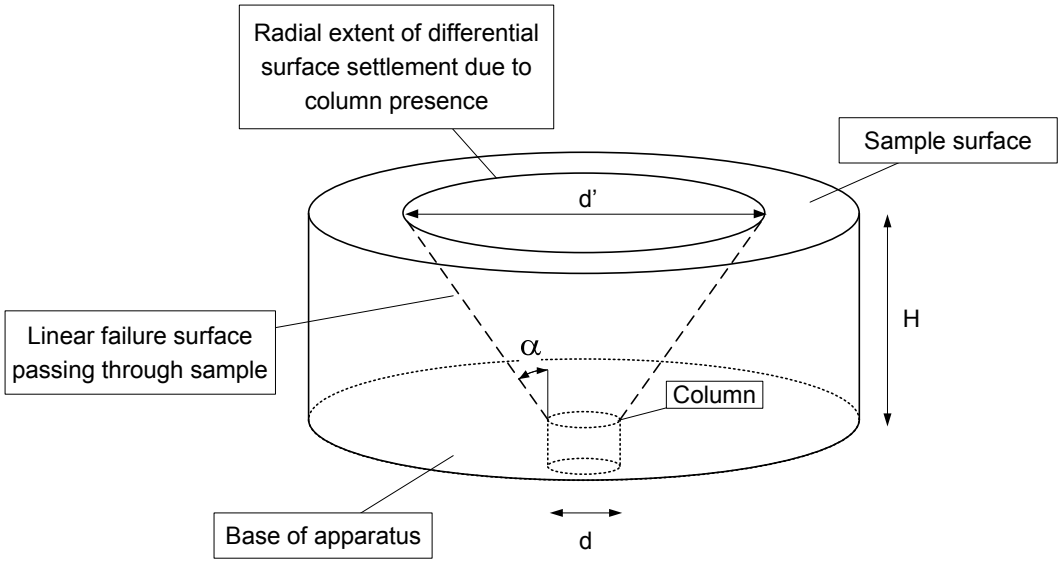

Figure 4.2 Using the angle α to described the limits of differential surface settlement

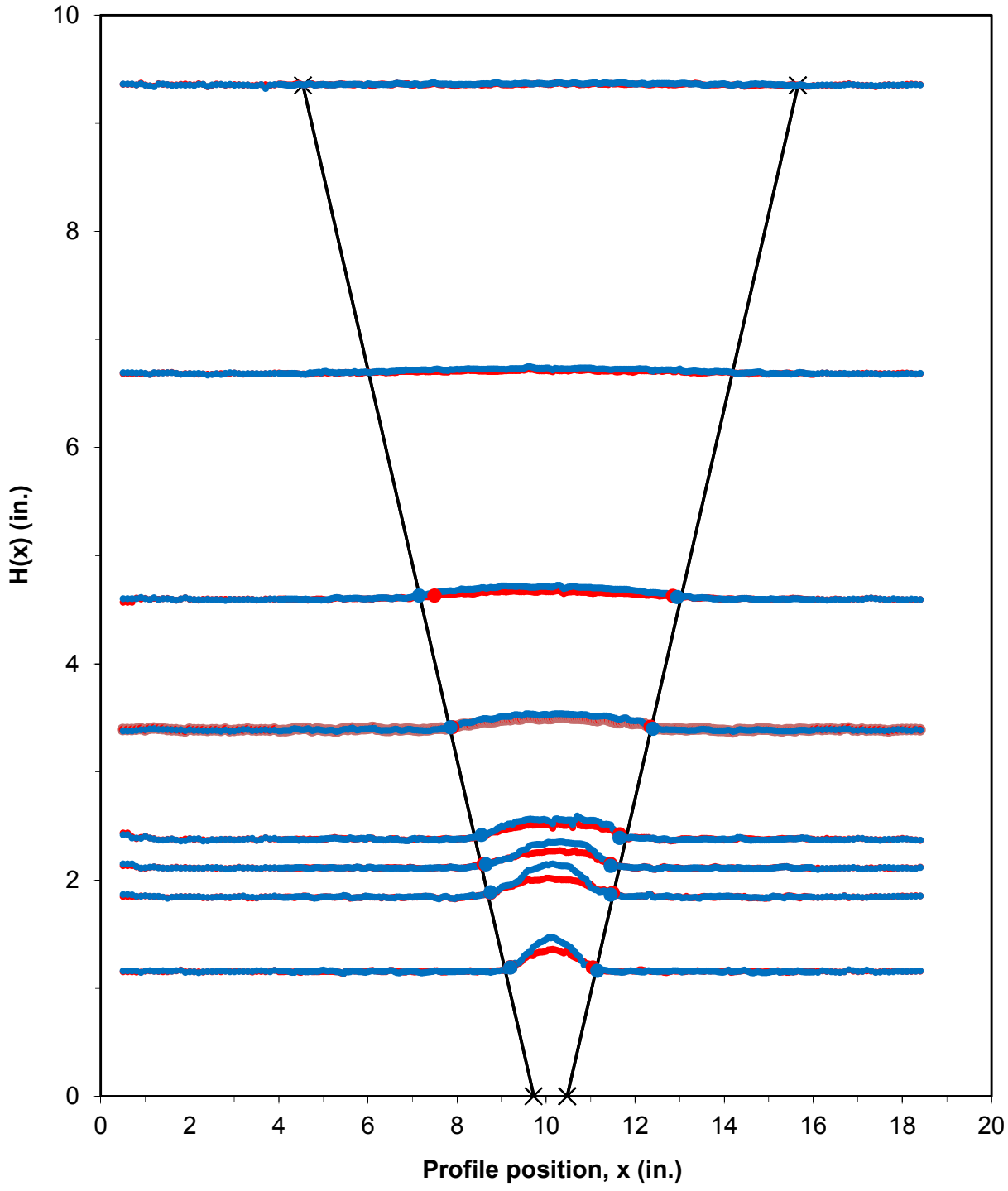

Figure 4.3 Surface deformation profiles for unreinforced tests performed using a 0.75-inch diameter column at sample Density 2 plotted on a consistent vertical axis that has been exaggerated with respect to the horizontal axis. Red and blue lines reflect deformation resulting from 0.25 and 0.5 inches of base settlement, respectively.

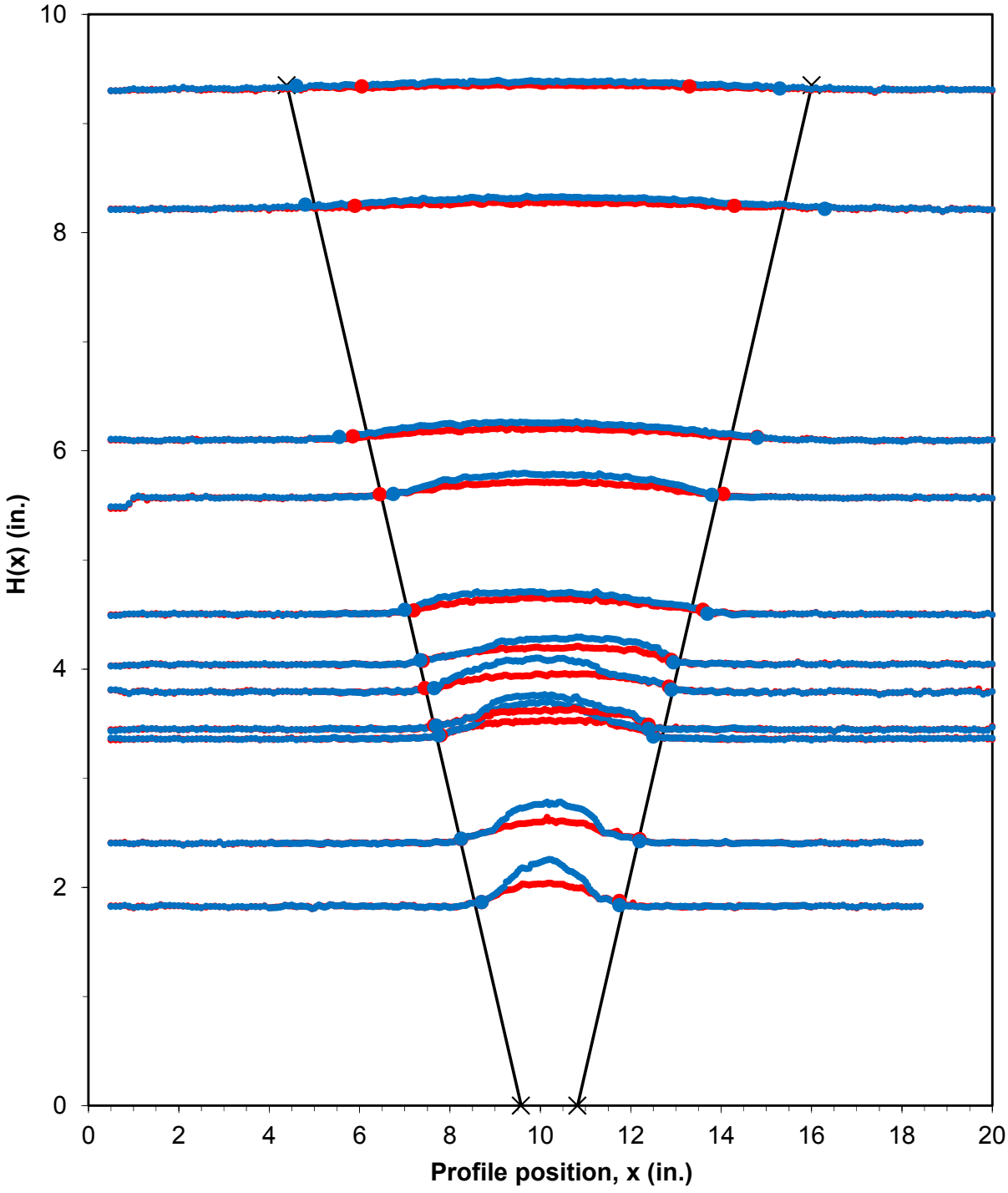

Figure 4.4 Surface deformation profiles for unreinforced tests performed using a 1.25-inch diameter column at Density 2 plotted on a consistent vertical axis that has been exaggerated with respect to the horizontal axis. Red and blue lines reflect deformation resulting from 0.25 and 0.5 inches of base settlement, respectively.

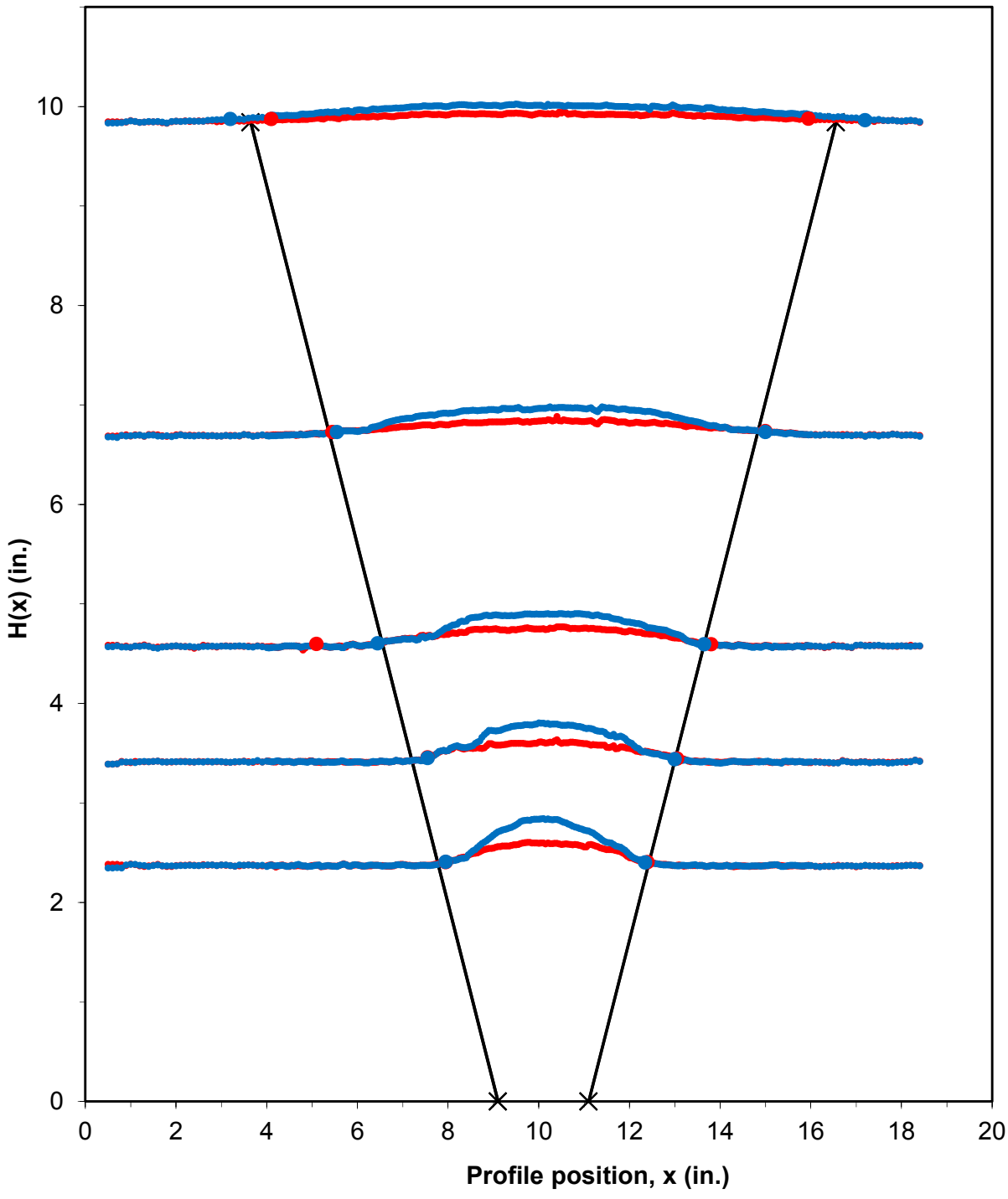

Figure 4.5 Surface deformation profiles for unreinforced tests performed using a 2.0-inch diameter column at Density 2 plotted on a consistent vertical axis that has been exaggerated with respect to the horizontal axis. Red and blue lines reflect deformation resulting from 0.25 and 0.5 inches of base settlement, respectively.

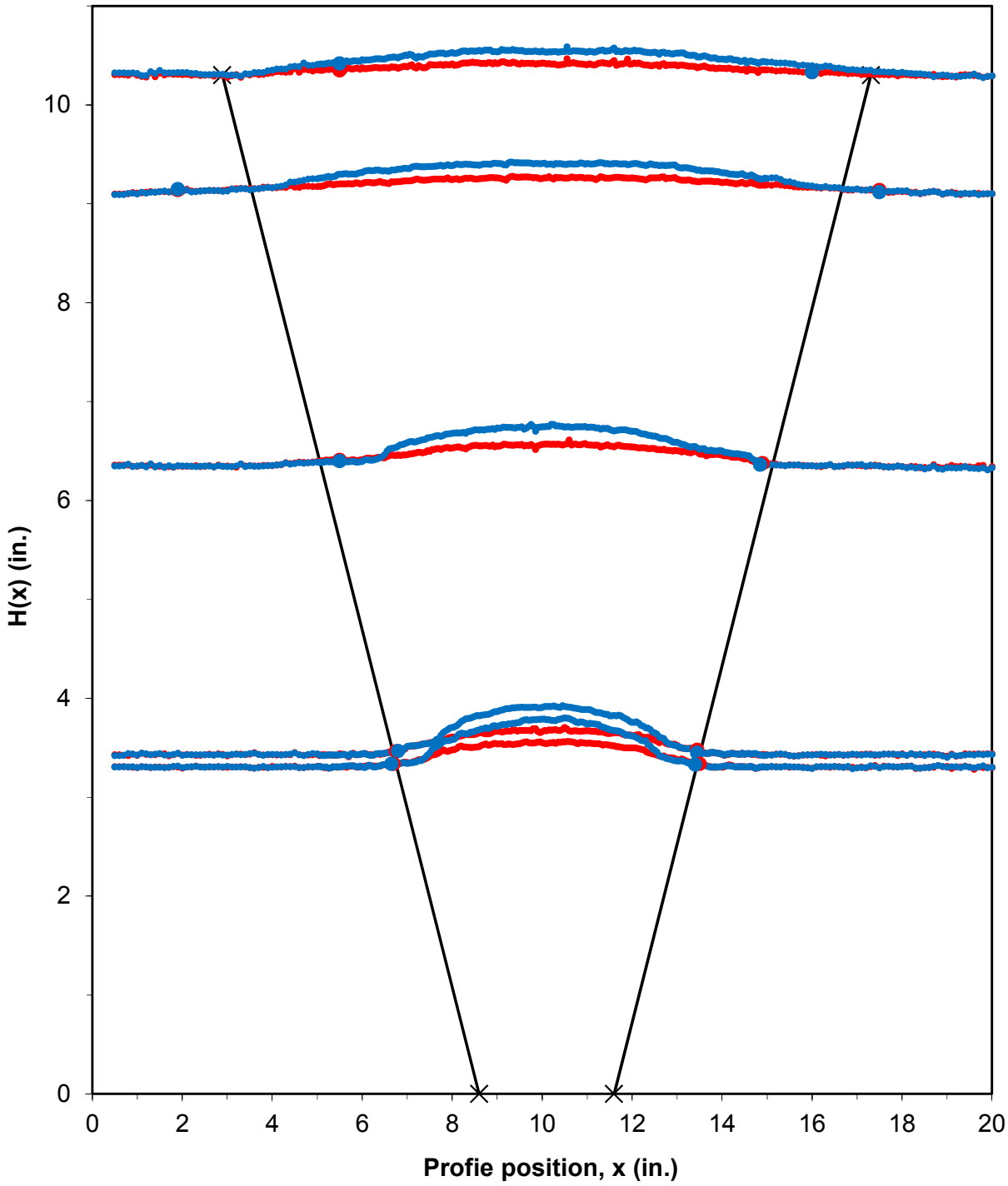

Figure 4.6 Surface deformation profiles for unreinforced tests performed using a 3.0-inch diameter column at Density 2 plotted on a consistent vertical axis that has been exaggerated with respect to the horizontal axis. Red and blue lines reflect deformation resulting from 0.25 and 0.5 inches of base settlement, respectively.

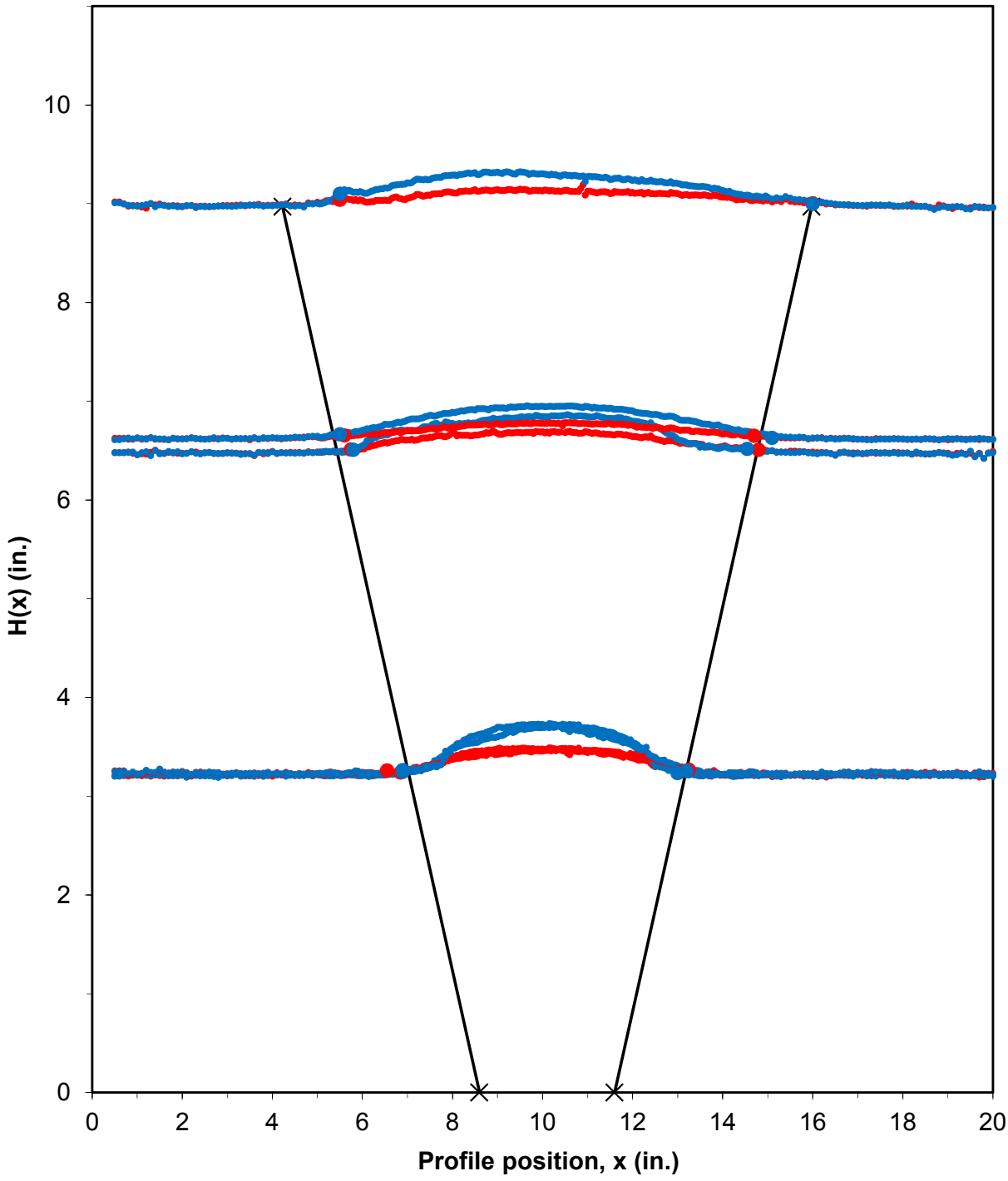

Figure 4.7 Surface deformation profiles for unreinforced tests performed using a 3.0-inch diameter column at Density 1 plotted on a consistent vertical axis that has been exaggerated with respect to the horizontal axis. Red and blue lines reflect deformation resulting from 0.25 and 0.5 inches of base settlement, respectively.

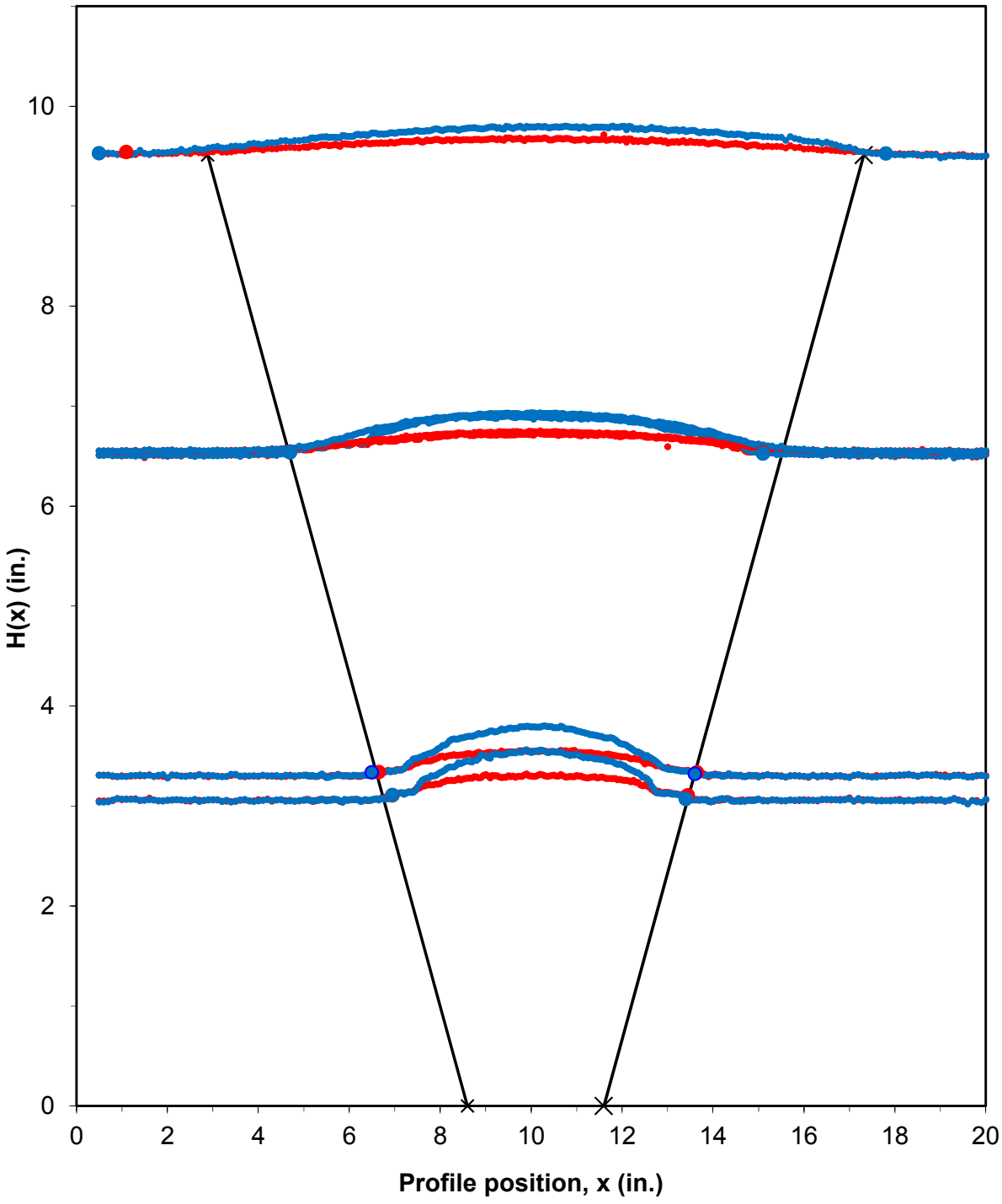

Figure 4.8 Surface deformation profiles for unreinforced tests performed using a 3.0-inch diameter column at Density 3 plotted on a consistent vertical axis that has been exaggerated with respect to the horizontal axis. Red and blue lines reflect deformation resulting from 0.25 and 0.5 inches of base settlement, respectively.

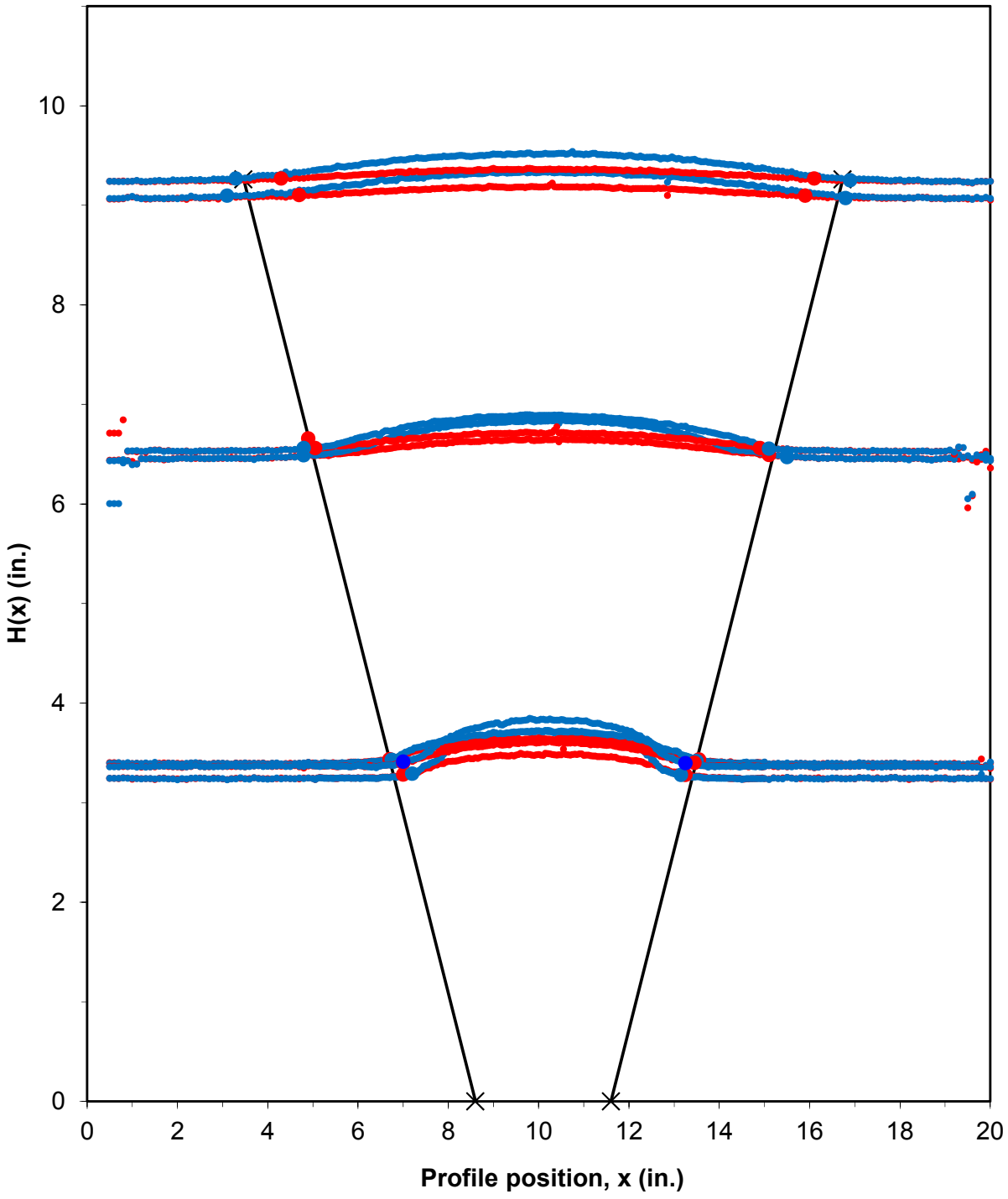

Figure 4.9 Surface deformation profiles for unreinforced tests performed at sub-atmospheric conditions using a 3.0-inch diameter column at Density 2 plotted on a consistent vertical axis that has been exaggerated with respect to the horizontal axis. Red and blue lines reflect deformation resulting from 0.25 and 0.5 inches of base settlement, respectively.

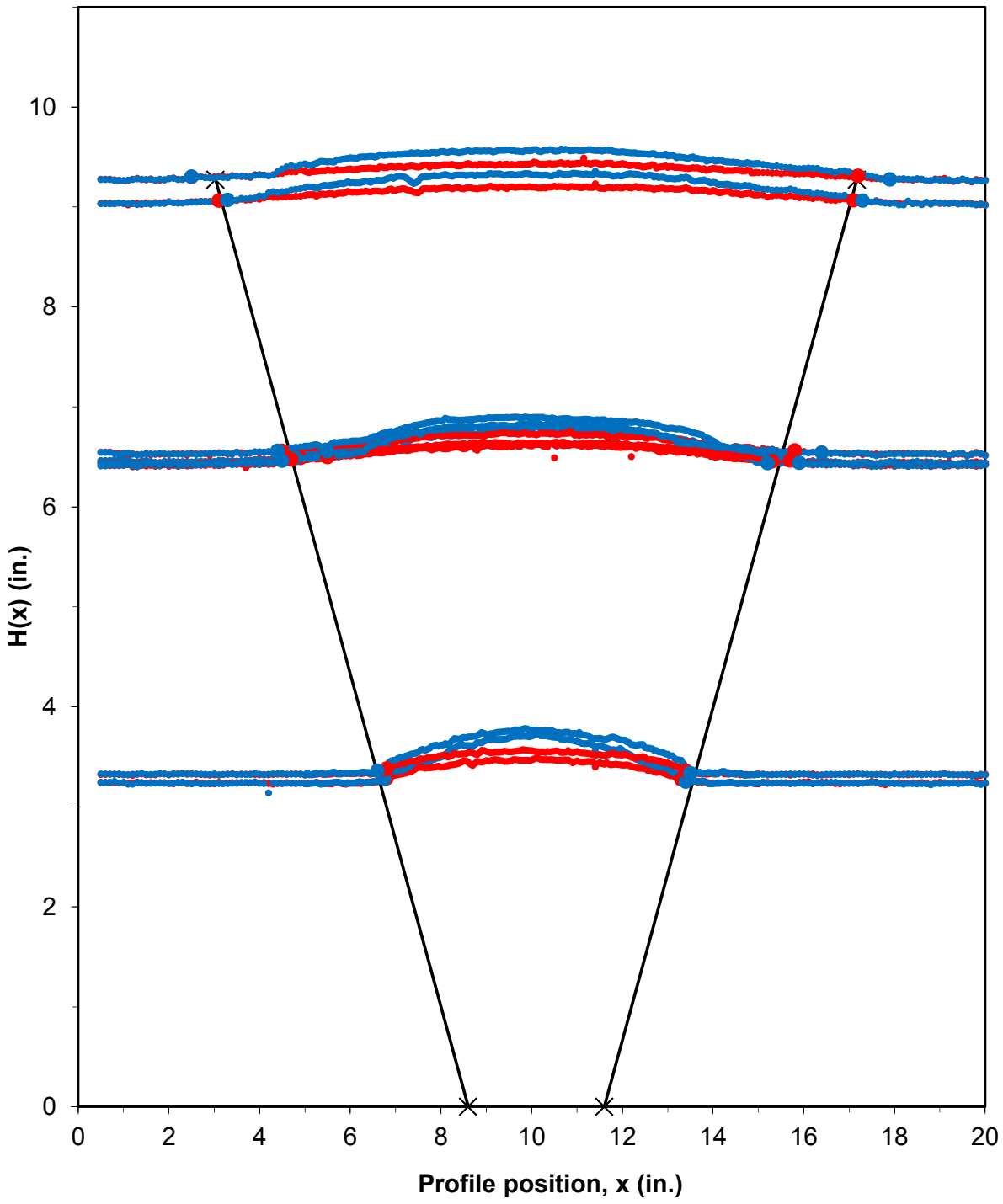

Figure 4.10 Surface deformation profiles for reinforced tests performed using a 3.0-inch diameter column at Density 2 plotted on a consistent vertical axis that has been exaggerated with respect to the horizontal axis. Red and blue lines reflect deformation resulting from 0.25 and 0.5 inches of base settlement, respectively.

The larger red and blue symbols shown in Figures 4.3 through 4.10 show the delineation of the limits of differential surface settlement. The locations were determined using an automatic routine in the analysis file which searches for the furthest distance away from the column axis in either direction where the change in the sample height, $\Delta H(x)$, exceeds 0.03 inches. The threshold value of $\Delta H(x) = 0.03$ inches is equal to twice the d_{50} particle size for Light Castle sand. In a few cases at higher sample heights, the symbols are omitted because the surface deformations are too small to identify the boundary. The black lines in the figures provide a good fit to the boundaries and were used to estimate values of α. This approach for delineating the boundaries of differential surface settlement suggests that sample height, surcharge pressure, and the magnitude of base settlement have little effect on the angle α. The results shown in Figures 4.3 through 4.10 are summarized in Table 4.2.

Table 4.2 Summary of results for delineating limits of differential surface settlement from single column tests

Figure	Test Condition	Estimate of α (deg)	α/ϕ	α/ψ
4.3	d = 0.75 in., Density 2, unreinforced	29	0.56	0.97
4.4	d = 1.25 in., Density 2, unreinforced	29	0.56	0.97
4.5	d = 2.00 in., Density 2, unreinforced	29	0.56	0.97
4.6	d = 3.00 in., Density 2, unreinforced	29	0.56	0.97
4.7	d = 3.00 in., Density 1, unreinforced	26	0.54	0.96
4.8	d = 3.00 in., Density 3, unreinforced	32	0.57	0.97
4.9	d = 3.00 in., Density 2, unreinforced, w/ surcharge	29	0.56	0.97
4.10	d = 3.00 in., Density 2, reinforced	31	0.60	1.03

Note: Values of friction angle, ϕ, and dilation angle, ψ, are reported in Section 3.3.1

The results shown in Figures 4.3 through 4.10 and summarized in Table 4.2 indicate that α for unreinforced samples increases approximately in proportion with peak friction and dilation angles according to Equations 4.2 and 4.3. The presence of reinforcement appears to have the effect of slightly increasing α.

$$\alpha \approx 0.56\phi \tag{4.2}$$

$$\alpha \approx 0.97\psi \tag{4.3}$$

The ratios α/ϕ and α/ψ provided in Equations 4.2 and 4.3 support the experimental findings by Ilamparuthi and Muthukrishnaiah (1999), Murray and Geddes (1989), and Vermeer and Sutjiadi (1985) during their research on embedded anchors discussed in Section 2.5.2.

4.1.2 Surface settlement over the column axis

This section describes how surface settlement directly over the axis of the column is influenced by sample height, column diameter, sample density, reinforcement condition, application of surcharge pressure, and magnitude of base settlement.

As described in Sections 3.2.2 and 3.5, the settlement over the axis of the column is measured during profiling of the sample surface at each increment of base settlement. When the equipment is configured for testing a single column or column-centered unit cell, the surface settlement over the column axis is also measured between scans during column displacement. This measuring capability provides a detailed view of the relationship between surface settlement over the column and base settlement. Using the example test described at the beginning of the chapter, Figures 4.11 and 4.12 shows the two ways surface settlement over the column can be measured.

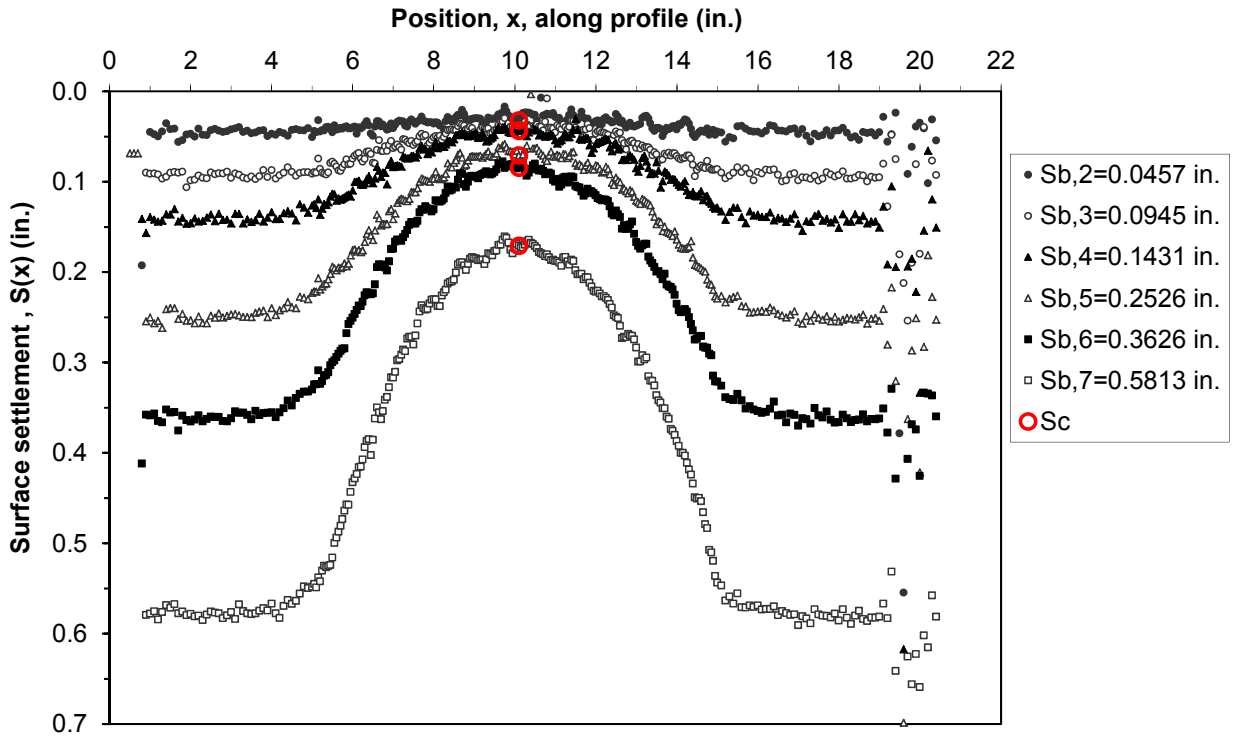

Figure 4.11 Example settlement profiles measured between increments of column displacement. The settlement measured over the column, S_c, is highlighted in red

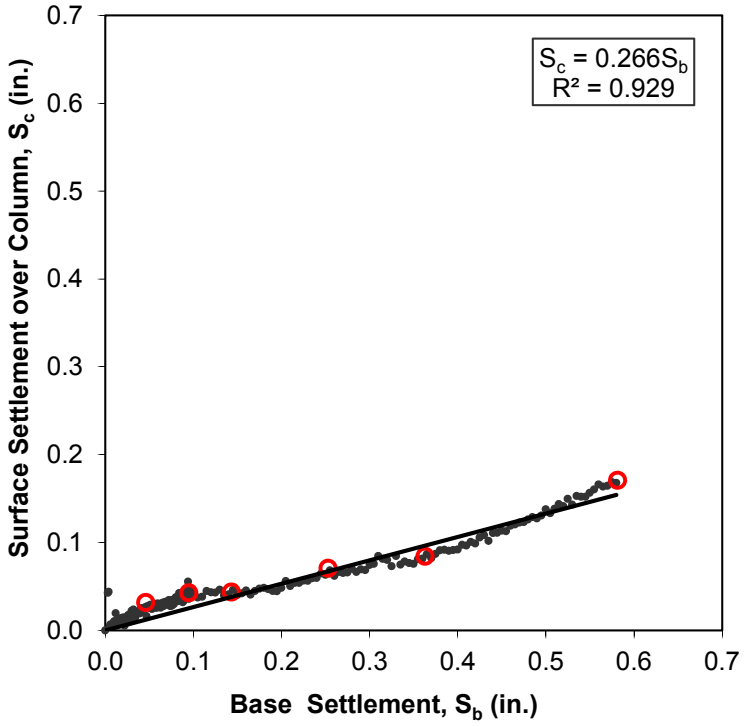

Figure 4.12 Example plot of surface settlement over the column, Sc, versus base settlement, Sb measured during column displacement. Measurements of S_c obtained between increments of column displacement shown in Figure 4.11 are superimposed in red.

As described in Section 1.4, it is convenient to describe the surface settlement over the column as a ratio of the base settlement. From Figure 4.12, the ratio S_c/S_b, referred to herein as SBR_c, can be reasonably approximately as linear. In the current example SBR_c is equal to 0.266. As described in Section 2.5, the experiments performed by Fadl (1981) on embedded anchors showed that SBR_c increases with sample height and tends to normalize for different anchor diameters when plotted against H/d.

The values of SBR_c obtained from single column testing on unreinforced samples prepared at Density 2 are shown in Figure 4.13. The figure shows that SBR_c equals zero at H/d approximately equal to unity, meaning that the surface over the column axis does not experience any settlement due to base settlement. At the other extreme, when H/d exceeds about 13.5, the column has essentially no influence on surface settlement over the column axis. This value of H/d agrees well with Meyerhof and Adam's (1968) recommendations for estimating the critical embedment ratio, H^*/d, based on friction angle. As discussed in Section 2.5, the critical embedment ratio is the anchor depth where the failure mode transitions from a shallow mode that reaches the ground surface to a deep mode that is contained within a bulb of soil above the

anchor. Figure 4.14 is a reproduction of Figure 2.15 in Section 2.5 showing the agreement between the recommendations by Meyerhof and Adams (1968) and the current results.

In Section 2.5, the results from single column testing were also compared to the anchor pullout test results obtained by Fadl (1981). Figure 4.15 is a reproduction of Figure 2.14 showing the agreement between Fadl's results for dense samples and the current results. Most of the current test results classify as dense samples.

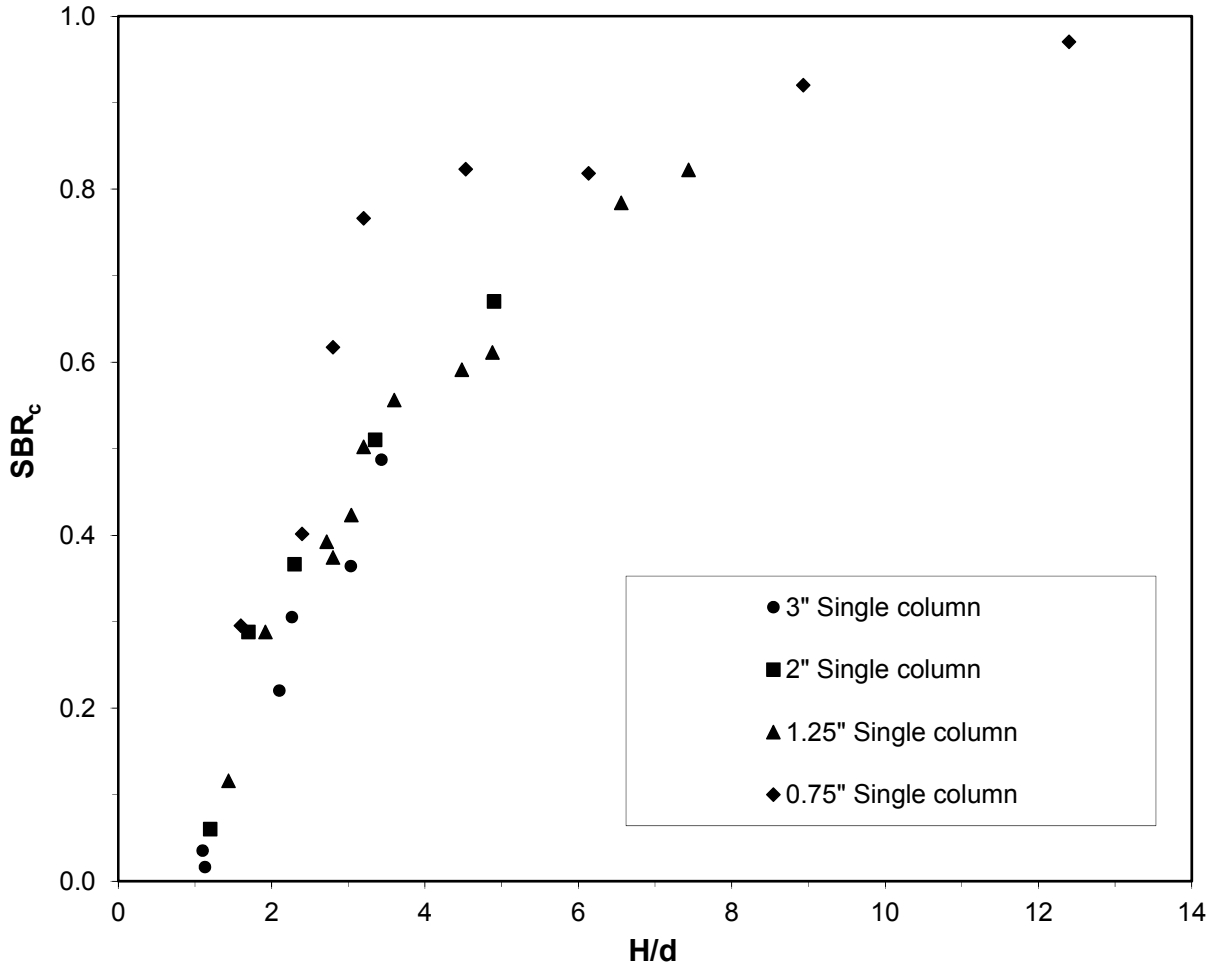

Figure 4.13 Ratio of surface settlement over column to base settlement, SBR_c, versus H/d for unreinforced single column tests prepared at Density 2

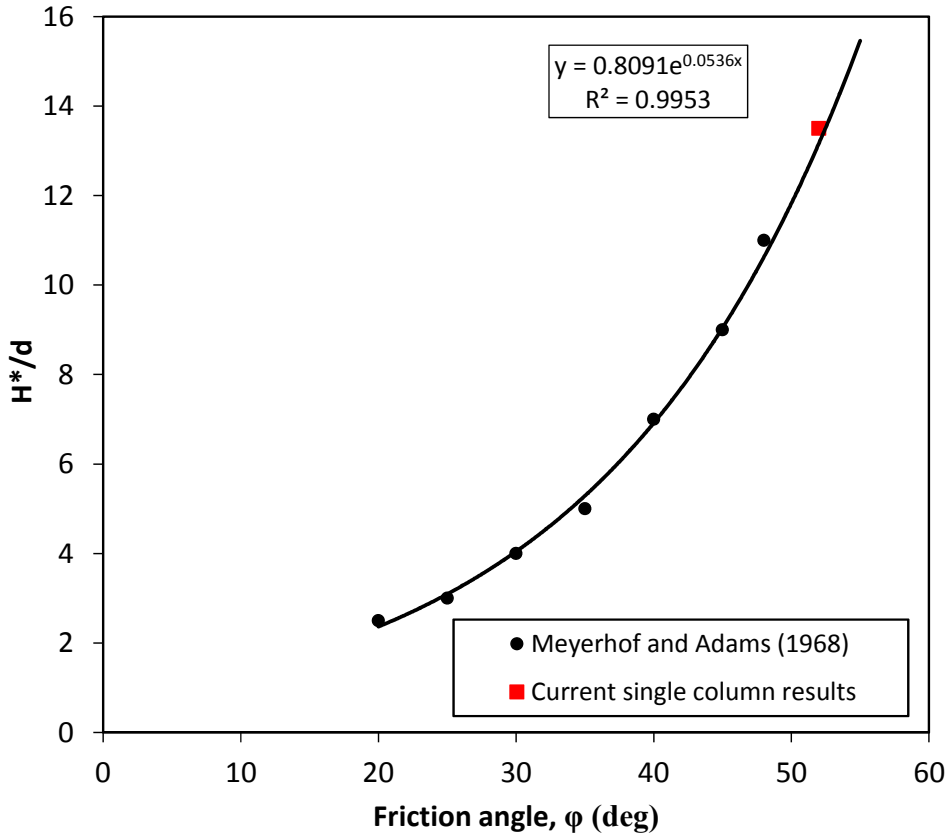

Figure 4.14 Meyerhof and Adam's (1968) relationship between critical embedment ratio. H^*/d, and friction angle. Extrapolation of current results shown in red ($\phi = 52^o$ at Density 2, Section 3.3.1)

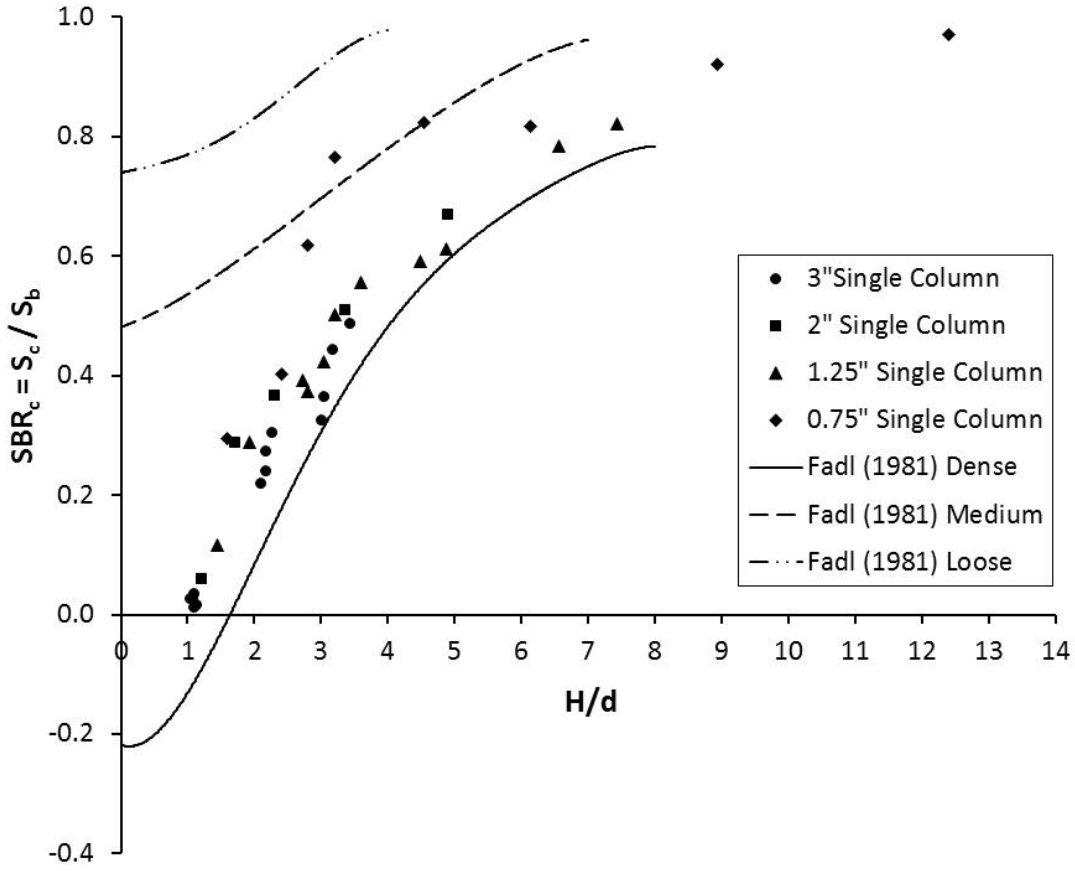

Figure 4.15 Settlement ratio, SBR_c determined using results by Fadl (1981) with results from single column tests

Figure 4.16 shows the impact of density on SBR_c for unreinforced tests. Over the range of densities evaluated, no trend is evident and no conclusions can be drawn. As shown in Figure 4.15, Fadl (1981) observed that settlement over the anchor increases with decreasing relative density.

Figure 4.17 shows the influence of a surcharge pressure applied using the vacuum system described in Section 3.2.3. The magnitude of applied surcharge pressure used in the tests varied from 200 to 425 psf. Similar to the variation in sample density, it is difficult to distinguish the influence of an applied surcharge pressure on SBR_c over the range of surcharge pressures evaluated. However, there appears to be a slight increase in SBR_c for the tests with applied surcharge. Except for the two tests with normalized sample heights exceeding 3, SBR_c increases with the magnitude of surcharge pressure. One possible explanation for this behavior is that the surcharge pressure contributes to the stress concentration over the column induced by base

settlement. The higher stresses in the soils over the column lead to greater compression, which has the effect of increasing SBR_c.

Figure 4.18 shows the influence of incorporating the reinforcement described in Section 3.4 in the samples. The test results using different reinforcement stiffnesses and number of reinforcing layers are lumped together in the figure. The results suggest that, in general, the presence of reinforcement does not have a large impact on SBR_c compared to the unreinforced tests. However, at low normalized sample heights, two tests suggest that the presence of reinforcement may increase SBR_c. Of the two tests showing an increase in SBR_c at low values of H/d, one sample incorporated one layer of Stiffness 1 (least stiff) reinforcement, while the other sample incorporated two layers of Stiffness 1 reinforcement. The measured value of SBR_c for the sample with two layers of reinforcement is higher than the measured value for one layer. Therefore, based on a limited number of observations, there is evidence that at low sample heights, the presence of reinforcement increases SBR_c and the number of layers magnifies the effect. One possible explanation for this behavior is that the vertical component of tension in the reinforcement compresses the soil between the reinforcement and the top of the column. This explanation is supported by the fact that an additional layer of reinforcement results in a greater increase in SBR_c. As described in Section 3.4, a ½ inch layer of sand was placed between the column and the bottom layer of reinforcement and another ½ inch layer of sand separated the bottom and top reinforcement layers. The tests where the increase in SBR_c was observed had sample heights around 3.4 inches, so the added compression of the soil below the reinforcement layers could have a significant impact on SBR_c for the conditions associated with the bench-scale tests.

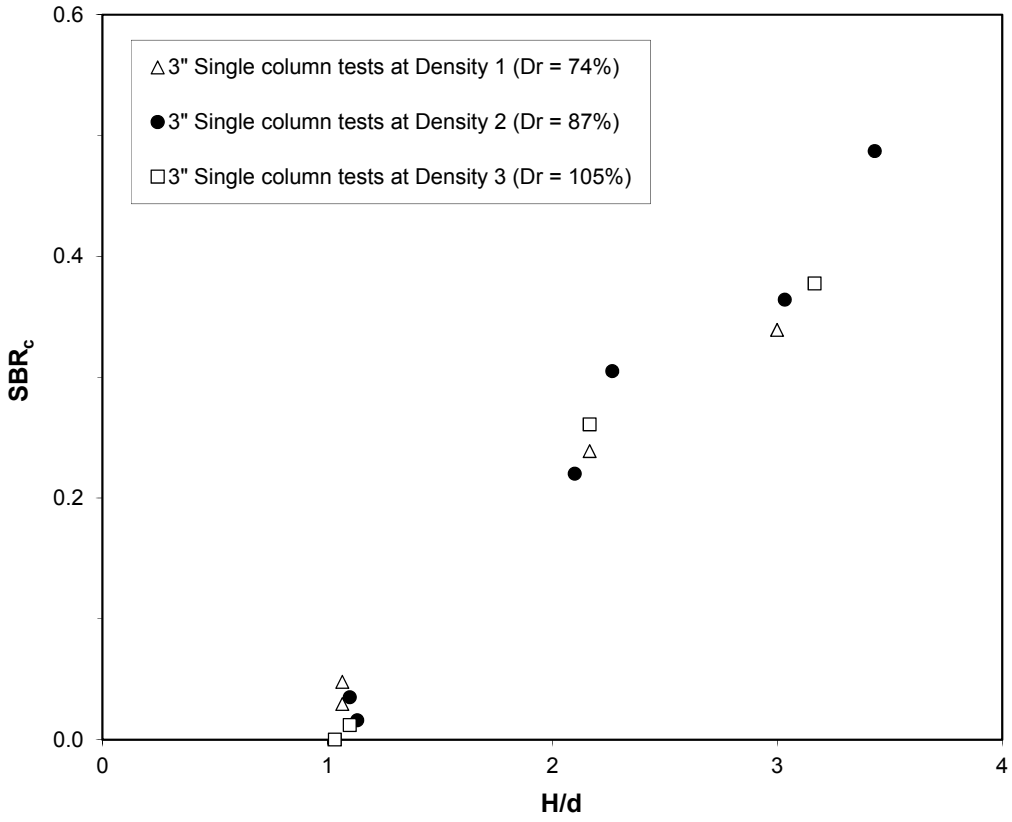

Figure 4.16 Measured impact of relative density on SBR_c

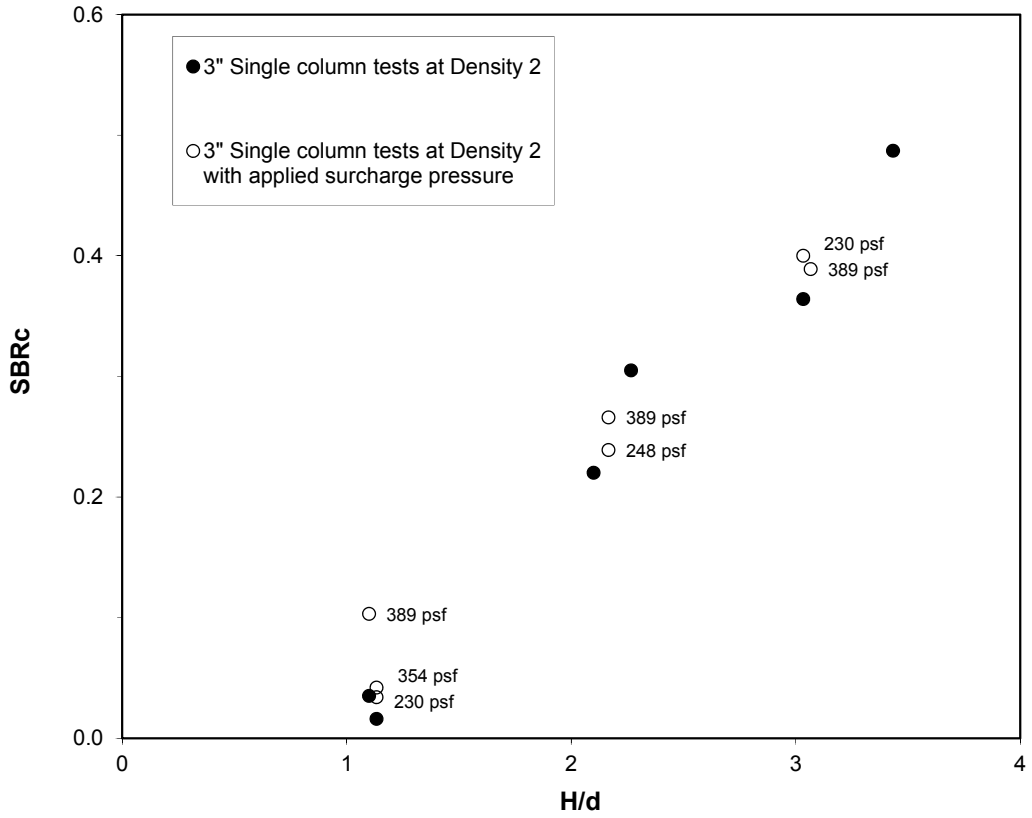

Figure 4.17 Measured influence of applied surcharge pressure on SBR_c. Data labels indicate the magnitude of applied surcharge pressure.

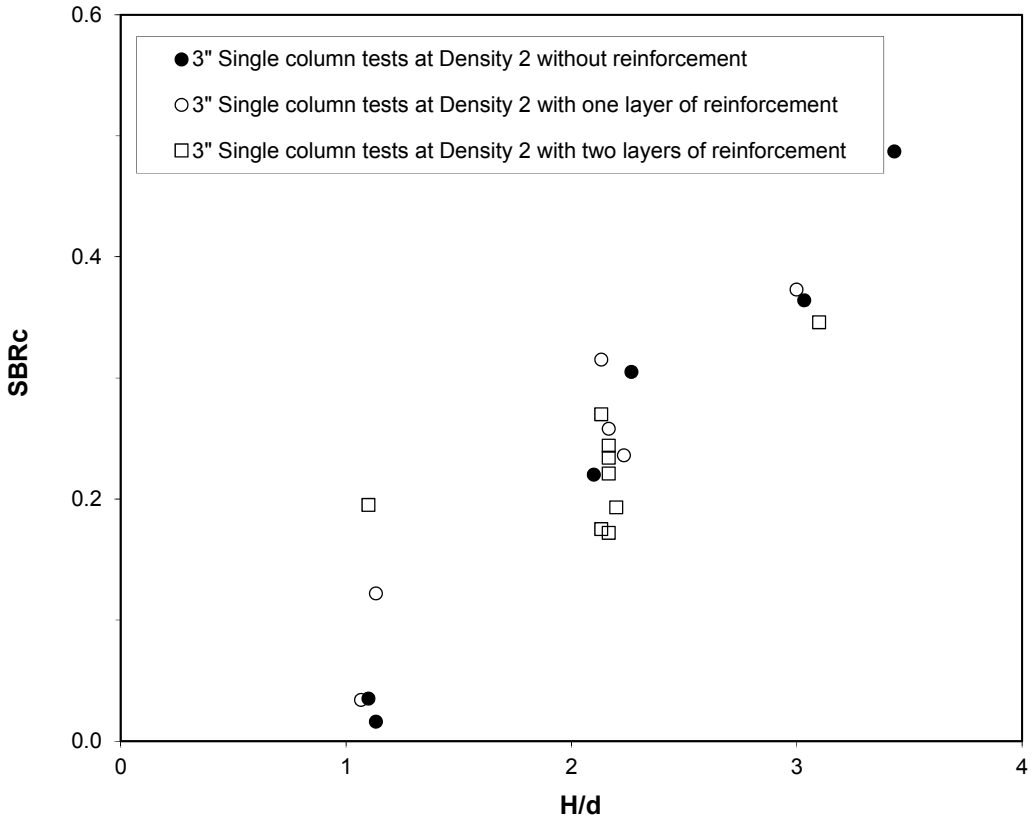

Figure 4.18 Measured influence of reinforcement on SBR_c

4.2 Volume Change

Volume change in the sample was determined by subtracting the initial sample volume from the volume calculated at increments of base settlement. Sample volume was calculated using the procedures described in Section 3.7.2. Sample volume calculations at increments of base settlement were performed for tests using the 1.25 and 3.00 inch diameter columns only. Figure 4.19 shows the change in sample volume with increasing base settlement for the example test described at the beginning of the chapter. As the figure shows, the sample continues to dilate even at the highest magnitude of base settlement, although the rate of dilation is decreased compared to lower magnitudes of base settlement.

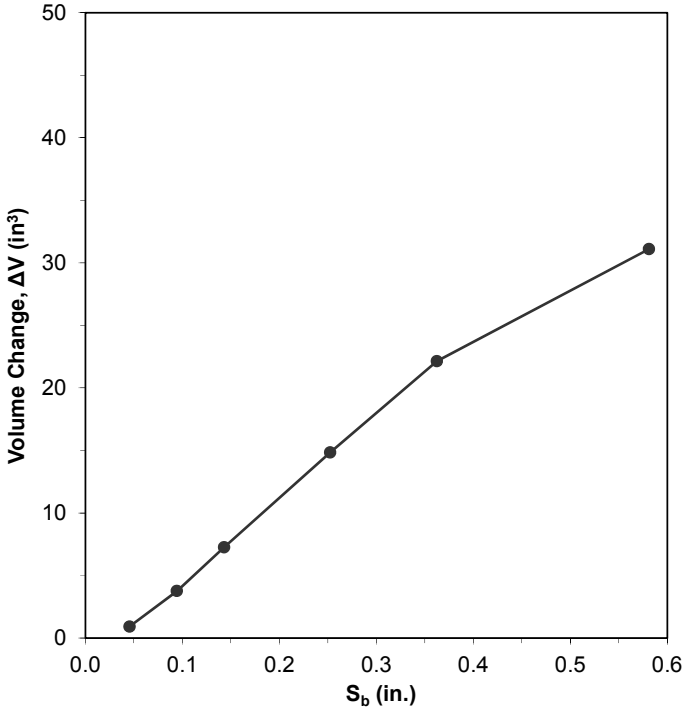

Figure 4.19 Volume change in sample versus base settlement magnitude for example test

Figure 4.20 shows volume change versus base settlement for unreinforced single column tests performed on samples prepared at Density 2 using column diameters of 1.25 and 3.00 inches. The test data is organized by column diameter and normalized sample height, H/d. As expected, for a particular sample height and base settlement magnitude, the volume change produced by the 3-inch column is greater than the volume change due to the 1.25-inch column. Using this plot, it is difficult to determine how sample height influences the magnitude of volume change, but it appears that taller samples generally experience more cumulative volume change than shorter samples. This is likely because, even at tall sample heights, the confining stresses are not sufficient to significantly suppress dilation. The volume change per unit volume of soil influenced by the column can be determined by dividing the magnitude of volume change by the volume of the influenced soil mass shown in Figures 4.2 and 4.21. The volume of the influenced soil mass, V_f, is a truncated cone, or frustum, which can be determined according to Equation 4.4. For the current test results, the angle α was found in Section 4.1.1 to have values shown in Table 4.2.

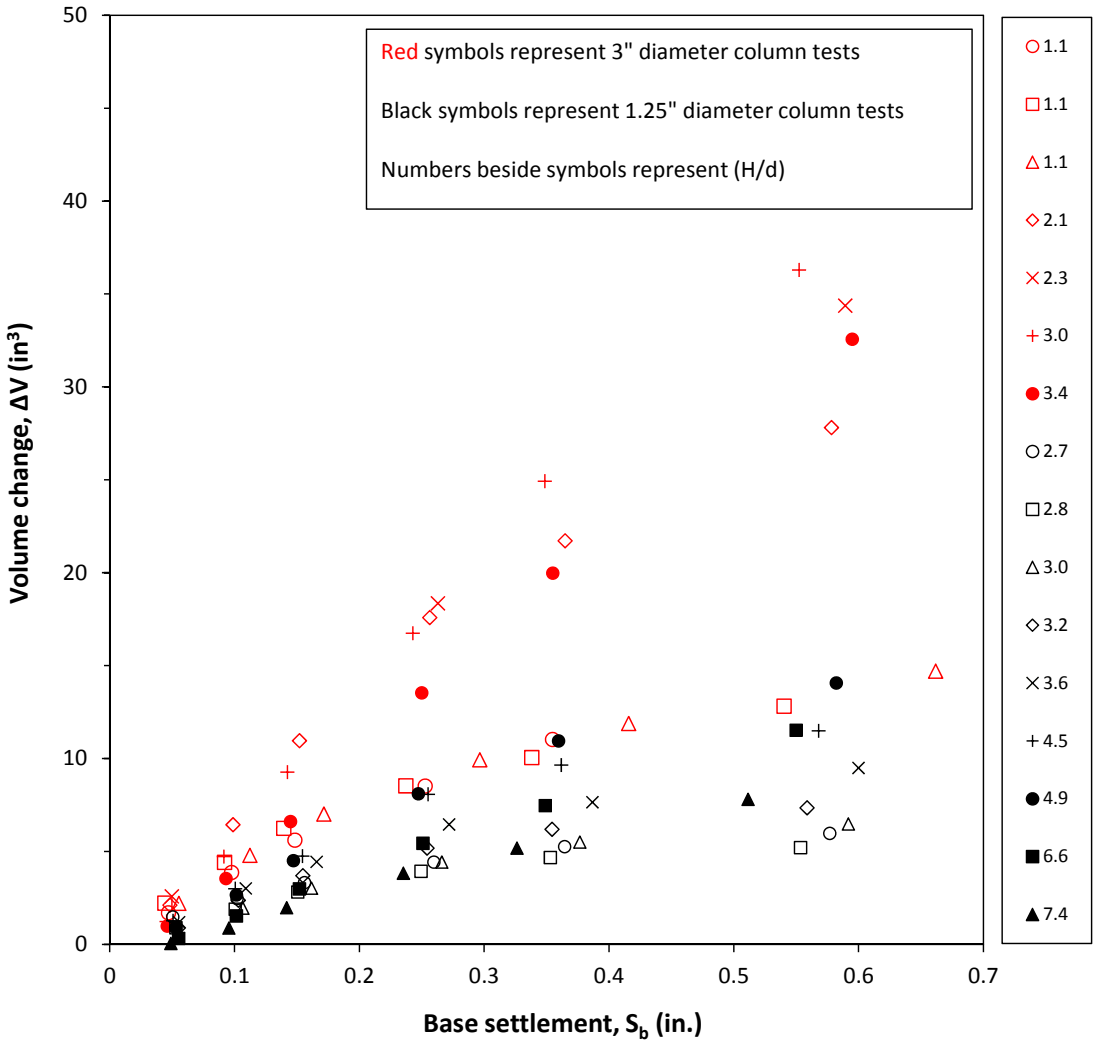

Figure 4.20 Volume change versus base settlement for unreinforced samples prepared at Density 2

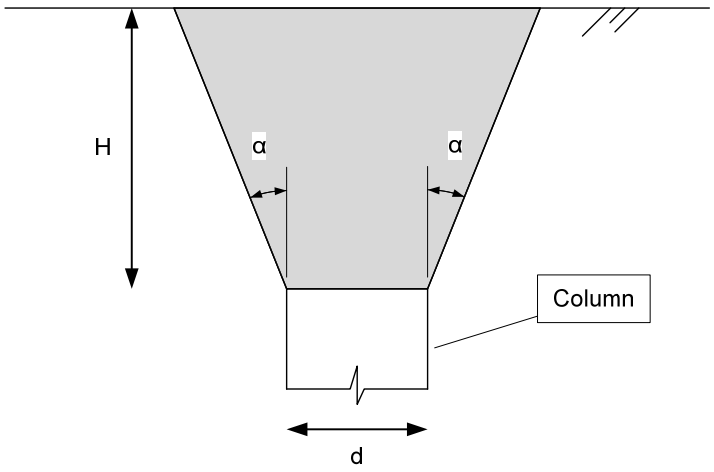

Figure 4.21 Profile view with shaded portion indicating the soil volume infuenced by the column

$$V_f = \frac{\pi}{12}\left[4H^3 \tan^2\alpha + 6H^2 d \tan\alpha + 3Hd^2\right] \quad (4.4)$$

Figure 4.22 shows volume change normalized by the volume of soil influenced by the column, $\Delta V/V_f$, versus the base settlement magnitude normalized by column diameter for unreinforced samples prepared at Density 2 tested using 1.25 and 3.00-inch single columns. Plotting the data in this way shows that, on a unit volume basis, shorter samples dilate more intensely than taller samples. Figure 4.23, which only shows the two tests that have the same normalized height but different column diameters, indicates that the unit volume change does not normalize by H/d. This outcome suggests that volume change is not only tied to the geometric relationship between sample height and column diameter, but also involves other factors such as confining stress. Because the data does not normalize by geometry, the remainder of the comparisons are made by plotting volume change versus base settlement.

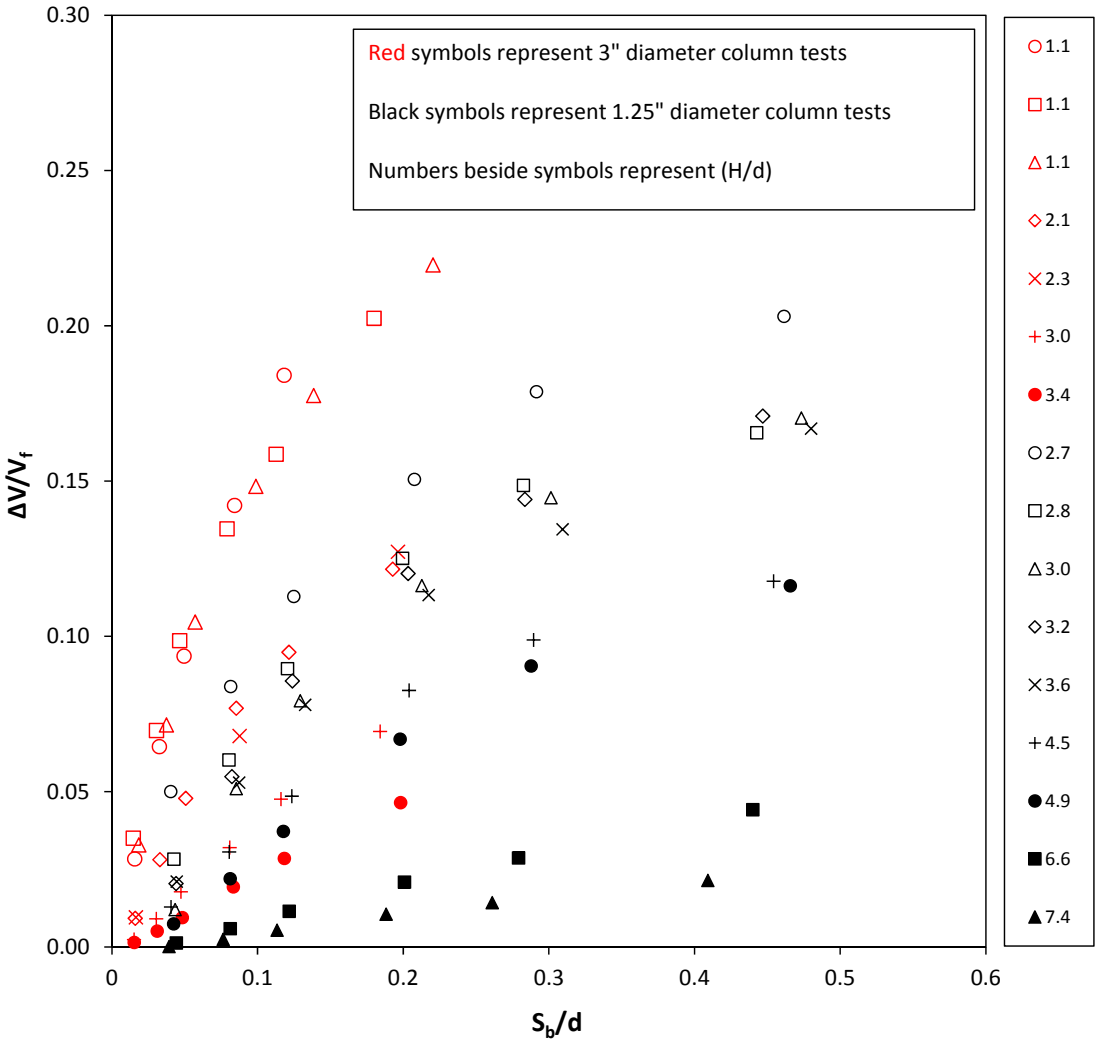

Figure 4.22 Plot of volume change normalized by volume of soil influenced by column versus base settlement normalized by column diameter for unreinforced samples prepared at Density 2

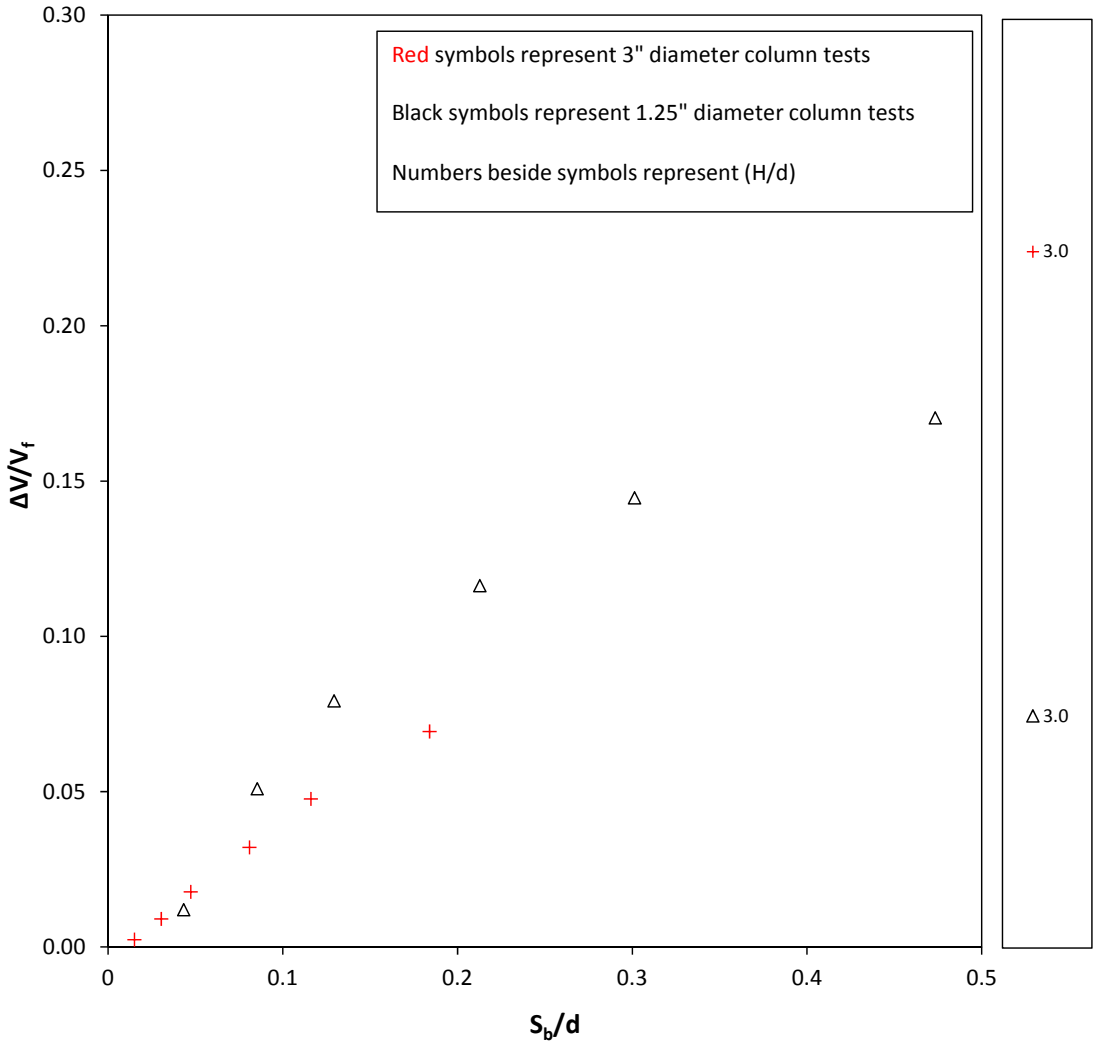

Figure 4.23 Reprint of Figure 4.22 only showing tests performed using different column diameters but having the same normalized sample height

Figure 4.24 shows comparison of the volume change experienced by samples performed with and without application of a surcharge pressure. The results suggest that, with all other parameters consistent, the application of a surcharge pressure slightly suppresses dilation of the sample, however all samples, regardless of surcharge pressure, dilated due to base settlement.

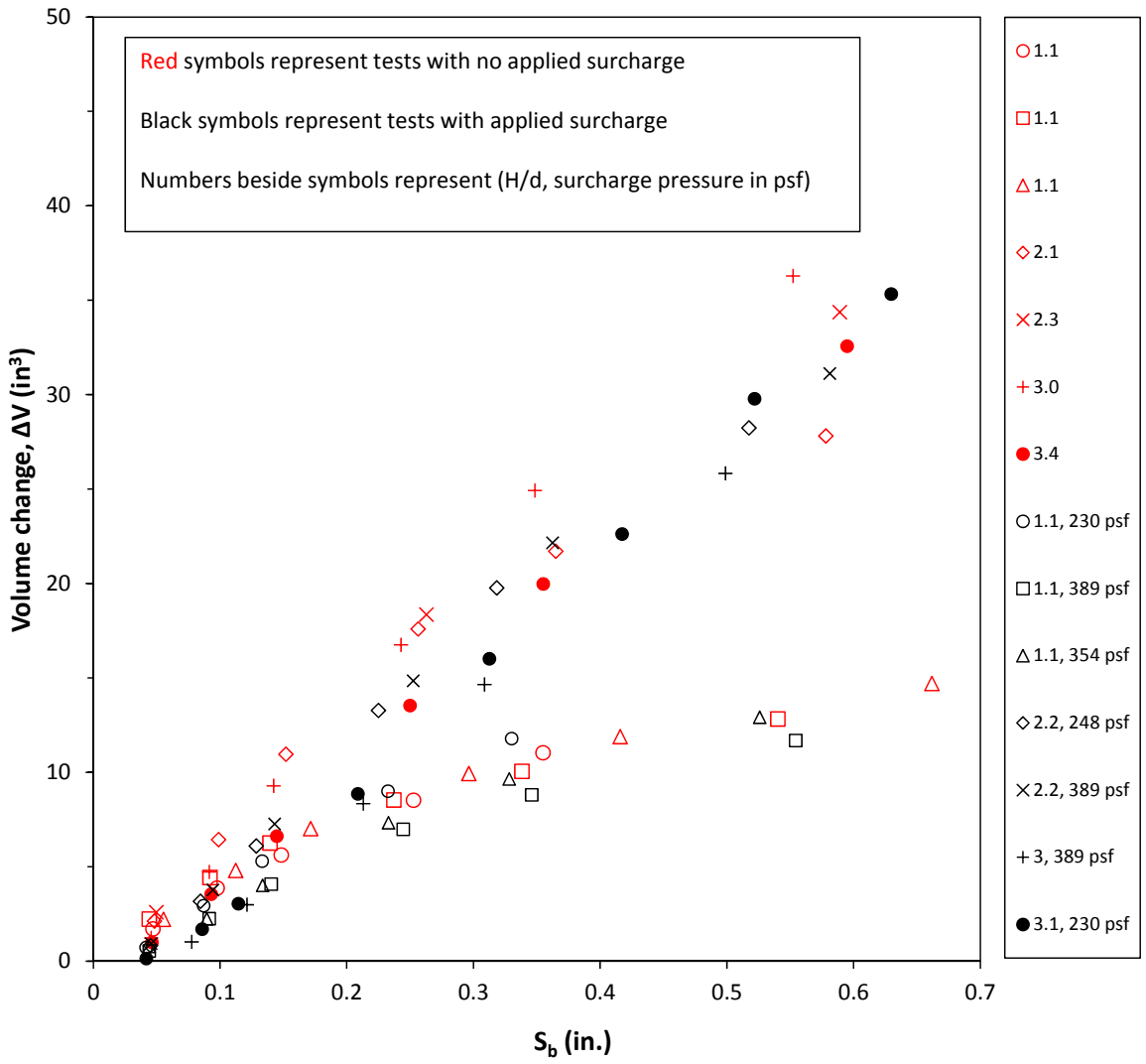

Figure 4.24 Volume change versus base settlement for unreinforced samples with and without applied surcharge, prepared at Density 2, and tested using a single 3-inch diameter column

Figure 4.25 shows the comparison of volume change in samples prepared at different densities. The results indicate that, with all other parameters being consistent, dilation generally increases with the relative density of the sample. This outcome is expected because dense samples have a higher dilation angle than loose samples under the same initial state of stress.

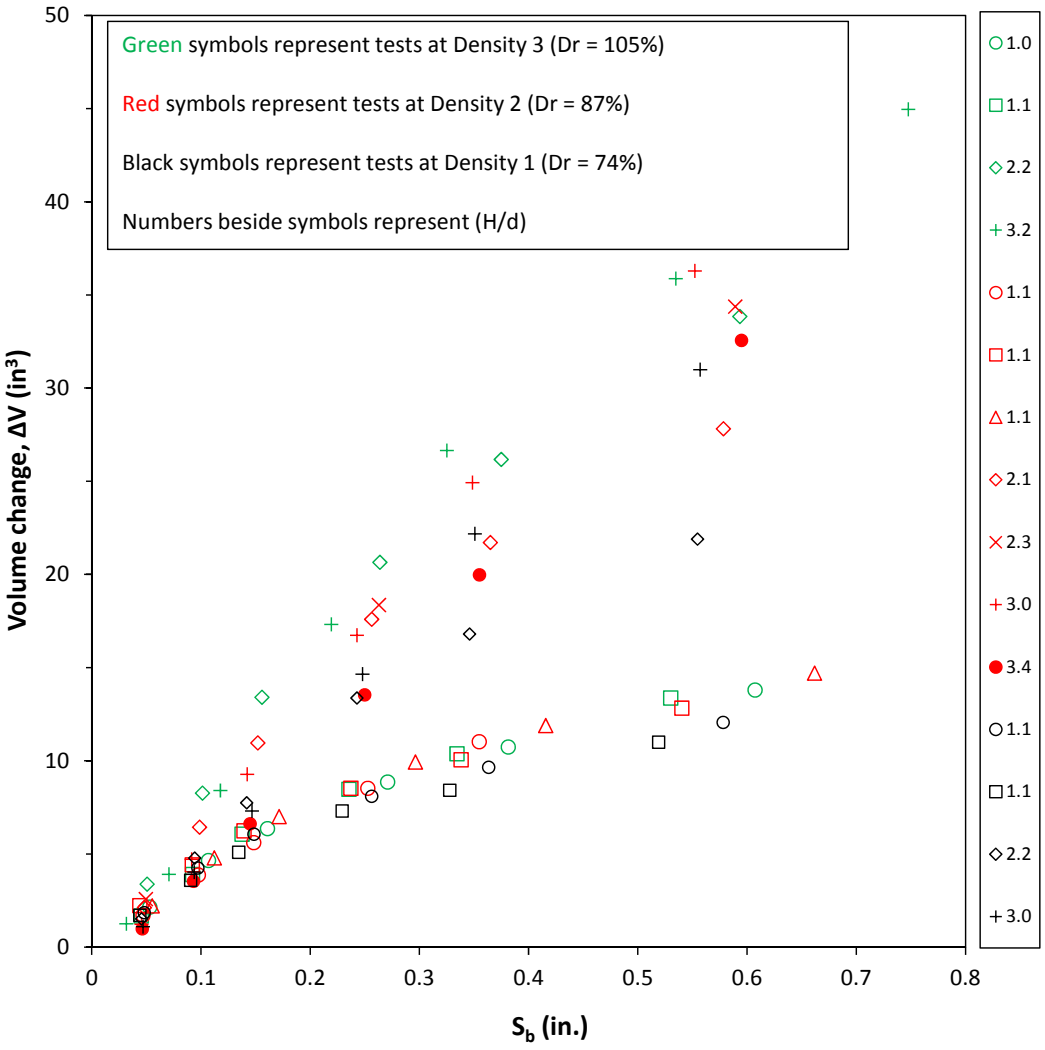

Figure 4.25 Volume change versus base settlement for unreinforced samples prepared at different densities and tested using a single 3-inch diameter column

Figure 4.26 compares the volume change resulting from base settlement for samples tested with and without reinforcement. The results indicate that, with all other parameters being consistent, reinforced samples experience greater volume change than unreinforced samples. One explanation for this outcome is that some soil may be retained on top of the reinforcement as it deforms in response to differential base settlement. Since settlement of the base around the column is uniform, this behavior would create a low-density zone of soil below the reinforcement where it spans between the column and the settling base. A low-density zone would occupy more volume, resulting in greater volume change, than if the same mass of soil

remained at a higher density. Another potential reason volume change is greater in reinforced samples is that the angle α defining the volume of soil influenced by the column increases slightly with the presence of reinforcement. Therefore, for the same volume change per unit volume, reinforced samples will experience more total volume change since the volume of soil influenced by the column is greater than for unreinforced samples.

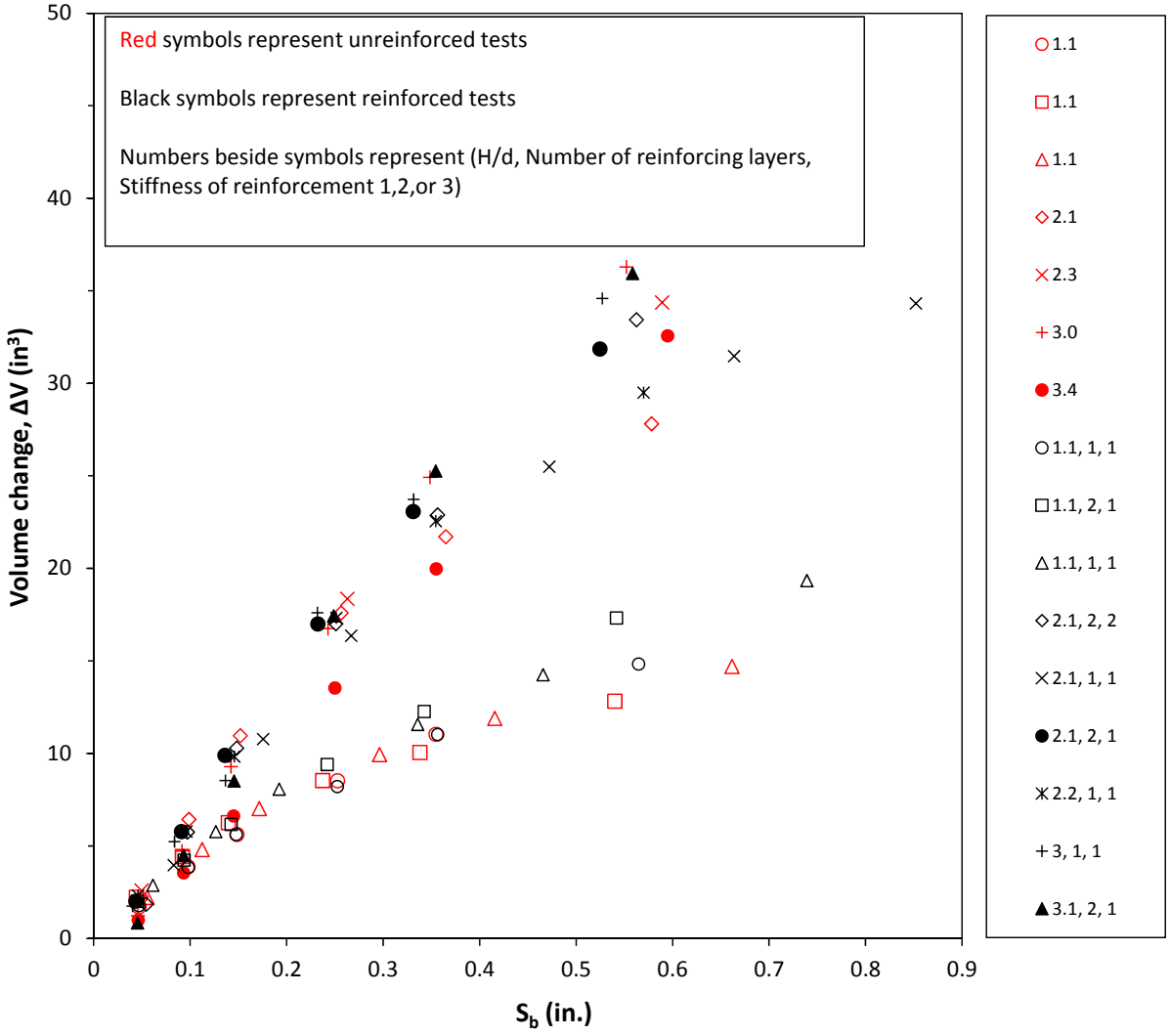

Figure 4.26 Volume change versus base settlement for samples with and without reinforcement prepared at Density 2 and tested using a single 3-inch diameter column

4.3 Column Stress-Displacement Relationship

The relationship between column stress and base settlement was determined by plotting the column stress, σ_{col}, determined from the measured load acting on the column corrected for friction in the apparatus divided by column area, versus base settlement, S_b, determined from the measured relative displacement between the column and the base of the sample tank. As described in Section 3.2.1, only the 3-inch single column configuration included a load cell. The column stress-displacement plot for the example test described at the beginning of the chapter is provided in Figure 4.27

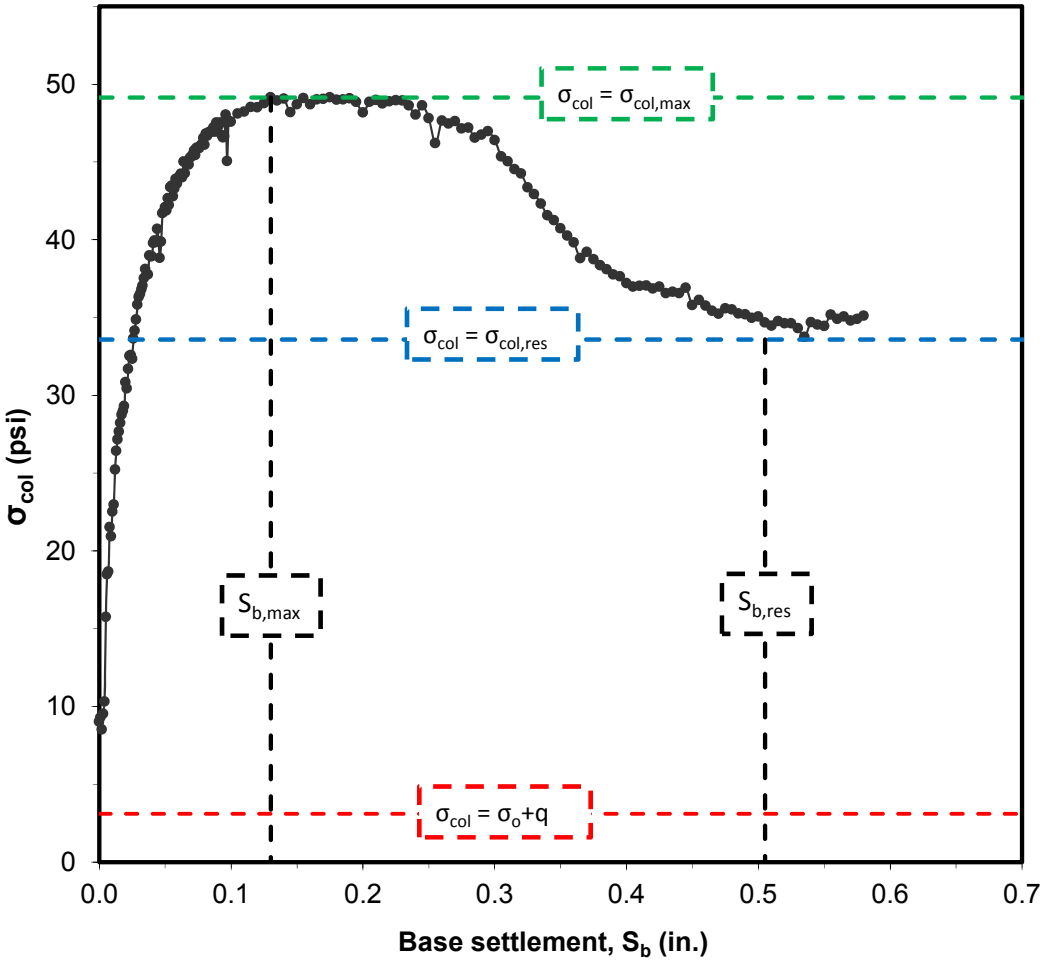

Figure 4.27 Column stress versus base settlement for example test.

The relationship between column stress and base settlement can be characterized by a rapid increase in stress over the stress due to overburden and surcharge, σ_o+q, to peak stress, $\sigma_{col,max}$, followed by a decrease in stress to a residual value, $\sigma_{col,res}$, that remains approximately constant, or decreases slightly, with increasing base settlement magnitude. As described in Section 2.5, this behavior is analogous to the load-displacement response of an embedded anchor during pullout. As shown in Figure 4.27, the column stresses and base settlements defined in Table 4.3 can be used to describe the key aspects of the relationship between column stress and base settlement.

Table 4.3 Key descriptors to describe relationship between column stress and base settlement

Base Settlement	Column Stress	Description
$S_b = 0$	σ_o+q	The column stress before any base settlement
$S_{b,max}$	$\sigma_{col,max}$	The base settlement corresponding to the maximum column stress
$S_{b,res}$	$\sigma_{col,res}$	The base settlement at the onset of an approximately stable post-peak column stress

Section 4.3.1 presents the findings related to $\sigma_{col,max}$ and $S_{b,max}$ and Section 4.3.2 describes $\sigma_{col,res}$ and $S_{b,res}$ for unreinforced samples. Section 4.3.3 discusses the results obtained from tests performed on samples incorporating reinforcement. The column stresses are presented as ratios to the initial vertical stress, σ_o+q. As described in Section 1.4, the column stress ratio, CSR, is often used to describe load transfer in GRCSEs. Similar stress ratios are used for describing the pullout capacity of embedded anchors. The ratio of column stress to initial vertical stress for a single column is different than CSR for a column array since there is not the influence of soil arching between adjacent columns. Because of the distinction, the term CSR will not be used in this section to avoid confusion. Instead, the term 'column stress factor' will be used to refer to the ratio of column stress to initial vertical stress for single columns.

The very low initial vertical stress associated with testing low height samples without application of a surcharge caused the calculation of column stress ratios to be prone to scatter. As such, tests performed on samples shorter than 6 inches without a surcharge pressure were omitted from the analysis. The application of surcharge pressure using the vacuum system described in Section 3.2.3 significantly increased the overall quality of the load cell data.

4.3.1 Peak column stress

Figure 4.28 shows the ratio of peak column stress to initial vertical stress versus normalized sample height for tests performed on samples without reinforcement. The results indicate that the peak column stress factor increases with normalized height. The results from testing at a normalized height of about 2.2 with an applied surcharge, which seems to make the load cell data more reliable, suggest that the peak column stress factor increases as sample density is increased.

In Section 2.5, a simple method was developed to estimate the breakout factor for embedded anchors. The breakout factor is the ratio of the peak anchor resistance to the initial vertical stress and is analogous to the peak column stress factor used here for the single column tests. The method introduced in Equation 2.16 and redefined below as Equation 4.5 was found to be adaptable to seven published methods for estimating the breakout factor.

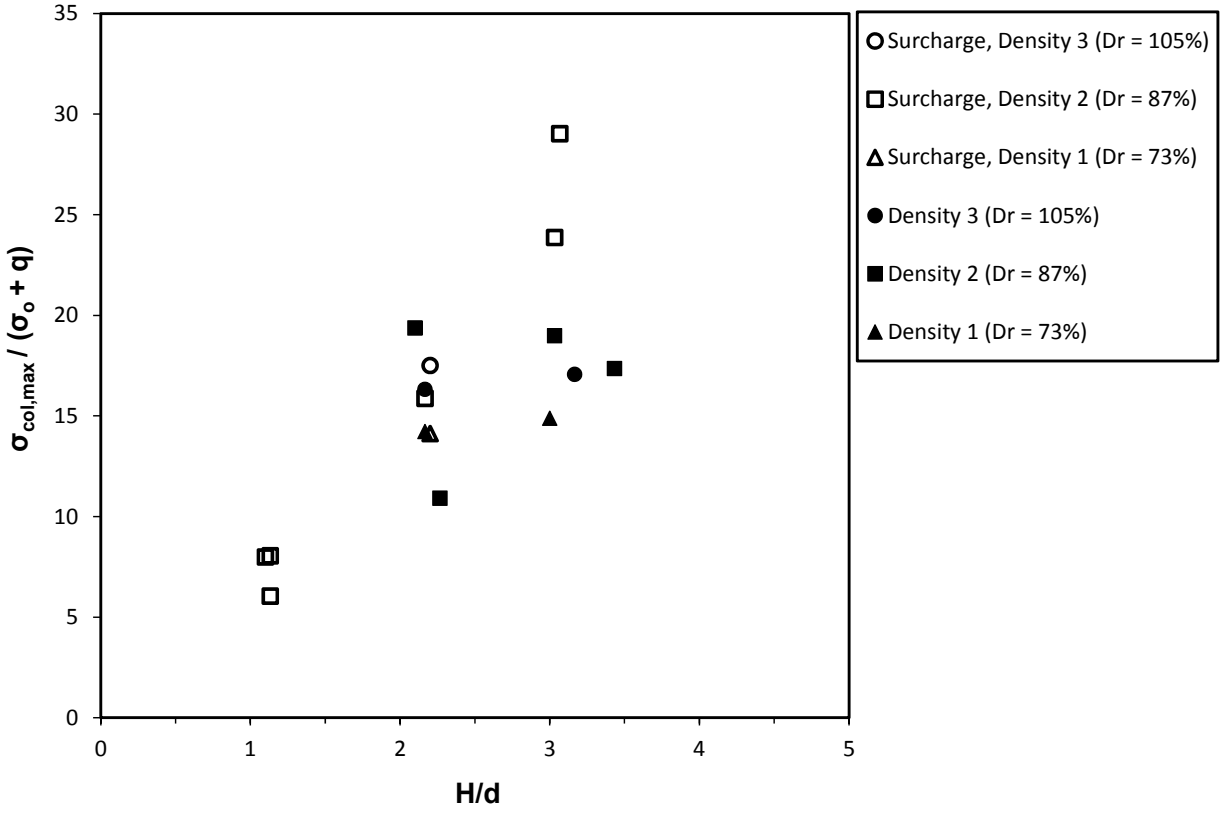

Figure 4.28 Peak column stress factor versus normalized sample height

$$\frac{\sigma_{col,max}}{\sigma_o + q} = A\left(N^*\right)^2 + B\left(N^*\right) + 1$$

where

$$N^* = \tan\phi\left(\frac{H}{d}\right)\left(\frac{2q + \sigma_o}{q + \sigma_o}\right) \tag{4.5}$$

Figure 4.29 shows peak column stress factor plotted against the dimensionless factor N* defined in Equation 4.3. A second order polynomial was fitted to the tests with applied surcharge pressure to determine values of the coefficients A and B in Equation 4.5 equal to 0.298 and 1.409, respectively. These values are compared in Table 2.6 in Section 2.5 to the coefficient values fitted to eight published methods for estimating breakout factor.

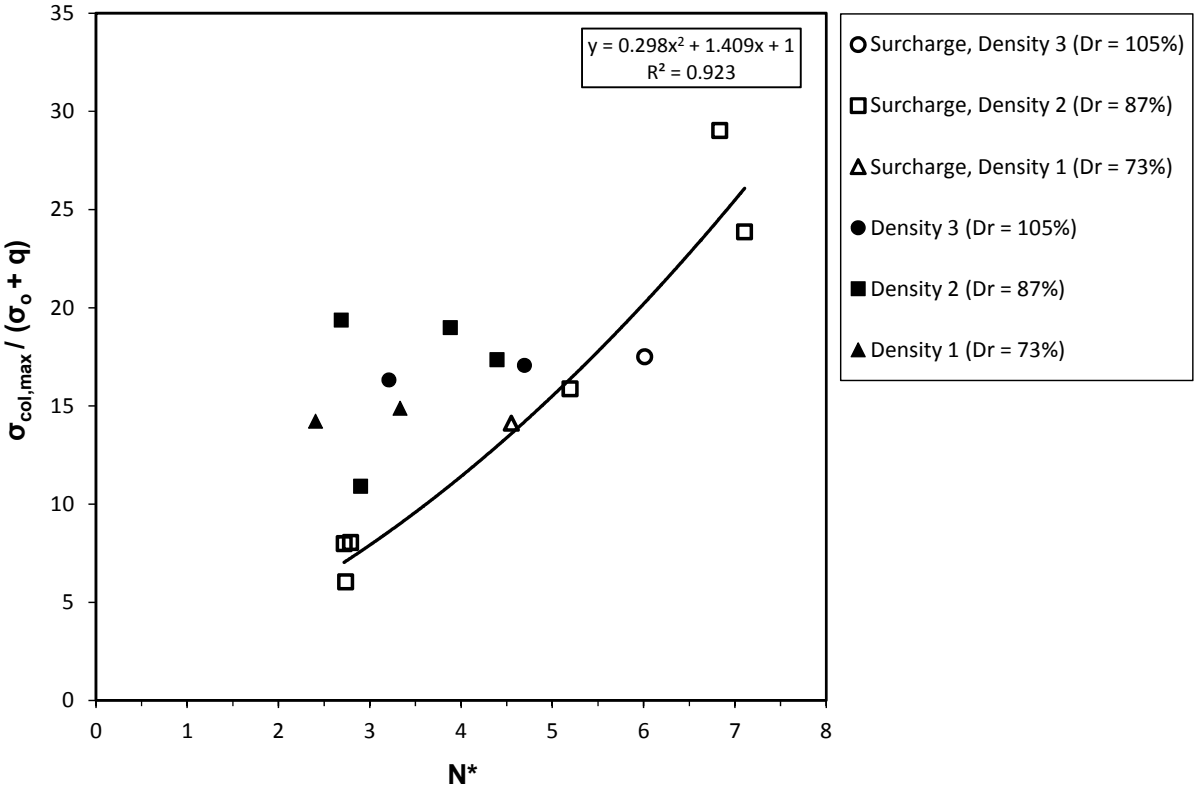

Figure 4.29 Peak column stress factor versus dimensionless parameter N*

In Figure 4.30, the base settlement at the peak column stress factor was expressed as a ratio of the column diameter and plotted against normalized sample height. Figure 4.30 suggests

a weak trend exists whereby base settlement corresponding to peak column stress increases as the initial sample height increases. The application of surcharge pressure also appears to have the effect of increasing the base settlement at peak column stress. There is not sufficient evidence to draw conclusions about the influence of sample density; however, it is expected that $S_{b,max}$ decreases as sample density increases since dense samples tend to have a stiffer stress/strain response to peak strength than loose samples.

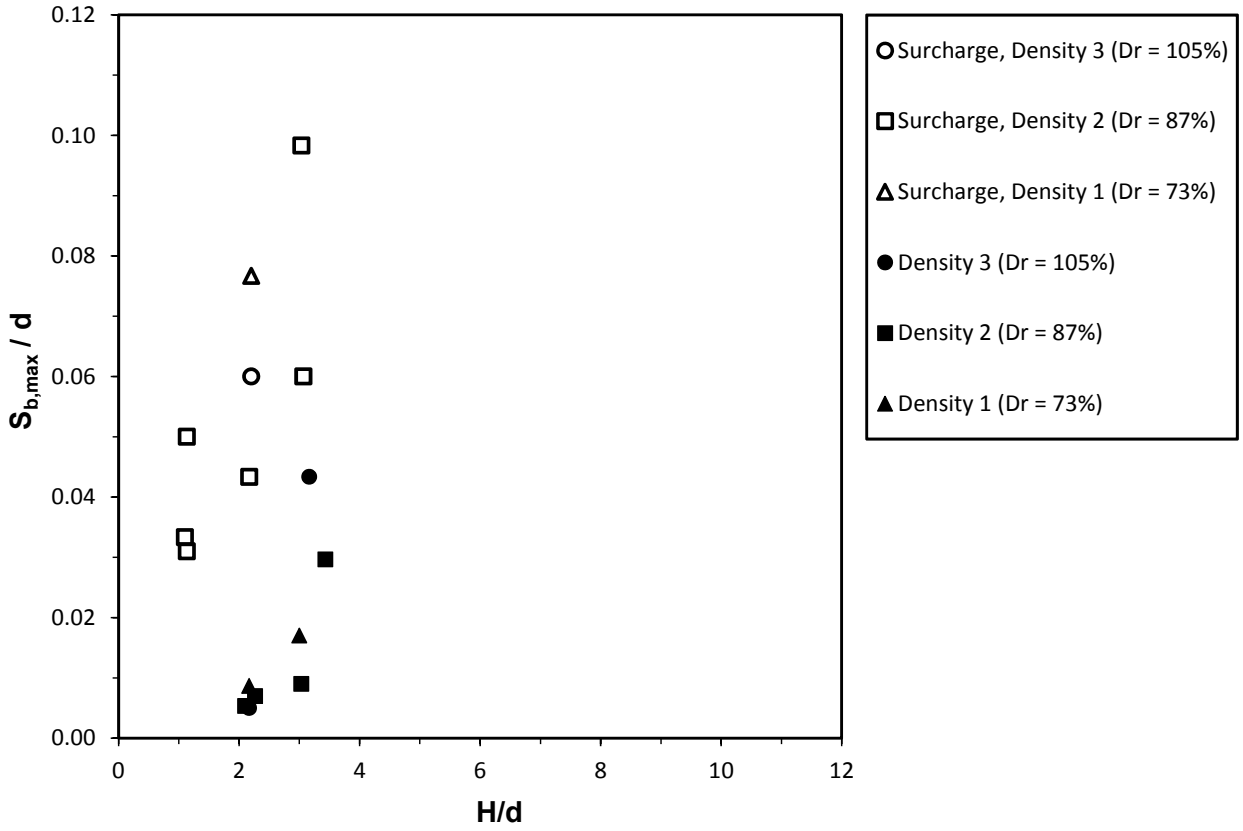

Figure 4.30 Relationship between normalized base settlement at maximum column stress versus normalized sample height

4.3.2 Column stress at large base settlements

Figure 4.31 shows the relationship between the residual column stress factor, which is the residual column stress divided by the initial vertical column stress, versus normalized sample height. The figure suggests that the column stress at large magnitudes of base settlement

increases with sample height, sample density, and applied surcharge. The trend between residual column stress and sample density is weak compared to the trends with sample height and surcharge pressure. Based on the test results, the residual stress was found to be suitably approximated as the weight acting over the area of the column of the soil volume influenced by the column, as defined in Equation 4.4, plus the surcharge pressure acting over the circular area defined by the influence diameter given in equation 4.1. This approximation is given in Equation 4.6. Combining Equations 4.2, 4.4, and 4.6 and solving for the residual column stress factor produces Equation 4.7. Equation 4.7 is similar to Equation 4.5 for estimating the peak column stress factor, except fitting parameters A and B are not needed. Figure 4.32 shows the measured residual column stress factor plotted against the predicted value using Equation 4.7.

$$\sigma_{col,res} = \frac{1}{d^2}\left[\frac{4V_f\gamma}{\pi} + q\left(d + 2H\tan\alpha\right)^2\right] \tag{4.6}$$

$$\frac{\sigma_{col,res}}{\sigma_o + q} = \frac{4\left(\frac{\sigma_o}{3} + q\right)}{\left(\sigma_o + q\right)}\left[\tan\left(0.56\phi\right)\frac{H}{d}\right]^2 + \frac{2\left(\sigma_o + 2q\right)}{\left(\sigma_o + q\right)}\left[\tan\left(0.56\phi\right)\frac{H}{d}\right] + 1 \tag{4.7}$$

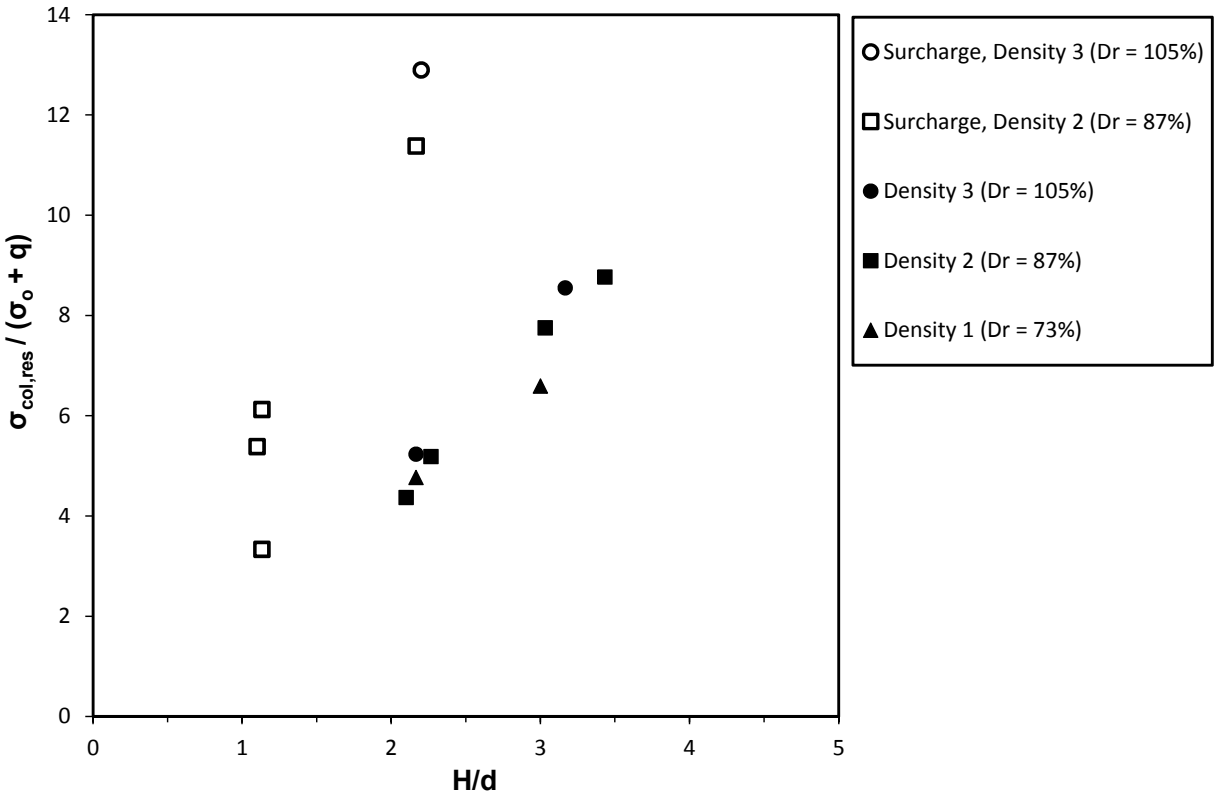

Figure 4.31 Residual column stress factor versus normalized sample height

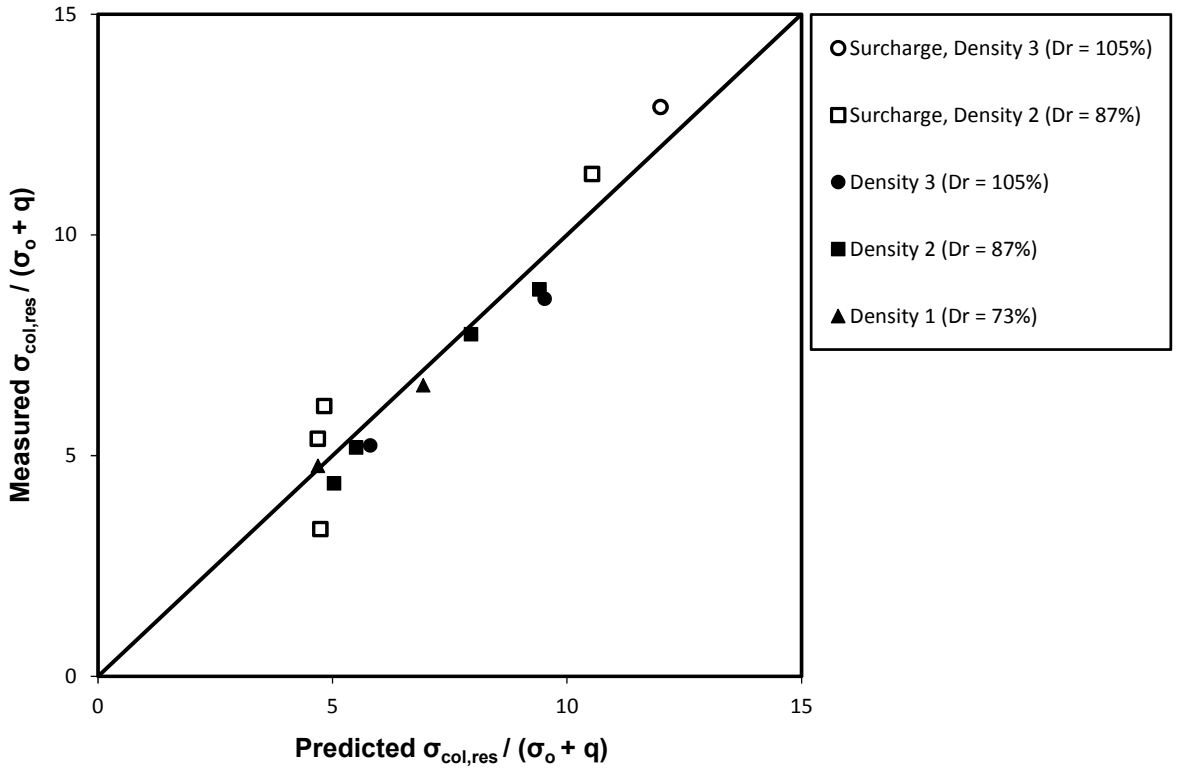

Figure 4.32 Measured residual column stress factor versus values predicted using Equation 4.7

As can be seen in Figure 4.32, the approximation given in Equation 4.7 is in fairly good agreement with measured values for tests with and without a surcharge. As Figure 4.33 shows, a multiplier equal to 1.56 can be applied to Equation 4.7 to predict the peak column stress factor for tests performed with an applied surcharge. This approximation is given in Equation 4.8, and it can also be stated that the residual column stress is about 64 percent of the maximum value. This means that at large base settlements ($S_b \geq S_{b,res}$), the load transfer to the column is about 64 percent of the amount at $S_{b,max}$.

$$\frac{\sigma_{col,max}}{\sigma_{col,res}} \approx 1.56 \tag{4.8}$$

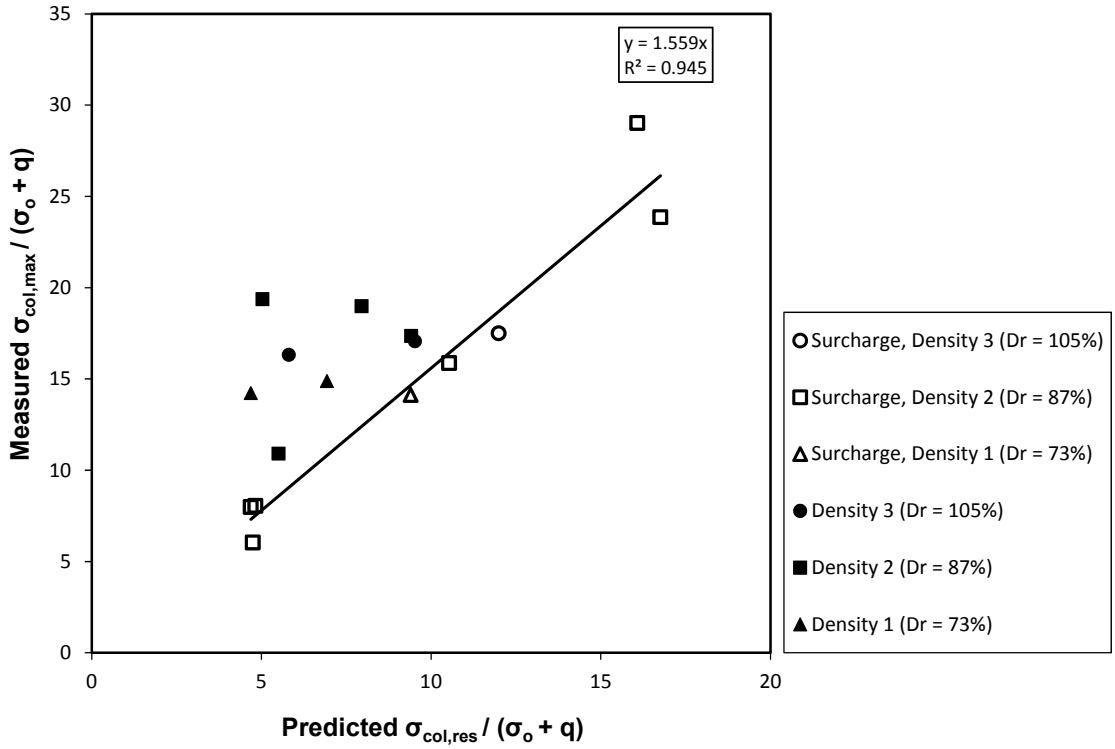

Figure 4.33 Relationship between measured peak column stress factor and predicted residual column stress factor

As shown in Figure 4.34, the magnitude of base settlement present when the column stress reaches a residual value is variable when plotted against the normalized sample height, H/d. Some of the tests did not reach a residual column stress by the end of the test. Despite this variability, the figure suggests that a residual column stress value is reached when base settlement is at least 9 percent of the column diameter.

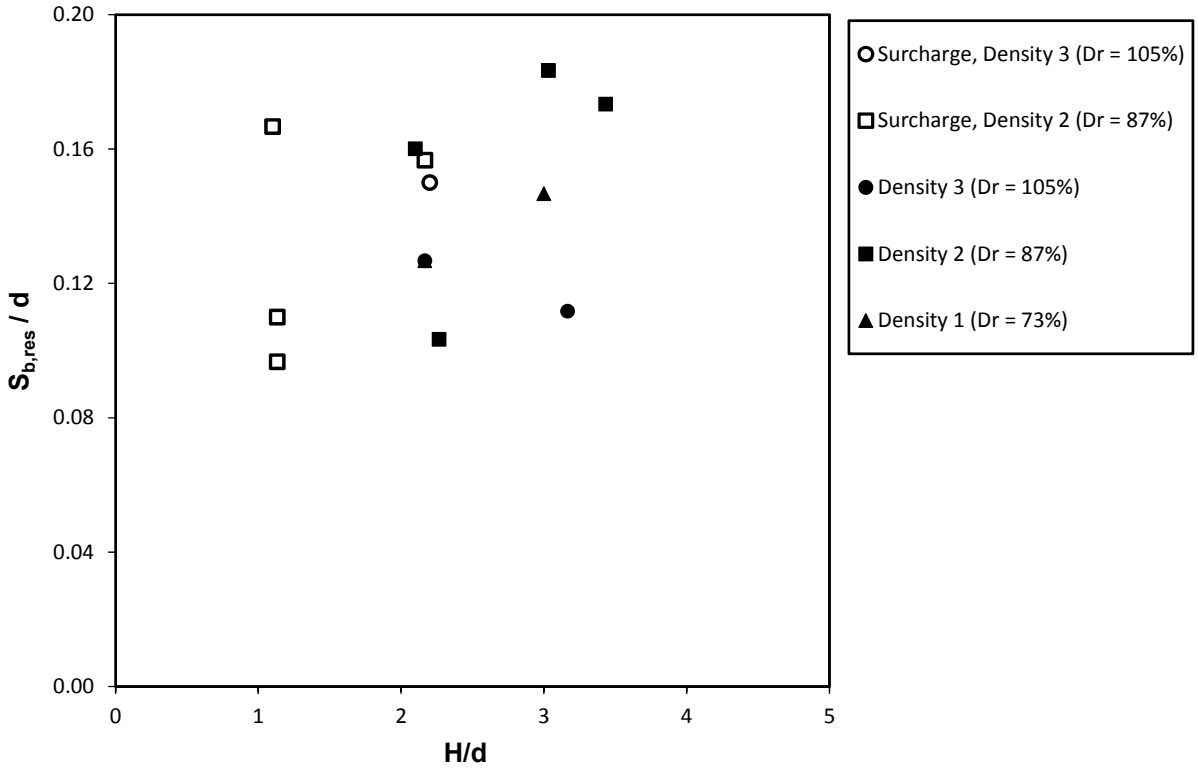

Figure 4.34 Normalized base settlement when column stress reaches a residual value versus normalized sample height

4.3.3 Column stress-displacement relationship for reinforced samples

In general, the tests performed on samples incorporating reinforcement exhibited a relationship between column stress and base settlement that was similar to the relationship for the unreinforced tests. In the case of reinforced samples, the measured column stress is equivalent to $\sigma_{col,geobot}$ defined in Section 1.4. As expected, the measured values of peak and residual column stress are typically higher for samples incorporating reinforcement. Additional load is transferred to the column through the vertical component of tension developed in the reinforcement. In the case of a single column, the tension developed in the reinforcement must be counteracted by the pullout resistance between the reinforcement and the sand. Based on the test procedures described in Section 3.5, the reinforcement was not restricted from moving vertically or radially and no measurements were made to determine if radial movement occurred during a test. In a column array sufficiently far away from any boundaries, symmetry prevents relative in-plane movement between the reinforcement and the embankment material at mid-span. Furthermore, as described in Section 3.1, since base settlement is uniform and

displacement controlled, the deformed shape of the reinforcement is likely different than expected in a GRCSE under field conditions. Since both of these differences are sensitive to the magnitude of base settlement, it is likely that the current results for peak column stress are more applicable to GRCSEs than the post-peak behavior since the peak stress condition generally occurs when base settlement is small.

Figure 4.35 shows a layer of reinforcement that was exhumed from a sample following the completion of testing. There is some permanent deformation visible in the vicinity of the column. By counting the number of reinforcement strands, which are spaced 0.25 inches apart, the diameter of the permanently deformed reinforcement is about 5 inches. The concentration of the permanent deformation close to the column location suggests that the abrupt differential settlement between the column and the base produces high localized strains in the reinforcement.

Figures 4.36 through 4.41 present the results for peak and post-peak column stresses obtained from reinforced samples. The blue symbols are used to indicate tests that were performed with an applied surcharge and the red symbols indicate tests performed without a surcharge. As with the unreinforced tests, the tests performed with an applied surcharge are believed to be more reliable than the tests performed without a surcharge. The data labels indicate the number of reinforcement layers in the sample and the type of reinforcement used. As described in Section 3.4, the type of reinforcement is identified as Stiffness 1, 2, or 3, with Stiffness 3 being the stiffest.

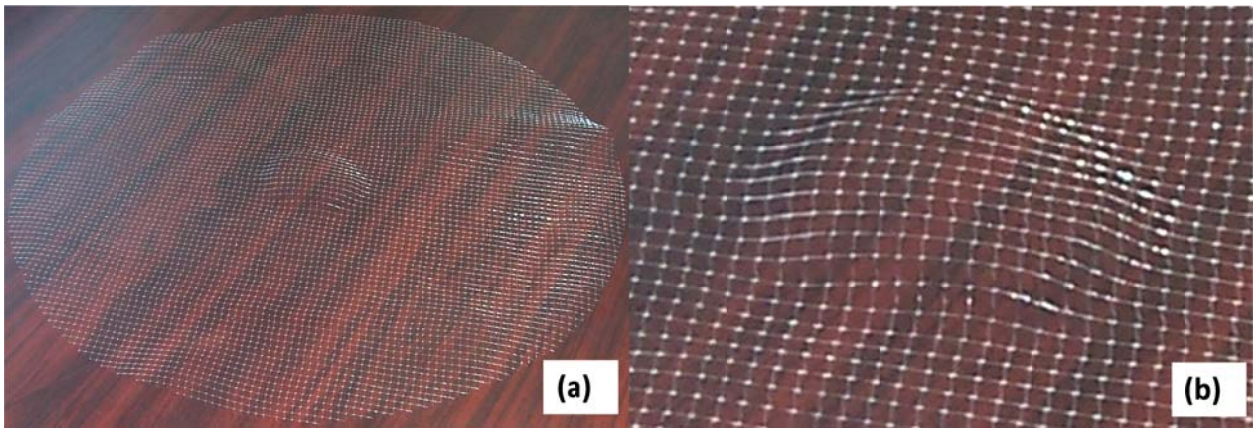

Figure 4.35 Reinforcement exhumed from a test showing permanent deformation. Figure (a) shows the radial extent of the permanent deformation. Figure (b) shows a detail of the deformed shape. Note that reinforcement strands have a 0.25-inch spacing

The influence of reinforcement on the peak and residual column stress is summarized in Table 4.4. The stiffness and number of reinforcing layers was not found to produce a measurable difference in the peak or residual column stresses under the testing conditions.

Table 4.4 Summary of the influence of reinforcement of the column stress-displacement relationship

Parameter	Influence of Reinforcement
$\sigma_{col,max} / \sigma_o+q$	Tests performed with applied surcharge do not show a significant increase in peak column stress due to presence of reinforcement. Tests performed without an applied surcharge generally exhibited an increase in peak column stress.
$S_{b,max}$	The tests show that the presence of reinforcement does not have a significant impact on the magnitude of base settlement at peak column stress
$\sigma_{col,res} / \sigma_o+q$	The tests show that the presence of reinforcement generally increases the residual column stress.
$S_{b,res}$	With the exception of a few tests performed without a surcharge, the presence of reinforcement was not found to impact the base settlement when the column stress reaches a residual magnitude.

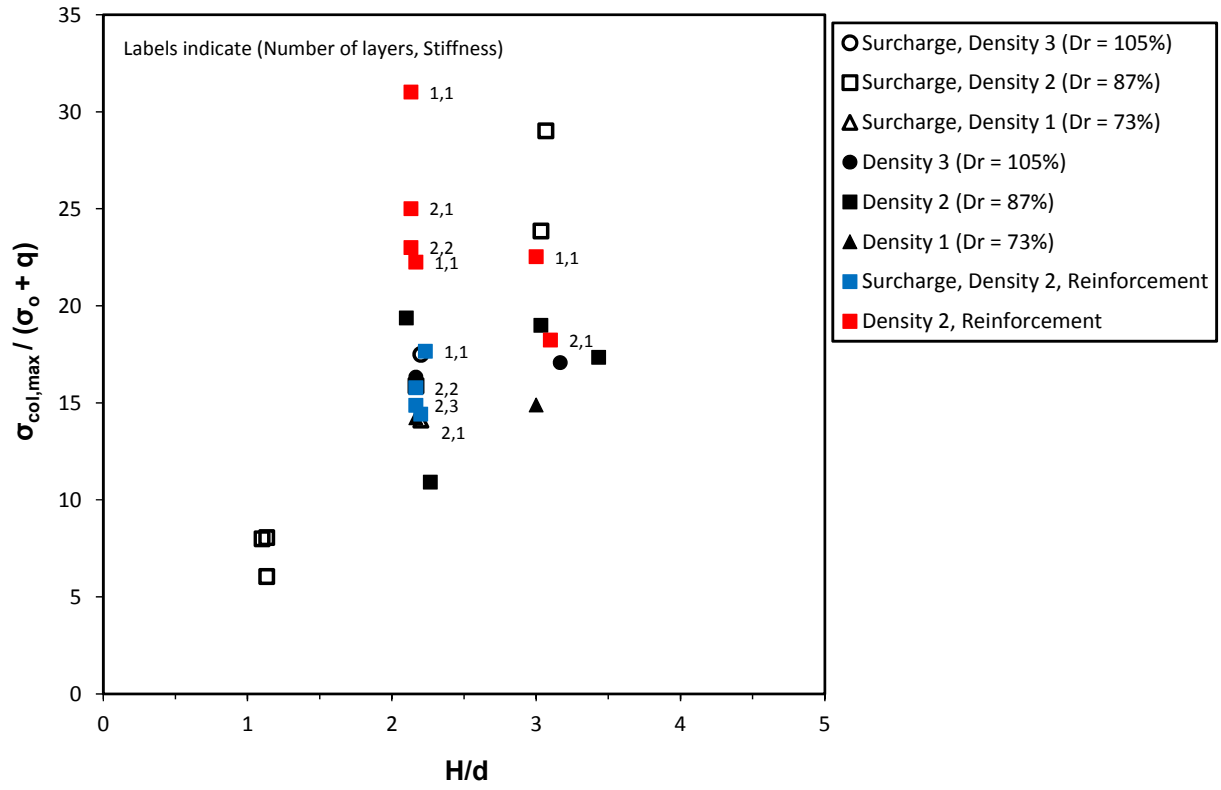

Figure 4.36 Peak column stress factor versus normalized sample height showing tests performed on reinforced samples

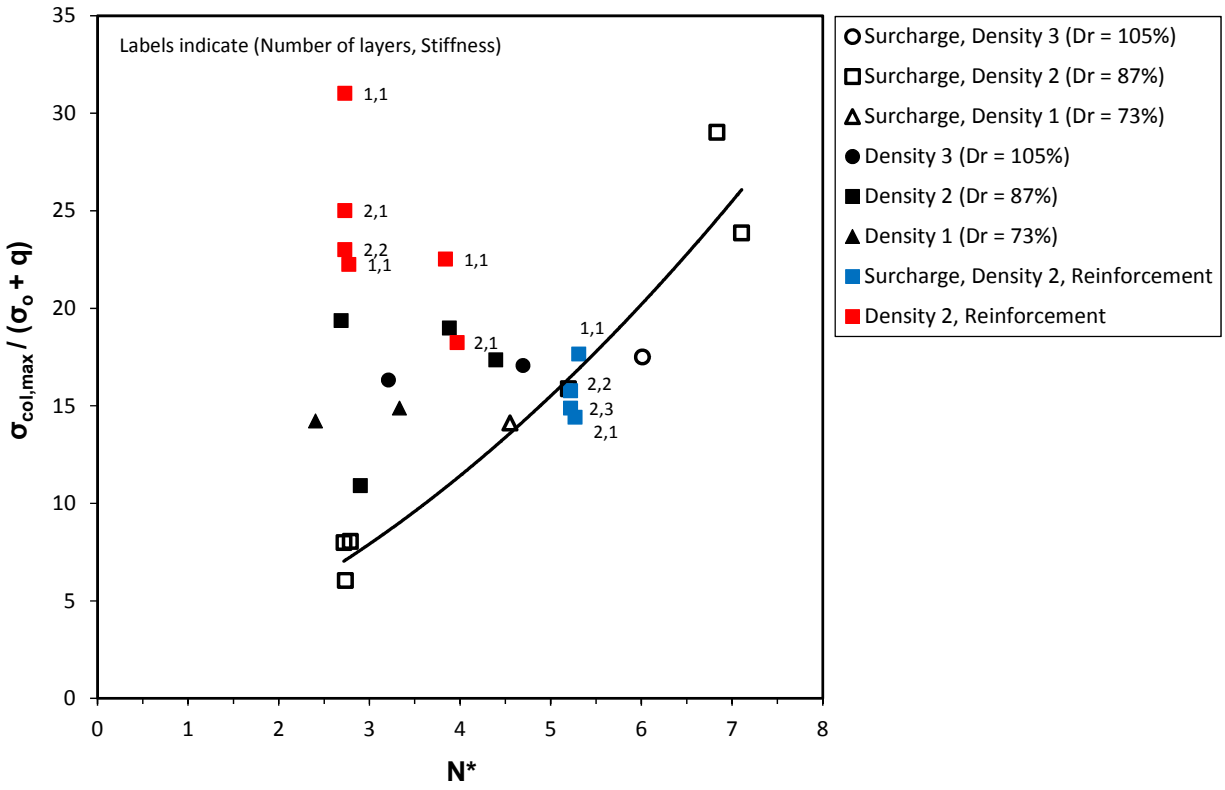

Figure 4.37 Peak column stress factor versus dimensionless parameter N* showing results from reinforced samples

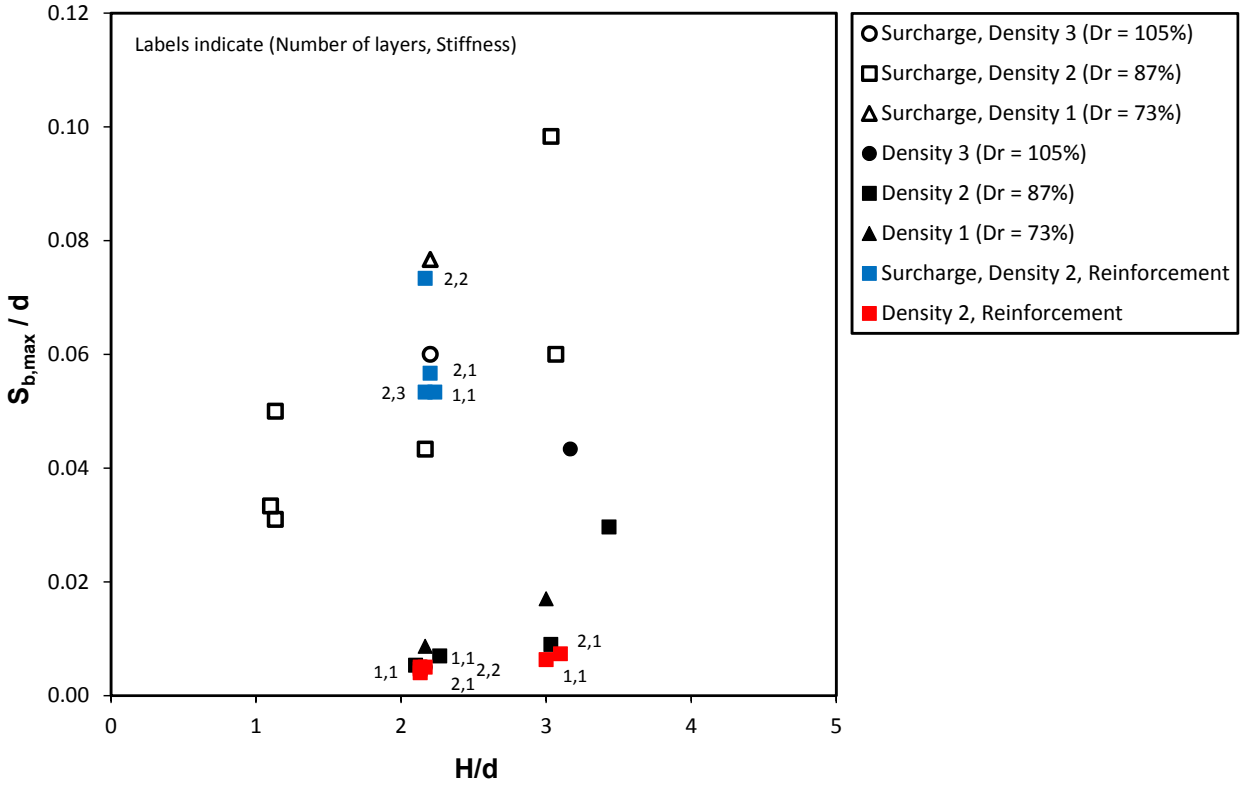

Figure 4.38 Normalized base settlement at peak column stress versus normalized sample height showing results from reinforced samples

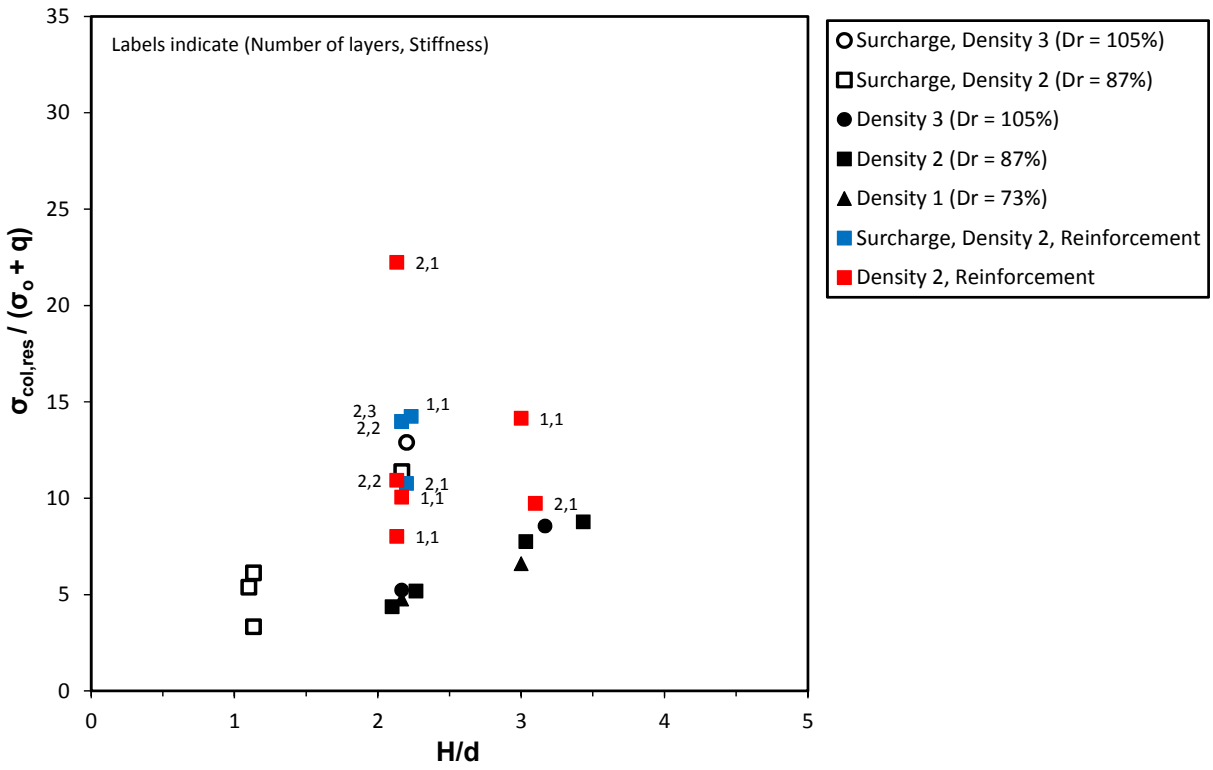

Figure 4.39 Residual column stress factor versus normalized sample height showing results from reinforced samples

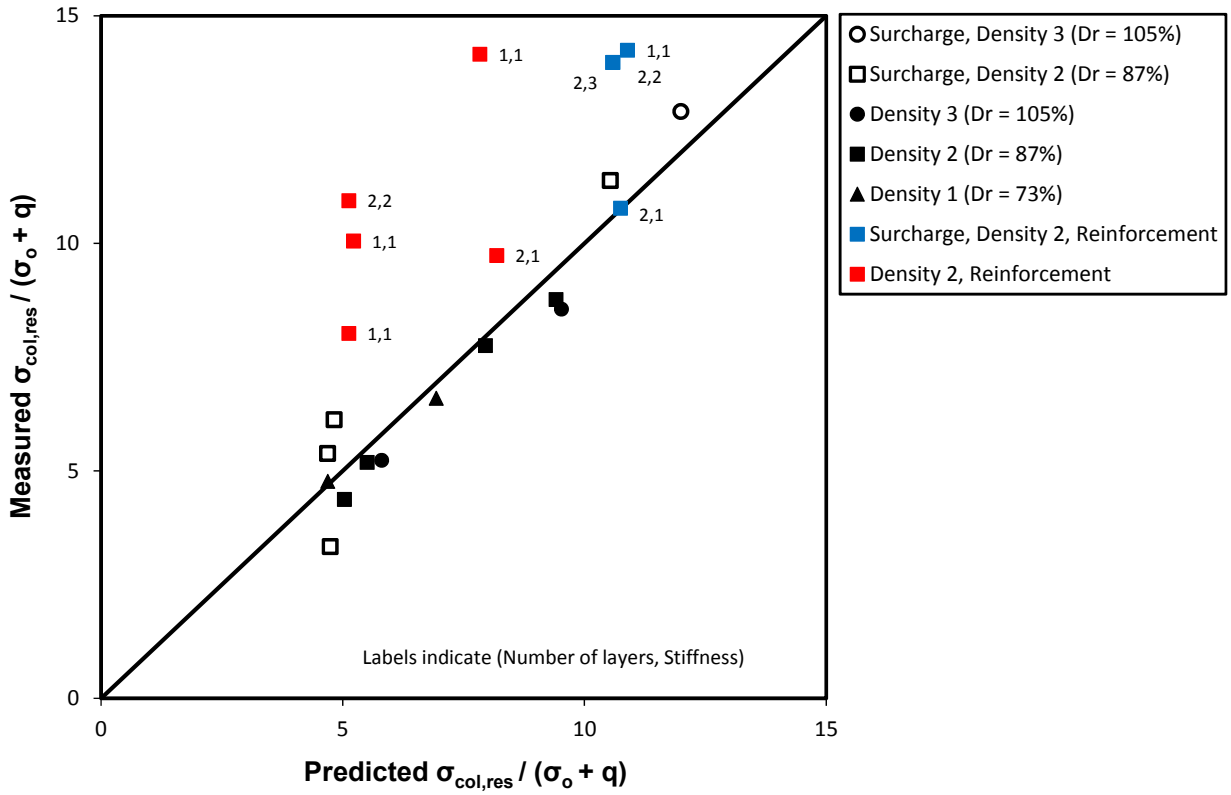

Figure 4.40 Measured residual column stress factor versus value predicted using Equation 4.7 showing results from reinforced samples

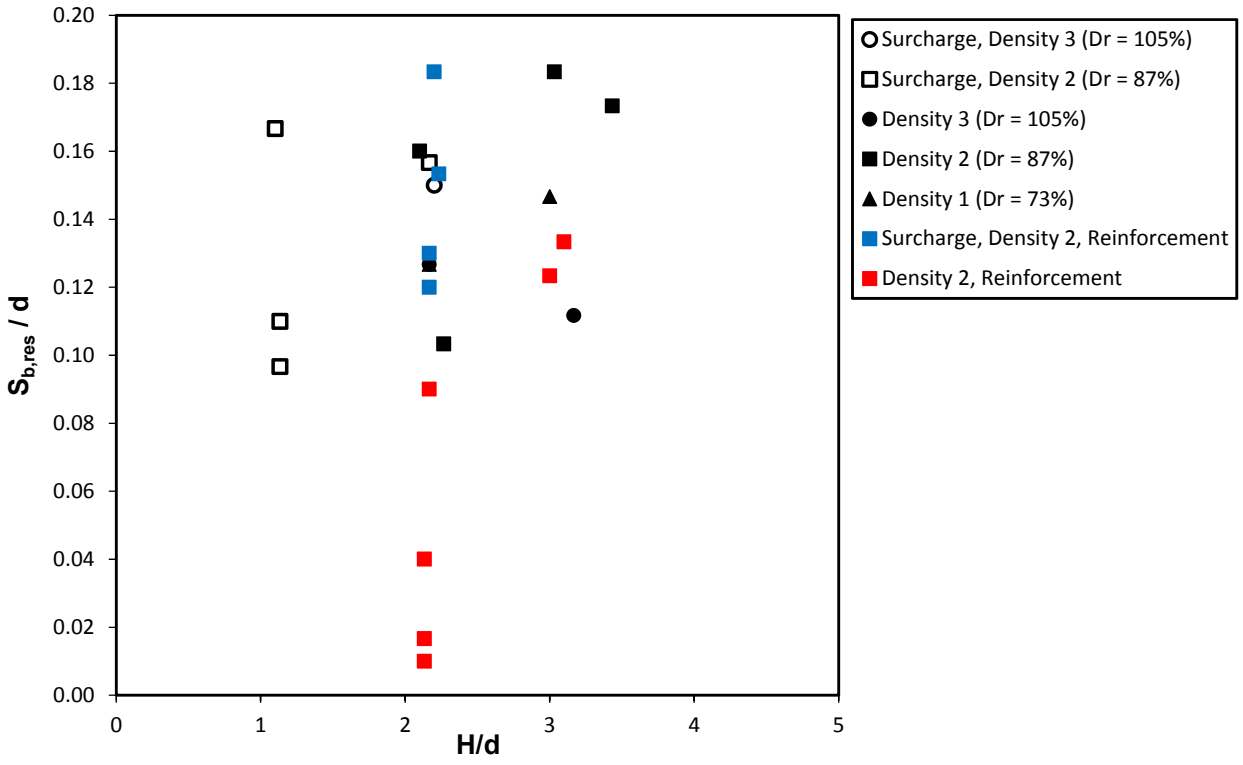

Figure 4.41 Normalized base settlement at the onset of residual column stress versus normalized sample height showing results from reinforced samples

4.4 Summary

A total of 63 single column tests were performed using different column diameters, sample heights, sample densities, number and stiffness of reinforcing layers, and magnitude of applied surcharge pressure. The test results were used to investigate the influence of the test parameters on surface settlement, volume change, and change in stress acting on the column due to differential settlement between the column and the base. The key findings from the single column tests are listed below:

1. When viewed from above, the limit of differential surface settlement produced by the influence of a single round column is a circle with a diameter, d', equal to d+2Htanα. The angle α defines the inclination from vertical of the linear approximation of the shearing surface extending from the column edge to the sample surface. The angle α increased proportionately with friction angle and dilation angle. The presence of reinforcement

appeared to slightly increase α, while the application of surcharge pressure did not have a measureable effect.

2. For a fixed sample height, the ratio of surface settlement over the column to base settlement, SBR_c, can be approximated as being linear over the range of base settlements evaluated. Values of SBR_c obtained from tests using different column diameters tend to normalize when plotted against normalized sample height, H/d. SBR_c increases non-linearly with H/d and was observed to have a value equal to zero at H/d=1 and a value equal to unity when results were extrapolated to H/d=13.5.
3. Measured values of SBR_c appear largely insensitive to the variation in relative density or application of surcharge pressure. Apparent trends suggest that SBR_c increases as the initial relative density of the sample decreases and when the magnitude of applied surcharge pressure increases. These trends are smaller than the scatter in the data. There was no clear influence of reinforcement on SBR_c; however, there was a weak trend suggesting that at low sample heights, the presence of reinforcement increases SBR_c and the number of layers magnifies the effect.
4. The samples were observed to dilate over the range of base settlements evaluated, although the rate of dilation decreases as the magnitude of base settlement increases. On a unit volume basis of soil influenced by the column, shorter samples dilate more than taller samples. Dilation increases as the initial relative density of the samples increased. The application of surcharge pressure was observed to decrease dilation, while the presence of reinforcement was found to increase dilation.
5. The relationship between column stress and base settlement can be characterized by a rapid increase in stress over the stress due to overburden and surcharge, σ_o+q, to peak stress, $\sigma_{col,max}$, followed by a decrease in stress to a residual value, $\sigma_{col,res}$, that remains approximately constant with base settlement magnitude. The ratio of the residual value of vertical column stress to the initial value can be estimated using Equation 4.7. The ratio of the peak column stress to the initial column stress can be estimated using either Equation 4.5, which requires two fitting parameters, or Equation 4.8 which requires a single fitting parameter representing the ratio between peak and residual values of column stress. The presence of reinforcement did not significantly increase $\sigma_{col,max}$ for tests performed with an applied surcharge pressure. The presence of reinforcement generally increased $\sigma_{col,max}$ for tests performed without an applied surcharge. The tests performed with an applied surcharge are believed to have more reliable measurement of column stress than the tests performed without a surcharge. The presence of reinforcement generally increased the magnitude of the residual column stress.

6. Under all testing conditions, samples reached a condition of peak column stress at base settlement magnitudes less than about 10 percent of the column diameter. Without applied surcharge pressure, samples reached peak column stress at base settlement magnitudes less than 5 percent of the column diameter. The base settlement magnitude at peak column stress was observed to increase with increasing sample height. For all testing conditions, the residual column stress was reached at base settlements between about 9 and 20 percent of the column diameter. The presence of reinforcement did not have a significant impact on the magnitudes of base settlement at peak and residual column stress conditions.

5 Multi-Column Test Results

This section describes the results from the laboratory experiments performed using columns arrays. As described in Chapter 3, a total of 120 tests were performed using the configurations shown below in Table 5.1, which is adapted from Table 3.2 in Chapter 3. Tests were performed for a range of sample heights, sample densities, and reinforcement conditions. A summary of parameter variations is provided in Table 3.11 in Chapter 3. The notation used in this chapter is described in Section 1.4. Chapter 4 covers the results and findings from the single column tests, which serve as the starting point for the discussion of the multi-column tests.

Table 5.1 Configurations of testing equipment used for multi-column tests

Apparatus Configuration	2x2 Array 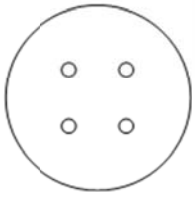	5x5 Array 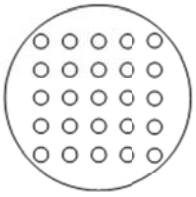
Column Spacing (s), inches	7.00	3.50
Column Diameter (d), inches	0.75 - 2.00 -	0.75 1.25 2.00 -
Area Replacement Ratio (a_s), %	1 - 6 -	4 10 26 -

The primary objective of conducting the multi-column tests was to observe the surface deformation occurring within a unit cell defined according to Figure 1.2 in Chapter 1 in response to differential settlement between the columns and the base of the sample tank. Key locations for describing surface deformation are defined in Table 1.4 of Chapter 1 and reproduced below as Figure 5.1 for a square array. The surface settlement over the axis of the columns, S_c, was described in Section 4.1.2 for the single column tests. Settlements S_i and S_d are the minimum and maximum surface settlements, respectively, at the unit cell boundary. As described in Section 1.4, the location of the settlement S_d is the distance s' from the edge of any round column. The

surface settlements are described as ratios of the base settlement, S_b, according to Table 1.5 in Chapter 1 which is reproduced below as Table 5.2. The principal outcome of the multi-column tests is the development of a relationship between unit cell geometry and the critical sample height. The critical height, H_{crit}, is the height at which surface settlement becomes uniform. Since the settlement over the column, S_c, is the minimum surface settlement in the unit cell and S_d is the maximum settlement in the unit cell, the differential settlement, S_c-S_d, occurring over a distance of s'+d/2, is critical for determining the critical height. Therefore, using the current notation, the critical height is defined as the height at which the settlement ratio $DSBR_d$ reaches zero.

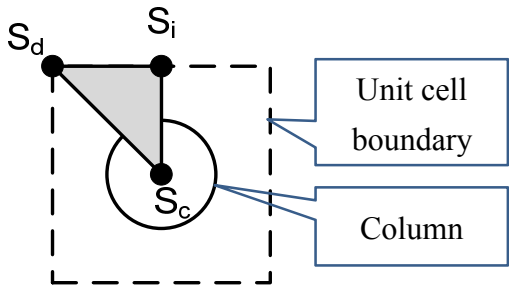

Figure 5.1 Key locations of surface settlement within a square unit cell

Table 5.2 Definition of surface settlement ratios

Settlement Ratio	Definition
SBR_c	S_c / S_b
SBR_d	S_d / S_b
SBR_i	S_i / S_b
$DSBR_d$	$(S_d - S_c) / S_b$
$DSBR_i$	$(S_i - S_c) / S_b$

Measurement of surface settlement within the unit cell was obtained from profiles taken at various increments of base settlement, S_b. The equipment and procedures used to obtain surface measurement during profiling are described in Sections 3.2.2 and 3.5. The methods used to reduce the data are discussed in Section 3.7.1. Figure 5.2 provides a plan view sketch of the settlement measurements extracted from the profiles. For 5x5 column arrays, the focus is on a column-centered unit cell at the center of the array and for 2x2 column arrays, the focus is on the soil-centered unit cell formed by the four columns. The extracted measurements, labeled A

through L, were used according to Table 5.3 and Table 5.4 to determine the reported values for the settlement over the column, S_c, and at the unit cell boundary, S_d and S_i. The settlement ratios SBR_c, SBR_d, and SBR_i are determined as the slope of the best fit line through S_c, S_d, and S_i versus base settlement magnitude, S_b, at each increment of column displacement. The intercept of the best fit line with the settlement axis is not reported here, but was generally negative with a magnitude less than 0.05. Because of nonlinearities and data scatter that may exist, the calculated ratios can differ from the secant ratio at a given increment of base settlement. The settlement ratios $DSBR_d$ and $DSBR_i$ are determined by subtracting SBR_c from the respective values of SBR_d and SBR_i.

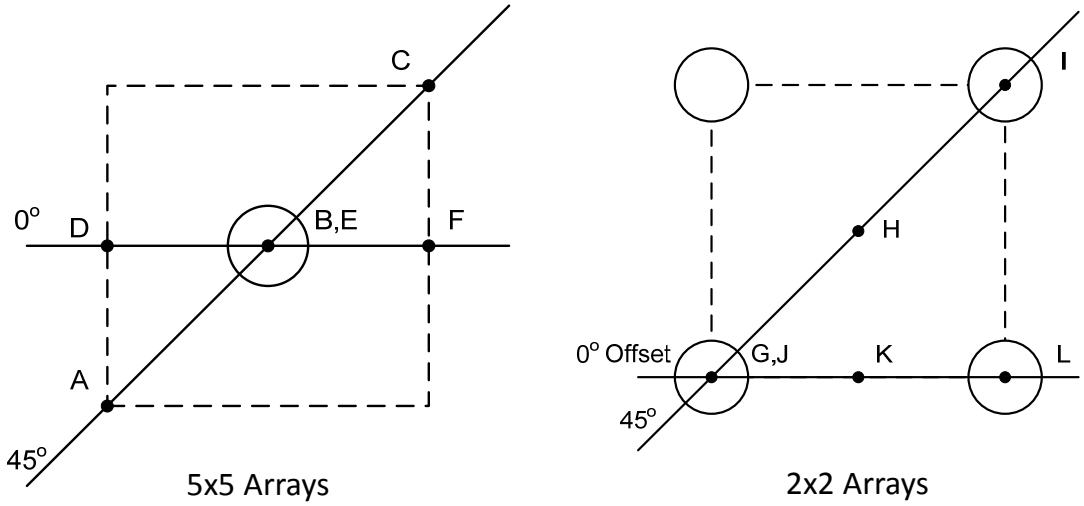

Figure 5.2 Surface settlement measurements extracted from profiles performed along the 45°, 0°, and 0° Offset orientations defined in Figure 3.8 in Chapter 3

Table 5.3 Use of surface measurements obtained during profiling for 5x5 column arrays

Profile Orientation	S_c	S_d	S_i
45°	B	Avg(A,C)	-
0°	E	-	Avg(D,F)
Reported	Avg(B,E)	Avg(A,C)	Avg(D,F)

Table 5.4 Use of surface measurements obtained during profiling for 2x2 column arrays

Profile Orientation	S_c	S_d	S_i
45°	Avg(G,I)	H	-
0° Offset	Avg(J,L)	-	K
Reported	Avg(G,I,J,L)	H	K

The base settlement and surface settlement at the center of the tank were also measured during continuous displacement of the columns relative to the base of the sample tank. The profiler measured settlement over the column, S_c, for 5x5 arrays and at the centroid of the soil-centered unit cell, S_d, for 2x2 arrays during column displacement. This capability allowed for a detailed look at the relationship between settlement at the surface measuring location and base settlement.

Similar to Chapter 4, Chapter 5 proceeds using examples in order to detail each component of the analysis. Two tests were selected as examples, one representing the results from a 5x5 column array and the other representing a 2x2 column array. The test parameter values associated with the examples are provided in Table 5.5.

Table 5.5 Test parameter values for tests highlighted as examples

Tests used as examples		
Test parameter	**Value**	
Test ID	7AMD22	4AMD4
Array type	5x5	2x2
Column diameter (in.)	0.75	2.00
Column spacing (in.)	3.5	7.0
Sample height (in.)	1.8	4.6
Sample density	Density 2 (D_r = 87%)	Density 2 (D_r = 87%)
Reinforcement	None	None

Chapter 5 is organized as follows: Section 5.1 describes the relationship between surface settlement directly over the axis of the columns and base settlement for samples below the critical height, Section 5.2 presents the relationship between surface settlement at the unit cell boundary and base settlement for samples below the critical height, Section 5.3 is focused on differential surface settlement and the determination of critical height, Section 5.4 describes the uniform surface settlement that occurs in response to base settlement for samples above the critical height, and Section 5.5 describes volume change within the unit cell resulting from base settlement. The influence of reinforcement and sample density on surface settlement is described in terms of differential settlement in Section 5.3. Additional discussion of the impact of reinforcement and density on surface settlement over the column and volume change for single column tests is presented in Chapter 4.

5.1 Surface Settlement over the Columns below the Critical Height

This section describes the surface settlement occurring over the axis of the columns due to base settlement. Figure 5.3 through Figure 5.6 show example profiles diagonal and along the column lines obtained at various increments of base settlement for 2x2 and 5x5 arrays. The measurement of S_c over the central column in the 5x5 column array is highlighted in red. In Figure 5.7, the measurements of S_c obtained during profiling are superimposed on a plot of S_c versus S_b obtained from measurements taken during column displacement. The figure shows that there is good correspondence between the methods of measurement.

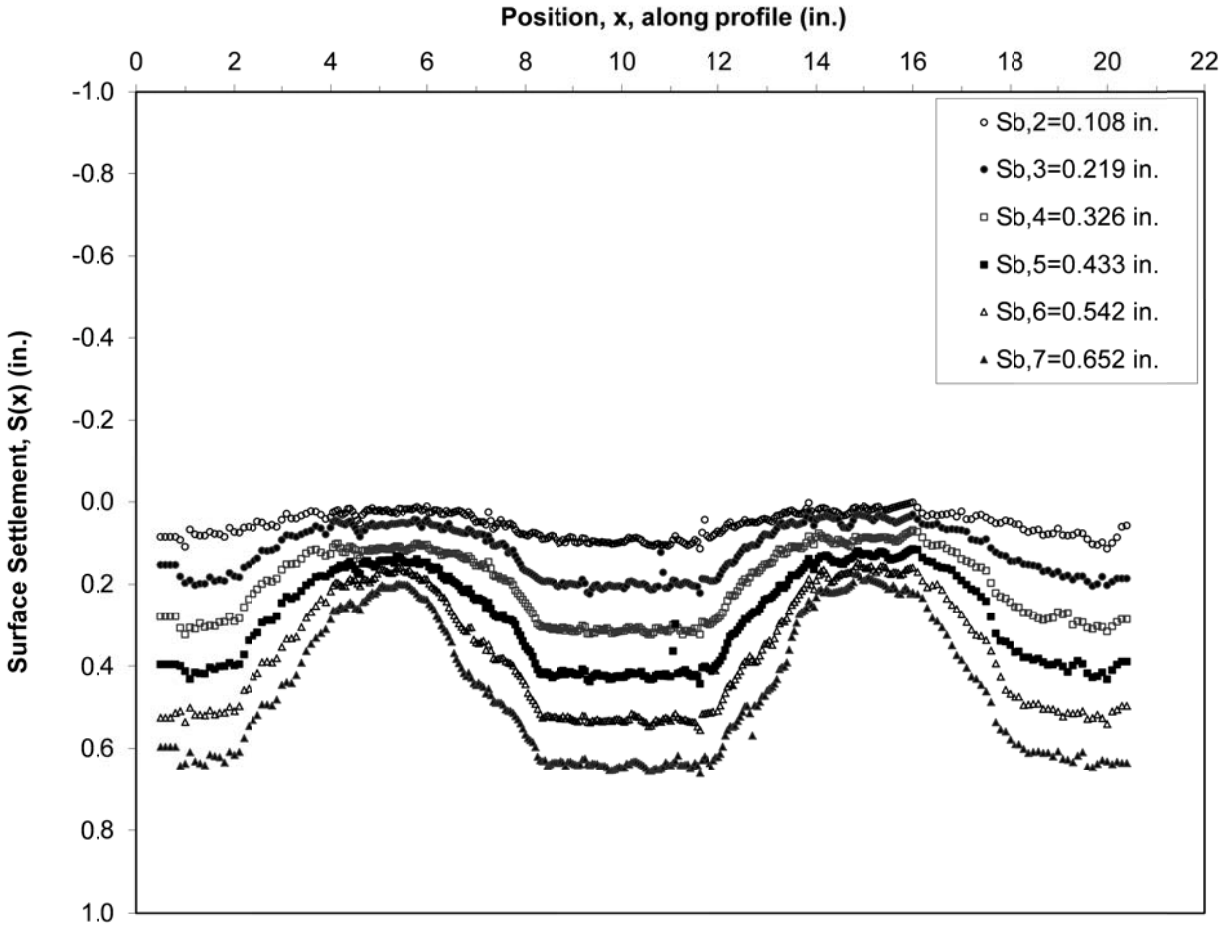

Figure 5.3 Example settlement profiles diagonal to the column lines at various increments of base settlement for 2x2 array

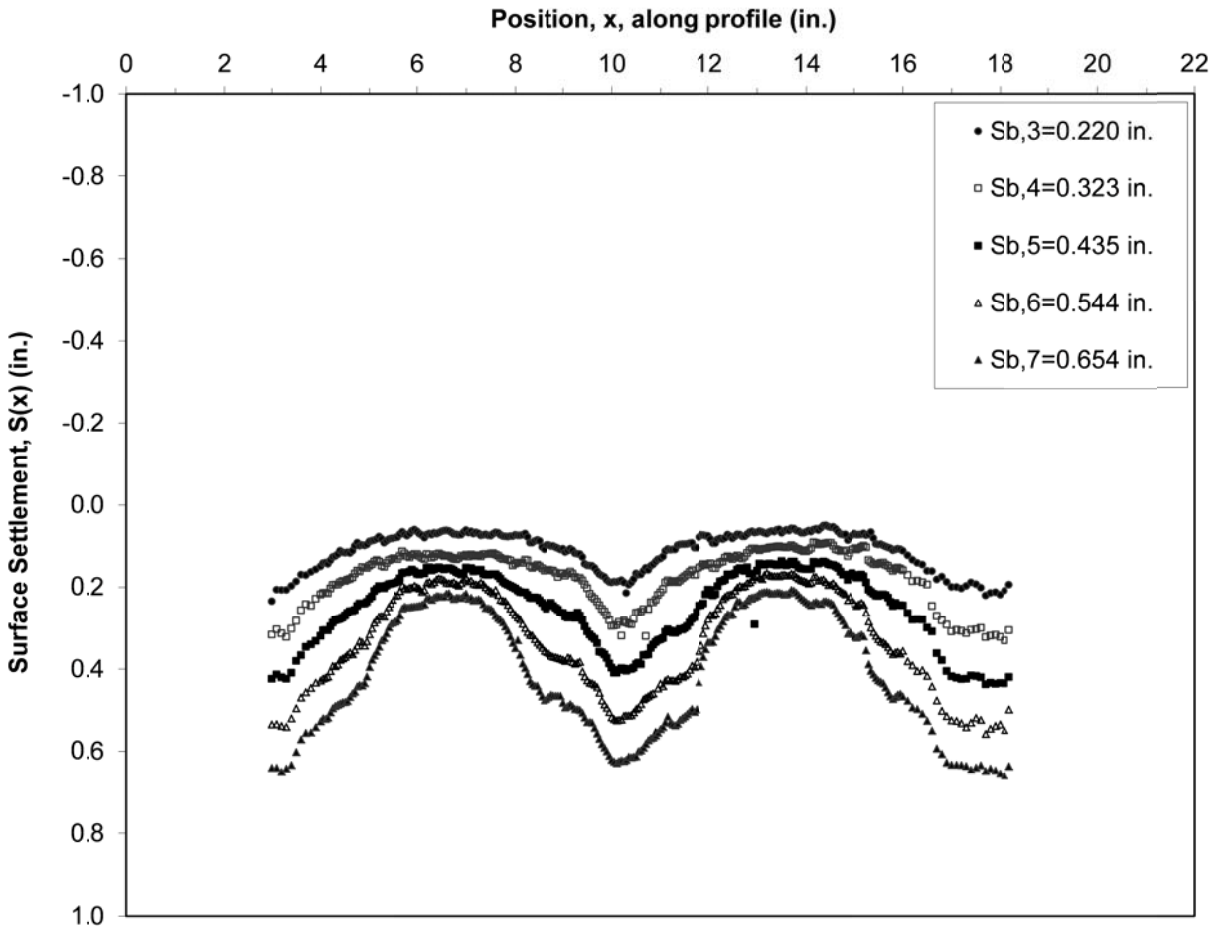

Figure 5.4 Example settlement profiles along the column lines at various increments of base settlement for 2x2 array

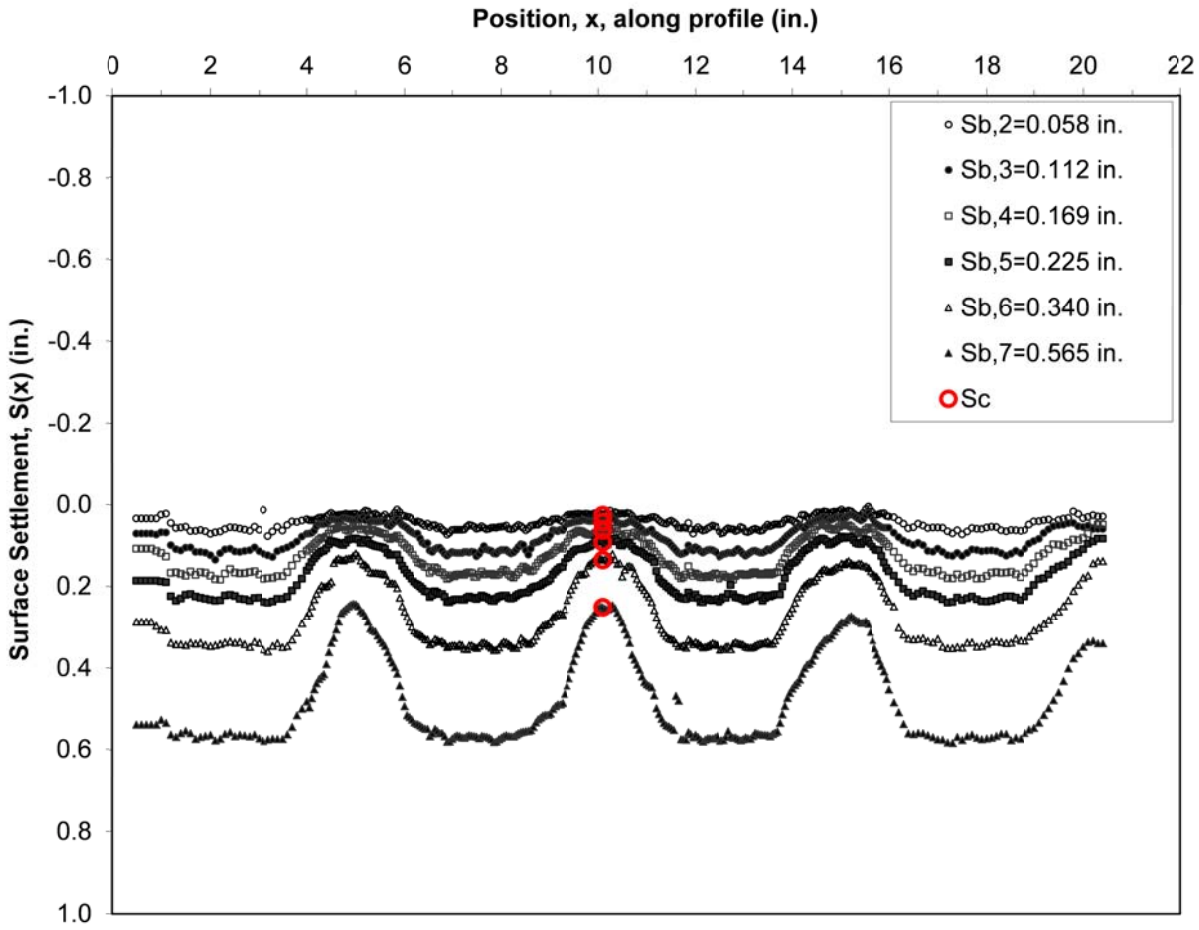

Figure 5.5 Example settlement profiles diagonal to the column lines at various increments of base settlement for 5x5 array. The settlement measured over the column, S_c, is highlighted in red.

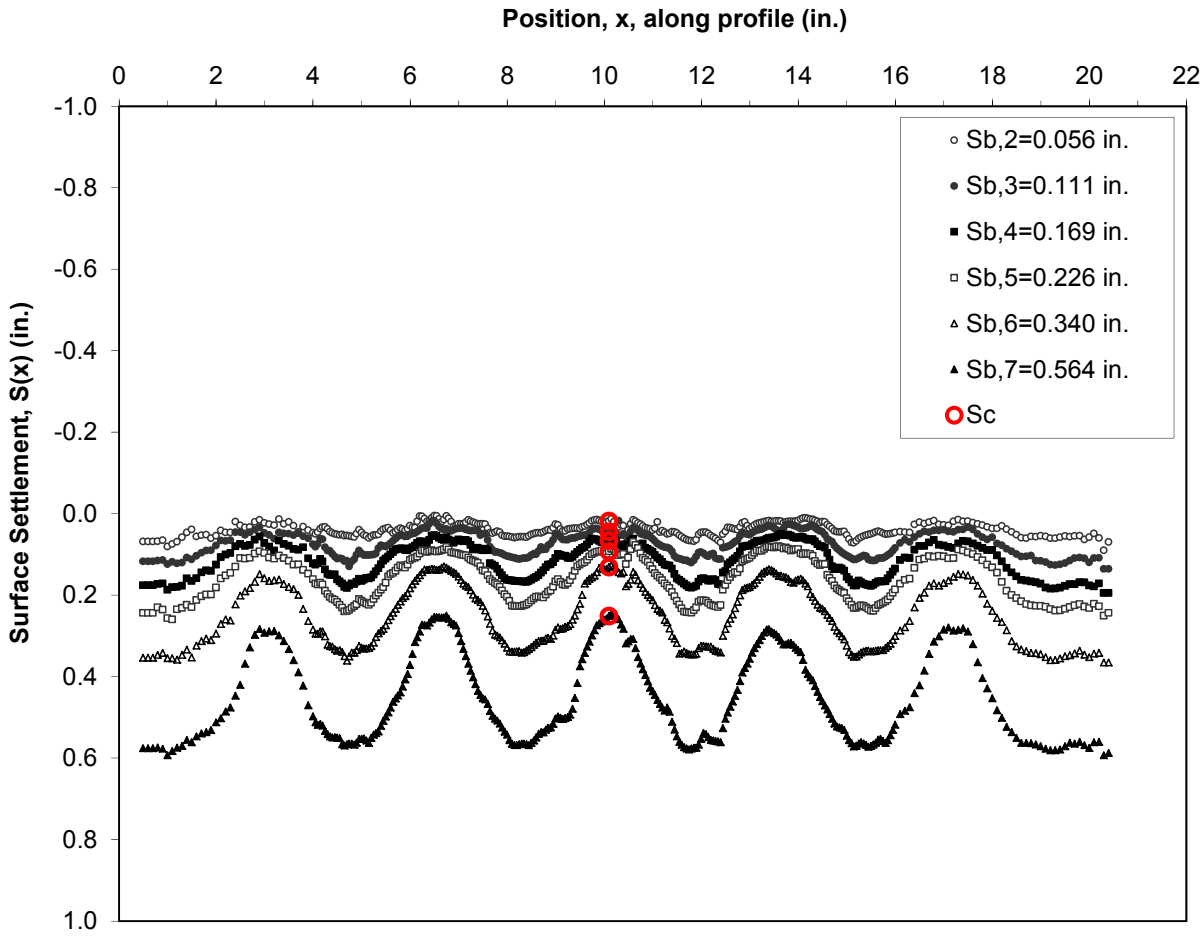

Figure 5.6 Example settlement profiles along the column lines at various increments of base settlement for 5x5 array. The settlement measured over the column, S_c, is highlighted in red.

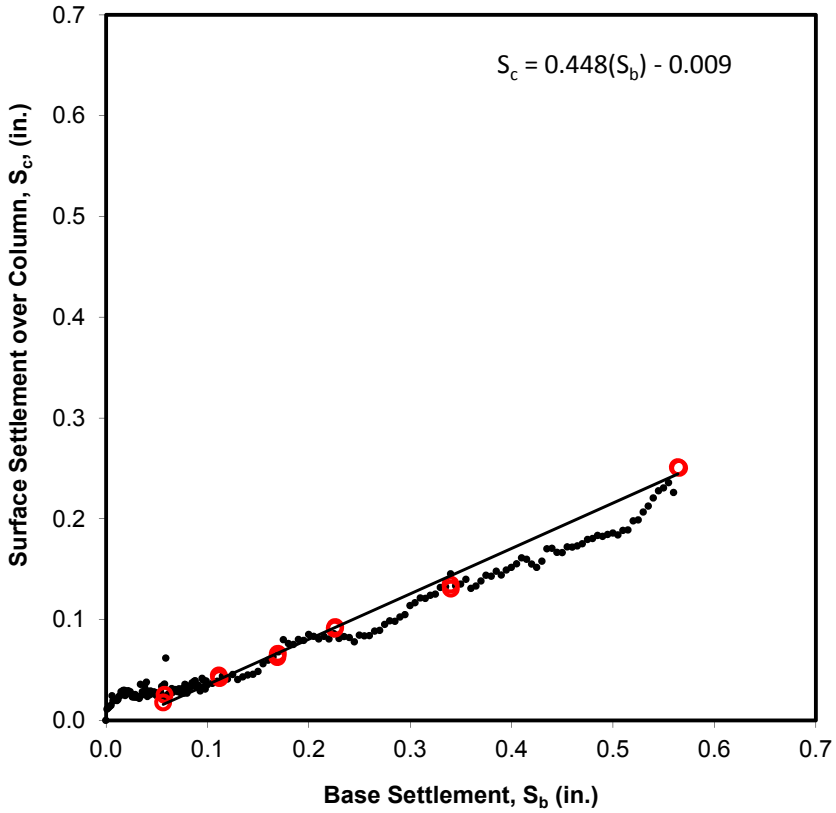

Figure 5.7 Example plot of surface settlement over column, S_c, versus base settlement, S_b, measured during column displacement for the 5x5 array. Measurements of S_c obtained during profiling diagonal and parallel to column lines as shown in Figures 5.4 and 5.5 are superimposed in red.

As shown in Figure 5.7, the settlement ratio SBR_c can be reasonably approximated as constant. Using the procedures described at the beginning of Chapter 5, Table 5.6 provides the settlement ratios defined in Table 5.2 for the example tests. As discussed in Section 5.2, since both of the samples are both below the interaction height, H_i, the settlement ratios at the unit cell boundary are approximately equal to unity.

Table 5.6 Settlement ratios determined for example tests outlined in Table 5.5

Test ID	SBR_c	SBR_d	SBR_i	$DSBR_d$	$DSBR_i$
7AMD22	0.448	1.009	1.002	0.561	0.554
4AMD73	0.344	1.005	1.005	0.661	0.661

The procedures for determining settlement ratios were followed for all multi-column tests and the resulting values of SBR_c for unreinforced multi-column experiments below the critical height performed at Density 2 (D_r = 87%) are shown in Figure 5.8 along with the results from

single column experiments described in Chapter 4. Inspection of Figure 5.8 indicates that below a normalized height of about 3, there is not much difference between the values of SBR_c determined from a single column test configuration and from a multi-column test performed below the critical height. Figure 5.9 shows single and multi-column tests performed using the same diameter columns at the same sample normalized sample height, H/d, and the resulting calculated values of SBR_c are nearly identical.

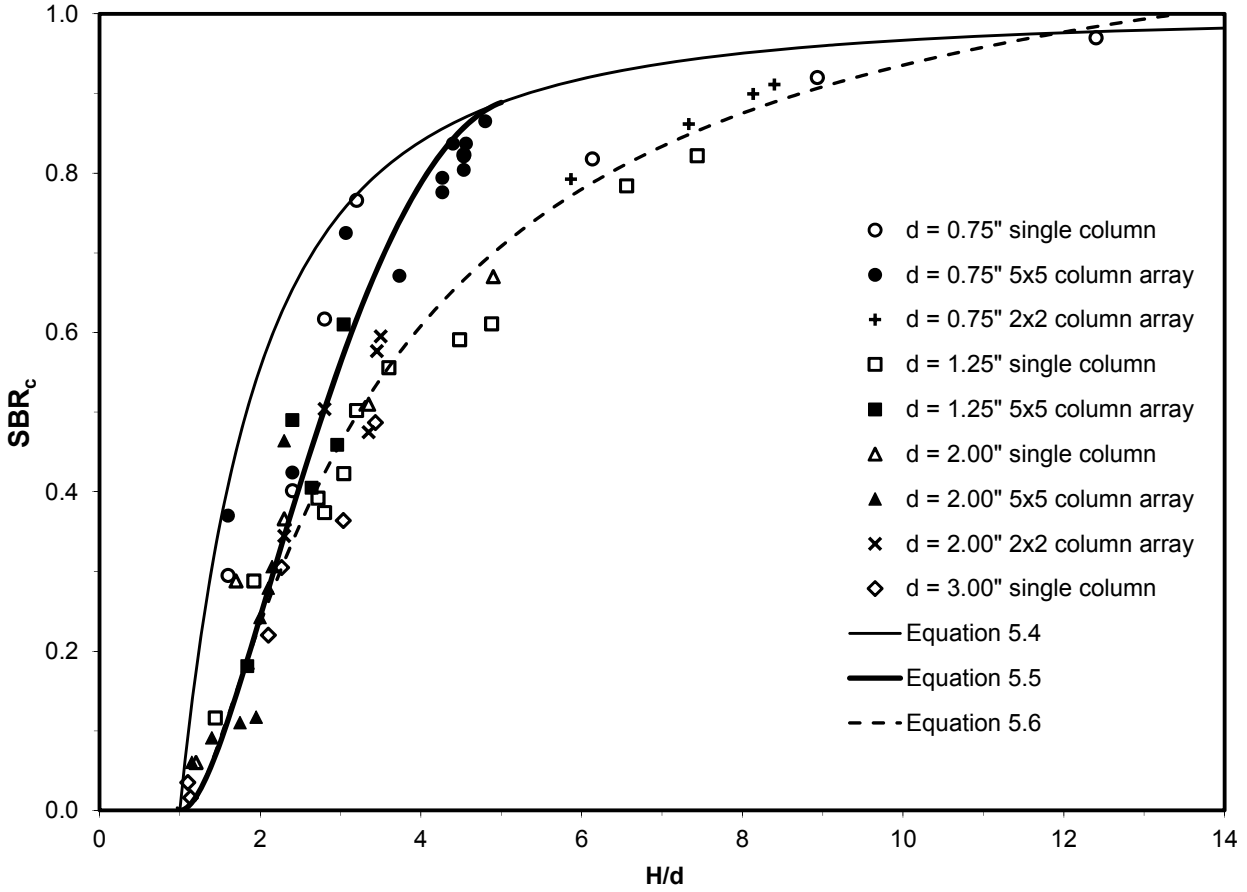

Figure 5.8 Measurements of SBR_c for unreinforced samples at Density 2 (D_r = 87%) for tests using single and multi-column configurations. Only multi-column tests performed below the critical sample height are shown.

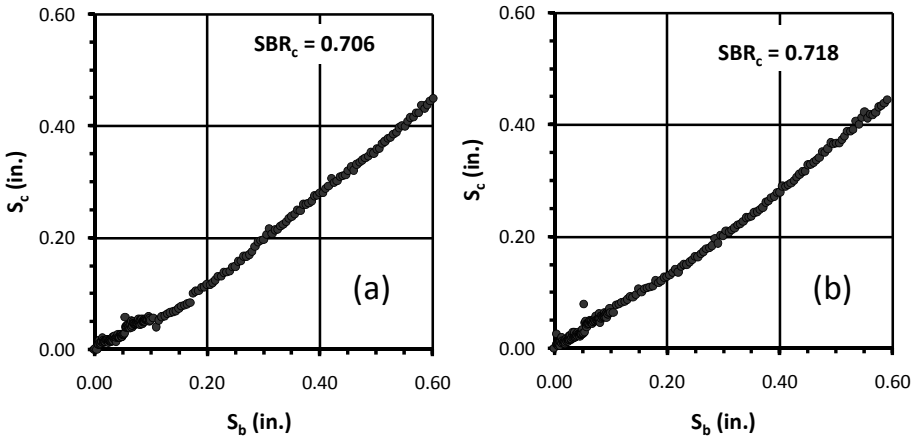

Figure 5.9 SBR$_c$ determined for 3.4-inch unreinforced samples at Density 2 tested using the following testing configurations: (a) 0.75- inch single column, (b) 5x5 array, d = 0.75, s = 3.5

The thin solid black line defining the upper boundary of the measurements of SBR$_c$ was generated using a simple model shown in profile view in Figure 5.10. As described in Section 4.1.1, the boundaries of the soil volume whose deformation is influenced by the presence of an individual column can be approximated by a truncated cone, or frustum, extending from the column to the sample surface with sides inclined at an angle α from vertical. The diameter of the cone at the surface of the sample is equal to d+2Htanα. If distortion, but no volume change, is allowed to occur within the cone of soil influenced by the column during settlement of the base, the dimension ΔH shown in Figure 5.10 is given by Equation 5.1. Described from a reference frame at the base of the settling sample, the volume of soil displaced by the column equals the volume of soil displaced at the sample surface. Using this relationship, which assumes that the surface influenced by the column deforms uniformly, the settlement ratio over the column is given by Equation 5.2. By adding a fitting parameter, C, to the expression, the relationship can be simplified to Equation 5.3. Since Figure 5.8 shows that the measurements of SBR$_c$ reach zero at a normalized sample height approximately equal to unity, assigning the fitting parameter a value equal to 4 results in the thin solid black line shown in Figure 5.8. The expression given in Equation 5.4 serves as the basis for fitting an expression to the data from multi-column tests below the critical height. Equation 5.5 includes an additional term used to fit the data for normalized heights less than 5. The data from single column tests do not follow the same trend and can be represented by the polynomial provided in Equation 5.6. Figure 5.11 through Figure 5.13 show fitted lines applied to the data sorted by column diameter.

From Figure 5.11 through Figure 5.13, it appears that the values of SBR$_c$ measured for four of the five unit cell geometries evaluated can be reasonably approximated by Equation 5.5.

The data from testing using the 2x2 array of 0.75-inch diameter columns does not follow same trend as the other arrays and are better approximated by the single column trend defined by Equation 5.6. It appears that the spacing for the 2x2 array of 0.75-inch diameter columns is so large compared to the column diameter that, below the critical height, the influence on SBR_c by neighboring columns is insignificant. Such a low area replacement ratio (A_s=1%) is likely not realistic for field conditions for a variety of reasons including, as described in Section 8.3.1, the small amount of settlement reduction achieved. Therefore, the trend defined by Equation 5.5, should be considered the default trend for column arrays.

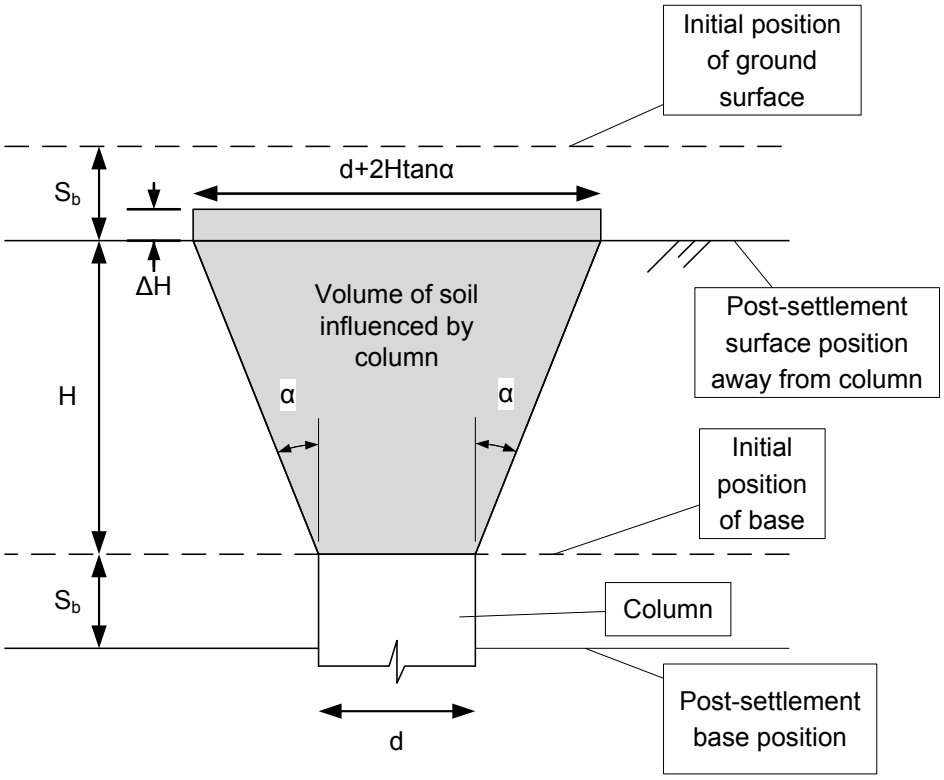

Figure 5.10 Simple model to estimate SBR_c

$$\Delta H = S_b \frac{d^2}{\left(d + 2H\tan\alpha\right)^2} \tag{5.1}$$

$$SBR_c = 1 - \frac{1}{\left(1 + 2\frac{H}{d}\tan\alpha\right)^2} \tag{5.2}$$

$$SBR_c = 1 - C\left(1 + \frac{H}{d}\right)^{-2} \tag{5.3}$$

$$SBR_c = 1 - 4\left(1 + \frac{H}{d}\right)^{-2} \quad \text{for } H/d \geq 1 \tag{5.4}$$

$$SBR_c = \left(1 - \frac{1}{16}\left(5 - \frac{H}{d}\right)^2\right)\left(1 - 4\left(1 + \frac{H}{d}\right)^{-2}\right) \quad \text{for } 1 \leq H/d \leq 5 \tag{5.5}$$

$$SBR_c = -0.3865\left(\frac{H}{d}\right)^{-3} + 2.0452\left(\frac{H}{d}\right)^{-2} - 2.8603\left(\frac{H}{d}\right)^{-1} + 1.2016 \text{ for } 1 \leq H/d \leq 13.5 \tag{5.6}$$

The performance of Equations 5.5 and 5.6 was evaluated by comparing the predicted values of SBR_c to the measured values from the experiments. Deviation of the measured values from the trend lines is due to variability in the measurements and testing conditions, as well as inaccuracies and omissions with curve fitting. Equation 5.5 was compared to multi-column test results below the critical height, except for tests performed using a 2x2 array of 0.75-inch diameter columns, and Equation 5.6 was compared to the results from single column tests and the multi-column tests using a 2x2 array of 0.75-inch diameter columns. The approach used to compared Equations 5.5 and 5.6 to the measurements of SBR_c was based on approximate application of regression analysis. Figure 5.14 shows the residuals (i.e. $SBR_{c,predicted} - SBR_{c,measured}$) determined using Equations 5.5 and 5.6 and the measurements of SBR_c from single and multi-column experiments performed for the full range of sample densities, applied surcharge pressures, and reinforcement conditions. The tests results were not filtered by testing condition since the findings from Chapter 4 suggest that the impacts of relative density, reinforcement, and applied surcharge pressure on SBR_c are small. The residuals indicate that Equation 5.5 slightly underpredicts SBR_c at low normalized heights and overpredicts SBR_c at high normalized heights. The residuals are essentially randomly distributed for Equation 5.6. In order to simplify the analysis of variation, the biases in Equations 5.5 and 5.6 were ignored and the variation of the data points from the trend lines was assumed to be normally distributed and independent of normalized height. Using these assumptions and simplifications, the standard deviations of the data from the trend lines were determined and are summarized below in Table 5.6. If all the conditions for regression analysis were met, the results in Table 5.7 would indicate that about 68 percent of the measured values of SBR_c fall within one standard deviation of the predicted values and there is 95 percent confidence that the mean of the data at a given normalized height is within 0.02 of the predicted value.

Table 5.7 Variability in values of SBRc predicted using Equations 5.5 and 5.6

	Equation 5.5	Equation 5.6
Average residual	0.01	0.00
Standard deviation	0.09	0.08
95% Confidence interval	Predicted SBR_c ±0.02	Predicted SBR_c ±0.02
Sample size	77 tests	67 tests

In a practical context, the results of the simplified analysis indicate that there are some small biases in the curve fitting to the data; however, the small confidence interval suggests that placement of the trend lines is reasonably good. The standard deviation values are about 10 percent of the full scale of SBR_c which indicates that the predictive accuracy of the trend lines is not very high.

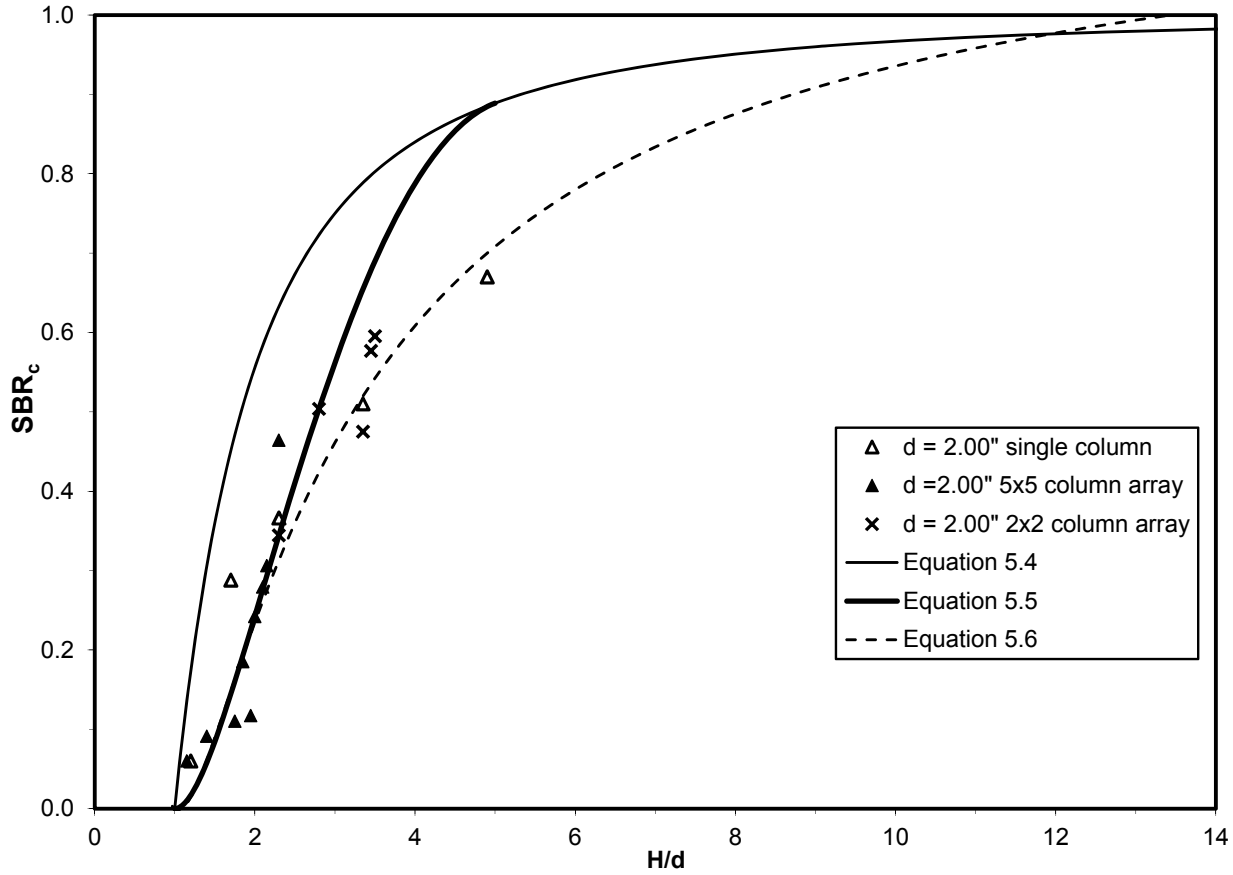

Figure 5.11 Measured values of SBR_c for unreinforced tests performed at Density 2 with 2.00" diameter column(s) versus normalized sample height showing fitted relationships.

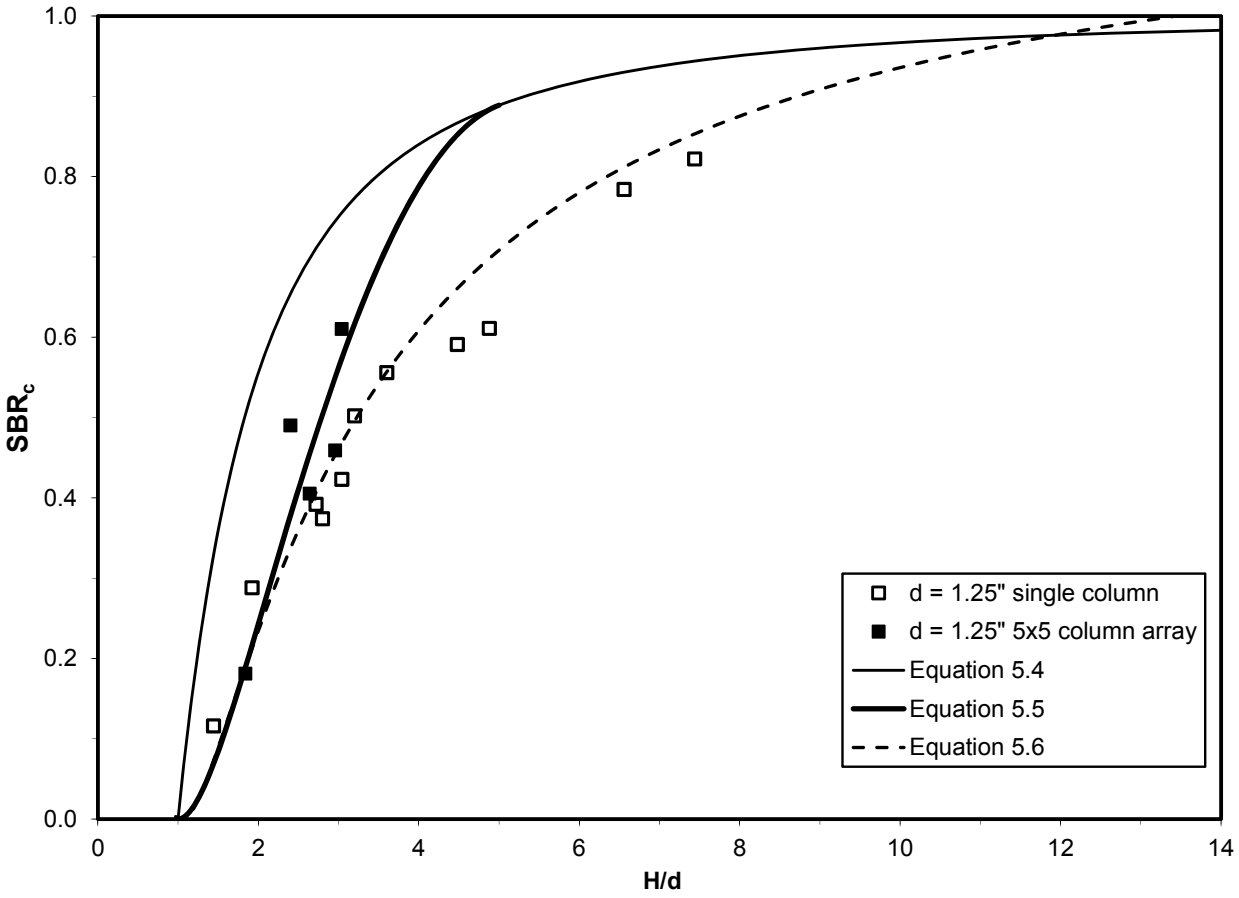

Figure 5.12 Measured values of SBR_c for unreinforced tests performed at Density 2 with 1.25" diameter column(s) versus normalized sample height showing fitted relationships.

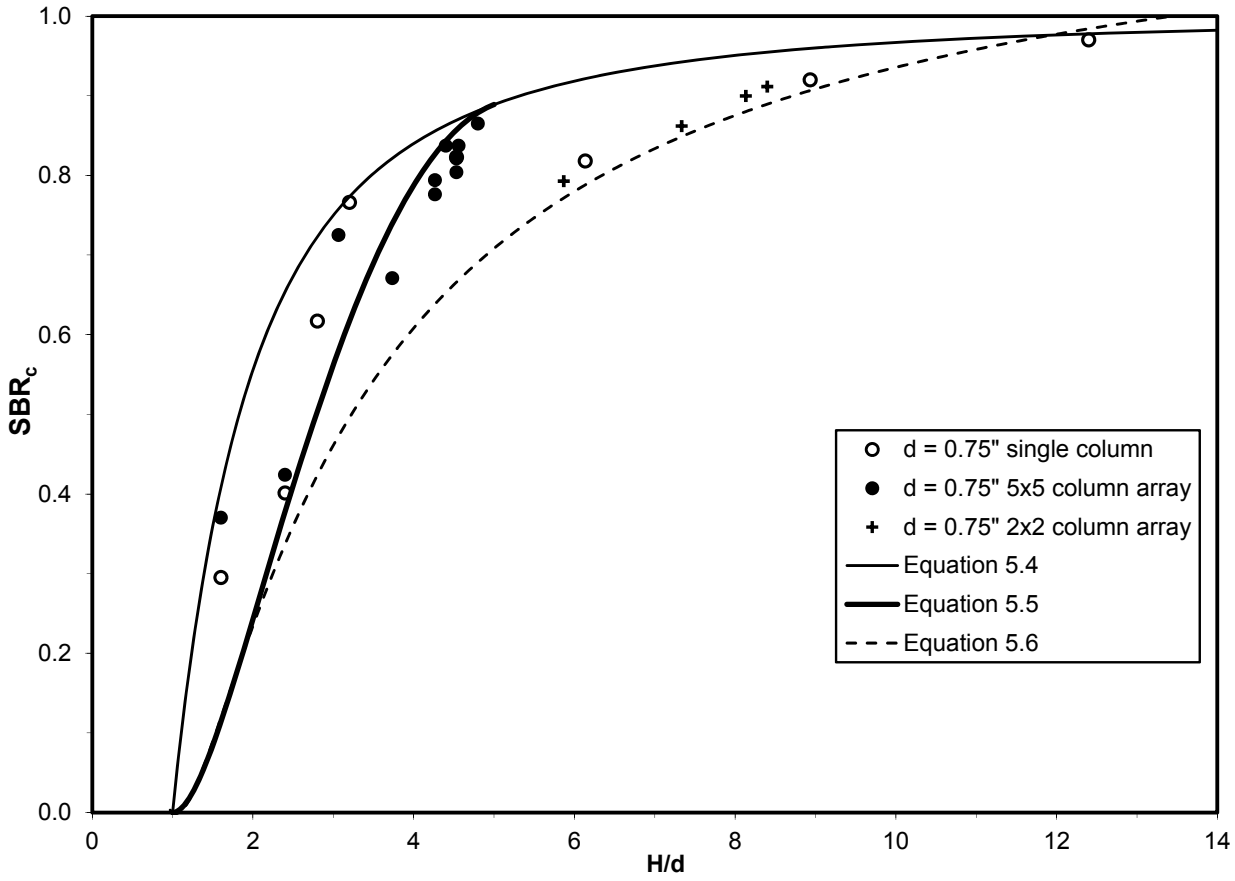

Figure 5.13 Measured values of SBR_c for unreinforced tests performed at Density 2 with 0.75" diameter column(s) versus normalized sample height showing fitted relationships.

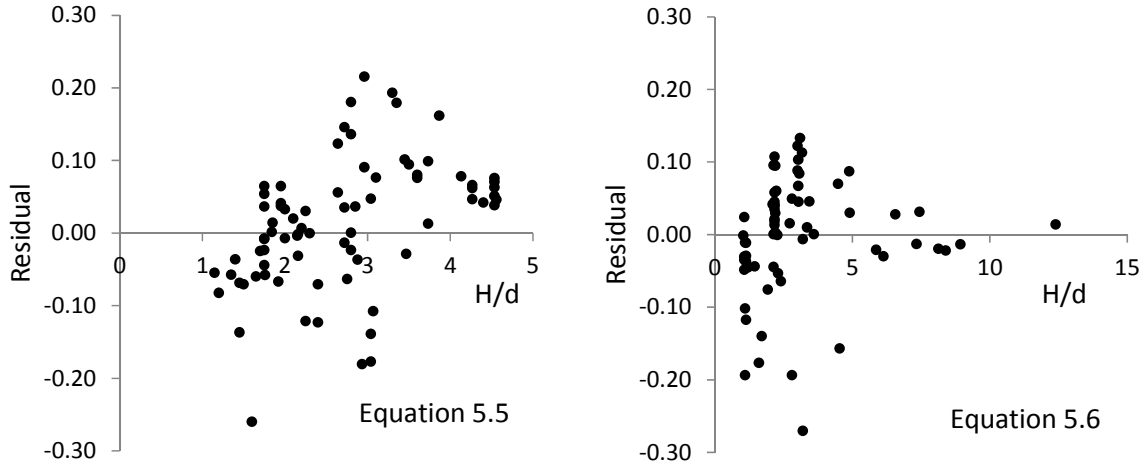

Figure 5.14 Difference between measured and predicted values of SBR_c for multi-column tests below the critical height and single column tests.

5.2 Surface Settlement at the Unit Cell Boundary below the Critical Height

This section describes the surface settlement occurring at the unit cell boundary for tests performed below the critical height. The surface settlement at the unit cell boundary reaches a maximum value, S_d, a distance s' from the edge of any round column and a minimum value, S_i, mid-span along a line of columns. The locations of S_d and S_i are defined for a square column array in Figure 5.1 and for all types of arrays in Section 1.4. Since the locations in the unit cell that receive the least support from the column control the critical height, the focus in this section will be primarily on S_d. For 5x5 and 2x2 column arrays, S_d and S_i are measured during profiling of the sample in between increments of base settlement. This type of measurement is shown in Figure 5.15 through Figure 5.18 for profiles diagonal and along the column lines, with the measurement of S_d highlighted in red for the 2x2 array. The equipment and procedures used to obtain surface measurement during profiling are described in Sections 3.2.2 and 3.5. The methods used to reduce the data are discussed in Section 3.7.1. When the equipment is configured to test 2x2 column arrays, S_d is also measured during the displacement of the columns relative to the base of the sample tank as shown in Figure 5.19. The measurements of S_d obtained during profiling are superimposed on the plot in Figure 5.19 using red symbols to show the correspondence between methods of measurement.

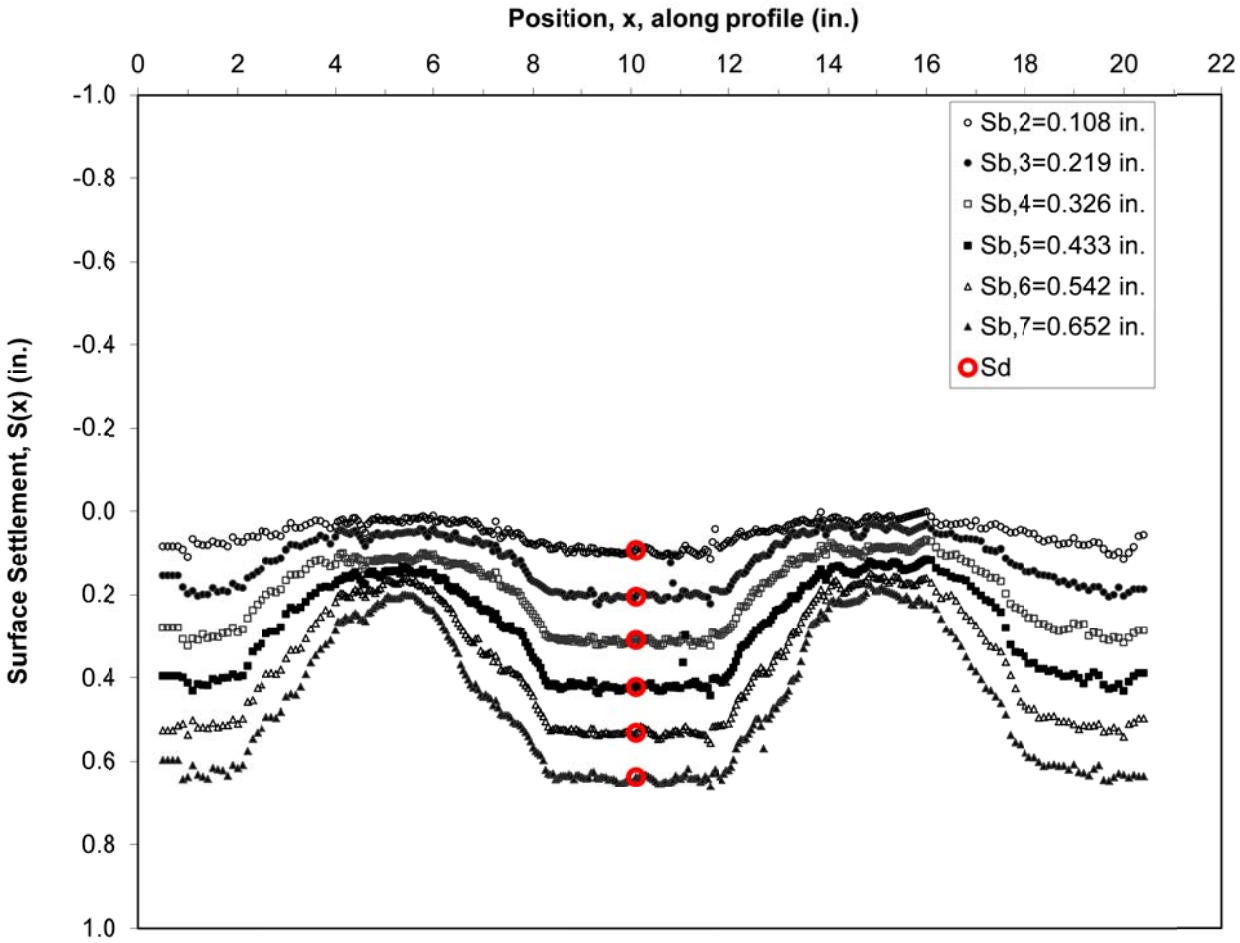

Figure 5.15 Example settlement profiles diagonal to the column lines at various increments of base settlement for 2x2 array. The measured surface settlement, S_d, is highlighted in red.

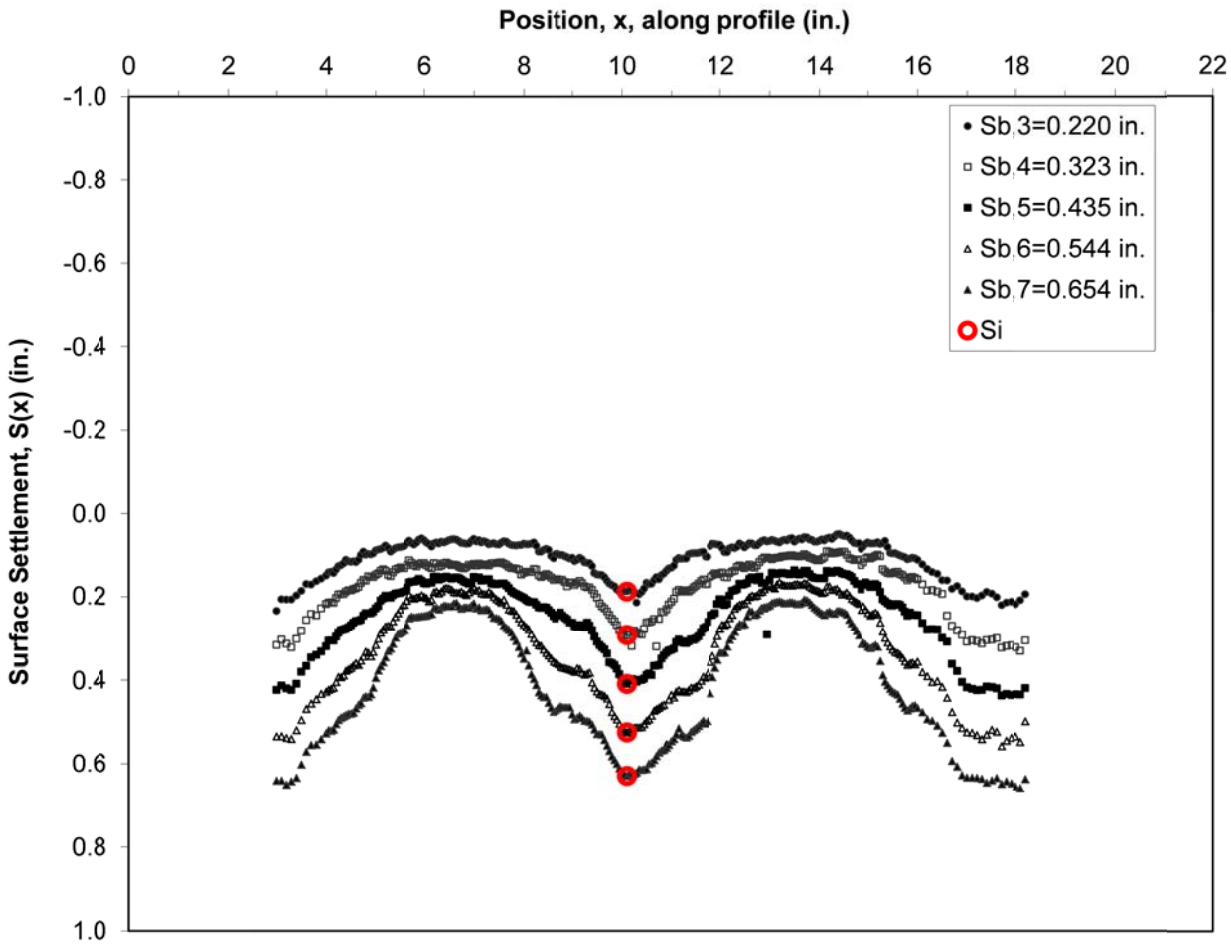

Figure 5.16 Example settlement profiles along the column lines at various increments of base settlement for 2x2 array. The measured surface settlement, S_i, is highlighted in red.

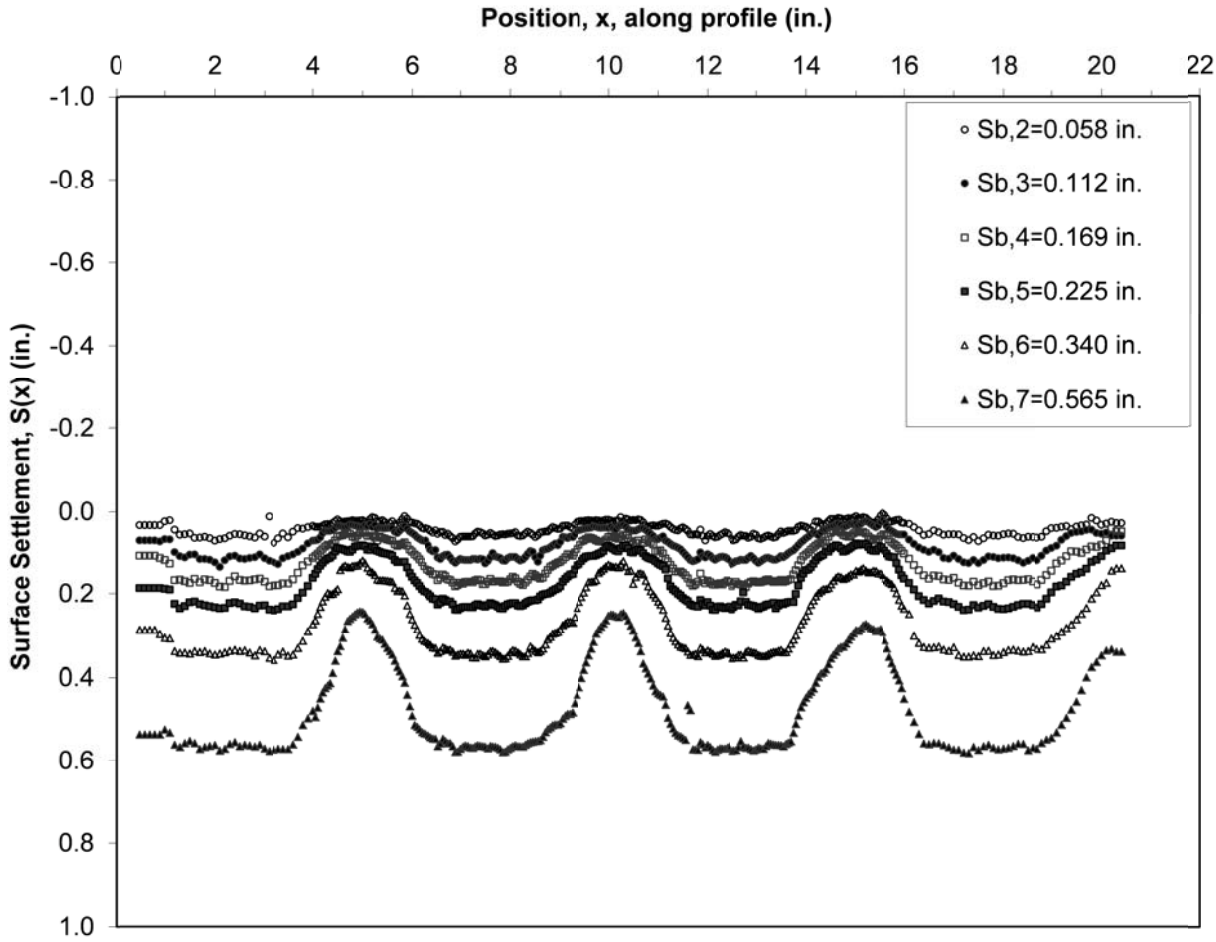

Figure 5.17 Example settlement profiles diagonal to the column lines at various increments of base settlement for 5x5 array.

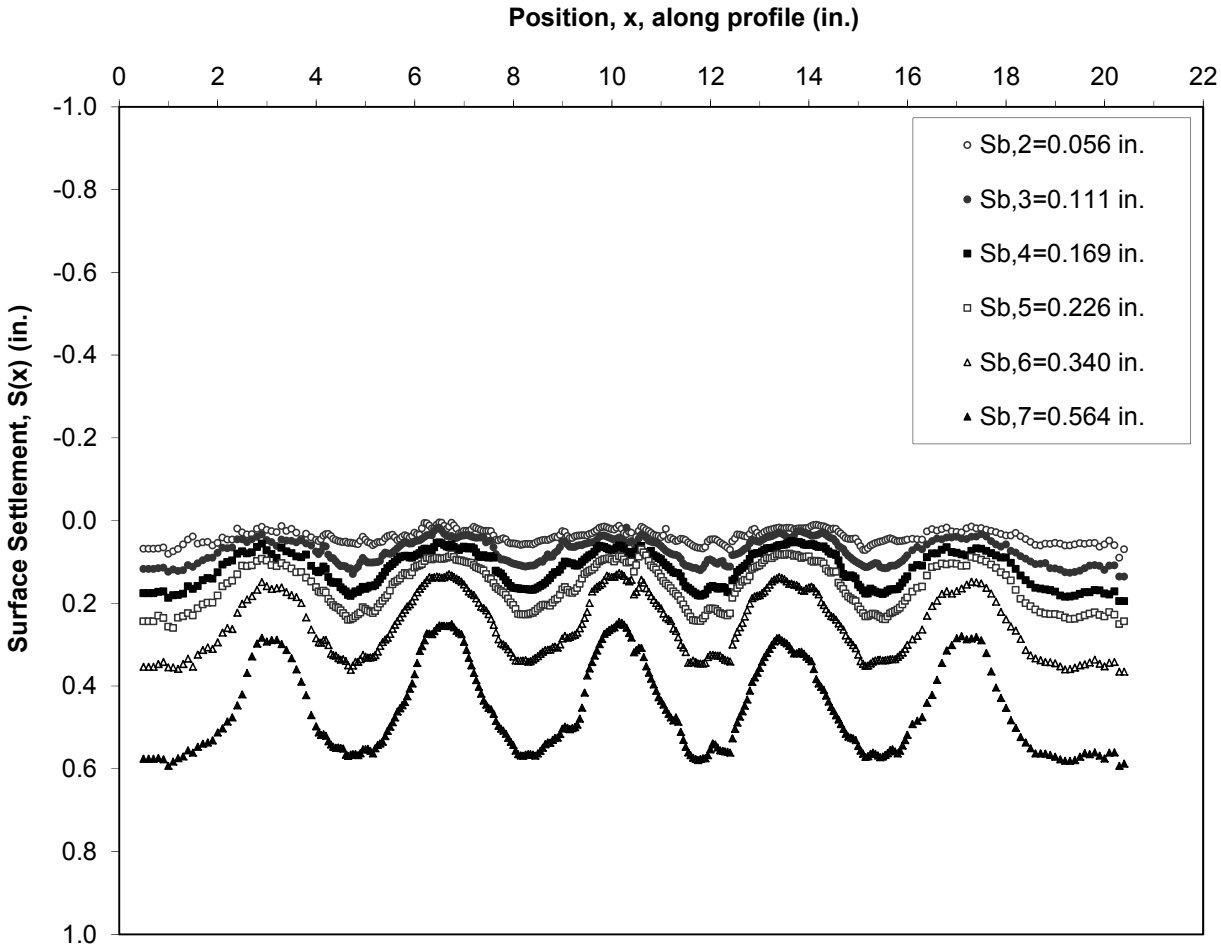

Figure 5.18 Example settlement profiles along the column lines at various increments of base settlement for 5x5 array.

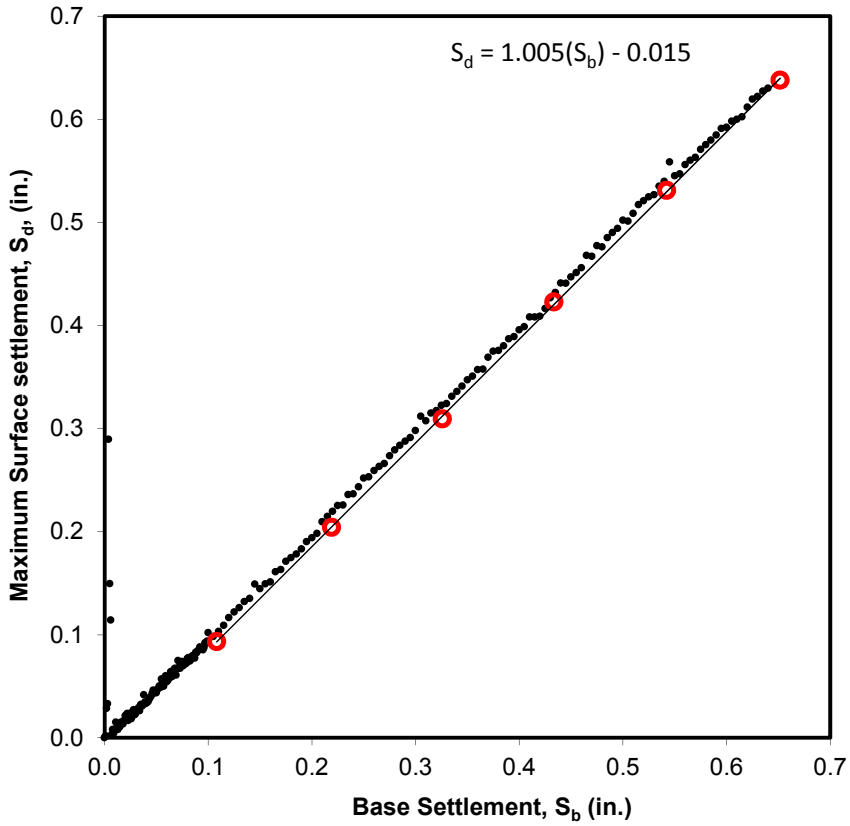

Figure 5.19 Example plot of surface settlement at unit cell boundary, S_d, versus base settlement, S_b, measured during column displacement for 2x2 array. Measurements of S_d obtained during profiling diagonal to the column lines orientations shown in Figure 5.13 is superimposed in red.

The ratio of S_d to S_b is defined as SBR_d in Table 5.2. For the example shown in Figure 5.19, SBR_d is calculated as 1.005, which is essentially equal to unity. The settlement ratios for both example tests defined in Table 5.5 are provided in Table 5.6. Figure 5.20 through Figure 5.24 show SBR_d determined for each unit cell geometry over a range of normalized sample heights. The results show that SBR_d is initially equal to unity when the influence of the individual columns does not extend completely to the unit cell boundary. A value of SBR_d equal to unity means that the surface settlement at the centroid of the soil-centered unit cell, a distance s' from any round column, is equal to the base settlement. As defined in Section 1.4, the interaction height, H_i, is the height above which S_d becomes less than S_b. Assuming that the interaction height is equal to the height where linear shearing surfaces from adjacent columns intersect, the interaction height can be determined for the unit cell geometries defined in Section 1.4 according to Equation 5.7. As described in Section 2.5, Kumar and Kouzer (2008b) used a similar approach for estimating the ultimate capacity of a group of embedded anchors.

$$H_i = \frac{s'}{\tan \alpha} \tag{5.7}$$

Values of α observed during single column testing are reported in Table 4.2 of Chapter 4, where α is the inclination from vertical of the linear shearing surface from the edge of the column to the surface. The red symbols in Figure 5.20 through Figure 5.24 show the interaction height calculated using Equation 5.7 with α equal to 29° plotted at SBR_d equal to unity. For the arrays using 1.25 and 2.00-inch diameter columns, the predicted interaction height agrees well with the observations. The observed interaction heights for the arrays using 0.75-inch columns, which also have the lowest area replacement ratios, are less than the predicted values. The green vertical line included in each plot indicates the normalized critical height, H_{crit}/d, determined in Section 5.3 for each unit cell geometry. The relationship between SBR_d and normalized height is approximtely linear between the observed interaction height and the critical height. Beyond the critical height when surface settlement is uniform, SBR_d converges to SBR_{tot}, which is discussed in Section 5.4.

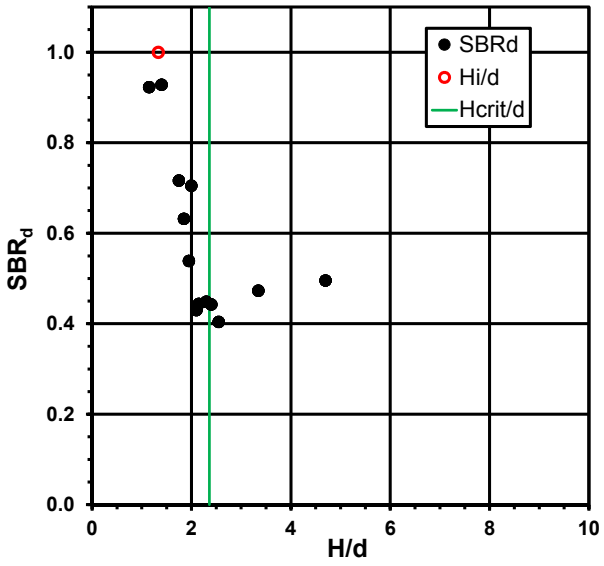

Figure 5.20 SBR_d versus H/d for array geometry defined by s = 3.50 in., d = 2.00 in. Plot shows interaction height, H_i, calculated using Equation 5.7 with α = 29° and critical height determined in Section 5.3.

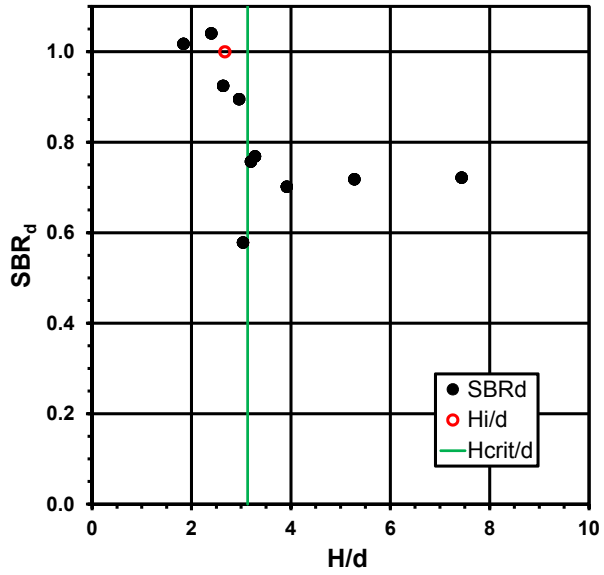

Figure 5.21 SBR$_d$ versus H/d for array geometry defined by s = 3.50 in., d = 1.25 in. Plot shows interaction height, H$_i$, calculated using Equation 5.7 with α = 29^o and critical height determined in Section 5.3.

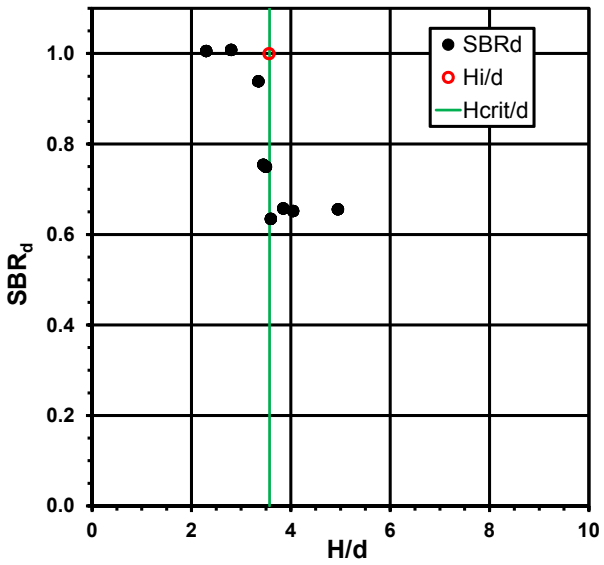

Figure 5.22 SBR$_d$ versus H/d for array geometry defined by s = 7.00 in., d = 2.00 in. Plot shows interaction height, H$_i$, calculated using Equation 5.7 with α = 29^o and critical height determined in Section 5.3.

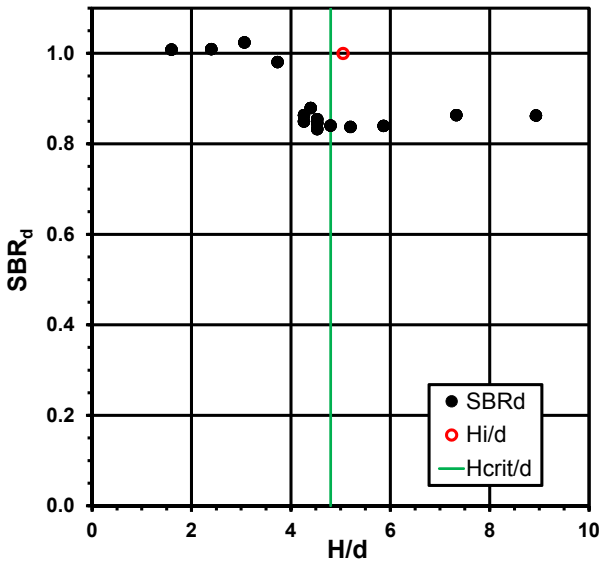

Figure 5.23 SBR_d versus H/d for array geometry defined by s = 3.50 in., d = 0.75 in. Plot shows interaction height, H_i, calculated using Equation 5.7 with $\alpha = 29^o$ and critical height determined in Section 5.3.

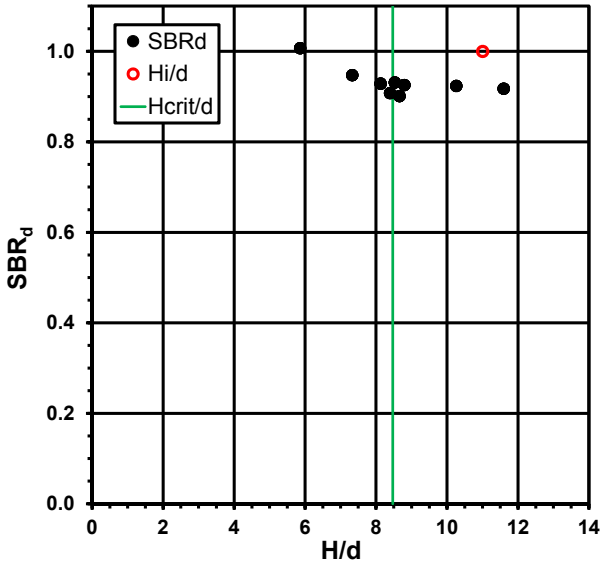

Figure 5.24 SBR_d versus H/d for array geometry defined by s = 7.00 in., d = 0.75 in. Plot shows interaction height, H_i, calculated using Equation 5.7 with $\alpha = 29^o$ and critical height determined in Section 5.3.

5.3 Differential Settlement and Critical Height

Sections 5.1 and 5.2 describe surface settlement occurring over the column, S_c, and at the unit cell boundary, S_d and S_i, resulting from base settlement, S_b, when sample height is less than the critical height. The results show that the surface settlement over the column increases and the

settlement at the unit cell boundary decreases for an increment of base settlement as sample height is increased. The net effect of these trends is a reduction of differential surface settlement between the column and the unit cell boundary, S_d-S_c and S_i-S_c, produced by an increment of base settlement as sample height is increased. This section describes the influence of unit cell geometry, sample density, and reinforcement on differential surface settlement and the determination of critical height, H_{crit}. The settlement ratios $DSBR_d$ and $DSBR_i$ defined in Section 1.4 and reintroduced in Table 5.2 are used to describe the relationship between differential surface settlement and base settlement. The values of $DSBR_d$ and $DSBR_i$ for the example tests outlined in Table 5.5 are provided in Table 5.6. Equations 5.8 and 5.9 show the relationship between the settlement ratios for differential settlement and the ratios for total settlement.

$$DSBR_d = SBR_d - SBR_c \tag{5.8}$$

$$DSBR_i = SBR_i - SBR_c \tag{5.9}$$

Figure 5.29 through Figure 5.52, which are provided at the end of Section 5.3 for convenient , show the relationships between DSBR in the diagonal (45^o) and in-line directions ($0^o/0^o$ Offset) versus normalized sample height. The figures show that DSBR decreases in a fairly linear fashion as normalized sample height is increased. The normalized height where $DSBR_d$ reaches zero is interpreted as the critical height. Table 5.8 lists the normalized heights in the diagonal and in-line direction where differential surface settlement no longer occurs.

Table 5.8 Summary of parameters defining the relationship between normalized height (h/d) and DSBR

			Diagonal			In-Line			
A_s	Column diameter, d (in.)	Column spacing, s (in.)	Spanning ratio, s'/d	H/d at $DSBR_d$ =0	Unreinforced, β (deg.)	Reinforced β (deg.)	H/d at $DSBR_i$ =0	Unreinforced, β (deg.)	Reinforced β (deg.)
26%	2.00	3.50	0.74	2.36	81-**83**-85	81-**82**-85	2.20	77-**79**-82	73-**77**-82
10%	1.25	3.50	1.48	3.13	81-**84**-87	78-**80**-87	3.13	80-**82**-87	73-**75**-85
6%	2.00	7.00	1.97	3.57	79-**83**-87	79-**83**-87[1]	3.57	79-**83**-87	70-**83**-87[1]
4%	0.75	3.50	2.80	4.80	63-**66**-72	**45**[2]	4.50	65-**68**-74	**43**[2]
1%	0.75	7.00	6.10	8.47	37-**38**-41	--	8.47	37-**38**-41	--

Notes:

Three numbers separated by dashes are reported for the angle β. The first number is minimum value indicated by the data, the third number is the maximum value, and the second number in bold is the representative value

1. In this case, the values for β are based on very limited testing
2. In this case, a single value for β captures the trend of the data

In two of the five geometries evaluated, DSBR reached a value of zero at a lower height in the in-line direction than in the diagonal direction. This behavior is not surprising since the location that receives the least support from the column is located along the diagonal between adjacent columns. There is no obvious explanation why some geometries had different heights where DSBR reached zero for the diagonal and in-line directions and others did not.

The presence and stiffness of reinforcement was not found to change the critical height. As discussed in Chapters 2 and 8, this outcome is consistent with the findings of others.

The range of relative densities used during testing (74%-105%) was also not found to have a clear measurable impact on critical height. As described in Section 5.5, surface measurements indicate that the sample volume within the unit cell dilates in response to differential base settlement. Furthermore, samples above the critical height were observed to settle uniformly even at large magnitudes of base settlement. This suggests that critical height may be insensitive to initial relative density. This assertion is further supported in Chapter 7 by comparing critical heights interpreted from experimental and numerical studies performed by others using different sample materials and initial relative densities than in the current study.

Figure 5.25 shows values of critical height listed in Table 5.8 plotted against spanning ratio. The relationship indicated by the results is provided in Equation 5.10.

$$H_{crit} = 1.15(s') + 1.44d \tag{5.10}$$

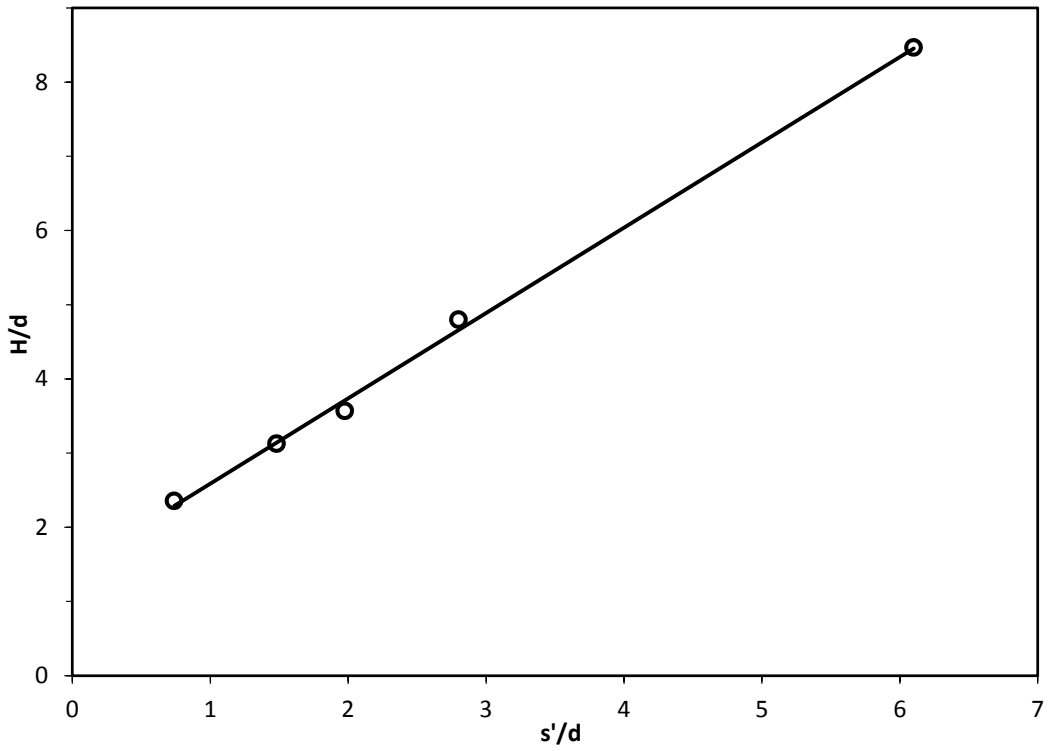

Figure 5.25 Critical heights interpreted from the results of the current study

To understand the impact of unit cell geometry, sample density, and reinforcement on differential settlement below the critical height, the angle β was defined to describe the trend of DSBR versus H/d. In Figure 5.29 through Figure 5.52 provided at the end of Section 5.3, DSBR spans a range from 0 to 1 while H/d spans a range from 0 to 10. If the horizontal axis is scaled down by a factor of 10, a trend line originating at H/d where DBSR equals zero makes an angle above the horizontal equal to β.

The angle β provides a relative indication of how DSBR increases as normalized height decreases below the height where DSBR equals zero. For example, in Figure 5.29, the trend of $DSBR_d$ with respect to H/d for column spacing equal to 3.50 in. and column diameter equal to 2.00 in., is represented by β equal to 83°, whereas Figure 5.45 shows β equal to 66° for column

spacing equal to 3.50 in. and column diameter equal to 0.75 in. For an increment of normalized height below the critical height, DSBR is greater for the unit cell geometry with the higher value of β.

Values for the angle β were determined using the bench-scale test results and are depicted in Figure 5.29 through Figure 5.52. As shown in Figure 5.35 and Figure 5.41, a range of values for the angle β was considered before selecting the representative value. The minimum, maximum, and representative values of β are provided in Table 5.8. The angle β was found to be sensitive to unit cell geometry and reinforcement as described below. There was not a measurable change in β over the range of sample relative densities evaluated.

Figure 5.26 and Figure 5.27 provide plots of the angle β versus spanning ratio in the diagonal and in-line directions. The circle symbols indicate the representative values and the error bars indicate the minimum and maximum estimates of β provided in Table 5.8. In the diagonal direction, the plot suggests that between the minimum spanning ratio investigated equal to 0.73 to about 2.00, β for unreinforced samples can be approximated by a constant value equal to 83^o. For a square array of columns, a fixed value of β equal to 83^o covers area replacement ratios from about 6 to 26 percent. Beyond a spanning ratio of 2.00, β decreases as spanning ratio increases. Between a spanning ratio of 2.00 and the maximum spanning ratio investigated equal to 6.10, β for unreinforced samples can be estimated using Equation 5.11. The relationship between β and spanning ratio is indicated in Figure 5.26 by the dashed line. In the in-line direction, β for unreinforced samples can be approximated as increasing linearly from a value of 79^o at a spanning ratio of 0.73 to a value of 83^o at a spanning ratio of 2.00. Beyond a spanning ratio of 2.00, the relationship provided in Equation 5.11 for the diagonal direction can also reasonably be applied to the in-line direction. The dashed line in Figure 5.27 indicates the approximated relationship between spanning ratio and β for the in-line direction.

$$\beta = 135\left(\frac{s'}{d}\right)^{-0.7} \tag{5.11}$$

Figure 5.26 and Figure 5.27 show that the inclusion of reinforcement decreases β, corresponding to reduced differential settlement versus the unreinforced case at fixed magnitudes of spanning ratio, sample height, and base settlement. The available data indicates that the decrease in β increases as spanning ratio increases. The influence of reinforcement on β is revisited in Chapter 7.

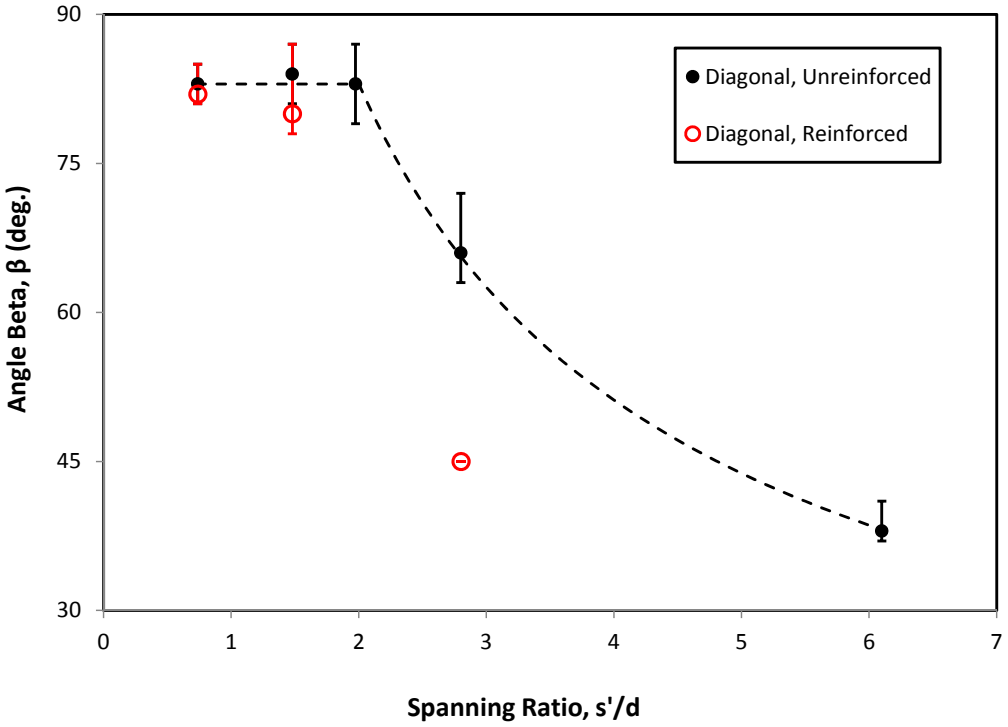

Figure 5.26 Relationship between β and spanning ratio diagonal to adjacent columns

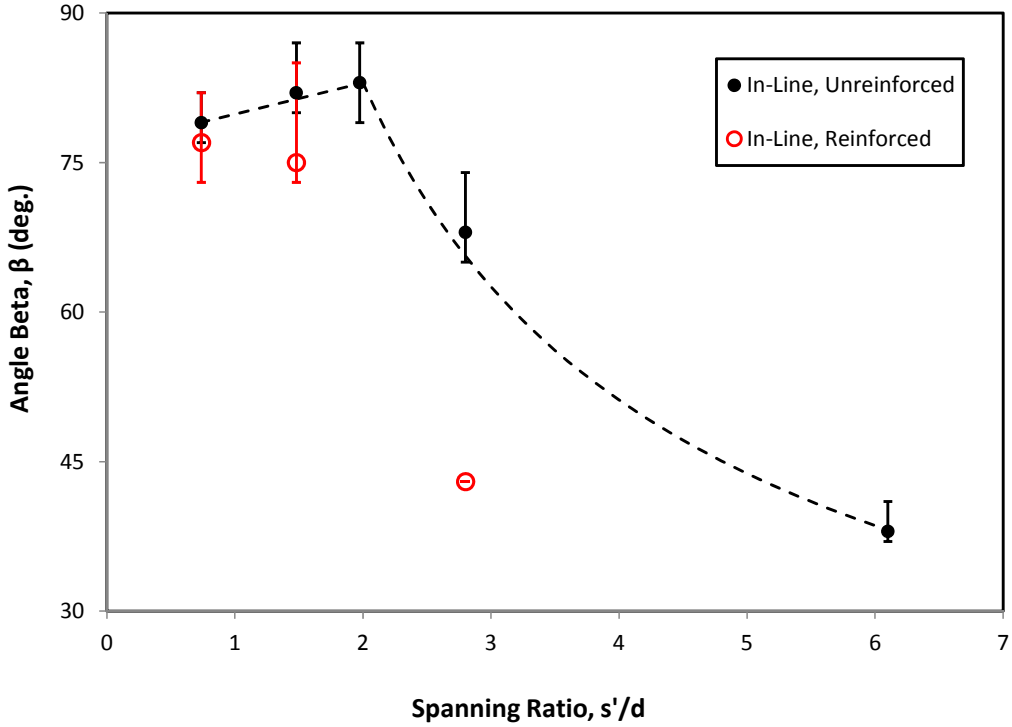

Figure 5.27 Relationship between β and spanning ratio in-line with adjacent columns

The angle β can be used to estimate $DSBR_d$ using Equation 5.12. Other inputs to Equation 5.12 are the critical height, H_{crit}, estimated using Equation 5.10, the sample height of interest below the critical height, H, and the settlement ratio, SBR_c, estimated using Equation 5.5. Equation 5.12 is only relevant for $H<H_{crit}$ since $DSBR_d$ equals zero at and above the critical height.

$$DSBR_d = \min\left\{\begin{array}{c} 1-SBR_c \\ \dfrac{H_{crit}-H}{d}\left(\dfrac{\tan\beta}{10}\right) \end{array}\right. \tag{5.12}$$

Equations 5.10, 5.11, and 5.12 can be combined into Equation 5.13 to estimate the maximum differential surface settlement below the critical height for unreinforced samples. For example, in a case where column spacing equals 3.50-inches, column diameter equals 2.00-inches, and sample height equals 3-inches, $DSBR_d$ is estimated using Equation 5.13 to equal 0.64. Therefore, for a base settlement equal to 1 inch, there would be 0.64 inches of differential surface settlement.

$$DSBR_d = \min\left\{\begin{array}{c} 1-SBR_c \\ \left(0.115\dfrac{s'}{d}-\dfrac{H}{10d}+0.144\right)\tan\left(\min\left\{\begin{array}{c} 83^o \\ 135\left(\dfrac{s'}{d}\right)^{-0.7} \end{array}\right.\right) \end{array}\right. \tag{5.13}$$

The performance of Equation 5.13 was evaluated by comparing the predicted values of $DSBR_d$ to the measured values from the experiments. The same approach used in Section 5.1 to assess the prediction of SBR_c was applied to the prediction of $DSBR_d$. Figure 5.28 shows the residuals (i.e. $DSBR_{d,predicted} - DSBR_{d,measured}$) determined using Equation 5.13 and the measurements of $DSBR_d$ from unreinforced multi-column experiments performed for the full range of sample densities. Reinforced tests were not included in the assessment of Equation 5.13 because reinforcement reduces differential surface settlement. The residuals indicate that Equation 5.13 is slightly biased in a manner that underpredicts $DSBR_d$; however, the variation is essentially independent of normalized height. In order to simplify the analysis of variation, the bias in Equation 5.13 was ignored and the variation of the data points from the trend lines was

assumed to be normally distributed and independent of normalized height. Using these assumptions and simplifications, the standard deviations of the data from the trend lines were determined and are summarized below in Table 5.9. If all the conditions for regression analysis were met, the results in Table 5.9 would indicate that about 68 percent of the measured values of SBR_c fall within one standard deviation of the predicted values and there is 95 percent confidence that the mean of the data at a given normalized height is within 0.03 of the predicted value.

Table 5.9 Variability in values of $DSBR_d$ predicted using Equation 5.13

	Equation 5.13
Average residual	-0.06
Standard deviation	0.12
95% Confidence interval	Predicted $DSBR_d$ ±0.03
Sample size	53 tests

Based on the simplified analysis, the fit of the trend line given by Equation 5.13 is reasonably good, however there is a tendency for the predicted values of $DSBR_d$ to be less than the measured values. The standard deviation is slightly over 10 percent of the full scale of $DSBR_d$ which indicates that the predictive accuracy of the trend lines is not very high. The low predictive accuracy is partially due to the high sensitivity of differential surface settlement to the normalized sample height, as evidenced by high angles of β, as sample height decreases below the critical height.

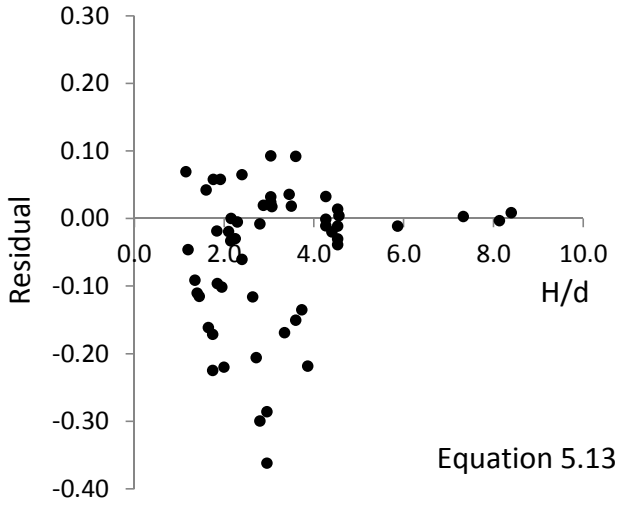

Figure 5.28 Difference between measured and predicted values of $DSBR_d$ for unreinforced multi-column tests below the critical height.

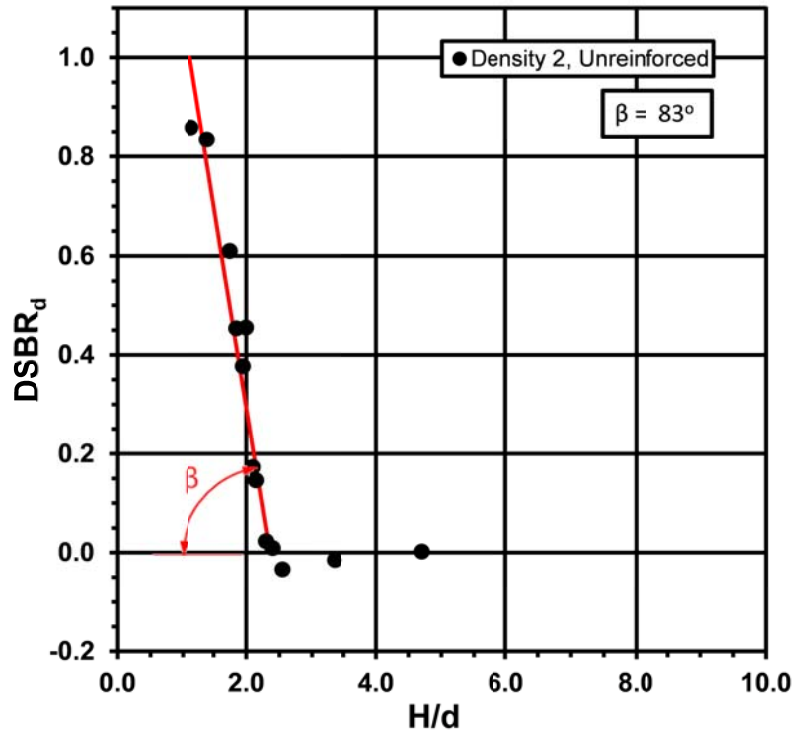

Figure 5.29 DSBR$_d$ versus H/d for d = 2.00 in., s = 3.50 in.

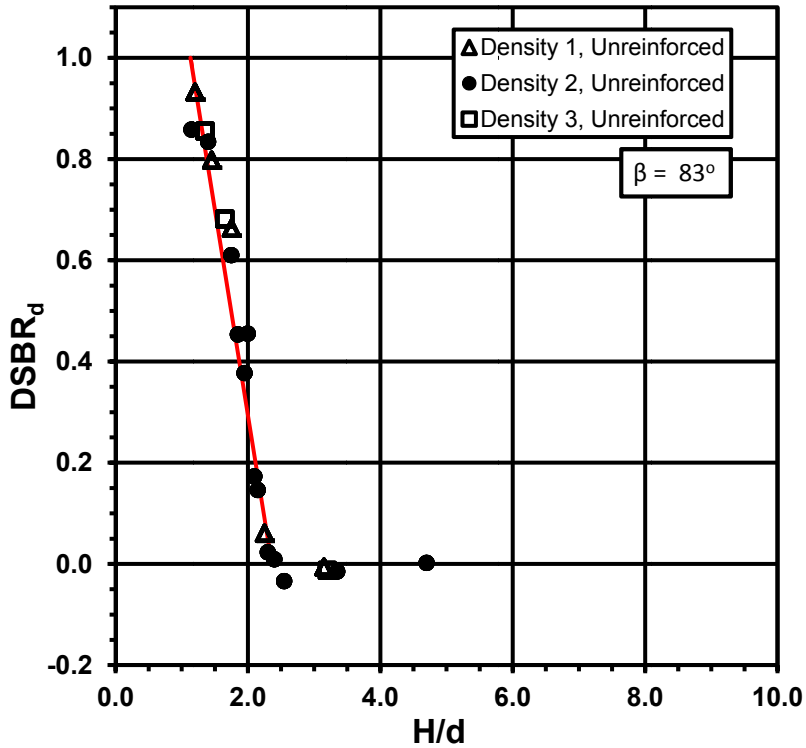

Figure 5.30 DSBR$_d$ versus H/d for d = 2.00 in., s = 3.50 in., comparing sample density

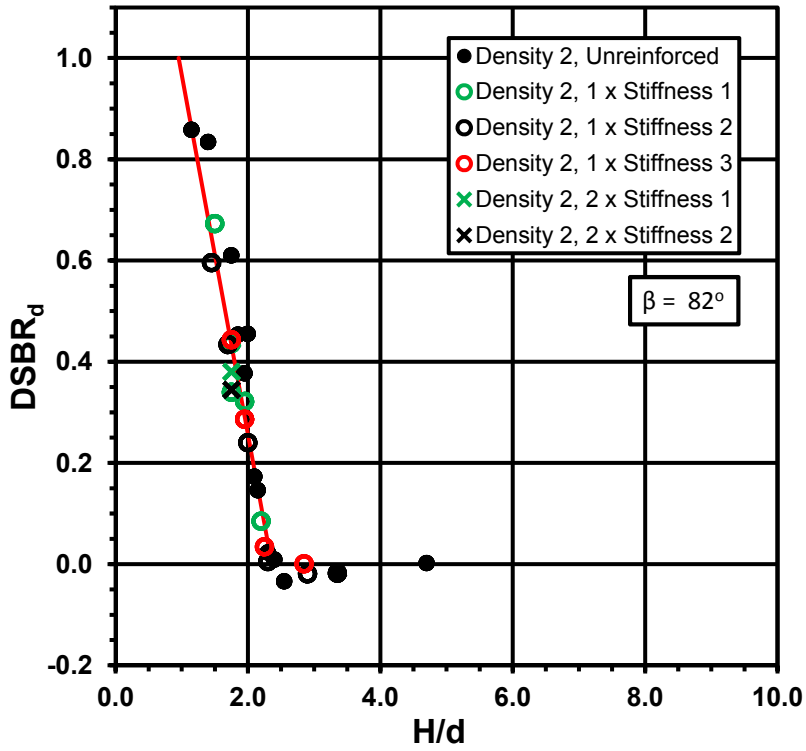

Figure 5.31 $DSBR_d$ versus H/d for d = 2.00 in., s = 3.50 in., comparing reinforcement

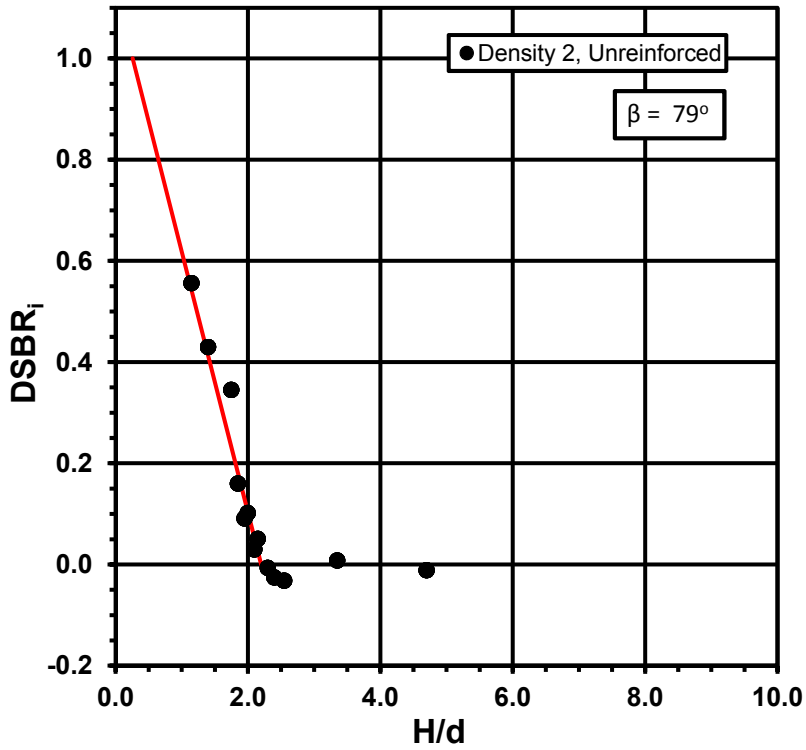

Figure 5.32 $DSBR_i$ versus H/d for d = 2.00 in., s = 3.50 in.

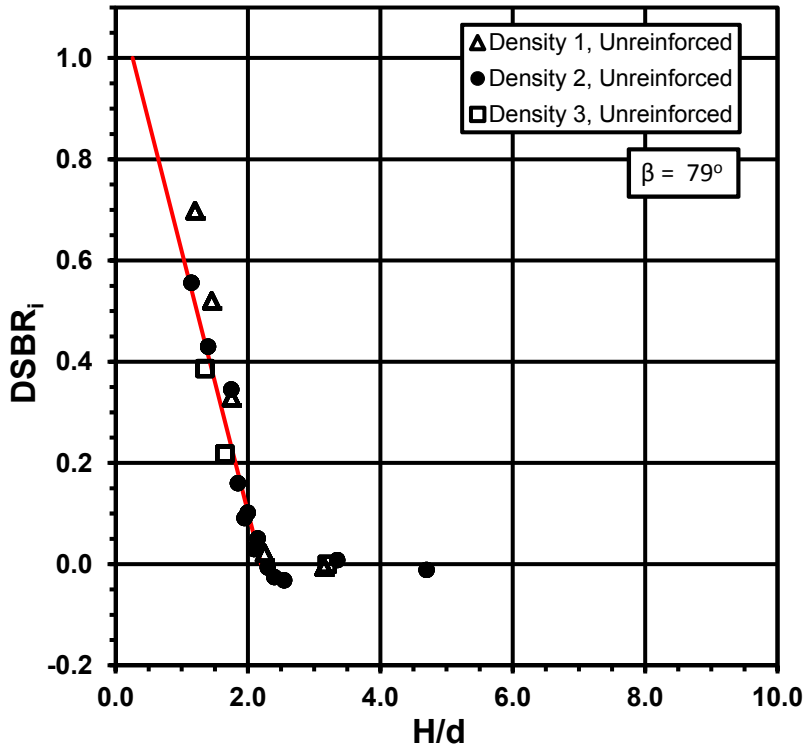

Figure 5.33 DSBR$_i$ versus H/d for d = 2.00 in., s = 3.50 in., comparing sample density

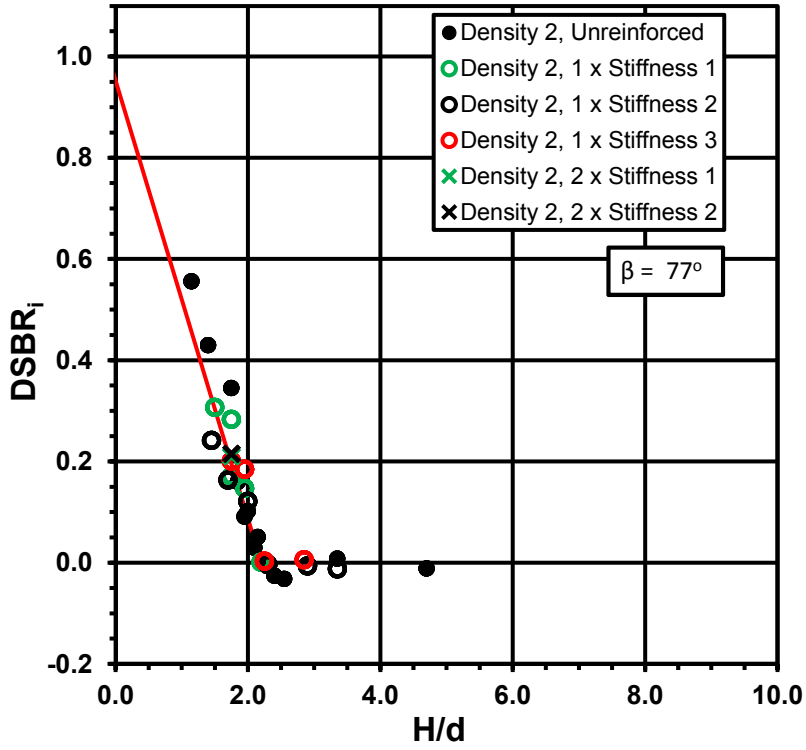

Figure 5.34 DSBR$_i$ versus H/d for d = 2.00 in., s = 3.50 in., comparing reinforcement

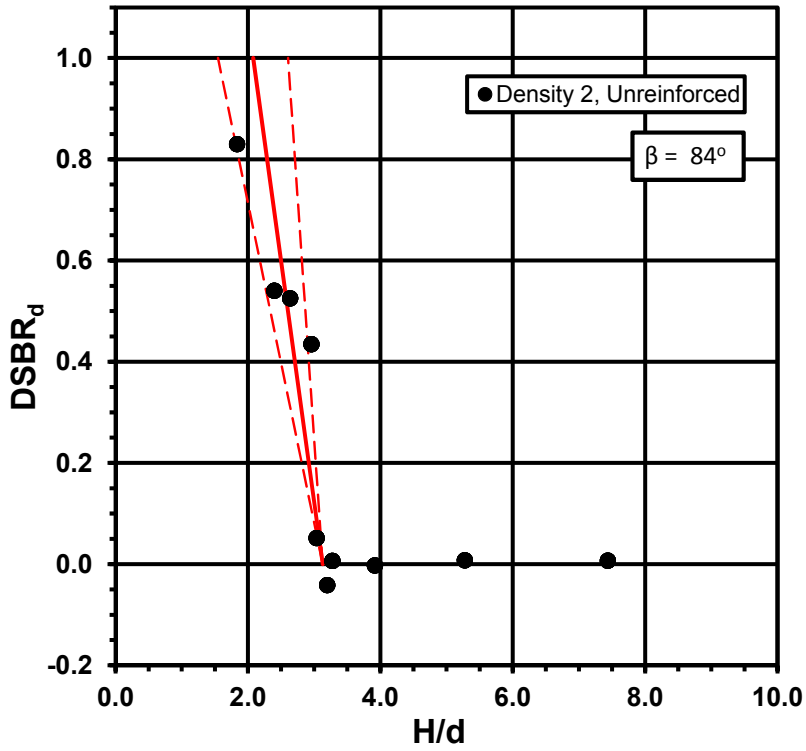

Figure 5.35 $DSBR_d$ versus H/d for d = 1.25 in., s = 3.50 in.

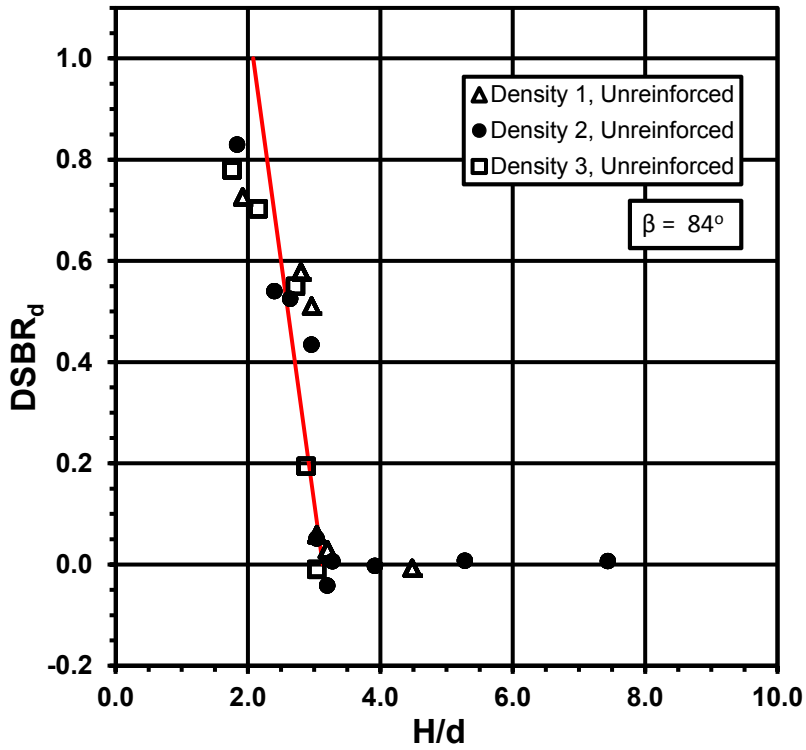

Figure 5.36 $DSBR_d$ versus H/d for d = 1.25 in., s = 3.50 in., comparing sample density

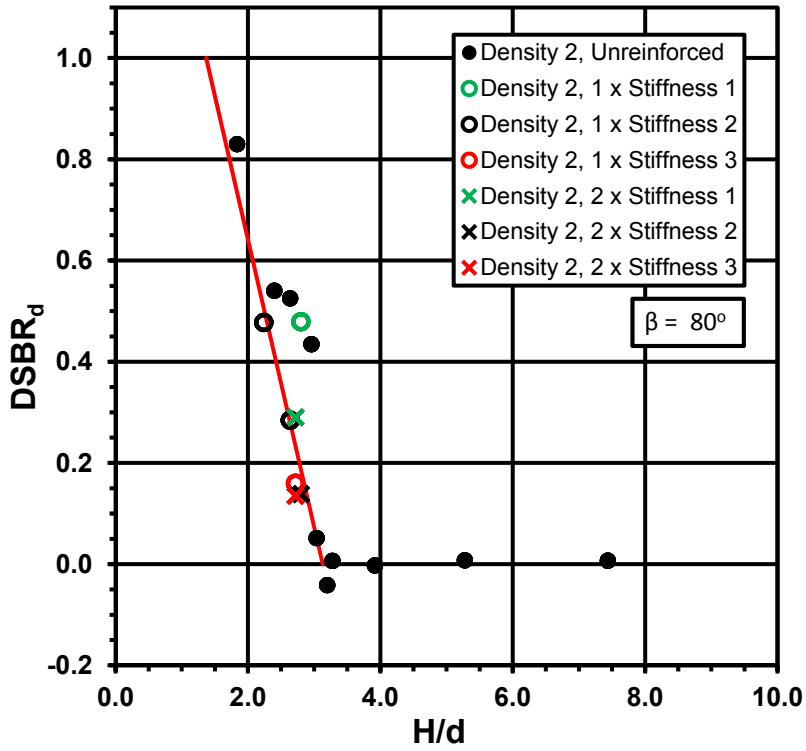

Figure 5.37 $DSBR_d$ versus H/d for d = 1.25 in., s = 3.50 in., comparing reinforcement

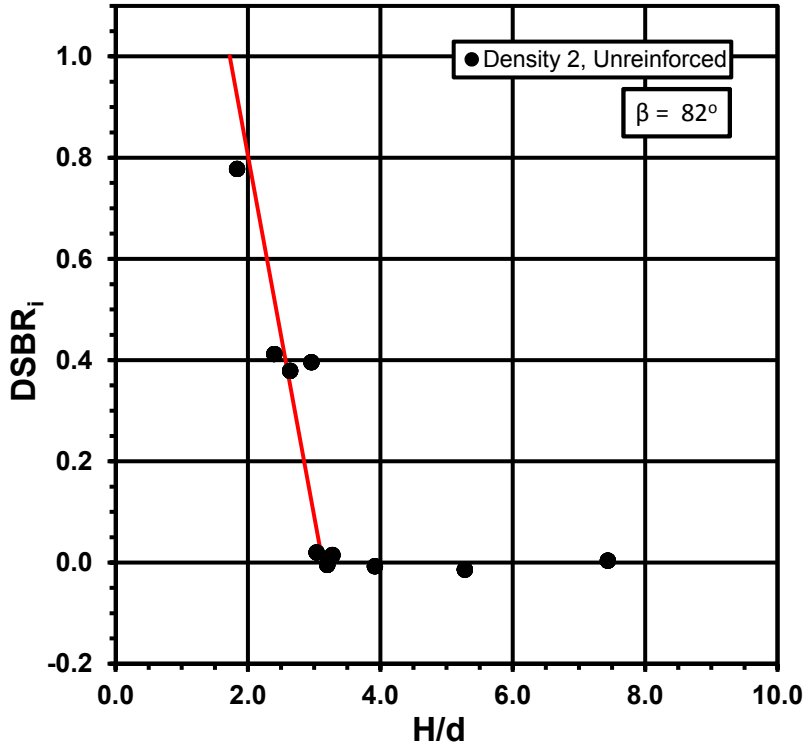

Figure 5.38 $DSBR_i$ versus H/d for d = 1.25 in., s = 3.50 in.

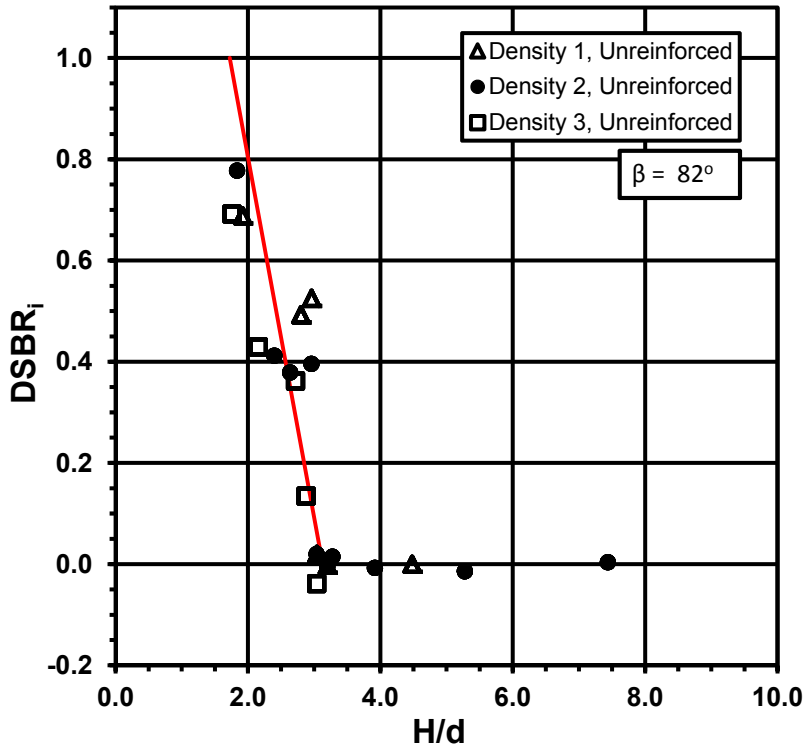

Figure 5.39 DSBR$_i$ versus H/d for d = 1.25 in., s = 3.50 in., comparing sample density

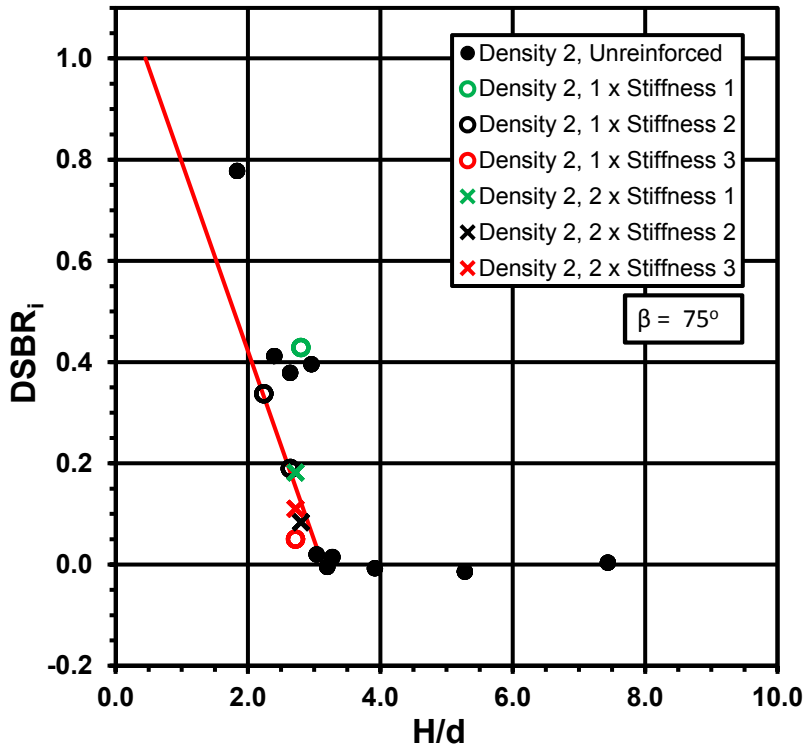

Figure 5.40 DSBR$_i$ versus H/d for d = 1.25 in., s = 3.50 in., comparing reinforcement

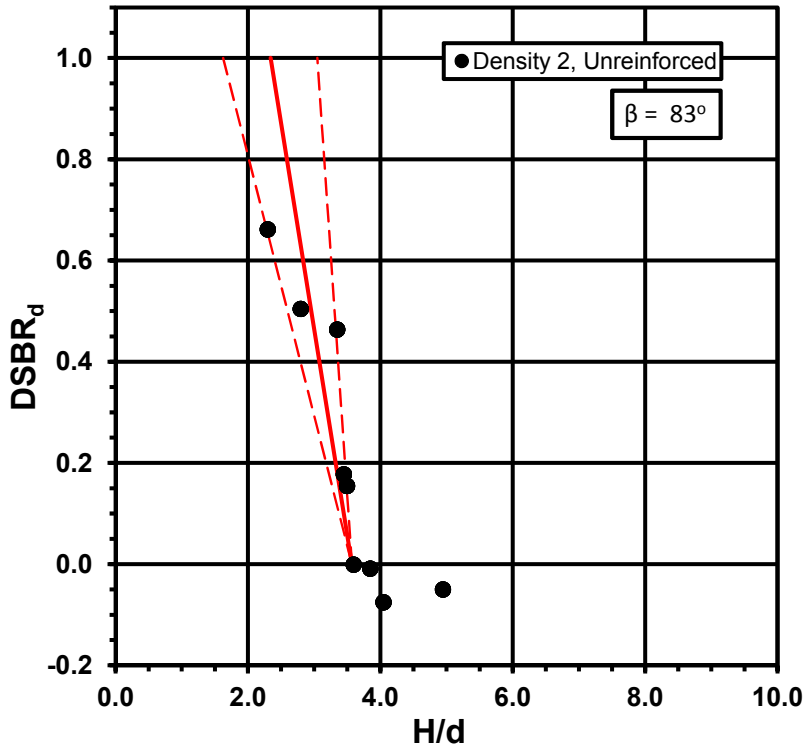

Figure 5.41 $DSBR_d$ versus H/d for d = 2.00 in., s = 7.00 in.

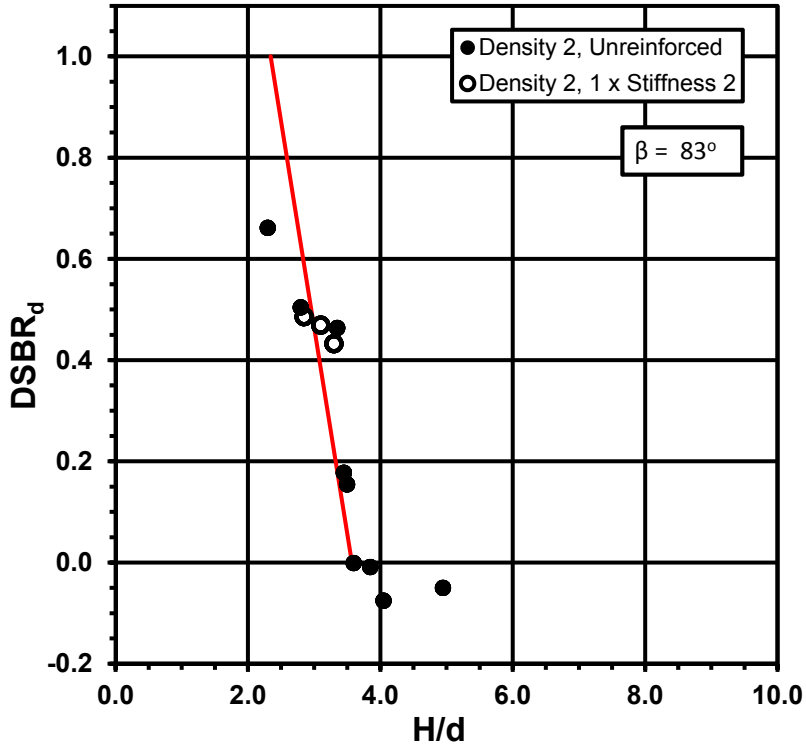

Figure 5.42 $DSBR_d$ versus H/d for d = 2.00 in., s = 7.00 in, comparing reinforcement

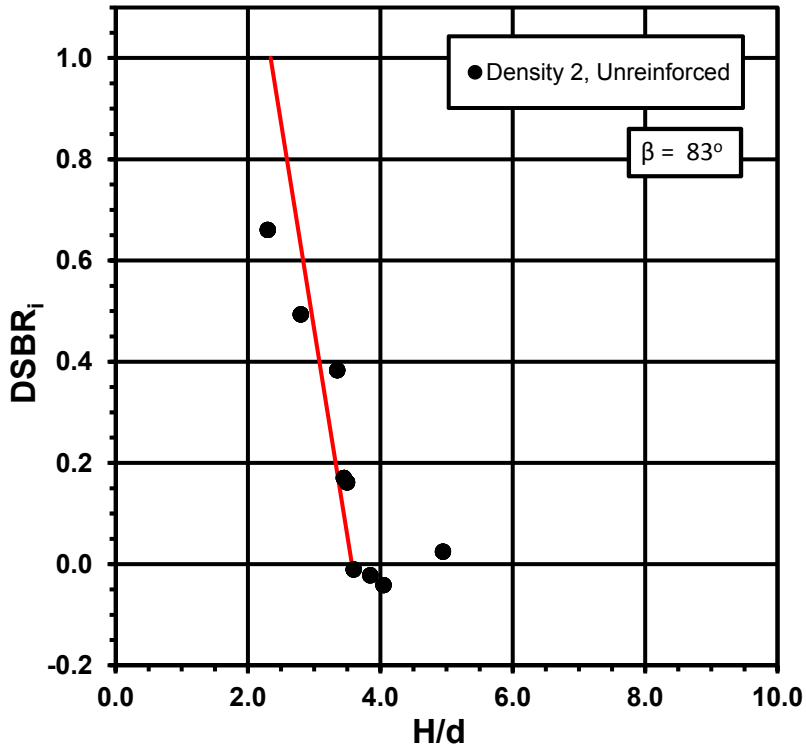

Figure 5.43 DSBR$_i$ versus H/d for d = 2.00 in., s = 7.00 in.

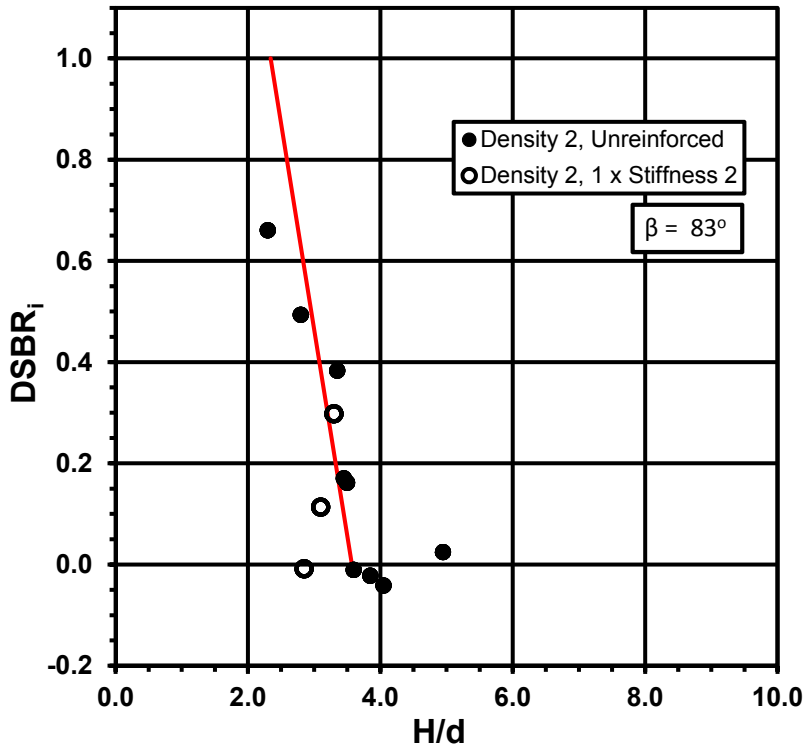

Figure 5.44 DSBR$_i$ versus H/d for d = 2.00 in., s = 7.00 in., comparing reinforcement

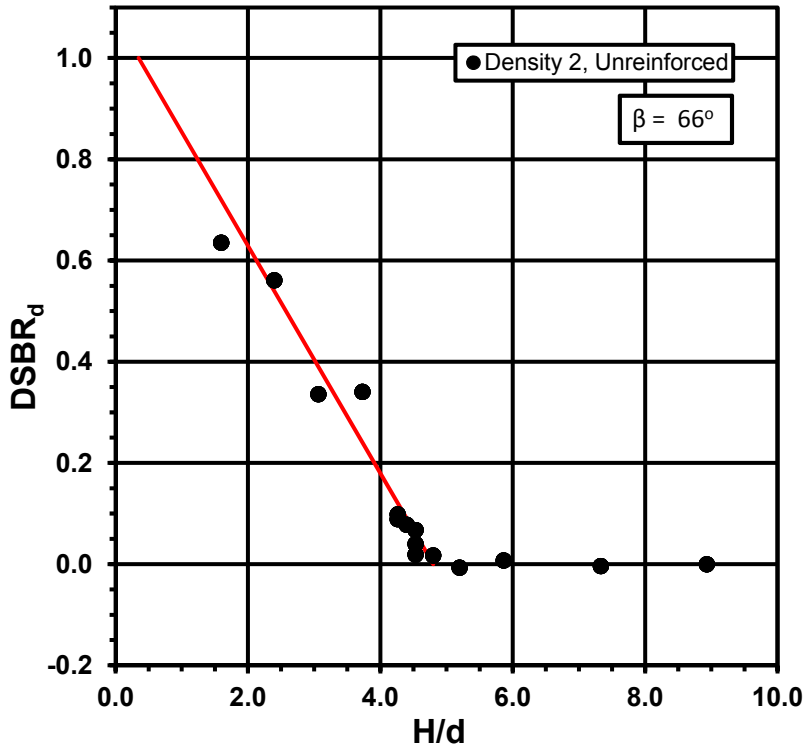

Figure 5.45 $DSBR_d$ versus H/d for d = 0.75 in., s = 3.50 in.

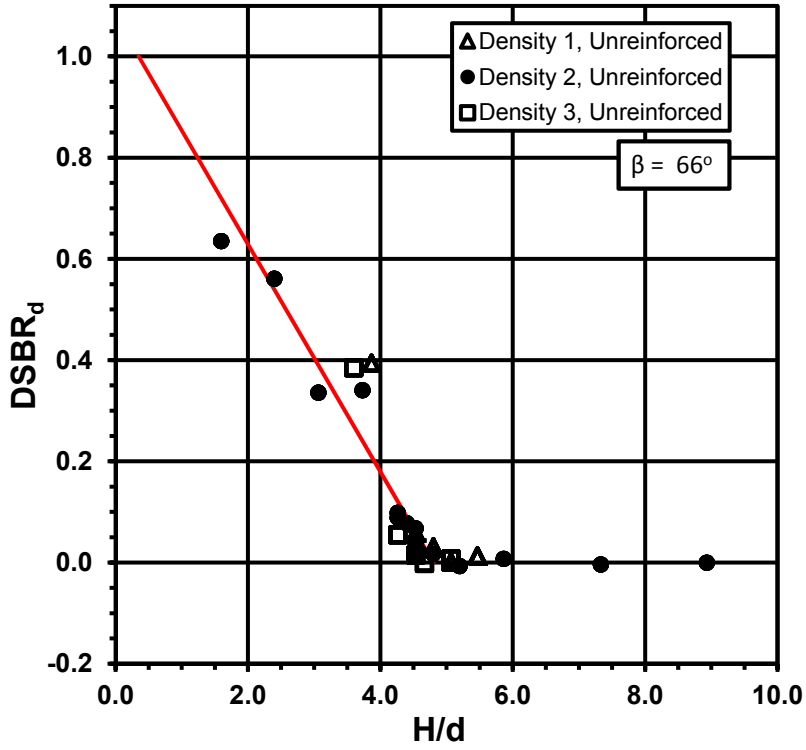

Figure 5.46 $DSBR_d$ versus H/d for d = 0.75 in., s = 3.50 in., comparing sample density

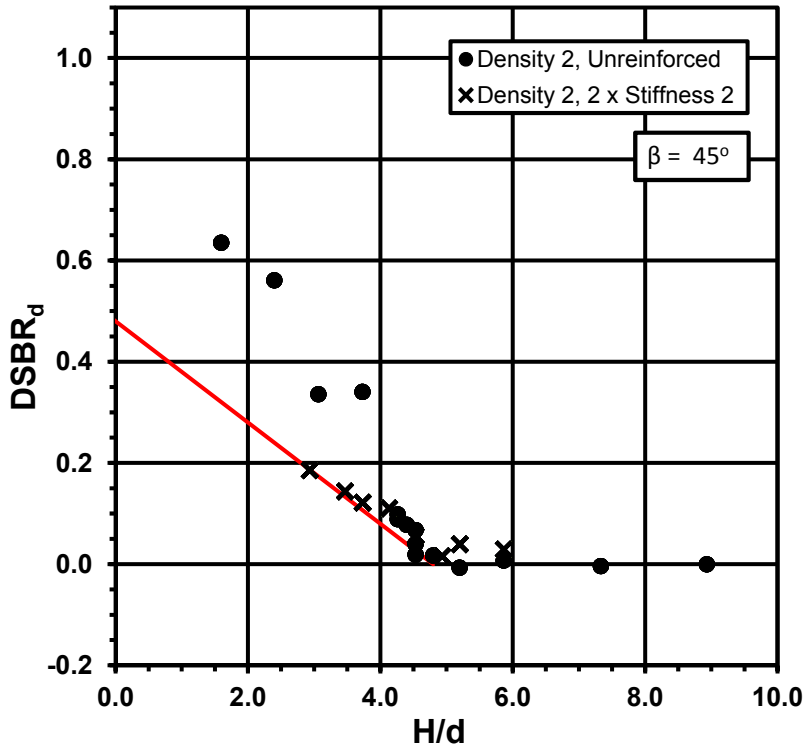

Figure 5.47 $DSBR_d$ versus H/d for d = 0.75 in., s = 3.50 in., comparing reinforcement

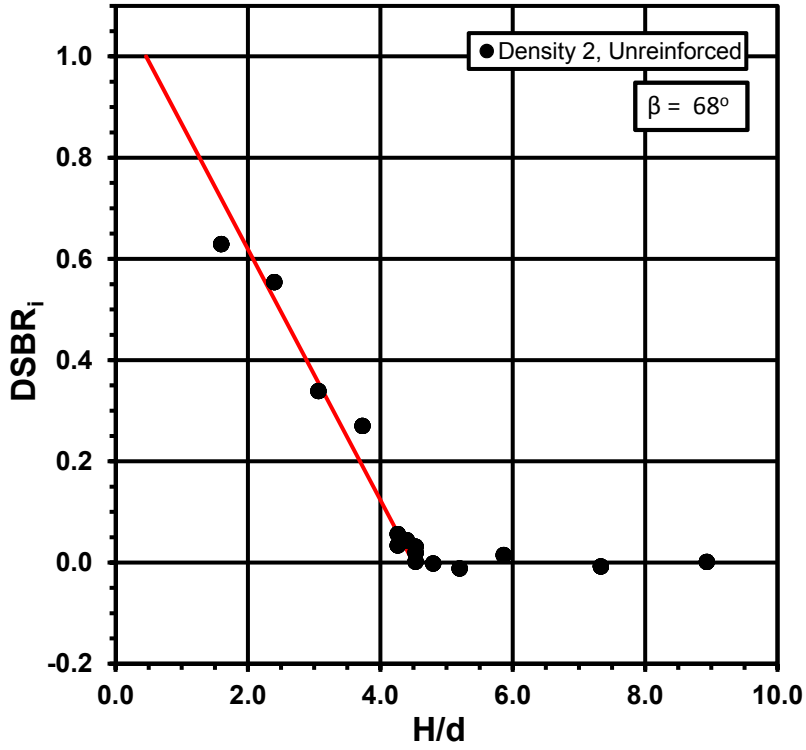

Figure 5.48 $DSBR_i$ versus H/d for d = 0.75 in., s = 3.50 in.

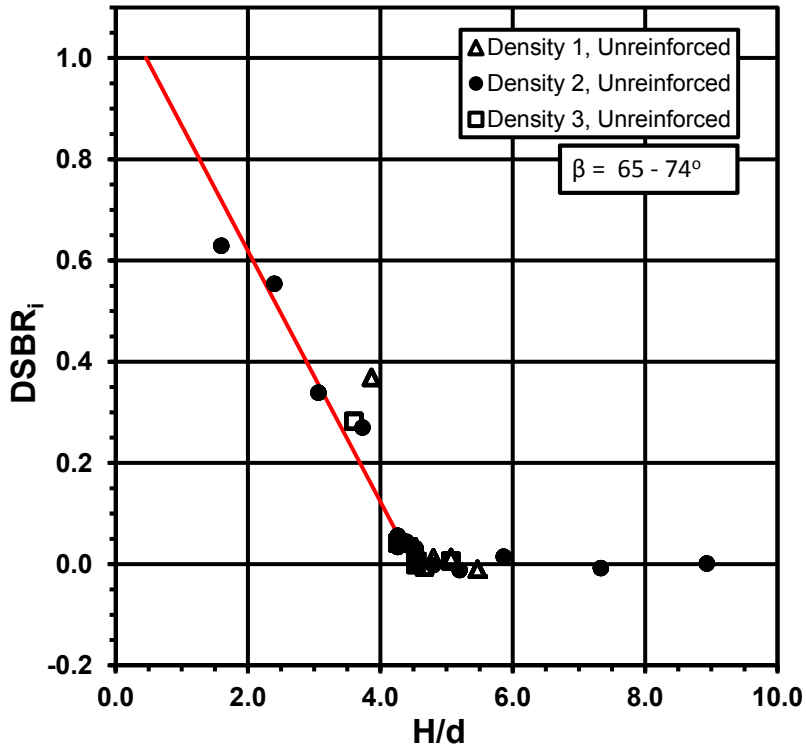

Figure 5.49 DSBR$_i$ versus H/d for d = 0.75 in., s = 3.50 in., comparing sample density

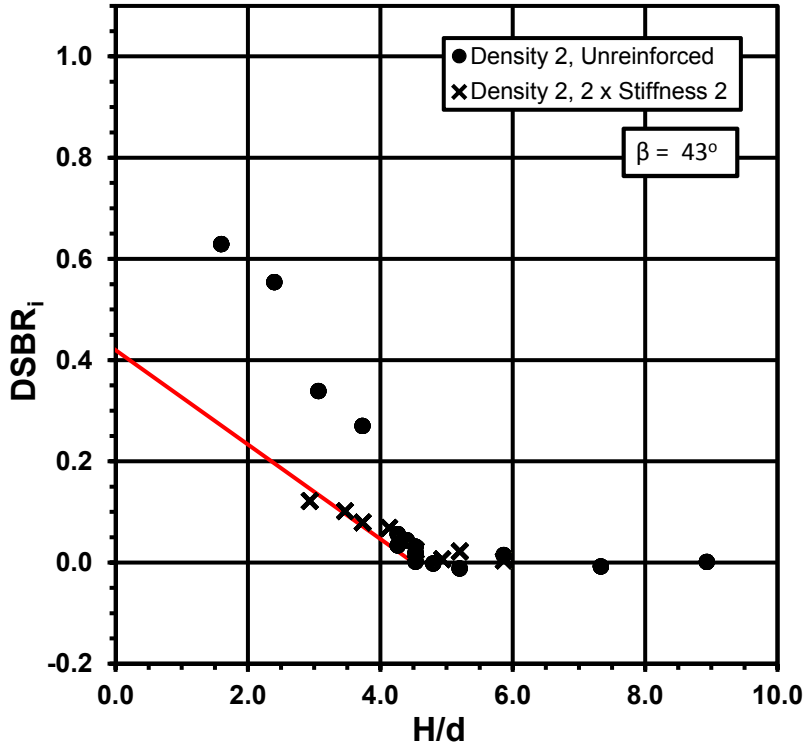

Figure 5.50 DSBR$_i$ versus H/d for d = 0.75 in., s = 3.50 in., comparing reinforcement

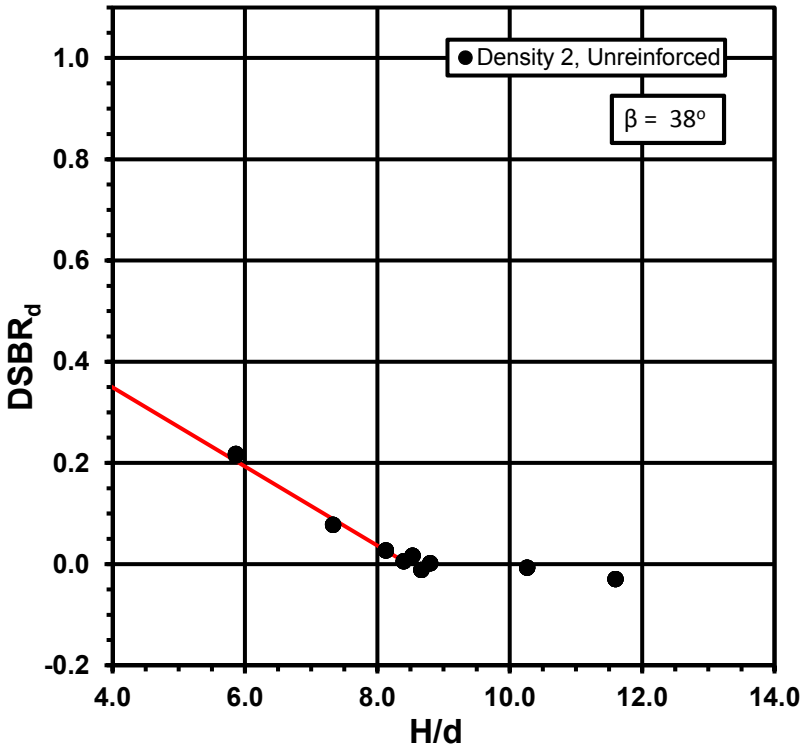

Figure 5.51 $DSBR_d$ versus H/d for d = 0.75 in., s = 7.00 in.

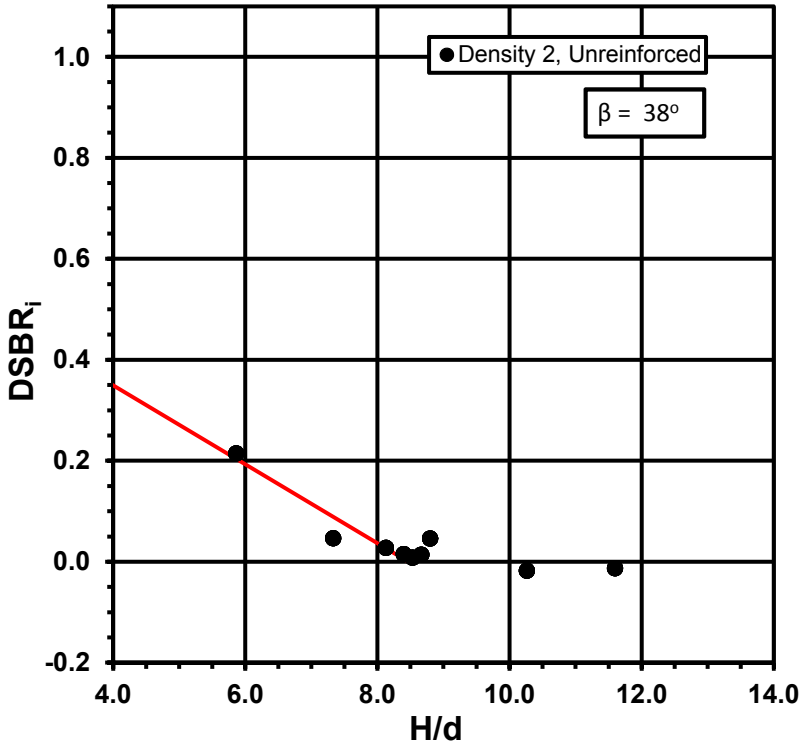

Figure 5.52 $DSBR_i$ versus H/d for d = 0.75 in., s = 7.00 in.

5.4 Surface Settlement above the Critical Height

Above the critical height, the sample surface settles uniformly in response to base settlement. Figure 5.53 through Figure 5.57 show how the settlement ratios over the column, SBR_c, and at the unit cell boundary, SBR_d, converge at the critical height, which is indicated by a vertical green line. Beyond the critical height, the ratio of the total surface settlement to the base settlement is defined as SBR_{tot}, which is indicated by the horizontal red line in the figures. The results shown in Figure 5.53 through Figure 5.57 indicate that each unit cell geometry has an approximately constant value of SBR_{tot} over the range of sample heights evaluated. As discussed at the beginning of the chapter, settlement ratios are based on best-fit linear relationships between surface settlement and corresponding magnitudes of base settlement. Some tests exhibited nonlinearity between total surface settlement and base settlement. Nonlinearity was particularly apparent for unit cell geometries with low spanning ratios at low magnitudes of base settlement. As described in Section 5.5, the rate of dilation is typically very high for geometries with a low spanning ratio at low magnitudes of base settlement. To address nonlinearity, secant values of SBR_{tot} were determined by dividing surface settlement by base settlement at base settlement equal to 20 percent of the column diameter, $S_b/d = 0.2$. A ratio of base settlement to column diameter equal to 0.2 is used in Section 5.5 to compare volume change across all the tests. Table 5.10 summarizes the values of SBR_{tot} for the unit cell geometries evaluated during the experimental study.

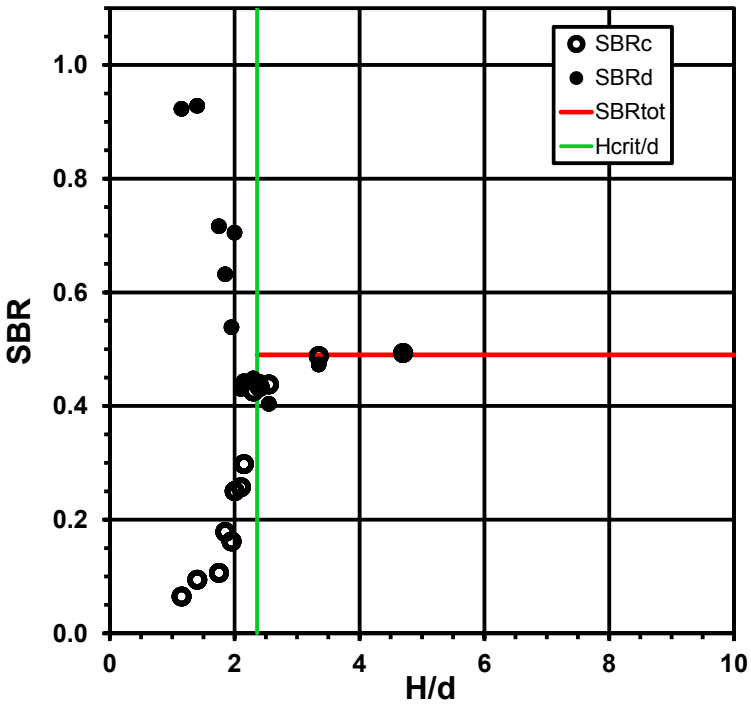

Figure 5.53 Convergence of surface settlements to uniform ratio with base settlement beyond the critical height (d = 2.00 in., s = 3.50 in.)

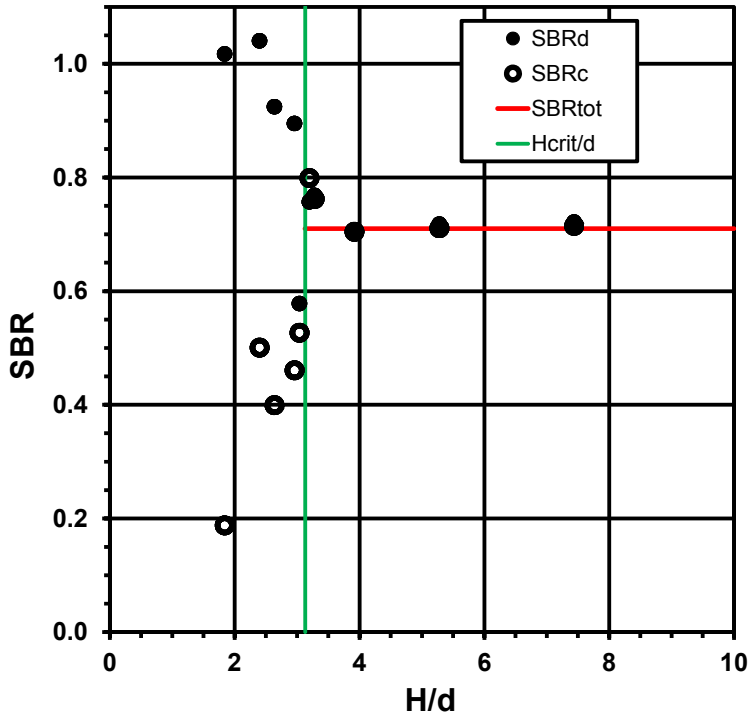

Figure 5.54 Convergence of surface settlements to uniform ratio with base settlement beyond the critical height (d = 1.25 in., s = 3.50 in.)

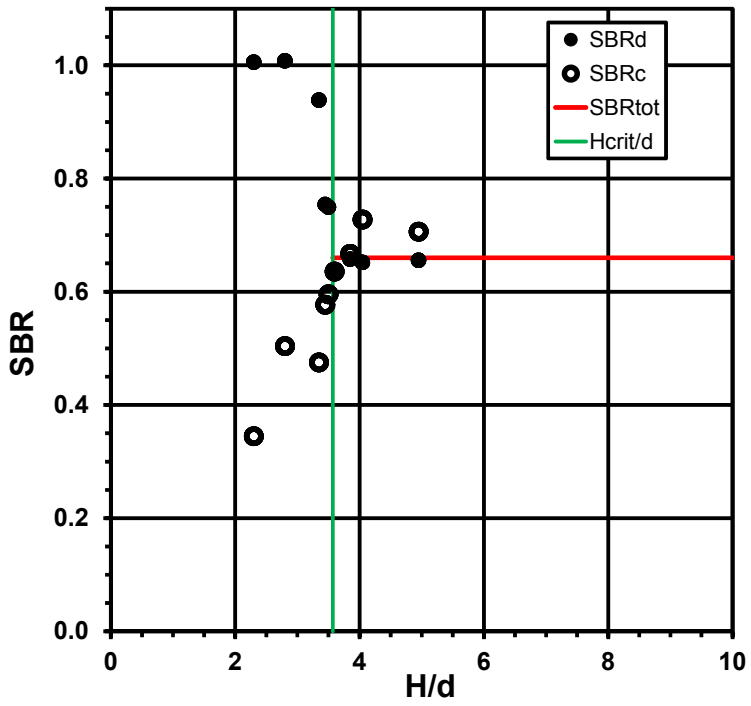

Figure 5.55 Convergence of surface settlements to uniform ratio with base settlement beyond the critical height (d = 2.00 in., s = 7.00 in.)

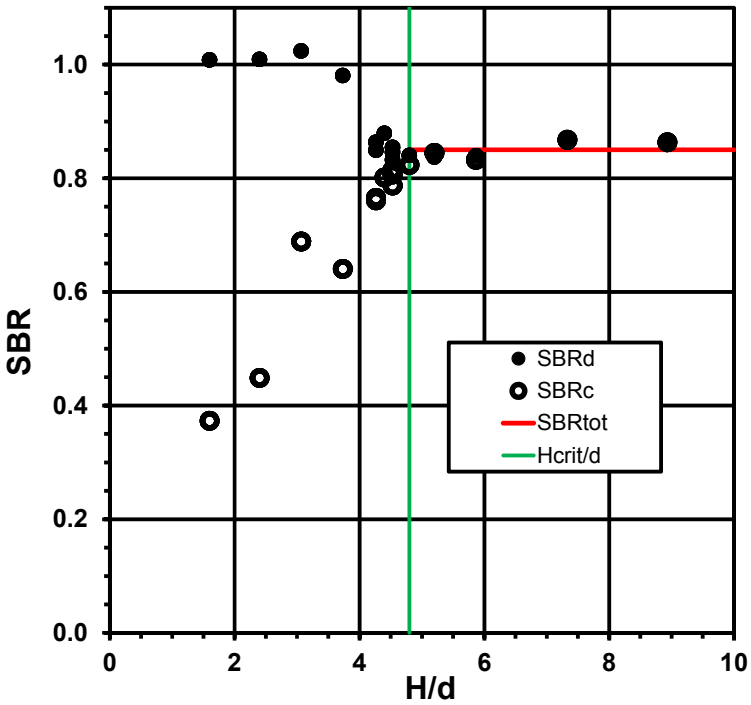

Figure 5.56 Convergence of surface settlements to uniform ratio with base settlement beyond the critical height (d = 0.75 in., s = 3.50 in.)

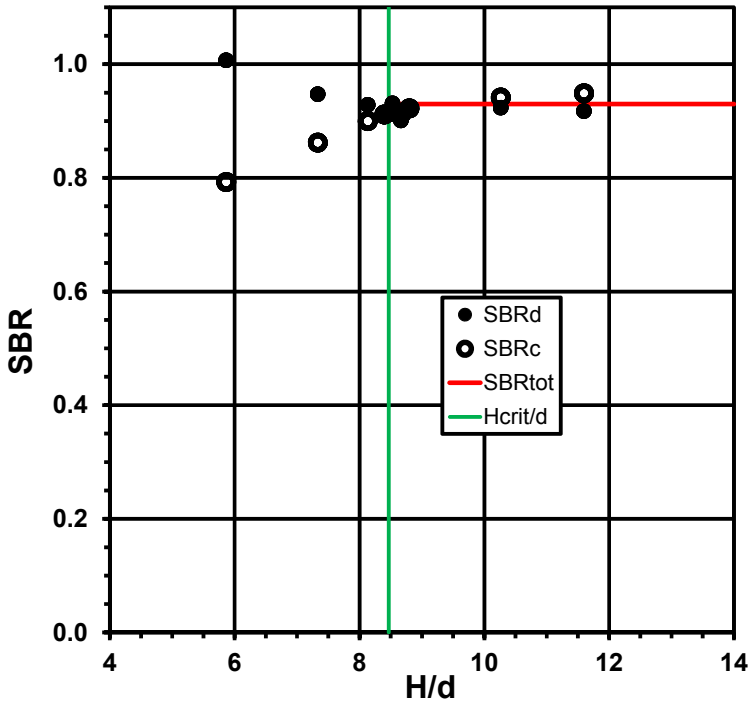

Figure 5.57 Convergence of surface settlements to uniform ratio with base settlement beyond the critical height (d = 0.75 in., s = 7.00 in.)

Table 5.10 Ratio of total surface settlement to base settlement for unit cell geometries evaluated

Area replacement ratio, As (%)	Column Diameter, d (in.)	Column Spacing, s (in.)	Spanning Ratio, s'/d	Best Fit SBRtot	Average Secant SBR_{tot} at $S_b/d = 0.2$
26%	2.00	3.50	0.74	0.49	0.34
10%	1.25	3.50	1.48	0.71	0.53
6%	2.00	7.00	1.97	0.66	0.58
4%	0.75	3.50	2.80	0.85	0.75
1%	0.75	7.00	6.10	0.93	0.92

The study by Russell et al. (2003) provides guidance on estimating the ratio between the total surface settlement to the maximum base settlement. Their approach uses an assumption of no volume change in the embankment and assumes that the ratio of the peak base settlement to the average base settlement is between 1.0 and 2.0, with 2.0 being the default value. Equation 5.14 provides the relationship developed by Russell et al. (2003) using the current notation for circular pile caps. Equation 5.15 provides the same relationship expressed using area replacement ratio, A_s. In both equations $S_{b,d}/S_{b,avg}$ is the ratio of the maximum base settlement to the average base settlement. For the multi-column tests described here, the maximum and

average base settlements have the same value since settlement is uniform. A method for estimating the maximum and average base settlements when base settlement is non-uniform is presented in Section 7.2.3. Relationships equivalent to Equations 5.14 and 5.15 can be developed in terms of spanning ratio using the relationships between area replacement ratio and spanning ratio provided in Section 1.4.

$$SBR_{tot} = \frac{s^2 - \frac{\pi}{4}d^2}{\left(S_{b,d}/S_{b,avg}\right)s^2} \tag{5.14}$$

$$SBR_{tot} = \frac{1 - A_s}{\left(S_{b,d}/S_{b,avg}\right)} \tag{5.15}$$

Figure 5.58 plots the measured best-fit and secant values of SBR_{tot} listed in Table 5.10 versus area replacement ratio. The relationship proposed by Russell et el. (2003) for uniform base settlement plots consistently above the measured best-fit and secant values of SBR_{tot}.

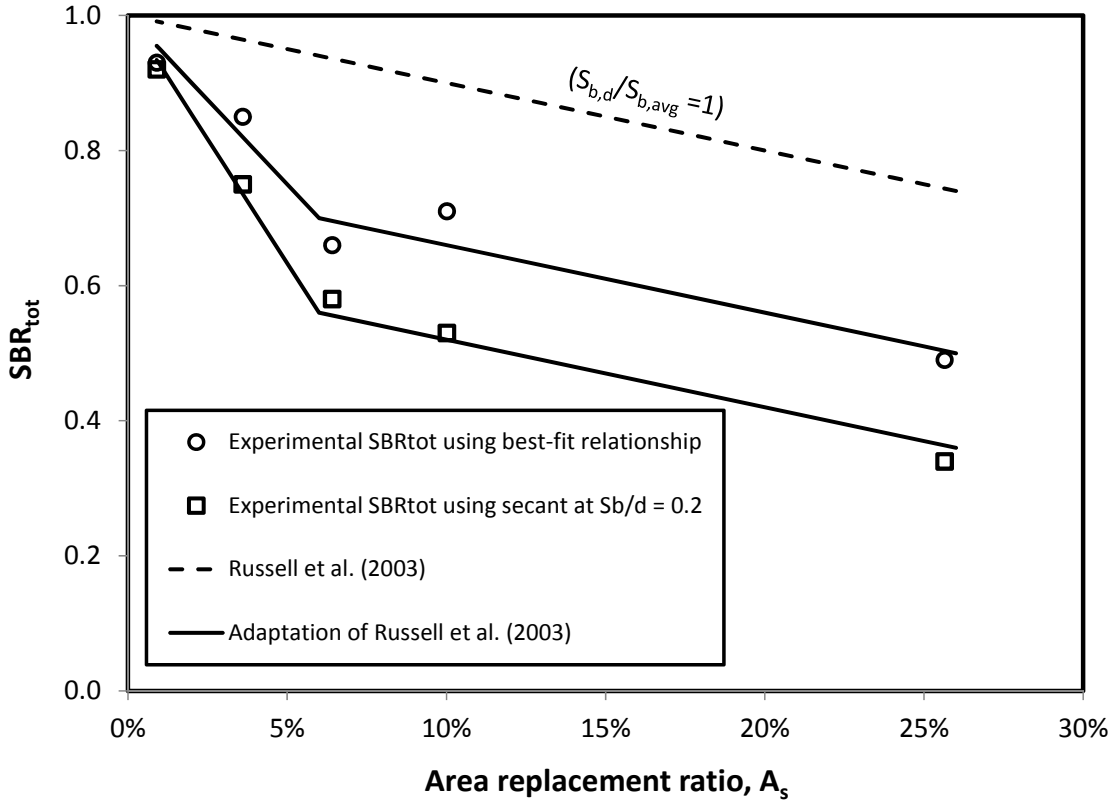

Figure 5.58 Relationship between SBR_{tot} and area replacement ratio, A_s

The results provided in Section 5.5 show that the sample dilates over the range of base settlements evaluated. Equation 5.20 in Section 5.5 expresses the unit volume change within the unit cell as a function of unit cell geometry, uniform base settlement, total surface settlement, and sample height. Rearranging this expression as shown in Equation 5.16 results in the relationship for uniform settlement without requiring the assumption of zero volume change. When volume change is zero, Equation 5.16 reduces to Equation 5.15 for uniform base settlement.

$$SBR_{tot} = 1 - A_s - \frac{\Delta V_u}{V_u}\frac{H}{S_b} \tag{5.16}$$

The contribution of volume change can be seen in Figure 5.59 by subtracting the measured value of SBR_{tot}, which includes volume change, from the value estimated by $(1\text{-}A_s)$, which assumes no volume change. The secant values show the contribution of volume change at $S_b/d = 0.2$.

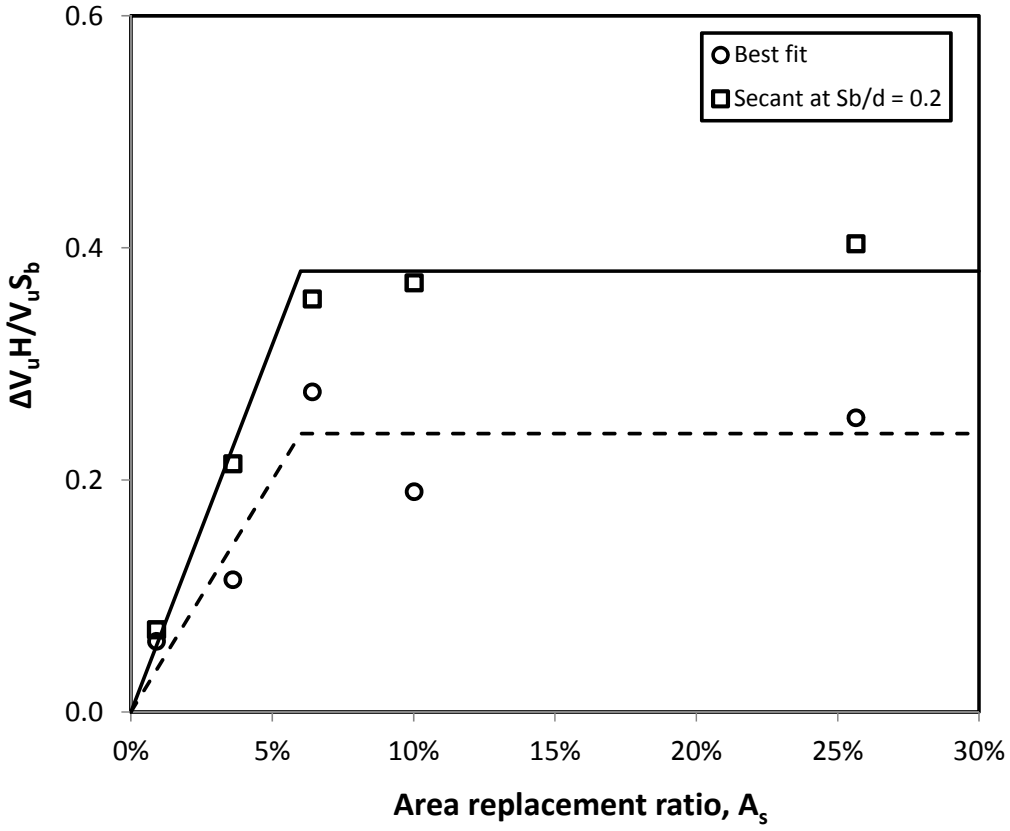

Figure 5.59 Contribution of volume change to SBR_{tot}

As shown by the trend lines in Figure 5.59, the contribution of volume change for the experimental conditions can be approximated by Equation 5.17 for secant values of SBR_{tot} at S_b/d =0.2 and Equation 5.18 for best-fit values of SBR_{tot}. Substituting Equations 5.17 and 5.18 for the volume change term in Equation 5.16 give the solid trend lines shown in Figure 5.58.

$$\frac{\Delta V_u H}{V_u S_b} = \text{Min}\begin{cases} 0.38 \\ 0.38\left(A_s/6\%\right) \end{cases} \tag{5.17}$$

$$\frac{\Delta V_u H}{V_u S_b} = \text{Min}\begin{cases} 0.24 \\ 0.24\left(A_s/6\%\right) \end{cases} \tag{5.18}$$

The approximations given by Equations 5.17 and 5.18 for the contribution of volume change are specific to the conditions associated with the bench-scale experiments. The properties of the embankment material, embankment height, unit cell geometry, and magnitude of uniform base settlement influence how volume change contributes to SBR_{tot}. Section 7.2.3 adapts Equation 5.16 for conditions where base settlement is non-uniform.

5.5 Volume Change in Unit Cell

This section describes the volume change within the unit cell, ΔV_u, due to differential base settlement, S_b. The unit cell volume, V_u, is defined as the unit cell area multiplied by the sample height. For a square array of columns, V_u equals $(H)s^2$. The procedures used to calculate volume change using surface measurements are described in Section 3.7.2. Volume change in the unit cell was measured for 5x5 column arrays. Figure 5.60 shows volume change as a percentage of the initial volume, $\Delta V_u/V_u$, plotted against base settlement normalized by column diameter, S_b/d. Plotting volume change this way allows for the most direct comparison of the degree of volume change that occurs for a particular unit cell geometry. Figure 5.60 includes the example test introduced at the beginning of the chapter (7AMD22), as well as two additional tests performed with different column diameters but having the same normalized height. The results show that the samples dilate in response to base settlement, with the percentage increase in volume at a particular normalize base settlement increasing as spanning ratio decreases. The results also show that the rate of dilation is not constant and is highest at small magnitudes of base settlement.

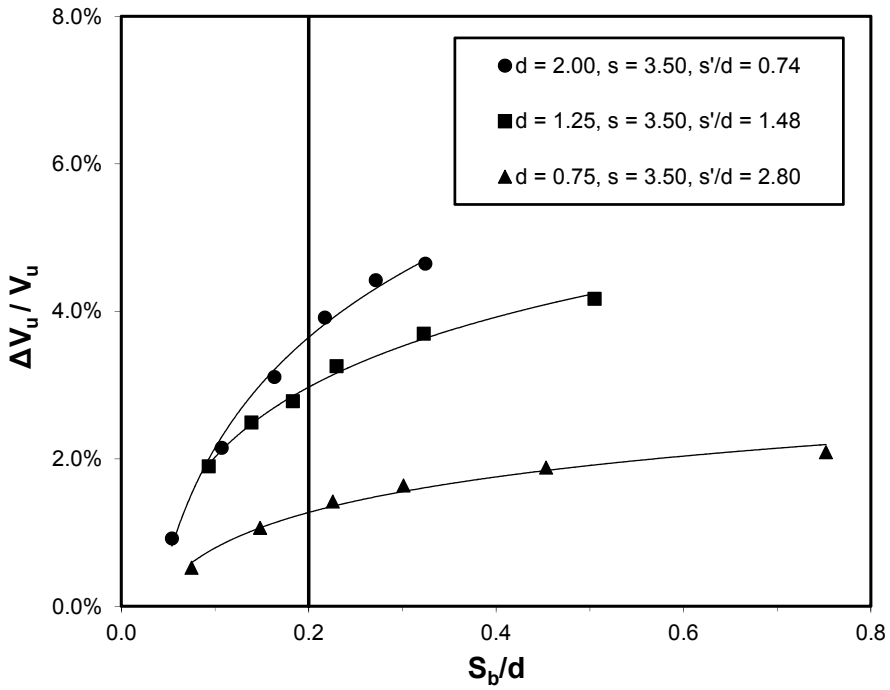

Figure 5.60 Ratio of volume change to unit cell volume versus base settlement normalized by column diameter. All tests shown had H/d = 2.4, were unreinforced, and prepared at Density 2.

In order to compare volume change across all the tests performed, the percentage volume change at base settlement equal to 20 percent of the column diameter was determined, $\Delta V_{u,20}/V_u$, and plotted against normalized sample height as shown in Figure 5.61 through Figure 5.67. Dividing $\Delta V_{u,20}/V_u$ by 0.2d provides a secant value of the rate of dilation for base settlement that is equal 20 percent of the column diameter. A normalized base settlement of 0.2 was selected because all tests were performed to a settlement magnitude of at least 20 percent of the column diameter.

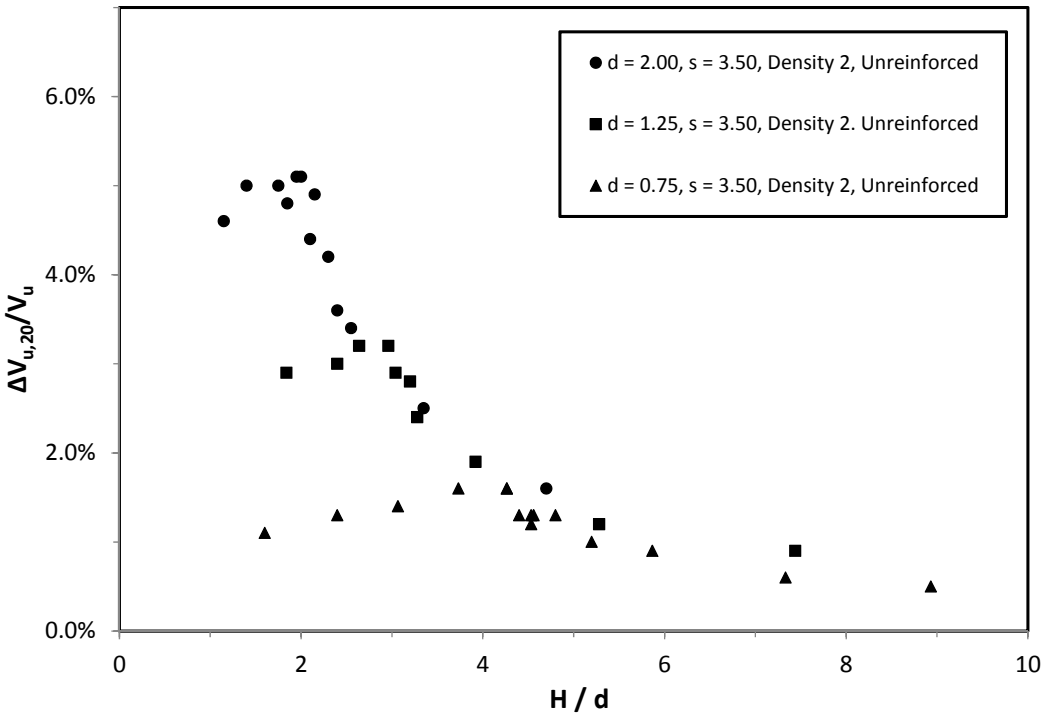

Figure 5.61 Percentage change in volume at base settlement equal to 20% of column diameter, highlighting influence of geometry

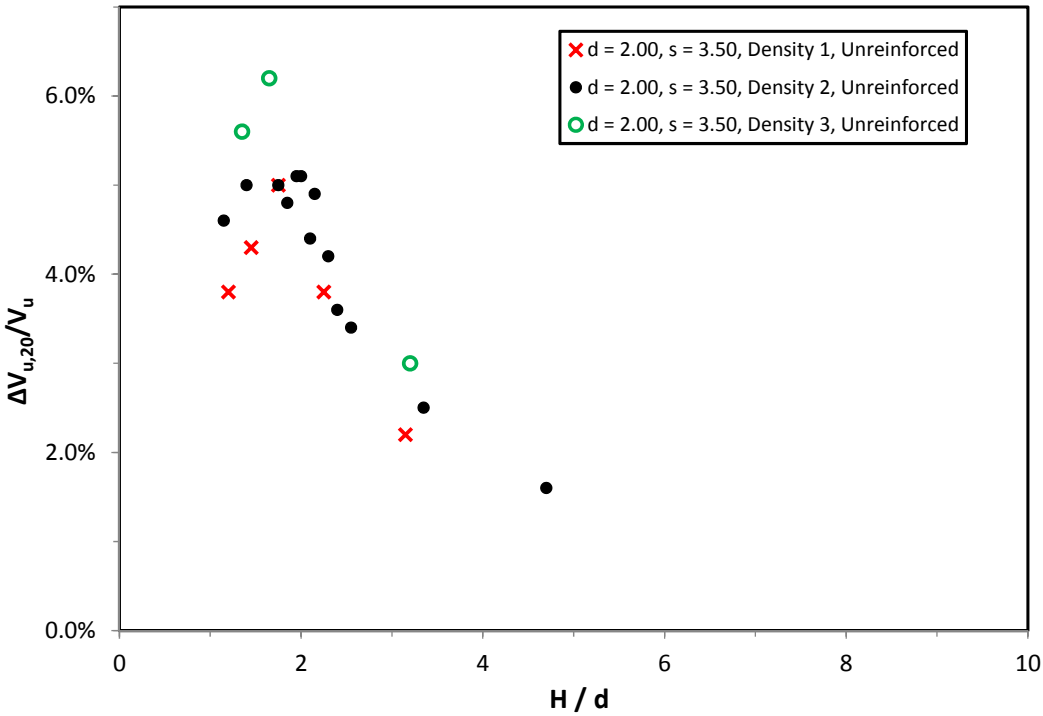

Figure 5.62 Percentage change in volume at base settlement equal to 20% of column diameter for spanning ratio equal to 0.74, highlighting influence of initial sample density

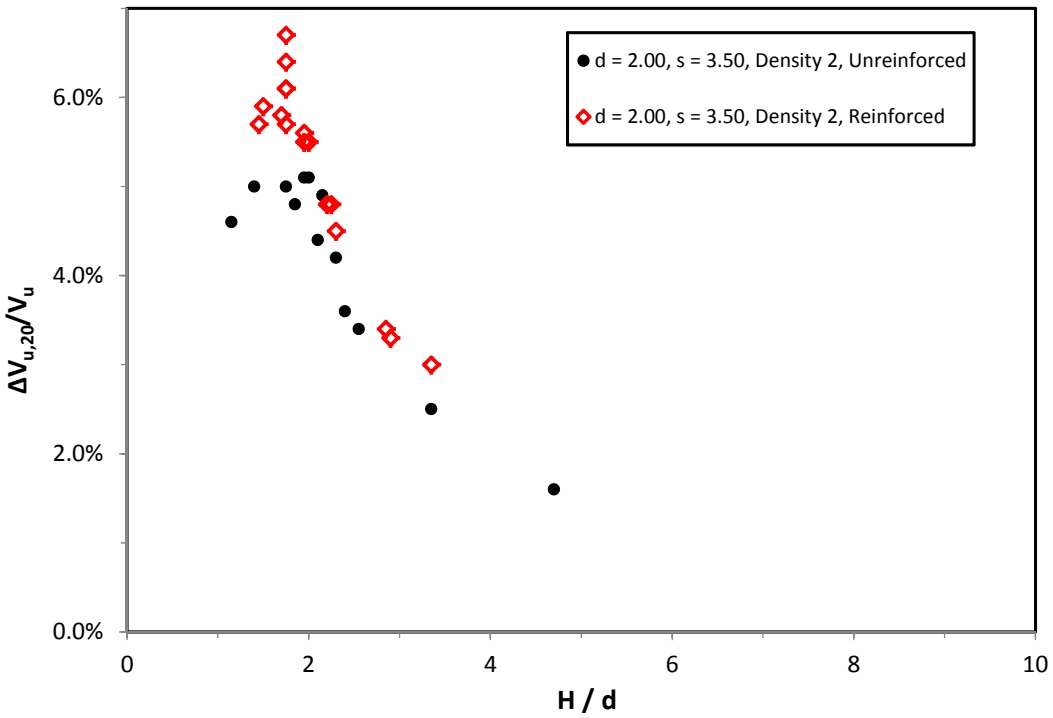

Figure 5.63 Percentage change in volume at base settlement equal to 20% of column diameter for spanning ratio equal to 0.74, highlighting influence of reinforcement

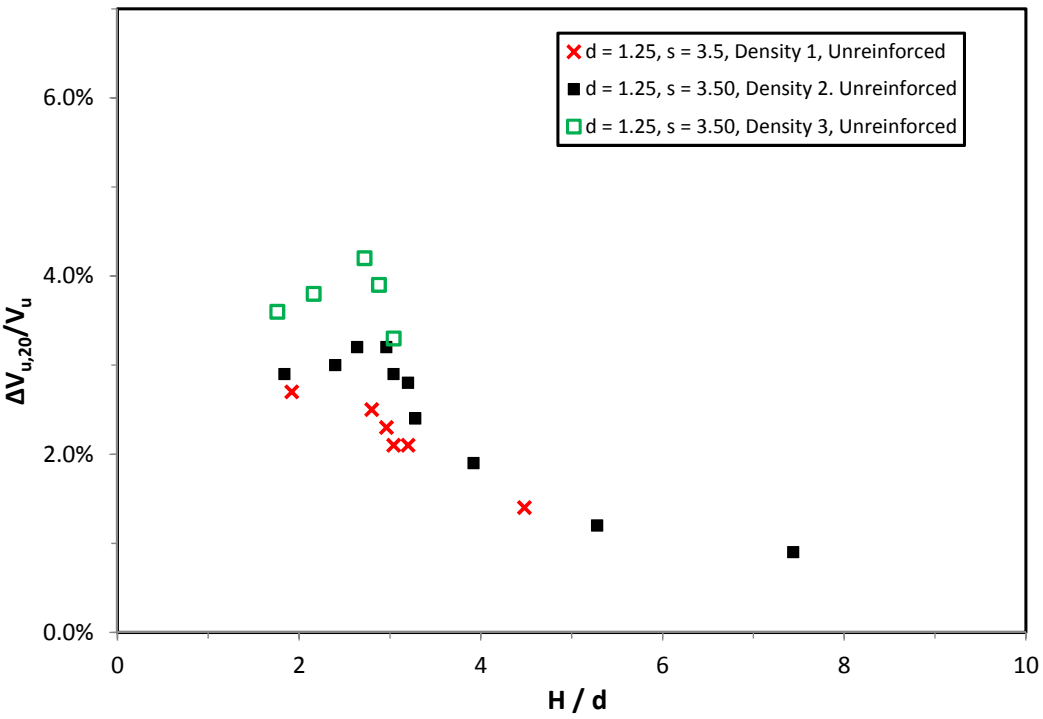

Figure 5.64 Percentage change in volume at base settlement equal to 20% of column diameter for spanning ratio equal to 1.48, highlighting influence of initial sample density

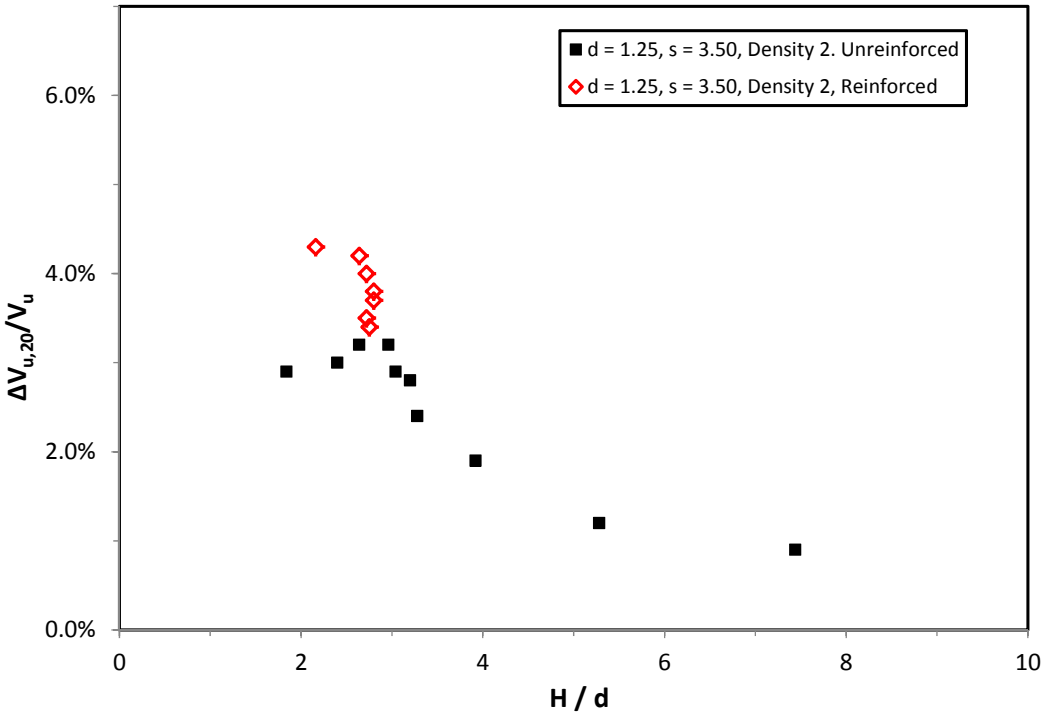

Figure 5.65 Percentage change in volume at base settlement equal to 20% of column diameter for spanning ratio equal to 1.48, highlighting influence of reinforcement

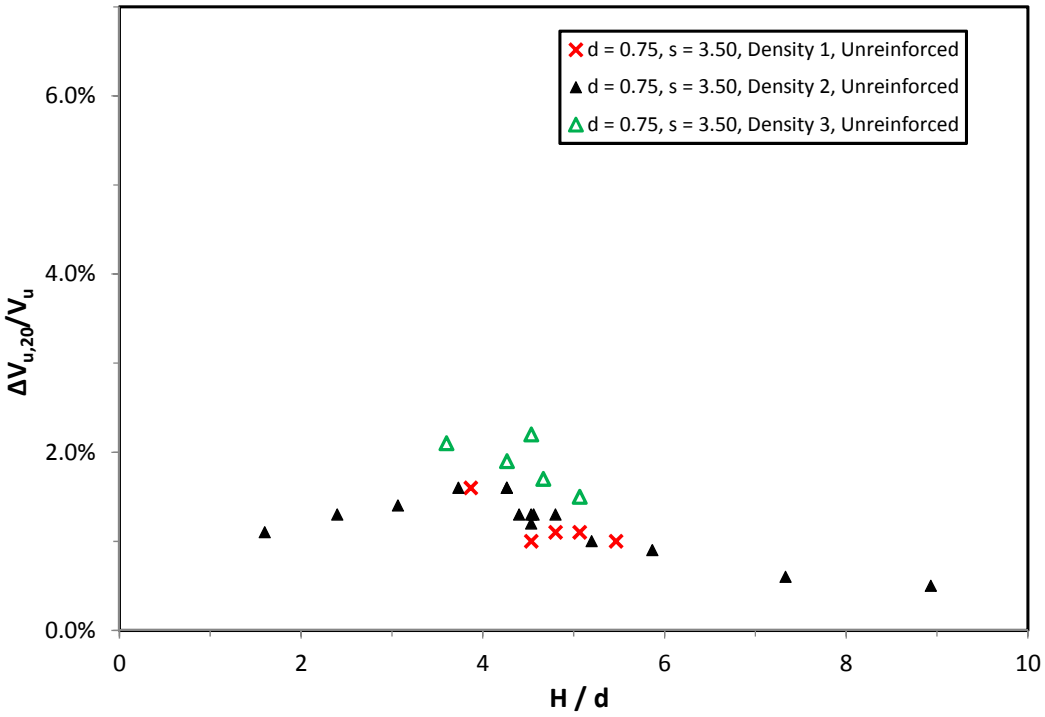

Figure 5.66 Percentage change in volume at base settlement equal to 20% of column diameter for spanning ratio equal to 2.80, highlighting influence of initial sample density

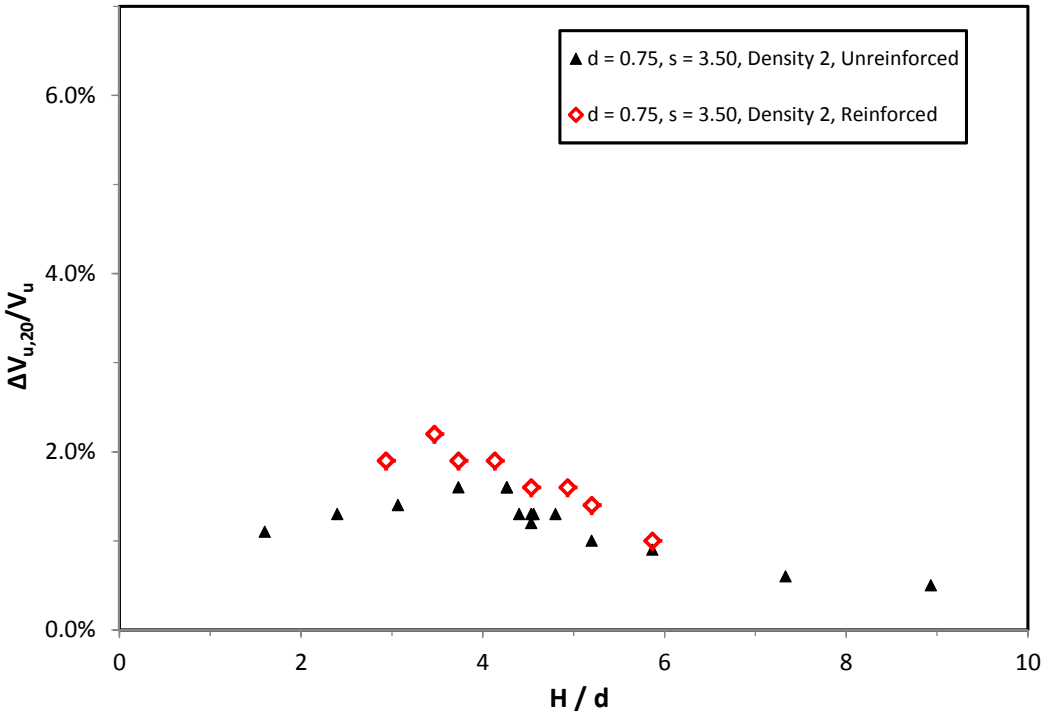

Figure 5.67 Percentage change in volume at base settlement equal to 20% of column diameter for spanning ratio equal to 2.80, highlighting influence of reinforcement

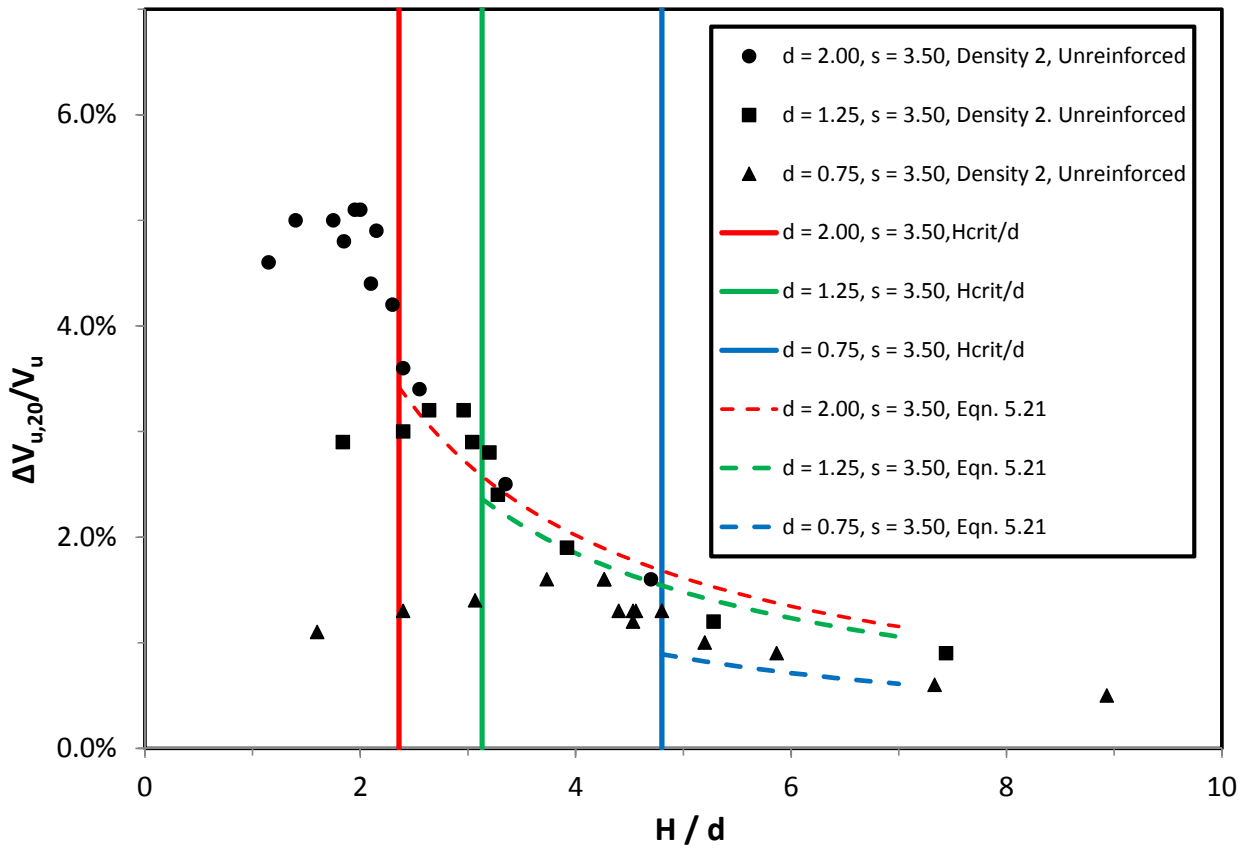

Figure 5.68 Trend for volume change above and below critical height for three unit cell geometries. The black dashed line is the trend above the critical height given by Equation 5.21

Using the experimental results shown in Figure 5.61 through Figure 5.67 and the interpreted results shown in Figure 5.68, the following conclusions can be made regarding volume change within the unit cell:

1) Below the critical height $\Delta V_{u,20}/V_u$ is sensitive to unit cell geometry, initial sample density, and reinforcement condition. Dilation increases as spanning ratio decreases, as initial sample density increases, and when reinforcement is present. The data from reinforced samples follow essentially the same trend regardless of the number and stiffness of reinforcing layers.
2) The secant rate of dilation for base settlements equal to 20 percent of the column diameter reaches a maximum just below the critical height.
3) Above the critical height, the relationship between $\Delta V_{u,20}/V_u$ and H/d can reasonably be approximated by Equation 5.21 over the range of sample heights, densities, and reinforcement conditions considered. Equations 5.19 and 5.20 provide the supporting derivation using unit cell geometry and settlement measurements. The dashed lines in

Figure 5.68 are based on Equation 5.21 using corresponding secant values of SBR_{tot} provided in Table 5.10.

$$\frac{\Delta V_u}{V_u} = \frac{\left(S_b - S_{tot}\right)s^2 - \frac{\pi}{4}d^2 S_b}{\left(H\right)s^2} \tag{5.19}$$

$$\frac{\Delta V_u}{V_u} = \frac{S_b}{H}\left[1 - SBR_{tot} - A_s\right] \tag{5.20}$$

$$\frac{\Delta V_{u,20}}{V_u} = \frac{0.2d}{H}\left[1 - SBR_{tot} - A_s\right] \text{ when } \frac{S_b}{d} = 0.2 \tag{5.21}$$

5.6 Summary

A total of 120 multi-column tests were performed using five different unit cell geometries as well as a range of sample heights, sample densities, and number and stiffness of reinforcing layers. The purpose of the tests was to observe deformation of the surface of the unit cell resulting from differential settlement between the columns and the rigid base. The key findings from the multi-column tests are listed below:

1. Below the critical height, the ratio of surface settlement over the column axis to base settlement, SBR_c, was observed to have a value equal to zero for $H/d \leq 1$ and increase nonlinearly as sample height increased. For four of the five unit cell geometries evaluated during the bench-scale testing, which had area replacement ratios greater than 1 percent, the relationship between SBR_c and sample height can be approximated using Equation 5.5. For the conditions evaluated using the single column tests described in Chapter 4 and the unit cell geometry evaluated experimentally with an area replacement ratio equal to 1 percent, the relationship between SBR_c and sample height can be approximated using Equation 5.6.
2. For the unit cell geometries evaluated with an area replacement ratio greater than 4 percent, the interaction height, H_i, where S_d becomes less than S_b, was estimated reasonably well by s'/tanα, where α was assigned a value of 29 degrees based on results from the single column testing in Chapter 4.
3. Between the interaction height and the critical height, the ratio of the surface settlement to base settlement at the unit cell boundary location furthest from the column, SBR_d, decreased from unity in an approximately linear fashion. A similar relationship was also

observed for the settlement ratio, SBR_i, at the unit cell boundary location closest to the column.

4. Below the critical height, the ratios of differential surface settlement to base settlement, $DSBR_d$ and $DSBR_i$, decreased in an approximately linear fashion as sample height increased. The differential settlement ratio $DSBR_i$ reached zero, indicating no differential settlement, at sample heights less than or equal to the height where $DSBR_d$ reached zero.
5. For the range of relative densities evaluated ($73\% \leq D_r \leq 105\%$), there was not sufficient evidence to determine a trend between DSBR and relative density.
6. The values of DSBR for samples incorporating reinforcement were equal to or less than the values from equivalent unreinforced samples. The reduction in DSBR due to the presence of reinforcement increased as the spanning ratio of the unit cell geometry increased. Since the experimental tests were displacement controlled, the reduction in differential surface settlement due to the presence of reinforcement does not include the reduction in base settlement due to load transfer to the columns by the reinforcement.
7. The magnitude of maximum differential surface settlement can be estimated for unreinforced conditions using Equation 5.13. Except at low area replacement ratios, the ratio of differential surface settlement to base settlement increases rapidly as normalized sample height decreases below the critical height. The steepness of the trend between differential surface settlement and normalized sample height contributes to the low predictive accuracy of Equation 5.13.
8. Critical height, defined as the sample height where $DSBR_d$ reaches zero, was observed to be related to unit cell geometry according to the following expression: $H_{crit}=1.15(s')+1.44d$. The presence and stiffness of reinforcement did not have a measurable influence on critical height, nor did the variation of sample density over the range of relative densities evaluated.
9. Above the critical height, the surface settles uniformly ($SBR_c=SBR_d=SBR_i$). Over the range of base settlements and sample heights considered, the ratio of the total surface settlement to the base settlement, SBR_{tot}, can reasonably be approximated as constant for a particular unit cell geometry.
10. For the conditions considered, the settlement ratio SBR_{tot} can be estimated as a using a relationship with area replacement ratio modified from the approach by Russell et al. (2003). The ratio of total surface settlement to base settlement increased as area replacement ratio decreased. Variation of sample density and the presence and stiffness of reinforcement had no measurable effect on SBR_{tot}.

11. In all of the tests, the samples dilated in response to differential base settlement. The rate of dilation was observed to be highest at small magnitudes of base settlement and to decrease as base settlement magnitude increases. In the analysis, the unit volume change was determined as volume change in the unit cell divided by the initial unit cell volume. The tests were compared using the unit volume change at base settlement equal to 20 percent of the column diameter. The results show that sample height significantly influences volume change. Well below the critical height, the unit volume change increased as sample height increased and reached a maximum value just below the critical height. Beyond the critical height, the unit volume change declined gradually but remained positive over the range of sample heights evaluated.
12. Below the critical height the unit volume change was sensitive to unit cell geometry, initial sample density, and reinforcement condition. Dilation was observed to increase as spanning ratio decreased, initial sample density increased, and when reinforcement is present. The unit volume change for reinforced samples followed essentially the same trend with respect to normalized sample height regardless of the number and stiffness of reinforcement layers. Above the critical height, the sensitivity of unit volume change to the range of sample densities and reinforcement conditions diminished.
13. When base settlement is uniform, the unit volume change above the critical height can be estimated using Equation 5.20. The unit volume change provides the average volume change in the unit cell volume. It is likely that localized volume change within the unit cell volume is spatially dependent and may deviate significantly from the average value.

6 Numerical Modeling of GRCSE Unit Cell in FLAC3D

This chapter describes the use of FLAC3D, developed by Itasca Consulting Group, Inc. (2008) of Minneapolis, Minnesota, to model the multi-column experimental tests described in Chapter 5 and investigate the impact of scale on calculated surface deformations. The primary goals of the numerical modeling efforts are listed below.

1) Determine if a fairly simple three-dimensional numerical model can calculate surface deformations that agree with the experimental results using a consistent set of material properties.
2) Evaluate whether increasing the scale of the numerical model to ten times larger than the experimental model has an impact on calculated surface deformations.
3) Observe the relationship between column stress and base settlement.

A 3D model was used in the current study because, as described in Kempton et al. (1998), the support provided by an array of individual columns to the overlying embankment cannot be completely described in 2D. Berilgen et al. (2008) concluded that 2D plane strain analyses and 3D analyses of the same GRCSE resulted in different results for deformation and load transfer. Smith (2005) showed that 2D axisymmetric analyses can be used to calculate load transfer between the columns and foundation soil that agrees with field measurements obtained from a full-scale embankment founded on a triangular array of columns; however, as described in Chapter 7, 2D plane strain and axisymmetric analyses with and without reinforcement have not been successful at calculating critical heights for 3D unit cell geometries.

The numerical model was developed to study a square array of circular columns without the inclusion of reinforcement. All five unit cell geometries used during the experimental testing were analyzed numerically. In addition, three of the five geometries used during the experiments were scaled by a factor of ten to evaluate whether scale has an impact of calculated surface deformation. All of the analyses evaluating deformation used material properties for the embankment based on the properties estimated for Light Castle sand prepared dry at Density 2. The notation and terminology used in this chapter is consistent with the definitions provided in Section 1.4. An example analysis for a model with a column diameter of 1.25 in., a column spacing of 3.50 in., and a sample height of 3.75 in. is used in Sections 6.1 through 6.6 to explain the modeling process and interpretation of results.

6.1 Model Discretization and Boundary Conditions

Because of the symmetries that exist, one quarter of the unit cell was modeled using three basic components: the embankment soil, the column, and the foundation soil. Like the experimental model, the foundation soil was treated as a rigid base and the column was pushed up into the bottom of the embankment soil to represent differential settlement. Roller supports were applied to the four sides of the embankment soil and the top of the sample was left free to deform in response to the displacement of the column. Interface elements were used to connect the rigid base and column to the embankment soil. Figure 6.1 shows a typical grid for the embankment soil, containing 5120 zones, generated by the geometry input file developed for the model. Results of a mesh refinement study are presented in Section 6.5.

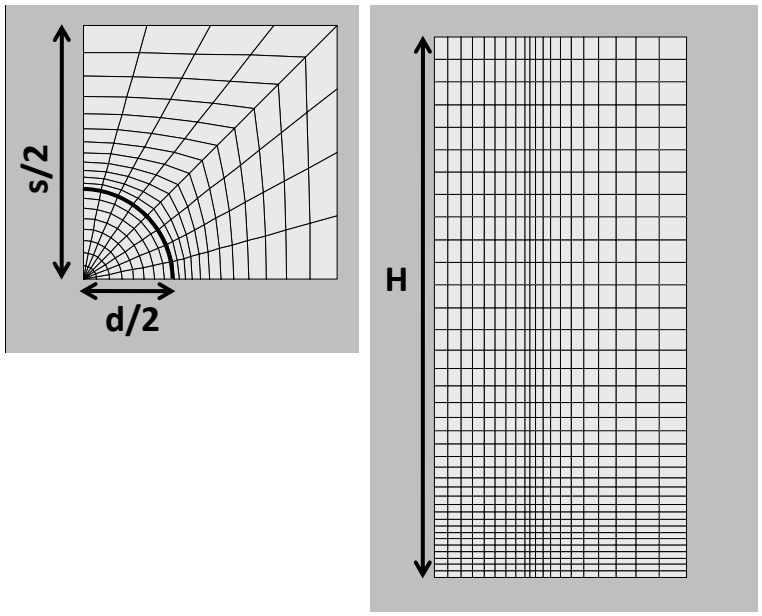

Figure 6.1 Discretization of the embankment soil model for d = 1.25 in., s = 3.50 in., H = 3.75 in.

6.2 Initial Conditions

To establish the initial stress conditions, the soil model was first assigned elastic properties and brought into equilibrium with gravity. After coming into equilibrium, the soil was assigned Mohr-Coulomb properties, and the model was again brought into equilibrium. Figure 6.2 shows an example of the vertical stress contours after the model is initialized to gravity loads.

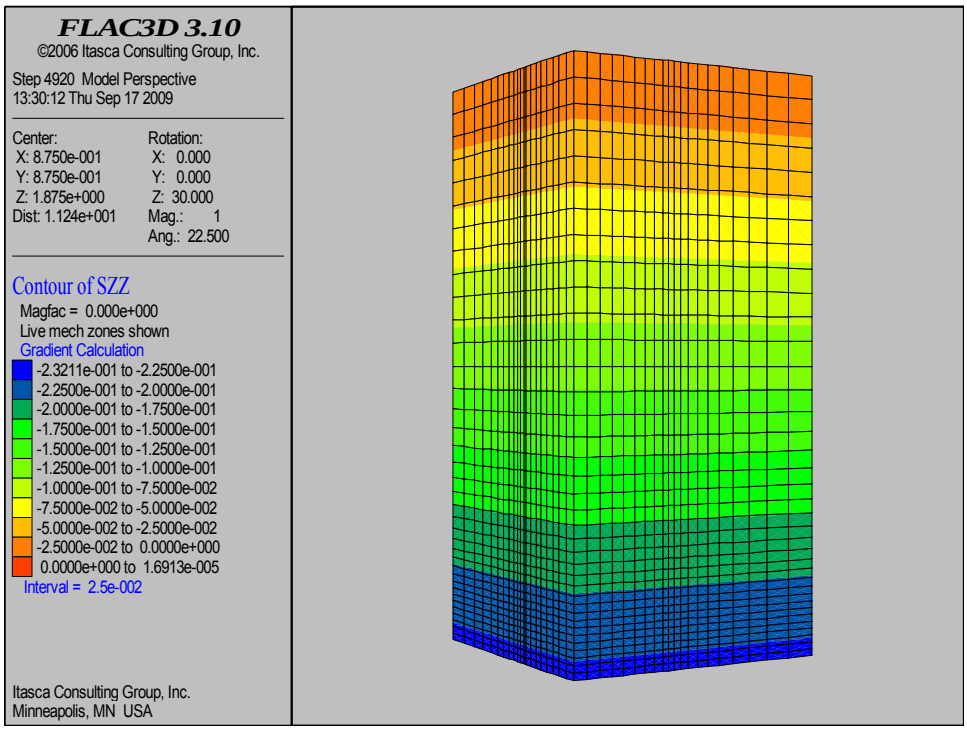

Figure 6.2: Typical vertical stress contours once the model is brought into equilibrium with gravity

6.3 Material Properties

The embankment soil was modeled as a cohesionless Mohr-Coulomb material with non-associated flow rule for shear failure. The Mohr-Coulomb model has an elastic region up to a failure surface defined by the Mohr-Coulomb criteria (c, ϕ). Shear stresses at failure result in perfectly plastic behavior. The properties of the embankment soil were based on the properties estimated for Light Castle sand prepared dry at Density 2. Section 3.3.1 discusses material properties for Light Castle sand and the relationship between confining pressure and values of friction angle and dilation angle. A series of preliminary analyses were performed to determine the sensitivity of surface settlements over the column and at the unit cell boundary to values of friction angle and dilation angle. Friction and dilation angles were varied between the peak (ϕ = 52^o, ψ = 30^o) and critical state (ϕ = 32^o, ψ = 0^o) values listed for Density 2 in Table 3.5 in Section 3.3.1. The analyses revealed that surface deformation above the column decreases as friction angle increases and becomes essentially insensitive to friction angle above a value of 35 degrees. Surface deformation above the column decreases as dilation angle increases and becomes relatively insensitive to dilation angle above a value of 15 degrees. At the unit cell boundary, surface deformation was insensitive to friction angle. Surface deformation at the unit cell

boundary decreased as dilation angle increased over the full range of values considered. Since portions of the model were expected to be sheared well past peak conditions, it was decided to use a friction angle of 45 degrees and a dilation angle of 15 degrees in the analyses. These values are about halfway between peak and critical state values.

The values of bulk modulus and shear modulus were assigned based on elastic relationships with Youngs Modulus for a selected value of Poissons Ratio. The relationship between the initial tangent modulus and confining pressure given by Janbu (1963) was used for selecting a value of Youngs Modulus. This relationship is shown below in Equation 6.1. In the expression, σ'_3 is the effective confining stress, P_a is atmospheric pressure expressed in consistent units with σ'_3, K is a dimensionless modulus number, and n is a coefficient. A value of K equal to 1500 and n equal to 0.75 were used in the analyses based on experimental tests performed by Lade (1971) and reported by Duncan et al. (1980) on Monterey No. 0 sand, which is similar to Light Castle Sand.

$$E_i = KP_a\left(\frac{\sigma'_3}{P_a}\right)^n \tag{6.1}$$

As previously mentioned, the soil was initially modeled as an elastic material to reduce computation time during gravity turn-on. The value of bulk modulus during this phase was assigned based on elastic relationship with Youngs Modulus for a Poissons Ratio equal to $K_o/(1+K_o)$, where K_o is the at rest earth pressure coefficient estimated by 1-sin(ϕ). Following initialization of the model to gravity loads, the embankment soil was assigned a Poissons ratio equal to 0.3, which is consistent with the value used by Smith (2005) for axisymmetric numerical modeling of GRCSEs.

Table 6.1 provides example material property values used for a case where the column spacing, s, is equal to 3.5 inches, the column diameter, d, is equal to 1.25 inches, and the sample height, H, is equal to 3.75 inches. A confining pressure, σ'_3, equal to 0.077 psi was calculated using Equation 6.2 to estimate Youngs Modulus. Since the deformation of the soil near the column is significantly greater than the average deformation in the model, Equation 6.2 uses the vertical effective stress at a depth equal to two-thirds of the sample height and a lateral earth pressure coefficient of 0.5, which is higher than the at-rest value to account for stress changes due to the development of soil arching.

$$\sigma_3' = \frac{H\gamma}{3} \tag{6.2}$$

Two values of bulk modulus are listed in Table 6.1. The value, Kmod, is related to Youngs Modulus, Emod, using a Poissons Ratio equal to the variable pois, while K_elas is related to Emod by Poissons Ratio equal to the variable nu_elas.

Table 6.1 An example of the material properties used in the FLAC3D model

Property	FLAC3D variable	Value for d = 1.25 in., s = 3.5 in., H = 3.75 in.
Friction angle	phi	45^o
Dilation angle	psi	15^o
Poissons Ratio	pois	0.3
Poissons Ratio for Elas. Soln.	nu_elas	0.226
Atmospheric pressure	Pa	14.7 psi
Modulus number	K	1500
n	n	0.75
At rest E.P. coef	Ko	0.293
Unit Weight	uwght	107 pcf
Mass Density	mds	1.6e-4 lbs-s^2/in^4
Youngs Modulus	Emod	431 psi
Shear Modulus	Gmod	166 psi
Bulk Modulus	Kmod	359 pci
Bulk Mod. for Elas. Soln.	K_elas	262 pci

6.4 Modeling Differential Settlement

To introduce differential settlement between the column and base, the column was advanced slowly into the soil using the displacement control regime shown in Figure 6.3. The variable *ncut* represents the number of time steps needed to bring the column into steady state motion and *col_disp* is the number of time steps required to achieve the target magnitude of column displacement. The values of *ncut* and *col_disp* were selected such that the maximum acceleration of the column was approximately 3.6e-11 inches/(time step)^2 and the maximum velocity was approximately 7.1e-7 inches/(time step). These values are sufficiently low to keep the FLAC3D model stable during the computation process.

Column displacement magnitudes were limited to 0.2 inches or less at the experimental scale and 1 inch at 10x scale in the FLAC3D model. In the vicinity of the column, the soil undergoes large strains even at modest column displacement magnitudes. For this reason, the

FLAC3D model was set to large strain mode which updated the mesh during computation every 100 time steps.

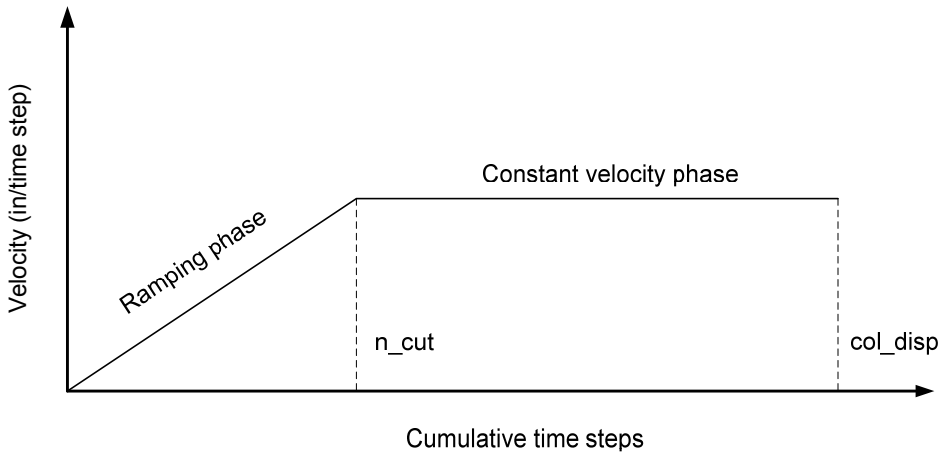

Figure 6.3: Velocity ramping process used during column displacement

Figure 6.4a-c shows typical plots of the shear strain contours following column displacement into the soil for three samples with the same column diameter and spacing, arranged in order of increasing height from left to right. The samples shown in Figure 6.4a and Figure 6.4b are below the critical height, while the sample shown in Figure 6.4c is above the critical height. The sample with lowest height, shown in Figure 6.4a, experiences little soil arching and the shear bands initiating from the column edge reach the surface. The sample shown in Figure 6.4b is just below the critical height and, while the shear bands still reach the surface, there is significant soil arching between adjacent unit cells. The sample shown in Figure 6.4c is above the critical height and areas experiencing significant shearing are contained to the soil arches.

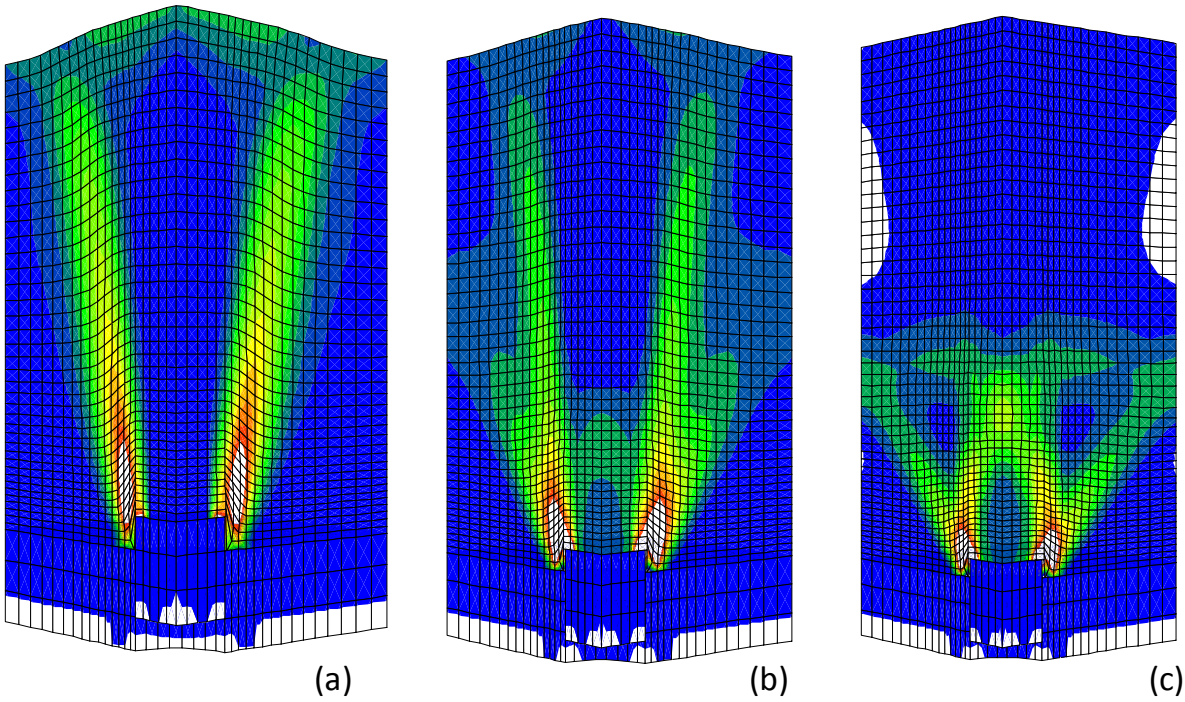

Figure 6.4: Typical deformed mesh showing shear strain contours for sample heights, H: H(a) < H(b) < H_{crit} < H(c) (samples shown at different scales).

6.5 Measuring Surface Settlements within the Unit Cell

The surface displacements calculated during differential movement between the column and base can be expressed in terms of settlement using the equivalency between displacing the column up into the base of the sample, while holding the base fixed, and holding the column fixed and lowering the base. Figure 6.5 shows SBR_c, SBR_d and SBR_i plotted against S_b and Figure 6.6 shows $DSBR_d$ versus S_b for the case where column spacing is equal to 3.50 inches, column size is 1.25 inches, sample height is 3.75 inches, and the material properties are those given in Table 6.1. Recall that SBR_c, SBR_d and SBR_i are the ratios of the surface settlements over the column and unit cell boundary at locations defined in Section 1.4 to base settlement, S_b. The settlement ratio $DSBR_d$ is equal to SBR_d minus SBR_c and represents differential surface settlement occurring between locations in the unit cell with the greatest and least amounts of support from the column.

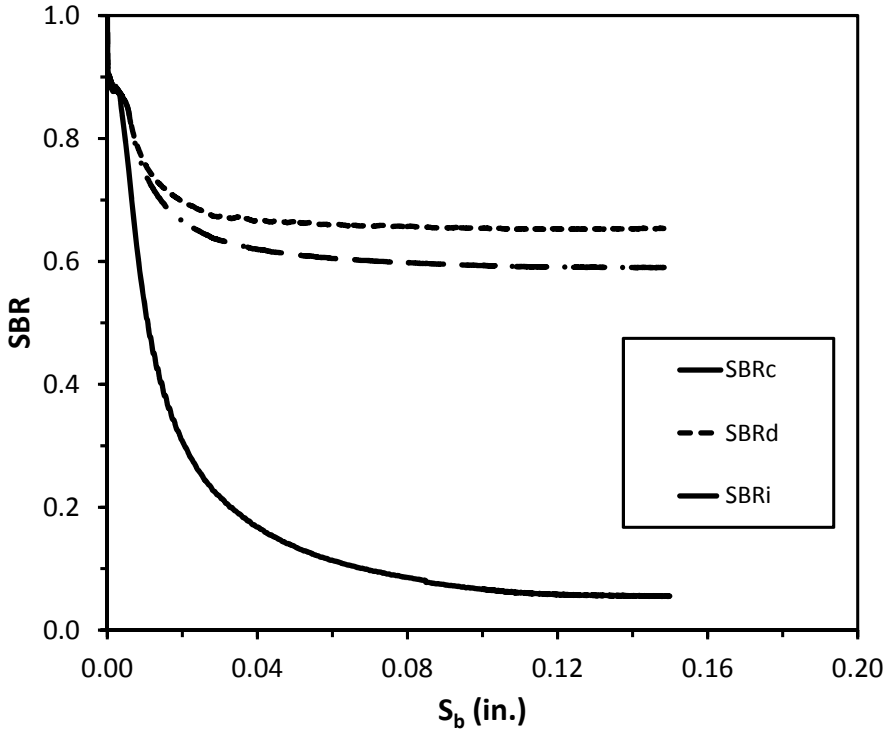

Figure 6.5: SBR versus S_b for d = 1.25 in., s = 3.50 in., H = 3.75 in.

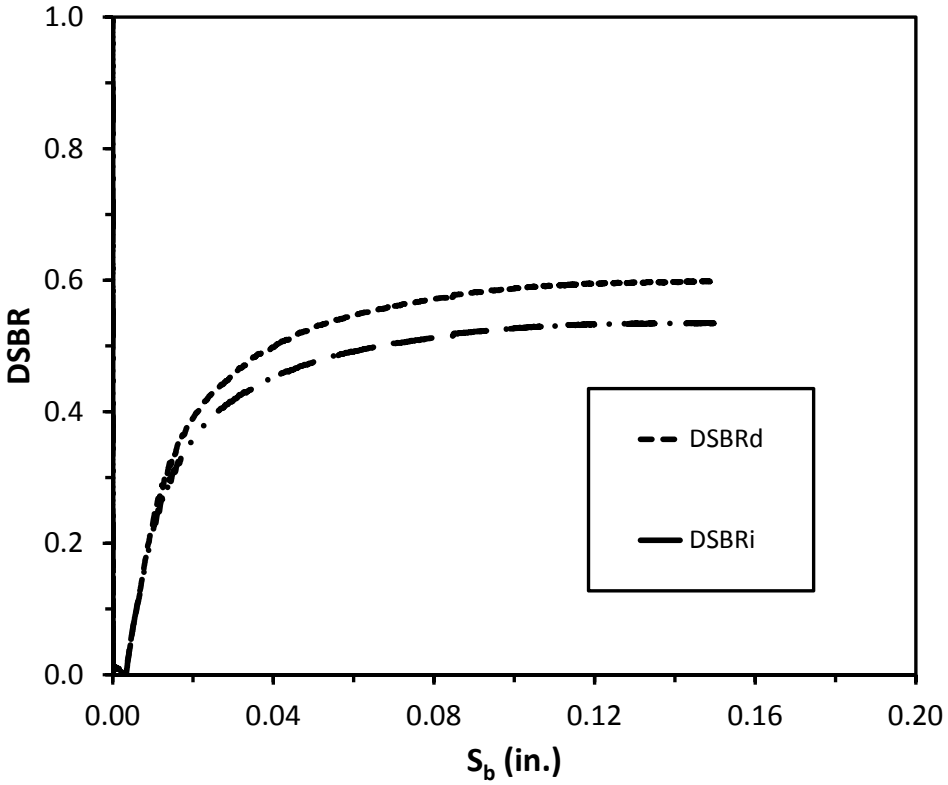

Figure 6.6: DSBR versus S_b for d = 1.25 in., s = 3.50 in., H = 3.75 in.

At small values of S_b, the values of SBR_c SBR_d, and SBR_i, determined in FLAC3D are sensitive to the magnitude of base settlement. Some nonlinearity in the relationship between surface settlement and base settlement was observed in the experimental results, but not to the degree exhibited by the numerical results. The settlement ratios calculated in FLAC at higher magnitudes of S_b, which were essentially stable with respect to base settlement, are used in Section 6.6 for comparison to the experimental values.

The mesh used in the numerical analyses is described in Section 6.1. A check was performed to determine the sensitivity of the calculated settlement ratio to the mesh refinement. Using the example analysis with geometry and material properties defined in Table 6.1, analyses were performed using the standard mesh (5120 zones), a mesh half as refined as the standard mesh (612 zones), and a mesh that was twice as refined as the standard mesh (39040 zones). The number of zones for the three levels of refinement are not exactly related by $(1/2)^3$:1:2^3 because the vertical refinement of the rigid base and column was not changed. Analyses using the three meshes were performed to a maximum base settlement of 0.05 inches due to the extended computation time of the model with the highly refined mesh. Table 6.2 summarizes the resulting settlement ratios calculated at 0.05 inches of base settlement for the three levels of refinement. The results indicate that the model with the standard mesh refinement calculates settlement ratios similar to the model with double the mesh refinement. The primary reason for the observed differences is that at a base settlement of 0.05 inches, the settlement ratios are still somewhat sensitive to the base settlement magnitude. The settlement ratios calculated for the model with half the mesh refinement are also close to the values calculated using the standard refinement. The largest discrepancy is for settlement along the in-line direction. The results of the refinement study suggest that the model is not strongly sensitive to mesh refinement over the levels of refinement evaluated. Therefore, it was concluded that the standard mesh refinement was suitable for the analyses performed in this study.

Table 6.2 Settlement ratios calculated for models with three different levels of mesh refinement

Settlement Ratio	Half refinement (612 zones)	Standard refinement (5,120 zones)	2X refinement (39,040 zones)
SBR_c	0.12	0.14	0.10
SBR_d	0.64	0.66	0.67
SBR_i	0.48	0.61	0.63
$DSBR_d$	0.52	0.52	0.57
$DSBR_i$	0.36	0.47	0.53

6.6 Simulation of Multi-Column Experiments

The multi-column experimental tests described in Chapter 5 were simulated using the 3D numerical model described in the preceding sections. In addition, the impact of model scale on surface deformations was investigated by performing analyses where the geometries of three of the five unit cells evaluated experimentally were scaled by a factor of ten.

The results presented herein focus on the settlement ratio $DSBR_d$, which is used to define the critical height, and the ratios SBR_c and SBR_d which are used to determine $DSBR_d$. As described in Section 6.5, the settlement ratios calculated at base settlement magnitudes where sensitivity to S_b diminishes were used for comparison to the experimental results. Figures 6.7 through 6.21 show the results for SBR_c, SBR_d, and $DSBR_d$ obtained from the FLAC3D analyses compared to the corresponding experimental results. The vertical green line provided in each figure represents the critical heights determined from the multi-column experiments.

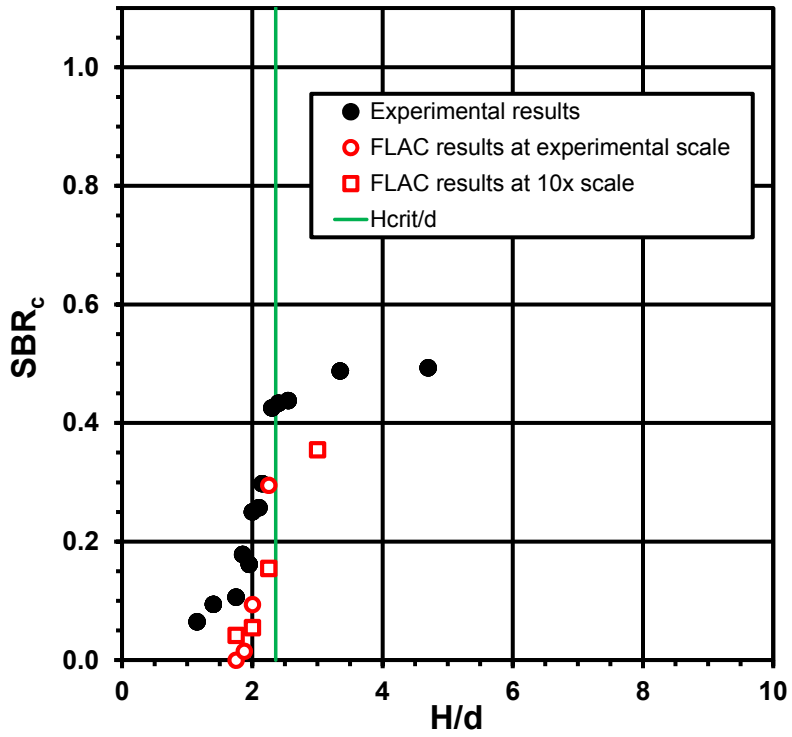

Figure 6.7 SBR_c versus H/d based on experimental and numerical results for d = 2.00 in., s = 3.50 in.

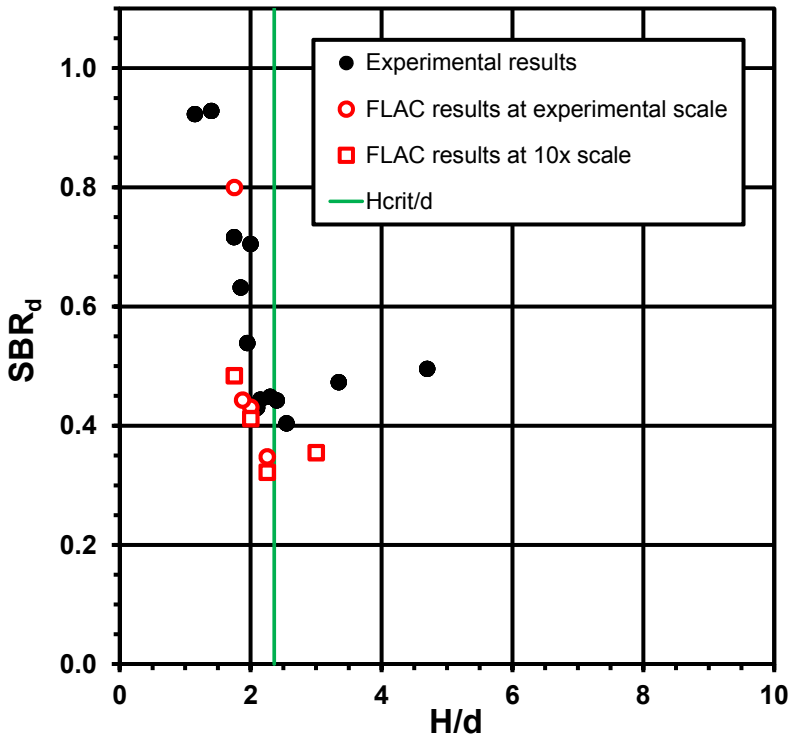

Figure 6.8 SBR_d versus H/d based on experimental and numerical results for d = 2.00 in., s = 3.50 in.

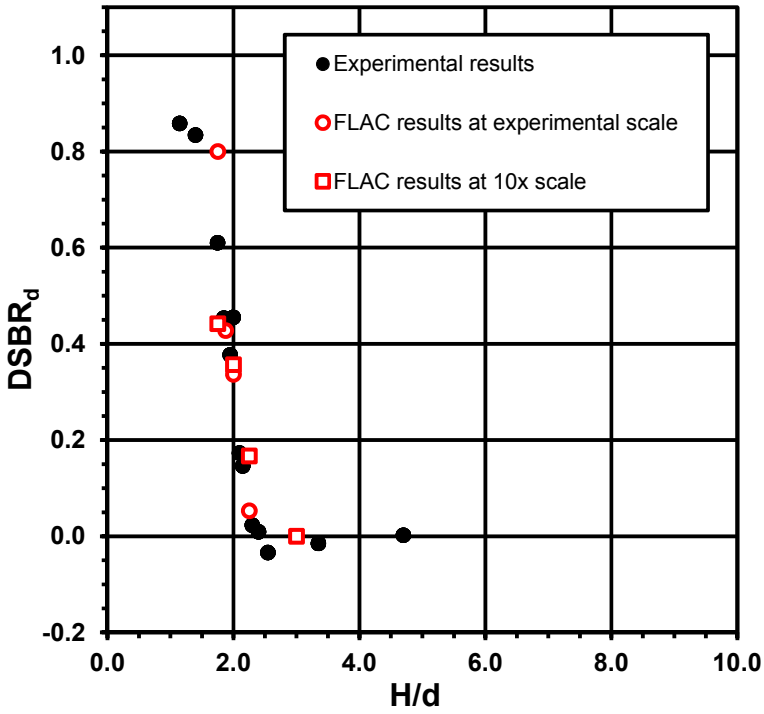

Figure 6.9 $DSBR_d$ versus H/d based on experimental and numerical results for d = 2.00 in., s = 3.50 in.

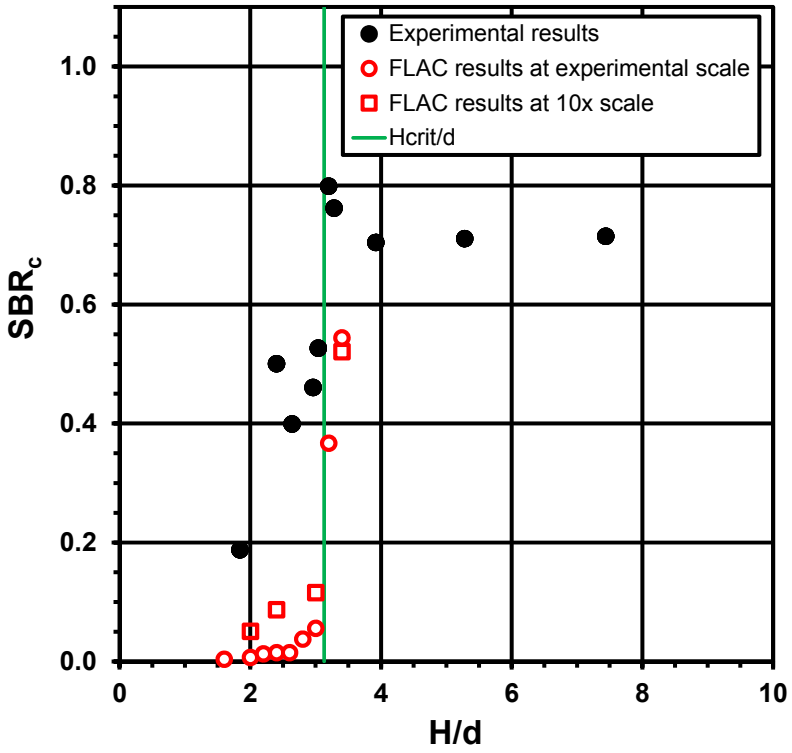

Figure 6.10 SBR_c versus H/d based on experimental and numerical results for d = 1.25 in., s = 3.50 in.

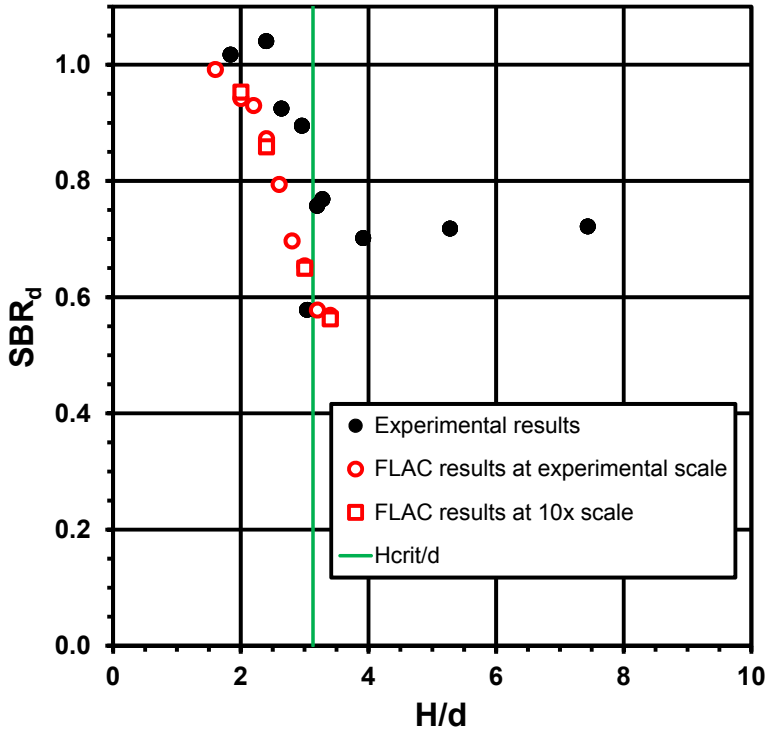

Figure 6.11 SBR_d versus H/d based on experimental and numerical results for d = 1.25 in., s = 3.50 in.

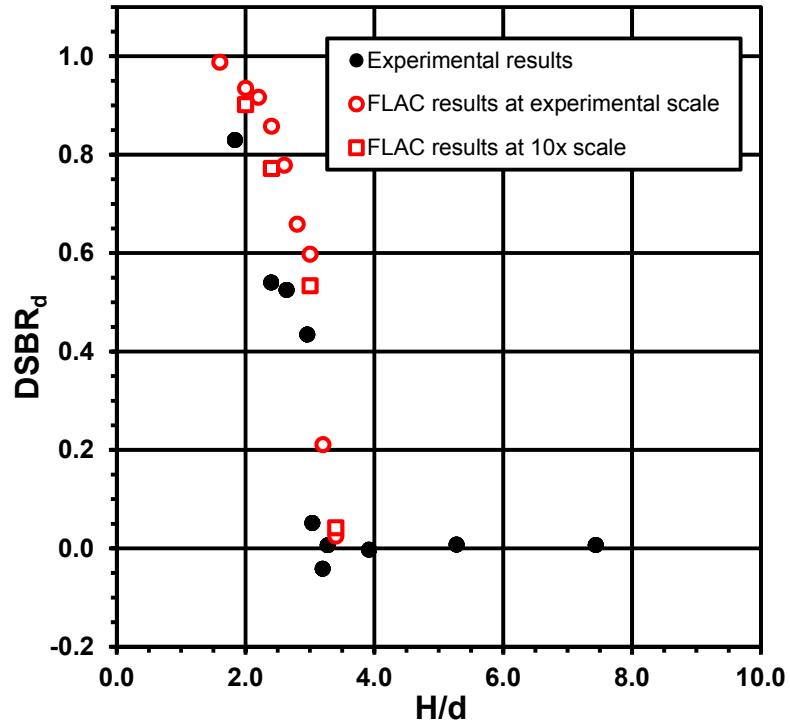

Figure 6.12 DSBR$_d$ versus H/d based on experimental and numerical results for d = 1.25 in., s = 3.50 in.

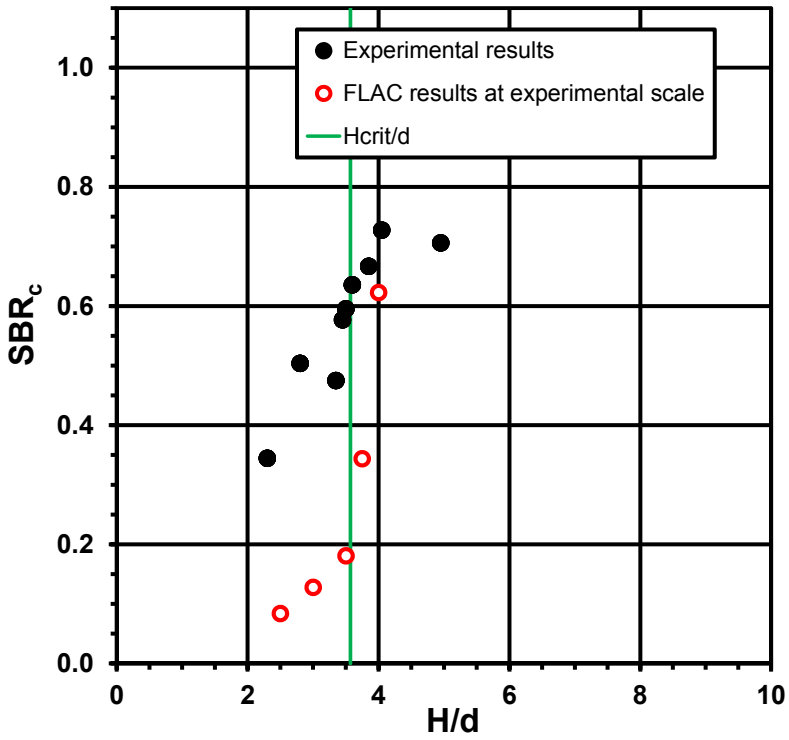

Figure 6.13 SBR$_c$ versus H/d based on experimental and numerical results for d = 2.00 in., s = 7.00 in.

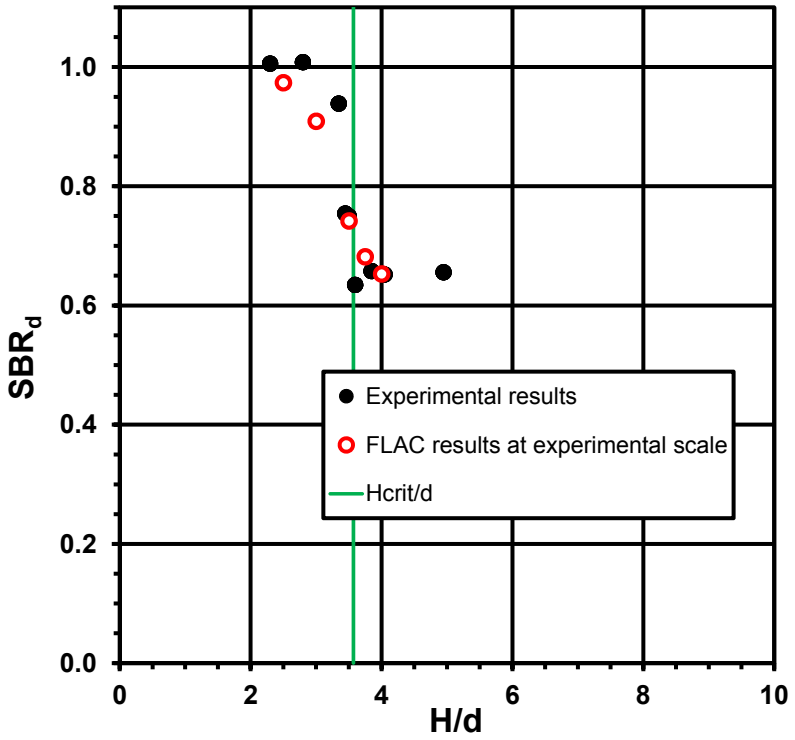

Figure 6.14 SBR$_d$ versus H/d based on experimental and numerical results for d = 2.00 in., s = 7.00 in.

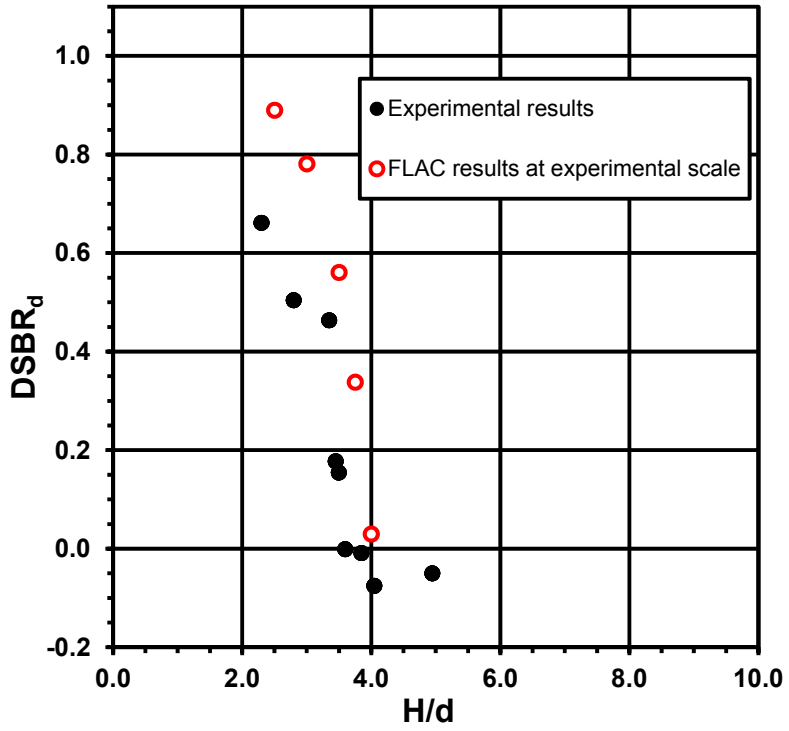

Figure 6.15 DSBR$_d$ versus H/d based on experimental and numerical results for d = 2.00 in., s = 7.00 in.

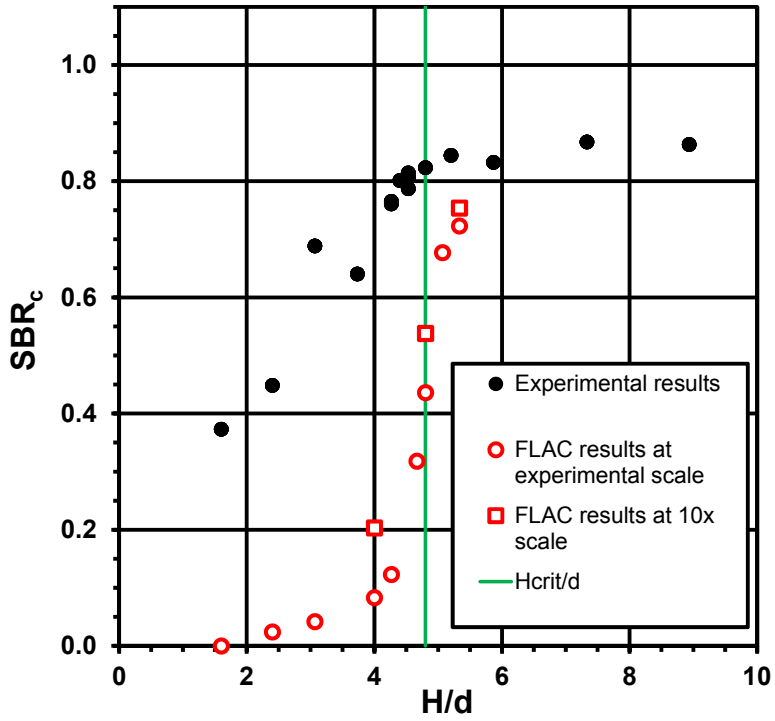

Figure 6.16 SBR_c versus H/d based on experimental and numerical results for d = 0.75 in., s = 3.50 in.

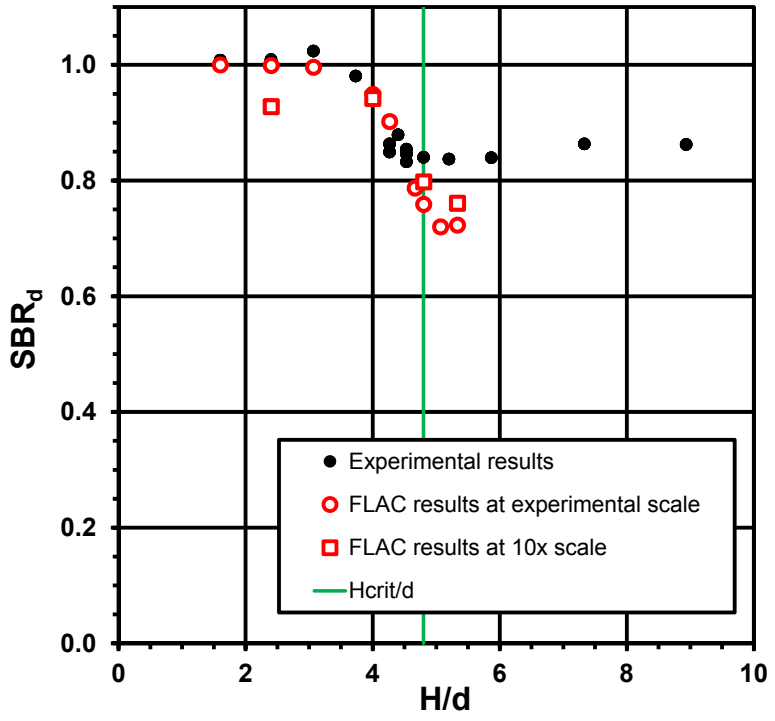

Figure 6.17 SBR_d versus H/d based on experimental and numerical results for d = 0.75 in., s = 3.50 in.

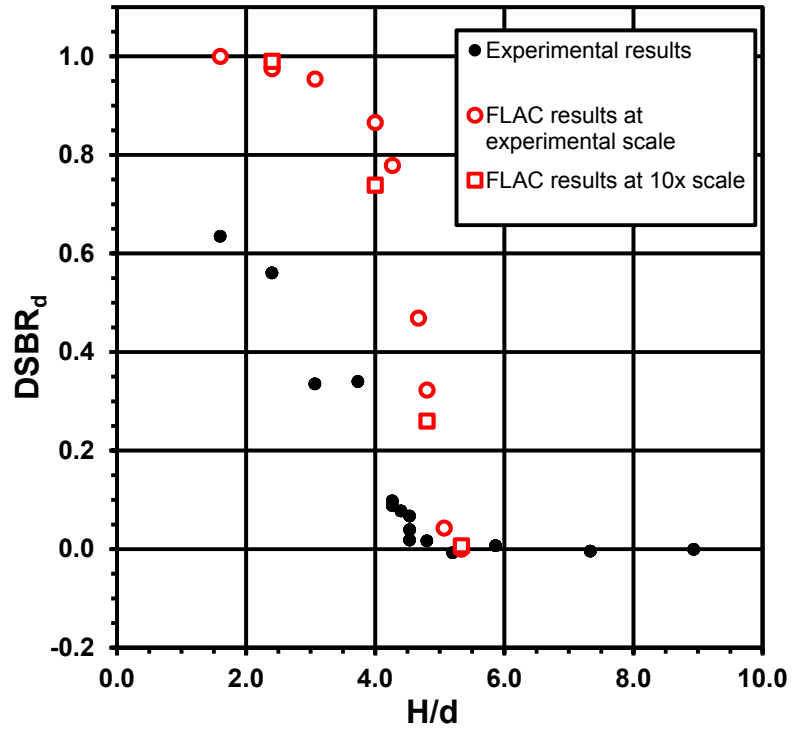

Figure 6.18 DSBR$_d$ versus H/d based on experimental and numerical results for d = 0.75 in., s = 3.50 in.

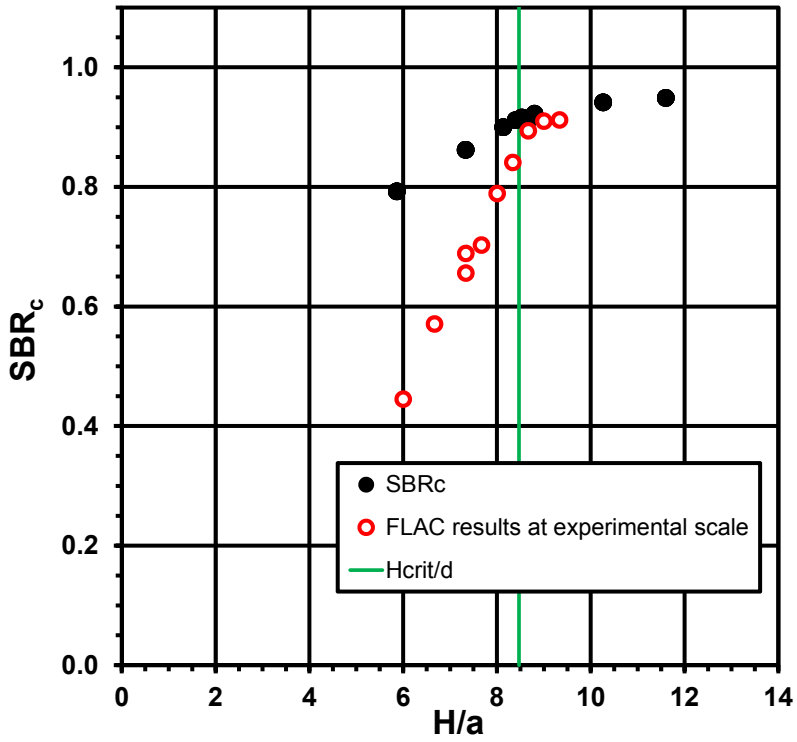

Figure 6.19 SBR$_c$ versus H/d based on experimental and numerical results for d = 0.75 in., s = 7.00 in.

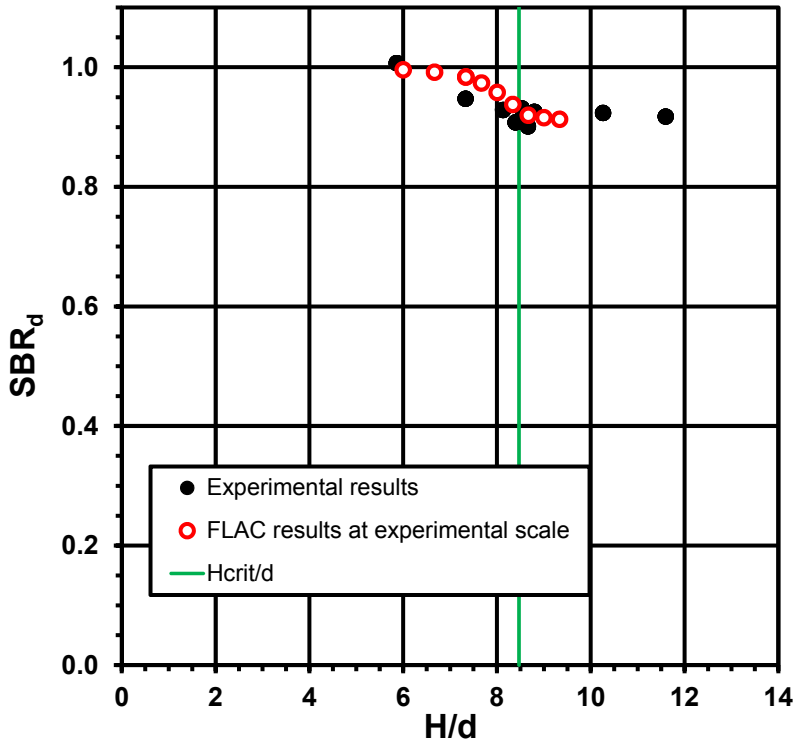

Figure 6.20 SBR$_d$ versus H/d based on experimental and numerical results for d = 0.75 in., s = 7.00 in.

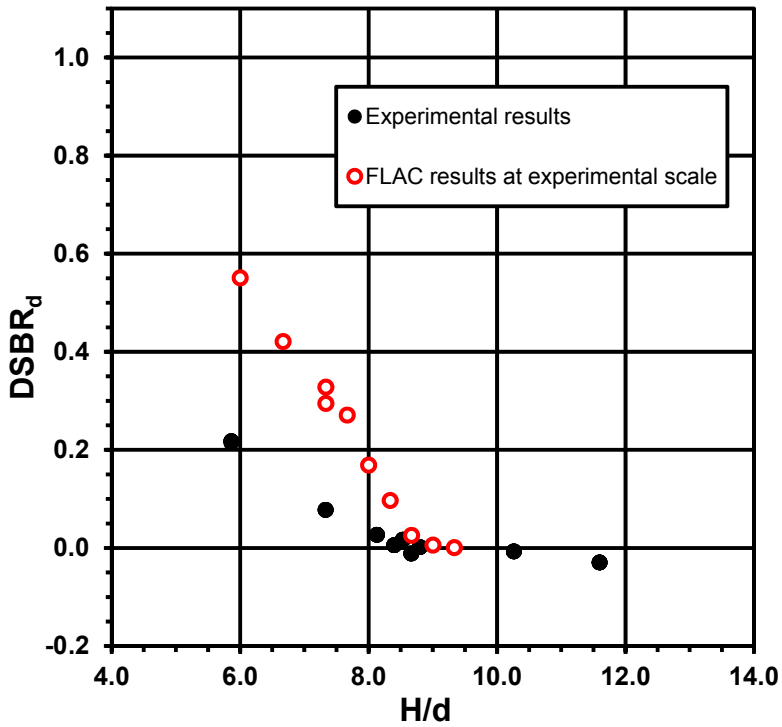

Figure 6.21 DSBR$_d$ versus H/d based on experimental and numerical results for d = 0.75 in., s = 7.00 in.

The results shown in Figures 6.7 through 6.21 indicate that, in general, the numerical analyses calculate significantly lower values of SBR_c and values of SBR_d that ranged from about the same to significantly lower than the experimental values. The calculated values of $DSBR_d$ range from about the same to significantly higher than the experimental values. Demerdash (1996) used a 2D numerical model and an experimental model with a square unit cell and also observed underestimation of settlement over the columns and overestimation of differential settlement. However, despite these differences, the critical heights from the current numerical analyses for all five unit cell geometries are practically identical to those determined experimentally. Furthermore, the scale of the numerical model had no practical impact on calculated settlement ratios and critical heights. This result is supported in Chapter 7 by evidence that suggests a relationship exists between critical height and unit cell geometry that is not dependent on scale.

An attempt was made to decrease the discrepancy between the measured and calculated values of SBR_c by incorporating strain softening into the model. According to the hyperbolic model proposed by Duncan and Chang (1970), the tangent modulus varies from E_i determined according to Equation 6.1 when stress conditions are isotropic to a value equal to $(1-R_f)^2E_i$ at peak deviatoric stress conditions determined using the Mohr-Coulomb failure criterion for the current confining stress. The fitting parameter R_f is explained by Duncan and Chang (1970) and always has a value between 0 and 1. To determine whether incorporating strain softening in the model would resolve the discrepancy between measured and calculated values of SBR_c, a series of analyses were performed using successively lower values of the coefficient K in Equation 6.1 until the model became unstable. Using this approach it was possible to observe the trend for surface deformation at very low embankment material stiffness. The outcome of the analyses suggested that incorporating strain softening into the model would not resolve the discrepancy between measured and calculated values of SBR_c. The discrepancy between calculated and measured values of settlement ratios may be the result of other limitations of the Mohr-Coulomb constitutive model or of modeling the unit cell as a continuum rather than as discrete elements.

6.7 Load Transfer

The relationship between column stress and relative displacement with the rigid base representing the foundation soils is presented herein for a square unit cell with a column diameter of 1.25 inches and a column spacing of 3.50 inches. Figure 6.22 provides an example of

the stress displacement relationships for the column and base. The model parameters are the same as the example defined at the beginning of the chapter except that sample height is 4 inches instead of 3.75 inches. The Column Stress Ratio, CSR, and the Stress Reduction Ratio, SRR, represent the vertical stresses acting of the column and base, respectively, normalized by the initial overburden stress. The plot shows load transfer from the base to the column at the onset of differential settlement. The red circle indicates the interpreted value of the maximum column stress ratio, $CSR_{max,}$ which has a value of 7.98. The peak column stress occurs at a base settlement equal to 0.42 percent of the column diameter. This means the stress acting on the column increases by about 8 times when the base settles 0.00525 inches relative to the column. At higher magnitudes of base settlement, the values of CSR calculated from the numerical analyses remain approximately constant or decrease gradually as shown in Figure 6.22. As described in Section 1.4, SRR is related to CSR according to the relationship $1=CSR(A_s)+SRR(1-A_s)$, where A_s is the area replacement ratio. Theoretically, CSR could reach a maximum value of $1/A_s$ if the load from the unit cell could be completely transferred to the column.

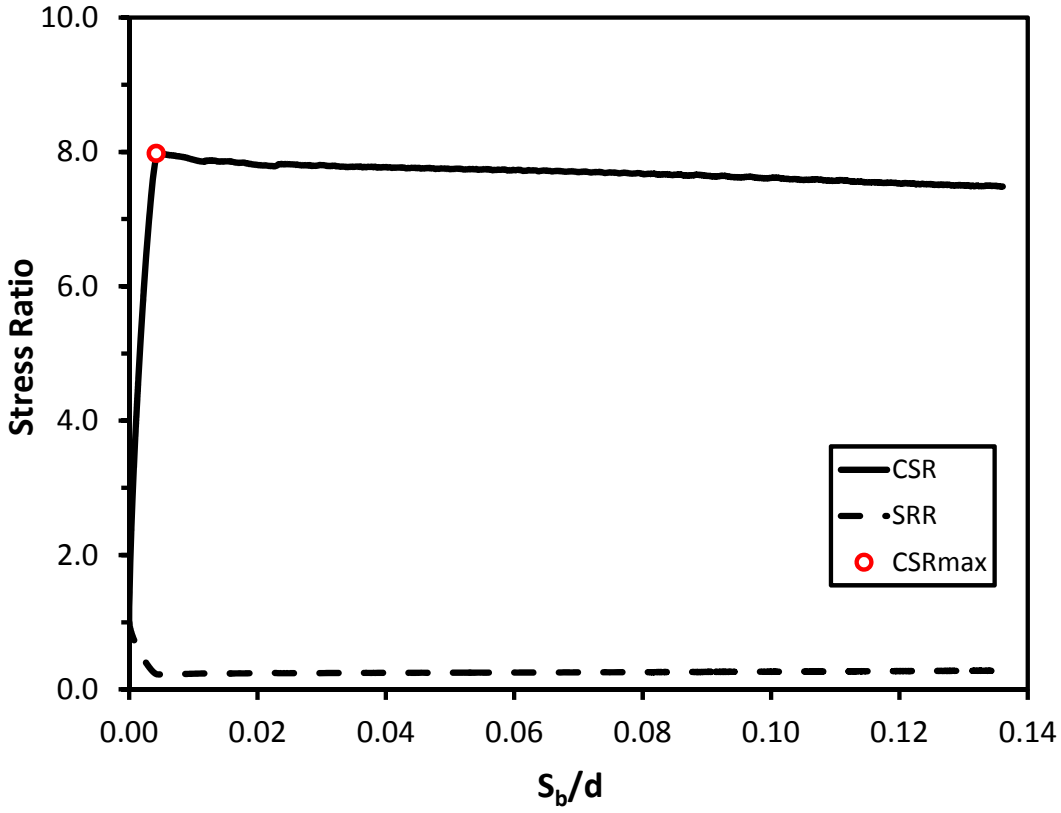

Figure 6.22: Stress displacement relationships for column and base for d = 1.25 in., s = 3.50 in., H = 4.00 in.

For each numerical analysis where CSR and SRR were tracked, the value of CSR_{max} was determined and plotted against the corresponding normalized sample height, H/d, as shown in Figure 6.23. Three sets of analyses were performed to observe the impact of simultaneous changes in friction angle and dilation angle on load transfer by soil arching. In the figure, "phi" represents the friction angle and "psi" represents the dilation angle. The results show that more load transfer occurs for soils that are stronger and more dilative. The results also indicate that CSR_{max} increases as normalized height increases.

Figure 6.24 shows $S_{b,max}/d$, which is the base settlement corresponding to CSR_{max}, plotted against normalized sample height, H/d, for the three sets of strength parameter values analyzed. The results indicate that, for dilative soils, greater displacement is required to reach CSR_{max} as strength and dilatency are increased. It also appears that $S_{d,max}/d$ is not strongly sensitive to H/d, for dilative soils. For the analyses performed with dilation angle equal to zero, $S_{b,max}/d$ increases as H/d increases.

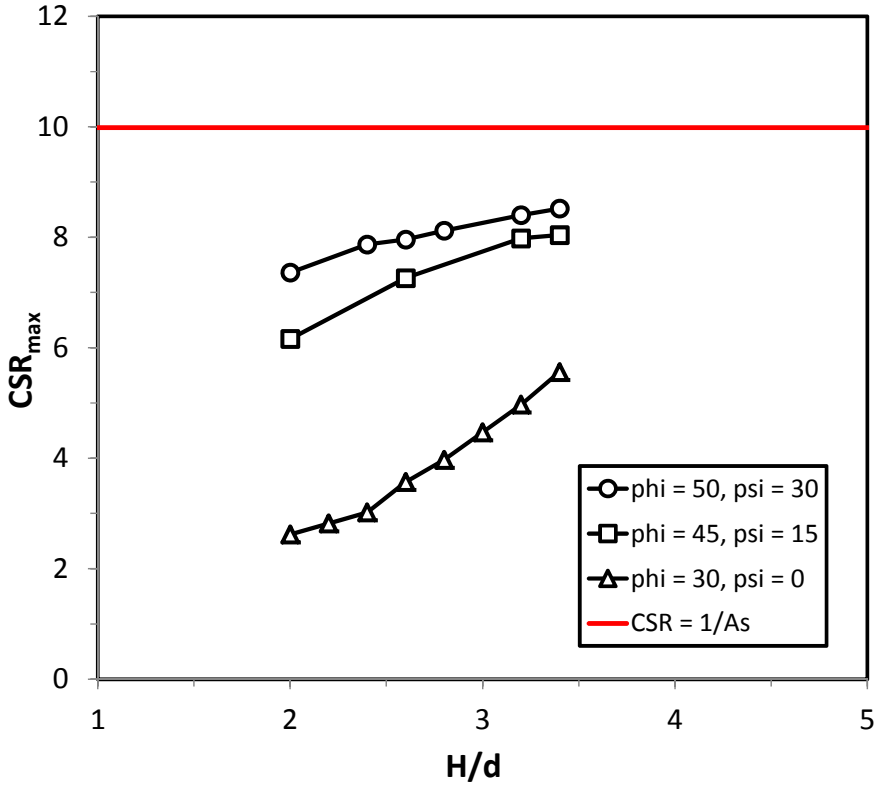

Figure 6.23 Relationship between CSR_{max} and H/d analyzed using three sets of strength parameter values for d = 1.25 in., s = 3.50 in.

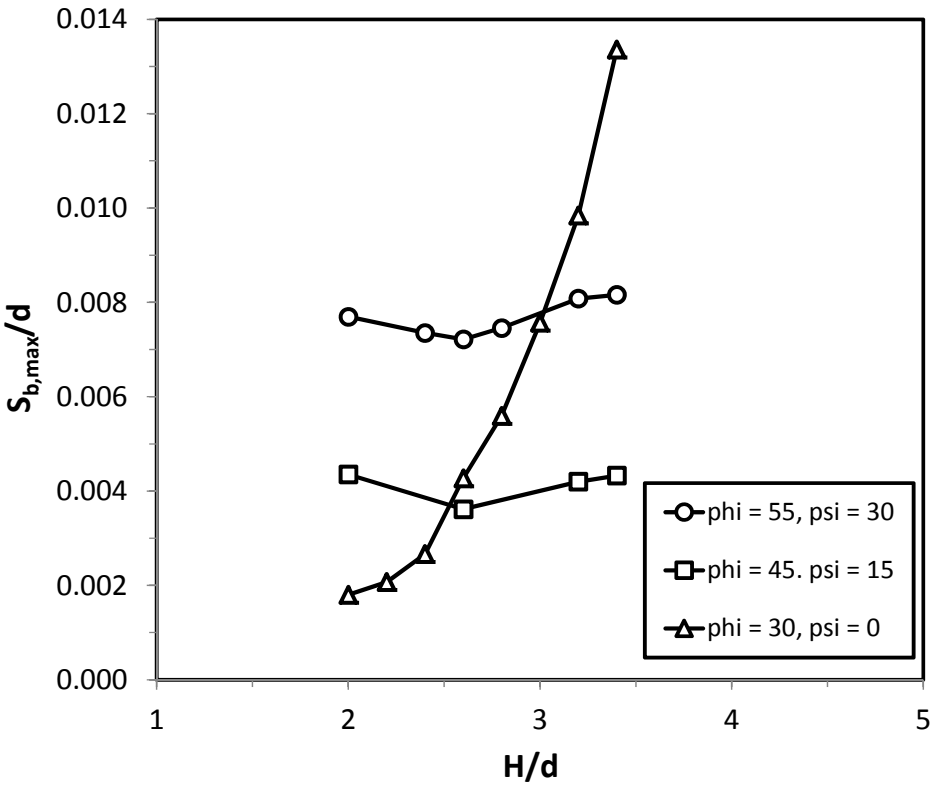

Figure 6.24 Relationship between $S_{b,max}/d$ and H/d analyzed using three sets of strength parameter values for d = 1.25 in., s = 3.50 in.

6.8 Summary

A three-dimensional numerical model of a square unit cell with round columns was developed using the finite difference code FLAC3D, developed by Itasca Consulting Group, Inc. The embankment soil was modeled as an elastic perfectly-plastic material with a Mohr-Coulomb failure criterion and was assigned material properties based on the properties for Light Castle sand used in the experimental testing. The column and base were modeled as essentially rigid. The model was used to simulate the multi-column tests described in Chapter 5 and evaluate whether a fairly simple numerical model using a consistent set of material properties could calculate surface deformations that agreed with the experimental measurements. In addition, the model was used to investigate whether calculated deformations were sensitive to scale and to observe the relationship between column stress and differential settlement between the column and base. The key findings from the numerical modeling study are listed below:

1. The numerical model generally calculated significantly lower surface settlements over the axis of the columns compared to the experimental model. For the conditions

evaluated, the settlement over the column decreased as friction angle increased until reaching a friction angle of 35 degrees beyond which point settlement over the column became essentially insensitive to friction angle. Settlement over the column decreased as dilation angle increased until reaching a value of 15 degrees, beyond which point settlement over the column became essentially insensitive to dilation angle.

2. The numerical model calculated surface settlement settlements at the unit cell boundary that ranged from about the same to significantly lower than the experimental measurements. Over the full range of conditions evaluated, the settlement at the unit cell boundary was essentially insensitive to the value of friction angle and decreased as dilation angle increased.
3. The calculated values of differential settlements ranged from about the same to significantly greater than the experimental measurements.
4. Progressively softening the elastic response of the embankment material did not remedy discrepancies between the calculated and measured surface settlements.
5. Despite the differences between calculated and measured surface settlements, the critical heights from the results of the numerical model were essentially identical to the heights interpreted from the experiments for all of the unit cell geometries evaluated.
6. Calculated peak load transfer to the columns, expressed as a ratio of the peak column stress to the initial column stress, CSR_{max}, increased as the friction angle and dilation angle were simultaneously increased. CSR_{max} also increased as sample height increased.
7. For the conditions evaluated, calculated peak load transfer occurred at base settlements that were a small percentage of the column diameter. When the assigned dilation angle was greater than zero, peak load transfer occurred at base settlements that were less than one percent of the column diameter for the range of sample heights evaluated. When the assigned dilation angle was equal to zero, the base settlement at peak load transfer increased sharply as sample height increased.

7 Integrated Findings

This chapter incorporates the findings from the literature review (Chapter 2), experimental testing (Chapters 3, 4, and 5) and numerical modeling (Chapter 6). The findings discussed herein pertain to critical height, surface settlement above and below the critical height, and the magnitude of base deformation at peak load on the columns.

The primary goals of the integrated analysis are to:

1) Validate the relationship between unit cell geometry and critical height observed from the results of the multi-column tests described in Chapter 5.
2) Determine the appropriate extrapolation of surface deformations observed during the bench-scale testing above and below the critical height to other conditions.
3) Demonstrate that the relationship between normalized embankment height, H/d, and the magnitude of maximum base settlement at peak soil stress on the column, $S_{b,max}$, described in Chapter 4 is similar for single and multi-column arrangements.

Chapter 7 is organized into three sections. Section 7.1 presents and compares values of critical height determined during the experimental testing program, numerical modeling study, and interpreted from previous work by others. Section 7.1 also comments on the contribution of reinforcement and stiff near-surface foundation materials on differential surface settlement. Section 7.2 compares the surface deformations measured above and below the critical height during the current bench-scale test program to surface deformations observed at the laboratory scale and field scale. Section 7.2 also provides some observations about surface deformations calculated using 2D and 3D numerical models. Section 7.3 compares the stress-displacement relationships observed during the single column tests described in Chapter 4 and observed by others for embedded anchors to the column stress-displacement relationships observed by others for multi-column arrangements.

7.1 Critical Height

As defined in Section 1.4, critical height, H_{crit}, is the height of the embankment or sample where $DSBR_d$ reaches zero. In Chapter 2, the results from 53 experimental and numerical studies performed by others as well as 24 published case histories were reviewed and summarized. Of

these sources, critical heights were determined for five square unit cell geometries, one triangular unit cell geometry, one axisymmetric geometry, and seven plane strain geometries. In addition, case histories and the results of 16 experimental studies were interpreted with respect to surface deformation by evaluating whether differential surface settlement was reported for the type of unit cell geometry and embankment height present. In Chapter 5, critical heights were determined for five square unit cell geometries with area replacement ratios, A_s, ranging from 1 to 26 percent. In Chapter 6, a 3D numerical modeling study performed using FLAC3D calculated critical heights that were in very close agreement with the experimental results discussed in Chapter 5 for the five unit cell geometries evaluated.

In Chapter 5, a relationship between critical height and unit cell geometry was developed from the experimental findings. The relationship, which is reproduced below as Equation 7.1, was supported by the results from the numerical modeling study described in Chapter 6. The relationship is validated separately in this chapter against the interpreted results described in Chapter 2 for 3D unit cell geometries and for plane strain and axisymmetric geometries. Figure 7.1 shows the relationship between unit cell geometry and critical height given by Equation 7.1 as a solid black line along with the critical heights determined from the current study and the critical heights interpreted from other published studies for 3D unit cell geometries. Critical heights are indicated in the figure using open diamond symbols. In some cases, there was insufficient data to 'pinpoint' a single value for the critical height, so the possible range for the critical height was determined and provided on the plot as two symbols connected by a vertical line. Also included in Figure 7.1 are points representing the spanning ratio and normalized embankment height for the conditions described in the case histories and experimental studies. Open circular symbols are used for cases where no differential surface settlement was reported in the published source and filled black square symbols are used for cases that did report differential surface settlement. As described in Section 2.4, in some cases, the embankment surface was described as having 'insignificant' differential settlement or the embankment was reported to be in service without any problems. These instances were interpreted as not having differential surface settlement. The data labels adjacent to each symbol in Figure 7.1 refer to the sources listed in Tables 7.1 through 7.3, which are adapted from Tables 2.7 through 2.9 in Chapter 2. The notes below Table 7.1 also apply to Tables 7.2 and 7.3.

$$\frac{H_{crit}}{d} = 1.15\left(\frac{s'}{d}\right) + 1.44 \qquad (7.1)$$

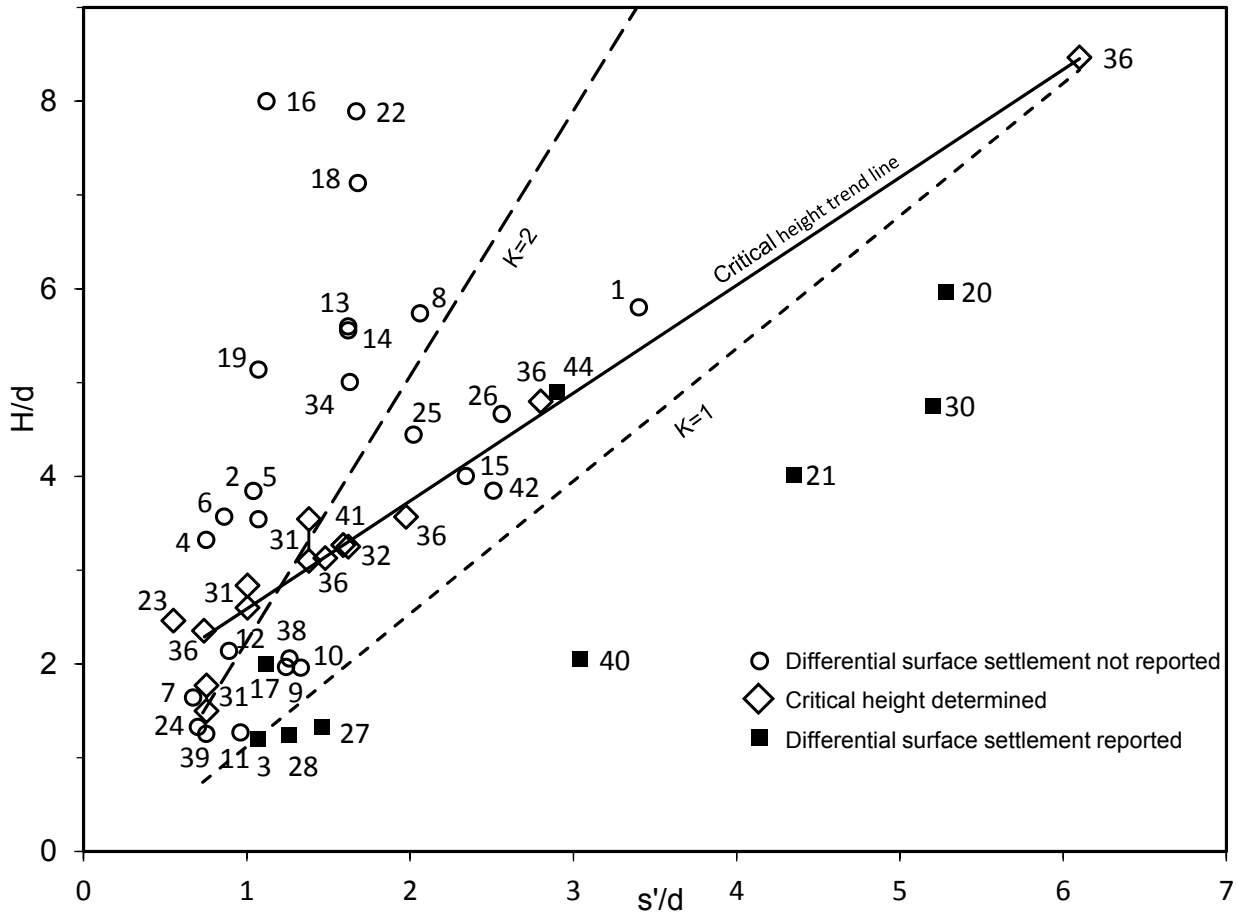

Figure 7.1 Normalized embankment height versus spanning ratio for 3D unit cells. The solid black line is the trend given by Equation 7.1.

Table 7.1 Case histories with reference to data points in Figures 7.1 and 7.2

Ref	Case History	Array type [1]	Column spacing (ft)	Cap diameter or equivalent diameter (ft)	Embankment height (ft)	Spanning Ratio	Reinforcement used in embankment	Differential surface settlement reported
1	Alexiew (2000, 1996)	S	6.23	1.13	6.56	3.40	•	
2	Alexiew (2000)	ET	5.24	1.96	7.54	1.04	•	
3	Camp and Siegel (2006) and S&ME (2004)	ET	8.20	3.00	2.16 to 3.6	1.07	•	•
4	Chen et al. (2010)	S	6.56 to 9.84	3.70 to 5.92	19.68	0.68 to 0.75		
5	Chen et al. (2010)	S	6.56 to 8.20	3.33 to 3.70	13.12	0.89 to 1.07	•	
6	Chen et al. (2010)	T	7.21 to 8.86	4.59	16.40	0.61 to 0.86	•	
7	Chin (1985)	IT	10.49 to 12.47	6.66	10.95 to 18.96	0.48 to 0.67		
	Coghlin (2005)	ET	?	?	?		•	•
8	Collin et al. (2005b)	ET	8.00 to 8.86	2.00	11.48	1.80 to 2.06	•	
9	Gwede and Horgan (2008)	S	8.20	3.33	6.56	1.24	•	
	Han and Akins (2002)	?	8.53 to 9.84	2.25	12.14	?	•	
10	Habib et al. (2002)	ET	8.20	2.59	5.08	1.33	•	
11	Hoppe and Hite (2006)	S	7.00	3.38	4.3 to 6.3	0.96	•	
12	Jones et al. (1990)	S	9.02	4.59	9.84 to 16.40	0.89	•	
13	Liu et al. (2007)	S	9.84	3.28	18.37	1.62	•	
14	Livesey et al. (2008)	R	9.51 x 8.20	2.95	<16.4	1.62	•	
15	Maddison et al. (1996)	ET	7.21 to 8.86	1.80	7.21 to 18.7	1.81 to 2.34	•	
16	Miki (1997)	S	7.54	3.28	26.25	1.12		
17	Miki (1997)	S	7.54	3.28	5.24 to 6.56	1.12		•
18	Pearlman and Porbaha (2006)	S	3.28	1.38	9.84 to 24.61	1.68	•	
19	Russell and Pierpoint (1997)	S	8.20	3.70	19.02	1.07		
20	Ryan et al. (2004)	R	6.89 x 3.28	0.49 to 0.66	3.94	5.28 to 7.29	•	•
21	Ryan et al. (2004)	R	6.89 x 6.56	0.98	3.94	4.35	•	•
	de Mello et al. (2008)	ET	5.90 to 7.22	2.30	16.4 to 27.9	0.98 to 1.31		
22	Smith (2005), Stewart et al. (2004)	T	6.00 to 10.00	2.66	21	0.8 to 1.67		
23	Ting et. al (1994)	IT	11.15 to 13.78	6.66	10.83 to 19.03	0.55 to 0.79		•
OC [2]	Ting et. al (1994)	S	4.72	2.22	49.21	1.00		
24	Ting et. al (1994)	S	5.90 to 7.54	2.96 to 4.44	5.90 to 18.04	0.70 to 0.91		
25	Wood et al. (2004)	S	8.86 to 10.50	2.95	13.12 to 31.17	1.62 to 2.02	•	

Notes:
1. A key for interpreting array type is provided in Chapter 2
2. OC means that the data point plots off the chart above the trend line

Table 7.2 Experimental studies with reference to data points in Figures 7.1 and 7.2

Ref	Experimental studies	Array type	Column spacing (ft)	Cap diameter or equivalent diameter (ft)	Embankment height (ft)	Spanning Ratio	Reinforcement used in embankment	Differential surface settlement reported
26	Abdullah and Edil (2007a)	S	8.20 to 10.66	2.46	11.48	1.86 to 2.56	•	
27	Almeida et al. (2008, 2007)	S	8.2	2.96	3.94	1.46	•	•
28	Almeida et al. (2008)	S	9.20	3.70	4.59	1.26	•	•
30	Chew et al. (2004)	R	6.82 x 3.94	0.69	1.64 to 3.28	5.20	•	•
33	Fluet et al. (1986)	P	15.42	8.20	4.92	0.44	•	•
34	Hossain and Rao (2006)	S	3.94	1.31	6.56	1.63		
37	Miki (1997)	P	4.26 to 7.54	3.28	6.56	0.15 to 0.65		
OC	Oh and Shin (2007)	S	1.97	0.56	8.86	1.99		
OC	Oh and Shin (2007)	S	1.97 to 3.11	0.56	8.86	1.99 to 3.43	•	
38	Quigley et al. (2003)	ET	9.02	2.95	6.07	1.26	•	
39	Rogbeck et al. (1998)	S	7.87	4.44	5.58	0.75		
40	Sloan (2011)	S	10.00	2.00	4.10	3.04	•	•
42	Van Eekelen et al (2008)	S	4.17	0.98	3.77	2.51		
43	Van Eekelen et al (2003)	P	3.77	0.49	2.30	3.33		•
44	Villard et al. (2004)	ET	3.94	0.67	1.64 to 3.28	2.90	•	•
OC	Xu et al. (2007)	ET	6.56	1.31	20.64	2.39	•	

Table 7.3 Critical heights with reference to data points in Figures 7.1 and 7.2

Ref	Reference	(E)Xperimental study, (N)umerical study, (C)ase history	Reinforcement Array Type		Column spacing,s (in.)	Column diameter, d [1] (in.)	Spanning ratio, s'/d	Critical height, H_{crit} [2] (in.)	H_{crit}/d
36	Current Study	E	S		3.50	2.00	0.74	4.72	2.36
36	Current Study	E	S		3.50	1.25	1.48	3.91	3.13
36	Current Study	E	S		7.00	2.00	1.97	7.14	3.57
36	Current Study	E	S		3.50	0.75	2.80	3.60	4.80
36	Current Study	E	S		7.00	0.75	6.10	6.35	8.47
29	Chen et al. (2008)	E	P		29.53	5.90	2.00	33.07 to 37.80	5.60 to 6.41
31	Demerdash (1996)	E	S	•[3]	23.62	8.88	1.38	27.53 to 31.52	3.10 to 3.55
31	Demerdash (1996)	E	S	•[4]	23.62	8.88	1.38	25.31 to 31.52	2.85 to 3.55
31	Demerdash (1996)	E	S	•[5]	23.62	8.88	1.38	27.08 to 31.52	3.05 to 3.55
31	Demerdash (1996)	E	S	•[3]	23.62	11.11	1.00	28.89 to 31.55	2.60 to 2.84
31	Demerdash (1996)	E	S	•[3]	23.62	13.33	0.75	20.00 to 23.59	1.50 to 1.77
45	Demerdash (1996)	N	P	•	78.74	39.37	0.91	118.00	3.00
45	Demerdash (1996)	N	P	•	118.11	39.37	1.62	157.00	4.00
45	Demerdash (1996)	N	P	•	157.48	39.37	2.33	236.00	6.00
32	Ellis and Aslam (2009a,b)	E	S		118.11	39.98	1.59	130.63	3.27
46	Han and Gabr (2002)	N	A	•	118.11	27.56	1.64	118.11	4.29
35	Jenck et al. (2007)	E,N	P		12.60	3.94	1.10	10.24 to 13.40	2.60 to 3.40
35	Jenck et al. (2007)	E,N	P		17.72	3.94	1.75	15.76 to 19.70	4.00 to 5.00
35	Jenck et al. (2007)	E,N	P		25.60	3.94	2.75	15.76 to 23.64	4.00 to 6.00
41	Sloan (2011)	E	S	•	72.00	24.00	1.62	78.00	3.25
23	Ting et al. (1994)	C	IT		133.86	79.92	0.55	196.85	2.46

Notes:

1. Square pile caps are expressed as circular caps of equal area
2. Range of heights reflect max. and min. interpretation of data. See corresponding appendices for details.
3. Default reinforcement stiffness. See Appendix E for details.
4. 1/3 of default reinforcement stiffness. See Appendix E for details.
5. 4/7 of default reinforcement stiffness. See Appendix E for details.

Based on the results in Figure 7.1, the following statements can be made for 3D unit cell geometries:

1. The critical heights interpreted from experiments and case studies generally agree with the trend given by Equation 7.1
2. All of the cases where differential surface settlement was reported fall below or touch the trend line.
3. A majority of the cases where differential surface settlement was not reported are above the trend line.

The primary implication from the above statements is that the relationship between critical height and unit cell geometry determined from the multi-column experiments described in Chapter 5 and the numerical study described in Chapter 6 can be reasonably applied to cases with different scale, embankment material properties, reinforcement condition, and whether base settlement is uniform or non-uniform. This means that critical height is primarily controlled by unit cell geometry, which can be normalized and expressed as the spanning ratio.

When the data for plane strain conditions is plotted in the same manner as Figure 7.1, the critical heights plot consistently above the trend line from Equation 7.1. If a factor of 1.5 is applied to the spanning ratio, as shown in Figure 7.2, the results fit the trend line reasonably well. As shown in Figure 7.3, there is no out-of-plane support provided by other columns for the plane strain case. This means that a 3D unit cell provides more support to the overlying embankment than a plane strain with the same spanning ratio. Equation 7.2 is the same as Equation 7.1 but includes the adjustment factor of 1.5 applied to the spanning ratio to account for the lack of out-of-plane support.

$$\frac{H_{crit}}{d} = 1.15\left(1.5\frac{s'}{d}\right)_{2D} + 1.44 \qquad (7.2)$$

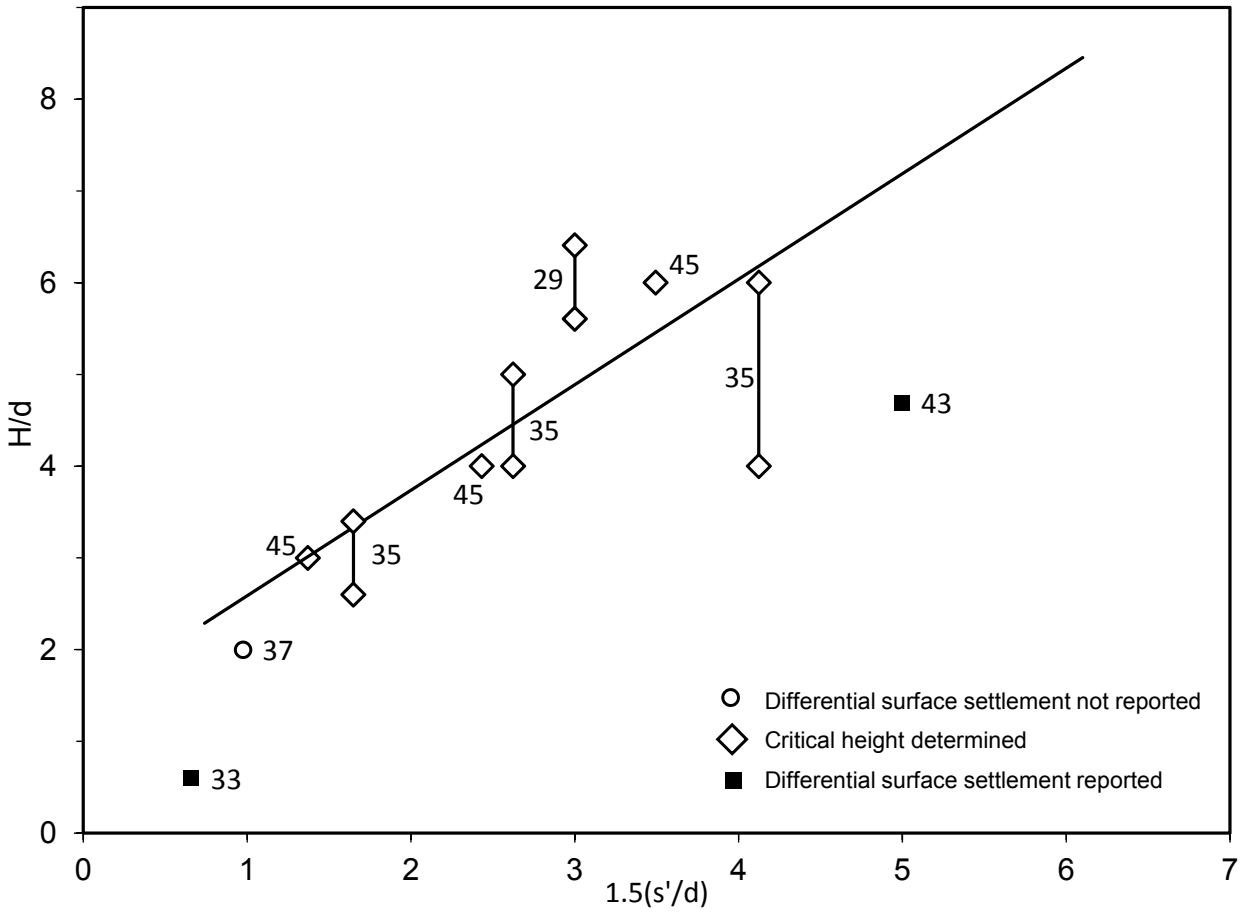

Figure 7.2 Normalized embankment height versus spanning ratio for plane strain geometries. The solid black line is the trend given by Equation 7.2.

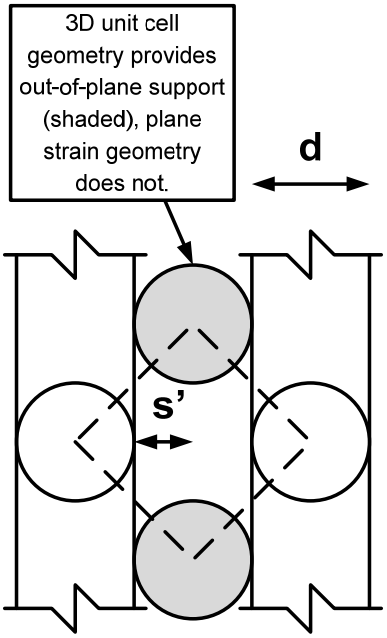

Figure 7.3 Difference in support provided by plane strain and 3D unit cell geometries with the same spanning ratio

The numerical study performed by Han and Gabr (2002) provides the only information about critical height for axisymmetric conditions. The geometry evaluated by Han and Gabr (2002) had a spanning ratio equal to 1.64 which, according to Equation 7.1, translates to a normalized critical height equal to 3.33. The normalized critical height interpreted from Han and Gabr's analyses is equal to 4.29. A spanning ratio equal to 2.48, is needed in Equation 7.1 to calculate a normalized critical height equal to 4.29. A spanning ratio of 2.48 is 1.51 times larger than the value of 1.64 determined using the definition of spanning ratio for axisymmetric conditions provided in Chapter 1. In their analysis, Han and Gabr (2002) used the axisymmetric approximation to study a square unit cell with an area replacement ratio of 5.4 percent. Using the relationships between area replacement ratio and spanning ratio provided in Table 1.2, the left side of Table 7.4 provides the spanning ratios at increasing levels of area replacement for square, isosceles triangular, equilateral triangular, and axisymmetric unit cell geometries. The last three columns of the right side of Table 7.4 provide the ratio of the spanning ratio for 3D geometries to the spanning ratio of an axisymmetric geometry. At an area replacement ratio of 5.4 percent, the spanning ratio for an axisymmetric geometry is 1.33 times larger than the spanning ratio for a square unit cell geometry with equivalent area replacement. While 1.33 is smaller than the factor of 1.51 needed for Equation 7.1 to correctly predict the normalized critical height interpreted from Han and Gabr's results, it demonstrates that differences in spanning ratio between the 3D geometry and the axisymmetric approximation may explain why Equation 7.1 is not directly

applicable to the axisymmetric case. Additional numerical analyses using a range of axisymmetric geometries are needed to fully explain this issue.

Table 7.4 Comparison of spanning ratios at various area replacement ratios for 3D and axisymmetric unit cell geometries

	Spanning Ratio, s'/d				$(s'/d)_{3D}/(s'/d)_{axi}$		
	3D arrays						
As %	Square	Isosceles Triangular (s_1=s_2)	Equilateral Triangular	Axisymmetric	Square	Isosceles Triangular (s1=s2)	Equilateral Triangular
1	5.77	5.04	5.00	4.50	1.28	1.12	1.11
2	3.93	3.42	3.39	3.04	1.30	1.13	1.12
4	2.63	2.27	2.25	2.00	1.32	1.13	1.12
6	2.06	1.76	1.74	1.54	1.34	1.14	1.13
8	1.72	1.46	1.44	1.27	1.35	1.15	1.14
10	1.48	1.25	1.24	1.08	1.37	1.16	1.15
12	1.31	1.10	1.09	0.94	1.39	1.16	1.15
14	1.17	0.98	0.97	0.84	1.40	1.17	1.16
16	1.07	0.88	0.87	0.75	1.42	1.18	1.17
18	0.98	0.81	0.80	0.68	1.44	1.19	1.17
20	0.90	0.74	0.73	0.62	1.46	1.19	1.18
24	0.78	0.63	0.62	0.52	1.50	1.21	1.20
28	0.68	0.55	0.54	0.44	1.54	1.23	1.21
32	0.61	0.48	0.47	0.38	1.58	1.25	1.23

For the cases in Figures 7.1 and 7.2 that fall below the trend line, the published sources were checked to see if the embankments were reinforced and whether stiff near surface foundation materials were reported. Examples of stiff near-surface materials include permanent working platforms, existing fill, natural sand deposits, and desiccated clay crusts. Table 7.4 summarizes the findings for the cases that fall below the trend line in Figure 7.1. As shown in Figure 7.4, of the cases falling below the trend line that reported stiff near surface materials, only 33 percent indicated differential surface settlement. When stiff near surface materials were not reported, 62 percent of cases falling below the trend line indicated differential surface settlement. The results were more evenly split for the influence of reinforcement with 56 percent of the cases falling below the trend line experiencing differential surface settlement. Four cases without reinforcement fell below the trend line and one of the cases experienced differential surface settlement.

These findings suggest that the likelihood of an embankment experiencing significant differential surface settlement decreases when stiff near-surface materials are present. Filz and Smith (2006) noted the benefits of stiff near-surface materials in reducing foundation settlement. The stiff materials transfer embankment loads to the columns and occupy space where vertical stress change in the foundation soil is highest. Furthermore, the load transfer mechanisms in near-surface soils, including arching within the soil and skin friction between the soil and column, require little deformation to be mobilized. These factors can considerably reduce compression of the underlying soft foundation soils, which can result in differential surface settlement being reduced to insignificant levels.

Reinforcement, which initially provides no out-of-plane stiffness, requires considerably more vertical deformation before load transfer to the column occurs. This means that, unless measures are taken, such as those described in Gwede and Horgan (2008), to deform and develop strain in the reinforcement prior to completing the embankment, there is opportunity for significant base settlement to occur and be expressed at the ground surface, even with basal reinforcement.

Table 7.5 Reinforcement and near-surface soil conditions for data points falling below trend line in Figures 7.1 and 7.2

Ref	Reference	Reinforcement	Stiff near-surface materials reported	Differential surface settlement
27	Almeida et al. (2008)	•	~3 ft working platform	•
28	Almeida et al. (2008, 2007)	•	~3 ft working platform	•
3	Camp and Siegel (2006) and S&ME (2004)	•	About 6.6 ft of existing sand fill	•
30	Chew et al. (2004)	•	No subgrade support	•
7	Chin (1985)		Not reported	
33	Fluet et al. (1986)	•	None, adjustable pneumatic base	•
9	Gwede and Horgan (2008)	•	Temp. working platform removed, compressible peat placed between caps, LTP surcharged prior to surfacing	
10	Habib et al. (2002)	•	Not reported	
11	Hoppe and Hite (2006)	•	18 ft of silty sand fill (SPT N = 5-9)	
12	Jones et al. (1990)	•	Working platform shown in cross section	
15	Maddison et al. (1996)	•	0.98 ft working platform + dessicated clay crust	
17	Miki (1997)		Not reported	•
37	Miki (1997)		None, moveable base support	
38	Quigley et al. (2003)	•	1.3 ft working platform + dessicated clay crust	
39	Rogbeck et al. (1998)		3 to 10 ft of existing fill	
20	Ryan et al. (2004)	•	Not reported	•
21	Ryan et al. (2004)	•	Not reported	•
40	Sloan (2011)	•	No subgrade support	•
24	Ting et. al (1994)		Not reported	
43	Van Eekelen et al (2003)		None, compressible foam rubber	•
42	Van Eekelen et al (2008)		Not reported	
44	Villard et al. (2004)	•	No subgrade support	•

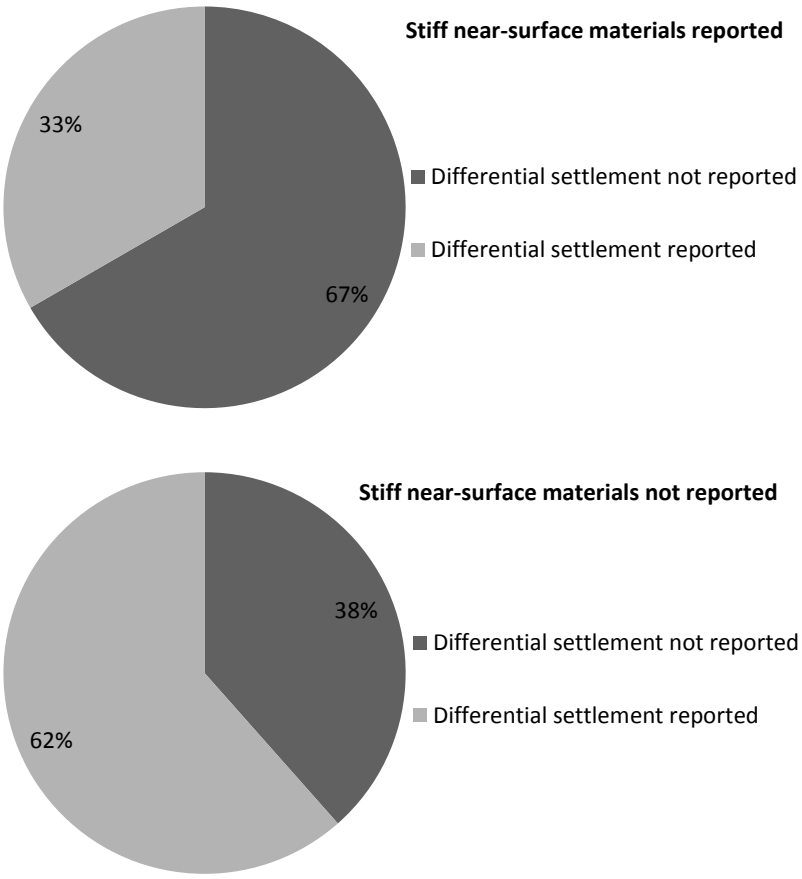

Figure 7.4 Pie charts showing the association between reported stiff near-surface soils and reported differential surface settlement for cases listed in Table 7.4

Sloan (2011) determined critical height from his field-scale experiments before and after the embankment surface was trafficked by a small skid-steer loader. The critical height determined before trafficking, which is shown in Figure 7.1, falls on the trend line given by Equation 7.1. The critical height determined after trafficking, which is not shown in Figure 7.1, is higher than the before trafficking case and thus would plot above the trend line. The only critical height data plotted on Figure 7.1 that includes the influence of traffic is from the case history described by Ting el al. (1994) (Reference #23 on the plot) and it too plots slightly above the trend line. Table 7.5 summarizes the critical heights determined from the studies by Sloan (2011) and Ting et al. (1994) before and after traffic loading.

Table 7.6 Critical heights determined for 3D unit cells with the influence of traffic loading

Case	Author	H_{crit}/d before traffic predicted using Eq. 7.1	Measured H_{crit}/d after traffic	Ratio H_{crit}/d (after/before traffic)	Difference in critical height, ft (after - before traffic)
41	Sloan (2011)	3.30 (3.25 meas.)	3.75	1.14 (1.15 meas.)	0.9 (1.0 meas.)
23	Ting et al. (1994)	2.07	2.46	1.19	2.6

The increase in critical height due to traffic is likely sensitive to the unit cell geometry and the intensity and dynamic characteristics of the traffic loading. It is hypothesized here that the increase in critical height due to traffic decreases as the critical height before trafficking and column diameter increases. A possible relationship to account for the influence of traffic is given below as Equation 7.3, where $H_{crit,traffic}$ is the critical height under design traffic conditions, κ is a coefficient that depends on the nature of the design traffic loading, and H_{crit} is determined using either Equation 7.1 or 7.2. Equation 7.3 is provided to illustrate the concept only since currently there is not sufficient data to develop reliable values of κ.

$$H_{crit,traffic} = H_{crit} + \frac{\kappa \cdot s'}{H_{crit}} \tag{7.3}$$

In Table 7.6, the observed increases in critical height due to traffic are less than 20 percent. The fact that none of the cases reporting differential surface settlement plot above the trend line and the fact that some of the cases located close to the line not reporting differential surface settlement, such as Case 15, included traffic, suggest that the increase in critical height due to traffic does not exceed 20 percent of the before-traffic value for typical embankment geometries and roadway traffic conditions. Research by Heitz (2006) and Zaeske (2001), described briefly in English by Raithel et al. (2008), indicates that soil arching is not strongly affected when traffic loading is less than about 300 psf.

7.2 Surface Deformations

This section describes findings related to surface deformation for cases that are above and below the critical height. Surface settlements are described using the settlement ratios defined in Table 1.5 of Section 1.4. As discussed in Chapters 4 and 5, SBR_c $DSBR_d$, and SRB_{tot} can be

approximated as being independent of base settlement magnitude for a particular combination of unit cell geometry, sample height, and reinforcement condition. Below the critical height, the ratio SBR_c is primarily controlled by the sample height and the column diameter. Equations 5.5 and 5.6 provide relationships between SBR_c and the ratio of sample height to column diameter, H/d. The ratio $DSBR_d$ is primarily controlled by column spacing, column diameter, sample height, and reinforcement condition. Equation 5.13 provides a relationship among $DSBR_d$, unit cell geometry, and sample height for unreinforced samples. In the review of previous research discussed in Chapter 2, studies by Demerdash (1996), Fadl (1981), and Sloan (2011) were identified as providing measurements of surface and base deformation that can be interpreted as the settlement ratios SBR_c, $DSBR_d$, and SBR_{tot}.

Section 7.2 is divided into four parts: Section 7.2.1 describes findings related to SBR_c, Section 7.2.2 describes findings related to $DSBR_d$, Section 7.2.3 describes findings related to SBR_{tot}, and Section 7.2.3 discusses some observations regarding surface deformations calculated using numerical modeling methods.

7.2.1 Surface settlement over the column axis

The laboratory experiments performed by Fadl (1981) studied the load-displacement response of embedded anchors in dry sand. Since the behavior of embedded anchors during pullout is analogous to base settlement occurring around a single column, Fadl's results were used to validate the single column experiments described in Chapter 4. As described in Chapter 2, Fadl's results, expressed as SBR_c, showed good correspondence to the current single column experiments. The key figure from Chapter 2 showing the correspondence between Fald's results and the current single column test results is reproduced below as Figure 7.5. For the multi-column tests described in Chapter 5, it was observed that values of SBR_c determined at low normalized sample height, where there is minimal interaction between adjacent columns, are essentially the same as values measured for a single column test with the same normalized sample height. Therefore, Fadl's experimental results indirectly validate measurements of SBR_c from the multi-column experiments at low embankment heights.

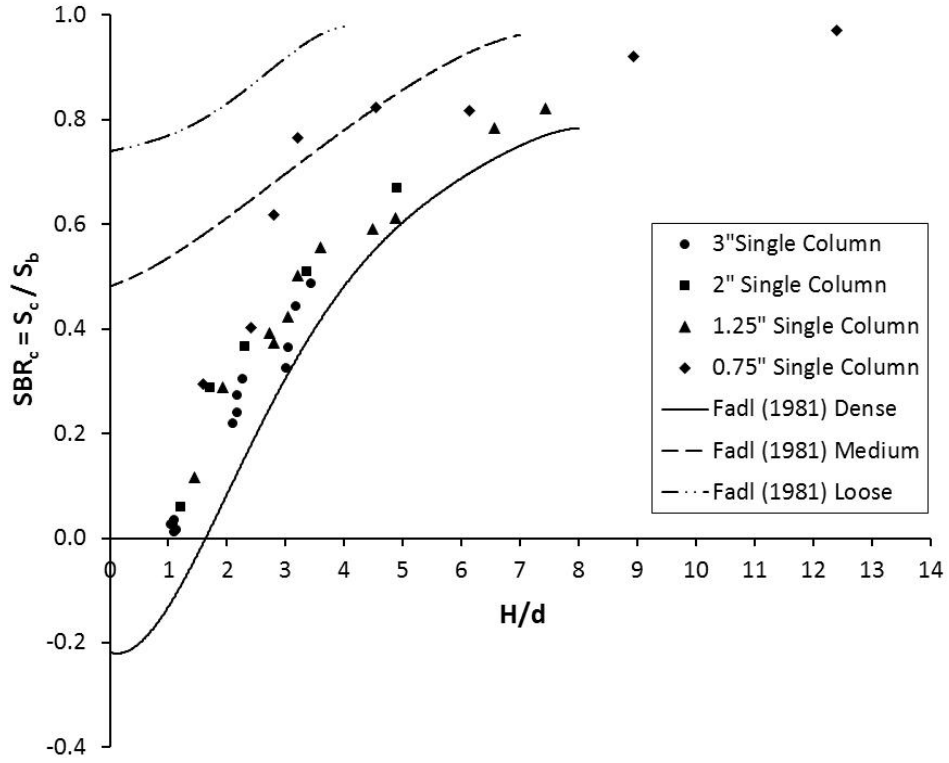

Figure 7.5 Settlement ratio, SBR_c determined using results by Fadl (1981) with overlay of measurements from single column test results described in Chapter 4

The laboratory-scale tests performed by Demerdash (1996) are summarized in Appendix E. Some key differences between Demerdash's experiments and the multi-column tests described in Chapter 5 are: 1) Demerdash's experimental scale is larger than the bench-scale experiments, 2) base settlement is uniform for the bench-scale experiments and non-uniform for Demerdash's experiments, and 3) material properties of the sand and reinforcement. Figure 7.6 shows the comparison of Demerdash's measurements, expressed as SBR_c, to values of SBR_c measured from the multi-column tests. The number and letter combinations in the legend correspond to the unit cell geometry and type of reinforcement used for the experiment. Appendix E provides detailed information about each geometry and reinforcement material used in Demerdash's experiments. The comparison shows that there is good agreement between Demerdash's results and the bench-scale tests when normalized sample height is greater than about 2. Below H/d =2, Demerdash's measurements suggest that SBR_c levels off at about 0.2, while the current tests indicate that SBR_c reaches zero at H/d equal to unity. The agreement between the current results and those by Demerdash suggests that SBR_c is not significantly affected by change from bench-scale to laboratory scale and from uniform to non-uniform base settlement.

The field-scale measurements of SBR_c by Sloan (2011) before trafficking are also shown in Figure 7.6 and are considerably lower than the values measured in the current study multi-column tests and by Demerdash (1996). As shown in Figure 7.7, Sloan (2011) found that trafficking the embankment surface increased SBR_c by only 0.06 to 0.08. Since the before traffic values of SBR_c are so small, the percentage increase due to trafficking is very large. Given the available data, it is not clear how to update Equations 5.5 and 5.6 to account for the influence of traffic loading.

A possible explanation for the discrepancy between the field-scale experiments by Slaon (2011) and the experiments at reduced scale is that higher confining stress associated with the field-scale tests reduces compliance in the material overlying the columns. Another significant difference is that Sloan (2011) used a dense-graded aggregate at field moisture content for constructing the embankment while the reduced-scale experiments used dry sand.

In light of these findings, it appears that Equations 5.5 and 5.6 in Chapter 5 can reasonably be applied to laboratory conditions using dry sand whether base settlement is uniform or not, but it is unclear whether predicted values of SBR_c are applicable to typical field conditions.

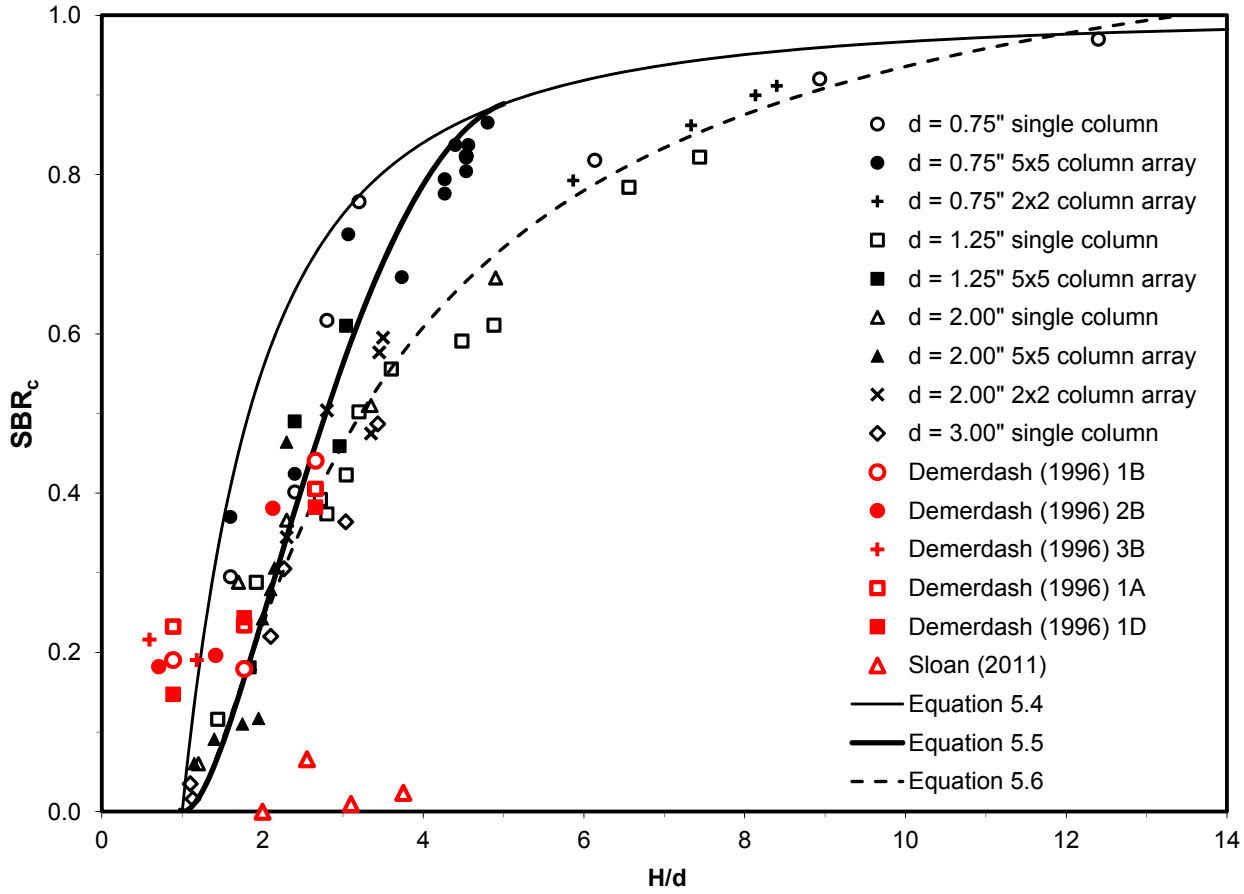

Figure 7.6 SBRc versus normalized sample height from current bench-scale multi-column tests, laboratory-scale experiments by Demerdash (1996), and field-scale experiments by Sloan (2011).

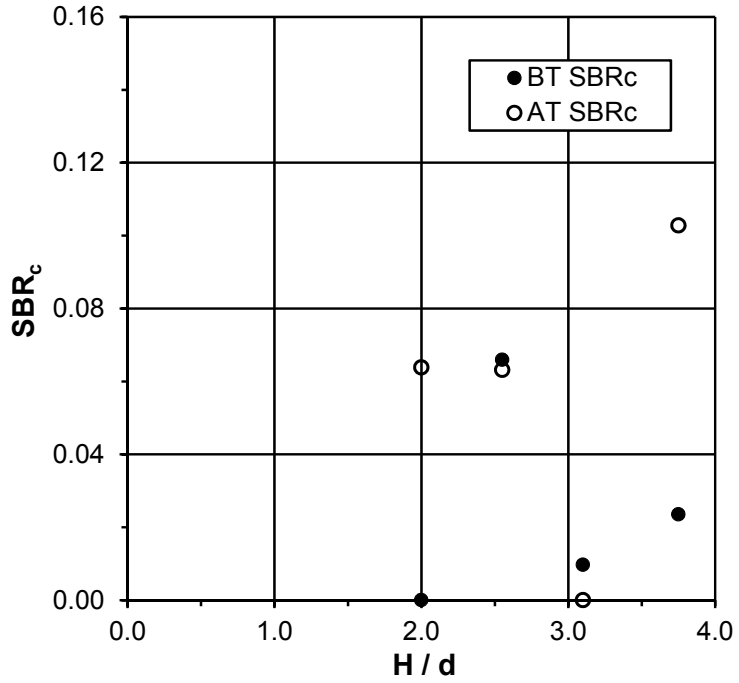

Figure 7.7 SBRc measured by Sloan (2011) before (BT) and after (AT) trafficking the embankment surface

7.2.2 Differential surface settlement

In Chapter 5, the angle β was defined in order to describe the rate at which $DSBR_d$ increases as normalized sample height is decreased below the critical height. Measured values of β from the bench-scale experiments are shown in Figure 7.8 along with the trend line between β and spanning ratio for unreinforced samples. The results show that reinforcement decreases β, which indicates reduced differential surface settlement, particularly at high values of spanning ratio. The results discussed in Chapter 5 also indicate that initial relative density did not consistently affect β over the range of densities evaluated. For unreinforced samples below the critical height, a relationship, given by Equation 5.13, was found among unit cell geometry, sample height, and differential surface settlement. Equation 5.13 is not directly applicable to field conditions since base settlement is typically non-uniform. The testing conditions used by Demerdash (1996) and Sloan (2011) did not include subgrade support, so the deflected shape of the reinforcement under the weight of the embankment defined the settlement of the base. Many authors, including Demerdash (1996) and Sloan (2011), assume that the deflected shape of the reinforcement is parabolic when viewed in two dimensions. The resulting values of β for these cases are provided in Figure 7.8. When base settlement is non-uniform, $DSBR_d$ is defined as the ratio of the differential surface settlement (S_d-S_c) to the maximum base settlement, $S_{b,d}$, which

occurs distance s' from the edge of any round column. The values of β determined for reinforced experiments with non-uniform base settlement plot below the trend line developed from the un-reinforced bench-scale experiments with uniform base settlement. The trend between β and spanning ratio for reinforced conditions with non-uniform base settlement is conservatively given by the straight dash-dot line in Figure 7.8 and by Equation 7.13. The bounds on Equation 7.13 equate to area replacement ratios for square column arrays from about 9 to 26 percent.

$$\beta = 90 - 10\left(\frac{s'}{d}\right) \text{ for } 0.73 \le \frac{s'}{d} \le 1.62 \qquad (7.13)$$

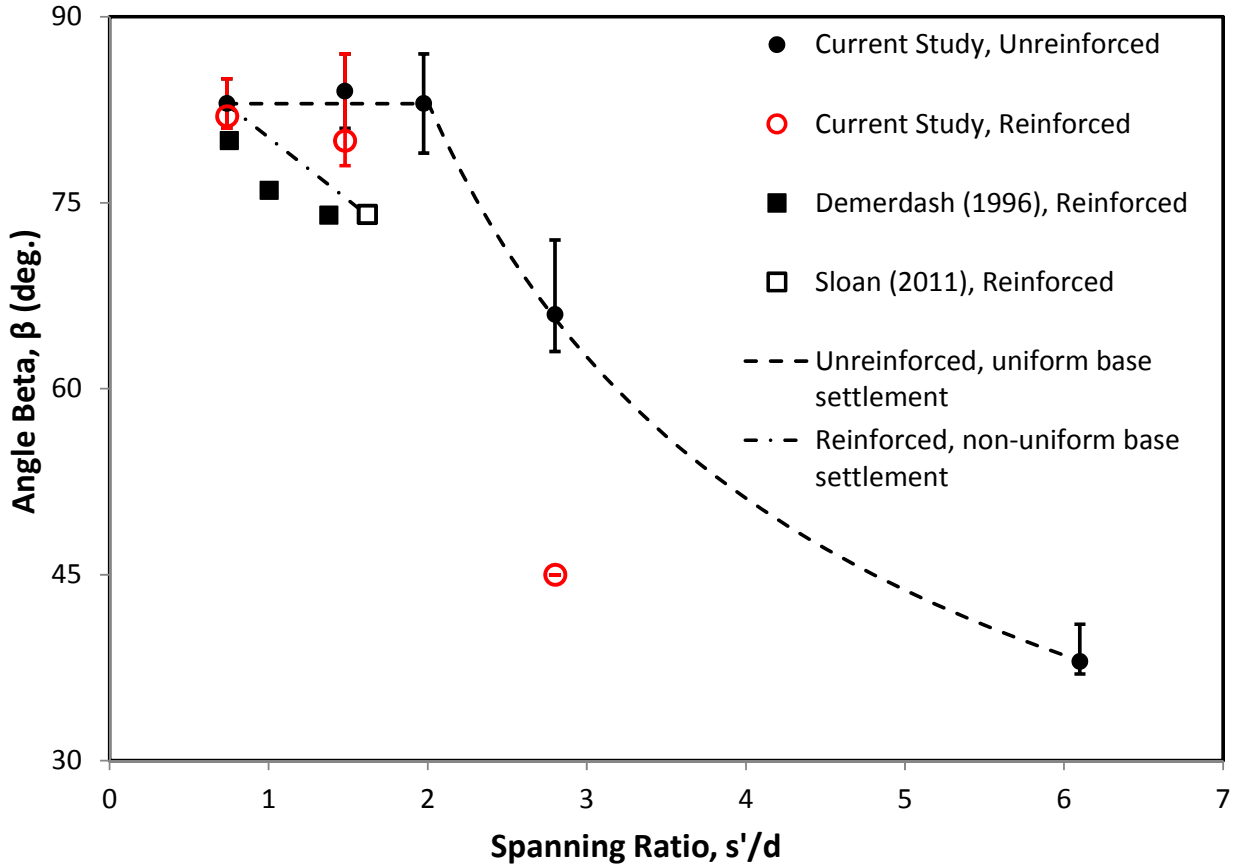

Figure 7.8 Relationship between β and spanning ratio for maximum differential surface settlement

Using the relationship between β and spanning ratio given by Equation 7.13, $DSBR_d$ for cases where base settlement is non-uniform can be estimated by modification of Equation 5.13 to

produce Equation 7.14. As described above, SBR_c in Equation 7.14 can be estimated using Equations 5.5 or 5.6 since Demerdash's measurements of SBR_c for non-uniform base settlement agree fairly well with the bench-scale measurements with uniform settlement.

$$DSBR_d = \min\left\{\left(0.115\frac{s'}{d} - \frac{H}{10d} + 0.144\right)\tan\left(90 - 10\left(\frac{s'}{d}\right)\right), \; 1 - SBR_c\right\} \text{ for } 0.73 \le \frac{s'}{d} \le 1.62 \qquad (7.14)$$

It is hypothesized here that Equation 7.14 is valid regardless of reinforcement stiffness (including zero stiffness) as long as the deformed shape of the base is approximately parabolic in two dimensions as assumed by Demerdash (1996) and Sloan (2011). For example, when there is no subgrade support, the maximum base settlement, $S_{b,d}$ is controlled by the vertical stress acting on the reinforcement, the in-plane tensile stiffness of the reinforcement, and the unit cell geometry. For cases with the same $DSBR_d$, but different reinforcement stiffnesses, the case with the stiffer reinforcement will experience less differential surface settlement since $S_{b,d}$ will be smaller. For field-conditions with subgrade support, the compressibility of the foundation soil will also influence the magnitude of $S_{b,d}$ and thus the magnitude of differential surface settlement. If the shape of the base settlement is somewhere between uniform and a parabola, an estimate of $DSBR_d$ can be made by interpolating between values estimated using Equation 5.13 for uniform settlement and Equation 7.14 for parabolic settlement.

For the bench-scale multi-column tests that included reinforcement, in order for base settlement to remain uniform, sand would have to be able to freely pass through the apertures in the reinforcement. If sand passes freely through the reinforcement, the net vertical stress acting on the reinforcement would be very low. As shown in Figure 4.35 in Chapter 4, reinforcement exhumed from a single column experiment experienced plastic yielding in the vicinity of the column. This observation suggests that net vertical stress on the reinforcement was not very low and, thus, the reinforcement provided vertical support to portions of the overlying sand. If arching of sand grains around the apertures partially or completely supports the overlying sand, base settlement becomes non-uniform with less settlement occurring closer to the columns because the columns support the reinforcement. If the reinforcement completely supports the sand around the column, a void would form between the reinforcement and the rigid base. If the reinforcement partially supported the sand around the column, a zone of low density sand would form between the reinforcement and the rigid base. As described in Section 5.5, samples below the critical height incorporating reinforcement experienced greater volume change than

unreinforced samples. This observation supports the notion that the reinforcement is providing at least partial vertical support to portions of the sample. Russell et al. (2003) describes the condition where portions of the embankment near the columns are primarily supported by the reinforcement while portions away from the columns are supported by the subgrade. The fact that the symbols in Figure 7.8 representing values of β estimated for reinforced multi-column tests with spanning ratios up to about 1.6 fall between the trend for uniform base settlement and parabolic base settlement supports the notion that a portion of the sand is being supported by the reinforcement and a portion is supported by the rigid base.

Sloan (2011) also measured differential surface settlement after trafficking the embankment surface with a small skid-steer loader. As shown in Figure 7.9, trafficking the embankment surface impacts the critical height, however the trend lines through the data before and after trafficking have about the same slope. Since the trend lines have the same slope, they have the same value of the angle β. Reliable methods for estimating SBR_c and H_{crit} after traffic are needed to adapt Equations 5.13 and 7.14 to include the influence of traffic on the value of $DSBR_d$.

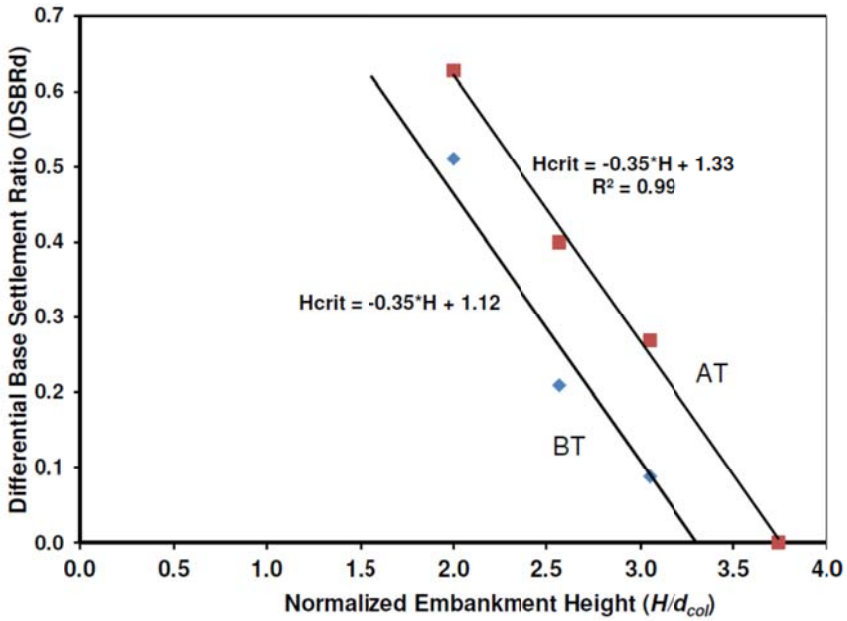

Figure 7.9 Impact of trafficking embankment surface on $DSBR_d$ (from Sloan, 2011 with permission). The equations provided in the figure should read $DSBR_d$ instead of H_{crit} and H/d instead of H. BT = before traffic, AT= after traffic.

7.2.3 Total surface settlement above the critical height

Section 5.4 discusses the ratio of total surface settlement to base settlement measured from the current multi-column experiments. The results were used to adapt a relationship between the maximum base settlement and total surface settlement proposed by Russell et al. (2003) to incorporate the influence of deformation-related volume change in the embankment. As discussed in Section 5.5, the samples from the bench-scale experiments dilated due to differential base settlement. Dilation has the effect of reducing total surface settlement resulting from base settlement. Equation 5.16 incorporates the influence of volume change into the expression proposed by Russell et al. (2003) when base settlement is uniform.

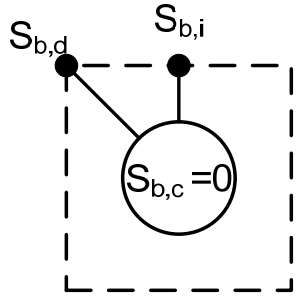

Figure 7.10 Definitions of base settlement locations for square unit cell

Figure 7.10 reintroduces the notation used for base settlement in a square unit cell when base settlement is non-uniform. Table 1.4 in Section 1.4 can be used as a guide for defining base settlement for other unit cell geometries. When base settlement is non-uniform, the average base settlement, $S_{b,avg}$, and the maximum base settlement, $S_{b,d}$, have different values. The maximum base settlement in the unit cell occurs where vertical stress acting on the base is highest and the influence of skin friction provided by the columns is lowest. In plan view, this location at the base corresponds to the location at the surface where support provided by the columns is at a minimum. The average base settlement, $S_{b,avg}$, depends on the distribution of base settlement over the unit cell area. If base settlement is assumed to be parabolic when viewed in two dimensions, the average settlement along a given 2D profile is equal to two thirds of the maximum value. If $S_{b,avg,d}$ and $S_{b,avg,i}$ represent, respectively, the average base settlements along the diagonal and in-line directions and the settlement between these profile directions is assumed to vary parabolically, the average base settlement is given by Equation 7.15. If $S_{b,i}$ is assumed to be proportional to $S_{b,d}$ according to their respective distances from the center of the column, the ratio ($S_{b,i}/S_{b,d}$) has values equal to $1/\sqrt{2}$ and $\sqrt{3}/2$, respectively, for square and equilateral triangular arrays of round columns. Using this assumption and the assumption that S_b varies

parabolically from the diagonal profile to the inline profile, Equation 7.16 expresses the ratio of maximum base settlement to average base settlement for a square array of circular columns when base settlement varies parabolically. The ratio given by Equation 7.16 falls between the range of 1 to 2 recommended by Russell et al. (2003).

$$S_{b,avg} = \frac{2}{3} S_{b,i} + \frac{4}{9}\left(S_{b,d} - S_{b,i}\right) \tag{7.15}$$

$$\frac{S_{b,d}}{S_{b,avg}} = 1.67 \tag{7.16}$$

The influence of parabolically-distributed base settlement can be incorporated into the relationship between unit cell geometry and volume change given by Equation 5.16. If uniform base settlement, S_b, is assumed to have the same influence on total surface settlement as average base settlement, $S_{b,avg}$, Equation 5.16, can be rewritten as Equation 7.17. Dividing Equation 7.17 by $S_{b,d}$ gives an expression for SBR_{tot} that is consistent with the definition by Russell et al. (2003). Substituting the ratio between maximum and average base settlements provided in Equation 7.16 into Equation 7.18 produces the expression for SBR_{tot} when base settlement varies parabolically. Since average base settlement is assumed to have the same influence on total surface settlement as uniform base settlement, the term in Equation 7.19 accounting for volume change can be replaced by the approximations given in Equations 5.17 and 5.18. Equation 7.20 provides the final version of the expression for secant values of SBR_{tot}.

$$S_{tot} = S_{b,avg}\left(1 - A_s\right) - \frac{\Delta V_u}{V_u} H \tag{7.17}$$

$$SBR_{tot} = \frac{1 - A_s}{\left(S_{b,d}/S_{b,avg}\right)} - \frac{\Delta V_u}{V_u}\frac{H}{S_{b,d}} \tag{7.18}$$

$$SBR_{tot} = 0.6\left[1 - A_s - \frac{\Delta V_u}{V_u}\frac{H}{S_{b,avg}}\right] \tag{7.19}$$

$$SBR_{tot} = 0.6\left[1 - A_s - \text{Min}\begin{Bmatrix} 0.38 \\ 0.38\left(A_s/6\%\right) \end{Bmatrix}\right] \tag{7.20}$$

The studies by Demerdash (1996) and Sloan (2011) provide measurements of surface and base settlement above the critical height which can be interpreted to produce secant values of SBR_{tot}. In Chapter 5, secant values of SBR_{tot} were defined as the ratio of the total surface

settlement to the maximum base settlement. In both studies, base settlements were observed by the authors to vary in an approximately parabolic fashion when viewed in two dimensions. Table 7.7 summarizes the secant values of SBR_{tot} extracted from the studies by Demerdash (1996) and Sloan (2011). The number and letter combinations in each entry from Demerdash's study represent the unit cell geometry and type of reinforcement used in the experiment. Appendix E contains the details of each unit cell geometry and reinforcement type used.

Table 7.7 SBR_{tot} calculated for cases with non-uniform base settlement

Case	**A_s (%)**	**S_{tot} (in.)**	**$S_{b,d}$ (in.)**	**$SBR_{tot} = S_{tot}/S_{b,d}$**
Demerdash (1996) 1B	11	0.47	1.10	0.43
Demerdash (1996) 2B	17	0.28	0.79	0.35
Demerdash (1996) 3B	25	0.16	0.49	0.33
Demerdash (1996) 1A	11	0.43	1.46	0.29
Demerdash (1996) 1D	11	0.47	1.22	0.38
Sloan (2011) BT, before traffic	9	0.20	8.50	0.02
Sloan (2011) AT, after traffic	9	1.10	10.70	0.10

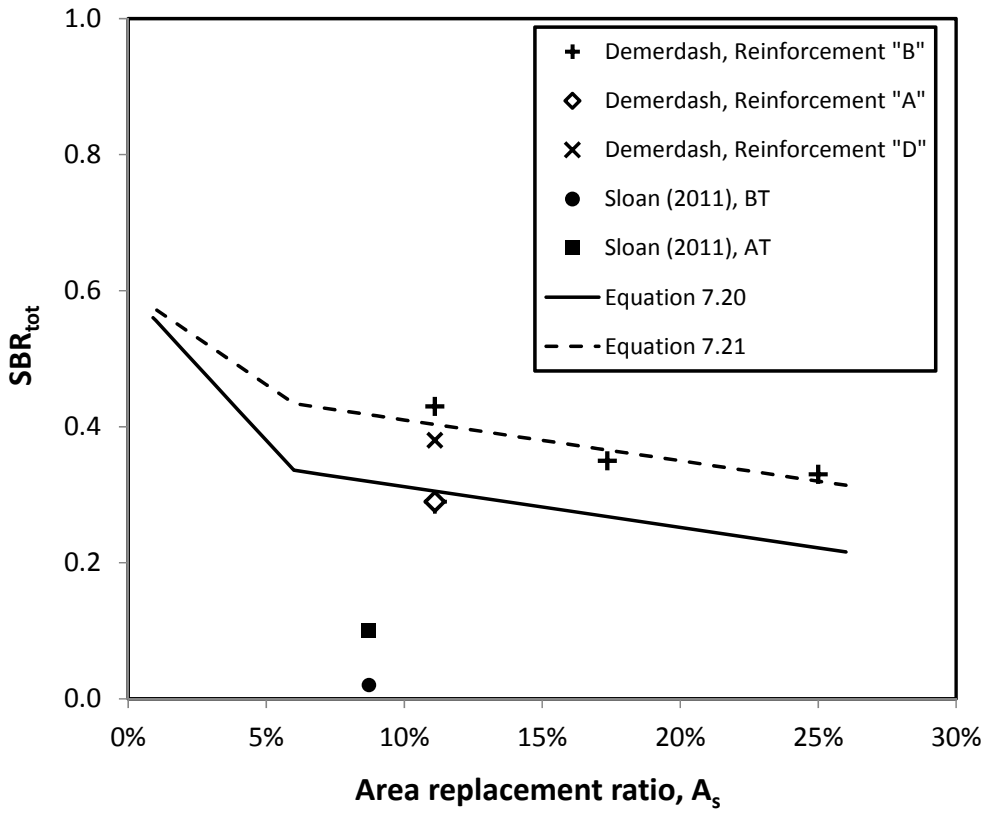

Figure 7.11 SBRtot versus area replacement ratio for cases with base settlement that varies parabolically

Figure 7.11 shows the secant values of SBR_{tot} from Table 7.7 plotted with the trend given by Equation 7.20. The comparison shows that Equation 7.20 does a good job of predicting SBR_{tot} for one case but underpredicts the remainder of the data points from Demerdash (1996) and considerably overpredicts for the data points from Sloan (2011). Equation 7.21 provides a better fit to the data points from Demerdash (1996) for Reinforcement B and D. The fact that the volume change term in Equation 7.21 is smaller than in Equation 7.20 means that, on average, the samples tested by Demerdash dilated less than the samples from the bench-scale tests. This outcome makes sense since the typical confining pressures at the bench-scale are considerably less than the typical confining pressures from the laboratory-scale experiments. The results from the field-scale tests by Sloan (2011) indicate that trafficking the embankment surface increases SBR_{tot}; however, there is not sufficient data to draw a general conclusion on how to adjust values of SBR_{tot} to account for traffic.

$$SBR_{tot} = 0.6\left[1 - A_s - \text{Min}\begin{Bmatrix} 0.22 \\ 0.22\left(A_s/6\%\right) \end{Bmatrix}\right] \tag{7.21}$$

7.2.4 Surface settlements calculated using numerical modeling methods

This section briefly summarizes observations regarding the calculation of surface deformations using numerical modeling methods. Of the numerical studies reviewed in Chapter 2, the plane strain model developed in FLAC2D by Demerdash (1996) was the only study in which calculated surface deformations were compared to experimental measurements. A summary of Demerdash's numerical study is contained in Appendix E. Demerdash found that his numerical model overestimated differential surface settlement compared to the experimental measurements. The greatest discrepancy he observed between the measured and calculated surface settlements was over the column axis, S_c, where the numerical analyses consistently underpredicted settlement. Chapter 6 describes the numerical model developed in FLAC3D that was compared to the multi-column tests described in Chapter 5. The FLAC3D model also consistently underpredicted surface settlement over the column and generally overpredicted differential surface settlement compared to the experimental measurements. Attempts to incorporate strain softening into the model did not resolve the differences between calculated and measured values of SBR_c. The discrepancies between the measured and calculated surface measurements may be due to the inherent limitations of the Mohr-Coulomb constitutive model or of modeling the unit cell as a continuum rather than as discrete elements.

The FLAC3D model described in Chapter 6 did a very good job of calculating critical heights that agreed with the values measured for the five unit cell geometries evaluated with the bench-scale experiments. This agreement suggests that a fairly simple 3D model utilizing a simple linear elastic perfectly-plastic constitutive model can calculate the correct critical height, even though the calculated surface deformations are incorrect.

The available data from the numerical study by Demerdash (1996) does not include a direct comparison of the critical height measured experimentally for square unit cells to the critical height calculated by the numerical model for corresponding plane strain approximations. Figure 7.12 shows the values of normalized critical height measured from Demerdash's laboratory-scale experiments and the calculated values of normalized critical height from Demerdash's plane strain numerical model. The results show that the experimental measurements plot below or touch the trend line while the numerical results consistently plot above the trend line. As discussed in Section 7.1, two dimensional unit cell geometries lack out-of-plane support, which results in higher critical height for the same spanning ratio.

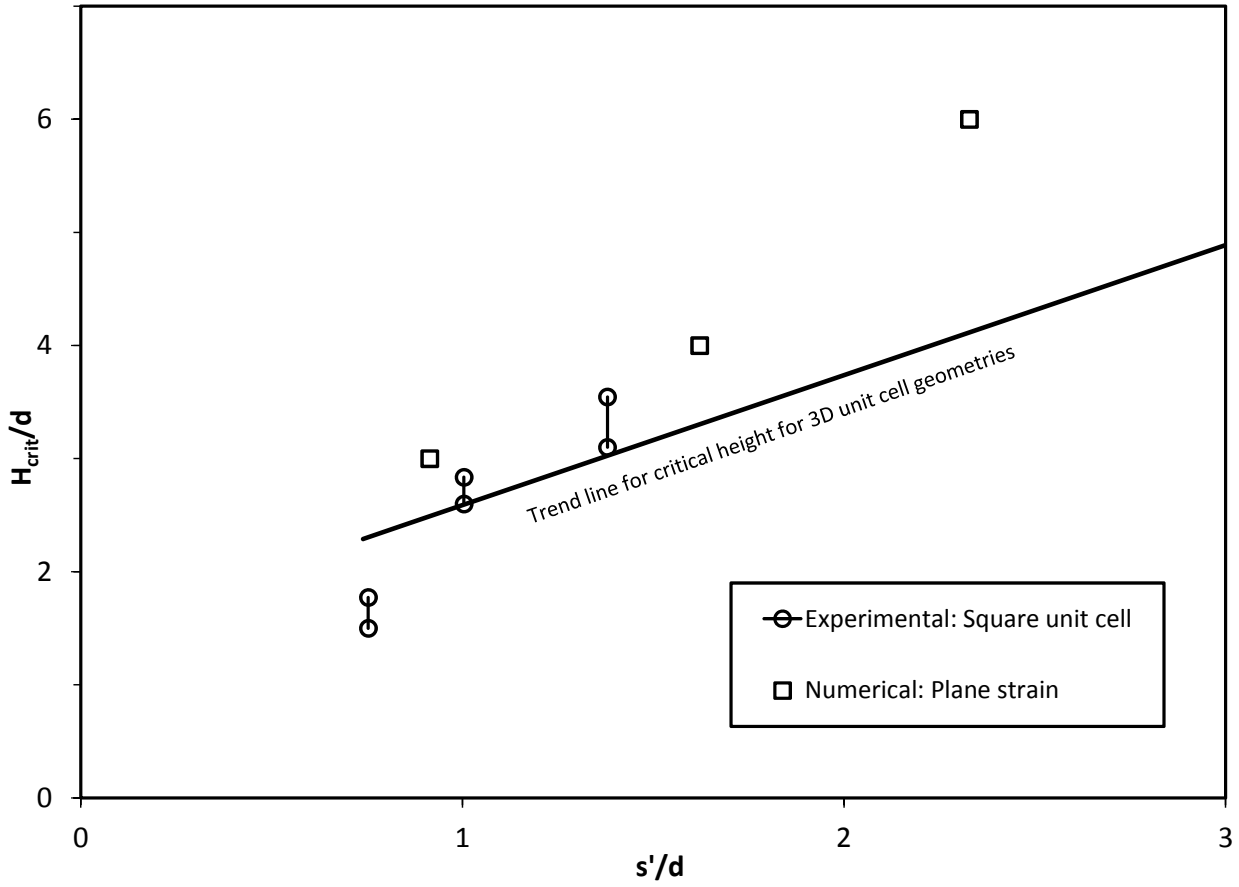

Figure 7.12 Comparison of measured critical heights for 3D unit cell geometries to calculated critical heights for plane strain geometries using data from Demerdash (1996)

7.3 Relationship between Column Stress and Base Settlement

As summarized in Table 7.8, the relationship between vertical stress acting on the column and base settlement was explored in several ways. The literature review described in Chapter 2 focused heavily on the stress-displacement relationship of embedded anchors because there is a considerable amount of research and experimental data in this area that, to the author's knowledge, has not previously been applied to research on column-supported embankments. It is intended that the content in Sections 2.5.3 and 4.3 can serve as a starting point for future research focused on the stress-displacement behavior of columns used in column-supported embankments.

Table 7.8 Summary of information relevant to the relationship between column stress and base settlement

Source	Described in	Provides
Chen et al. (2008)	Section 2.3 and Appendix D	Load-displacement behavior for plane strain conditions
Demerdash (1996)	Section 2.3 and Appendix E	Load-displacement behavior for square unit cell
Published studies on the behavior of embedded anchors	Section 2.5.3	Load-displacement behavior for embedded plate anchors which is analogous to the load-displacement behavior of a single column
Current single column tests	Section 4.3	Load-displacement conditions for a single column.

One aspect discussed here is the relationship between the magnitude of maximum base settlement at peak column stress, $S_{b,max}$, versus sample height. Figure 7.13 provides a plot of available data normalized by column or anchor diameter. Table 7.9 provides a key to interpreting Figure 7.13. For experiments studying embedded anchors, the peak stress on the anchor was treated as the peak column stress and the corresponding anchor displacement was interpreted as the magnitude of base settlement. None of the results shown include load transfer by tension in the reinforcement. Despite the scatter in the data there appears to be a trend, provided in Equation 7.22, suggesting that the magnitude of maximum base settlement at full mobilization of the strength in the sample increases as the normalized sample height increases. Another key finding is that the results from experiments by Demerdash (1996) and Chen (1996), which studied arching in 3D and plane strain conditions, fit within, albeit slightly biased below, the trend of the data from tests using a single column or embedded anchor. This suggests that the displacement to fully mobilize the pullout capacity of an embedded anchor or the push-out capacity of a single column is comparable to the differential base settlement to fully mobilize soil arching in a column-supported embankment.

$$S_{b,max} = (d)\max\begin{Bmatrix} 2\% \\ \frac{2}{3}\left(\frac{4H}{d} - 5\right) \end{Bmatrix} \tag{7.22}$$

In terms of load transfer, it is conservative to treat the change from initial to peak column stress as linear from zero base settlement to $S_{b,max}$. Single column tests in Chapter 4 showed a 36% decline in column stress as base settlement accumulated beyond $S_{b.max.}$ The experimental results using multi-column arrangements by Chen et al. (2008), Demerdash (1996), and Sloan (2011) exhibited a less severe drop in load transfer when base settlement exceeded $S_{b,max}$.

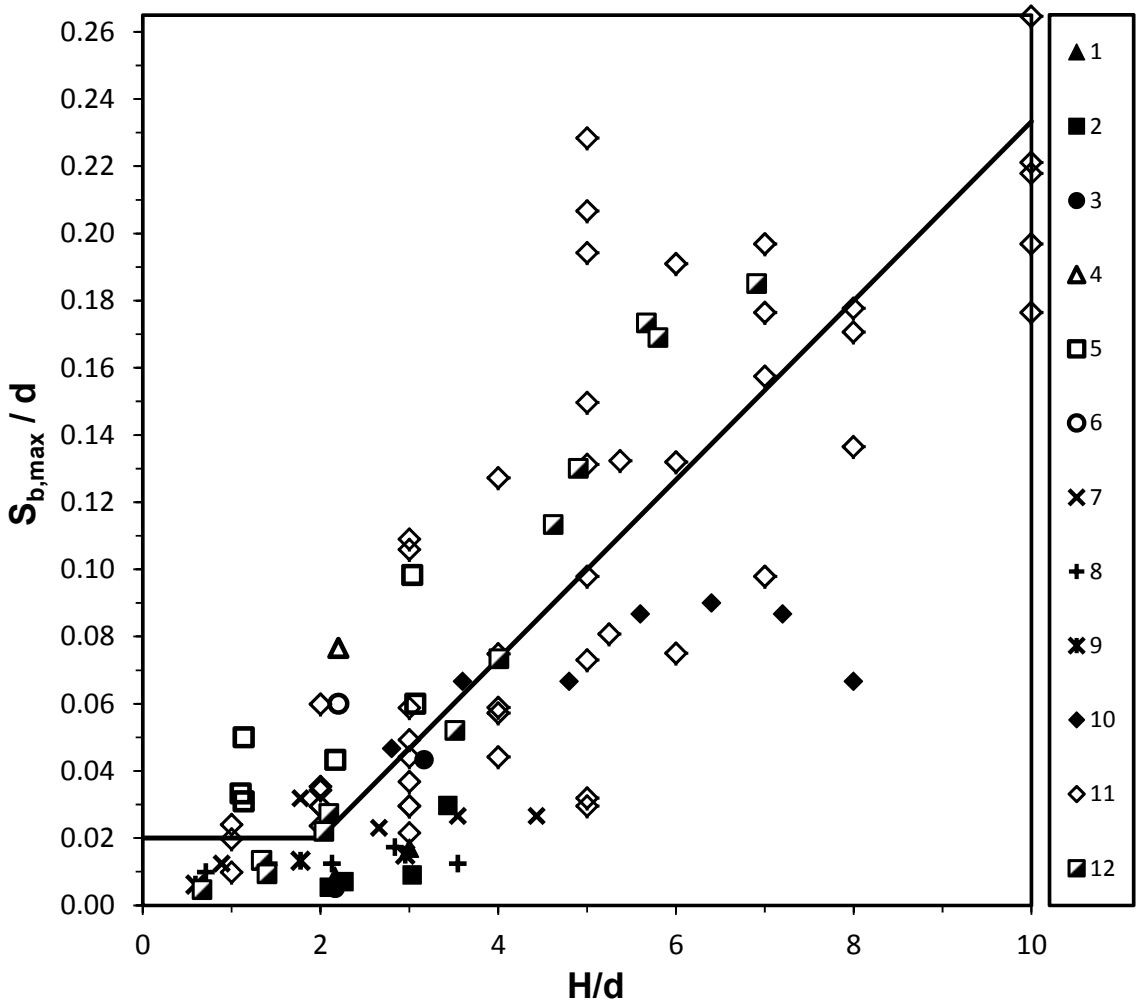

Figure 7.13 Relationship between base settlement at peak column stress versus sample height

Table 7.9 Key for interpreting Figure 7.13

Ref	Source	Remarks
1	Single column tests, Chapter 4	Density 1, unreinforced tests
2	Single column tests, Chapter 4	Density 2, unreinforced tests
3	Single column tests, Chapter 4	Density 3, unreinforced tests
4	Single column tests, Chapter 4	Density 1, unreinforced tests with applied surcharge
5	Single column tests, Chapter 4	Density 2, unreinforced tests with applied surcharge
6	Single column tests, Chapter 4	Density 3, unreinforced tests with applied surcharge
7	Demerdash (1996)	Laboratory-scale experiments using square unit cell, geometry/reinforcement combination 1B
8	Demerdash (1996)	Laboratory-scale experiments using square unit cell, geometry/reinforcement combination 2B
9	Demerdash (1996)	Laboratory-scale experiments using square unit cell, geometry/reinforcement combination 3B
10	Chen et al. (2008)	Laboratory-scale experiments using approximated plane strain conditions, geometry/reinforcement combination 1A
11	Fadl (1981)	Laboratory-scale experiments on embedded anchors
12	Ilamparuthi and Muthukrishnaiah (1999)	Laboratory-scale experiments on embedded anchors

7.4 Summary

Chapter 7 incorporates the results from research performed by others with the results obtained from the current experiment and numerical studies to draw conclusions about critical height and surface deformation of column-supported embankments. The key findings are listed below.

1. The trend developed in Chapter 5 between critical height and unit cell geometry was evaluated using the results of 24 case histories and 16 experimental studies identified in Chapter 2. All of the cases where differential surface settlement was reported fall below the trend line and a majority of the cases where differential surface settlement was not reported are above the trend line. A total of 21 measurements of critical height, including 5 measurements from the current study, were compared to the trend line. The critical heights obtained from 3D unit cell geometries were in good agreement with the trend

given by H_{crit} = 1.15s'+1.44d. Critical heights determined from plane strain and axisymmetric geometries appear to follow a different trend given by: H_{crit} = 1.72s'+1.44d. A likely reason for this difference is the lack of out-of-plane support for plane strain and axisymmetric conditions.

2. Only 33 percent of the case history and experimental data that plotted below the trends for critical height and reported the presence of stiff near-surface foundation materials also reported differential surface settlement. When stiff near-surface soils were not reported, 62 percent of cases falling below the trends for critical height reported differential surface settlement. The presence of reinforcement did not have a significant impact on whether cases below the trend lines reported differential surface settlement.
3. Based on a limited amount of experimental and case history data, the application of traffic loading typical of construction and roadway traffic increases the critical height by less than 20 percent of the pre-traffic value. Research by Heitz (2006) and Zaeske (2001) indicates that soil arching is not strongly affected when traffic loading is less than about 300 psf.
4. The trend between surface settlement over the column axis and base settlement established from the bench-scale single- and multi-column tests is reasonably applicable to the measurements made by Demerdash (1996) at the laboratory-scale. Besides scale, a key difference between these studies is that the base settlement in Demerdash's model was non-uniform whereas the base settlement was uniform for the bench-scale experiments. The measurements made by Sloan (2011) at the field-scale were much lower than the trend from the bench-scale testing. A possible explanation for the difference is that the dense-graded crushed stone at field moisture content used by Sloan (2011) was less compliant at the confining stress levels associated with the field scale than the dry sands used in the experiments at the bench- and laboratory-scale.
5. If base settlement is approximately parabolic when viewed along a profile, Equation 7.14 can be used to estimate the maximum differential surface settlement for embankments below the critical height. When the distribution of base settlement is somewhere between uniform and parabolic, the results of the application of Equations 5.13 and 7.14 can be interpolated to estimate maximum differential surface settlement. Except at very low area replacement ratios, the ratio of differential surface settlement to base settlement increases sharply as the embankment height decreases below the critical height. Since the change in differential settlement is large for a small change in embankment height, the predictive accuracy of Equations 5.13 and 7.14 is fairly low.
6. The approach proposed by Russell et al. (2003) and modified in Chapter 5 for estimating the surface settlement above the critical height was found to compare reasonably well to

the laboratory-scale measurements by Demerdash (1996); however, the influence of volume change on surface settlement was slightly greater for the bench-scale tests. The surface settlements measured by Sloan (2011) above the critical height were much lower than predicted using the modification of the approach proposed by Russell et al. (2003).

7. The displacement required to mobilize peak capacity on an embedded anchor is comparable to the base settlement required to fully mobilize load transfer to the columns by soil arching. The magnitude of base settlement at peak soil arching can be estimated using Equation 7.22. For an embankment height equal to 10 ft and a column diameter equal to 2 ft, the relationship suggests that peak soil arching is mobilized when maximum base settlement reaches 2.4 inches.

8 Summary and Recommendations

This chapter provides a summary of work accomplished, conclusions, design recommendations, and recommendations for further research. The contents are organized in the following sections:

Section 8.1: Summary of work accomplished
Section 8.2: Conclusions
Section 8.3: Recommendations for GRCSE design
Section 8.4: Recommendations for further research

8.1 Summary of Work Accomplished

The following summarizes the work accomplished in this study:

- An extensive literature review was performed to gather information from previous experimental studies, numerical studies, and case histories. Key items extracted from these sources included: unit cell geometry, embankment height, whether reinforcement was used, whether near-surface foundation soils were competent, whether the embankment was subjected to traffic, and whether differential surface settlement was reported. The literature review also involved compiling existing recommendations for estimating critical height, load transfer to columns, and tension developed in the reinforcement.
- In the paper by McGuire and Filz (2008), which is provided in Appendix A, 10 published methods for estimating the vertical stress acting on the reinforcement and 5 methods for estimating the tension developed in the reinforcement were compared and evaluated using a simple parametric study.
- In the paper by McGuire et al. (2009), which is provided in Appendix B, the Filz and Smith Method (Filz and Smith, 2006), also known as the Load-displacement Compatibility (LDC) Method, was applied, and the results were compared to measurements from an instrumented low-height GRCSE constructed in Brazil.
- In the paper by McGuire and Filz (2010), which is provided in Appendix C, the Parabolic Method for estimating tension and deflection of the reinforcement, as in BS8006 (1995),

was expanded to incorporate the influence of initial slack and creep of the geosynthetic reinforcement.

- A separate extensive literature review was performed to gather relevant information from other topics of research that are analogous to the research of deformation and load transfer in column-supported embankments. These topics are pullout of embedded anchors and the propagation of fault rupture through a soil profile.
- The bench-scale testing apparatus described in Chapter 3 was designed and constructed. To the author's knowledge, this is the first study in this area of research to: 1) use vacuum to apply surcharge pressure to a model embankment without disturbing or obstructing the sample surface, 2) use a non-contact laser distance transducer to obtain high-resolution measurements of surface deformation, and 3) physically evaluate a very wide range of unit cell geometries for a variety of sample densities and reinforcement conditions using a single apparatus.
- Published material properties for Light Castle Sand were evaluated, and additional vacuum triaxial tests were performed to develop estimates of friction angle and dilation angle at very low confining pressures. A separate literature review of the strength and dilatency of sand at low confining pressures was performed to compile available guidance and correlations.
- A total of 183 bench-scale experiments were performed, and they are described in Chapters 4 and 5. Of this total, 63 tests were performed using a single column configuration and 120 tests were performed using one of five multi-column configurations.
- A system of notation and terminology, including *spanning ratio* to describe unit cell geometry and *settlement ratios* to describe settlement at the embankment surface, was developed.
- Using the results from the bench-scale experiments and from 21 previous experimental studies, 4 numerical studies, and 24 case histories, relationships were developed for plane strain and 3D column arrangements between unit cell geometry and critical height. The relationships are substantially different from existing recommendations for estimating critical height.
- An approach was proposed to account for the influence of typical roadway traffic loading on critical height based on field-scale experiments by Sloan (2011), the case study by Ting et al. (1994), and research performed by Zaeske (2001) and Heitz (2006).

- Empirical relationships were developed between surface settlement for embankments below the critical height and unit cell geometry, sample height, and magnitude of base settlement.
- The relationship between maximum base settlement and surface settlement proposed by Russell et al. (2003) for embankments above the critical height was evaluated against the bench-scale test results, field-scale experimental results by Sloan (1996), and laboratory-scale experimental results by Demerdash (1996). The relationship proposed by Russell et al. (2003) was modified to account for volume change and parabolic distribution of base settlement.
- A numerical modeling study was performed using FLAC3D and compared to the results from the bench-scale experiments.

8.2 Conclusions

Conclusions are provided at the end of Chapters 4 through 7. The findings from the single column tests are provided in Section 4.4, the multi-column tests in Section 5.6, the numerical modeling study in Section 6.8, and the integrated analysis in Section 7.4. The primary conclusions of this study are summarized here.

- The critical height, which is the minimum embankment height where differential surface settlement does not occur due to differential base settlement, is primarily controlled by unit cell geometry, which can be expressed in dimensionless form using the spanning ratio. The presence and stiffness of geosynthetic reinforcement was not observed to have a measureable effect on critical height. The range of initial relative densities evaluated in the bench-scale experiments (D_r = 74 to 105%) also did not have a measurable effect on critical height.
- The trend between critical height and unit cell geometry developed from the bench-scale experiments also appears to be representative of the data obtained from many previous investigations and case histories with three-dimensional unit cells. Critical heights determined from plane strain and axisymmetric geometries are higher than the trend for three-dimensional geometries for the definition of spanning ratio adopted here. In total, the trends between critical height and unit cell geometry for plane strain and three-dimensional column arrangements were evaluated against 24 case histories, 21 experimental studies, and 4 numerical studies. This pool of data represents both full and

reduced-scale embankments as well as a wide range of unit cell geometries, reinforcement properties, and embankment material types.

- Expressing the critical height as a fixed ratio of the clear span between adjacent columns, which is the current state of practice, does not adequately represent the complete trend of the data set produced and reviewed during this study.
- Based on the results from the case history by Ting et al. (1994) and the field scale study by Sloan (2011), it appears that traffic loading typical of roadways increases the critical height by less than 20 percent.
- For embankments below the predicted critical height, the available case history data suggests that the presence of stiff near-surface materials decreases the likelihood of significant differential settlement occurring at the embankment surface. Stiff near-surface materials include permanent working platforms, desiccated clay crusts, existing compacted fills, and natural sand deposits. It is believed that the benefit of stiff-near surface materials in preventing significant differential surface settlement may be due to reduction in base settlement rather than lowering the critical height.
- Based on results from the bench-scale tests and interpreted results from laboratory and field-scale experiments performed by others, the embankment material typically dilates in response to differential settlement between the column and the compressible foundation soil. The rate of dilation is highest when the magnitude of differential base settlement is small. During the bench-scale testing, the rate of dilation was observed to increase slightly with higher initial relative density over the range of densities evaluated.
- For a fixed embankment height and location on the embankment surface, the ratio of settlement of the embankment surface to base settlement can be approximated as constant even though some nonlinearity exists. Nonlinearity tends to be most significant at small magnitudes of base settlement. Dilation of the embankment material has a significant influence on surface settlements. Nonlinearity in the relationship between surface and base settlement is likely attributed to decreasing dilation rate with increasing base settlement. Since the impact of initial sample density on dilation was small for the range of densities considered, there was not a measurable influence of initial sample density on the ratio between surface settlement and base settlement.
- Below the critical height, the ratio between surface settlement over the axis of the column to base settlement increases as embankment height increases. This result is due to compliance of the embankment material overlying the column. When the embankment height is low relative to the column diameter, stress concentration over the column is low and the embankment material does not displace or compress significantly. When the embankment is high relative to the column diameter, stress concentration over the

column is high and the embankment material displaces and compresses resulting in greater settlement at the embankment surface.

- At very low embankment height, the columns independently provide support to the overlying embankment. The outer-most shearing surface around a column within a unit cell that develops through the embankment due to differential settlement between the column and the foundation soil can be approximated as an inverted truncated cone or frustum. In elevation view, the shearing surface makes an angle from vertical that can be correlated to either the peak friction or dilation angle of the embankment material. The shearing surface becomes more inclined from vertical as the friction and dilation angles increase. In plan view, the rupture of the outer shear bands produced by round columns makes a circle on the embankment surface equal to the diameter of the column plus the spread due to the inclination of the shear surface. As embankment height increases, the shearing surfaces produced by individual columns begin to interact. The interaction of shearing surfaces between adjacent columns is necessary for development of soil arching from column to column. Soil arching influences both the load transfer to the columns and deformation of the embankment. The height at which soil arching begins to develop between columns is the interaction height. The interaction height can be estimated using unit cell geometry and the assumption that the outer shear bands remain at approximately the same inclination from the column edges to their intersection point. The FLAC3D analyses described in Chapter 6 suggest that the shear bands become increasingly bell-shaped as they interact to form arches, therefore the linear approximation tends to overpredict the interaction height.
- Below the critical height, the maximum surface settlement occurs a distance s' from the edge of any round column, where s' is the maximum distance a location within the unit cell can be from the edge of a column. Below the interaction height, the settlement at this location equals the base settlement. As the embankment height is increased above the interaction height, the surface settlement decreases below the magnitude of the base settlement. Therefore, as embankment height increases from the interaction height to the critical height, the surface settlement over the axis of the column increases and the settlements a distance s' from any round column decreases. Since the surface settlement over the axis of the column represents the minimum surface settlement in the unit cell and the settlements at distances s' from any column edge represents the maximum settlement, the difference in the settlement between these locations is the maximum differential surface settlement. At the critical height, the surface settlement over the column axis equals the settlement a distance s' from the column, thus eliminating differential surface settlement.

- Below the critical height, the magnitude of maximum differential surface settlement can be estimated as a function of the base settlement, unit cell geometry, and sample height. Except at very low area replacement ratios, the ratio between maximum differential surface settlement and base settlement increases sharply as the embankment height decreases below the critical height. This observation indicates that an embankment and its supporting columns should be designed such that the embankment is safely above the critical height if significant base settlements are anticipated and there is low tolerance for differential surface settlement.
- For the same unit cell geometry and embankment height, uniform base settlement produces greater differential surface settlement than when base settlement is distributed parabolically, with the maximum base settlement equal to the magnitude of the uniform base settlement. If the average base settlement for the parabolic case equals the uniform base settlement, the case with the higher differential surface settlement depends on the spanning ratio of the unit cell geometry. At higher values of spanning ratio, uniform base settlement produces more differential surface settlement. At low values of spanning ratio, the parabolic base settlement case produces more differential surface settlement.
- At and above the critical height, the settlement of the embankment surface is uniform. The ratio between the surface settlement and maximum base settlement remains relatively constant as the embankment height increases above the critical height. The approach proposed by Russell et al. (2003) substantially overpredicts the ratio between surface settlement and maximum base settlement because it assumes zero volume change occurs within the embankment. If the approach is modified to account for volume change, it can be used to reasonably estimate surface settlement when base settlement is uniform or distributed parabolically. The results from the bench-scale testing suggests that the presence and stiffness of reinforcement does not influence the ratio of surface settlement to base settlement, though it is possible that this result is influenced by the fact that sand is able to flow through the apertures in the reinforcement.
- The FLAC3D model described in Chapter 6, as well as the FLAC2D model developed by Demerdash (1996), calculates surface settlements over the column axis that are significantly lower than experimental measurements. Both models also calculated settlements at the unit cell boundary that were generally lower than the experimental measurements; however, the discrepancy was smaller than the comparison to the settlement over the column. The differences between the calculated values of surface settlement to the measure values resulted in calculated differential settlements that were generally larger than the measured values. Despite these differences, the FLAC3D model

described used in the current study calculated critical heights that were essentially the same as the values measured using the bench-scale experiments.

8.3 Recommendations for GRCSE Design

This section provides practice-oriented recommendations for GRCSE design. The recommendations for selecting unit cell geometry with respect to the critical height are intended to supplement the design recommendations provided by Sloan (2011) and intended to be applicable to both field and reduced scale conditions. Recommendations for estimating surface deformation are provided, acknowledging the limitations of experimental testing at reduced scale, the fact embankment materials used in the field may be significantly different from the dry sand used in the experiments, and that the predictive accuracy of the proposed methods is generally low. Based on comparison to the results of the field tests by Sloan (2011), the recommendations for estimating differential surface settlement are reasonably applicable to field conditions, while the recommendations for estimating surface settlement over the column and total surface settlement above the critical height are very conservative. Table 8.1 provides recommended procedures for estimating critical height and embankment settlement. Additional guidance is provided in the following subsections:

Section 8.3.1: Selecting unit cell geometry
Section 8.3.2: Accounting for the presence of stiff near-surface foundation materials
Section 8.3.3: Estimating base settlements

Table 8.1 Recommendations for GRCSE design

Calculation	Limitations	Recommendation	Remarks
Critical height, H_{crit}	3D unit cell, Before traffic, $0.55 \le s'/d \le 6.10$	$H_{crit} = 1.15s' + 1.44d$	
	Plane strain unit cells, Before traffic $0.75 \le s'/d \le 2.75$	$H_{crit} = 1.72s' + 1.44d$	
	After traffic[1], $q \le 300psf$ (15kPa), $1.62 \le s'/d$	$H_{crit,traffic} = H_{crit} + Max\begin{cases} 1ft \\ 0.2H_{crit} \end{cases}$	A 20% increase in critical height due to typical roadway traffic loading is likely conservative for conditions with at least moderate subgrade support and construction trafficking prior to surface finishing.
Surface settlement over the column axis, S_c	Square unit cell, Before traffic, $H < H_{crit}$, $1 \le H/d \le 5$, $0.73 \le s'/d \le 2.80$	$S_c = S_{b,d}\left(1 - \frac{1}{16}\left(5 - \frac{H}{d}\right)^2\right)\left(1 - 4\left(1 + \frac{H}{d}\right)^{-2}\right)$	Sloan (2011) measured values of S_c at the field-scale that were much lower than predicted using the expression given here.
Maximum differential surface settlement, $(S_d - S_c)$	Square unit cell, Before traffic, Uniform base settlement, $H < H_{crit}$, $0.73 \le s'/d \le 2.80$	$(S_d - S_c) = \min\begin{cases} S_b - S_c \\ S_b\left(0.115\frac{s'}{d} - \frac{H}{10d} + 0.144\right)\tan\left(\min\begin{cases} 83^o \\ 135\left(\frac{s'}{d}\right)^{-0.7} \end{cases}\right) \end{cases}$	For application to field conditions, S_c can conservatively be given a value of zero.

Calculation	Limitations	Recommendation	Remarks
	Square unit cell, Before traffic, Parabolic base settlement, $H < H_{crit}$, $0.73 \le s'/d \le 1.62$	$(S_d - S_c) = \min\left\{ \begin{array}{c} S_{b,d} - S_c \\ S_{b,d}\left(0.115\frac{s'}{d} - \frac{H}{10d} + 0.144\right)\tan\left(90^o - 10^o\left(\frac{s'}{d}\right)\right) \end{array} \right.$	
Uniform surface settlement, S_{tot}	Square unit cell, Before traffic, Uniform base settlement, $H \ge H_{crit}$, $0.73 \le s'/d \le 6.10$	$S_{tot} = S_b\left(1 - A_s - \frac{\Delta V_u}{V_u}\frac{H}{S_b}\right)$ where, $\frac{\Delta V_u H}{V_u S_b} = \text{Min}\left\{ \begin{array}{c} 0.38 \\ 0.38(A_s/6\%) \end{array} \right.$ for $\frac{S_b}{d} \le 0.2$ $\frac{\Delta V_u H}{V_u S_b} = \text{Min}\left\{ \begin{array}{c} 0.24 \\ 0.24(A_s/6\%) \end{array} \right.$ for $\frac{S_b}{d} > 0.2$	Surface settlement measured by Sloan (2011) at the field-scale before and after traffic was significantly less than predicted using the guidance given here. It is recognized that the estimate of S_c just below H_{crit} was not developed to be continuous with the estimate of S_{tot} just above H_{crit}. The influence of volume change is based on limited available data and provided conservative results at the laboratory and field scale.
	Square unit cell, Before traffic, Parabolic base settlement, $H \ge H_{crit}$, $0.73 \le s'/d \le 6.10$	$S_{tot} = 0.6S_{b,d}\left(1 - A_s - \frac{\Delta V_u}{V_u}\frac{H}{S_{b,d}}\right)$ where $\frac{\Delta V_u H}{V_u S_{b,d}} = \text{Min}\left\{ \begin{array}{c} 0.38 \\ 0.38(A_s/6\%) \end{array} \right.$ for $\frac{S_{b,d}}{d} \le 0.2$ $\frac{\Delta V_u H}{V_u S_{b,d}} = \text{Min}\left\{ \begin{array}{c} 0.24 \\ 0.24(A_s/6\%) \end{array} \right.$ for $\frac{S_{b,d}}{d} > 0.2$	
Notes: 1. Dynamic qualities of loading should be typical of roadway traffic.			

8.3.1 Selecting unit cell geometry

The primary performance criteria for the serviceability of GRCSEs are settlement and ride quality. Both of these criteria are heavily tied to the unit cell geometry. For good overall ride quality, the proposed embankment height should be greater than or equal to the critical height for the selected geometry. In terms of settlement of the embankment surface, the embankment should be designed such that the expected foundation settlement multiplied by the settlement ratio SBR_{tot} is less than the limit on total settlement. As shown in Table 8.1, critical height and the ratio SBR_{tot} can be determined from the unit cell geometry. Figure 8.1 shows the measured values of normalized critical height and SBR_{tot} determined from the bench-scale testing along with the recommended trend lines listed in Table 8.1 plotted against area replacement ratio for a square column arrangement.

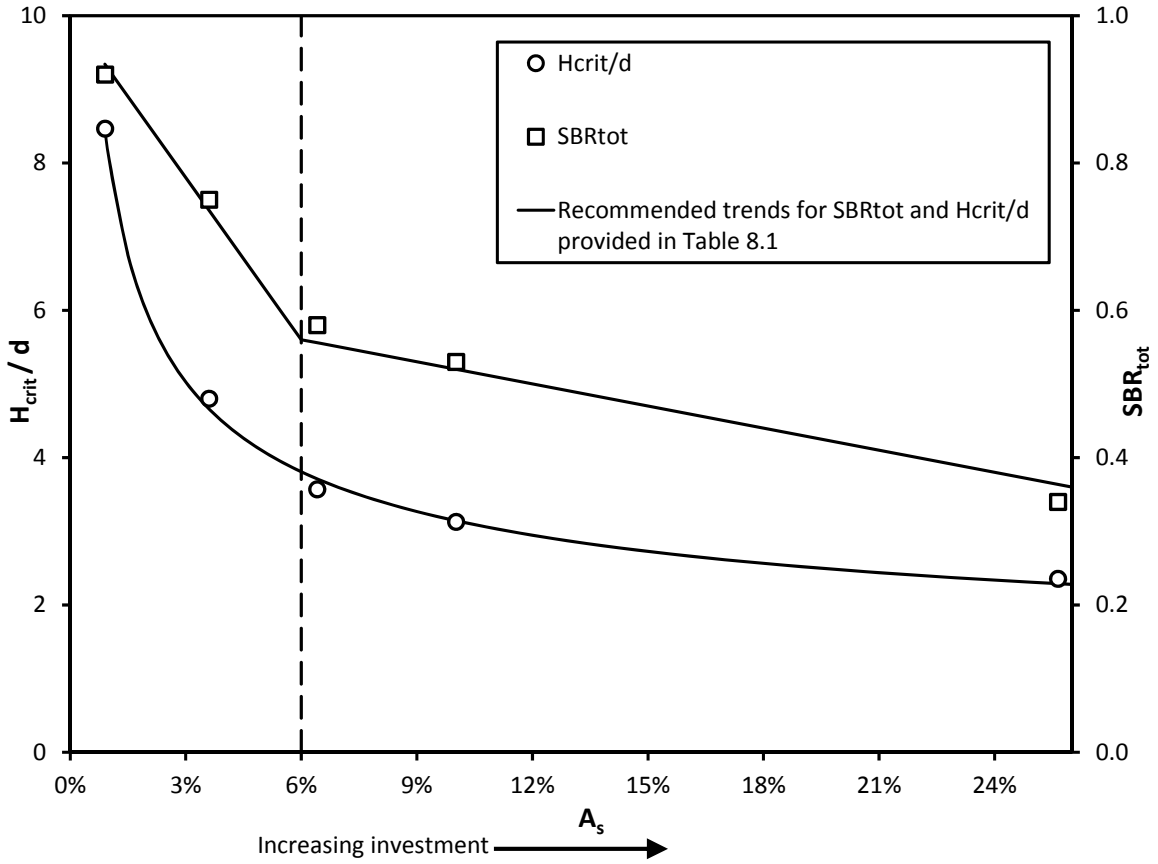

Figure 8.1 Normalized critical height and SBR_{tot} versus area replacement ratio

The figure shows that both H_{crit}/d and SBR_{tot} increase sharply below an area replacement ratio of about 6 percent. The area replacement ratio provides an indication of the investment in time and materials required to install the columns for embankment support. Figure 8.1 shows that there is a large incremental return on investment, in terms of settlement reduction through the embankment, for area replacement ratios up to 6 percent.

Figure 8.2 was adapted from the parametric analysis performed by McGuire and Filz (2008) and shows the stress reduction ratio, SRR_{emb}, as defined in Section 1.4, due to arching versus area replacement ratio. Further details on the parametric analysis can be found in McGuire and Filz (2008), which is provided in Appendix A. The three methods shown on the plot suggest that more stress reduction by soil arching occurs as area replacement ratio increases. Since the magnitude of vertical stress acting on the reinforcement or foundation soil directly impacts the magnitude of foundation settlement, the stress reduction ratio provides an indication of the settlement reduction for a particular investment of time and materials associated with column construction. However, unlike SBR_{tot}, which is a reduction of settlement through the embankment, SRR_{emb} is a reduction in stress.

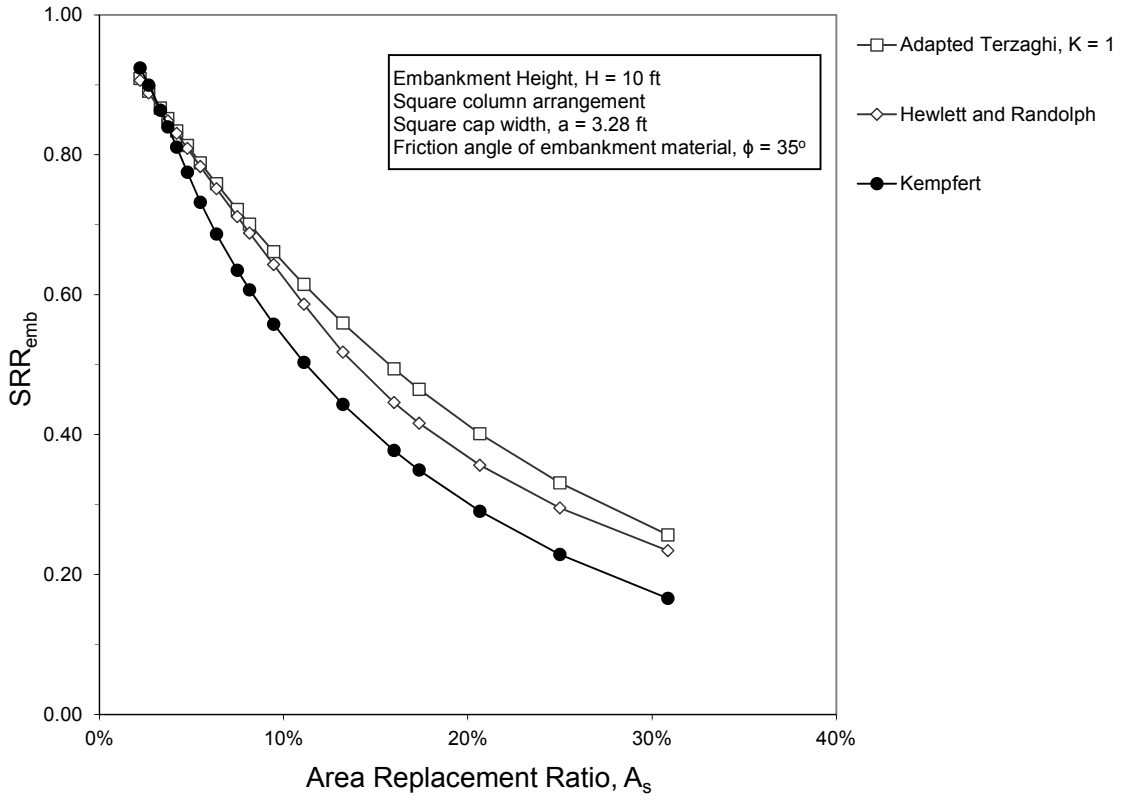

Figure 8.2 Stress reduction by arching versus area replacement ratio (Adapted from McGuire and Filz, 2008)

The reduction in foundation settlement due to the reduction in applied stress by soil arching can be estimated by making some simplifying assumptions regarding the mechanisms of load transfer and foundation soil compression. Equation 8.1 illustrates how SRR_{emb} reduces foundation settlement if load transfer by the reinforcement and stress reduction below the foundation level are ignored and foundation settlement is assumed to be uniform and occur only after the embankment reaches full height. In the expression, H_{clay} is the thickness of the compressible clay foundation soil, M represents the one-dimensional compression modulus, and ($H\gamma$+q) equals the applied embankment stress. For the case where no columns are present, SRR_{emb} equals unity. If the one-dimensional compression modulus is assumed to be insensitive to stress level, then Equation 8.2 represents the Settlement Reduction Factor at the base of the embankment, SRF_{base}, which is ratio of base settlement with arching to the base settlement without arching. Using the simplifying assumptions, which ignores the non-linear relationship between stress and strain in the foundation soil, SRF_{base} equals SRR_{emb}.

$$S_b = H_{clay}\frac{(H\gamma + q)SRR_{emb}}{M} \tag{8.1}$$

$$SRF_{base} = SRR_{emb} \tag{8.2}$$

Figure 8.3 shows the reduction of settlement at the base of the embankment, SRF_{base}, due to soil arching, the reduction of settlement through the embankment, SRF_{emb}, equal to SBR_{tot}, and the reduction of settlement at the embankment surface, SRF_{surf}, which is equal to the product of SRF_{base} and SRF_{emb}. The settlement reduction ratio SRF_{surf} represents the combined effect of the reduction of settlement at the base of the embankment due to soil arching and the settlement reduction through the embankment. For the conditions used in this example at an area replacement ratio equal to 6 percent the surface settlement is predicted to be 45 percent of the estimated foundation settlement without improvement by columns. This percentage does not account for stress reduction by the reinforcement (SRR_{net}), load transfer below the foundation level, or settlement that occurs during construction. Procedures such as the Filz and Smith Method (2006), which considers load transfer below the foundation level and by the reinforcement, can be applied to specific conditions to estimate post-construction foundation settlement.

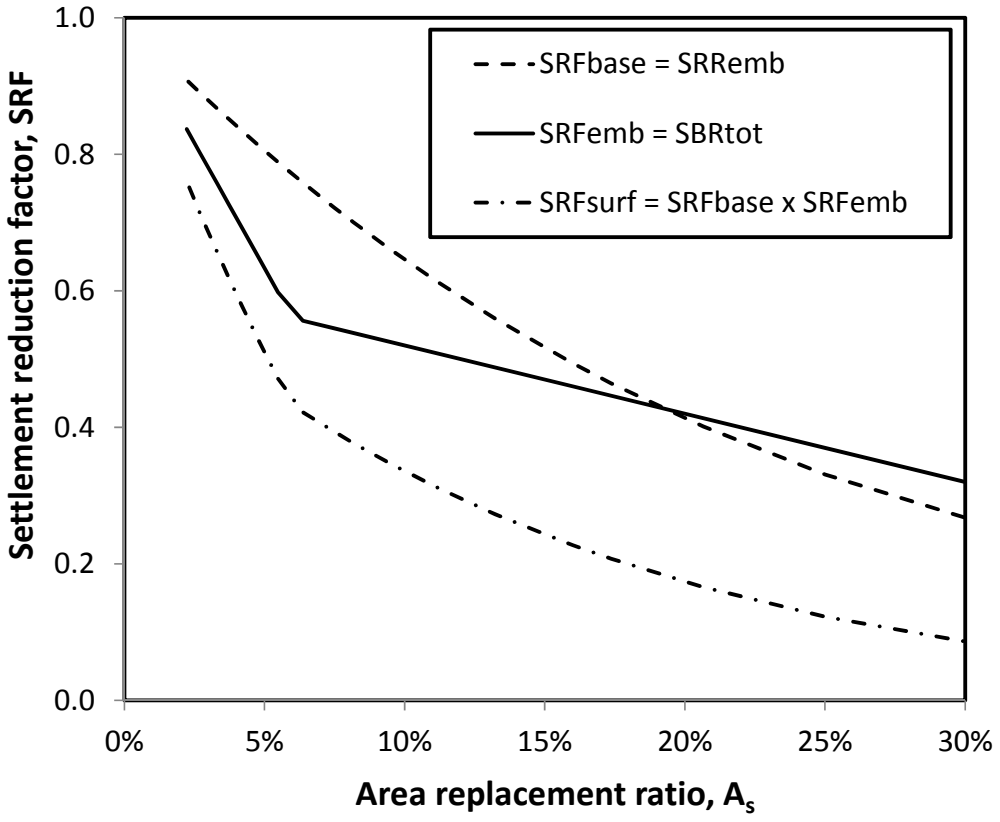

Figure 8.3 Settlement reduction at the base of the embankment due to load transfer by soil arching, SRF_{base}, settlement reduction through the embankment, SRF_{emb}, and the settlement reduction at the embankment surface, SRF_{surf} for the conditions outlined in Figure 8.2 using the Adapted Terzaghi Method for K=1.

8.3.2 Accounting for the presence of stiff near-surface foundation materials

Sloan (2011) defines competent near-surface soils as having a relative density of medium dense or above (D_r > 40%, N > 10 blows/ft) for cohesionless soils and a consistency of medium-stiff or above (S_u=500 psf) for clays. Sloan (2011) recommends that load transfer to the columns by the stiff near-surface materials can be accounted for using a conservative estimate of the thickness of the stiff near-surface soils, t, and estimating an effective pile diameter, d', using the relationship d' = d+0.5t. The effective pile diameter is used in conjunction with an arching theory, such as the Adapted Terzaghi Method, to estimate load transfer to columns by soil arching within the embankment.

The question addressed here is whether the effective pile diameter, as defined by Sloan (2011) or some similar definition, should be applied to procedures to estimate critical height and embankment settlement. Currently, there is not experimental data that directly provides an answer to this issue; however, as mentioned in Section 8.2, it is believed that the benefit of stiff near-surface soils is in reducing foundation settlement rather than lowering the critical height. The impact of combining the recommendations for estimating effective pile diameter proposed by Sloan (2011) with the relationship between unit cell geometry and critical height provided in Table 8.1 was investigated by comparing the equation for critical height using the actual pile diameter to the equation for critical height with effective pile diameter used in place of the actual pile diameter. The comparison shows that the critical height increases by an amount equal to 0.4325 multiplied by the thickness of the stiff near-surface soil, t. It does not seem logical for the critical height to increase if competent near-surface soils are present. Therefore, it is recommended that the effective column diameter as defined by Sloan (2011) not be applied to the procedures for estimating critical height and embankment surface settlement provided in Table 8.1.

8.3.3 Estimating base settlements

Procedures for estimating foundation settlement in GRCSEs are provided by Filz and Smith (2006). GeogridBridge1.2 is a Microsoft Excel spreadsheet implementation of the procedures developed by Filz and Smith (2006) and is available online by searching "GeogridBridge" at http://vtrc.virginiadot.org/PUBS.aspx. The original method proposed by Russell et al. (2003) is currently integrated in the method to estimate settlement at the embankment surface from differential base settlement.

As this research suggests, the original method by Russell et al. (2003) overestimates the ratio between surface settlement and maximum differential base settlement. Table 8.2 provides the operations and cell references needed to extract the values needed to apply the recommendations provided in Table 8.1. Instructions for using GeogridBridge1.2 are provided by Filz and Smith (2006). By default, the worksheets in GeogridBridge are protected and must be unprotected to add the operations shown in Table 8.2 to an existing worksheet. GeogridBridge1.2 is limited to square column arrangements; however, a future version will accommodate triangular column arrangements as described in Sloan et al. (2011).

Table 8.2 Extraction of data from GeogridBridge1.1 to estimate embankment surface settlement

Quantity		Calculation using cell references in GeogridBridge1.1 (Filz and Smith, 2006) http://vtrc.virginiadot.org/PUBS.aspx
1	Ultimate average differential foundation settlement ($S_{b,avg}$)[1]	SRRq!AG38
2	Ultimate column compression due to all sources, C_{col}	SRRq!AO38
3	Average compression of sand layers subjected to preload, if present	SRRp!U24-SRRp!U25
4	Ultimate average compression of clay layers subjected to preload, if present	SRRp!U25-SRRp!U26
5	Column compression due to interface with sand layers subjected to preload, if present	SRRp!V24-SRRp!V25
6	Ultimate column compression due to interface with clay layers subjected to preload, if present	SRRp!V25-SRRp!V26
7	Janbu degree of consolidation, U%	SRRp!V18
8	Post-construction average differential foundation settlement ($S_{b,avg,post}$)[1]	SRRq!AG38-(SRRp!U24-SRRp!U25)-SRRp!V18(SRRp!U25-SRRp!U26)
9	Post-construction column compression due to all sources, $C_{col,post}$	SRRq!AO38-(SRRp!V24-SRRp!V25)-SRRp!V18(SRRp!V25-SRRp!V26)
10	Settlement of foundation below the tip elevation of columns, S_u	Not determined in GeogridBridge

Note: 1. The average differential base settlement calculated in GeogridBridge can be treated as equivalent to uniform base settlement, S_b.

The settlements estimated using the procedure listed in Table 8.1 are referenced to the original elevation of the top of the column or pile cap, if present. If total values of settlement are desired, the magnitude of column compression and settlement of the foundation below the tip elevation of the columns, if significant, must be added to the estimated surface settlement referenced to the top of the column.

As shown in Table 8.1, the recommended procedure for estimating surface settlement above the critical height incorporates volume change, which is sensitive to the magnitude of base settlement. Using the notation defined in Table 8.2 and treating the calculated average base settlement as equivalent to uniform base settlement, Table 8.3 provides the recommended procedures for estimating post-construction surface settlement for embankments above the critical height. Similar procedures can be developed for settlements that occur during construction.

Table 8.3 Recommended calculations for estimating post-construction surface settlement using values calculated by GeogridBridge1.2

If $S_{b,avg}<0.2d$ $S_{tot,post} = S_{b,avg,post}\left(1 - A_s - \text{Min}\left\{\begin{matrix}0.38\\0.38\left(A_s/6\%\right)\end{matrix}\right.\right)$
If $(S_{b,avg} - S_{b,avg,post}) \leq 0.2d \leq S_{b,avg}$ $S_{tot,post} = S_{b,avg,post}\left(1-A_s\right) - \left(0.2d + S_{b,avg,post} - S_{b,avg}\right)\text{Min}\left\{\begin{matrix}0.38\\0.38\left(A_s/6\%\right)\end{matrix}\right.$ $-\left(S_{b,avg} - 0.2d\right)\text{Min}\left\{\begin{matrix}0.24\\0.24\left(A_s/6\%\right)\end{matrix}\right.$
If $0.2d<(S_{b,avg} - S_{b,avg,post})$ $S_{tot,post} = S_{b,avg,post}\left(1 - A_s - \text{Min}\left\{\begin{matrix}0.24\\0.24\left(A_s/6\%\right)\end{matrix}\right.\right)$

8.4 Recommendations for Further Research

A well-developed list of recommendations for further research is provided by Sloan (2011). The recommendations include performing additional field-scale experiments to produce three additional measurements of critical height and conducting tests that use triangular column arrangements. A supplement or alternative to performing field-scale tests using triangular column arrangements would be to perform the experiments at the bench-scale or some other reduced scale using triangular arrangements. As of August 2011, the bench-scale apparatus used in this study has been mostly dismantled and placed in storage. Roughly 400 hours would be required to re-assemble and configure the equipment to test triangular column arrangements.

Additional recommendations for further research not already provided by Sloan (2011) are listed below:

- Perform numerical and/or experimental research to further investigate how the distribution of base settlement (uniform or non-uniform) affects settlements at the embankment surface. The results of such research would help refine estimates of surface settlement using calculations of average base settlement, as in GeogridBridge. If a numerical approach is used, the model should first be calibrated against the bench-scale testing results for uniform base settlement. As described in Chapter 6, the model developed using FLAC3D was not successful at

calculating surface settlements that agreed with the experimental measurements. An advanced constitutive model in finite element analyses and/or use of the discrete element method may be necessary to produce realistic calculations.

- Develop an analytical model that explains the observed relationship between critical height and unit cell geometry.
- The additional experiments and numerical modeling recommended by Sloan (2011) to investigate critical height, should also include tests performed sufficiently above the critical height to further refine the modified approach by Russell et al. (2003) to estimate total surface settlement resulting from maximum differential base settlement for non-uniform base settlement.
- Investigate how load transfer by arching in multi-column arrangements is affected by continued base settlement beyond $S_{b,max}$. The results from single column testing described in Chapter 4 and the results from several experimental studies on the load-displacement behavior of embedded anchors during pullout suggest that load transfer reaches a peak value and then declines to a residual value with continued displacement.

References

Abdullah, C. H., and Edil, T. B. (2007). "Behaviour of geogrid-reinforced load transfer platforms for embankment on rammed aggregate piers." *Geosynthics International*, 14(3), 141-153.

Abdullah, C. H., and Edil, T. B. (2007). "Numerical analysis of catenary load transfer platform for Geopier-supported embankment." *GSP 173 Advances in Measurement and Modeling of Soil Behavior*.

Alexiew, D. (1996). "Modified redistribution of tensile forces of biaxial span reinforcement between the pile caps." HUESKER Synthetic, internal report.

Alexiew, D. (2000). "Reinforced embankments on piles for railroads: German experience." *GEOTECH-YEAR 2000: Developments in Geotechnical Engineering*, Bangkok, Thailand, 575-584.

Almeida, M. S. S., Ehrlich, M., Spotti, A. P., and Marques, M. E. S. (2007). "Embankment supported on piles with biaxial geogrids." *Geotechnical Engineering*, 160(GE4), 185-192.

Almeida, M. S. S., Marques, M. E. S., Almeida, M. C. F., and Mendonca, M. B. (2008). "Performance of two "low" piled embankments with geogrids at Rio de Janeiro." *The First Pan American Geosynthetics Conference and Exhibition*, Cancun, Mexico.

Alshibli, K. A., Batiste, S. N., and Sture, S. (2003). "Strain localization in sand: plane strain versus triaxial compression." *Jouranl of Geotechnical and Geoenvironmental Engineering*, 129(6), 483-494.

Anastasopoulos, I., Gazetas, G., Bransby, M. F., Davies, M. C. R., and Nahas, A. (2007). "Fault rupture propagation through sand: finite element analysis and validation through centrifuge experiments." *ASCE Journal of Geotechnical and Geoenvironmental Engineering*, 133(8), 943-958.

Bell, A. L., Jenner, C., Maddison, J. D., and Vignoles, J. (1994). "Embankment support using geogrids with vibro concrete columns." *Proceedings Title: Proceedings, 5th International Conference on Geotextiles, Geomembranes, and Related Products*, Singapore, 335-338.

Berilgen, M., Edil, T. B., and Ozaydin, I. K. (2008). "Comparison of 3D and 2D modeling of geosynthetics-reinforced load transfer platforms." *The First Pan American Geosynthetics Conference and Exhibition,*, Cancun, Mexico, 1323-1331.

Bolton, M. D. (1986). "The strength and dilatancy of sands." *Geotechnique*, 36(1), 65-78.

Bonita, J. A. (2000). "The effects of vibration on the penetration resistance and pore water pressure in sand." PhD Dissertation, Virginia Polytechnic Institute and State University, Blacksburg, Virginia.

Bray, J., Seed, R. B., Cluff, L. S., and Seed, H. B. (1994). "Earthquake fault rupture propagation through soil." *Journal of Geotechnical Engineering*, 120(3), 543-561.

Bray, J., Seed, R. B., Cluff, L. S., and Seed, H. B. (1994). "Earthquake fault rupture propagation through soil." *ASCE Journal of Geotechnical and Geoenvironmental Engineering*, 120(3), 543-561.

British Standards, I. (1995). *BS8006 Code of Practice for Strengthened/Reinforced Soils and Other Fills*, BSI, London, U.K.

Broms, B. B. (1979). "Problems and solutions to construction in soft clay." *Proceedings, Sixth Asain Regional Geotechnical Conference on Soil Mechanics and Foundation Engineering*, Bangkok, Thailand, 3-38.

Camp, W. M., and Siegel, T. C. (2006). "Failure of a column-supported embankment over soft ground." *Proceedings of the 4th International Conference on Soft Soils Engineering*, Vancouver, Canada.
Carlsson, B. (1987). "Reinforced soil, principles for calculation." Terratema AB, Linköping, Sweden.
Casagrande, A. (1936). "Characteristics of cohesionless soils affecting the stability of slopes and earth fills." *Journal of the Boston Society of Civil Engineers*.
Chen, R. P., Chen, Y. M., and Xu, Z. Z. (2006). "Interaction of rigid pile-supported embankment on soft soil." *Advances in Earth Structures: Research to Practice*, ASCE (GSP151).
Chen, R. P., Xu, Z. Z., Chen, Y. M., Ling, D. S., and Zhu, B. (2010). "Field tests on pile-supported embankments over soft ground." *ASCE Journal of Geotechnical and Geoenvironmental Engineering*, 136(6), 777-785.
Chen, Y. M., Cao, W. P., and Chen, R. P. (2008). "An experimental investigation of soil arching within basal reinforced and unreinforced piled embankments." *Geotextiles and Geomembranes*, 26, 164-174.
Chew, S. H., Phoon, H. L., Loke, K. H., and Lim, L. K. (2004). "Geotextile reinforced piled embankment for highway bridges." *8th International Conference on Applications of Advanced Technologies in Transportation Engineering*, Beijing, China.
Chin, F. K. (1985). "Design and construction of high embankments on soft clay." *Eighth Southeast Asian Geotechnical Conference,*, Kuala Lumpur, 42-59.
Coghlin, J. (2005). "Brian Blair and Joan Blair (and other individuals identified in the schedule attached to the writ summons dates 17 April 2003) v AWG Residential Limited and Brendan Loughran, Edna Loughran, Dermot Loughran and Eunin Loughran Trading as Brendan Loughran and Sons and Rosorry Development and TPA Taylor, GI Black, RG Kerr and N Magill Practising as Taylor and Boyd (a firm) and Tensar International Limited." *Neutral Citation, No. 2005 NIQB 68.* , N. I. C. Service, ed.
Cole, D. A., and Lade, P. (1984). "Influence zones in alluvium over dip-slip faults." *ASCE Journal of Geotechnical Engineering*, 110(5), 599-615.
Collin, J. G. (2004). "Column supported embankment design considerations." *52nd Annual Geotechnical Engineering Conference,* , University of Minnesota.
Collin, J. G. (2007). "U.S. state-of-practice for the design of geosynthetic reinforced load transfer platforms in column supported embankments." *GeoDenver,* , Denver, Colorado.
Collin, J. G., Han, J., and Huang, J. (2006). "Design Recommendations for Column-Supported Embankments." FHWA-HRT-.
Collin, J. G., Watson, C. H., and Han, J. (2005). "Column-supported embankment solves time constraint for new road construction." *ASCE GeoFrontiers,* , Austin, Texas.
Combarieu, O. (1989). "Remblais sur sols mous améliorés par inclusions verticales rigides." *Proceedings of the Twelfth International Conference on Soil Mechanics and Foundation Engineering*, Rio de Janeiro, 1723-1724.
Cornforth, D. H. (1973). "Prediction of drained strength of sands from relative density measurements." *Evaluation of relative density and its role in geotechnical projects involving cohesionless soil, ASTM Special Technical Publication 523*, American Society for Testing and Materials, Philadelphia, 281-303.
Das, B. M., and Seeley, G. (1975). "Breakout resistance of shallow horizontal anchors." *Journal of Geotechnical Engineering*, 101(GT9), 999-1003.
Demerdash, M. A. (1996). "An experimental study of piled embankments incorporating

geosynthetic basal reinforcement." Doctoral Disseration, University of Newcastle-Upon-Tyne, Department of Civil Engineering.
Dickin, E. A., and Laman, M. (2007). "Uplift response of strip anchors in cohesionless soil." *Advances in Engineering Software*, 38(8-9), 618-625.
Duncan, J. M. (2004). "Friction angles for sand, gravel and rockfill." *Notes of a lecture presented at the Kenneth L. Lee Memorial Seminar,* Long Beach, California.
Duncan, J. M., Byrne, P. M., Wong, K. S., and Mabry, P. (1980). "Strength, Stress-Strain and Bulk Modulus Parameters for Finite Element Analyses of Stress and Movements in Soil Masses." University of California, Berkeley, California.
Duncan, J. M., and Chang, C. Y. (1970). "Nonlinear analysis of stress and strain in soils." *ASCE Journal of the Soil Mechanics and Foundation Division*, 96, 1629-1653.
Duncan, J. M., and Filz, G. M. (1995). "Capacities of drilled shafts in sand subjected to overturning and torsion." *Bengt B. Broms Symposium in Geotechnical Engineering*, Singapore, 97-111.
Eid, W. K. (1987). "Scaling effect in cone penetration testing in sand." PhD Dissertation, Virginia Polytechnic Institute and State University, Blacksburg, Virginia.
Ellis, E. A., and Aslam, R. (2009). "Arching in piled embankments: comparison of centrifuge tests and predictive methods - part 1 of 2." *Ground Engineering*, 42(6), 34-38.
Ellis, E. A., and Aslam, R. (2009). "Arching in piled embankements: comparison of centrifuge tests and predictive methods - part 2 of 2." *Ground Engineering*, 42(7), 28-31.
Fadl, M. O. (1981). "The behavior of plate anchors in sand." PhD, University of Glasgow, Glasgow.
Filz, G. M. (1992). "An experimental and analutic study of earth loads on rigid retaining walls." PhD Dissertation, Virginia Polytechnic Institute and State University, Blacksburg, Virginia.
Filz, G. M. (2001). "Columnar reinforcement of soft ground beneath roadway embankments." *A Research Proposal to Virginia Transportation Research Council*.
Filz, G. M., and Plaut, R. H. (2009). "Practical implications of numerical analyses of geosynthetic reinforcement in column-supported embankments." *2009 US-China Workshop on Ground Improvement Technologies*, Orlando, Florida.
Filz, G. M., and Smith, M. E. (2006). "Design of Bridging Layers in Geosynthetic-Reinforced, Column-Supported Embankments." Virginia Transportation Research Council, Charlottesville, Virginia, 46p.
Fluet Jr, J. E., Christopher, B. R., and Slaters Jr, A. R. (1986). "Geosynthetic stress-strain response under embankment loading conditions." *Third Internation Conference on Geotextiles*, 175-180.
Fukushima, S., and Tatsuoka, F. (1984). "Strength and deformation characteristics of saturated sand at extremely low pressures." *Soils and Foundations*, 24(4), 30-48.
Gomez, J. E. (2000). "Development of an extended hyperbolic model for concrete-to-soil interfaces." PhD Dissertation, Virginia Polytechnic Institute and State University, Blacksburg, Virginia.
Guido, V. A., Knueppel, J. D., and Sweeny, M. A. (1987). "Plate loading tests on geogrid-reinforced earth slabs." *Geosynthetic '87 Conference*, New Orleans, 216-225.
Gulin, K., and Wikström, R. "Stabilization of horizontal movements in weak organic clay layers."
Gwede, D., and Horgan, G. (2008). "Design, construction and in-service performance of a low

height geosynthetic reinforced piled embankment: A650 Bingley Relief Road." *EuroGeo4*, Edinborough, Scotland, Paper number 256.
Habib, H. A. A., Brugman, M. H. A., and Uijting, B. J. "Widening of Road N247 founded on a geogrid reinforced mattress on piles." Swets & Zeitlinger, 369-372.
Halvordson, K., Plaut, R. H., and Filz, G. M. (2010). "Analysis of geosynthetic reinforcement in pile-supported embankments. Part II: 3D cable-net model." *Geosynthics International*, 17(2), 68-76.
Han, J., and Akins, K. (2002). "Use of geogrid-reinforced and pile-supported earth structures." *International Deep Foundation Congress, ASCE*, Orlando, FL., 668-679.
Han, J., and Gabr, M. A. (2002). "Numerical analysis of geosynthetic-reinforced and pile-supported earth platforms over soft soil." *Journal of Geotechnical and Geoenvironmental Engineering*, 128(1), 44-53.
Han, J., and Huang, J. (2007). "Validation of constitutive models for geosynthetic-reinforced column-supported embankments." *International Workshop on Constitutive Modeling*, Hong Kong, China.
Han, J., Huang, J., and Porbaha, A. (2005). "2D numerical modeling of a constructed geosynthetic-reinforced embankment over deep mixed columns." *Geo-Frontiers 2005*, Austin, Texas.
Han, J., Oztoprak, S., Parsons, R. L., and Huang, J. (2007). "Numerical analysis of foundation columns to support widening of embankments." *Computers and Geotechnics*, 34, 435-438.
Heitz, C. (2006). "Bodengewolbe unter ruhender und nichtruhender Belastung bei Berucksichtigung von Bewehrungseinlagen aus Geogittern (in German)." Schriftenreihe Geotechnik Universitat Kassel, Kassel, Germany.
Hewlett, W. J., and Randolph, M. F. (1988). "Analysis of piled embankments." *Ground Engineering*, 21(3), 12-18.
Hite, S. L., and Hoppe, E. J. (2006). "Performance of a pile-supported embankment." *06-R36*, Virginia Transportation Research Council, Charlottesville, Virginia.
Horgan, G. J., and Sarsby, R. W. "The arching effect of soils over voids and piles incorporating geosynthetic reinforcement." Swets & Zetilinger, 373-378.
Hossain, S., and Rao, K. N. (2006). "Performance evaluation and numerical modeling of embankment over soft clayey soil improved with Chemico-Pile." *Transportation Research Record*, 1952, 80-89.
Huang, C., Han, J., and Porbaha, A. (2006). "Two and three-dimensional modeling of DM columns under embankments." *GeoCongress: Geotechnical Engineering in the Information Technology Age*, Atlanta, Georgia.
Huang, J., and Han, J. (2008). "Critical height of deep mixed column-supported embankment under an undrained condition." *GeoCongress: Geosustainability and Geohazard Mitigation*, New Orleans, Louisiana.
Huang, J., Han, J., and Collin, J. G. "Geogrid-reinforced pile-supported railway embankments - three dimensional numerical analyses."
Huang, J., Han, J., and Collin, J. G. (2006). "Serviceability analysis of geomembrane in geosynthetic-reinforced column-support platforms." *GeoShanghai, Advances in Earth Structures: Research to Practice (GSP 151)*, Shanghai, China.
Huang, J., Han, J., and Collin, J. G. (2006). "Deformations of geosynthetic-reinforced column-supported embankments." *8th International Geosynthetics Conference*, Yokohama,

Japan, 1029-1032.
Huang, J., Han, J., and Oztoprak, S. (2009). "Coupled mechanical and hydraulic modeling of geosynthetic-reinforced column-supported embankments." *Jouranl of Geotechnical and Geoenvironmental Engineering*, 135(8), 1011-1021.
Huang, J., Han, J., and Parsons, R. L. (2008). "Two-dimensional paramtetric study on geosynthetic-reinforced column-supported embankments over soft soil." *The First Pan American Goesynthetics Conference and Exhibition*, Cancun, Mexico, 1275-1284.
Huat, B. B. K., Craig, W. H., and Ali, P. "The mechanics of piled embankment." 1069-1082.
Ilamparuthi, K., and Muthukrishnaiah, K. (1999). "Anchor in sand bed: delineation of rupture surface." *Ocean Engineering*, 26(12), 1249-1273.
ITASCA Consulting Group (2008). *FLAC3D Fast Lagrangian Analysis of Continua in 3 Dimensions*, ITASCA Consulting Group, Minneapolis, Minnesota.
Janbu, N. (1963). "Soil compressibility as determined by oedometer and triaxial tests." *European Conference on Soil Mechanics and Foundation Engineering*, Weisbaden, Germany, 19-25.
Jenck, O., Dias, D., and Kastner, R. (2007). "Two-dimnesional physical and numerical modeling of a pile-supported eath platform over soft soil." *ASCE Journal of Geotechnical and Geoenvironmental Engineering*, 133(3), 295- 305.
Jones, B. M., Plaut, R. H., and Filz, G. M. (2010). "Analysis of geosynthetic reinforcement in pile-supported embankments. Part I: 3D plate model." *Geosynthics International*, 17(2), 59-67.
Jones, C. J. F. P., Lawson, C. R., and Ayres, D. J. "Geotextile reinforced piled embankments." 155-160.
Kempfert, H. G., Gobel, C., Alexiew, D., and Heitz, C. (2004). "German recommendations for reinforced embankments on pile-similar elements." 279-284.
Kempton, G., and Naughton, P. "Piled embankments with basal reinforcement: development of design methods and state of the art."
Kempton, G., Russell, D., Pierpoint, N. D., and Jones, C. J. F. P. (1998). "Two- and three-dimensional numerical analysis of the performance of piled embankments." *Proceedings, 6th International Conference on Geosynthetics*, 767-772.
Koutsabeloulis, N. C., and Griffiths, D. V. (1989). "Numerical modeling of the trap door problem." *Geotechnique*, 39(1), 77-89.
Kumar, J., and Kouzer, K. M. (2008). "Vertical uplift capacity of a group of shallow horizontal anchors in sand." *Geotechnique*, 58(10), 821-823.
Kumar, J., and Kouzer, K. M. (2008). "Vertical uplift capacity of horizontal anchors using upper bound limit analysis and finite elements." *Canadian Geotechnical Journal*, 45, 698-704.
Laboratory Technologies Corporation (1994). "Labtech Notebook Pro v8."
Lade, P. (1971). "The stress-strain and strength characteristics of cohesionless soils." PhD dissertation, University of California, Berkeley.
Liu, H. L., Ng, C. W. W., and Fei, K. (2007). "Performance of a geogrid-reinforced and pile-supported highway embankment over soft clay: case study." *ASCE Journal of Geotechnical and Geoenvironmental Engineering*, 133(12), 1483-1493.
Livesey, J., Webber, I., Whaley, A., and Horgan, G. (2008). "Design, construction and in-service performance of a low height geosynthetic reinforced piled embankment: A614 Welham Bridge to Spaldington." *EuroGeo4*, Edinborough, Scotland, Paper number 253.
Low, B. K., Tang, S. K., and Choa, V. (1994). "Arching in piled embankments." *Journal of*

Geotechnical Engineering, 120(11), 1917-1938.
Maddison, J. D., Jones, D. B., Bell, A. L., and Jenner, C. G. "Design and performance of an embankment supported using low strength geogrids and vibro concrete columns." A.A. Balkema, 325-332.
Matsuo, M. (1967). "Study of uplift resistance of footing (I)." *Soils and Foundations*, 7(4).
Matsuo, M. (1968). "Study on the uplift resistance of footing (II)." *Soils and Foundations*, 8(1), 18-48.
McGuire, M. P., and Filz, G. M. (2008). "Quantitative comparison of theories for geosynthetic reinforcement of column-supported embankments." *GeoAmericas 2008, First Pan American American Geosynthetics Conference and Exhibition*, Cancun, Mexico, 1303-1312.
McGuire, M. P., and Filz, G. M. (2010). "Incorporation of slack and creep in the British Standard code of practice for calculating tension and deflection of geosynthetic reinforcement used in column-supported embankments." *9th International Conference on Geosynthetics*, Guaruja, Brazil.
McGuire, M. P., Filz, G. M., and Almeida, M. S. S. (2009). "Load-displacement compatibility analysis of a low-height column-supported embankment." *International Foundation Congress and Equipment Expo*, Orlando, Florida.
Merifield, R. S., and Sloan, S. W. (2006). "The ultimate pullout capacity of anchors in frictional soils." *Canadian Geotechnical Journal*, 43, 852-868.
Meyerhof, G. G., and Adams, J. I. (1968). "The ultimate uplift capacity of foundations." *Canadian Geotechnical Journal*, 5(4), 225-244.
Miki, H. (1997). "Design of deep mixing method of stabilization with low improvement ratio." *1st Seminar on Ground Improvement in Highways*, 197-204.
Miki, H., and Nozu, M. (2004). "Design and numerical analysis of road embankment with low improvement ratio deep mixing method." *Proceedings of Geo-Trans 2004, Geotechnical Engineering for Transportation Projects*, Los Angeles, California, 1395-1402.
Murray, E. J., and Geddes, J. D. (1987). "Uplift of anchor plates in sand." *Journal of Geotechnical Engineering*, 113(3), 202-215.
Naughton, P. (2007). "The significance of critical height in the design of piled embankments." *Geo-Denver 2007: New Peaks in Geotechnics*, Denver, CO.
Naughton, P. J., and Kempton, G. T. (2005). "Comparison of analytical and numerical analysis design methods for piled embankments." *GeoFontiers 2005*, Austin, Texas.
NGG (2002). "Nordic Handbook - Reinforced soils and fills."Nordic Geotechnical Society, Stockholm, Sweden.
Oh, Y. I., and Shin, E. C. (2007). "Reinforcement and arching effect of geogrid-reinforced and pile-supported embankment on marine soft ground." *Marine Georesources and Geotechnology*, 25(2), 97-118.
Pearlman, S. L., and Porbaha, A. (2006). "Design and monitoring of an embankment on controlled modulus columns." *Transportation Research Record*, 1975, 96-103.
Plaut, R. H., and Filz, G. M. (2010). "Analysis of geosynthetic reinforcement in pile-supported embankments. Part III: Axisymmetric model." *Geosynthetics International*, 17(2), 77-85.
Ponce, M. V., and Bell, J. M. (1971). "Shear strength of sand at extremely low pressures." *ASCE Journal Soil Mechanics and Foundations Division*, 97(SM4), 625-638.
Porter, J. R. (1998). "An examination of the validity of steady state shear strength determination using isotropically consolidated undrained triaxial tests." PhD Dissertation, Virginia

Polytechnic Institute and State University, Blacksburg, Virginia.
Poulos, H. G., and Davis, E. H. (1974). *Elastic Solution for Soil and Rock Mechanics*, John wiley & Sons, Inc., New York.
Quigley, P. (2003). "Performance of a trial piled embankment constructed on soft compressible esturine deposits at Shannon, Ireland." *International Workshop on Geotechnics of Soft Soils-Theory and Practice*.
Rad, N. S., and Tumay, M. T. (1986). "Effect of cementation on the cone penetration resistance of sand." *Use of In Situ Tests in Geotechnical Engineering*.
Raithel, M., Kirchner, A., and Kempfert, H. G. (2008). "Pile-supported embankments on soft ground for a high speed railway: Load transfer, distribution and concentration by different construction methods." *Advances in Transportation Geotechnics* Nottingham, England.
Rathmeyer, H. (1975). "Piled embankment supported by single pile caps." *Proceedings, Conference on Soil Mechanics and Foundation Engineering*, Istanbul, 283-290.
Rogbeck, Y., Gustavsson, S., Sodergren, I., and Lindquist, D. (1998). "Reinforced piled embankments in Sweden - design aspects." *Proceedings, Sixth International Conference on Geosynthetics*, 755-762.
Rowe, R. K., and Davis, E. H. (1982). "The behavior of anchor plates in sand " *Geotechnique*, 32(1), 25-41.
Russell, D., Naughton, P. J., and Kempton, G. (2003). "A new design procedure for piled embankments." *Proceedings of the 56th Canadian Geotechnical Conference and the NAGS Conference*, Winnipeg, Canada, 858-865.
Russell, D., and Pierpoint, N. (1997). "An assessment of design methods for piled embankments." *Ground Engineering*, 30(11), 39-44.
Ryan, T., McGill, C., and Quigley, P. (2004). "A timber piled road over deep peat in North West Ireland." *6th International Symposium on Pavements Unbound (UNBAR 6)*, Nottingham, England, 239-245.
Salgado, R. (2008). *The Engineering of Foundations*, McGraw-Hill, New York, NY.
Schanz, T., and Vermeer, P. A. (1996). "Angles of friction and dilatancy of sand." *Geotechnique*, 46(1), 145-151.
Sloan, J. A. (2011). "Column-supported embankments: Full-scale tests and design recommendations." PhD Dissertation, Virginia Polytechnic Institute and State University, Blacksburg.
Sloan, J. A., Filz, G. M., and Collin, J. G. (2011). "A generalized formulation of the adapted terzaghi method for arching in column-supported embankments." *Geo-Frontiers 2011: Advances in Geotechnical Engineering*, Dallas, TX, 798-805.
Smith, M. E. (2005). "Design of bridging layers in geosynthetic-reinforced column-supported embankments." PhD Dissertation, Virginia Polytechnic Institute and State University, Blacksburg.
Smith, M. E., and Filz, G. M. (2007). "Axisymmetric numerical modeling of a unit cell in geosynthetic-reinforced, column-supported embankments." *Geosynthetics International*, 14(1), 13-22.
Stewart, M. E., and Filz, G. M. (2005). "Factors affecting load transfer to deep mixing columns from embankments without geosynthetic reinforcement." *Deep Mixing*, Stockholm, Sweden, 305-314.
Stewart, M. E., and Filz, G. M. (2005). "Influence of clay compressibility of geosynthetic loads

in bridging layers for column-supported embankments." *Geo-Frontiers: Contemporary Issues in Foundation Engineering*.
Stewart, M. E., Navin, M. P., and Filz, G. M. "Analysis of a column-supported test embankment at th eI-95/Route 1 interchange." ASCE, 1337-1346.
Sture, S., Costes, N. C., Batiste, S. N., Lankton, M., Alshibli, K. A., Jeremic, B., and Swanson, R. A. (1998). "Mechanics of granular materials at low effective stresses." *Journal of Aerospace Engineering*, 11(3), 67-72.
Sutherland, H. B. (1965). "Model studies for shaft raising through cohesionless soils." *Sixth International Conference on Soil Mechanics and Foundation Engineering*, 410-413.
Sutherland, H. B. (1988). "Uplift resistance of soils." *Geotechnique*, 38(4), 493-516.
Svano, G., Ilstad, T., Eiksund, G., and Watn, A. (2000). "Alternative calculation principle for design of piled embankments with base reinforcement." *4th conference on Grouting Soil Improvement Ecosystems including reinforcement, GIGS*, Finland, 541-548.
Swedish Road Board (1974). "Embankment Piles." *Report No. TV121*.
Tanaka, T., and Sakai, T. (1993). "Progressive failure and scale effects of trap-door problems with granular materials." *Soils and Foundations, Japanese Society of Soil Mechanics and Foundation Engineering*, 33(1), 11-22.
Tatsuoka, T., Sakamoto, M., Kawamura, T., and Fukushima, S. (1986). "Strength and deformation characteristics of sand in plane strain compression at extremely low pressures." *Soils and Foundations, Japanese Society of Soil Mechanics and Foundation Engineering*, 26(1), 65-84.
Terzaghi, K. (1943). *Theoretical Soil Mechanics*, John Wiley and Sons, Inc., New York.
Ting, W. H., Chan, S. F., and Ooi, T. A. (1994). "Design methodology and experiences with pile supported embankments." *Development in Geotechnical Engineeering*, Balkema, Rotterdam, 419-432.
Van Eekelen, S., Bezuijen, A., and Alexiew, D. (2008). "Piled embankments in the Netherlands, a full-scale test, comparing 2 years of measurements with design calculations." *EuroGeo4*, Edinburgh, Scotland.
Van Eekelen, S. J. M., and Oung, A. B. O. (2003). *Foundations: innovations, observations, design, and practice*, Thomas Telford, London, England.
Vardoulakis, I., Graf, B., and Gudehus, G. (1981). "Trap-door problem with dry sand: A statical approach based upon model test kinematics." *International Journal for Numerical and Analytical Methods in Geomechanics*, 5, 57-78.
Vermeer, P. A., and Sutjiadi, W. "The uplift resistance of shallow embedded anchors." *Proc., Proceedings of the 11th international conference on soil mechanics and foundation engineering*

Vesic, A. S. (1971). "Expansion of cavaties in infinite soil mass." *Journal of Soil Mechanics and Foundation Division, ASCE*, 98(SM3), 1183-1205.
Villard, P., Le Hello, B., Chew, S. H., Nancey, A., Delmas, P., Loke, K. H., and Mannsbart, G. (2004). "Use of high-strength geotextiles over piles - results from a full-scale test." *EuroGeo3 - Thrid European Geosynthetics Conference, Geotechnical Engineering with Geosynthetics*, Munich, Germany, 295-298.
Wood, H., Horgan, G., and Pedley, M. (2004). "A63 Selby Bypass - Design and construction of a 1.6 km geosynthetic reinforced piled embankment." *EuroGeo3*, Munich, Germany.
Xu, L. R., Lu, D. W., and Niu, J. D. (2007). "Formula of pile-soil stress ratio in pile-net

composite ground." *Journal of the Southest Asain Geotechnical Society*, 38(1), 8-15.
Yan, L., Yang, J. S., and Han, J. (2006). "Parametric study on geosynthetic-reinforced pile-supported embankments." *GeoShanghai, Advances in Earth Structures: Research to Practice (GSP 151)*, Shanghai, China, 255-261.
Zaeske, D. (2001). "Zur Wirkungsweise von unbewehrten und bewehrten mineralischen Tragschichten über pfahlartigen Gründungselementen." Schriftenreihe Geotechnik, Universität Gh-Kassel, Heft 10.

Appendix A: McGuire, M. P., and Filz, G. M. (2008). "Quantitative comparison of theories for geosynthetic reinforcement of column-supported embankments."

(Reproduced with permission from IGS)

The First Pan American Geosynthetics Conference & Exhibition
2-5 March 2008, Cancun, Mexico

Quantitative Comparison of Theories for Geosynthetic Reinforcement of Column-Supported Embankments

M.P. McGuire, Civil and Environmental Engineering Department, Virginia Tech, Blacksburg, Virginia, U.S.A.
G.M. Filz, Civil and Environmental Engineering Department, Virginia Tech, Blacksburg, Virginia, U.S.A.

ABSTRACT
Several theories have been published and used to calculate the vertical pressure that acts on, and the resulting tensile force that develops in, geosynthetic reinforcement at the base of column-supported embankments. This paper compares the results of these theories for a broad range of conditions of practical importance.

1. INTRODUCTION

Geosynthetic-reinforced, column-supported embankments have been used in soft ground conditions when there is a need to accelerate construction and/or protect adjacent facilities from the settlement that would otherwise be induced by the new embankment load. The columns in column-supported embankments can be driven piles or various types of formed-in-place columns. If driven piles are used, they are often fitted with pile caps to help transfer the embankment load to the piles. A bridging layer consisting of several feet of sand or sand and gravel is often used to help transfer the embankment load to the columns.

Geosynthetic-reinforced, column-supported embankments concentrate the embankment stress and live loads to the stiff columns through stress redistribution both above and below the foundation subgrade level. Mechanisms of load transfer present above the subgrade level consist of (1) arching within the embankment fill and (2) the vertical component of tension developed in the geosynthetic reinforcement. Below the foundation subgrade level, load transfer occurs via negative skin friction acting down on the column. Mobilization of these load transfer mechanisms requires differential settlement between the column and the soft foundation soil.

Several methods to calculate the vertical stress acting on and the resulting tension developed in the geosynthetic reinforcement are described in the published literature. The values of stress and tension predicted by these methods vary greatly in some cases, and there is not agreement on which method is correct. Inconsistencies among existing methods for determining the vertical stress on the reinforcement have been demonstrated by Habib et al. 2002, Horgan and Sarsby 2002, and Naughton and Kempton 2005 for certain conditions. This paper presents a comparison of existing methods for calculating the stress acting on and the resulting tension developed in the geosynthetic reinforcement over a broad range of conditions of practical importance.

2. METHODS STUDIED

2.1 Notation and Terminology

Consistent notation will be used throughout this paper, and consequently, it may differ from the source literature in some cases. The unit cell for a square array of columns is shown in Figure 1, and the contributing area of reinforcement for determining tension by the Parabolic Method, which is discussed below, is given in Figure 2.

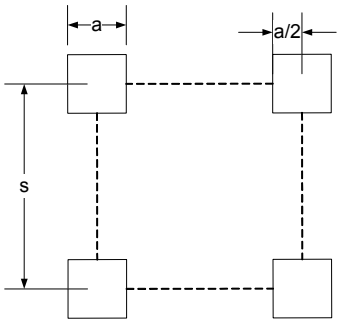

Figure 1. Unit cell for square array of columns.

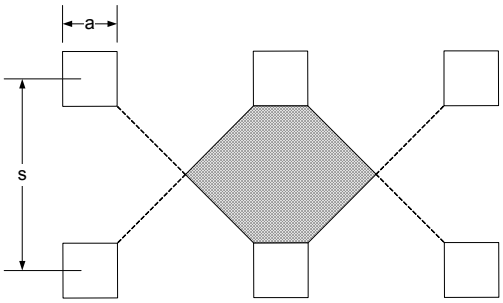

Figure 2. Contributing area that produces tension in reinforcement spanning the columns.

The following terminology is employed: γ = unit weight of embankment fill [kN/m^3], q = surcharge [kN/m^2], H = embankment height [m], H_{crit} = critical embankment height [m], A_{col} = area of column top or pile cap [m^2], A_{soil} = area of soil in one unit cell [m^2], A_t = total area of unit cell [m^2], a_s = area replacement ratio = A_{col}/A_t, p = net vertical stress acting on geosynthetic reinforcement [kN/m^2], SRR = stress reduction ratio = $p/(\gamma H + q)$, E = Efficacy = (stress on top of columns)$a_s/(\gamma H + q) = 1 - SRR(1 - a_s)$, T = tension in the reinforcement [kN/m], K = coefficient of lateral earth pressure in the Adapted Terzaghi Methods, K_p = Rankine coefficient of passive lateral earth pressure, and J = tensile stiffness of the reinforcement [kN/m].

2.2 Vertical Stress Acting on Geosynthetic Reinforcement

2.2.1 British Standard BS8006

The British Standard (BS8006 1995) "Code of Practice for strengthened/reinforced soils and other fills" has adopted the empirical method developed by Jones et al. (1990). The load on the area not supported by columns is treated as a uniform vertical line load, W_T, between adjacent supports for the purpose of determining the tension in the geosynthetic. Support from the foundation subgrade is not part of this method, which considers two possible cases depending on whether the embankment height is below H_{crit} = 1.4(s - a):

$$W_T = \frac{s\cdot(\gamma H+q)}{s^2-a^2}\left[s^2 - a^2\left(\frac{p_c}{\gamma H+q}\right)\right] \text{ for H } \le \text{ 1.4(s-a)} \quad [1a]$$

$$W_T = \frac{1.4\cdot s\cdot\gamma(s-a)}{s^2-a^2}\left[s^2 - a^2\left(\frac{p_c}{\gamma H+q}\right)\right] \text{ for H > 1.4(s-a)} \quad [1b]$$

where $p_c/(\gamma H + q) = (C_c/H)^2$. The term p_c is the vertical stress on the columns or pile caps determined based on Marston's equation for positive projecting subsurface conduits and C_c is the arching coefficient, which is dependent upon the height of the fill, the width of the pile caps, and the rigidity of the piles or columns, as follows: 1) for non-yielding piles, such as steel or concrete piles founded on an incompressible stratum, C_c = 1.95(H/a) - 0.18, 2) for steel or concrete friction piles, or timber piles, C_c = 1.70 (H/a) – 0.12 (Lawson 1992), and 3) for stone columns, lime columns, and sand compaction columns, C_c = 1.5 (H/a) - 0.07. The vertical line load, W_T, carries the entire load in the shaded area shown in Figure 2. Because the area of the shaded zone is equal to (s^2 - a^2)/2 and the line load distance is s - a, the vertical stress acting on the reinforcement can be found according to Equation 2.

$$p = \frac{2W_T}{s+a} \quad [2]$$

2.2.2 Adapted Terzaghi Methods

Russell and Pierpoint (1997) adapted Terzaghi's arching theory to take into account the three-dimensional nature of column arrangements. The settling soil mass is assumed to be cruciform in plan, as shown in Figure 1. The resulting stress reduction ratio, SRR, for this method is presented in Equation 3. Russell and Pierpoint (1997) assume a value of K equal to unity. This method does not consider subgrade support.

$$SRR = \frac{s^2-a^2}{4H\cdot a\cdot K\cdot\tan\phi}\left\{1-\exp\frac{-4H\cdot a\cdot K\cdot\tan\phi}{s^2-a^2}\right\} \quad [3]$$

Russell et al. (2003) presented a modified version of the Adapted Terzaghi Method. It was assumed that the portion of the embankment fill that settles as a cruciform has a height of ($n\cdot H$), and the embankment fill above this height is treated as a surcharge. The resulting stress reduction ratio is expressed in Equation 4.

$$SRR = \frac{\left(s^2-a^2\right)\gamma}{4\left(\gamma H+q\right)\cdot a\cdot K\cdot\tan\phi}\left\{1-\exp\frac{-4H\cdot a\cdot K\cdot\tan\phi}{s^2-a^2}\right\} + \frac{\gamma(1-n)H+q}{\gamma H+q}\exp\frac{-4H\cdot a\cdot K\cdot\tan\phi\cdot n}{s^2-a^2} \quad [4]$$

The coefficient, n, in Equation 4 is equal to unity for the ultimate limit state condition and 0.8 for serviceability limit state conditions. Russell et al. (2003) assume a value for the coefficient of passive lateral earth pressure equal to 0.5. Load transfer from the clay to the piles is based on a total stress analysis, but that aspect is not considered here.

By inspection, the expressions for stress reduction ratio for both Adapted Terzaghi Methods differ only in their assumed value of *K*, for the ultimate limit state condition when no surcharge is present. The stress acting on the geosynthetic reinforcement for both Adapted Terzaghi Methods is given by Equation 5.

$$p = SRR \cdot (\gamma H + q) \quad [5]$$

2.2.3 Hewlett and Randolph Method

Hewlett and Randolph (1988) presented theoretical methods for determining the embankment loads applied to columns and the foundation soil due to arching based on the limiting equilibrium of stresses in a hemispherical domed region of embankment fill over the piles. Hewlett and Randolph (1988) state that the domed regions will fail either at the crown of the arch or at the top of the column. Load concentration is evaluated in terms of efficacy, with the efficacy value at the crown of the arch given by Equation 6a and, at the top of the column, by Equation 6b.

$$E = 1 - \left[1 - \left(\frac{a}{s}\right)^2\right] \cdot \left[\left(1 - \frac{a}{s}\right)^{2(K_p - 1)} \left(1 - \frac{s \cdot 2(K_p - 1)}{\sqrt{2} \cdot H \cdot (2K_p - 3)}\right) + \left(\frac{(s - a) \cdot 2(K_p - 1)}{\sqrt{2} \cdot H \cdot (2K_p - 3)}\right)\right] \quad [6a]$$

$$E = \frac{\beta}{1 + \beta} \qquad \text{where } \beta = \left(\frac{2K_p}{K_p + 1}\right)\left(\frac{1}{1 + \frac{a}{s}}\right)\left[\left(1 - \frac{a}{s}\right)^{-K_p} - \left(1 + \frac{a}{s} \cdot K_p\right)\right] \quad [6b]$$

The critical efficacy, as determined from Equations 6, is the lower of the two values. At low embankment heights the critical efficacy is governed by the condition at the arch crown, and as embankment height increases, the critical region transfers to the top of the columns. Using the critical value of efficacy, the vertical pressure acting on the geosynthetic reinforcement can be found using Equation 7.

$$p = \frac{(1 - E)(\gamma H + q)}{(1 - a_s)} \quad [7]$$

Kempfert et al. (1997) indicate that the method proposed by Hewlett and Randolph (1988) is valid as long as the height of the embankment is equal to or greater than the pile spacing. Kempfert et al. (1997) recommend that the efficacy for embankment heights less than the pile spacing be determined by linear interpolation between the values of efficacy at the critical height and the value of efficacy for no arching, which is simply the area replacement ratio.

2.2.4 Kempfert Method

Kempfert et al. (2004) present a method for calculating the vertical stress acting on the top side of the reinforcement using a domed analytical model based on plasticity theory. This calculated stress, which incorporates the effects of stress reduction due to soil arching within the embankment, is given by Equation 8.

$$p = \lambda_1^{\chi}\left(\gamma + \frac{q}{H}\right)\left[H\left(\lambda_1 + h_g^2\lambda_2\right)^{-\chi} + h_g\left(\left(\lambda_1 + \frac{h_g^2\lambda_2}{4}\right)^{-\chi} - \left(\lambda_1 + h_g^2\lambda_2\right)^{-\chi}\right)\right] \quad [8]$$

where s_g = 1.414(*s*), d_c = column diameter = 1.128(*a*), $\lambda_1 = (s_g - d_c)^2/8$, $\lambda_2 = (s_g^2 + 2d_c s_g - d_c^2)/(2s_g^2)$, $\chi = d_c(K_p - 1)/(\lambda_2 s_g)$, $h_g = s_g/2$ for $H > s_g/2$, and $h_g = H$ for $H < s_g/2$. The influence of subgrade support is accounted for by considering a modulus of subgrade reaction of the foundation soil during calculation of the tension developed within the reinforcement. For the purposes of this study, no subgrade support will be considered, although an adjustment to *p* during the strain calculation step is believed to be possible to account for subgrade support.

2.2.5 Adapted Guido Method

Guido et al. (1987) showed that inclusion of stiff geogrids in granular layers beneath spread footings can improve bearing capacity. Bell et al. (1994) applied this finding to evaluate an embankment with two layers of geosynthetic reinforcement supported on vibro-concrete columns. Russell and Pierpoint (1997) adapted the approach by Bell et al. (1994) to determine an *SRR* value based on a single layer of reinforcement at the base of an embankment fill. Russell and Pierpoint (1997) assumed that the geosynthetic reinforcement carries a pyramid of soil that is not supported by the piles, with ridge lines of the pyramid at an angle of 45 degrees above the horizontal and a square base with side lengths of (*s* - *a*). The vertical pressure for this method is given in Equation 9, which is based on an

interior area of $(s - a)^2$, rather than the cruciform area ($s^2 - a^2$). This method does not incorporate support provided by the foundation soil.

$$p = \frac{(s-a)}{3\sqrt{2}}(\gamma) \quad [9]$$

2.2.6 Swedish Method

Carlsson (1987) presents in Swedish a method for calculating the vertical pressure on geosynthetic reinforcement using a two-dimensional triangular wedge of soil with an internal angle at the apex equal to 30 degrees and a base equal to the clear spacing of the columns (s - a). This method is discussed in English by Rogbeck et al. (1998). The wedge of soil carried by the reinforcement has a weight given by $(s - a)^2\gamma/(4 \tan 15°)$. This weight acts over the length of the clear span, $(s - a)$, without support from the foundation subgrade. So, for a unit length of the soil wedge, the average pressure acting on the geosynthetic reinforcement is given by Equation 10.

$$p = \frac{s-a}{4\tan 15}\gamma \quad [10]$$

For embankment heights less than the critical height of 1/(2 tan15°), the upper part of the 2D wedge can be truncated by the difference between the critical height and the actual embankment height, and the remaining area is used to calculate the weight of soil supported by the reinforcement.

2.2.7 Naughton Method

The Naughton (2007) method is based on the assertion by Terzaghi (1943) that the shear planes produced at the edges of a trap door opening are log-spiral in shape. Naughton (2007) applied the log-spiral shape to the shear planes developed in the embankment fill due to arching for embankments with columns laid out in a square array. This method does not consider support from the foundation subgrade. The resulting expression for the vertical stress acting on the geosynthetic reinforcement is given by Equation 11, where ϕ is the friction angle of the embankment fill.

$$p = \frac{(s-a)(\gamma H + q)}{2H}\exp\left(\frac{\pi}{2}\tan\phi\right) \quad [11]$$

2.2.8 Collin Method

This method presented in Collin (2004, 2007) is similar to the Adapted Guido method presented by Bell et al. (1994) in that the stress acting on the geosynthetic reinforcement is based on an unsupported soil mass in the shape a pyramid. The pyramid in the Collin Method has faces inclined at 45 degrees above horizontal, rather than the ridge lines as with the Adapted Guido Method. The Collin Method considers a minimum of three layers of geosynthetic within the height of the soil pyramid, plus an additional layer referred to as the “catenary layer” at the foundation subgrade. For the purposes of this study, the same approach used by Russell and Pierpoint (1997) for adaptation of the Bell et al. (1994) method, which also utilized multiple layers of reinforcement, will be applied to the Collin method, with the weight of the entire unsupported pyramid applied to the bottom catenary layer of reinforcement. For a square array of columns, the vertical pressure acting on the reinforcement is given by Equation 12.

$$p = \frac{s-a}{6}\gamma \quad [12]$$

2.2.9 Filz and Smith Method

The Filz and Smith (2006) method is based on load-displacement compatibility among the embankment, columns, geosynthetic reinforcement, and foundation soil. Differential settlement between the columns and the foundation soil is determined as the difference between the vertical elastic deformation of the column and the settlement of the foundation soil, which comprises elastic compression of granular foundation soils, if present, and nonlinear compression of clay foundation soils. Friction between the settling foundation soils and the columns is accounted for by considering the interface friction angle and the lateral pressure produced by column installation as well as Poisson effects from the embankment load determined according to a concentric cylinder model (Davis and Poulos 1974).

The load-deflection response of geosynthetic reinforcement is obtained from axisymmetric numerical analyses of an annular membrane. The load-deflection relationship for the column or pile cap penetrating up, relatively, into the embankment is assumed to be linear up to a maximum load condition. The linear part is approximated using the

linear-elastic solution for displacement of a rigid circular loaded area on a semi-infinite mass (Davis and Poulos 1974). The maximum load condition on the column area above the reinforcement level is established by setting a lower limit on the value of *SRR* using the Adapted Terzaghi Method with an assumed value of K_p equal to 0.75, which is between the values of 1.0 used by Russell and Pierpoint (1997) and 0.5 used by Russell et al. (2003), and which provides reasonable agreement with numerical analyses used to calibrate the method.

The simultaneous solution among the load-displacement compatibility relations for the embankment fill, geosynthetic reinforcement, columns, and foundation soils is performed using an iterative technique implemented in a Microsoft Excel® spreadsheet, which calculates the net vertical stress acting down on the geosynthetic reinforcement.

2.3 Tension within Geosynthetic Reinforcement

This section describes three approaches for determining the tension developed within the geosynthetic reinforcement due to the net vertical load. Reinforcement can also provide resistance to outward thrust load due to lateral spreading of the embankment, but this component of tension is not included in the current study.

2.3.1 Parabolic Methods

The method for reinforcement tension presented in both the British Standard BS8006 method and the Swedish method (Rogbeck et al. 1998) calculates tension in the geosynthetic reinforcement based on the assumption that the two-dimensional projection of the deflected shape of the reinforcement is parabolic across the clear span, (s - a), of the columns and that tension is uniform and critical in the reinforcement spanning directly between adjacent columns in the area equal to (a)·(s - a). Vertical equilibrium requires that the vertical component of this tension equals the applied load, $W_T(s - a)$, which also equals the vertical pressure times the shaded area of Figure 2, $p(s^2 - a^2)/2$. Giroud (1995) showed that, if the ratio between the maximum vertical deflection and the clear span is small, the strain in parabolically deforming reinforcement can be reasonably approximated by $\varepsilon = 8d^2/[3(s - a)^2]$. Based on these assumptions, the tension can be determined according to Equation 13.

$$T = \frac{p(s^2 - a^2)}{4a}\sqrt{1 + \frac{1}{6\varepsilon}} \qquad [13]$$

Both the BS8006 and Swedish methods calculate tension based on an assumed design value for strain, typically about 5% or 6%. However, stress-strain compatibility can be applied by substituting $\varepsilon = (T/J)$ into Equation 13 giving Equation 14, which can be solved to give the tension without having to assume a value of strain.

$$96T^3 - 6\hat{K}_g^2 T - \hat{K}_g^2 J = 0 \quad \text{where } \hat{K}_g = \left(\frac{p(s^2 - a^2)}{a}\right) \qquad [14]$$

2.3.2 Tensioned Membrane Method

The Tensioned Membrane Method is presented in Collin (2004, 2007) and is an adaptation of the work by Giroud (1990) for calculating tension in geosynthetics spanning voids. For a single layer of reinforcement at the subgrade level, this procedure assumes a circular void exists beneath the reinforcement with a diameter equal to the diagonal clear spacing, $\sqrt{2}\cdot(s - a)$, for a square array of columns. Tensioned membrane theory assumes the deflected shape of the reinforcement is a circular arc. The approach is derived in Giroud (1990) for an infinitely long void and assumes that the strain in the reinforcement overlying the void is uniform and that no strain exists beyond the extent of the void. Giroud gives recommendations for adapting the infinitely long void case to a circular void, and he indicates that the difference in deflected shape allows only for an approximation of the average tension. For the case of a circular void, the tension in the membrane is provided by Equation 15.

$$T = \frac{p(s - a)\Omega}{\sqrt{2}} \quad \text{where } \Omega \text{ is a dimensionless coefficient determined by } 1 + \varepsilon = 2\Omega \sin^{-1}\left[\frac{1}{2\Omega}\right] \qquad [15]$$

The approach by Collin (2004, 2007) uses an assumed design value of strain not to exceed 5%. However, stress-strain compatibility, $\varepsilon = (T/J)$, can be applied to Equation 15 yielding Equation 16 which can be solved to give the tension without having to assume a value of strain.

$$\left(\frac{2\sqrt{2}\cdot T \cdot J}{p(s - a)}\right)\sin^{-1}\left(\frac{p(s - a)}{2\sqrt{2}\cdot T}\right) - T - J = 0 \qquad [16]$$

2.3.3 Kempfert Method

Kempfert et al. (2004) present a method for evaluating the tension in the geosynthetic reinforcement. In practice, strain is determined using dimensionless design charts and the tension is determined by stress-strain compatibility. Application of a subgrade reaction modulus acts to reduce reinforcement strain, but that effect is not studied here.

3. PARAMETRIC STUDY

A parametric study was conducted to evaluate the methods described herein for determining the net vertical load acting on and the resulting tension developed within the geosynthetic reinforcement. A simple column-supported geosynthetic-reinforced embankment shown in Figure 3 was considered for this analysis. Table 1 shows the parameters studied and the range considered in this analysis. For the purposes of this analysis, input parameters that could be determined or estimated from parameters in Table 1 were considered dependent parameters, and they were assigned values consistent with the values of the independent parameters.

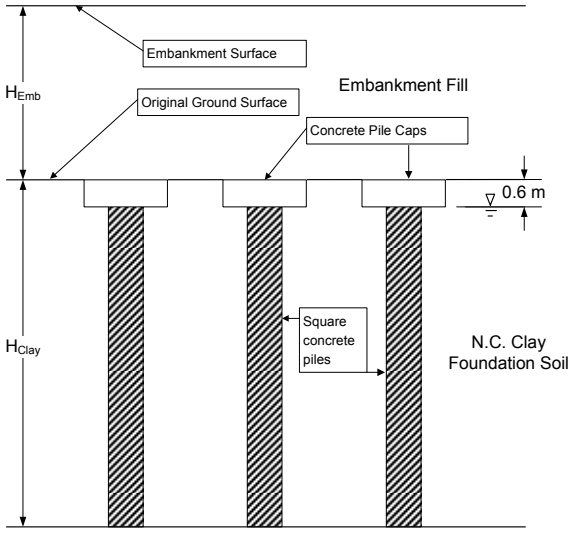

Figure 3. Embankment Cross-section.

Table 1. Parameter values.

Embankment Parameters	Base Case	Parametric Range
Height of Embankment	**2.50**	(1.25 - 5.00)
Properties of Embankment Fill		
Total Unit Weight (kN/m3)	**19**	(16 - 22)
Friction Angle (deg)	**35**	(30 - 40)
N.C. Clay Properties		
Thickness of Clay (m)	**7.5**	(3.5 - 11.0)
Total Unit Weight (kN/m3)	**16.5**	(13.0 - 19.5)
Compression Ratio, Cec	**0.2**	(0.01 - 0.50)
Column Properties		
Column Spacing (m)	**2.50**	(1.80 - 3.50)
Column width (m)	**0.46**	
Cap Width (m)	**1**	(0.6 - 1.5)
Cap Thickness (m)	**0.6**	
Reinforcement Properties		
Tensile Stiffness, J (kN/m)	**914**	

Figures 4 through 10 show the vertical stress acting down on the geosynthetic versus parameter variations for ten calculation methods. Figures 11 through 15 show the tension that develops in the geosynthetic versus parameter variations for five calculation methods, for which stress-strain consistency is incorporated in the "Parabolic Curve," "Tensioned Membrane," and "Kempfert" methods, but 5% strain has been assumed and stress-strain consistency is not incorporated in the "Assumed Strain Parabolic Curve" and "Assumed Strain Tensioned Membrane" methods.

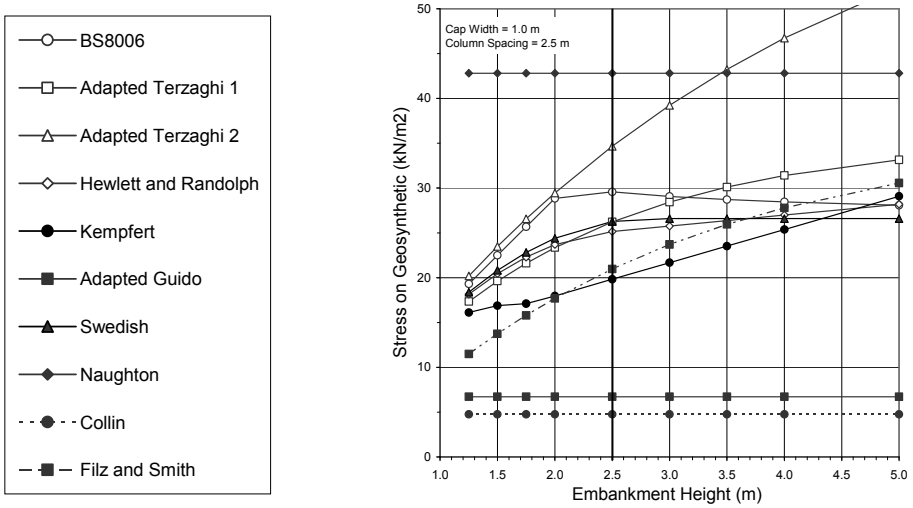

Figure 4. Legend for Figures 4 through 10, and Stress on Geosynthetic Reinforcement Versus Embankment Height.

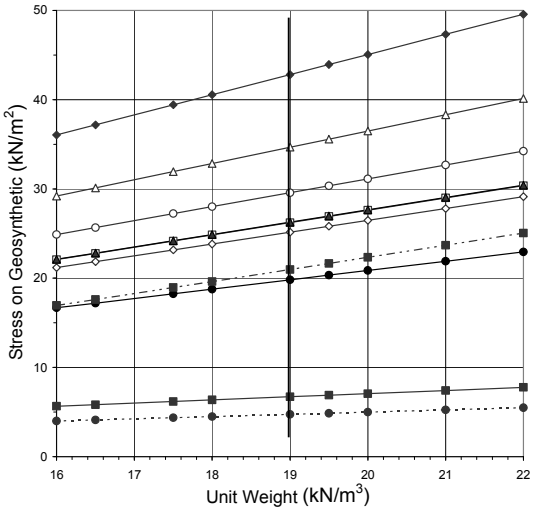

Figure 5. Stress on Geosynthetic Reinforcement Versus Unit Weight of Embankment Fill.

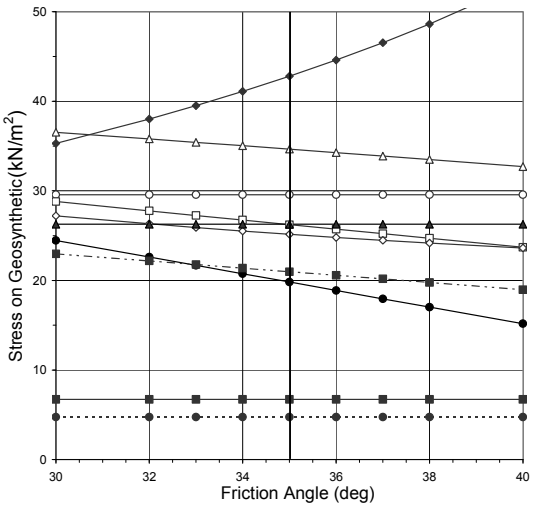

Figure 6. Stress on Geosynthetic Reinforcement Versus Friction Angle of Embankment Fill.

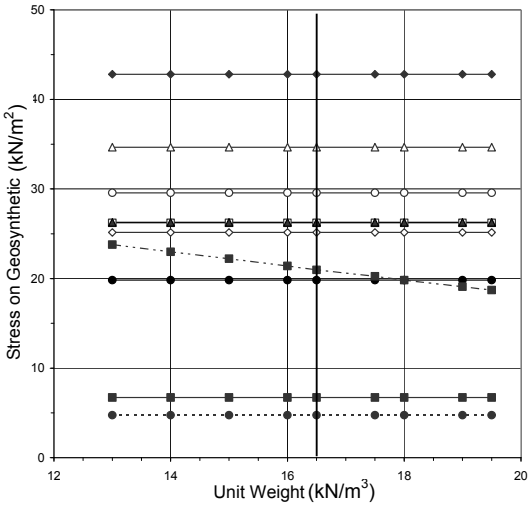

Figure 7. Stress on Geosynthetic Reinforcement Versus Unit Weight of Clay Foundation Soil.

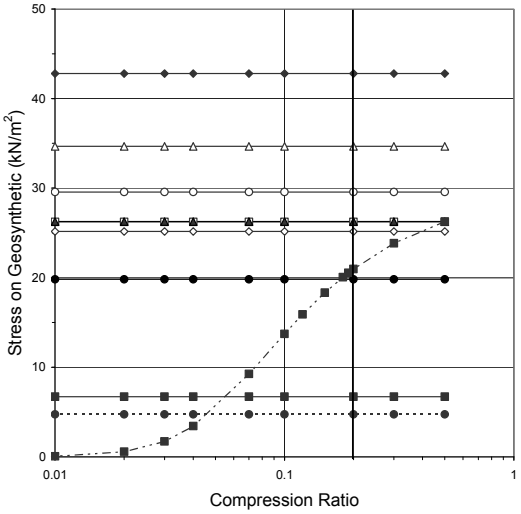

Figure 8. Stress on Geosynthetic Reinforment Versus Compression Ratio of Clay Foundation Soil.

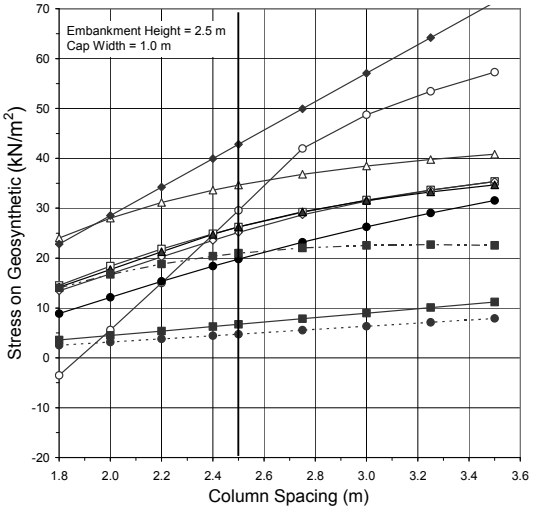

Figure 9. Stress on Geosynthetic Reinforcement Versus Column Spacing.

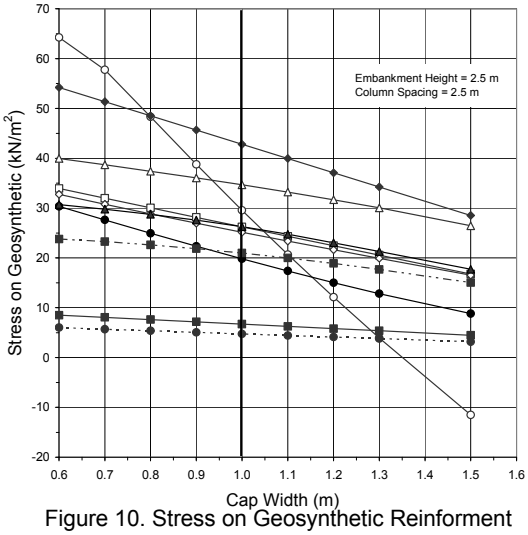

Figure 10. Stress on Geosynthetic Reinforment Versus Pile Cap Width.

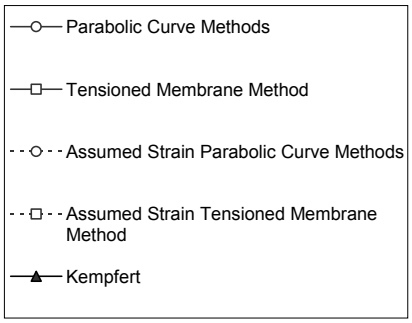

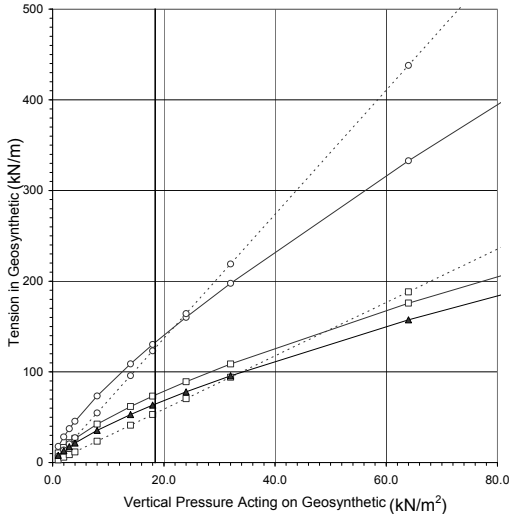

Figure 11. Legend for Figures 11 through 15, and Tension in Geosynthetic Reinforcement Versus Vertical Pressure.

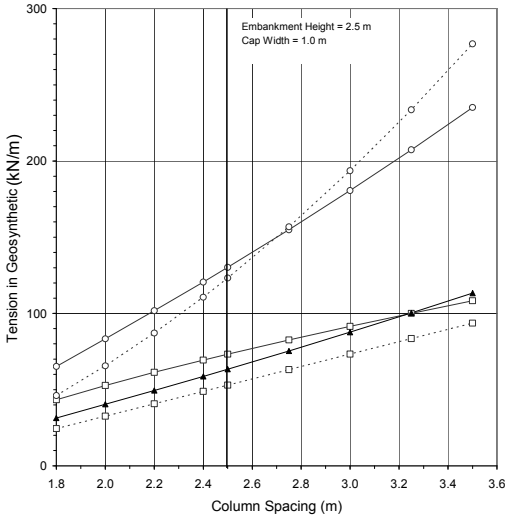

Figure 12. Tension in Geosynthetic Reinforcement Versus Column Spacing.

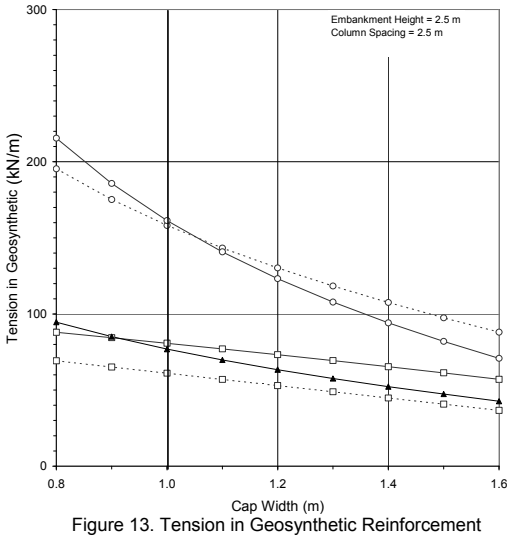

Figure 13. Tension in Geosynthetic Reinforcement Versus Pile Cap Width.

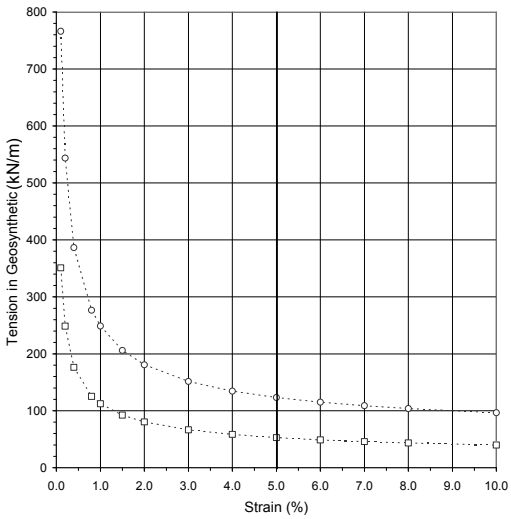

Figure 14. Tension in Geosynthetic Reinforcement Versus Assumed Strain.

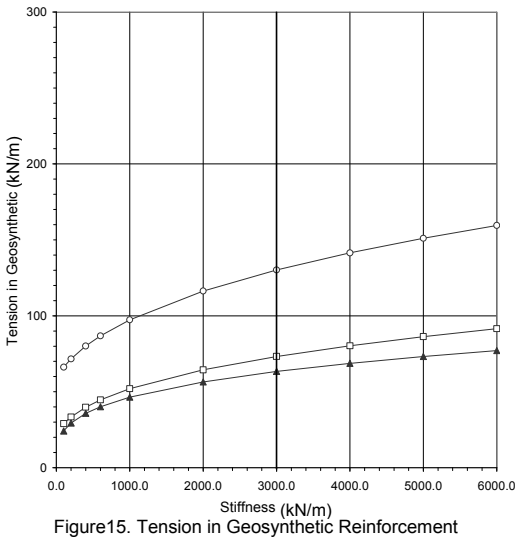

Figure15. Tension in Geosynthetic Reinforcement Versus Reinforcement Stiffness.

4. CONCLUSIONS AND COMMENTS

The following conclusions and comments regarding vertical pressure acting down on the geosynthetic reinforcement are offered, based on the results shown in Figures 4 through 10 for the ranges of parameter values investigated.

- Most methods show an increase in pressure as the embankment height increases. The Naughton, Adapted Guido, and Collin methods are insensitive to embankment height, and the BS8006 method shows an increase and then a slight decrease as embankment height increases.
- The Collin and Adapted Guido methods produce low values of pressure compared to the other methods.
- All methods show an increase in pressure as the unit weight of the embankment fill increases.
- The Adapted Terzaghi, Hewlett and Randolph, Kempfert, and Filz and Smith methods show decreasing pressure as the friction angle of the embankment fill increases. The BS8006, Swedish, Adapted Guido, and Collin methods are insensitive to friction angle of the embankment fill. Unlike all the other methods, the Naughton method exhibits an increase in pressure as the friction angle of the embankment fill increases.
- The pressure is insensitive to the characteristics of the clay foundation soil for all methods except the Filz and Smith method, which shows a slight decrease in net pressure as the unit weight of the clay soil increases and a large decrease in pressure as the compression ratio of the clay soil decreases. Both an increase in the unit weight and a decrease in the compression ratio correspond to decreases in the compressibility of the clay, which corresponds to increasing support provided by the clay soil and decreasing net pressure on the geosynthetic. According to the Filz and Smith method, subgrade support can have a dramatic impact on the net pressure applied to the geosynthetic reinforcement. It is recognized that the Kempfert method would also show this trend, if the subgrade support in that method were de-coupled from the strain calculation.
- All methods exhibit an increase in pressure with increased column spacing and a decrease in pressure with increased pile cap width. The BS8006 method is most dramatic in this regard, and it can even produce negative pressures for some system geometries.

The following conclusions and comments regarding tension developing in the geosynthetic reinforcement are offered, based on the results shown in Figures 11 through 15 for the ranges of parameter values investigated.

- All methods show an increase in tension as vertical pressure on the geosynthetic reinforcement increases.
- The parabolic method produces larger tension than the tensioned membrane or Kempfert methods, which produce similar values.
- The assumed strain methods are unconservative at low pressures and conservative at high pressures, when compared to the corresponding methods that incorporate stress-strain consistency.
- All methods show increases in tension with increasing column spacing and decreases in tension with increasing pile cap width.
- For the assumed strain methods, the tension decreases as the strain increases. This is not logical from a mechanics-of-materials perspective. It occurs because the impact of increased geosynthetic strain in these methods is only to increase the angle of the geosynthetic at its support location, which means that a smaller tension can produce the same vertical component needed to satisfy equilibrium with the applied vertical pressure.
- For the methods that incorporate stress-strain compatibility of the geosynthetic, the tension increases as the geosynthetic stiffness increases, as expected.

ACKNOWLEDGEMENTS

The information presented in this paper is based on work supported by the U.S. Department of Education and the U.S. National Science Foundation, whose support was provided under grant No. CMS-0408281. Any opinions, findings, conclusions, and recommendations in this paper are those of the authors and do not necessarily reflect the views of the U.S. Department of Education or the U.S. National Science Foundation.

REFERENCES

Bell, A. L., Jenner, C., Maddison, J. D., and Vignoles, J. (1994). Embankment support using geogrids with vibro concrete columns. *Proceedings, 5th International Conference on Geotextiles, Geomembranes, and Related Products,* Vol. 1, Karunaratne, Chew and Wong (eds), Singapore, pp. 335-338.

British Standards Institution. (1995). BS8006 Code of Practice for Strengthened/Reinforced Soils and Other Fills. London, U.K.

Collin, J.G. (2007) U.S. state-of practice for the design of the geosynthetic reinforced load transfer platform in column supported embankments. *Soil Improvement*, GSP 172, (on CD-ROM), ASCE, Reston, Virginia.

Collin, J. G. (2004). Column supported embankment design considerations. *Proceedings of the 52nd Annual Geotechnical Engineering Conference*, J.F. Labuz and J.G. Bentler (eds.), Minnesota, pp. 51-78.

Giroud, J.P. (1995). Determination of geosynthetic strain due to deflection, *Geosynthetics International*, Vol. 2, No. 3, pp. 635-641

Giroud, J.P., Bonaparte, R., Beech, J.F., and Gross, B.A. (1990). Design of soil layer – geosynthetic systems overlying voids, *Geotextile and Geomembranes*, Vol 9, pp. 11-50.

Guido, V. A., Knueppel, J.D. and Sweeny, M.A. (1987). Plate loading tests on geogrid-reinforced earth slabs. *Geosynthetic '87 Conference,* New Orleans, pp. 216-225.

Habib, H. A. A., Brugman, M.H.A. and Uijting, BG.J. (2002). Widening of Road N247 founded on a geogrid reinforced mattress on piles. *Proceedings, 7th International Conference on Geosynthetics*, Delmas, Gourc, & Girard (eds), Swets & Zeitlinger, Lisse, pp. 369-372.

Hewlett, W. J., and Randolph, M.F. (1998). Analysis of piled embankments. *Ground Engineering,* Vol. 22, No. 3, pp. 12-18.

Horgan, G. J., and Sarsby, R.W. (2002). The arching effect of soils over voids and piles incorporating geosynthetic reinforcement. *Proceedings, 7th International Conference on Geosynthetics*, Delmas, Gourc, & Girard (eds), Swets & Zeitlinger, Lisse, pp. 373-378.

Filz, G.M., and Smith, M.E. (2006). "Design of bridging layers in geosynthetic-reinforced, column-supported embankments." *Contract Report* VTRC 06-CR12, Virginia Transportation Research Council, Charlottesville.

John, N. W. M. (1987). *Geotextiles*. Blackie & Son Ltd., Glasgow and London.

Jones, C. J. F. P., Lawson, C.R., and Ayres, D.J. (1990). Geotextile reinforced piled embankments. *Proceedings, 4th International Conference on Geotextiles, Geomembranes, and Related Products,* Vol. 1, G. Den Hoedt (ed), The Hague, pp. 155-160.

Kempfert, H.-G., Gobel, C., Alexiew, D. and Heitz, C. (2004). German recommendations for reinforced embankments on pile-similar elements. *EuroGeo3 - Third European Geosynthetics Conference, Geotechnical Engineering with Geosynthetics,* pp. 279-284.

Kempfert, H. - G., Stadel, M. and Zaeske, D. (1997). Design of geosynthetic-reinforced bearing layers over piles. *Bautechnik*, Vol. 74, No. 12, pp. 818-825.

Lawson, C. R. (1992). Soil reinforcement with geosynthetics. *Applied Ground Improvement Techniques,* Southeast Asian Geotechnical Society (SEAGS), pp. 55-74.

Naughton, P.J. (2007). The significance of critical height in the design of piled embankments. *Soil Improvement*, GSP 172, (on CD-ROM), ASCE, Reston, Virginia.

Naughton, P.J., and Kempton, G.T. (2005). Comparison of analytical and numerical analysis design methods of piled embankments. *GeoFrontiers* 2005.

Rogbeck, Y., Gustavsson, S., Sodergren, I., and Lindquist, D. (1998). Reinforced piled embankments in Sweden - design aspects. *Proceedings, Sixth International Conference on Geosynthetics*, Vol. 2, Rowe, R.K. (ed.), Atlanta, Georgia, pp. 755-762.

Russell, D., Naughton, P.J. and G. Kempton, G. (2003). A new design procedure for piled embankments. *Proceedings of the 56th Canadian Geotechnical Conference and 2003 NAGS Conference,* Vol. 1, Winnipeg, MB, pp. 858-865.

Russell, D., and Pierpoint, N. (1997). An assessment of design methods for piled embankments. *Ground Engineering,* Vol. 30, No. 11, pp. 39-44.

Appendix B: McGuire, M. P., Filz, G. M., and Almeida, M. S. S. (2009). "Load-displacement compatibility analysis of a low-height column-supported embankment."

(Reproduced with permission from ASCE)

Load-Displacement Compatibility Analysis of a Low-Height Column-Supported Embankment

Michael P. McGuire, P.E.[1], George M. Filz, P.E.[2], and Marcio S.S. Almeida[3]

[1]PhD candidate, Dept. of Civil and Environmental Engineering, Virginia Polytechnic Institute and State Univ., Blacksburg, VA 24060-0105. Email: mcguirem@vt.edu
[2]Professor, Dept. of Civil and Environmental Engineering, Virginia Polytechnic Institute and State Univ., Blacksburg, VA 24060-0105. Email: filz@vt.edu
[3]Professor, Graduate School of Engineering, Federal University of Rio de Janeiro, Rio de Janeiro, Brazil. Email: almeida@coc.ufrj.br

ABSTRACT

This paper presents instrumentation results and analyses of a low-height, geosynthetic-reinforced, column-supported embankment constructed in Brazil. The approach involves back analyzing relevant properties of the embankment fill and geogrid reinforcement and applying the Load Displacement Compatibility (LDC) approach to calculate geogrid deflections in a unit cell of a square pile cap array. The results show that the LDC approach is consistent with the observed response of the embankment.

INTRODUCTION

Geosynthetic-reinforced, column-supported embankments (GRCSEs) are constructed over soft ground to accelerate construction, improve embankment stability, control total and differential settlements, and protect adjacent facilities from the settlement that would otherwise be induced by the new embankment load. The geosynthetic reinforcement generally consists of one or more layers of geogrid or high-strength woven fabric that are placed at the base of the embankment near the elevation of the top of the columns or pile caps. In addition to resisting lateral spreading, the purpose of the reinforcement is to aid in the transfer of embankment loads to the columns. One of several important design considerations for GRCSEs is limiting the strain and vertical deflection of the geogrid under service conditions. For instances when the embankment height is low relative to the clear spacing between adjacent columns, excessive levels of strain developing within the geosynthetic reinforcement can lead to surface expression of differential settlements between the columns and the soft soil at the foundation level.

This paper examines a full-scale GRCSE constructed in the Barra da Tijuca District of Rio de Janeiro, Brazil. This embankment was designed such that the clear spacing between columns exceeded the supported embankment height. A portion of this low-height embankment was instrumented to allow for measurement of the vertical deflection and strain of the reinforcement. Analyses and comparisons with deflection and strain measurements are presented.

CASE STUDY

A low-height GRCSE was constructed in 2004 on a pre-existing fill overlying an approximately 10 m thick layer of very soft clay in the Barra da Tijuca District of Rio de Janeiro. The roughly 2 m thick existing fill was placed in 1996 as part of the original plan to construct the embankment without columns by surcharging and accelerating consolidation with vertical drains. Lawsuits delayed construction, and eventually a decision was made to construct the embankment as a GRCSE. The second phase of embankment construction increased the embankment height, H, by roughly 1 to 1.3 meters. A portion of the GRCSE was instrumented and used as an experimental site, with three types of pile cap arrangements, as shown in Figure 1. For all three arrangements, square precast concrete piles with a width of 0.18 m were used to support the pile caps. At Locations A and B, the piles were driven in a square array with a 2.5 m center-to-center spacing, s, and square pile caps with a side length, a, of 0.8 m were used. At Locations C and D, 8.3 m long and 0.8 m wide cap beams were used with center-to-center spacings of 2.5 and 3.5 m, respectively. For all pile cap arrangements, the clear spacing, s - a, exceeds the embankment height of 1 to 1.3 m. Additional details regarding the experimental site can be found in Spotti (2006), Almeida et al. (2007), and Almeida et al. (2008).

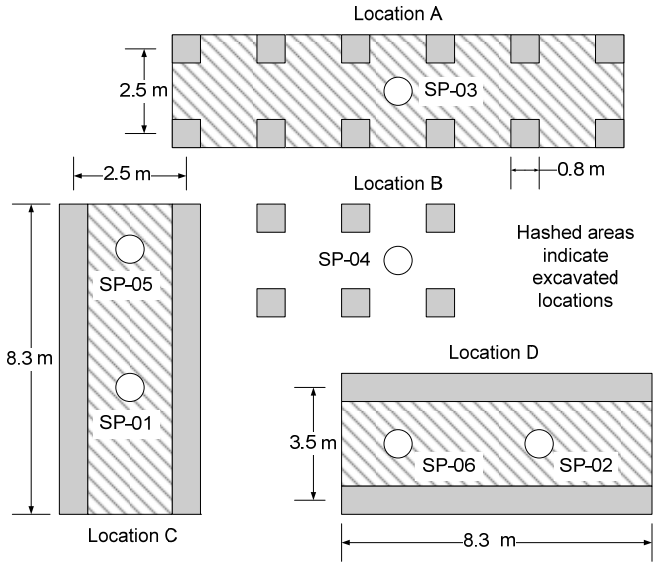

Figure 1: Layout of experimental site in the Barra da Tijuca District

A single layer of Huesker FORTRAC 200/200-30 polyester biaxial geogrid was placed over the pile caps with an underlying cushioning layer of non-woven geotextile to reduce abrasion. Field and laboratory testing was performed on the embankment material and underlying soft clay, and the details can be found in Spotti (2006). The embankment material used for both the 1996 and 2004 phases of construction consisted of a clayey sand compacted to at least 95% of the standard Proctor maximum and having a compacted unit weight, γ, of about 18 kN/m^3. The soft clay has a unit weight of about 12.5 kN/m^3, an undrained strength of 10 to 20 kPa, and a plasticity index of 120 to 250. The clay compressibility was assessed using conventional laboratory consolidation tests, which showed that the clay is normally consolidated with a representative compression ratio of 0.4 to 0.5. A stiff residual soil stratum underlies the clay layer.

To investigate the influence of subgrade support on load transfer mechanisms within the GRCSE, 1 m deep excavations were made prior to placement of the geogrid and embankment fill at Locations A, C, and D. An attempt to keep the geogrid taut was made by loading the edges with fill, although photos taken at the site indicate that some portions of the reinforcement did sag prior to placement of the embankment fill. Compaction of the lower lifts of fill material over the unsupported geogrid was performed with care using light equipment.

Instrumentation consisted of settlement plates (SP) installed at the level of the reinforcement at the locations shown in Figure 1 and strain gauges installed at Location A. Additional details regarding instrumentation can be found in Spotti (2006) and Almeida et al. (2007). Readings were taken over a period of 188 days after embankment construction. In all cases, the time history of the data indicates that the instrumentation readings had reached constant values during the monitoring period, which suggests that the soft clay had, for all practical purposes, completed primary consolidation.

ANALYSES

The settlement plate readings taken at Locations C and D were used to develop a single representative set of property values for the embankment material and geogrid reinforcement. These values were then used with the LDC approach (Filz and Smith 2006a) to produce calculated values of vertical geogrid deflection, which were compared to the settlement plate measurements.

Back Analysis of Embankment and Reinforcement Parameters

The method of back analysis was used to obtain representative properties of the embankment material and the geogrid reinforcement. The parameters varied in the back analyses were the shear strength properties (ϕ and c) of the embankment fill, the lateral earth pressure coefficient, K, used in the soil arching analysis (Terzaghi 1943, Russell et al. 2003), and the tensile stiffness, J, of the geogrid reinforcement. The back analyses were done in two dimensions because the cap beams are much longer than the clear span at Locations C and D. The two-dimensional approximation and the lack of subgrade support at both locations allows for direct application of

Terzaghi's (1943) expressions for estimating the vertical soil pressure acting on a downward yielding surface between two fixed supports. Using the current set of notation, the expression for calculating the net vertical pressure acting on the reinforcement, p, is

$$p = \frac{(s\text{-}a)\gamma\text{-}2c}{2K\tan\phi}\left(1 - e^{-2HK\tan\phi/(s-a)}\right) \tag{1}$$

The 2D parabolic approach provided by Carlsson (1987) in Rogbeck et al. (1998) was used for the load-deflection response of the geogrid. The tension, T, developed within the reinforcement can be determined using

$$T = \frac{p(s-a)}{2}\sqrt{1+\frac{1}{6\varepsilon}} \tag{2}$$

Stress-strain compatibility can be incorporated by substituting $\varepsilon = T/J$ into Eq. 2 yielding

$$24T^3 - 6\ddot{K}_g^2 - \ddot{K}_g^2 J = 0 \quad \text{where } \ddot{K}_g = p(s-a) \tag{3}$$

Eq (3) can be solved for T, which gives the strain using J. The maximum vertical deflection, d, for the assumed parabolic deformed shape of the reinforcement can be obtained from the reinforcement strain using $d \approx (s\text{-}a)\,(3\varepsilon/8)^{0.5}$.

Table 1 lists the final settlement plate readings at Locations C and D along with the corresponding embankment height at the settlement plate locations.

Table 1: Settlement plate readings 188 days following construction

Location	Settlement Plate	Embankment Height (m)	Measured Settlement (m)
C	SP-01	1.10	0.32
C	SP-05	1.14	0.22
D	SP-06	1.25	0.40
D	SP-02	1.28	0.37

The preceding expressions were used to calculate the geogrid deflections at the locations provided in Table 1. Initially, the shear strength parameters of the embankment fill, the earth pressure coefficient (K), and the geogrid stiffness were selected based on the available laboratory testing and the geogrid manufacturers specifications. These values were then incrementally adjusted independently such that good agreement between the predicted and measured values was achieved. It was not possible to choose one set of parameter values that simultaneously yielded good agreement at all four locations. It is believed that initial slack in the geogrid

reinforcement at the location of SP-01 lead to a measured deflection that incorporates the release of the slack under vertical loading in addition to the deflection produced by the developed strain. Justification for this lies in the fact that the measured deflection at SP-01 exceeds the calculated deflection, even for the case of no stress reduction, i.e., $p = \gamma H$. Parameter values that provided good agreement between the predicted and measured geogrid deflections at SP-05, SP-06, and SP-02 are given in the first row of Table 2.

Table 2: Relevant properties of geogrid and embankment

Fill material	ϕ	c (kPa)	K	J (kN/m)
Clayey sand	37	11	0.8	1600
Equivalent c = 0 soil	68	0	0.8	1600

Because the Adapted Terzaghi method used by the LDC approach for estimating the load-displacment behavior above the reinforcement was developed for a cohesionless embankment material, it was necessary to find equivalent c = 0 shear strength parameters for the fill. Examination of Eqs. (1) through (3) shows that all combinations of ϕ, c, and K that produce the same of value of p are entirely equivalent with respect to calculation of ε and d. Figure 2 shows values of ϕ and c that all produce the same value of p for a value of K = 0.8, and that a logical tradeoff between ϕ and c exists. Thus, even though the ϕ value for the equivalent c = 0 soil is unreasonably high, the equivalent c = 0 soil produces the same strain and deflection in the reinforcement.

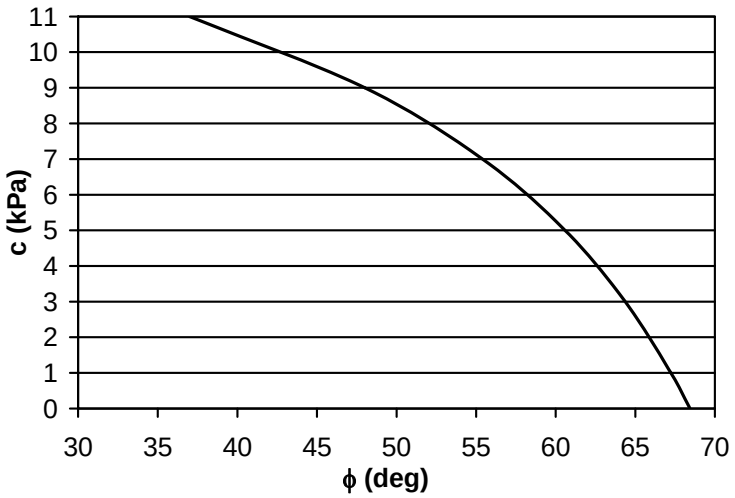

Figure 2: Equivalent shear strength parameters for the clayey sand fill

Table 3 shows the comparison between the measured and calcuated geogrid deflections at locations SP-05, SP-06, and SP-02 using the equivalent c = 0 shear strength values, and it can be seen that the agreement is good. On this basis, the values listed in Table 2 were used to calculate the performance at Locations A and B, as described in the next section.

Table 3: Comparison of predicted and measured deflection values

Settlement Plate	Measured Deflection (m)	Predicted Deflection (m)
SP-05	0.22	0.23
SP-06	0.40	0.39
SP-02	0.37	0.39

Analysis of Unit Cell of Square Pile Cap Array

The back analyzed parameter values for the embankment fill and geogrid were applied to Locations A and B using the LDC approach as implemented in an Excel spreadsheet named GeogridBridge 1.1 to predict the vertical deflection of the geogrid.

Load Displacement Compatibility (LDC) Approach

The LDC method is based on load and displacement compatibility among the embankment, columns, geosynthetic reinforcement, and foundation soil. Differential settlement between the columns and the foundation soil is determined as the difference between the vertical elastic deformation of the column and the settlement of the foundation soil, which includes linear compression of existing granular soil, if present, and nonlinear compression of clay. Friction between the settling foundation soils and the columns is accounted for by considering the interface friction angle and the lateral pressure produced by column installation as well as Poisson effects from the embankment load determined according to a concentric cylinder model (Davis and Poulos 1974).

The load-deflection response of geosynthetic reinforcement is obtained from axisymmetric numerical analyses of an annular membrane. The load-deflection relationship for the column or pile cap penetrating up, relatively, into the embankment is assumed to be linear up to a maximum load condition. The linear part is approximated using the linear solution for displacement of a rigid circular loaded area on a semi-infinite mass (Davis and Poulos 1974). The maximum load condition on the column area above the reinforcement level is established by setting a lower limit on the value of total vertical pressure acting down on the reinforcement using the Adapted Terzaghi Method with an earth pressure coefficient, K, equal to 0.8 for this particular case, which falls between the values of 1.0 used by Russell and Pierpoint (1997) and 0.5 used by Russell et al. (2003).

The simultaneous solution among the load-displacement compatibility relations for the embankment fill, geosynthetic reinforcement, columns, and foundation soils is performed using an iterative technique implemented in a Microsoft Excel® spreadsheet entitled GeogridBridge 1.1. Additional details regarding GeogridBridge 1.1 the LDC approach can be found in Filz and Smith (2006a,b).

Analysis of a 3D Unit Cell with Subgrade Support

Application of the LDC approach to Location B using the back-calculated property values from Locations C and D yield the results shown in Table 4. The good

agreement between measured and calculated magnitudes of geogrid deflection in Table 4 indicates that the parameter values from the 2D back analyses without subgrade support are also applicable to a 3D unit cell that includes the influence of subgrade support.

Table 4: Comparison of predicted and measured deflection values

Location	Settlement Plate	Measured Deflection (m)	Deflection Predicted from LDC Analysis (m)
B	SP-04	0.10	0.11

Analysis of a 3D Unit Cell without Subgrade Support

Table 5 presents the result of the LDC analysis at Location A. The condition of no subgrade support was simulated in the GeogridBridge spreadsheet by modeling the foundation soil as a granular elastic material and incrementally softening the system by reducing the soil modulus to a value approaching zero. Instrumentation at this unit cell included strain gauges in the geogrid. Using the relationship between vertical deflection and strain that is intrinsic to the parabolic deflection assumption, the vertical deflection of the geogrid can be determined both directly from the settlement plates and indirectly using the measured reinforcement strain. The fact that the deflection measured by the settlement plate is significantly larger than the calculated value suggests that the reinforcement was not initially taut at this location. This is further supported by the fact that the deflection determined from the strain gauge readings is significantly lower than the calculated value. Vertical equilibrium requires that the vertical component of the tension developed within the reinforcement counteract the vertical pressure produced by the overlying embankment. If the geogrid is allowed to sag prior to fill placement, the vertical component of the developed tension is larger, which means that less tension, and therefore strain, is necessary to satisfy equilibrium than for reinforcement without initial sag.

Table 5: Comparison of predicted and measured deflection values

Location	Settlement Plate	Deflection Measured from Settlement Plate (m)	Deflection Derived from Strain Measurements (m)	Deflection Predicted by LDC (m)
A	SP-03	0.36	0.12	0.19

CONCLUSIONS

From the analysis of the experimental site in the Barra da Tijuca District, it was found that reasonably accurate calculations of geogrid deflection for low-height embankments can be made. The data set is limited, but a single set of geogrid and embankment fill properties, along with laboratory determined values of compressibility of the soft clay, yielded calculated deflections in good agreement with the measured deflections at four settlement plate locations with different pile cap

configurations and subgrade support conditions. The analyses also demonstrate the significant contribution of subgrade support in limiting geogrid deflection, even when the subgrade is very soft. For conditions at Locations A and B, the calibrated calculations show that subgrade support reduces deflections by about 50%. The conclusion that subgrade support effects are considerable even for low height embankments is consistent with the findings of Rogbeck et al. (1998).

Results from the experimental site also show the significance of maintaining tautness in the reinforcement during embankment construction. If slack or wrinkling is initially present, the differential settlement between the foundation soil and the columns will not induce strain, and therefore tension, in the reinforcement until the slack is removed. This means that the reinforcement layer is providing no benefit to the load-transfer system until strain begins to develop.

The LDC approach as implemented in the GeogridBridge 1.1 spreadsheet was found to be capable of calculating accurate geogrid deflection for a condition with subgrade support and simulate a condition of no subgrade support.

REFERENCES

Almeida, M.S.S., Marques, M.E.S., Almeida, M.C.F., and Mendonca, M.B. (2008). "Performance on two low piled embankments with geogrids at Rio de Janeiro" *Proceedings, First Pan American Geosynthetics Conference and Exhibition,* Cancun, Mexico, pp. 1285 - 1295.

Almeida, M.S.S., Ehrlich, M., Spotti, A.P., and Marques, M.E.S. (2007). " Embankment supported on piles with biaxial geogrids" *Journal of Geotechnical Engineering*, Institution of Civil Engineers, ICE, UK, Vol. 160, No. 4, pp. 185-192.

Filz, G.M., and Smith, M.E. (2006a). "Design of bridging layers in geosynthetic-reinforced, column-supported embankments." *Contract Report* VTRC 06-CR12, Virginia Transportation Research Council, Charlottesville.

Filz, G.M., and Smith, M.E. (2006b). "Net vertical loads on geosynthetic reinforcement in column-supported embankments." *Proceedings*, *Geo-Denver: New Peaks in Geotechnics*, Soil Improvement, *Geotechnical Special Publication 172* (CD-ROM), ASCE, Reston, VA

Poulos, H.G., and Davis, E.H. (1970). *Elastic Solutions for Soil and Rock Mechanics*, John Wiley & Sons, Inc., New York, NY.

Rogbeck, Y., Gustavsson, S., Sodergren, I., and Lindquist, D. (1998). "Reinforced piled embankments in Sweden - design aspects." *Proceedings, Sixth International Conference on Geosynthetics*, Vol. 2, Rowe, R.K. (ed.), Atlanta, Georgia, pp. 755-762.

Russell, D., Naughton, P.J. and G. Kempton, G. (2003). "A new design procedure for piled embankments." *Proceedings of the 56th Canadian Geotechnical Conference and 2003 NAGS Conference*, Vol. 1, Winnipeg, MB, pp. 858-865.

Spotti, A. P. (2006). Monitoring results of a piled embankment with geogrids (in Portuguese). ScD Thesis, COPPE/UFRJ, Rio de Janeiro, Brazil

Terzaghi, K. (1943). *Theoretical Soil Mechanics*, J. Wiley & Sons, Inc., New York, NY.

Appendix C: McGuire, M. P., and Filz, G. M. (2010). "Incorporation of slack and creep in the British Standard code of practice for calculating tension and deflection of geosynthetic reinforcement used in column-supported embankments."

(Reproduced with permission from IGS)

Incorporation of slack and creep in the British Standard code of practice for calculating tension and deflection of geosynthetic reinforcement used in column-supported embankments

McGuire, M.P.
Civil and Environmental Engineering Department, Virginia Tech, Blacksburg, Virginia, U.S.A., mcguirem@vt.edu

Filz, G.M.
Civil and Environmental Engineering Department, Virginia Tech, Blacksburg, Virginia, U.S.A., filz@vt.edu

Keywords: column-supported embankment, reinforcement, BS8006, slack, creep

ABSTRACT: Geosynthetic reinforcement with adequate stiffness, durability, and resistance to creep is important for good long-term load transfer performance within a geosynthetic-reinforced column-supported embankment (GRCSE). The British Standard BS8006 code of practice provides a practical approach for estimating tension developed in the geosynthetic reinforcement due to the vertical stress imposed by the embankment weight reduced by soil arching. This paper shows that the BS8006 code of practice can be expanded to account for slack introduced in the reinforcement during installation and for long-term creep. Both of these influences result in higher predicted maximum deflection of the reinforcement and lower in-service tension when compared to considering elastic strain only. Consideration of creep is addressed using the concept of residual strength adopted by British Standards for determining the long-term strength of geosynthetics. A design approach is presented that is conservative for estimating both vertical deflection and in-service tension in the reinforcement.

1 INTRODUCTION

Geosynthetic-reinforced, column-supported embankments (GRCSEs) have been used in soft ground conditions when there is a need to accelerate construction and/or protect adjacent facilities from the settlement that would otherwise be induced by the new embankment load. The columns in column-supported embankments can be driven piles or various types of formed-in-place columns. If driven piles are used, they are often fitted with pile caps to help transfer the embankment load to the piles. GRCSEs reduce settlement of the soft foundation soils by concentrating the embankment stress and live loads to the stiff columns through stress redistribution both above and below the foundation subgrade level. One such mechanism of load transfer is through the vertical component of tension developed in the geosynthetic reinforcement in response to the applied embankment stress reduced by soil arching. The reinforcement undergoes strain due to the tension developed, and it deflects vertically in compatibility with the reinforcement strain and the settlement of the soft foundation soils.

The British Standard provides codes of practice for determining the vertical stress acting on the reinforcement and for estimating the tension and deflection developed in the geosynthetic reinforcement. The approach for estimating the tension and deflection of the reinforcement can be applied separately from the procedure for determining the vertical stress acting on the reinforcement. The code of practice considers that the two-dimensional projection of the deflected shape of the reinforcement is parabolic across the clear span between adjacent columns and that the tension is uniform. The Swedish method summarized in Rogbeck et al. (1998) relies on the same parabolic assumption.

This paper presents an expansion of the British Standard code of practice to incorporate the influence of initial slack and creep on the calculated values of tension and deflection. A practical design approach that is conservative for both tension and deflection is also presented.

2 OVERVIEW OF BRITISH STANDARD CODE OF PRACTICE BS8006

Development of the British Standard code of practice for estimating the tension and maximum vertical deflection of the geosynthetic reinforcement is given in Jones et al. (1990). In this method, the reinforcement spanning adjacent columns is treated as a 2D

cable segment and it is assumed to deform as a parabola in response to a uniformly applied vertical pressure, W_t. The arrangement for a 2D segment of geosynthetic reinforcement spanning adjacent columns is given in Figure 1.

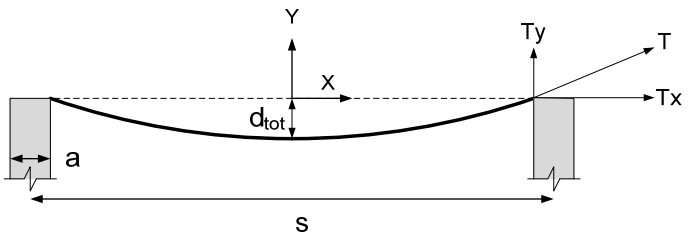

Figure 1: Parabolic approximation for reinforcement spanning adjacent columns

The center-to-center spacing of the columns is given by *s*, the width or diameter of the columns or caps is given by *a*, and the total maximum vertical deflection occurring at mid-span is represented by d_{tot}. The tension, *T*, in the reinforcement has vertical and horizontal components, T_y and T_x, which depend on the clear span (*s*-*a*) and the magnitudes of W_t and d_{tot}. The parabolic assumption has been shown to be reasonable for a cable with small vertical deflection relative to the clear span (Leonard 1988). For analysis of a 3D unit cell of a GRCSE, the magnitude of the uniform pressure acting across the clear span between adjacent columns can be approximated from the vertical embankment pressure reduced by arching, *P*, using the unit cell geometry. For a square array of columns, the ratio of W_t to *P* can be approximated by (*s*+*a*)/2*a*. McGuire and Filz (2008) discuss several methods for determining P, including some that consider the influence of subgrade support.

Vertical equilibrium requires that T_y equals W_t applied over half the clear span, giving the relationship between tension and deflection provided in Equation 1.

$$T = \frac{W_t\left(s-a\right)}{2}\sqrt{1+\frac{\left(s-a\right)^2}{16{d_{tot}}^2}} \qquad (1)$$

Equation 2 provides a binomial approximation for maximum deflection of the reinforcement based on the parabolic assumption. Equation 3, which is obtained by substituting Equation 2 into Equation 1 and applying the approximated ratio between W_t and *P*, provides the tension in the reinforcement as a function of geometry, stress, and total strain, ε_{tot}.

$$d_{tot} = \left(s-a\right)\sqrt{\frac{3}{8}\varepsilon_{tot}} \qquad (2)$$

$$T = \frac{\left(s^2-a^2\right)P}{4a}\sqrt{1+\frac{1}{6\varepsilon_{tot}}} \qquad (3)$$

The code of practice outlined in the British Standard uses an assumed strain approach whereby a value of working tensile strain, ε_t, usually 5 to 6 percent, and maximum creep strain, ε_c, of 2 per (3)ıre chosen to estimate tension and deflection of the reinforcement (Jones et al. 1990). Filz and Smith (2007) provide an approach that considers stress-strain compatibility within the parabolic method by substituting $\varepsilon_{tot} = T/J$ into Equation 3, where *J* is the tensile stiffness of the reinforcement.

$$96T^3 - 6\ddot{K}_g^2 T - \ddot{K}_g^2 J = 0 \qquad (4)$$

$$\text{where } \ddot{K}_g = P\left(s^2-a^2\right)/a$$

3 BASIS FOR INCORPORATING SLACK AND CREEP IN THE BRITISH STANDARD CODE OF PRACTICE

3.1 *Initial slack*

During construction of a GRCSE, the reinforcement is normally placed on top of a thin layer of granular material that acts as a cushion over the columns or pile caps. Tautness in the reinforcement is desired so that tension, resulting in load transfer to the columns, can develop at the onset of settlement of the foundation soils. Initial tautness in the reinforcement depends on the installation technique and quality of the workmanship at the project site. Factors such as poor grade control, construction traffic, and mismanagement of stormwater runoff can lead to an uneven cushion layer prior to reinforcement placement. Also, the flexural stiffness of some reinforcement may make it difficult for the reinforcement to lay flat. When perfect tautness is not maintained, the initial length of reinforcement spanning adjacent columns, L_o, exceeds (*s*-*a*). Slack, e_s, can be defined as a percentage of the clear span according to Equation 5.

$$e_s = \frac{L_0}{\left(s-a\right)} - 1 \qquad (5)$$

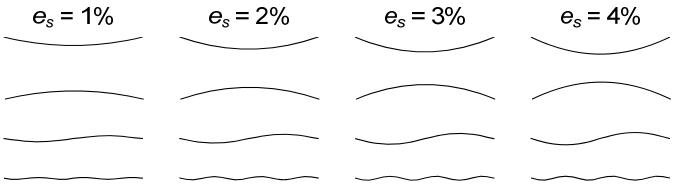

Figure 2: Graphic depiction of different magnitudes of initial slack

Figure 2 shows different magnitudes of slack without vertical exaggeration for reinforcement that initially takes on a shape approximated by a convex parabola, concave parabola, wrinkling that is one cycle of a sine function, or wrinkling that is three cycles of a sine function. Figure 2 shows that slacks of 1% to

2% could exist at some locations on a project site with average quality workmanship.

3.2 *Creep strain*

The accumulation of creep strain directly influences the magnitude of vertical deflection and total strain of the reinforcement. Less apparent are the effects of creep on the tensile strength and tensile stiffness of geosynthetic reinforcement. The International Organization of Standardization (ISO) Technical Report ISO/TR 20432:2007 has been adopted as the British Standard for determining the long-term strength of geosynthetics for soil reinforcement. In this report, the concept of residual strength (Naughton and Kempton 2004) suggests that there is essentially no degradation of tensile strength due to creep prior to creep rupture.

Naughton et al. (2005) showed that under light loading, the stress-strain relationship of aged polyester samples was almost identical to the virgin samples tested at the time of construction. Furthermore, it has been found that tensile stiffness of polyester materials can actually increase substantially under sustained load (Hirakawa et al. 2003). Therefore, in the absence of environmental degradation (e.g. hydrolysis) or installation damage, it may be acceptable to consider the tensile stiffness obtained from un-aged samples over the useful life of the embankment.

The creep rate is generally influenced by polymer type, stress level, temperature, stress relaxation through soil interaction, soil moisture, and geosynthetic structure (i.e. textile or rib structure) (Koerner 2005, Leshchinsky et al. 1997, ISO 2007). If the influences on creep rate are adequately captured for a particular application, the creep strain can be estimated as a function of time. Results of long-term creep tests showing creep strain versus time for a variety of geosynthetic reinforcement materials, load magnitude, and confinement conditions are available in published literature (Koerner et al. 1993, Greenwood et al. 2004, and Leshchinsky et al. 1997).

4 DEVELOPMENT AND CONSEQUENCE OF INCORPORATING CREEP AND SLACK IN THE BRITISH STANDARD CODE OF PRACTICE

Accounting for the influences of initial slack, tensile strain, and creep, the final length of the reinforcement spanning adjacent columns, L_{final}, is equal to $L_o(1 + \varepsilon_t + \varepsilon_c)$, where the tensile and creep strains are defined in terms of the initial length and $L_o = (s - a)(1 + e_s)$ from Equation 5. For the purposes of establishing the correct parabolic geometry, total strain can be defined according to Equation 6. Using this definition, we can express total strain in terms of slack, tensile strain, and creep strain by Equation 7. Over a range of reasonable values for e_s, ε_t, and ε_c, we can neglect the influence of second order terms without significant consequence to the calculated value of ε_{tot} allowing for simplification of Equation 7 to the form given in Equation 8.

$$\varepsilon_{tot} = \frac{L_{final}}{(s-a)} - 1 \tag{6}$$

$$\varepsilon_{tot} = e_s + \varepsilon_t + \varepsilon_c + e_s\varepsilon_t + e_s\varepsilon_c \tag{7}$$

$$\varepsilon_{tot} = e_s + \varepsilon_t + \varepsilon_c \tag{8}$$

The value of total strain, incorporating the effects of initial slack, tensile strain, and creep strain can be substituted into Equation 3 with $\varepsilon_t = T/J$ to provide the compatible solution for tension.

$$\left(96T^2 - 6\ddot{K}_g^2\right)\left(C_g + T\right) - \ddot{K}_g^2 J = 0 \quad \text{where } C_g = J\left(e_s + \varepsilon_c\right) \tag{9}$$

Due to the geometry of the parabolic assumption, the tension in the reinforcement satisfying vertical equilibrium decreases for a given clear spacing and magnitude of W_t as the value of $(e_s+\varepsilon_c)$ increases. Figures 3a and 3b illustrate this trend and the corresponding trend for tensile strain across a range of reinforcement stiffnesses for typical values of column diameter and spacing. These trends highlight an interesting outcome of the inclusion of initial slack and creep. Creep strains occur over the service life of the GRCSE and the resulting deflection due to creep can impact settlement sensitive elements, such as pavements. The impact of initial slack however, depends on whether the slack is released during embankment construction. The release of slack results in an increase in the value of d_{tot}, which corresponds to a reduced tension, T, required to maintain a constant vertical component of tension, T_y. For the case of slack released prior to installation of settlement sensitive elements, the presence of initial slack would be beneficial by reducing the increment of deformation needed to produce the vertical component of tension necessary to resist the increment in W_t.

5 DESIGN APPROACH USING THE EXPANDED BRITISH STANDARD CODE OF PRACTICE

When compared to considering tensile strain alone, the inclusion of the influences of initial slack and creep in the British Standard code of practice result in higher estimated vertical deflection of the reinforcement. As can be seen in Figure 1, larger vertical

deflection increases the vertical component of tension in the reinforcement thereby reducing the magnitude of tension required to satisfy vertical equilibrium with the applied pressure, W_t.

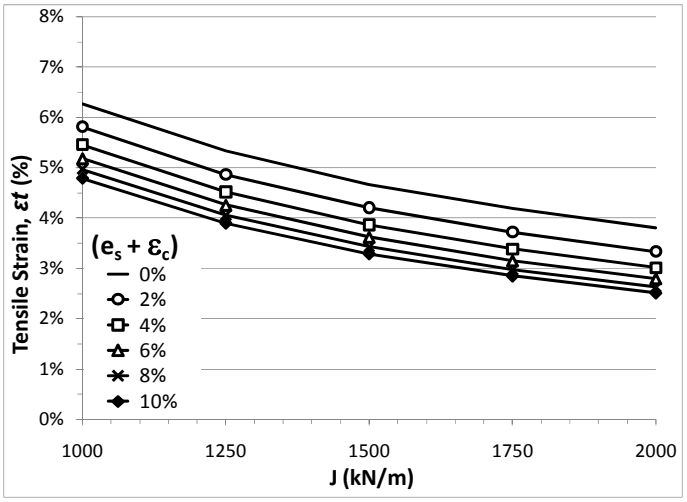

Figure 3a: Influence of initial slack and creep on in-service tension across a range of reinforcement stiffnesses

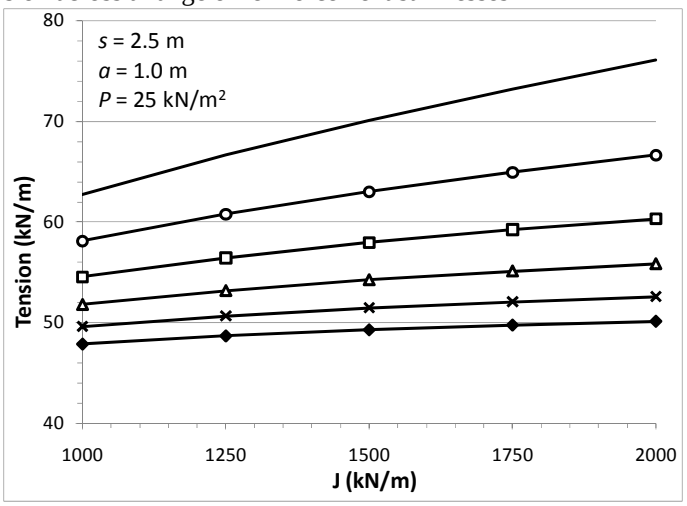

Figure 3b: Influence of initial slack and creep on in-service tensile strain across a range of reinforcement stiffnesses

Therefore, a reasonable design approach is to perform the analysis twice, once with the inclusion of creep and initial slack and once without. The tension estimated from the analysis ignoring creep and slack will be conservative for selecting a geosynthetic with adequate strength. The deflection estimated from the analysis including creep and initial slack will be conservative for the maximum deflection of the reinforcement at the time of interest and selecting a geosynthetic with acceptable creep behavior. The stiffness of the reinforcement considered for the analysis including creep should be the initial design value, including installation damage, reduced for environmental degradation expected at the time of interest.

Further development of this approach could include studies undertaken to determine appropriate values of e_s to use for design.

ACKNOWLEDGEMENTS

Special thanks go to Dr. Patrick Naughton of the Institute of Technology, Sligo, Ireland, and Dr. John Greenwood of Cobham plc, Dorset, U.K. for sharing their expertise on the long-term performance of geosynthetics. This research was funded in part by the Geosynthetic Institute.

REFERENCES

Filz, G.M., and Smith, M.E. 2007. Net vertical loads on geosynthetic reinforcement in column-supported embankments. *Proceedings, Geo- Denver, Geotechnical Special Publication 172*, ASCE, Reston, VA

Greenwood, J.H., Kempton, G.T., Brady, K.C., and Watts, G.R.A. 2004. Comparison between stepped isothermal method and long-term creep tests on geosynthetics. Proceedings of the 3rd European Conference on Geosynthetics, Munich, Gernany, pp. 527-532.

Hirakawa, D., Kongkitkul, W., Tatsuoka, F., Uchimura, T. 2003. Time-dependent stress-strain behavior due to viscous properties of geogrid reinforcement. *Geosynthetics International*, Vol. 10, No. 6, pp. 176-199.

IS0 2007. Guidelines for the determination of the long-term strength of geosynthetics for soil reinforcement. *Technical Report 20432*, Geneva, Switzerland.

Jones, C. J. F. P., Lawson, C.R., and Ayres, D.J. 1990. Geotextile reinforced piled embankments. *Proceedings, 4th International Conference on Geotextiles, Geomembranes, and Related Products*, Vol. 1, G. Den Hoedt (ed), The Hague, pp. 155-160.

Koerner, R.M. 2005. *Designing with Geosynthetics, 5th Edition*, Pearson Prentice Hall, New Jersey, USA.

Koerner, R.M., Hsuan, Y., and Lord, A.R. 1993. Remaining technical barriers to obtaining general acceptance of geosynthetics. *Geotextiles and Geomembranes*, Vol. 12, No. 1, pp. 1-52.

Leshchinsky, D., Dechasakulsom, M., Kaliakin, V.N. and Ling, H.I. 1997. Creep and stress relaxation of geogrids. Geosynthetics International, Vol. 4, No. 5, pp. 463-479.

Leonard, J.W. 1988. *Tension Structures*, McGraw Hill, New York, USA.

McGuire, M.P., Filz, G.M., and Almeida, M.S.S. 2009. Load-Displacement Compatibility Analysis of a Low-Height Column-Supported Embankment. *Proceedings, International Foundations Congress and Equipment Expo, Geotechnical Special Publication 187*, ASCE, Reston, VA

McGuire, M.P., and Filz, G.M., 2008, Quantitative comparison of theories for geosynthetic reinforcement of column-supported embankments, *Proceedings, GeoAmericas 2008*, Cancun, Mexico, 1303-1312.

Naughton, P.J., Balderson, T. & Laronzo, R., 2005. The properties of polyethylene encased high tenacity linear elements. *Geosynthetics and Geosynthetic-Engineered Soil Structures, Contributions from the Symposium Honoring Prof. Robert M. Koerner*, Ed Ling, H., Kaliakin, V.N. & Leshchinsky, D., pp 19-38.

Naughton, P.J. and Kempton, G.T. 2004. Creep strain in a residual strength procedure. *Proceedings, International Conference on Geosynthetics and Geo-Environmental Engineering*, Mumbai, India.

Rogbeck, Y., Gustavsson, S., Sodergren, I., and Lindquist, D. 1998. Reinforced piled embankments in Sweden - design aspects. *Proceedings, Sixth International Conference on Geosynthetics*, Vol. 2, Rowe, R.K. (ed.), Atlanta, Georgia, pp. 755-762.

Appendix D: Summary and interpretation of experimental study conducted by Chen et. al (2008)

D Summary of Experimental Study Conducted by Chen et al. (2008)

References:

Chen, Y. M., Cao, W. P., and Chen, R. P. (2008). "An experimental investigation of soil arching within basal reinforced and unreinforced piled embankments." *Geotextiles and Geomembranes*, 26, 164-174.

D.1 Overview of study:

Chen et al. (2008) describes a laboratory-scale experimental study to investigate load transfer and embankment deformation. The apparatus consisted of a tank with toughened glass walls measuring 1.5m long by 1.0m wide by 1.30m high. The tank rested on a brick base comprised of two side walls each having a 75mm wide ledge projecting beyond the walls of the tank and a middle beam which had a width of 150mm. The middle beam acted as a cap beam and the outer ledges each provided half a cap beam with the tank walls acting as planes of symmetry. This geometry was used for 13 of the 15 total tests performed. In the remaining two tests, toughen glass panels were fixed to the top of the middle beam and outer ledges to increase the cap beam widths to 180 and 250mm. Water bladders running the length of the tank were installed in the space between the cap beams to simulate settlement of the foundation soils. Initially, the water bladders were filled so they were flush with the top of the cap beams. During testing, water was released in increments to initiate differential settlement between the cap beams and the simulated compressible foundation soil. Samples of dry sand ranging from 420 to 1200mm high were prepared at a relative density of approximately 55 percent with and without the presence of biaxial reinforcement. Three different stiffnesses of reinforcement were used during the testing program.

Table D.1 summarizes the variation of test parameters during the experimental study using English units.

Table D.1 Variation of testing parameters during the experimental study conducted by Demerdash (1996)

	Config.	Array	s, in.	d[1], in.	H, in.	s'/d [2]
Geometry	1	Cap beams (Plane strain)	29.53	5.90	16.53 to 47.24	2.00
	2			7.09	16.53	1.58
	3			9.84	16.53	1.0

		Description	γ, pcf (D_r)	ϕ_{peak} (ϕ_{crit})	ψ_{peak}	c, psf
Embankment Material Properties		Qiantang River Beach sand	99.24 (55%)	44 (NG)	NG	0

	ID	Description	Layers	Position[4], in.	Stiffness, J, lbs/ft
Reinforcement[3]	A	None			
	B	Biaxial reinforcement	1	0	23.99
	C	Biaxial reinforcement	1	0	95.96
	D	Biaxial reinforcement	1	0	1542.13

Notes
1 Here, d is the width of the cap beams which approximate 2D plane strain conditions. As described in Section 1.4, no shape conversion is necessary for 2D plane strain conditions.
2 s'/d = s/(2d)-(1/2)
3 Reinforcement was only used in samples with a cap beam width of 5.90 in.
4 Vertical distance measured from the pile cap to the reinforcement
NG = Not Given

The apparatus was instrumented with seven soil stress transducers. Six of the soil stress transducers were placed over the water bladders at the elevation of the top of the cap beams. The seventh soil stress transducer was placed on top of the middle cap beam. The reinforcement was placed over the soil stress transducers, so the measured stress includes the contributions of soil arching and load transfer by the reinforcement. Settlement of the fill was measured using thin strips of marker paper placed at the front wall of the tank. Since the tank walls are transparent, the settlement of the fill could be tracked at various elevations within the sample.

D.2 Measurement of load transfer

Chen et al. (2008) used the measurements of settlement and stress over the water bladders and cap beams to develop relationships between the stress concentration ratio and the magnitude of differential settlement between the cap beams and the water bladders. Here, the stress

concentration ratio is defined as the stress measured on the middle cap beam divided by the average stress over the water bladders. The instruments used to measure load transfer were placed below the reinforcement, therefore, when reinforcement is present, the measured column stress is equivalent to $\sigma_{col,geobot}$ as defined in Section 1.4. Figure D.1 through Figure D.3 show the resulting relationships between load transfer and differential settlement. In Figure D.1, h/s is the sample height divided by the clear spacing between adjacent columns. Inspection of Figure D.2 and Figure D.3 indicate that the presence and stiffness of geosynthetic reinforcement increases the peak load transfer to the column but does not significantly change the differential settlement magnitude at the condition of peak column stress.

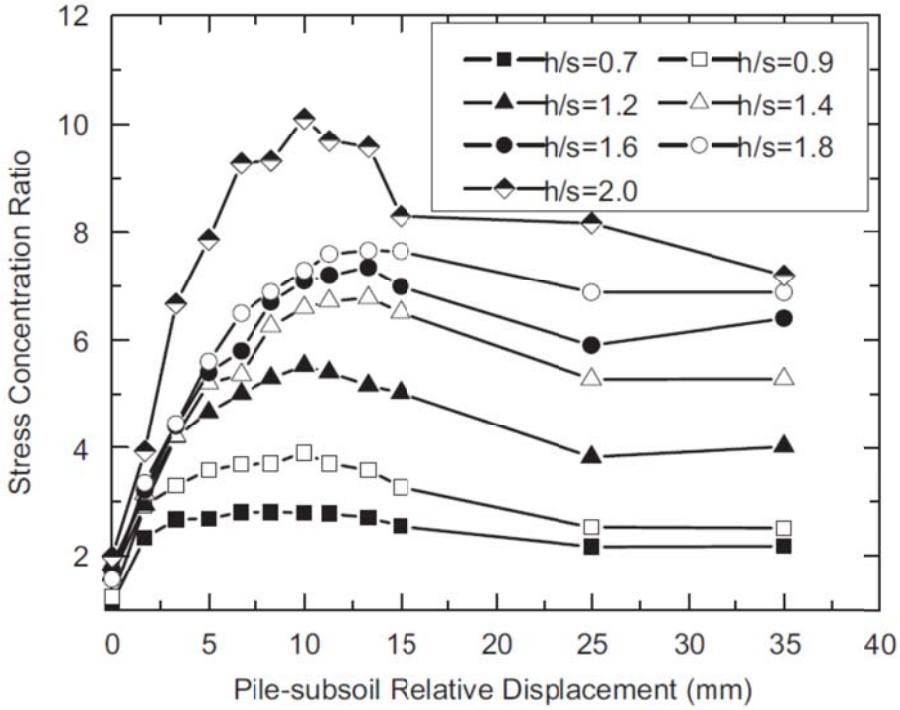

Figure D.1 Ratio of vertical stress over the cap beam to stress over the water bladders versus differential settlement for geometry/reinforcement combination 1A (Chen et al. 2008, fair use)

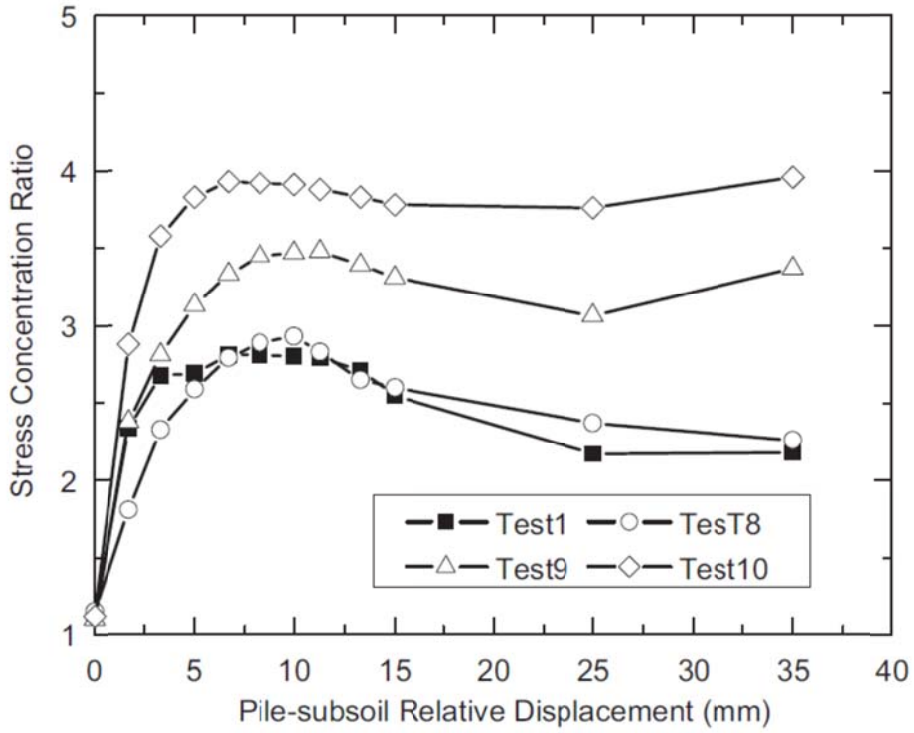

Figure D.2 Ratio of vertical stress over the cap beam to stress over the water bladders versus differential settlement for 16.53 inch high samples. Tests 1, 8, 9, and 10 used geometry/reinforcement combinations 1A, 1B, 1C, and 1D, respectively (Chen et al. 2008, fair use)

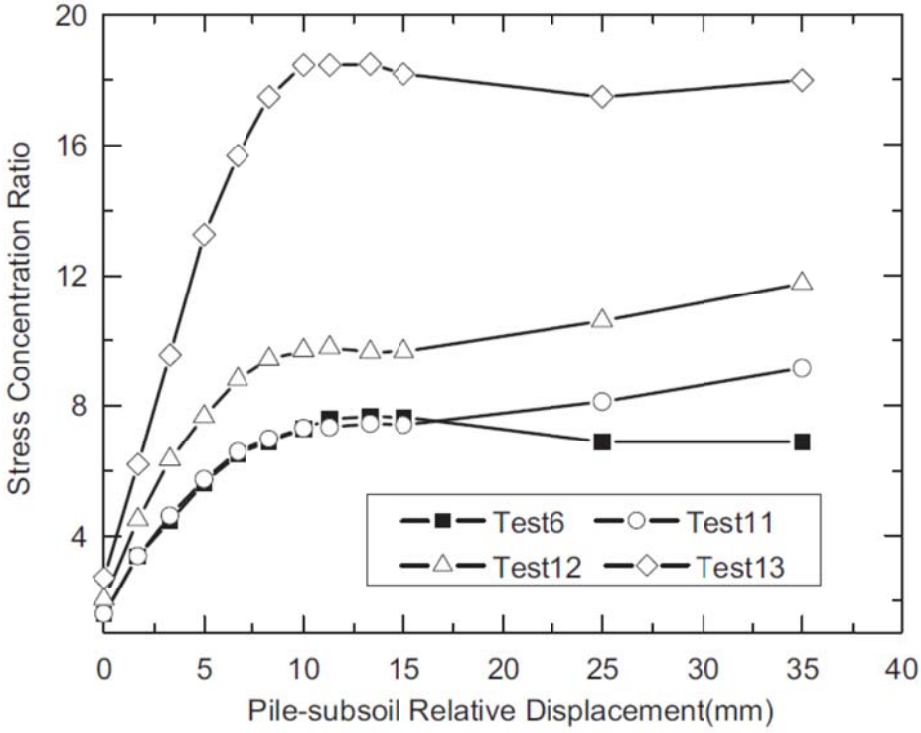

Figure D.3 Ratio of vertical stress over the cap beam to stress over the water bladders versus differential settlement for 42.52 inch high samples. Tests 6, 11, 12, and 13 used geometry/reinforcement combinations 1A, 1B, 1C, and 1D, respectively (Chen et al. 2008, fair use).

D.3 Measurement of settlement of the sample

Chen et al. (2008) contains two figures, reproduced below as Figure D.4 and Figure D.5, which show profiles of settlement through the sample. The profile in Figure D.4 is for a 16.53 in. high sample and Figure D.5 is for a 47.24 in. high sample. Both results are from tests performed using geometry/reinforcement combination 1A.

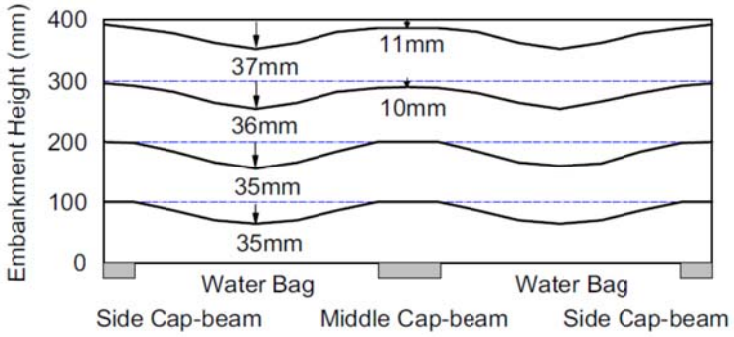

Figure D.4 Settlement profile through 16.53 in. sample tested using a geometry/reinforcement combination of 1A (Chen et al. 2008, fair use)

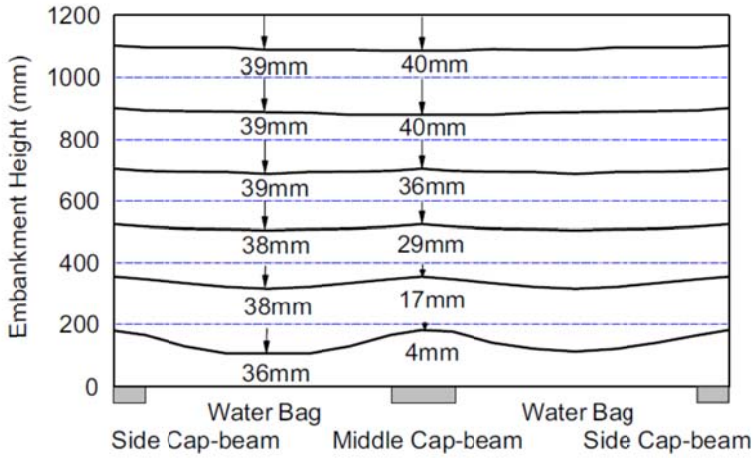

Figure D.5 Settlement profile through 47.24 in. sample tested using a geometry/reinforcement combination of 1A (Chen et al. 2008, fair use)

Chen et al. (2008) reports a critical height for Geometry A equal to 1.4 to 1.6 times the clear spacing between cap beams. This results equates to a critical height between 33.07 and 37.80 inches

D.4 Interpretation of results

Figure D.6 shows settlement at peak cap beam stress for unreinforced samples obtained by Chen et al. (2008) shown with the results obtained from 3D unit cells by Demerdash (1996) and from unreinforced single column tests described in Chapter 4. It is interesting that the tests performed without a surcharge pressure have a similar trend with respect to normalized sample height despite the differences in geometry, scale, material properties, and reinforcement condition.

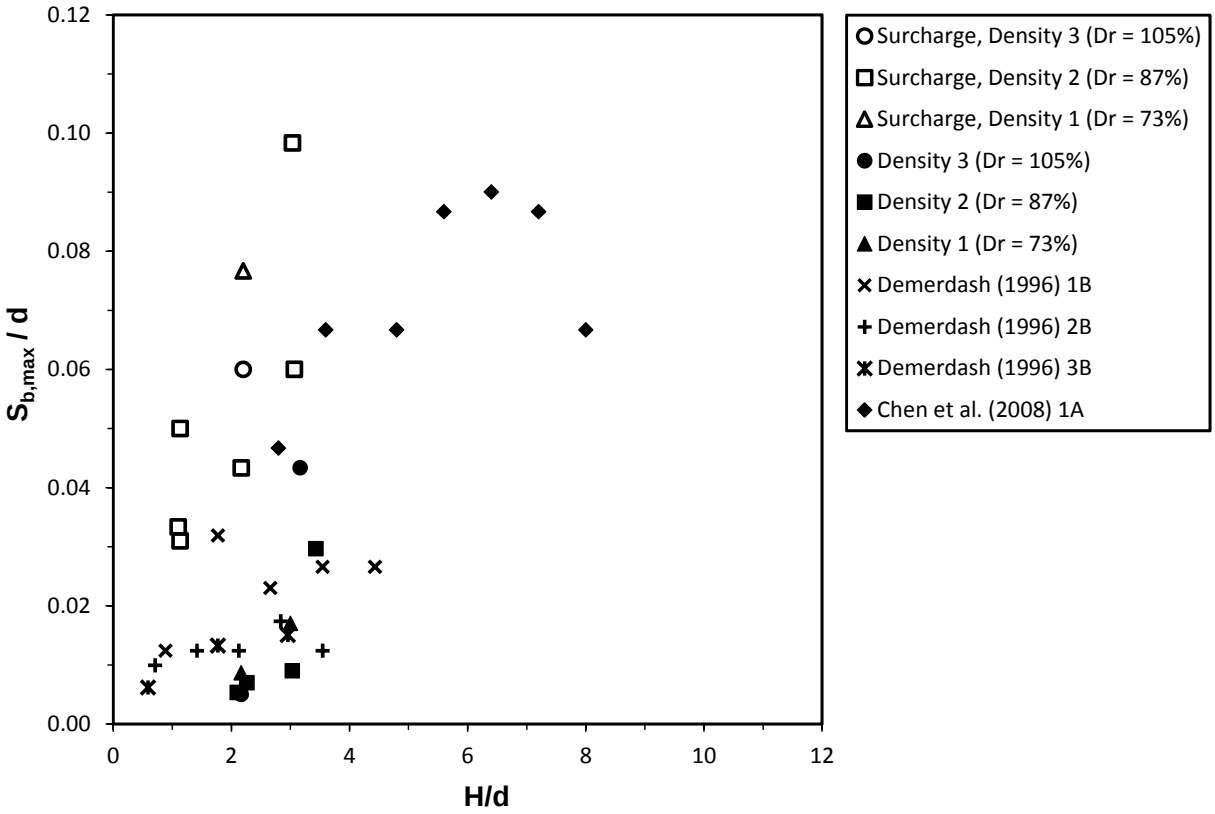

Figure D.6 Relationship between base settlement at maximum column stress and sample height. Note: The combinations of geometry and reinforcement provided in the legend for Demerdash (1996) are not the same as those provided in Table AA.1.

Table D.2 shows the critical height reported by Chen et al. (2008) compared to the critical height predicted using the trend developed form the results of the multi-column tests described in Chapter 5 for 3D unit cell geometries. The measured critical height is significantly higher than the predicted value. In Figure D.7, the results from Chen et al. (2008) are shown on a plot along with the calculated values of critical height determined by Demerdash (1996) using a 2D plane strain model and it appears that critical height for a condition of plane strain is higher than a square 3D unit cell with the same spanning ratio. This idea is discussed in detail in Section 7.1.

Table D.2 Comparison of measured to predicted values of critical height

Column spacing, s (in.)	Pile cap diameter, d[1] (in.)	Spanning ratio[2], s'/d	H_{crit} measured (in.)	H_{crit} predicted[3] (in.)
29.53	5.90	2.00	33.07 to 37.80	22.07

Notes

1 Here, d is the width of the cap beams which approximate 2D plane strain conditions. As described in Section 1.4, no shape conversion is necessary for 2D plane strain conditions.

2 s'/d = s/(2d)-(1/2)

3 $H_{crit}/d = 1.15(s'/d) + 1.438$

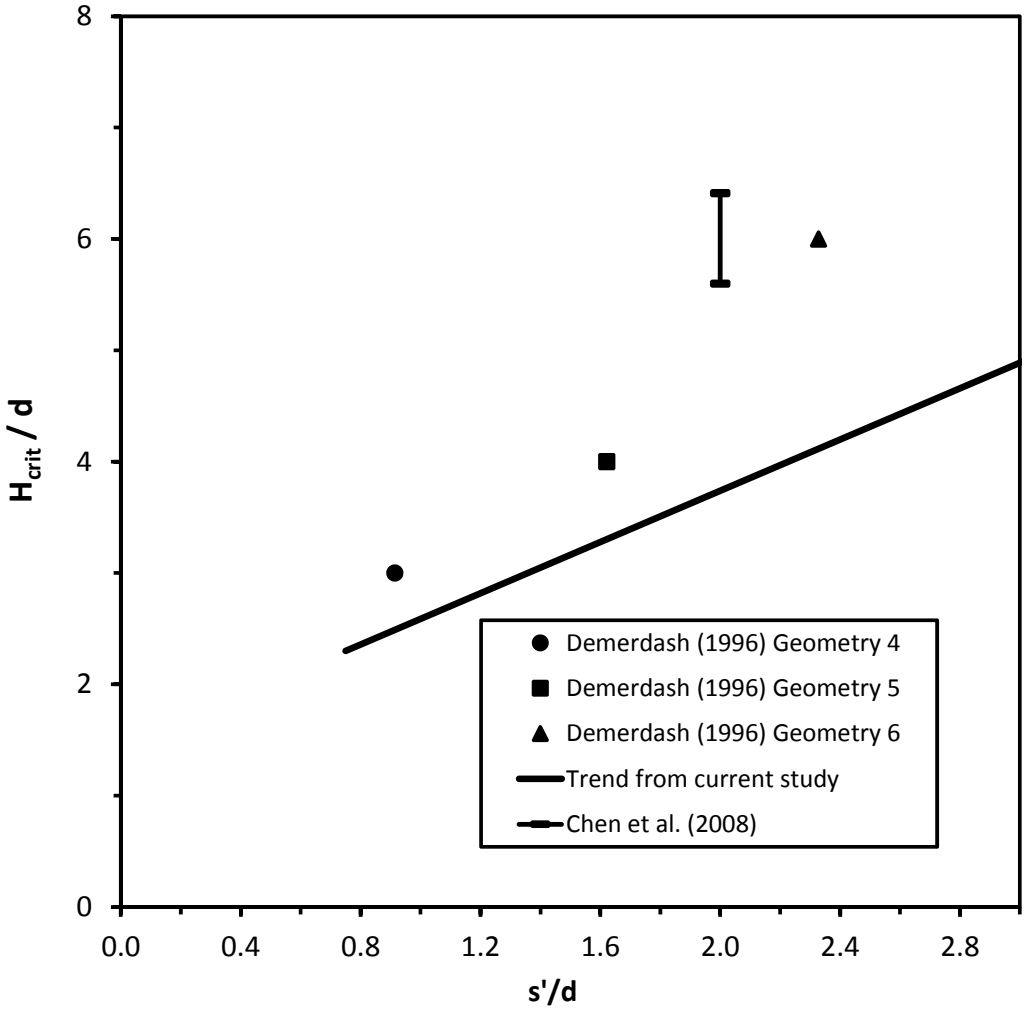

Figure D.7 Normalized critical height versus spanning ratio showing the results by Chen et al. (2008), the calculated results from the numerical model by Demerdash (1996), and the trend from the current multi-column tests.

Appendix E: Summary and interpretation of experimental and numerical studies conducted by Demerdash (1996)

E Summary of Experimental and Numerical Studies Conducted by Demerdash (1996)

Reference:

- Demerdash, M. A. (1996). "An experimental study of piled embankments incorporating geosynthetic basal reinforcement," University of Newcastle-Upon-Tyne, Department of Civil Engineering.

E.1 Summary of Experimental Work Related to Surface Deformation

E.1.1 Overview

Demerdash's dissertation focuses primarily on the load transfer due to soil arching in column-supported embankments with and without geosynthetic reinforcement. His approach included constructing a laboratory-scale apparatus capable of measuring vertical load acting on a square arrangement of four pile caps separated by a movable base used to simulate settlement of the foundation soils. Demerdash focused on the condition of zero subgrade support and therefore lowered the movable base of his model to a point where there was a loss of contact between the base and the reinforcement. His model also allowed for the study of the deflection and tension developed in the reinforcement from the embankment fill for various unit cell geometries. Demerdash used his experimental results to calibrate a numerical model developed using FLAC2D finite difference code. He compared the results from his investigation against other published models for estimating load transfer due to soil arching.

E.1.2 Description of experimental apparatus and testing materials

The apparatus developed by Demerdash utilizes a square test box with interior dimensions of 1.2 x 1.2 x 1.2 m. A square grid with a center-to-center spacing of 0.6 m was chosen for the four pile cap locations. Three cap sizes with side lengths of 200, 250, and 300 mm were selected to obtain area replacement ratios of 10, 17.4, and 25 percent, respectively. Figure E.1 shows a plan view sketch of the apparatus.

The soil used for the model tests was Leighton Buzzard sand falling between sieve numbers 14 and 25. The samples were prepared using air pluviation resulting in a relative density of 80%.

All tests were performed using geosynthetic reinforcement placed directly on top of the pile caps. Demerdash selected two scaled-down versions of polyester Paraweb strips arranged in two layers at right angles to each other to achieve biaxial load transfer. The stiffnesses of the scaled Paraweb strips were 165 and 500 kN/m. Two additional polyester reinforcement materials, Textomur and Stratagrid, were also used in the experimental apparatus. Textomur is a non-woven needle-punched geotextile and Stratagrid is a woven geogrid. The stiffnesses of Textomur and Stratagrid strips placed on 100 mm centers are 45 kN/m and 285 kN/m, respectively.

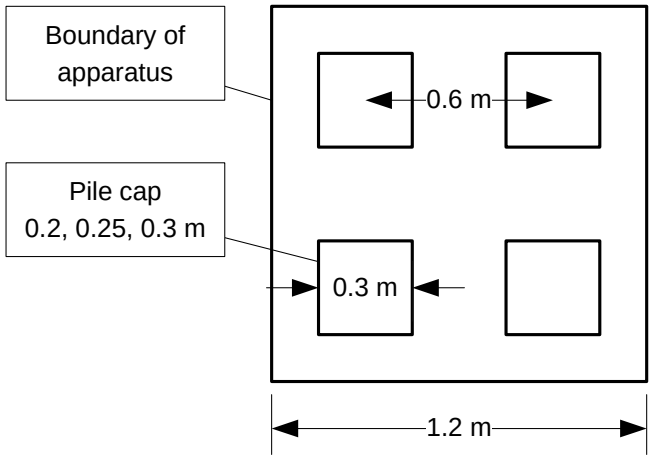

Figure E.1 Plan view sketch of the apparatus used by Demerdash

E.1.3 Testing procedures

During testing, the base of the apparatus was lowered until loss of contact occurred between the base and the reinforcement. Demerdash performed 28 'full height' tests which involved lowering the base once the intended sample height was reached. Full height tests were performed at sample heights of 0.2, 0.4, 0.6, 0.8, and 1.0 m. He also performed 5 'incremental' tests which involved lowering the base once a sample height of 0.2 m was reached and increasing the sample height in 0.2 m increments until a 1 m sample is obtained. During incremental testing, measurements of deformation and load were taken at each increment of sample height.

E.1.4 Test parameters

Table E.1 summarizes the variation of test parameters during the experimental study using English units. Table E.2 provides the combinations of geometry and reinforcement used during the testing program.

Table E.1 Variation of testing parameters during the experimental study conducted by Demerdash (1996)

	Config.	Array	s, in.	d[1], in.	H, in.	s'/d [2]
Geometry	1	Square	23.62	8.88	7.87 to 39.37	1.38
	2			11.10		1.00
	3			13.33		0.75

		Description	γ, pcf (D_r)	ϕ_{peak} (ϕ_{crit})	ψ_{peak}	c, psf
Embankment Material Properties		Leighton Buzzard sand	108.8 (80%)	45 (36)	NG	0

	ID	Description	Layers	Position[3], in.	Stiffness, J, lbs/ft
Reinforcement	A	Paraweb 165, Geosynthetic strips	1	0	11,306
	B	Paraweb 500, Geosynthetic strips	1	0	34,270
	C	Textomur, Needle-punched geotextile	1	0	3,083
	D	Stratagrid, Woven geogrid	1	0	19,528

Notes

1 Square pile caps were converted to round caps of equal area

2 $s'/d = s/(\sqrt{2}d)-0.5$

3 Vertical distance measured from the pile cap to the reinforcement

NG = Not Given

Table E.2 Combinations of geometry and reinforcement used during testing program

Test type	Combination of geometry and reinforcement
Full height	1B, 2B, 3B, 1A, 1D
Incremental	1B, 2B, 3B, 3A, 3C

E.1.5 Instrumentation

E.1.5.1 Instrumentation used to measure load transfer

The total vertical stress acting on two of the pile caps was captured by supporting each cap on a load cell. The other two caps were instrumented in a way to only capture the load due to soil arching within the embankment material. To achieve this, Demerdash used a second square bearing plate positioned to provide a small gap for the reinforcement to pass through. The upper plates were supported by threaded rods that transferred loads to load cells. In this way, Demerdash could determine what portion of the total column load was due to arching and which portion was due to the tension developed in the reinforcement.

E.1.5.2 Instrumentation used to measure deflection of the reinforcement

Demerdash used draw-wire sensors attached to the reinforcement at five locations in the unit cell to measure the vertical deflection of the reinforcement.

E.1.5.3 Measurement of surface deformation

Demerdash measured surface deformation during full height testing. Demerdash used a measuring stick outfitted with a flat end plate and a reference level. To make discrete measurements of the sample surface, he placed the flat end plate of the measuring stick on the sample surface and recorded the measurement at the reference elevation.

Measurements of the surface settlement were made at the center of the test box, S_d, over the center of each pile cap, S_c, and at mid-span between each of the pile caps, S_i. Figure E.2 shows the locations of the reported values of surface settlement.

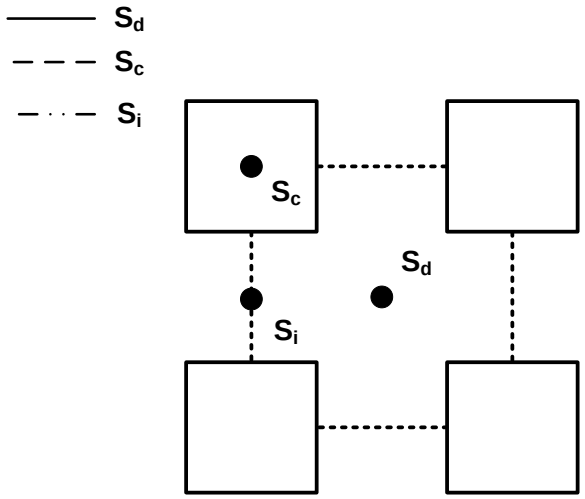

Figure E.2: Locations of surface settlement measurements

E.1.6 Results for surface deformation

Demerdash found that surface settlements measured over the pile caps increased with increasing embankment height to reach a limiting value at the critical height. He believes that the pile cap size controlled the height at which the limiting value was reached and its magnitude. He also reported that the mid-span surface settlement along the diagonal and inline directions decreased with increasing embankment height to reach a similar limiting value. Demerdash asserts that the height at which these limiting values coincide is the critical height. His observations are very similar to those observed during the current bench-scale experimental testing program.

Figure E.3 through Figure E.7 are extracted from Demerdash (1996) and provide his measurements of surface settlement obtained during full height testing. The line types used in the plots correspond to the settlement locations provided in Figure E.2.

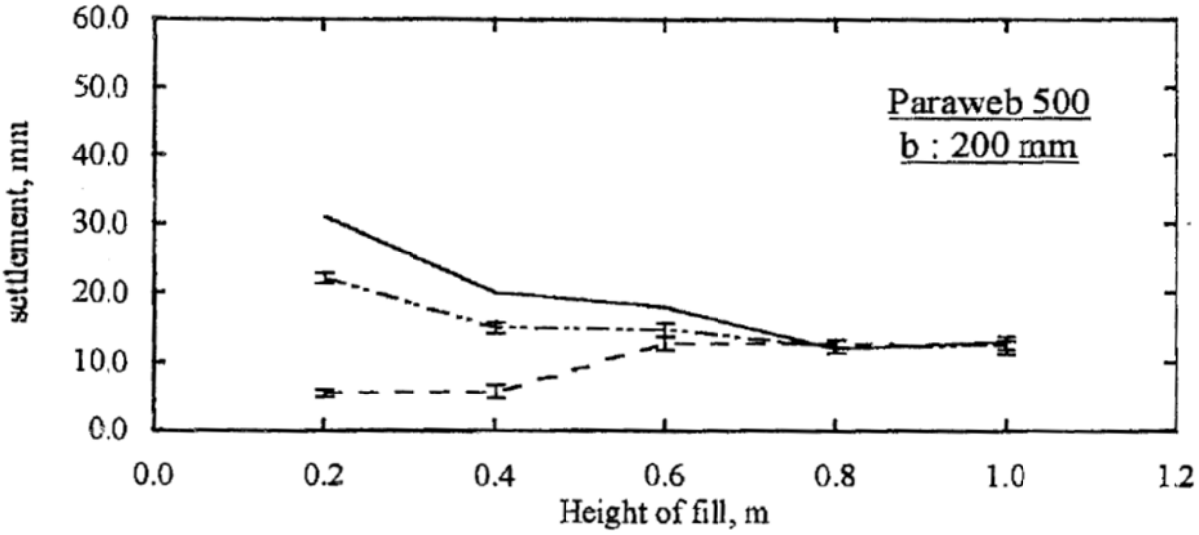

Figure E.3 Measured surface settlements versus sample height for geometry/reinforcement combination 1B (Demerdash 1996, fair use)

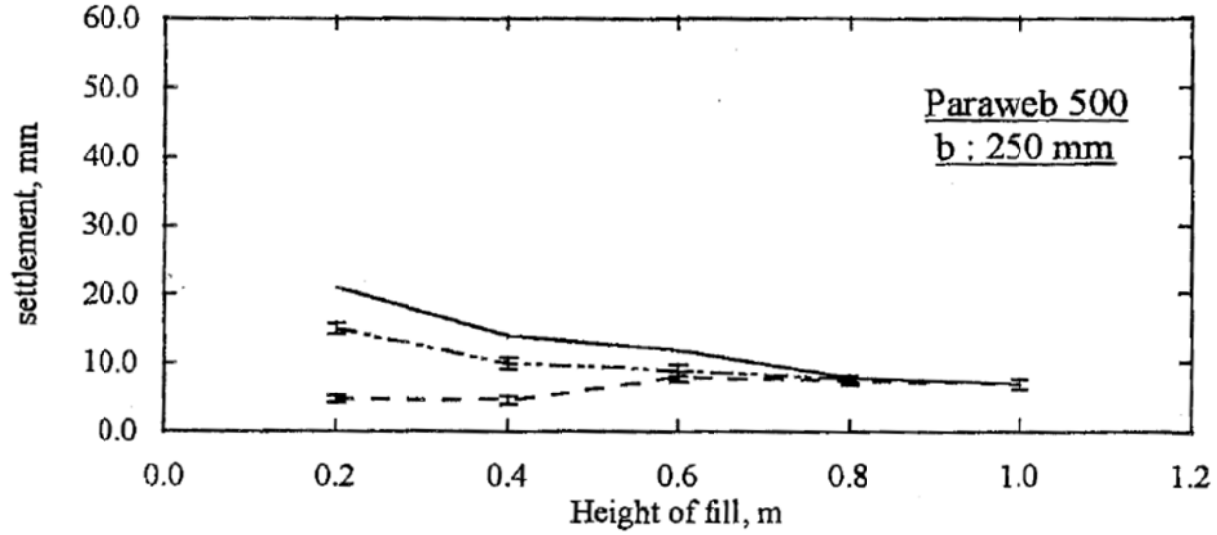

Figure E.4 Measured surface settlements versus sample height for geometry/reinforcement combination 2B (Demerdash 1996, fair use)

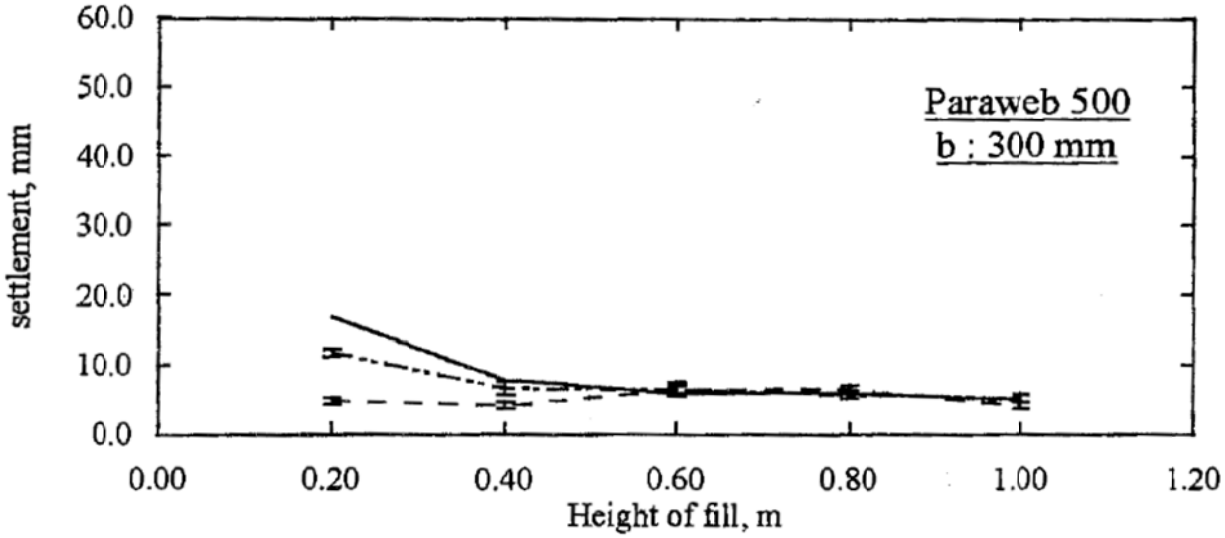

Figure E.5 Measured surface settlements versus sample height for geometry/reinforcement combination 3B (Demerdash 1996, fair use)

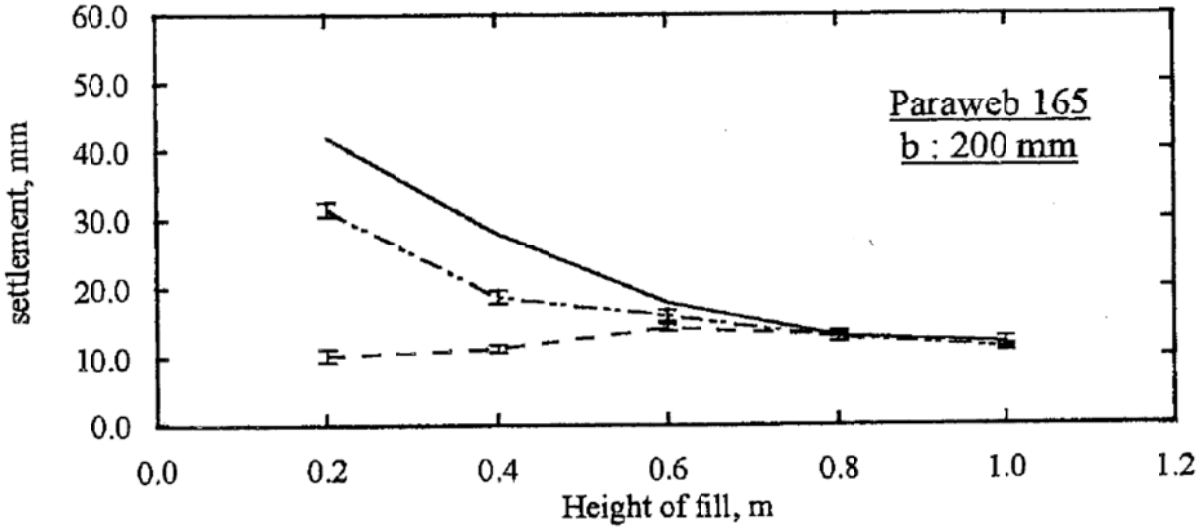

Figure E.6 Measured surface settlements versus sample height for geometry/reinforcement combination 1A (Demerdash 1996, fair use)

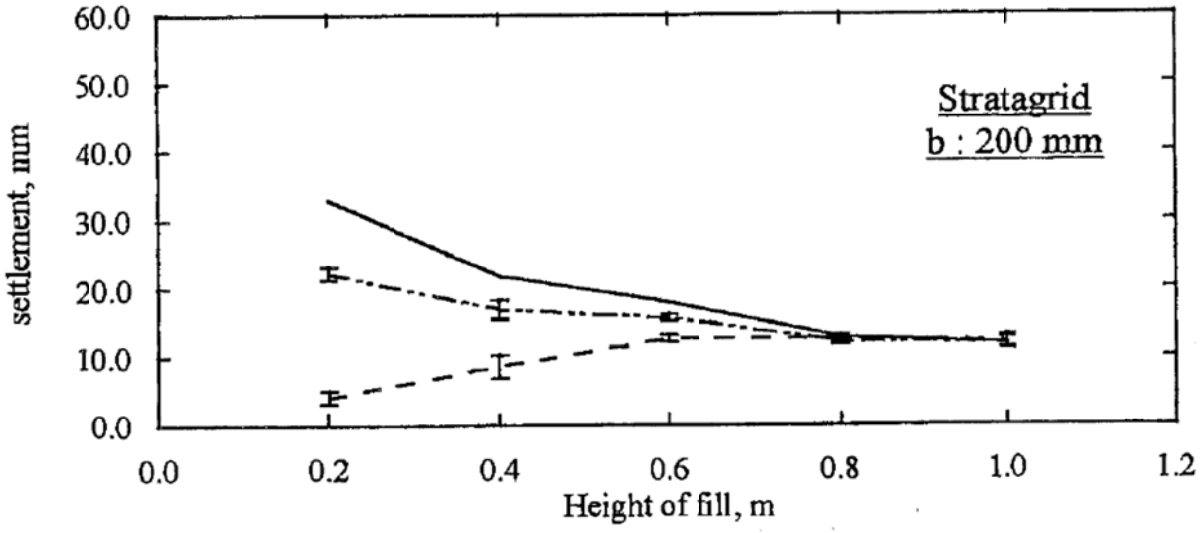

Figure E.7 Measured surface settlements versus sample height for geometry/reinforcement combination 1D (Demerdash 1996, fair use)

E.1.7 Results for base deformation

A difference between Demerdash's experiments and the bench-scale tests performed during the current study is that differential movement between the columns and base is uniform for the current tests and non-uniform for Demerdash's tests. Demerdash used an array of draw wire extensometers to measure the vertical deformation of the reinforcement at various locations in the unit cell. One of the locations was in the middle of the unit cell corresponding to the location of maximum base settlement, $S_{b,d}$ defined in Section 1.4. From the measurements of reinforcement deformation, Demerdash concluded that the deformation along a profile either diagonal or parallel to the column lines can be approximated by a parabola or circular arc. Figure E.9 through Figure E.13 are taken from Demerdash (1996) and show the measurements reinforcement deflection from full height tests. Figure E.8 shows the measurement location corresponding to each symbol type used in the plots.

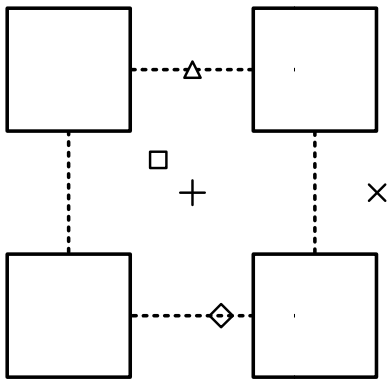

Figure E.8 Reinforcement deflection measurement locations

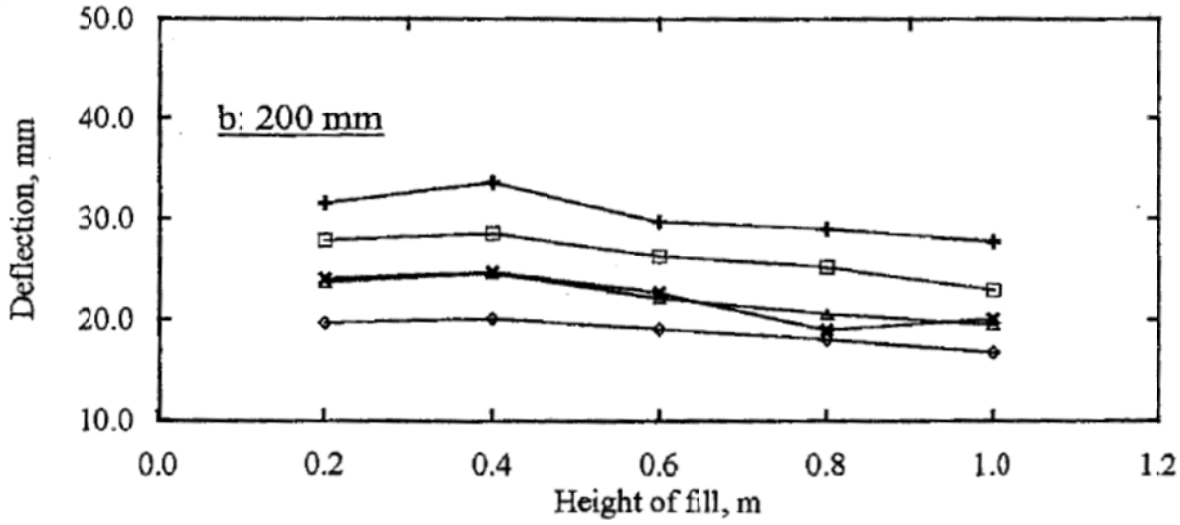

Figure E.9 Deflection of reinforcement versus sample height for geometry/reinforcement combination 1B (Demerdash 1996, fair use)

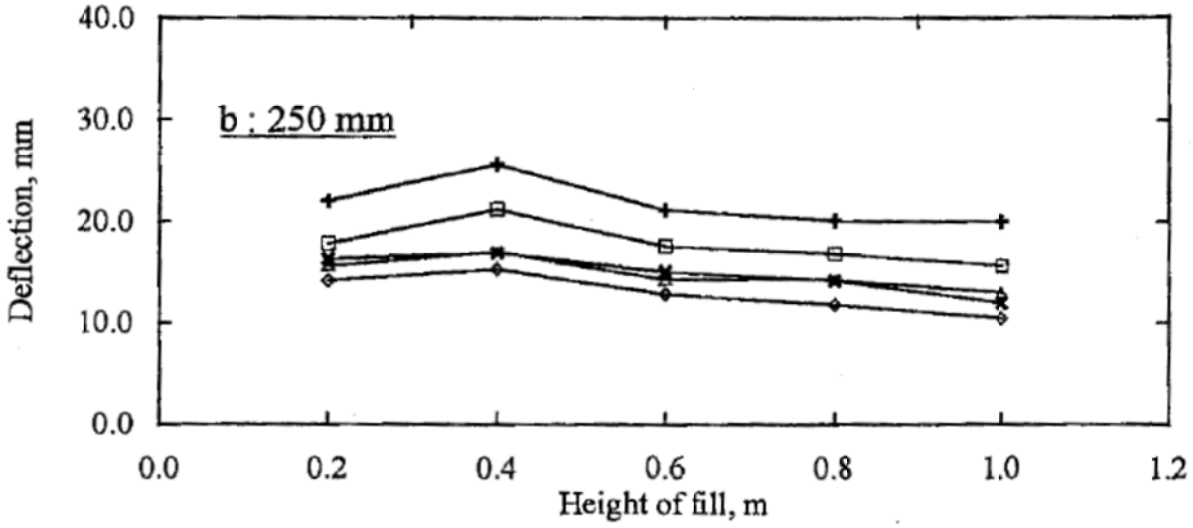

Figure E.10 Deflection of reinforcement versus sample height for geometry/reinforcement combination 2B (Demerdash 1996, fair use)

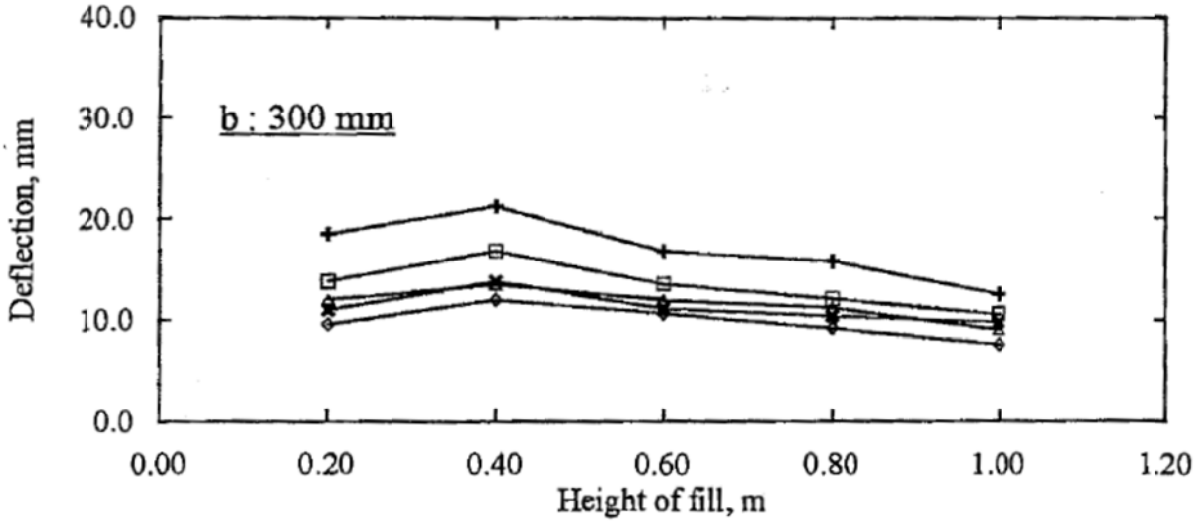

Figure E.11 Deflection of reinforcement versus sample height for geometry/reinforcement combination 3B (Demerdash 1996, fair use)

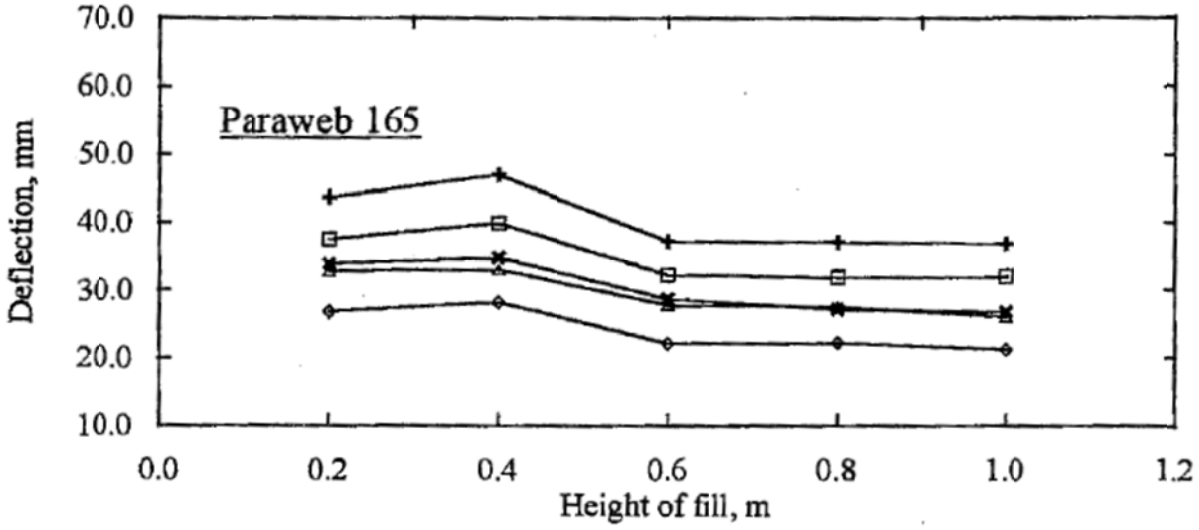

Figure E.12 Deflection of reinforcement versus sample height for geometry/reinforcement combination 1A (Demerdash 1996, fair use)

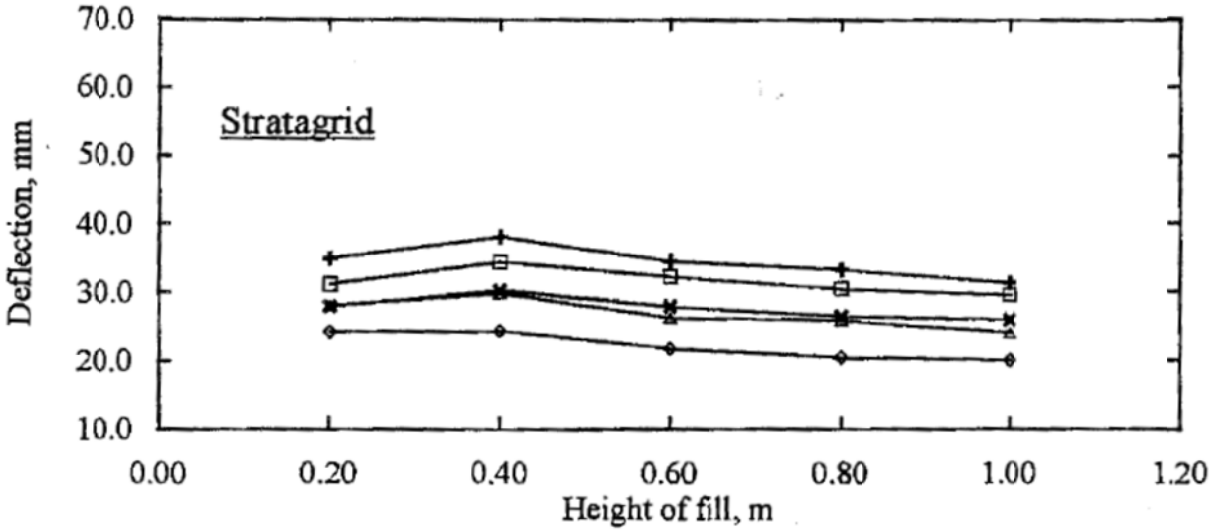

Figure E.13 Deflection of reinforcement versus sample height for geometry/reinforcement combination 1D (Demerdash 1996, fair use)

Demerdash comments on the fact that reinforcement deflection reaches a peak value at a sample height of 0.4 m, but he does not offer an explanation. One possibility is that better load transfer to the columns by arching is possible when sample height is greater than 0.4m.

E.1.8 Results for column stress-displacement behavior

Figure E.14 through Figure E.16 are adapted from Demerdash (1996) and show efficacy, which he defined as the percentage of the total weight of the soil within the unit cell carried by the pile caps due to arching, plotted against the maximum deflection of the reinforcement along the column line divided by the clear span, $S_{b,i}/(s-a)$. The figures are grouped by geometry and show the results for a range of sample heights expressed as a fraction of the clear span. All of the results provided are for tests performed using Reinforcement B.

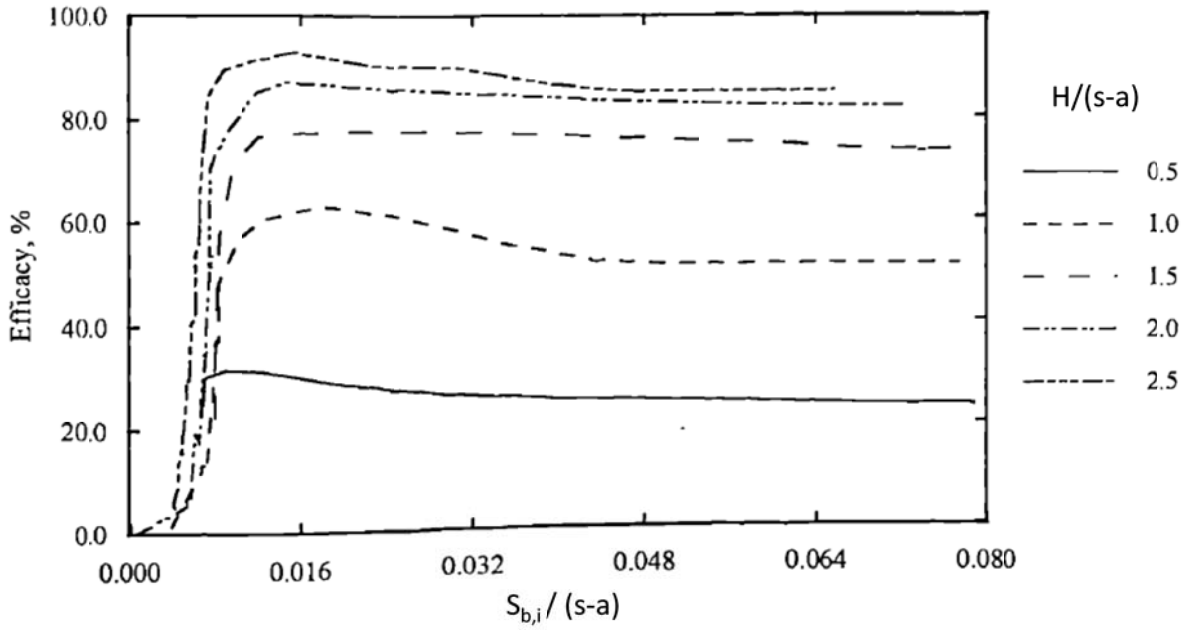

Figure E.14 Efficacy versus maximum base settlement along the column line divided by clear span, S_i / (s-a), for geometry/reinforcement combination 1B (Adapted from Demerdash 1996, fair use).

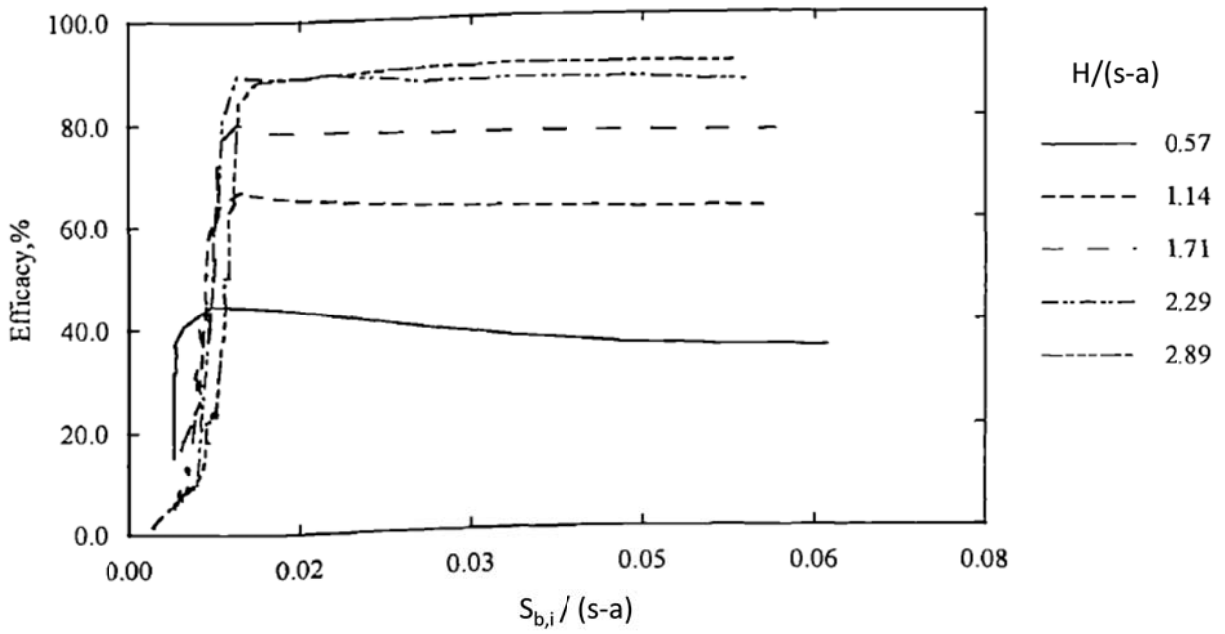

Figure E.15 Efficacy versus maximum base settlement along the column line divided by clear span, Si / (s-a), for geometry/reinforcement combination 2B (Adapted from Demerdash 1996, fair use).

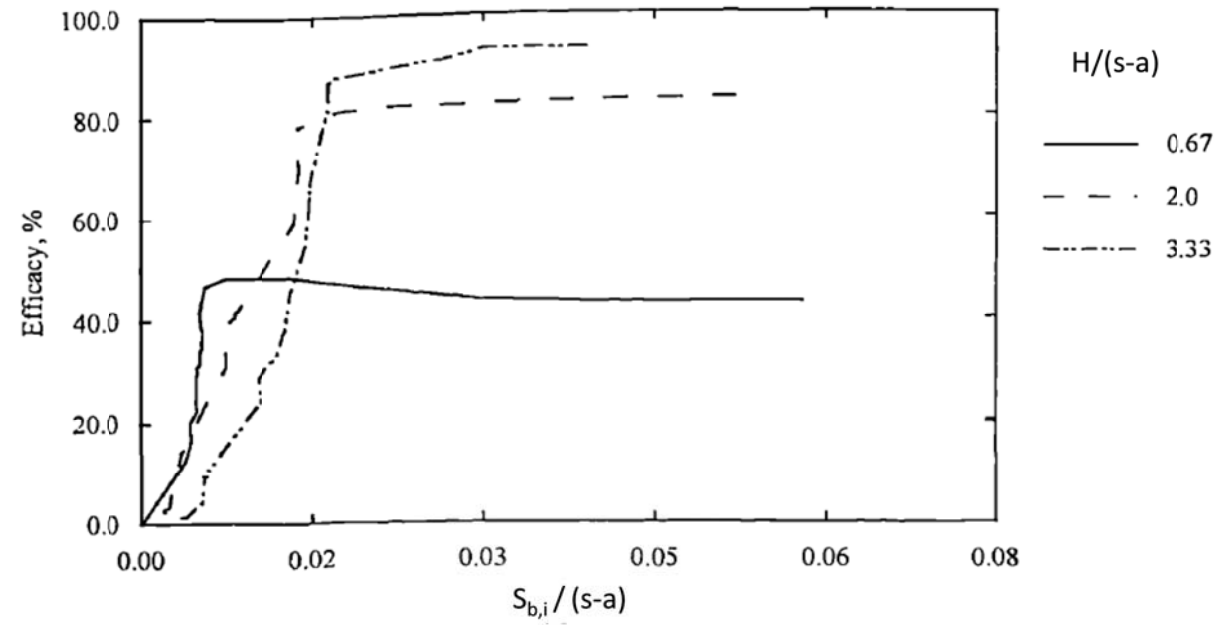

Figure E.16 Efficacy versus maximum base settlement along the column line divided by clear span, S_i / (s-a), for geometry/reinforcement combination 3B (Adapted from Demerdash 1996, fair use).

E.1.9 Interpretation of Demerdash's results for samples below critical height

The measurements of surface and base deformation provided in Figure E.3 through Figure E.7 and Figure E.9 through Figure E.13 were digitized and used to determine the ratio of the maximum differential surface settlement, S_d-S_c, to the maximum base settlement, which occurs at the center of the unit cell. This settlement ratio is equivalent to the ratio $DSBR_d$ used to analyze the current bench-scale test results except that the base settlement in non-uniform in the case of Demerdash's tests. Figure E.17 through Figure E.21, show plots of $DSBR_d$ versus normalized sample height, H/d, for Demerdash's results. As noted in Table E.1, the square pile caps used by Demerdash were converted to circular caps of equal area. The solid and dashed lines shown in each figure intersect the horizontal axis at the lowest and highest normalized heights reasonably possible for the critical height (i.e. the height where differential surface settlement becomes zero). Table E.3 summarizes the possible range for critical height for each of the geometry/reinforcement combinations. The results show that normalized critical height increases with spanning ratio. The results also indicate that $DSBR_d$ decreases slightly with a reduction in reinforcement stiffness. This result is counter-intuitive and likely the result of an increase in S_b without a proportional increase in S_d-S_c for a decrease in reinforcement stiffness. With a limited number of tests, this effect slightly lowers the minimum bound for critical height as reinforcement stiffness decreases. This outcome is not expected and is most likely due to the number of tests rather than an actual decrease in critical height with decreasing reinforcement stiffness. In his own interpretation of the test results, Demerdash concluded that reinforcement stiffness had an insignificant effect on critical height. Figure E.22 shows the range of normalized critical height versus spanning ratio, s'/d, for each combination of reinforcement and geometry along with the trend line for normalized critical height versus spanning ratio developed from the current bench-scale tests. The critical heights determined from Demerdash's tests using Geometry 1 and 2 agree fairly well with the current tests, however the predicted critical height for Geometry 3 is significantly higher than the measured value. Despite measures taken to reduce wall friction, it is possible that the proximity of the unit cell to the walls of Demerdash's apparatus is influencing the behavior of the sample. Geometry 3 uses the largest pile caps which come within 5.9 inches (0.15m) of the model boundary. The added support provided to the sample by any wall friction would have a tendency to lower the critical height.

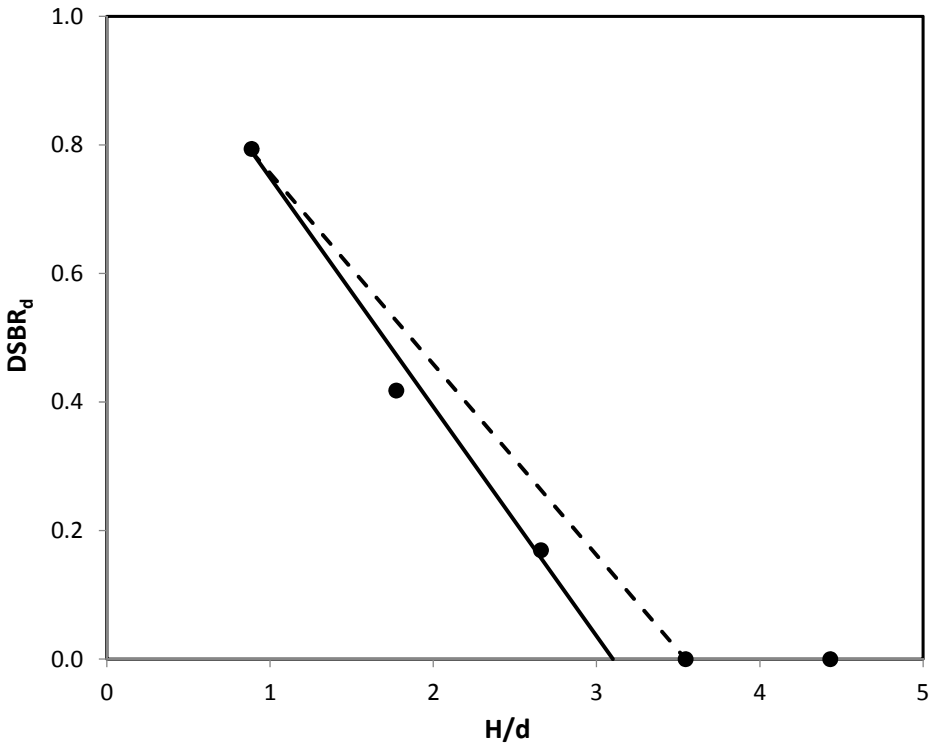

Figure E.17 DSBR$_d$ versus normalized sample height for geometry/reinforcement combination 1B

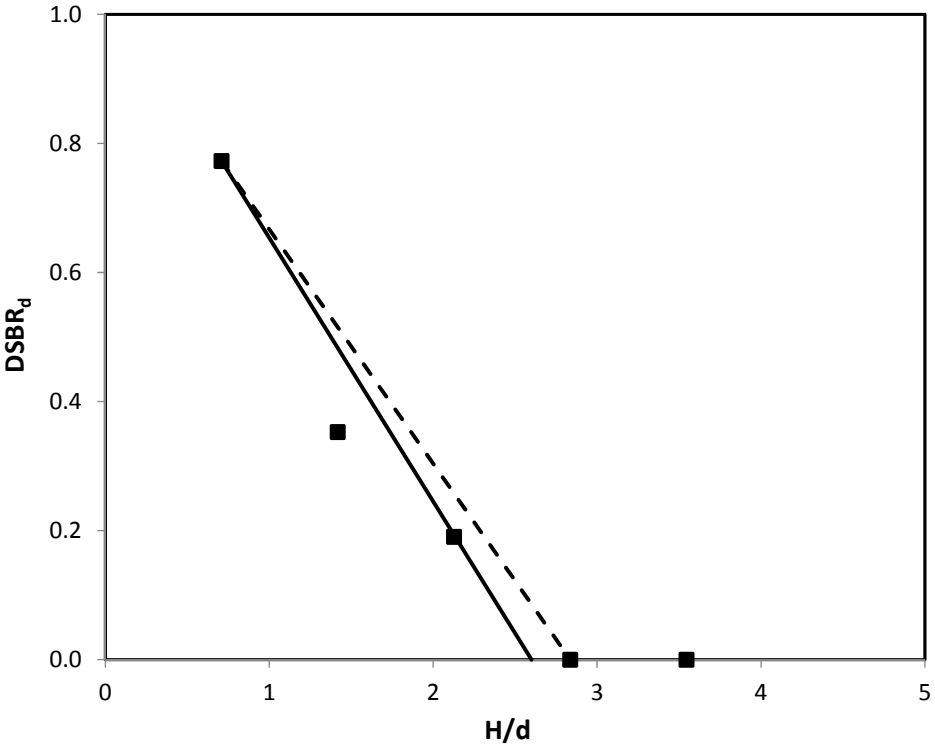

Figure E.18 DSBR$_d$ versus normalized sample height for geometry/reinforcement combination 2B

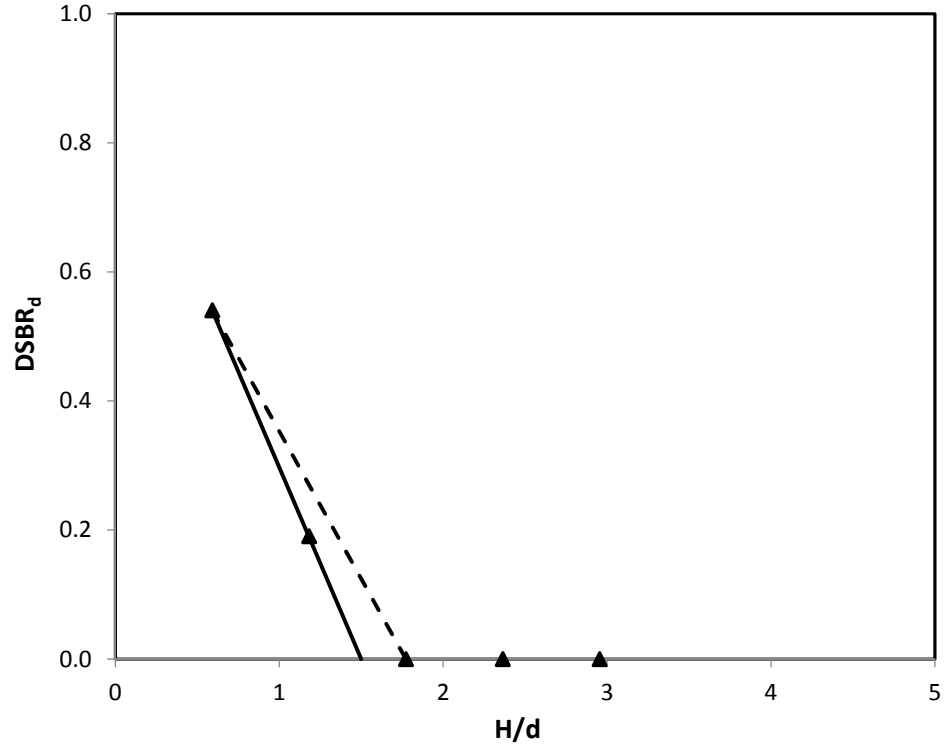

Figure E.19 DSBR$_d$ versus normalized sample height for geometry/reinforcement combination 3B

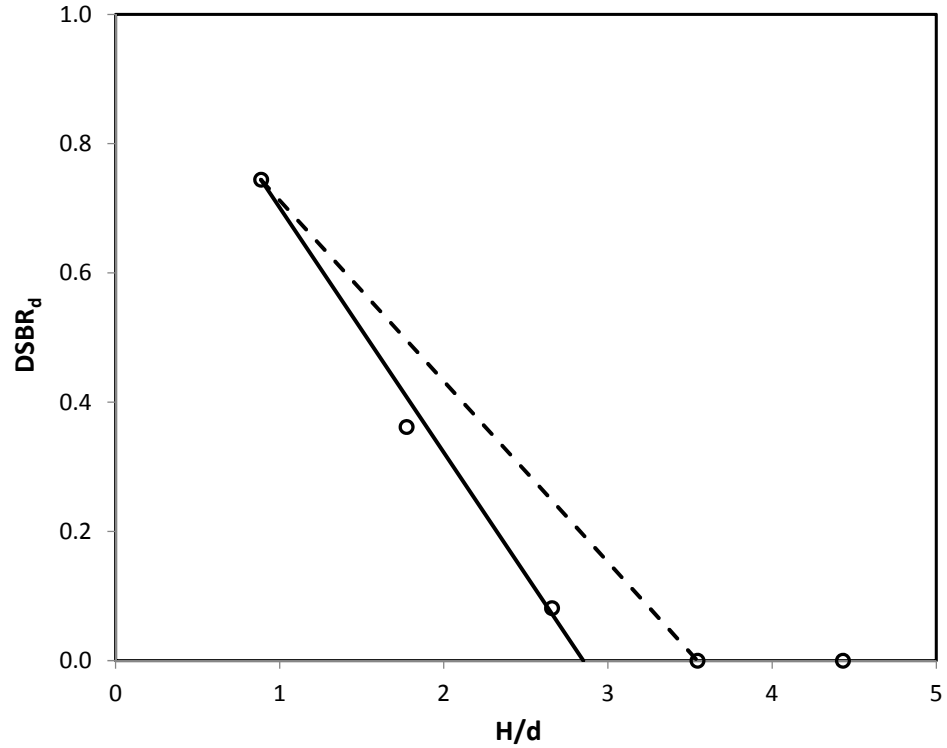

Figure E.20 DSBR$_d$ versus normalized sample height for geometry/reinforcement combination 1A

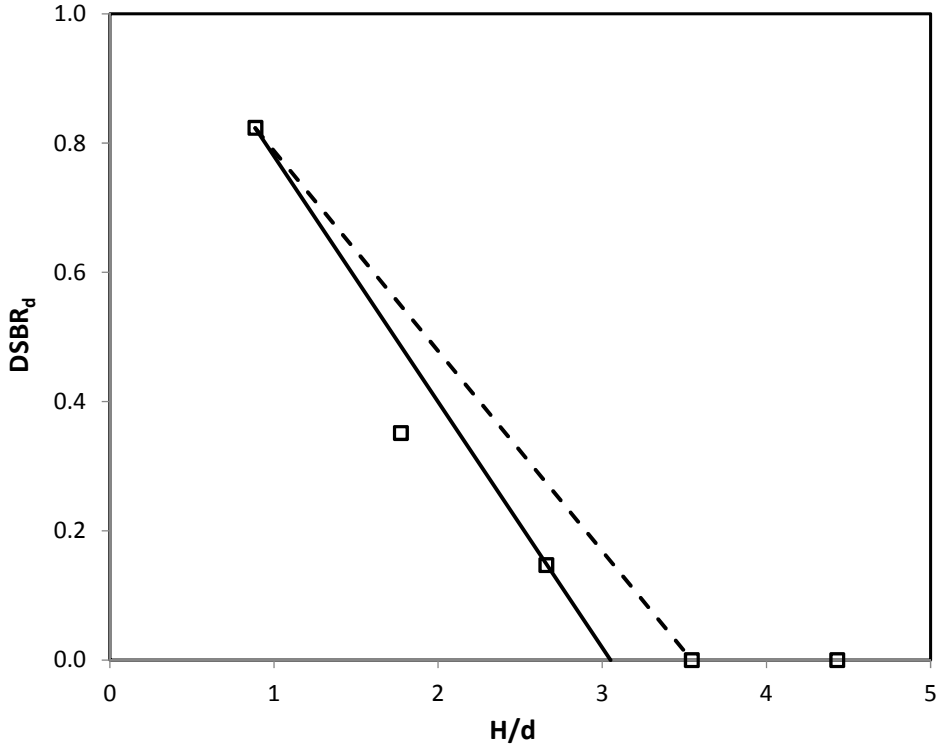

Figure E.21 DSBR$_d$ versus normalized sample height for geometry/reinforcement combination 1D

Table E.3 Range of normalized critical height for each geometry/reinforcement combination

Geometry	Reinforcement	s (in.)	a (in.)	d (in.)	s'/d	$H_{crit,min}/d$	$H_{crit,max}/d$
1	B	23.62	7.87	8.88	1.38	3.10	3.55
2	B	23.62	9.84	11.11	1.00	2.60	2.84
3	B	23.62	11.81	13.33	0.75	1.50	1.77
1	A	23.62	7.87	8.88	1.38	2.85	3.55
1	D	23.62	7.87	8.88	1.38	3.05	3.55

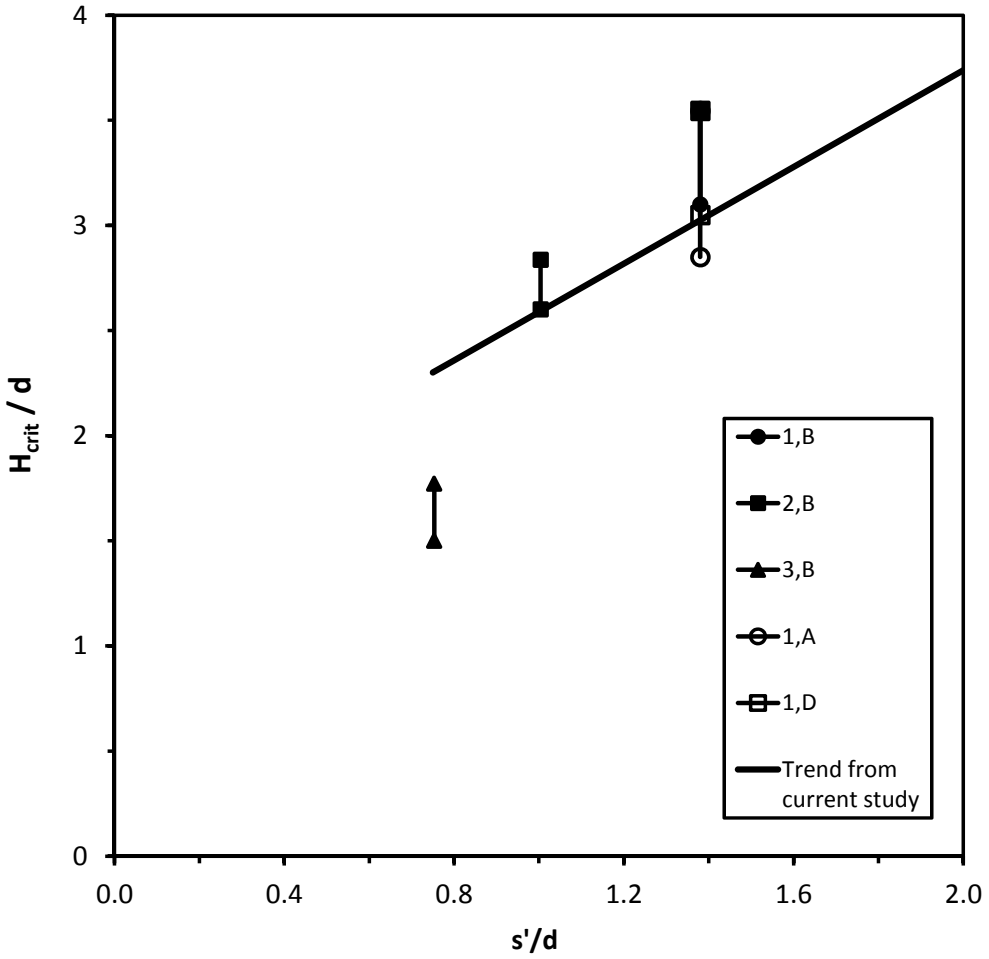

Figure E.22 Range of normalized critical height versus spanning ratio for the geometry/reinforcement combinations used by Demerdash (1996). The trend line developed from the current bench-scale tests is also provided.

E.1.10 Interpretation of Demerdash's results for samples above critical height

The results from the current bench-scale tests suggest that the ratio of total surface settlement to base settlement for samples above the critical height does not change significantly with further increase in height. Using Demerdash's test results, the ratio of total surface settlement to maximum base settlement above the critical height was determined by dividing the total settlement for tests with a 1 m sample height by the corresponding maximum base settlement. The resulting secant value of the settlement ratio, SBR_{tot}, for each geometry/reinforcement combination is provided in Table E.4. The results are plotted against area replacement ratio in Figure E.23. Excluding differences in material properties, there are two likely reasons why Demerdash's results plot slightly below the secant values of SBR_{tot} measured

from the experiments performed in the current study. The first likely reason is that, for Demerdash's tests, SBR_{tot} is determined using the maximum base settlement while SBR_{tot} is determined using the magnitude of uniform base settlement in the current tests. This difference is discussed in detail in Section 7.2. A second possible reason the values of SBR_{tot} determined from Demerdash's results plot below the trend line is the tendency for boundary effects in Demerdash's apparatus to become magnified as sample height increases. As sample height increases, there is a greater chance for a silo-effect to occur, whereby the sample arches between the walls of the apparatus rather than the pile caps. The additional support provided by the tank walls would have the effect of reducing total settlement above the critical height.

Table E.4 Ratio of total surface settlement to maximum base settlement, SBR_{tot}, for geometry/reinforcement combinations used in Demerdash's experimental study.

Geometry	Reinforcement	s (in.)	a (in.)	d (in.)	A_s	SBR_{tot}
1	B	23.62	7.87	8.88	11%	0.44
2	B	23.62	9.84	11.11	17%	0.35
3	B	23.62	11.81	13.33	25%	0.32
1	A	23.62	7.87	8.88	11%	0.30
1	D	23.62	7.87	8.88	11%	0.39

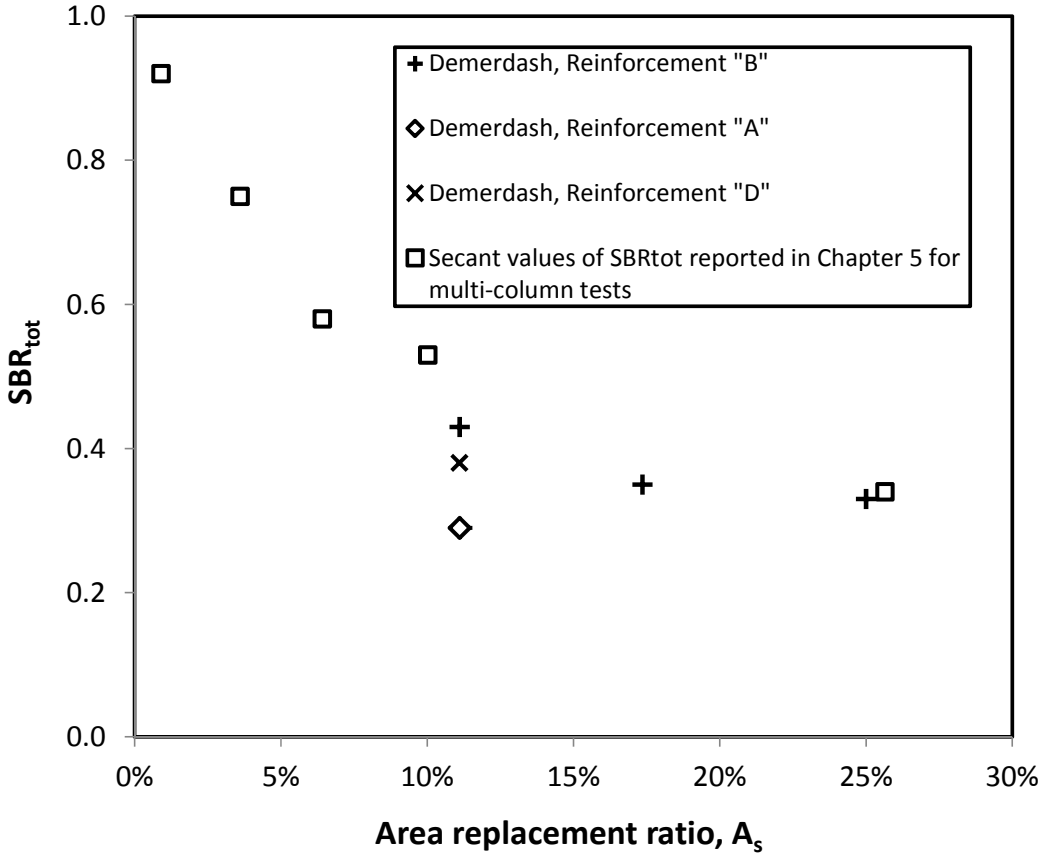

Figure E.23 Ratio of total surface settlement to maximum base settlement the geometry/reinforcement combinations used in Demerdash's experimental study.

E.1.11 Interpretation of Demerdash's results for the column stress-displacement relationship

The key findings from Demerdash's measurements shown in Figure E.14 through Figure E.16 are that: 1) the stress-displacement relationship is characterized by a sharp rise in column stress at the onset of base settlement followed by a leveling off or gradual decrease in stress, 2) the maximum stress acting over the columns above the reinforcement, as indicated by maximum efficacy, occurs at low magnitudes of base settlement, and 3) the base settlement required to reach maximum stress over the columns increases with sample height. These findings are similar to the results from the single column tests described in Chapter 4 and the results from pullout testing on embedded anchors described in Section 2.5. Since the multi-column tests described in Chapter 5 were not instrumented to measure column load, Demerdash's results provide an opportunity to compare the column-stress displacement relationships observed from single column testing to those observed from multi-column testing.

Demerdash's measurements of efficacy, E, can be converted to a column stress ratio, CSR, using the relationship CSR $= E/A_s$. In this case, since Demerdash measured efficacy above the reinforcement, the resulting value of CSR equals the ratio of $\sigma_{col,geotop}$ to the initial vertical stress as defined in Section 1.4. An in-depth analysis of Demerdash's measurements of efficacy was not performed as part of this study.

One straightforward comparison that can be made is the magnitude of base settlement required to reach peak column stress. Besides differences in material properties, the only significant difference between the interpretation of the results is that base settlements are uniform in the base of the current single column tests and non-uniform in the case of Demerdash's tests. Figure E.24 is a reproduction of Figure 4.30 in Chapter 4 with an overlay of Demerdash's results and the results from tests performed by Chen et al. (2008) discussed in Appendix D. The combined test data suggests that the magnitude of base settlement at peak column stress, $S_{b,max}$, for single column testing is similar to the base settlement required to reach peak column stress for multi-column testing.

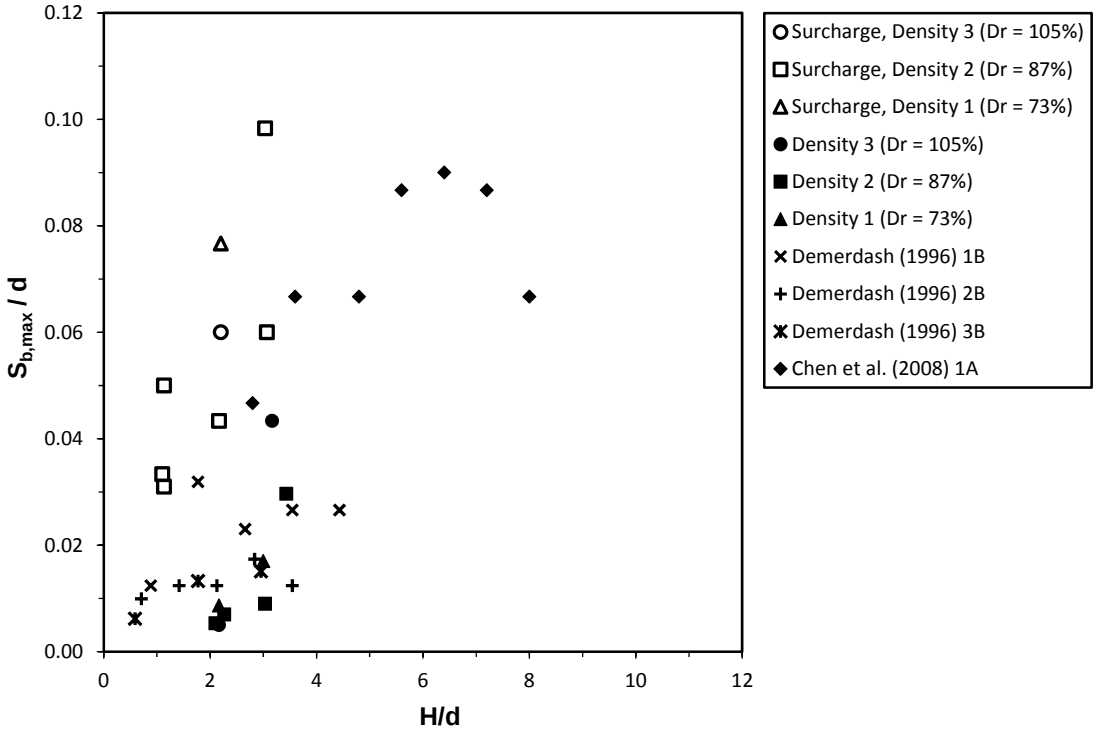

Figure E.24 Relationship between normalized base settlement at maximum column stress versus normalized sample height

E.2 Numerical Analysis using FLAC2D

Demerdash developed the model shown in Figure E.25 using FLAC2D. The embankment material was modeled as an isotropic linear elastic-perfectly plastic material with a Mohr-Coulomb failure criterion. The geosynthetic reinforcement was modeled using one dimensional cable elements and the soft sub-soil was modeled using Winkler springs. Using the model, Demerdash performed three different sets of analyses. The first set of analyses verified the model against plane strain experimental tests performed by Tang (1992). The second set of analyses modeled geometry/reinforcement combinations 1B and 3B from the experimental study with the goal of comparing the deformation and load transfer results. The third set of analyses used the unit cell geometries and material properties defined in Table E.5 to parametrically model range of conditions beyond those investigated during the experimental study. A broad range of reinforcement stiffnesses were used to evaluate the influences on load transfer and

surface deformation. Unfortunately, all the figures associated with the first two sets of analyses (verification and comparison studies) and some of the figures from the third set of analyses (parametric study) are missing from available electronic and hard copies of Demerdash's dissertation. The figures conveying calculated distortion between locations of maximum and minimum surface settlement from the parametric study are provided below as Figure E.26 and Figure E.28. The key findings described by Demerdash from the first two sets of analyses are that:

1) The 2D model calculates reinforcement deflection and load sharing between the columns and sub-soil that is in reasonable agreement with the 3D conditions associated with the experimental study.
2) Compared to the 3D experiments, the 2D model over-estimates differential surface settlement. The discrepancy between the calculated and measured values of surface settlement was greatest for the settlement measured over the axis of the pile cap, S_c, which was underestimated by FLAC2D.

The second conclusion agrees with the results of the current numerical study using FLAC3D described in Chapter 6. Therefore, the underestimation of S_c by FLAC does not appear to be primarily related to three dimensional effects.

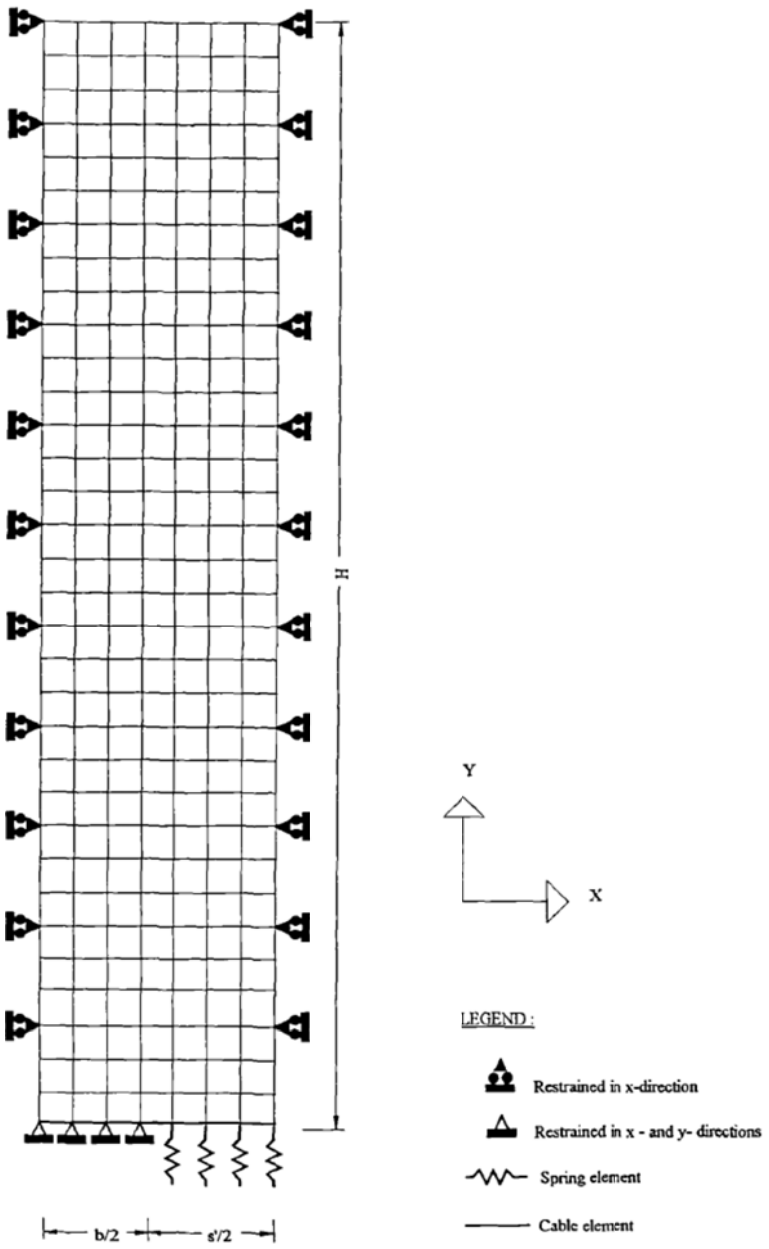

Figure E.25 Demerdash's numerical model developed in FLAC2D (Demerdash 1996, fair use)

Table E.5 Variation of testing parameters during the numerical parametric study conducted by Demerdash (1996) using FLAC2D

	Config.	Array	s, in.	d[1], in.	H, in.	s'/d [2]
Geometry	4	2D cap beams	78.74	39.37	19.7 to 354.3	0.5
	5		118.11			1.0
	6		157.48			1.5

		Description	γ, pcf	ϕ_{peak} (ϕ_{crit})	ψ_{peak}	c, psf
Embankment Material Properties		Isotropic linear elastic-perfectly plastic w/ Mohr-Coulomb failure criterion	127.3	38 (NG)	0	0

	ID	Description	Layers	Position[3], in.	Stiffness, J, lbs/ft
Reinforcement		Cable elements	1	0	3426 to 68522

Notes
1 Here, d is the width of the 2D cap beams. As described in Section 1.4, no shape conversion is necessary for 2D conditions.
2 s'/d = s/(2d)-(1/2)
3 Vertical distance measured from the pile cap to the reinforcement
NG = Not Given

The calculated surface distortions shown in Figure E.26 through Figure E.28 from Demerdash's numerical parametric study were used to determine the value of critical height for each geometry listed in Table E.5 by determining the height at which distortion reaches zero. For Geometry 6, the height at which distortion levels off at around 1 percent was considered to be the critical height. Table E.6 summaries the values of critical height calculated from Demerdash's numerical analyses.

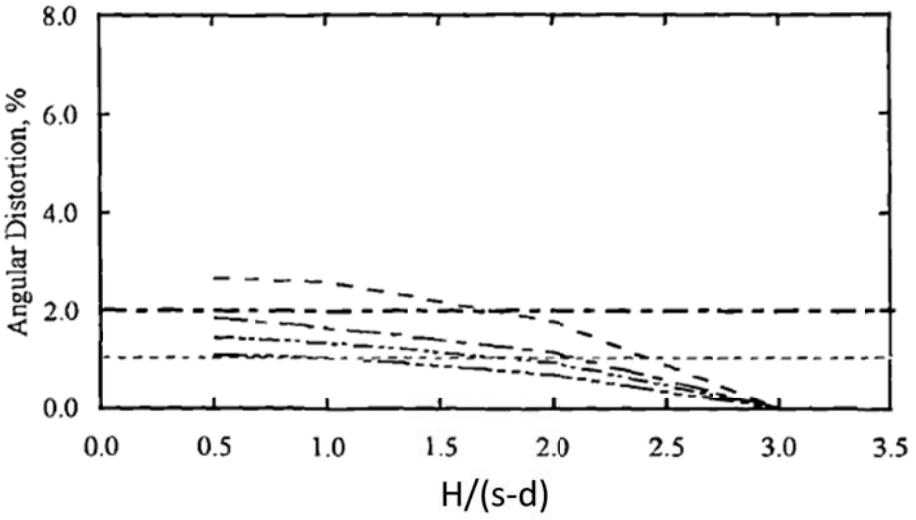

Figure E.26 Angular distortion between locations of maximum and minimum surface settlement versus sample height normalized by clear span between cap beams for Geometry 4. (Adapted from Demerdash, 1996, fair use)

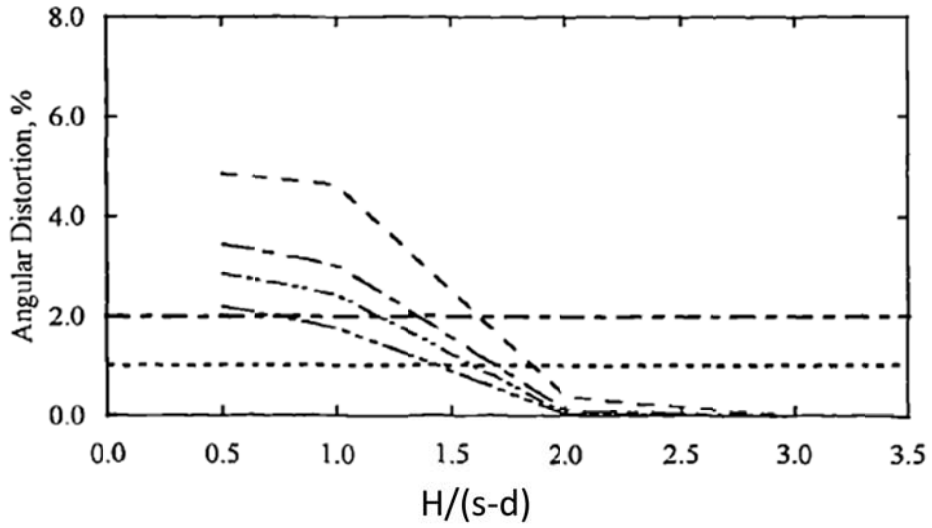

Figure E.27 Angular distortion between locations of maximum and minimum surface settlement versus sample height normalized by clear span between cap beams for Geometry 5. (Adapted from Demerdash, 1996, fair use)

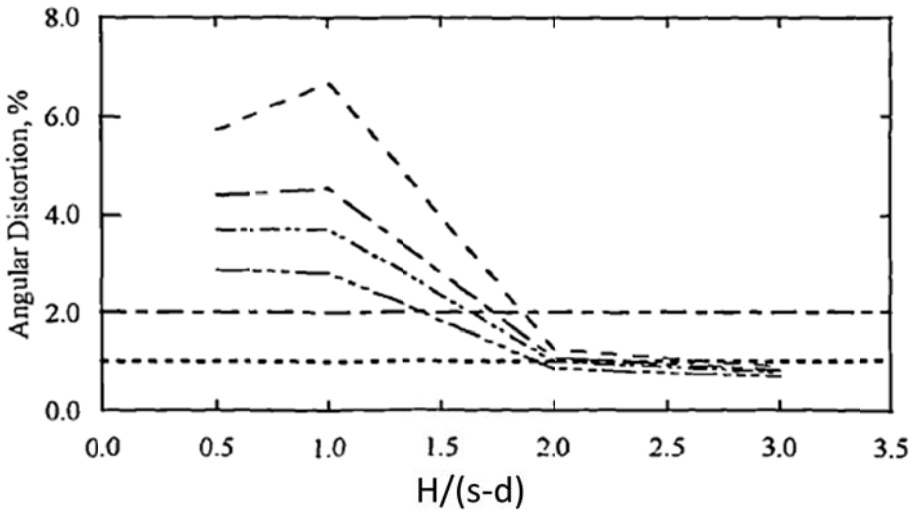

Figure E.28 Angular distortion between locations of maximum and minimum surface settlement versus sample height normalized by clear span between cap beams for Geometry 6. (Adapted from Demerdash, 1996, fair use)

Table E.6 Summary of critical heights determined for Geometries 4, 5, and 6

Geometry	Reinforcement	s (in.)	a (in.)	d (in.)	s'/d	H_{crit} (in.)	H_{crit}/d
4	Variable stiffness	78.74	39.37	39.37	0.91	118	3.00
5	Variable stiffness	118.11	39.37	39.37	1.62	157	4.00
6	Variable stiffness	157.48	39.37	39.37	2.33	236	6.00

Figure E.29 shows the normalized critical heights determined for Geometries 4, 5, and 6 plotted against spanning ratio along with the trend line developed from the bench-scale tests for 3D unit cell geometries. Demerdash's numerical results plot consistently above the trend line, which presents the possibility that critical heights determined for 2D conditions have a slightly different relationship with spanning ratio than critical heights determined for 3D conditions. This idea is discussed in detail in Section 7.1.

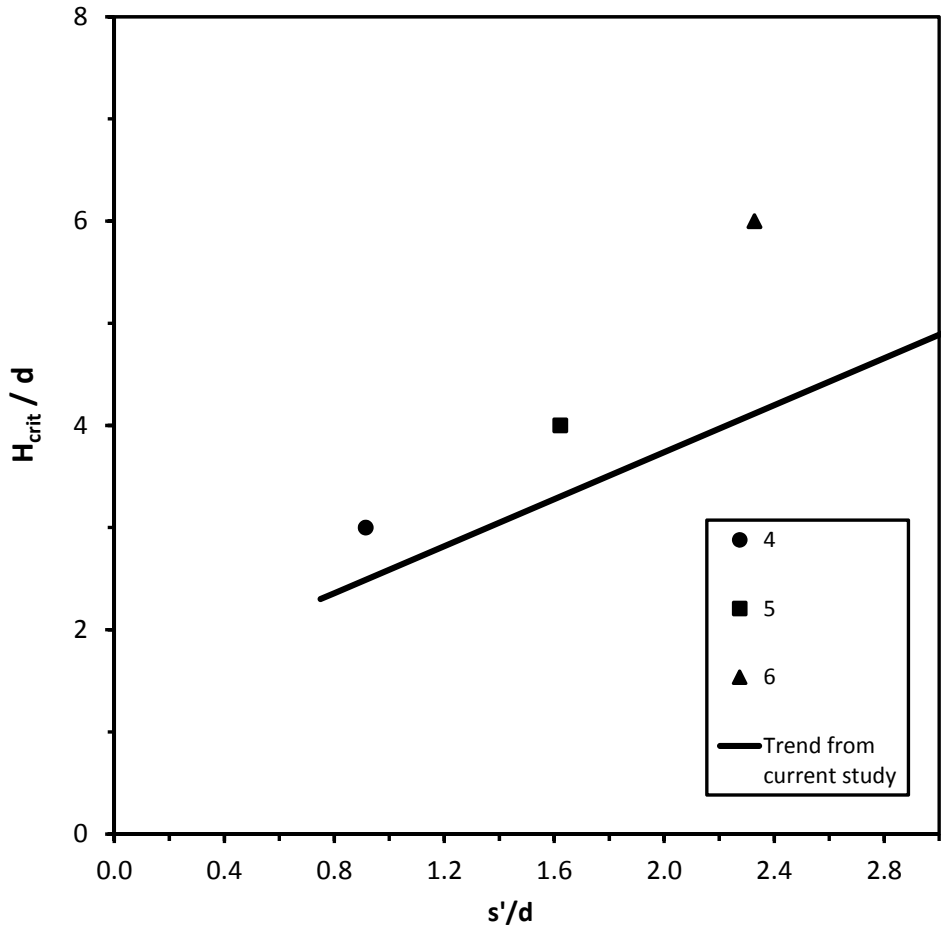

Figure E.29 Normalized critical heights calculated from the numerical parametric study for Geometries 4, 5, and 6 versus spanning ratio. The trend line obtained from the bench-scale experiments performed during the current study is also provided.

Appendix F: Summary and interpretation of experimental study conducted by Ellis and Aslam (2009a,b)

F Summary of Experimental Study Conducted by Ellis and Aslam (2009)

References:

Ellis, E. A., and Aslam, R. (2009). "Arching in piled embankments: comparison of centrifuge tests and predictive methods - part 1 of 2." *Ground Engineering*, 42(6), 34-38.

Ellis, E. A., and Aslam, R. (2009). "Arching in piled embankements: comparison of centrifuge tests and predictive methods - part 2 of 2." *Ground Engineering*, 42(7), 28-31.

F.1 Overview of study:

This study, covered in two parts in the journal *Ground Engineering*, uses a centrifuge test model of an unreinforced column-supported embankment. The model measured 300mm by 300mm in plan view and 500mm high. All model boundaries were covered in greased latex to minimize friction. The columns were constructed from 25mm diameter aluminum tube, with 30 mm square caps, and were arranged in a square grid of 3x3 and 4x4 piles on 100mm or 75mm centers, respectively. Compression on the foundation soil was considered using two different stiffnesses of expanded polystyrene stryrofoam (EPS) with a thickness of 180 mm. The embankment material consisted of Leighton Buzzard Fraction C sand. Samples ranging in height from 35 to 210mm were formed using dry air pluviation at high relative density of 90 to 95 percent. The sand had a critical state friction angle of 35 degrees, but the authors acknowledge that the peak friction angle is likely much higher due to the low confining stress, however no other values of friction angle are reported. A summary of the model geometry and material properties is provided using English units in Table F.1.

Table F.1 Variation of testing parameters during the experimental study conducted by Ellis and Aslam (2009a, 2009b)

	Config.	Array	s[1], in.	d[1,2], in.	H[1], in.	s'/d [3]
Geometry	1	Square	2.95	1.33	1.38 to 8.27	1.07
	2		3.94			1.59

		Description	γ, pcf (D_r)	ϕ_{peak} (ϕ_{crit})	ψ_{peak}	c, psf
Embankment Material Properties		Leighton Buzzard Fraction C sand	NG (90 -95 %)	NG (35)	NG	0

Reinforcement	ID	Description	Layers	Position[5], in.	Stiffness, J, lbs/ft
		None[4]			

Notes
1 Actual model dimensions. Scaled dimensions are 30 times larger at 30g level and 60 times larger at 60g level.
2 Square pile caps were converted to round caps of equal area
3 $s'/d = s/(\sqrt{2}d)-0.5$
4 All samples were unreinforced
5 Vertical distance measured from the pile cap to the reinforcement
NG = Not Given

During testing, the models were subjected to increasing g-levels in 10g intervals from 10g to 60g, thus increasing the scale of the model. Ellis and Aslam mention that at 30g, the model most closely represented typical embankment geometry with 0.9m column diameters and a center-to-center spacing of 2.25m.

The instrumentation used for to record the performance of the centrifuge model consisted of load cells to measure column load and a digital camera used to capture the deformation of the sample surface. The Particle Image Velocimetry (PIV) technique used to capture surface deformation had a maximum resolution of 0.2mm at 1g scale. Therefore, at 30g, the measurement system could discern differential settlement equivalent to 6 mm (0.24 in) at the model scale.

F.2 Measurement and interpretation of surface deformation

Ellis and Aslam report differential surface settlement versus sample height normalized by clear spacing, s-a, at 30 and 60 g-levels. A personal communication with Dr. Ellis indicated that

the tests that were below the critical height used a column spacing of 100 mm. For the tests using a 75 mm spacing, the lowest sample height evaluated was 75 mm and the resulting differential settlement was less than the measuring resolution of the PIV camera. Dr. Ellis also indicated that differential surface settlement was determined by eye using profiles similar to that given in Figure F.1.

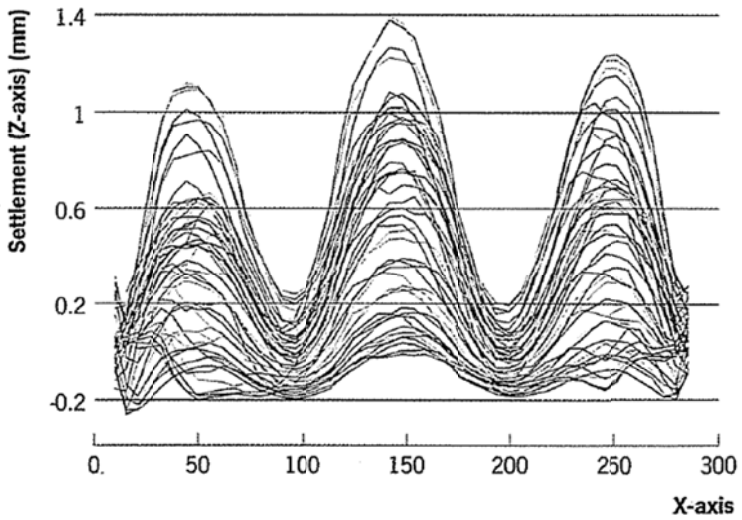

Figure F.1 Typical surface settlement profiles at different magnitudes of base settlement along column line obtained from PIV camera (Ellis and Aslam 2009b, fair use)

The orientation of the settlement profiles shown in Figure F.1 is parallel to the column lines. Experience from the current multi-column tests described in Chapter 5 has shown that the settlement along a profile diagonal to the column lines controls the values of critical height, however the difference in the critical heights determined in each direction is usually small enough to be insignificant. Figure F.2 shows the differential settlement versus sample height normalized by clear spacing for lower stiffness EPS foam subsoil. The plot shows a fairly linear relationship between the magnitude of differential settlement and the embankment height normalized by clear spacing similar to that observed during the current multi-column testing. It is worth noting that both the 30 and 60g levels have essentially the same critical height. This supports the notion that the influence of scale effects on the value of critical height are small. Scaling from the figure using the lines added to highlight the trend of the data suggests that the critical height is 1.58 times the clear spacing, which for a column spacing of 100mm and cap size of 30mm results in a critical height of 110.6mm at 1g and 3.32m at 30g. The differential settlement resulting from the samples using the higher stiffness EPS subsoil was significantly

smaller which made it not possible use a trend line of differential settlement versus sample height to determine the critical height.

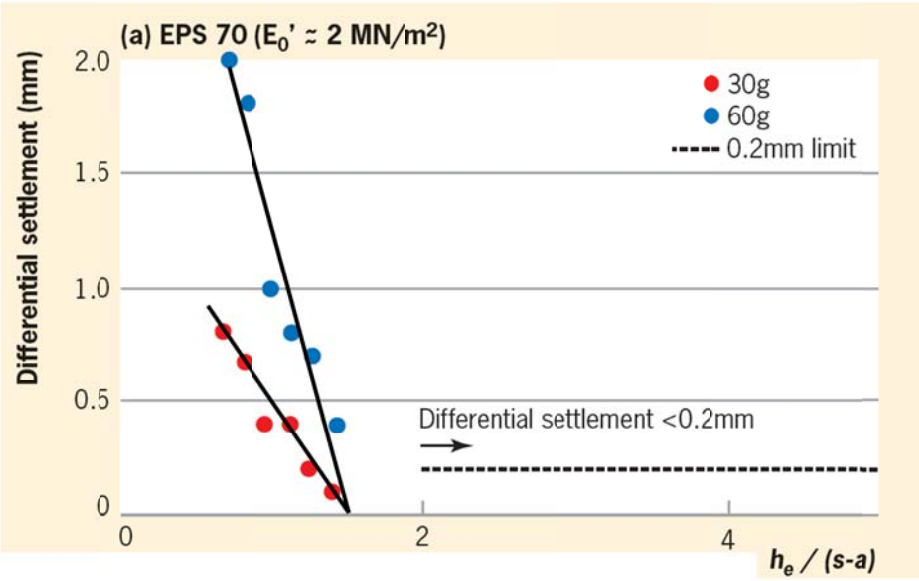

Figure F.2: Plot of differential settlement versus embankment height normalized by clear spacing. The black lines have been added here to determine the critical height from the trend of the data. (Adapted from Ellis and Aslam 2009b, fair use)

Table F.2 compares the critical height determined from Ellis and Aslam's results to the critical height predicted using the expression developed in Chapter 5.

Table F.2 Comparison of measured to predicted values of critical height

Column spacing[1], s (in.)	Pile cap width[1], a (in.)	Equivalent round pile cap diameter[2], d (in.)	Spanning ratio[3], s'/d	H_{crit} measured[1] (in.)	H_{crit} predicted (in.)
118.11	35.43	39.98	1.59	130.63	130.59

Notes

1 Dimensions are based on model scale at 30g

2 Based on equal area

3 See Section 1.4 for calculation of spanning ratio

4 $H_{crit}/d = 1.15(s'/d) + 1.438$

Appendix G: Summary and interpretation of numerical study conducted by Han and Gabr (2002)

G Summary of Numerical Study Conducted by Han and Gabr (2002)

Reference:

Han, J., and Gabr, M. A. (2002). "Numerical analysis of geosynthetic-reinforced and pile-supported earth platforms over soft soil." *Journal of Geotechnical and Geoenvironmental Engineering*, 128(1), 44-53.

G.1 Overview

Han and Gabr (2002) evaluated load and deformation behavior of GRCSEs using an axisymmetric approach in FLAC 2D. The fill and foundation soil were modeled using the nonlinear elastic Duncan Chang hyperbolic model under drained conditions. Piles with a length of 6 m consisted 0.7 m diameter linear elastic elements with a 3 m diameter of influence founded on a stiff stratum. Geosynthetic reinforcement was modeled as a linear elastic material. The reinforcement was assumed to be fully bonded to the soil and no creep was considered. A traffic surcharge of 10 kPa was applied to the top of the model during all analyses. Table G.1 summaries the geometry and material properties considered in the numerical study using English units.

The study by Han and Gabr focuses on load transfer to the columns, settlement of the foundation soil and ground surface, deformation of the reinforcement, and distribution of vertical stress across the model. The focus herein is on their results for surface settlement.

Table G.1 Variation of parameters during the numerical study conducted by Han and Gabr (2002)

		Array	s^1, in.	d , in.	H, in.	s'/d [2]
Geometry		2D axisymmetric	118.11	27.56	39.37 to 157.48	1.64

		Description	γ, pcf (D_r)	ϕ_{peak} (ϕ_{crit})	ψ_{peak}	c, psf
Embankment[3] Material Properties		Duncan and Chang (1970) nonlinear hyperbolic elastic with Mohr Coulomb failure criterion	NG (NG)	30 (NG)	NG	0

		Description	Layers	Position[4], in.	Stiffness, J, lbs/ft
Reinforcement		None			
		Linear elastic	1	3.94	58,943

Notes
1 Here, s is the diameter of the axisymmetric model.
2 s'/d = s/(2d)-(1/2)
3 A traffic surcharge of 1.45 psi (10kPa) was consider in all analyses
4 Vertical distance measured from the pile cap to the reinforcement
NG = Not Given

G.2 Results for surface deformation

Han and Gabr reported calculated maximum differential settlement at the ground surface for analyses performed with and without reinforcement. Figure G.1 is reproduced from Han and Gabr (2002) and shows an approximately linear decrease in differential settlement as the embankment fill height is increased. This outcome agrees with the results of the current multi-column tests described in Chapter 5. The critical height for the axisymmetric model geometry summarized in Table G.1 is 3 m regardless of whether the reinforcement is present. The independence of critical height on the presence and stiffness of reinforcement was also observed during the multi-column tests described in Chapter 5. Table G.2 compares the calculated critical height using the FLAC model to the critical height estimated using the expression developed from the results of the multi-column tests described in Chapter 5. The comparison indicates that the critical height for the model geometry calculated using Han and Gabr's results is higher than the height estimated using the expression developed form the current multi-column tests. Listed below are three possible explanations for the difference between the values:

1) The critical height calculated from Han and Gabr's results may be closer to the estimated value if more analyses were performed between embankment heights of 2 and 3 meters.
2) The tests results described in Chapter 5 suggest that critical height increases slightly with decreasing relative density (and estimated friction angle) of the embankment material. Han and Gabr used a fairly low value of friction angle in their model equal to 30^o which is much lower than the estimated friction angle equal to 52^o for Light Castle sand prepared at Density 2.
3) It is possible that 2D representations using either a plane strain or axisymmetric of a 3D unit cell overestimates the critical height. The results from the 2D plane strain numerical model developed by Demerdash (1996) also lead to higher calculated values of critical height than estimated using the trend from the current multi-column test results.

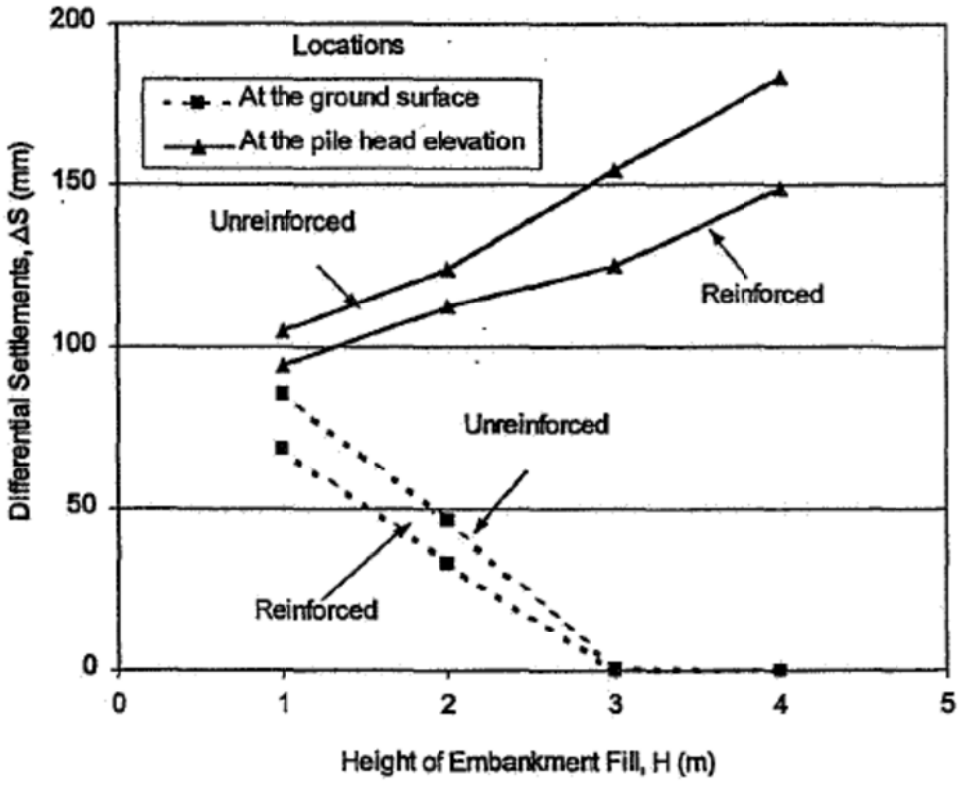

Figure G.1 Relationship between differential settlement and height of embankment fill (Han and Gabr 2002, used with permission from ASCE)

Table G.2 Comparison of measured to predicted values of critical height

Column spacing[1], s (in.)	Pile cap diameter, d (in.)	Spanning ratio[3], s'/d	H_{crit} measured[1] (in.)	H_{crit} predicted (in.)
118.11	27.56	1.64	118.11	91.60

Notes

1 Assumes that the diameter of the axisymmetric model is equivalent to column spacing

2 Based on equal area

3 See Section 1.4 for calculation of spanning ratio

4 $H_{crit}/d = 1.15(s'/d) + 1.438$

Appendix H: Summary and interpretation of experimental and numerical studies by Jenck et al. (2007)

H Summary of Experimental and Numerical Studies Performed by Jenck et al. (2007)

References:

Jenck, O., Dias, D., and Kastner, R. (2007). "Two-dimnesional physical and numerical modeling of a pile-supported eath platform over soft soil." *ASCE Journal of Geotechnical and Geoenvironmental Engineering*, 133(3), 295- 305.

H.1 Overview of experimental study:

The study by Jenck et al. (2007) has three primary components: 1) physical testing using a model approximating plane strain conditions, 2) calibration of a 2D numerical model and validation against the experimental tests and comparison of results using two constitutive models, and 3) a parametric study using the numerical model to investigate the influences of the material properties of the embankment and subsoil on load transfer and settlement at the embankment surface.

The experimental model developed by Jenck et al. (2007) consists of a bench-scale tank with Teflon-coated side walls and a transparent face. The width of the tank can be adjusted between 0.55m and 1.3 and the tank can accommodate a sample with a maximum height of 0.7 m. The base of the base has two 0.1 m wide platforms outfitted with load cells which act as cap beams. Three different geometries were evaluated by setting the c-c spacing between the caps to 0.32, 0.45, or 0.65 m. Compressible foam was used in between the cap beams to simulate compressible subsoil. Two different stiffness of foam were used during testing.

The sample material consisted of Schneebeli soil, which simulates the behavior of dense granular materials using a packing arrangement of steel rod segments. Calibration of the 2D numerical model indicated a friction angle of 24^o and zero cohesion if the Schneebeli soil is modeled as an elastic-perfectly plastic material with Mohr-Coulomb failure criterion and variable Young's Modulus. The Schneebeli soil has a unit weight of 62 kN/m^3 (395 lbs/ft^3).

During testing, the Schneebeli soil was added in 0.1 m lifts. The foam subsoil compressed with each lift causing the embankment to deform incrementally. Once the maximum sample height of 0.7 m was reached, an additional 5kPa surcharge was applied to the surface.

As mentioned above, the instrumentation consisted of load cells on each cap beam to determine load transfer occurring at each increment of sample height. Deformation of the embankment at each increment was measured using digital image processing.

Table H.1 summarizes the variation of test parameters during the experimental study using English units.

Table H.1 Variation of testing parameters during the experimental study conducted by Demerdash (1996)

	Config.	Array	s, in.	d[1], in.	H, in.	s'/d [2]
Geometry	1	Cap beams (Plane strain)	12.60	3.94	3.94 to 27.56	1.1
	2		17.72			1.75
	3		25.60			2.75

		Description	γ, pcf (D_r)	ϕ_{peak} (ϕ_{crit})	ψ_{peak}	c, psf
Embankment Material Properties		Schneebeli soil	395 (NG)	24 (NG)	4	0

Reinforcement	ID	Description	Layers	Position[3], in.	Stiffness, J, lbs/ft
	A	None			

Notes
1 Here, d is the width of the cap beams which approximate 2D plane strain conditions. As described in Section 1.4, no shape conversion is necessary for 2D plane strain conditions.
2 s'/d = s/(2d)-(1/2)
3 Vertical distance measured from the pile cap to the reinforcement
NG = Not Given

The focus of the current analysis of the study by Jenck et al. (2007) is the measurement of surface deformation. Jenck et al. (2007) only report peak load transfer at each increment, so there is no significant benefit to drawing comparison to the load-displacement results obtained from the single column tests described in Chapter 4.

H.2 Overview of numerical modeling

Jenck et al. (2007) developed a plane strain numerical model using FLAC that mimics the geometry and sample preparation procedures used for the physical experiments. The embankment material composed of Schneebeli soil and subsoil composed of foam were both modeled as elastic-perfectly plastic materials with Mohr-Coulomb failure criterion and variable Young's modulus or using a two-mechanism elastoplastic model with isotropic hardening. The behavior of the embankment material was calibrated against previous physical experiments performed by others and the behavior of the foam was calibrated using load tests performed by the authors. The calibrated model was validated against the bench-scale model tests and the results suggested that the simpler Mohr-Coulomb model was sufficient for estimating the system behavior.

Using the calibrated and validated model, Jenck et al. (2007) performed a parametric study whereby the properties of the embankment soil and subsoil were varied. The results for surface settlement are summarized in the next section.

H.3 Surface settlement results

Jenck et al. (2007) report the increment of surface distortion that occurs due to a 0.1 m increment increase in sample height. The surface distortion is measured as the difference between the settlement over the cap beam, S_c, to the settlement a distance s' from the cap beams, S_d, divided by the half the column spacing, s/2. Figure H.1 through Figure H.3 present their results measured experimentally and calculated using the numerical model using the current notation. In the figures, F1 indicates tests performed using the stiffer foam and F2 indicates tests performed using the softer foam. The value of α provided in each figure is the ratio of the cap beam width to the c-c spacing.

The author's principal findings from the parametric study related to surface settlements are: 1) increasing the shear strength of the embankment material reduces the magnitude of surface settlement and 2) the stiffness of the subsoil impacts the magnitude of differential surface settlement but does not significantly affect the critical height. In terms of displacements, the second finding suggests that the magnitude of base settlement does not significantly influence the critical height. This finding is consistent with the findings from the multi-column tests described in Chapter 5.

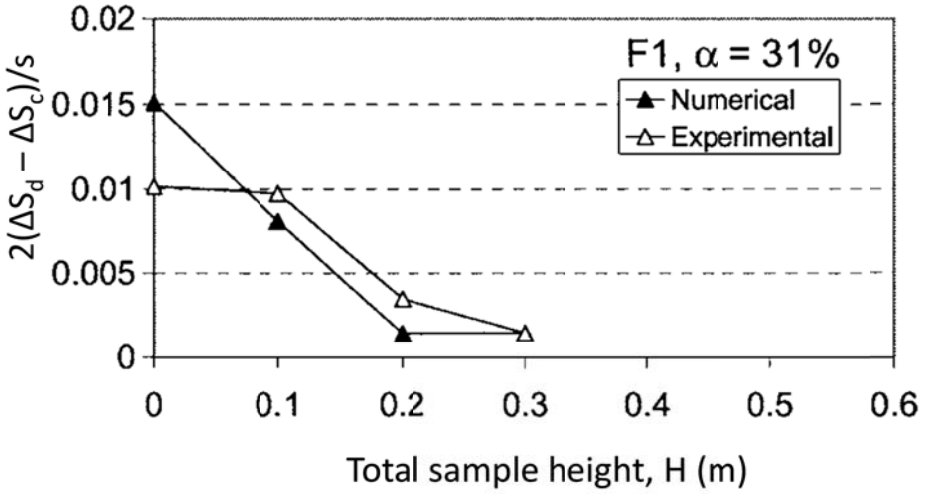

Figure H.1 Increment of surface distortion versus sample height for Geometry 1 (Adapted from Jenck et al. 2007, used with permission from ASCE).

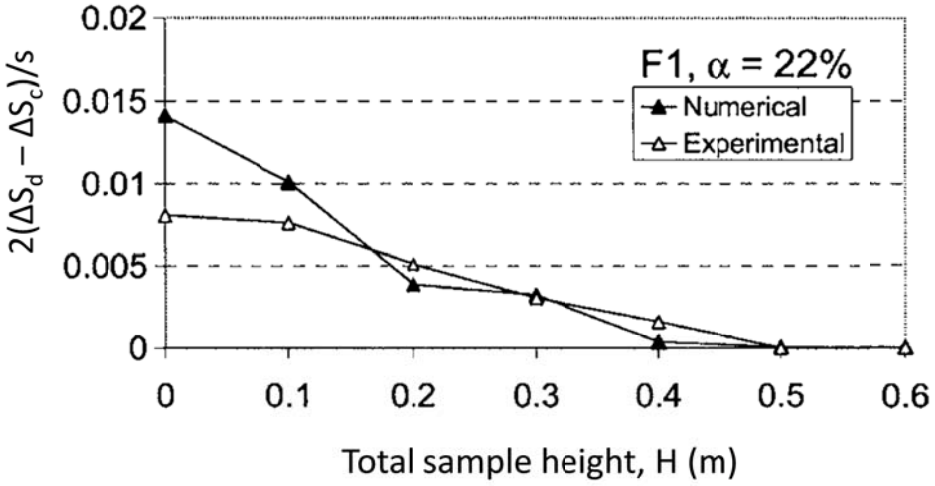

Figure H.2 Increment of surface distortion versus sample height for Geometry 2 (Adapted from Jenck et al. 2007, used with permission from ASCE).

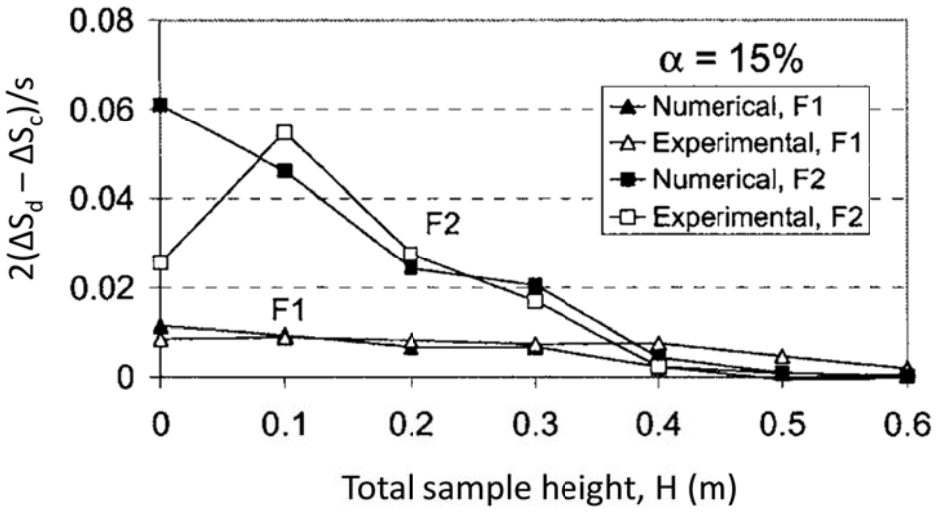

Figure H.3 Increment of surface distortion versus sample height for Geometry 3 (Adapted from Jenck et al. 2007, used with permission from ASCE).

H.4 Interpretation of results obtained by Jenck et al. (2007)

Critical heights for Geometries 1 through 3 were determined from the reported values of surface distortion shown in Figure H.1 through Figure H.3 by interpreting the height at which the increment of distortion equals zero. This approach is similar to the method used to determine critical height from the multi-column tests described in Chapter 5, except that in the experiments by Jenck et al. (2007) a single test with an incrementally increasing sample height is used whereas in the current study separate samples prepared to different heights are used. Therefore, in addition to the differences in boundary conditions (plan strain versus 3D unit cell) and material type (steel rods versus Light Castle sand), the samples used in the tests by Jenck et al. (2007) experience a number of episodes of shearing and stress change that is related to the position within the sample. For example, during the course of a test, the bottom 0.1 m thick layer undergoes 6 changes in overburden stress resulting in deformation, while the upper 0.1 m layer experiences no change in overburden pressure. The critical heights calculated using the results obtained by Jenck et al. (2007) compare reasonably well to the trend for plane strain conditions suggested by the results of experimental testing performed by Chen et al. (2008) as well as numerical modeling performed by Demerdash (1996) and Han and Gabr (2002). Table H.2 summarizes the calculated and predicted values of critical height normalized by the width of the cap beam. A range of normalized critical heights interpreted using the results obtained by Jenck et al. (2007) is provided in the table since there is some uncertainty as to the exact height where

differential settlement ceases to occur. The results are shown plotted against spanning ratio in Figure H.4 along with the trend line obtained from the multi-column tests described in Chapter 5.

The comparison of the interpreted range of critical heights from the studies by Jenck et al. (2007) to the results from the current study suggests that, while the trend observed for the conditions present during the current bench scale study consistently under-predicts the critical height for plane strain conditions, the differences are not radical. The tendency for the trend line to under-predict critical height for plane strain conditions was also observed during the interpretation of the experimental results by Chen et al. (2008) and the numerical results by Han and Gabr (2002) and Demerdash (1996).

Table H.2 Normalized critical heights determined from the experimental and numerical results by Jenck et al. (2007)

Geometry	Reinforcement	s (in.)	d^1 (in.)	s'/d	$H_{crit,min}/d$	$H_{crit,max}/d$
1	A (none)	12.60	3.94	1.10	2.60	3.40
2	A (none)	17.72	3.94	1.75	4.00	5.00
3	A (none)	25.60	3.94	2.75	4.00	6.00

Note: 1) Here, d, refers to the cap beam width and the equivalent diameter

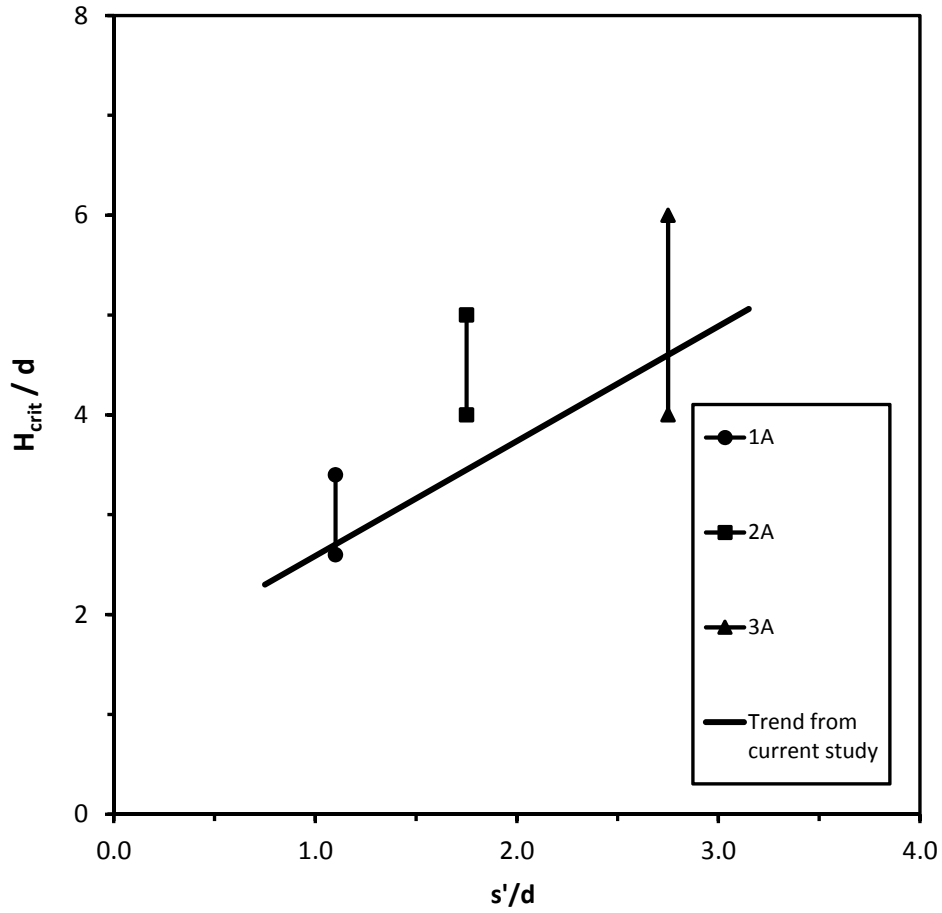

Figure H.4 Range of normalized critical heights determined from the results of the experimental and numerical studies by Jenck et al. (2007) versus spanning ratio. The trend developed from the multi-column test results described in Chapter 5 is also shown.

Appendix I: Summary and interpretation of Penang Bridge Approach case history described by Ting et al. (1994)

I Summary of Penang Bridge Approach Case History described in Ting et al. (1994)

References:

Ting, W. H., Chan, S. F., and Ooi, T. A. (1994). "Design methodology and experiences with pile supported embankments." *Development in Geotechnical Engineeering*, Balkema, Rotterdam, 419-432.

(2009) Personal communication with W.H. Ting

(2009) Personal communication with T.A. Ooi

I.1 Overview of case history and interpretation of measured settlements:

This case history is based on the results of an investigation carried out on behalf of the Malaysian Highway Authority and is described in brief in the paper by Ting et al. (1994). The eastern approach of the Penang Bridge was constructed as a column-supported embankment without the use of geosynthetic reinforcement. The portion of the sloping approach embankment supported on columns was estimated to be about 5.8 m to 3.3 m along the centerline profile as shown in Figure I.1 where surface settlements were reported.

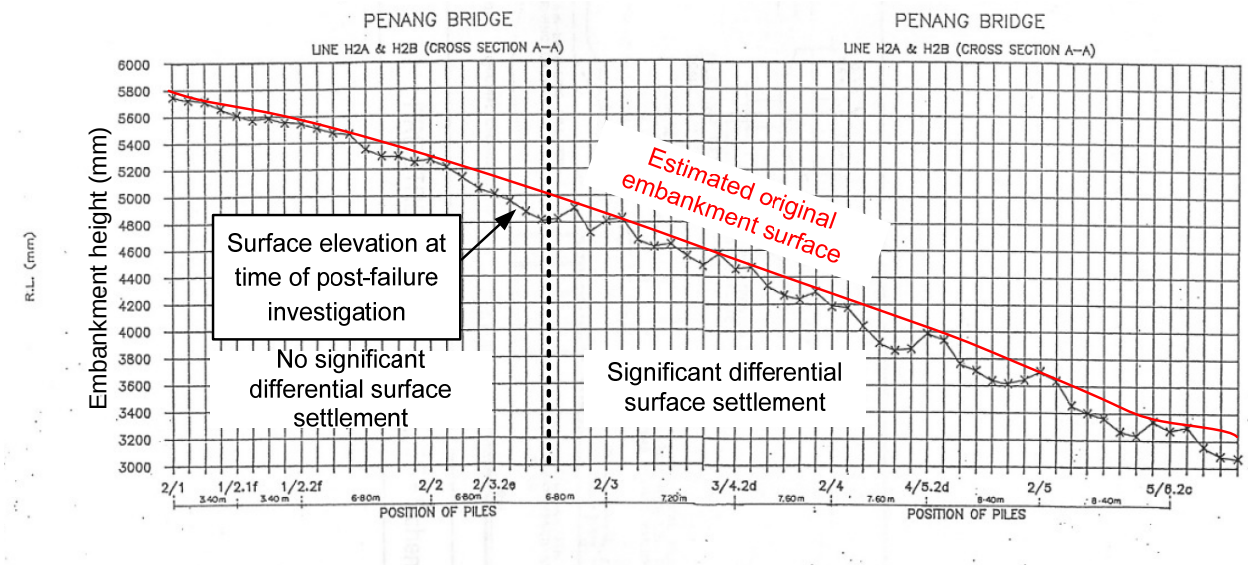

Figure I.1 Surface settlements along profile of failed column-supported embankment (adapted from Ting et al. 1994, fair use)

The columns consisted of 0.5 m diameter precast concrete cylinder piles fitted with square concrete caps having a side length of 1.8 m. The columns were installed on a staggered triangular array, as defined in Section 1.4, with spacing between adjacent rows and columns of 3.4 to 4.2 m. In an attempt to transition roadway settlements from the portion of the embankment supported on piles to the earth-supported portion, the column spacing was increased from 3.4 to 4.2 m as the embankment height decreased from 5.8 to 3.4 m.

Ting et al. (1994) reports that, within months of opening the approach ramp to traffic, differential settlement described as having a mushroom shape over each column developed over a portion of the column-supported roadway. The settlement profile shown in Figure I.1 was obtained at the start of an investigation into the failure of the embankment. The red line was added as part of the current analysis and indicates the estimated original height of the embankment. It was assumed that settlement of the embankment fill directly overlying the column is insignificant. The vertical dashed line, also added to the drawing, indicates the position along the profile of the commencement of differential surface settlement. The vertical dashed line intersects the red line at an embankment height of 5m, which is considered to be the critical height. Close inspection of Figure I.1 suggests the geometric arrangement presented in Table I.1. The column spacing at the critical height is 3.4 m corresponding to a spanning ratio of 0.55. Table I.2 compares the results of the current interpretation of critical height to the value of critical height estimated using the trend developed from the multi-column test results described in Chapter 5.

Table I.1 Embankment geometry interpreted from analysis of Figure AC.1

X position along profile (m)	Row and col. spacing, s (m)	Original embankment height, H (m)	Pile cap size, a (m)	Equiv. cap dia., d (m)	Normalized height, H/d	Spanning ratio, s'/d
0.0		5.80				
3.4	3.40	5.70	1.80	2.03	2.81	0.55
6.8	3.40	5.60	1.80	2.03	2.76	0.55
10.2	3.40	5.55	1.80	2.03	2.73	0.55
13.6	3.40	5.35	1.80	2.03	2.63	0.55
17.0	3.40	5.25	1.80	2.03	2.58	0.55
20.4	3.40	5.20	1.80	2.03	2.56	0.55
23.8	3.40	5.05	1.80	2.03	2.49	0.55
27.2	3.40	4.85	1.80	2.03	2.39	0.55
30.8	3.60	4.70	1.80	2.03	2.31	0.61
34.4	3.60	4.50	1.80	2.03	2.22	0.61
38.2	3.80	4.40	1.80	2.03	2.17	0.67
42.0	3.80	4.25	1.80	2.03	2.09	0.67
45.8	3.80	4.15	1.80	2.03	2.04	0.67
49.6	3.80	4.00	1.80	2.03	1.97	0.67
53.8	4.20	3.85	1.80	2.03	1.90	0.79
58.0	4.20	3.70	1.80	2.03	1.82	0.79
62.2	4.20	3.55	1.80	2.03	1.75	0.79
66.4	4.20	3.35	1.80	2.03	1.65	0.79

Note: Shaded portion indicates that embankment experienced differential surface settlement

Table I.2 Comparison of interpreted to predicted values of critical height

Column spacing, s (m)	Pile cap diameter, d[1] (m)	Spanning ratio[2], s'/d	H_{crit} measured (m)	H_{crit} predicted[3] (in.)
3.40	2.03	0.55	5.00	4.20

Notes

1 Square pile caps are converted to a circular cap of equal area.

2 s'/d = 0.625(s/d)-0.5

3 $H_{crit}/d = 1.15(s'/d) + 1.438$

Appendix J: List of test parameters

Test ID	Column Diamter, d (in.)	Column Spacing, s (in.)	H (in.)	Density[1]	Reinforcement[2]	Surcharge (psi)	SBR_c[3]	SBR_d[3]	SBR_i[3]	$\Delta V_{u,20}/V_u$[4]	$\sigma_{col,max}$[5] (psi)
HD6V	3.00	--	6.6	3	--	2.21	0.26	--	--	--	45.88
LD6V	3.00	--	6.6	1	--	2.21	0.29	--	--	--	40.19
MD3V	3.00	--	3.4	2	--	2.21	0.03	--	--	--	10.89
MD3V2	3.00	--	3.3	2	--	2.21	0.10	--	--	--	23.19
MD3V3	3.00	--	3.4	2	--	2.21	0.04	--	--	--	21.42
MD6V	3.00	--	6.5	2	--	2.21	0.24	--	--	--	-
MD6V2	3.00	--	6.5	2	--	2.21	0.27	--	--	--	49.13
MD9V	3.00	--	9.1	2	--	2.21	0.40	--	--	--	77.61
MD9V2	3.00	--	9.2	2	--	2.21	0.39	--	--	--	62.52
HD3	3.00	--	3.1	3	--	--	0.00	--	--	--	4.89
HD32	3.00	--	3.3	3	--	--	0.01	--	--	--	5.16
HD6	3.00	--	6.5	3	--	--	0.26	--	--	--	6.62
HD9	3.00	--	9.5	3	--	--	0.38	--	--	--	10.12
LD3	3.00	--	3.2	1	--	--	0.05	--	--	--	2.66
LD32	3.00	--	3.2	1	--	--	0.03	--	--	--	3.90
LD6	3.00	--	6.5	1	--	--	0.24	--	--	--	5.49
LD9	3.00	--	9.0	1	--	--	0.34	--	--	--	7.95
MD3L	3.00	--	3.2	2	--	--	-0.02	--	--	--	0.57
MD32	3.00	--	3.3	2	--	--	0.04	--	--	--	6.49
MD3B	3.00	--	3.4	2	--	--	0.02	--	--	--	1.92
MD6	3.00	--	6.3	2	--	--	0.22	--	--	--	7.40
MD62	3.00	--	6.8	2	--	--	0.31	--	--	--	4.50
MD92	3.00	--	9.1	2	--	--	0.36	--	--	--	10.48
MD9	3.00	--	10.3	2	--	--	0.49	--	--	--	10.84
MD3R2	3.00	--	3.2	2	1x1	--	0.03	--	--	--	6.32
MD3RR	3.00	--	3.3	2	2x1	--	0.20	--	--	--	7.03
MD3R	3.00	--	3.4	2	1x1	--	0.12	--	--	--	4.77
MD6RR5	3.00	--	6.4	2	2x2	--	0.27	--	--	--	8.93
MD6R	3.00	--	6.4	2	1x1	--	0.32	--	--	--	12.04
MD6RR	3.00	--	6.4	2	2x1	--	0.18	--	--	--	9.70
MD6R2	3.00	--	6.5	2	1x1	--	0.26	--	--	--	8.77
MD9R	3.00	--	9.0	2	1x1	--	0.37	--	--	--	12.29
MD9RR	3.00	--	9.3	2	2x1	--	0.35	--	--	--	10.28
MD6RRV5	3.00	--	6.5	2	2x3	2.95	0.17	--	--	--	49.68
MD6RRV4	3.00	--	6.5	2	2x2	2.95	0.23	--	--	--	52.68
MD6RRV	3.00	--	6.5	2	2x1	1.72	0.24	--	--	--	-
MD6RRV2	3.00	--	6.5	2	2x1	1.72	0.22	--	--	--	-
MD6RRV3	3.00	--	6.6	2	2x1	1.72	0.19	--	--	--	44.69
MD6RV	3.00	--	6.7	2	1x1	1.72	0.24	--	--	--	50.51
125MD1	1.25	--	1.8	2	--	--	0.12	--	--	--	--
125MD2	1.25	--	2.4	2	--	--	0.29	--	--	--	--
MD3S125	1.25	--	3.4	2	--	--	0.39	--	--	--	--
MD3S1252	1.25	--	3.5	2	--	--	0.37	--	--	--	--

Test ID	Column Diamter, d (in.)	Column Spacing, s (in.)	H (in.)	Density[1]	Reinforcement[2]	Surcharge (psi)	SBR_c[3]	SBR_d[3]	SBR_i[3]	$\Delta V_{u,20}/V_u$[4]	$\sigma_{col,max}$[5] (psi)
MD4S1253	1.25	--	3.8	2	--	--	0.42	--	--	--	--
MD4S1252	1.25	--	4.0	2	--	--	0.50	--	--	--	--
MD4S125	1.25	--	4.5	2	--	--	0.56	--	--	--	--
MD6S1252	1.25	--	5.6	2	--	--	0.59	--	--	--	--
MD6S125	1.25	--	6.1	2	--	--	0.61	--	--	--	--
MD9S1252	1.25	--	8.2	2	--	--	0.78	--	--	--	--
MD9S125	1.25	--	9.3	2	--	--	0.82	--	--	--	--
2MD2	2.00	--	2.4	2	--	--	0.06	--	--	--	--
2MD3	2.00	--	3.4	2	--	--	0.29	--	--	--	--
2MD4	2.00	--	4.6	2	--	--	0.37	--	--	--	--
2MD6	2.00	--	6.7	2	--	--	0.51	--	--	--	--
2MD9	2.00	--	9.8	2	--	--	0.67	--	--	--	--
75MD12	0.75	--	1.2	2	--	--	0.30	--	--	--	--
75MD1	0.75	--	1.8	2	--	--	0.40	--	--	--	--
75MD22	0.75	--	2.1	2	--	--	0.62	--	--	--	--
75MD2	0.75	--	2.4	2	--	--	0.77	--	--	--	--
75MD3	0.75	--	3.4	2	--	--	0.82	--	--	--	--
75MD4	0.75	--	4.6	2	--	--	0.82	--	--	--	--
75MD6	0.75	--	6.7	2	--	--	0.92	--	--	--	--
75MD9	0.75	--	9.3	2	--	--	0.97	--	--	--	--
AMD22	1.25	3.50	2.3	2	--	--	0.19	1.02	0.96	0.029	--
AMD2	1.25	3.50	3.0	2	--	--	0.50	1.04	0.91	0.030	--
AMD3	1.25	3.50	3.3	2	--	--	0.40	0.92	0.78	0.032	--
AMD32	1.25	3.50	3.7	2	--	--	0.46	0.89	0.86	0.032	--
AMD34	1.25	3.50	3.8	2	--	--	0.53	0.58	0.55	0.029	--
AMD33	1.25	3.50	4.0	2	--	--	0.80	0.76	0.79	0.028	--
AMD42	1.25	3.50	4.1	2	--	--	0.76	0.77	0.78	0.024	--
AMD4	1.25	3.50	4.9	2	--	--	0.70	0.70	0.70	0.019	--
AMD6	1.25	3.50	6.6	2	--	--	0.71	0.72	0.70	0.012	--
AMD9	1.25	3.50	9.3	2	--	--	0.71	0.72	0.72	0.009	--
AHD22	1.25	3.50	2.2	3	--	--	0.22	1.00	0.91	0.036	--
AHD2	1.25	3.50	2.7	3	--	--	0.30	1.00	0.73	0.038	--
AHD32	1.25	3.50	3.4	3	--	--	0.33	0.88	0.70	0.042	--
AHD33	1.25	3.50	3.6	3	--	--	0.56	0.76	0.70	0.039	--
AHD3	1.25	3.50	3.8	3	--	--	0.71	0.70	0.67	0.033	--
ALD2	1.25	3.50	2.4	1	--	--	0.28	1.01	0.97	0.027	--
ALD3	1.25	3.50	3.5	1	--	--	0.37	0.95	0.86	0.025	--
ALD34	1.25	3.50	3.7	1	--	--	0.34	0.85	0.86	0.023	--
ALD33	1.25	3.50	3.8	1	--	--	0.75	0.81	0.77	0.021	--
ALD32	1.25	3.50	4.0	1	--	--	0.74	0.77	0.74	0.021	--
ALD5	1.25	3.50	5.6	1	--	--	0.75	0.75	0.75	0.014	--
AMD3R53	1.25	3.50	2.7	2	1x2	--	0.33	0.81	0.67	0.043	--
AMD3R52	1.25	3.50	3.3	2	1x2	--	0.33	0.62	0.52	0.042	--

Test ID	Column Diamter, d (in.)	Column Spacing, s (in.)	H (in.)	Density[1]	Reinforcement[2]	Surcharge (psi)	SBR_c[3]	SBR_d[3]	SBR_i[3]	$\Delta V_{u,20}/V_u$[4]	$\sigma_{col,max}$[5] (psi)
AMD3RR6	1.25	3.50	3.4	2	2x1	--	0.44	0.74	0.63	0.035	--
AMD3RR3	1.25	3.50	3.4	2	2x3	--	0.49	0.63	0.60	0.040	--
AMD3R5	1.25	3.50	3.4	2	1x3	--	0.55	0.71	0.60	0.034	--
AMD3R	1.25	3.50	3.5	2	1x1	--	0.32	0.80	0.75	0.037	--
AMD3RR5	1.25	3.50	3.5	2	2x2	--	0.53	0.67	0.61	0.038	--
2AMD2	2.00	3.50	2.3	2	--	--	0.06	0.92	0.62	0.046	--
2AMD33	2.00	3.50	2.8	2	--	--	0.09	0.93	0.52	0.050	--
2AMD3	2.00	3.50	3.5	2	--	--	0.11	0.72	0.45	0.050	--
2AMD32	2.00	3.50	3.7	2	--	--	0.18	0.63	0.34	0.048	--
2AMD4	2.00	3.50	3.9	2	--	--	0.16	0.54	0.25	0.051	--
2AMD45	2.00	3.50	4.0	2	--	--	0.25	0.70	0.35	0.051	--
2AMD44	2.00	3.50	4.2	2	--	--	0.26	0.43	0.29	0.044	--
2AMD43	2.00	3.50	4.3	2	--	--	0.30	0.44	0.35	0.049	--
2AMD42	2.00	3.50	4.6	2	--	--	0.43	0.45	0.42	0.042	--
2AMD46	2.00	3.50	4.8	2	--	--	0.43	0.44	0.41	0.036	--
2AMD5	2.00	3.50	5.1	2	--	--	0.44	0.40	0.41	0.034	--
2AMD6	2.00	3.50	6.7	2	--	--	0.49	0.47	0.50	0.025	--
2AMD9	2.00	3.50	9.4	2	--	--	0.49	0.50	0.48	0.016	--
2ALD2	2.00	3.50	2.4	1	--	--	0.10	1.03	0.80	0.038	--
2ALD32	2.00	3.50	2.9	1	--	--	0.14	0.94	0.66	0.043	--
2ALD3	2.00	3.50	3.5	1	--	--	0.17	0.83	0.50	0.050	--
2ALD4	2.00	3.50	4.5	1	--	--	0.45	0.51	0.47	0.038	--
2ALD6	2.00	3.50	6.3	1	--	--	0.54	0.53	0.53	0.022	--
2AHD32	2.00	3.50	2.7	3	--	--	0.10	0.96	0.49	0.056	--
2AHD3	2.00	3.50	3.3	3	--	--	0.19	0.87	0.41	0.062	--
2AHD6	2.00	3.50	6.4	3	--	--	0.43	0.42	0.43	0.030	--
2AMD2R5	2.00	3.50	2.9	2	1x2	--	0.21	0.80	0.45	0.057	--
2AMD2R6	2.00	3.50	3.0	2	1x1	--	0.15	0.83	0.46	0.059	--
2AMD3R5	2.00	3.50	3.4	2	1x2	--	0.17	0.60	0.33	0.058	--
2AMD3R6	2.00	3.50	3.5	2	1x1	--	0.18	0.62	0.47	0.057	--
2AMD33R6	2.00	3.50	3.5	2	1x1	--	0.20	0.54	0.38	0.061	--
2AMD3R3	2.00	3.50	3.5	2	1x3	--	0.12	0.57	0.32	0.061	--
2AMD3RR5	2.00	3.50	3.5	2	2x2	--	0.10	0.48	0.31	0.067	--
2AMD3RR6	2.00	3.50	3.5	2	2x1	--	0.17	0.51	0.38	0.064	--
2AMD32R6	2.00	3.50	3.9	2	1x1	--	0.19	0.51	0.34	0.055	--
2AMD32R3	2.00	3.50	3.9	2	1x3	--	0.19	0.47	0.37	0.056	--
2AMD32R5	2.00	3.50	4.0	2	1x2	--	0.21	0.45	0.33	0.055	--
2AMD4R6	2.00	3.50	4.4	2	1x1	--	0.30	0.39	0.31	0.048	--
2AMD4R3	2.00	3.50	4.5	2	1x3	--	0.30	0.33	0.30	0.048	--
2AMD4R5	2.00	3.50	4.6	2	1x2	--	0.31	0.32	0.31	0.045	--
2AMD5R3	2.00	3.50	5.7	2	1x3	--	0.41	0.41	0.41	0.034	--
2AMD5R5	2.00	3.50	5.8	2	1x2	--	0.41	0.39	0.41	0.033	--
2AMD6R5	2.00	3.50	6.7	2	1x2	--	0.41	0.39	0.40	0.030	--

Test ID	Column Diamter, d (in.)	Column Spacing, s (in.)	H (in.)	Density[1]	Reinforcement[2]	Surcharge (psi)	SBR_c[3]	SBR_d[3]	SBR_i[3]	$\Delta V_{u,20}/V_u$[4]	$\sigma_{col,max}$[5] (psi)
4AMD4	2.00	7.00	4.6	2	--	--	0.34	1.01	1.00	--	--
4AMD5	2.00	7.00	5.6	2	--	--	0.50	1.01	1.00	--	--
4AMD6	2.00	7.00	6.7	2	--	--	0.48	0.94	0.86	--	--
4AMD74	2.00	7.00	6.9	2	--	--	0.58	0.75	0.75	--	--
4AMD73	2.00	7.00	7.0	2	--	--	0.60	0.75	0.76	--	--
4AMD72	2.00	7.00	7.2	2	--	--	0.64	0.63	0.62	--	--
4AMD7	2.00	7.00	7.7	2	--	--	0.67	0.66	0.64	--	--
4AMD8	2.00	7.00	8.1	2	--	--	0.73	0.65	0.69	--	--
4AMD9	2.00	7.00	9.9	2	--	--	0.71	0.66	0.73	--	--
4AMD5R5	2.00	7.00	5.7	2	1x2	--	0.48	0.97	0.47	--	--
4AMD62R5	2.00	7.00	6.2	2	1x2	--	0.51	0.98	0.63	--	--
4AMD6R	2.00	7.00	6.6	2	1x2	--	0.45	0.88	0.75	--	--
7AMD1	0.75	3.50	1.2	2	--	--	0.37	1.01	1.00	0.011	--
7AMD22	0.75	3.50	1.8	2	--	--	0.45	1.01	1.00	0.013	--
7AMD2	0.75	3.50	2.3	2	--	--	0.69	1.02	1.03	0.014	--
7AMD32	0.75	3.50	2.8	2	--	--	0.64	0.98	0.91	0.016	--
7AMD33	0.75	3.50	3.2	2	--	--	0.76	0.85	0.82	0.016	--
7AMD34	0.75	3.50	3.2	2	--	--	0.77	0.86	0.80	0.016	--
7AMD37	0.75	3.50	3.3	2	--	--	0.80	0.88	0.85	0.013	--
7AMD35	0.75	3.50	3.4	2	--	--	0.81	0.85	0.83	0.012	--
7AMD38	0.75	3.50	3.4	2	--	--	0.79	0.85	0.82	0.013	--
7AMD36	0.75	3.50	3.4	2	--	--	0.81	0.83	0.82	0.013	--
7AMD3	0.75	3.50	3.6	2	--	--	0.82	0.84	0.82	0.013	--
7AMD39	0.75	3.50	3.9	2	--	--	0.84	0.84	0.83	0.010	--
7AMD4	0.75	3.50	4.4	2	--	--	0.83	0.84	0.85	0.009	--
7AMD5	0.75	3.50	5.5	2	--	--	0.87	0.86	0.86	0.006	--
7AMD6	0.75	3.50	6.7	2	--	--	0.86	0.86	0.86	0.005	--
7AHD2	0.75	3.50	2.7	3	--	--	0.63	1.02	0.91	0.021	--
7AHD3	0.75	3.50	3.2	3	--	--	0.78	0.84	0.82	0.019	--
7AHD33	0.75	3.50	3.4	3	--	--	0.79	0.81	0.79	0.022	--
7AHD32	0.75	3.50	3.5	3	--	--	0.81	0.81	0.81	0.017	--
7AHD4	0.75	3.50	3.8	3	--	--	0.84	0.85	0.85	0.015	--
7ALD2	0.75	3.50	2.9	1	--	--	0.60	1.00	0.97	0.016	--
7ALD3	0.75	3.50	3.4	1	--	--	0.82	0.88	0.85	0.010	--
7ALD33	0.75	3.50	3.6	1	--	--	0.83	0.86	0.84	0.011	--
7ALD32	0.75	3.50	3.8	1	--	--	0.83	0.83	0.84	0.011	--
7ALD4	0.75	3.50	4.1	1	--	--	0.86	0.87	0.85	0.010	--
7AMD2RR2	0.75	3.50	2.2	2	2x2	--	0.72	0.91	0.85	0.019	--
7AMD2RR3	0.75	3.50	2.6	2	2x2	--	0.71	0.85	0.81	0.022	--
7AMD2RR	0.75	3.50	2.8	2	2x2	--	0.73	0.85	0.81	0.019	--
7AMD3RR2	0.75	3.50	3.1	2	2x2	--	0.73	0.84	0.80	0.019	--
7AMD3RR	0.75	3.50	3.4	2	2x2	--	0.78	0.84	0.81	0.016	--
7AMD3RR3	0.75	3.50	3.7	2	2x2	--	0.80	0.81	0.80	0.016	--

Test ID	Column Diamter, d (in.)	Column Spacing, s (in.)	H (in.)	Density[1]	Reinforcement[2]	Surcharge (psi)	SBR_c[3]	SBR_d[3]	SBR_i[3]	$\Delta V_{u,20}/V_u$[4]	$\sigma_{col,max}$[5] (psi)
7AMD4RR	0.75	3.50	3.9	2	2x2	--	0.78	0.82	0.80	0.014	--
7AMD5RR	0.75	3.50	4.4	2	2x2	--	0.80	0.83	0.81	0.010	--
74AMD4	0.75	7.00	4.4	2	--	--	0.79	1.01	1.01	--	--
74AMD5	0.75	7.00	5.5	2	--	--	0.86	0.95	0.91	--	--
74AMD62	0.75	7.00	6.1	2	--	--	0.90	0.93	0.93	--	--
74AMD63	0.75	7.00	6.3	2	--	--	0.91	0.91	0.93	--	--
74AMD64	0.75	7.00	6.4	2	--	--	0.92	0.93	0.92	--	--
74AMD65	0.75	7.00	6.5	2	--	--	0.91	0.90	0.93	--	--
74AMD6	0.75	7.00	6.6	2	--	--	0.92	0.93	0.97	--	--
74AMD7	0.75	7.00	7.7	2	--	--	0.94	0.92	0.92	--	--
74AMD9	0.75	7.00	8.7	2	--	--	0.95	0.92	0.94	--	--

Notes:

1. Densities are defined in Section 3.3
2. First number indicates the number of reinforcement layers, second number is the stiffness designation defined in Section 3.4
3. Settlement ratios are defined in Section 1.4
4. $\Delta V_{u,20}/V_u$ is defined in Section 5.5
5. $\sigma_{col,max}$ is defined in Section 1.4

Appendix K: Instrumentation calibration

K. Instrument Calibration

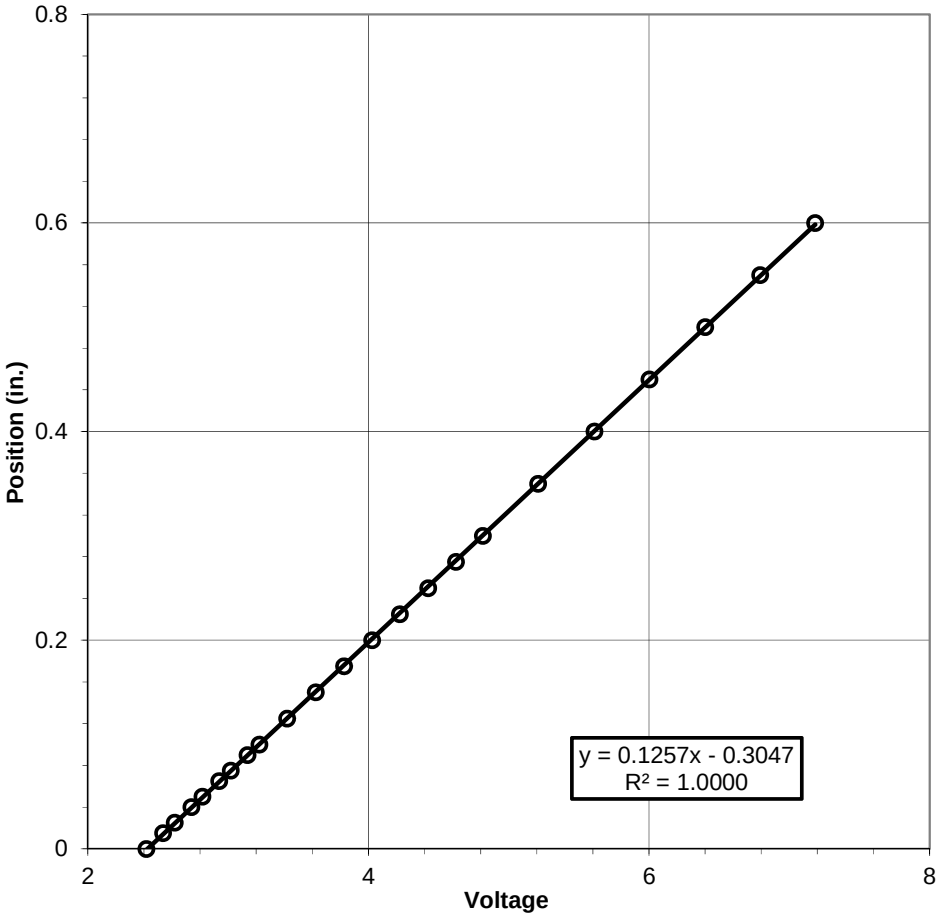

Figure K.1 Calibration of LVDT

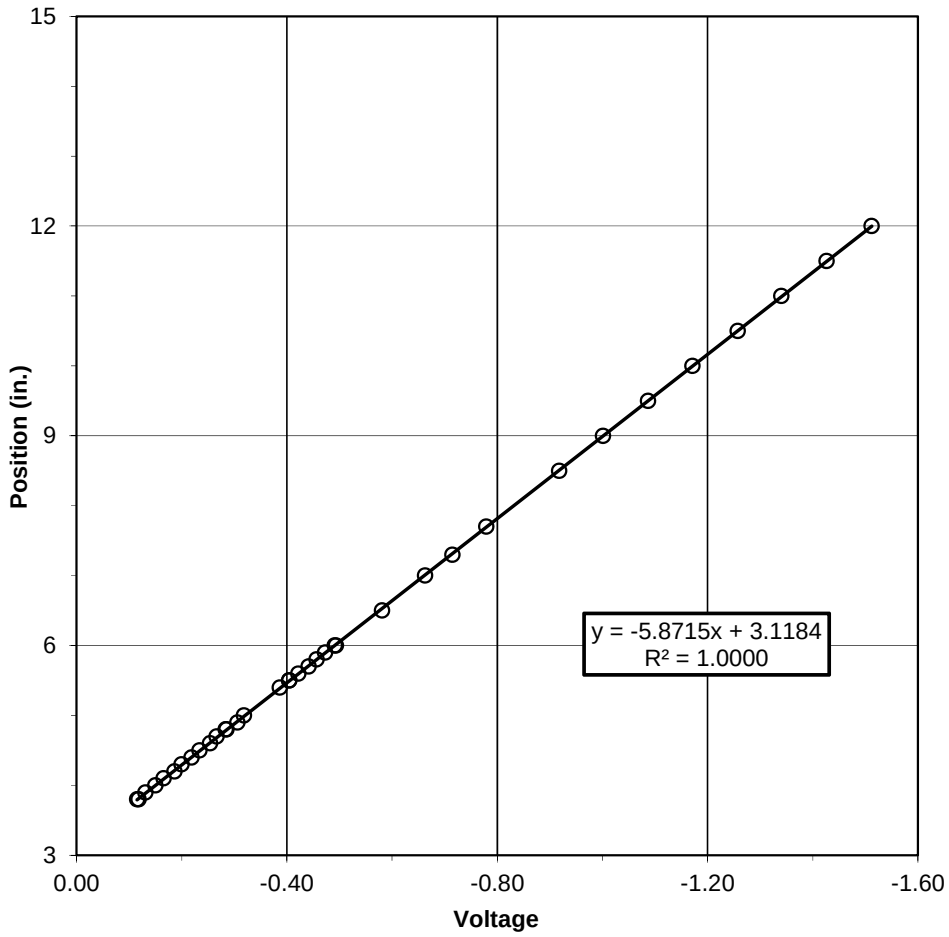

Figure K.2 Calibration of draw-wire sensor

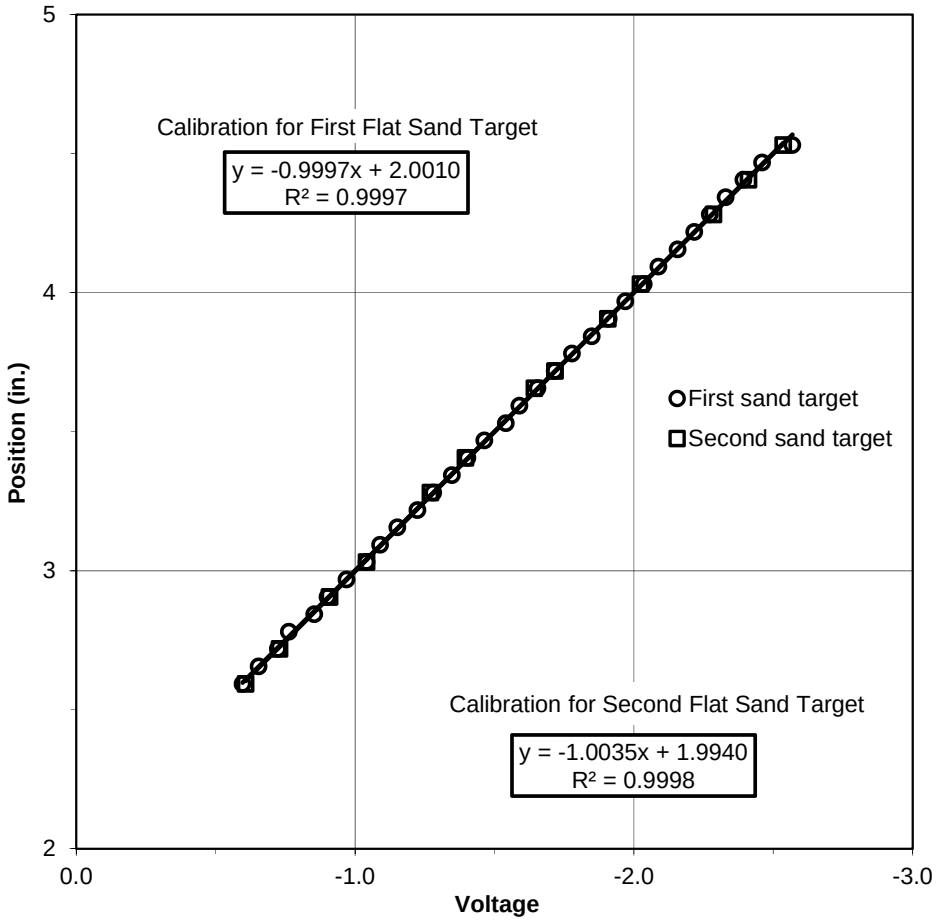

Figure K.3 Calibration of non-contact laser distance transducer on flat targets of Light Castle sand

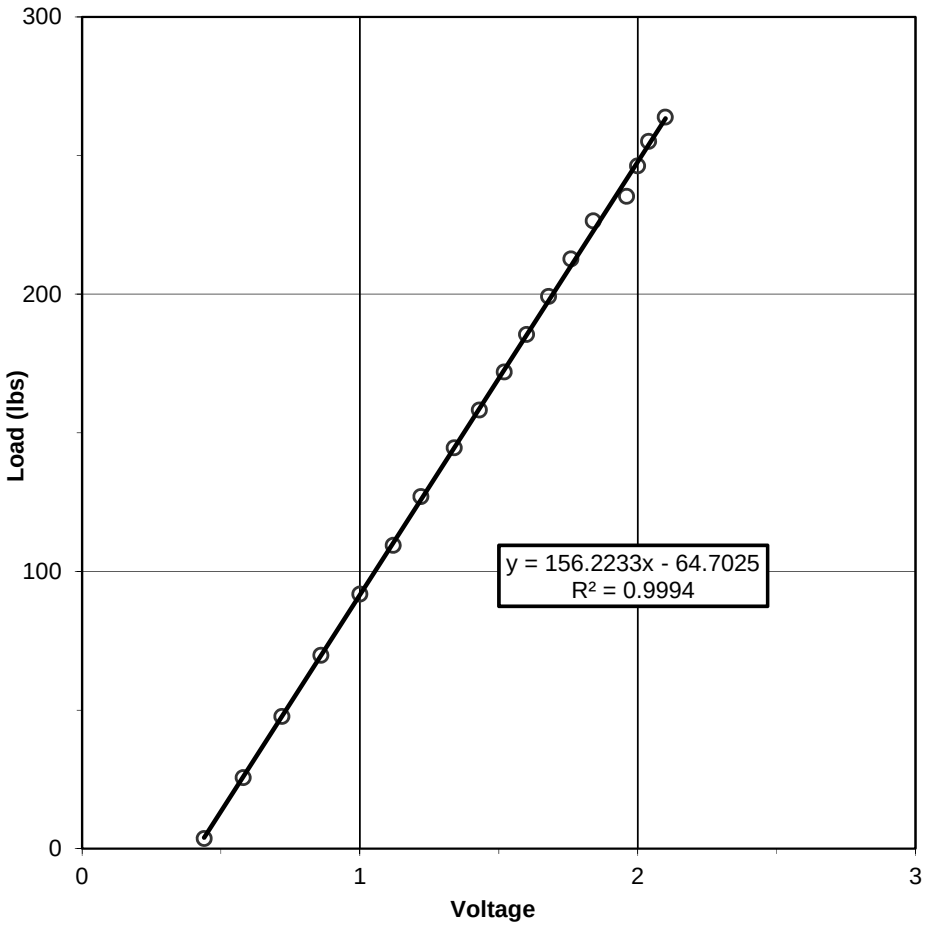

Figure K.4 Calibration of 500 lb load cell

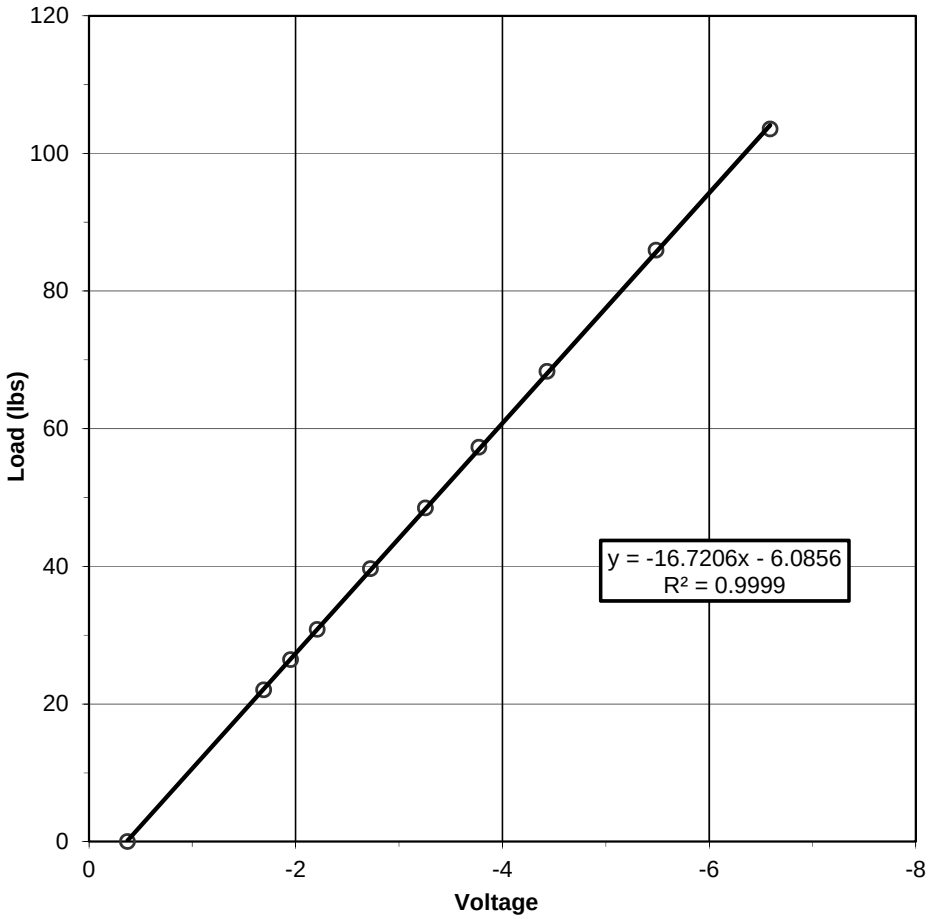

Figure K.5 Calibration of 250 lb load cell

Appendix L: Vacuum test results

L. Vacuum Triaxial Tests on Light Castle Sand

Table L.1 Summary of vacuum triaxial tests performed on Light Castle sand

Relative Density[1]	Confining Pressure, σ_3 (psi)	Deviatoric stress at failure, $\sigma_{d,f}$ (psi)	Peak friction angle, φ_{peak} (deg)	Axial strain at peak deviatoric stress (%)
62%	0.49	5.89	59.0	1.8%
72%	0.74	6.73	55.1	2.4%
53%	0.98	7.65	52.8	1.8%
58%	2.45	11.94	45.2	2.5%
55%	5.40	22.85	42.8	3.6%
52%	10.81	37.95	39.6	3.6%

Notes:

1. Relative density based on maximum and minimum void ratios provided in Table 3.5
2. Strain rate was 0.5%/min for all tests
3. Samples were approximately 6.9 inches high and 2.8 inches in diameter
4. Samples were pluviated and tamped in lifts

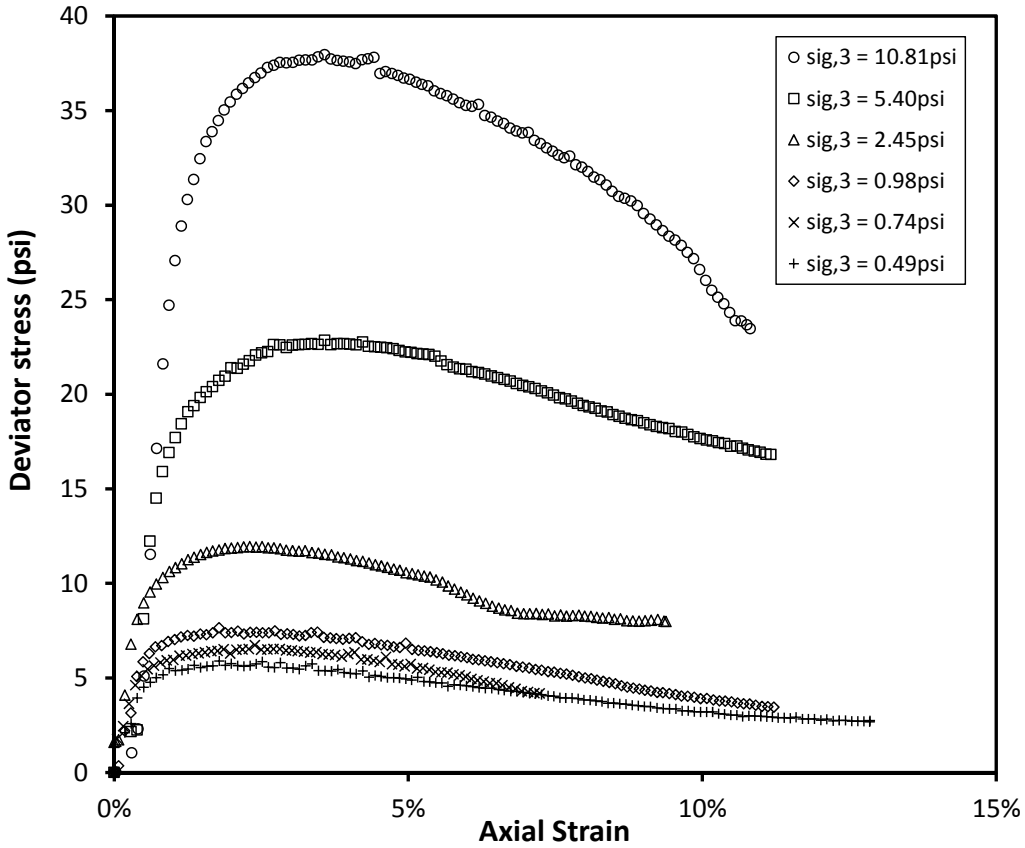

Figure L.1 Deviator stress versus axial strain